



Technical University of Crete
School of Production Engineering and Management
Production Systems Division
Turbomachines and Fluid Dynamics Laboratory

Design and Optimization of Diffuser-Augmented Wind Turbines

Stavros N. Leloudas

A dissertation submitted in partial fulfilment of the requirements for the degree of
Doctor of Philosophy in Engineering

Doctoral Advisor

Dr. Ioannis K. Nikolos, Professor

Chania, March 2024



Operational Programme
**Human Resources Development,
Education and Lifelong Learning**
Co-financed by Greece and the European Union



Copyright Statement

This doctoral dissertation is distributed under the terms and conditions of **Creative Commons Attribution-NonCommercial-NoDerivatives 4.0 International** (CC BY-NC-ND 4.0) License.



Citation

If you would like to cite this work, please use:

Stavros Leloudas, “Design and Optimization of Diffuser-Augmented Wind Turbines”, Doctoral Dissertation, School of Production Engineering and Management, Technical University of Crete, Chania, Greece, 2024.

or the following **BibTex** entry:

```
@phdthesis{Leloudas_PhD_2024,  
author = {Stavros N. Leloudas},  
title = {Design and Optimization of Diffuser-Augmented Wind Turbines},  
school = {School of Production Engineering and Management, Technical University of Crete},  
year = {2024},  
type = {Doctoral Dissertation},  
address = {Chania, Greece}  
}
```

Technical University of Crete

School of Production Engineering and Management
Turbomachines and Fluid Dynamics Laboratory

Doctoral Dissertation

Design and Optimization of Diffuser-Augmented Wind Turbines

by

Stavros N. Leloudas

Examination Committee:

1. **Ioannis K. Nikolos*, Professor**
Technical University of Crete
School of Production Engineering and Management
2. **Anargiros I. Delis*, Professor**
Technical University of Crete
School of Production Engineering and Management
3. **Fotios D. Kanellos*, Associate Professor**
Technical University of Crete
School of Electrical and Computer Engineering
4. **Kyriakos C. Giannakoglou, Professor**
National Technical University of Athens
School of Mechanical Engineering
5. **Spyridon G. Voutsinas, Professor**
National Technical University of Athens
School of Mechanical Engineering
6. **Vasilis A. Riziotis, Associate Professor**
National Technical University of Athens
School of Mechanical Engineering
7. **Georgios Arampatzis, Associate Professor**
Technical University of Crete
School of Production Engineering and Management

**Member of the Advisory Committee.*

Date Defended: **March 15th, 2024**



Π Ρ Α Κ Τ Ι Κ Ο
ΤΗΣ ΕΠΤΑΜΕΛΟΥΣ ΕΞΕΤΑΣΤΙΚΗΣ ΕΠΙΤΡΟΠΗΣ
ΓΙΑ ΤΗΝ ΚΡΙΣΗ ΤΗΣ ΔΙΔΑΚΤΟΡΙΚΗΣ ΔΙΑΤΡΙΒΗΣ

του Υποψήφιου Διδάκτορος

Σταύρου Ν. Αελούδα [Α.Μ. 2015019060]

ΔΙΠΛΩΜΑΤΟΥΧΟΥ

της Σχολής Μηχανικών Παραγωγής και Διοίκησης του Πολυτεχνείου Κρήτης.

Η Εξεταστική Επιτροπή, που διορίστηκε σύμφωνα με τις κείμενες διατάξεις και την απόφαση της Συνέλευσης της Σχολής Μηχανικών Παραγωγής και Διοίκησης στη 10η Συνεδρίαση στις 15-02-2024 για την κρίση της Διδακτορικής Διατριβής με τίτλο «Σχεδιασμός και Βελτιστοποίηση Ανεμογεννητριών Υποβοηθούμενων από Διαχύτη» και αγγλικό τίτλο «Design and Optimization of Diffuser-Augmented Wind Turbines», συνήλθε σε συνεδρίαση σήμερα την 15/3/2024 και παρακολούθησε την παρουσίαση της Διατριβής.

Τα μέλη της Επιτροπής υπέβαλαν ερωτήσεις στον Υποψήφιο Διδάκτορα. Ακολούθως η Επιτροπή συνεδρίασε χωρίς την παρουσία τρίτων και αξιολόγησε τη Διατριβή ως προς την ποιότητα, την πληρότητα, την πρωτότυπη σκέψη και τη συμβολή της στην επιστήμη. Με βάση τα ανωτέρω η Εξεταστική Επιτροπή κρίνει ότι η εξέταση ήταν επιτυχής και εγκρίνει τη διατριβή ως έχει.

Σύμφωνα με τον κανονισμό του Προγράμματος Διδακτορικών Σπουδών της Σχολής, για την επιτυχή εξέταση απαιτείται η σύμφωνη γνώμη τουλάχιστον πέντε μελών της Εξεταστικής Επιτροπής.

Η ΕΠΙΤΡΟΠΗ

1 Επιβλέπων: Ιωάννης Κ. Νικολός, Καθηγητής, Σχολή Μ.Π.Δ.,

Πολυτεχνείο Κρήτης.

2 Ανάργυρος Ι. Δελής, Καθηγητής, Σχολή Μ.Π.Δ.,

Πολυτεχνείο Κρήτης (Μέλος Τριμελούς Συμβουλευτικής Επιτροπής).

3 Φώτιος Κανέλλος, Αν. Καθηγητής, Σχολή Η.Μ.Μ.Υ.,

Πολυτεχνείο Κρήτης (Μέλος Τριμελούς Συμβουλευτικής Επιτροπής).

4 Κυριάκος Γιαννάκογλου, Καθηγητής, Σχολή Μηχανολόγων. Μηχ. Ε.Μ.Π.

5 Σπυρίδων Βουτσινάς, Καθηγητής, Σχολή Μηχανολόγων. Μηχ. Ε.Μ.Π.

6 Βασίλειος Ριζιώτης, Αν. Καθηγητής, Σχολή Μηχανολόγων. Μηχ. Ε.Μ.Π.

7 Γεώργιος Αραμπατζής, Αν. Καθηγητής, Σχολή Μ.Π.Δ., Πολυτεχνείο Κρήτης.

ΥΠΟΓΡΑΦΗ

Ioannis Nikolos Digitally signed by Ioannis Nikolos
Date: 2024.03.15 19:46:53 +02'00'

Anargyros Delis Digitally signed by Anargyros
Delis
Date: 2024.03.19 11:28:00
+02'00'

Fotios Kanellos Digitally signed by
Fotios Kanellos
Date: 2024.03.22
12:43:06 +02'00'

Kyriakos Giannakoglou Kyriakos Giannakoglou
16.03.2024 13:05

Spyridon Voutsinas Spyridon Voutsinas
19.03.2024 11:09

Vasileios Riziotis Vasileios Riziotis
17.03.2024 11:36

Georgios Arampatzis Digitally signed by Georgios
Arampatzis
Date: 2024.03.20 19:38:44
+02'00'

Summary

The concept of **diffuser-augmented or shrouded wind turbines** represents an attractive and highly versatile energy solution that has the potential to achieve power performance coefficients exceeding the Betz limit, and thus to improve the economic feasibility of renewable energy production under poor wind conditions, such as those prevailing within the urban environment. In that regard, shrouded wind turbines could eventually enable significant opportunities for more geographic dispersion of wind technology applications, growth in distributed energy deployments, and further expansion of renewable energy utilization on a global scale, contributing to the so-called energy transition. However, the achievement of widely adopted implementations and the consolidation of this promising technological application in the renewable energy market call for highly efficient and economically sustainable designs. Against this background, the present doctoral dissertation aims towards the development and validation of effective computational tools and numerical methodologies for, but not restricted to, the aerodynamic analysis, performance prediction, and design optimization of shrouded wind turbines.

Initially, the current doctoral study has been focused on the development and validation of an in-house Blade Element Momentum (BEM) code, which allows for the aerodynamic analysis and performance prediction of both conventional horizontal-axis and diffuser-augmented wind turbine rotors, in a remarkably short period of time. The proposed computational model is based on the extension of classical BEM theory to the case of shrouded rotors, which is actually implemented by introducing the velocity speed-up distribution over the rotor plane, for the unloaded diffuser configuration. Furthermore, the current BEM code has been enhanced with several empirical and analytical correction models, dealing with many of the inherent limitations of BEM theory; namely, two different correction models for capturing the power losses related to the blade tip and rotor hub, a drag correction model that accounts for the Reynolds number effects, and a detailed correction model for the accurate calculation of the axial induction factor, at the operating states of the rotor in which the Momentum theory is no longer valid. Besides, two different models for the extrapolation of the aerodynamic lift and drag coefficients to the entire range of angles of attack have been also implemented, based on the Montgomerie and Viterna-Corrigan extrapolation methods. Finally, the calculation of induced velocities at the rotor plane is achieved by applying a fixed-point iteration scheme, which is coupled with a typical relaxation procedure, aiming to dampen the fluctuating behaviour of the axial induction factor, during the iterative process. The accuracy of the entire BEM model, both in terms of conventional and shrouded wind turbines, is assessed against numerical and experimental data available in the literature, while

the impact of the tip loss correction model on the predicted power output of the rotor, is also examined.

Subsequently, the current doctoral dissertation features the application of Artificial Compressibility Method (ACM) for the numerical prediction of incompressible axisymmetric flows that involve swirling. The respective academic solver, named IGal2D, is based on the axisymmetric formulation of the Reynolds-Averaged Navier-Stokes (RANS) equations, which have been arranged in a pseudo-Cartesian form and enhanced by the addition of the circumferential momentum equation. The discretization of spatial derivative terms within the governing equations is performed via unstructured two-dimensional grid layouts, by employing a node-centered finite-volume scheme. For the evaluation of inviscid fluxes, the upwind Roe's approximate Riemann solver is applied, coupled with a higher-order accurate spatial reconstruction, whereas an element-based approach is used for the calculation of gradients required for the viscous fluxes. In addition, a detailed description of the convective flux Jacobian and the entire eigenvector system used within the Roe's approximate Riemann solver is provided, filling a respective gap in research literature. Time integration is succeeded through a second-order accurate four-stage Runge-Kutta method, adopting a local time-stepping technique. Further acceleration, in terms of computational time, is achieved by using an agglomeration multigrid scheme, incorporating the full approximation scheme in a V-cycle process, within an efficient edge-based data structure. A detailed validation of the proposed numerical methodology, and the respective flow solver, is performed by considering several non-swirling and swirling flows with axial symmetry. Regarding the numerical validation of the corresponding results, IGal2D solver is compared against the commercial software ANSYS Fluent, by adopting appropriate metrics and characteristic flow quantities, but also against experimental measurements, confirming the ability of the proposed methodology to predict such flows in terms of accuracy.

Additionally, this work reports the development and validation of an axisymmetric RANS - BEM model, which relies on the combination of the in-house BEM and IGal2D codes, for the simultaneous prediction of the wind turbine rotor performance and surrounding flow characteristics. The fundamental idea behind the proposed model is based on replacing the momentum part of the classical BEM theory with a more elaborate flow model, such as the Navier-Stokes equations, while assuming an actuator disc representation of the actual rotor geometry. Eventually, the rotor blades are modelled by means of body force terms, naturally included within the momentum conservation laws, and the Blade Element theory equations. The entire coupling procedure is fully coordinated by IGal2D software, while interaction between the involved codes is achieved via the aerodynamic blade loads and the velocity components at the rotor plane. The interpolation of the aforementioned quantities between the mesh nodes and the blade stations is implemented by custom Matlab scripts.

Despite the aforementioned analysis tools, this doctoral dissertation has been also focused on the design and aerodynamic evaluation a low Reynolds number airfoil family, for the entire blade span of small wind turbines, aiming to reduce the effects related to laminar separation, improve startup response, and meet acceptable levels of structural integrity. In particular, six airfoils of varying relative thickness have been designed, by increasing the thickness distribution of RG15 airfoil up to 50 percent, and adopting a rounded trailing edge, with a diameter equal to 1 percent of the chord length. The aerodynamic performance of RG15 family is initially evaluated by means of XFOIL code, at several low Reynolds numbers and angles of attack, while more elaborate RANS simulations are also conducted, in order to get additional information on the flow characteristics. Furthermore, the behavior of the recirculation area behind the rounded trailing edge, and that of the separation bubble near the leading edge for different values of relative thickness and angles of attack, is also examined. The computational results indicate that increasing the relative thickness of the airfoils has a beneficial impact on separation bubbles, while no significant effect of the rounded trailing edge on the aerodynamic characteristics of the airfoils has been observed.

Finally, this work presents the development and application of a modular optimization framework for the aerodynamic shape optimization of shrouded wind turbines, which combines the aforementioned analysis tools with a parallel and asynchronous version of a meta-model assisted Differential Evolution (DE) algorithm. When required, the parameterization/deformation of the computational mesh and design geometry are simultaneously succeeded, by employing a recently developed computational tool that is based on Free-Form Deformation (FFD) technique. The entire optimization process is implemented iteratively until the completion of the maximum number of generations, while the DE algorithm interacts with the parameterization, analysis, and post-processing software in a completely automated manner, by using specially developed scripts. Eventually, the proposed methodology is applied to three distinct design optimization cases, including:

- *The aerodynamic shape optimization of the rotor blades for a given shroud geometry.*
- *The aerodynamic shape optimization of an unloaded diffuser configuration.*
- *The simultaneous aerodynamic shape optimization of the blades and the diffuser.*

Keywords: Actuator Disc Model; Aerodynamics; Airfoil Design; Axisymmetric Flow; Blade Element Momentum Theory; Computational Fluid Dynamics; Diffuser-Augmented Wind Turbines; Ducted Wind Turbines; Differential Evolution Algorithm; Free-Form Deformation; Low Reynolds Airfoils; Mesh Morphing; RANS Equations; RG15 Airfoil Family; Shape Optimization; Shrouded Wind Turbines; SST Model; Swirling Flow; Wind Energy.

Σύνοψη – Summary in Greek

Οι ανεμογεννήτριες υποβοηθούμενες από διαχύτη (diffuser-augmented ή shrouded wind turbines) αντιπροσωπεύουν μια ευρεία κατηγορία εξαιρετικά ευέλικτων συστημάτων συγκομιδής αιολικής ενέργειας, τα οποία παρέχουν τη δυνατότητα επίτευξης συντελεστών ισχύος που υπερβαίνουν το θεωρητικό όριο του Betz, και συνεπώς μπορούν να συμβάλλουν στην οικονομική βιωσιμότητα της παραγωγής ανανεώσιμης ενέργειας σε περιοχές που χαρακτηρίζονται από χαμηλό αιολικό δυναμικό, όπως το αστικό περιβάλλον. Επομένως, η ευρύτερη υιοθέτηση και εγκατάσταση ανεμογεννητριών υποβοηθούμενων από διαχύτη θα μπορούσε τελικά να οδηγήσει σε μεγαλύτερη γεωγραφική διασπορά των εφαρμογών αιολικής ενέργειας, εδραίωση των συστημάτων διανεμημένης παραγωγής ισχύος, και περαιτέρω χρήση των ανανεώσιμων πηγών ενέργειας σε παγκόσμια κλίμακα, συμβάλλοντας έτσι σε μια ταχύτερη ενεργειακή μετάβαση. Ωστόσο, η επίτευξη ευρέως αποδεκτών προϊόντων και η εδραίωση αυτής της τεχνολογικής εφαρμογής στην παγκόσμια αγορά ανανεώσιμων πηγών ενέργειας απαιτούν εξαιρετικά αποδοτικές και οικονομικά βιώσιμες σχεδιάσεις. Σε αυτό το πλαίσιο, η παρούσα διδακτορική διατριβή στοχεύει στην ανάπτυξη και επικύρωση αποτελεσματικών υπολογιστικών εργαλείων και αριθμητικών μεθοδολογιών, για την αεροδυναμική ανάλυση και τη βελτιστοποίηση ανεμογεννητριών υποβοηθούμενων από διαχύτη.

Αρχικά, η παρούσα διδακτορική μελέτη εστιάζει στην ανάπτυξη και επικύρωση των αποτελεσμάτων ενός υπολογιστικού κώδικα που βασίζεται στη θεωρία Στοιχείων Πτερύγωσης - Δίσκου Ορμής (Blade Element Momentum – BEM). Το συγκεκριμένο υπολογιστικό μοντέλο χαρακτηρίζεται από την κατάλληλη τροποποίηση/επέκταση της κλασικής θεωρίας BEM για την περίπτωση ανεμογεννητριών υποβοηθούμενων από διαχύτη, η οποία υλοποιείται μέσω της αδιάστατης συνιστώσας της αξονικής ταχύτητας στο επίπεδο του ρότορα, υπό την απουσία φόρτισης. Συνεπώς, ο προτεινόμενος κώδικας παρέχει τη δυνατότητα αεροδυναμικής ανάλυσης και αξιολόγησης της απόδοσης του ρότορα, τόσο συμβατικών ανεμογεννητριών οριζοντίου άξονα, όσο και ανεμογεννητριών υποβοηθούμενων από διαχύτη. Επιπλέον, η συγκεκριμένη υλοποίηση έχει εμπλουτιστεί με αριθμό εμπειρικών και αναλυτικών μοντέλων διόρθωσης, που σχετίζονται με την αντιμετώπιση εγγενών περιορισμών της θεωρίας BEM. Αυτά συμπεριλαμβάνουν, δύο διαφορετικά μοντέλα διόρθωσης για τον υπολογισμό των απωλειών ισχύος από το ακροπτερύγιο και την πλήμνη, ένα μοντέλο διόρθωσης της τιμής του αεροδυναμικού συντελεστή αντίστασης λόγω των φαινομένων που σχετίζονται με τον αριθμό Reynolds, και ενός λεπτομερούς μοντέλου διόρθωσης για τον ορθό υπολογισμό του αξονικού συντελεστή επαγωγής στις περιοχές λειτουργίας του ρότορα, όπου η εγκυρότητα της

θεωρίας Δίσκου Ορμής παύει να ισχύει. Η προεκβολή των αεροδυναμικών συντελεστών άνωσης και αντίστασης σε ολόκληρο το εύρος γωνιών προσβολής πραγματοποιείται μέσω δύο διαφορετικών μοντέλων, που υλοποιήθηκαν στα πλαίσια της παρούσας διατριβής, και βασίζονται στις μεθόδους Montgomerie και Viterna-Corrigan. Τέλος, ο υπολογισμός των επαγόμενων ταχυτήτων στο επίπεδο του ρότορα επιτυγχάνεται μέσω της εφαρμογής μίας επαναληπτικής μεθόδου σταθερού σημείου, σε συνδυασμό με μια διαδικασία χαλάρωσης, στοχεύοντας στη μείωση των ταλαντώσεων της τιμής του αξονικού συντελεστή επαγωγής κατά τη διάρκεια της επαναληπτικής διαδικασίας. Η ακρίβεια των αποτελεσμάτων του προτεινόμενου υπολογιστικού μοντέλου – τόσο για την περίπτωση συμβατικών ανεμογεννητριών οριζοντίου άξονα, όσο και για αυτή ανεμογεννητριών υποβοηθούμενων από διαχύτη – επικυρώνεται μέσω της σύγκρισης των αντίστοιχων αποτελεσμάτων με αριθμητικά και πειραματικά δεδομένα από τη διεθνή βιβλιογραφία.

Στη συνέχεια, η παρούσα διδακτορική διατριβή περιγράφει την εφαρμογή της Μεθόδου Τεχνητής Συμπιεστότητας (Artificial Compressibility Method – ACM) για την αριθμητική πρόλεξη ασυμπίεστων και αξονοσυμμετρικών ροών, που χαρακτηρίζονται από την παρουσία περιφερειακής συνιστώσας της ταχύτητας (swirling velocity). Ο αντίστοιχος ακαδημαϊκός αριθμητικός επιλύτης που αναπτύχθηκε – εμπονομαζόμενος IGal2D – βασίζεται στην αξονοσυμμετρική μορφή των διαφορικών εξισώσεων Reynolds-Averaged Navier-Stokes (RANS), οι οποίες έχουν τελικά διατυπωθεί για ένα ψευδο-καρτεσιανό σύστημα αναφοράς και εμπλουτιστεί με την προσθήκη της περιφερειακής συνιστώσας της εξίσωσης της ορμής. Η διακριτοποίηση των χωρικών παραγώγων εντός του μοντέλου της ροής πραγματοποιείται μέσω της χρήσης μίας κεντροκομβικής μεθόδου πεπερασμένων όγκων (node-centered finite-volume method), επί διδιάστατων μη-δομημένων υπολογιστικών πλεγμάτων. Για την εκτίμηση των μη-συνεκτικών διανυσμάτων της ροής εφαρμόζεται ο προσεγγιστικός επιλύτης του Roe, ο οποίος θεωρεί ένα τοπικό μονοδιάστατο πρόβλημα Riemann στη διεπαφή των γειτονικών όγκων ελέγχου, ενώ η αύξηση της ακρίβειας του προαναφερθέντος υπολογισμού επιτυγχάνεται με την εφαρμογή ενός σχήματος δεύτερης τάξης χωρικής ακρίβειας, βασισμένο στην τεχνική Monotonic Upstream-centered Scheme for Conservation Laws (MUSCL). Από την άλλη, η εκτίμηση των συνεκτικών διανυσμάτων της ροής προϋποθέτει τον πρωτύερο υπολογισμό των παραγώγων των συνιστωσών της ταχύτητας στη διεπαφή των όγκων ελέγχου, η οποία συμπίπτει με το μέσο της ακμής που συνδέει τους αντίστοιχους υπολογιστικούς κόμβους, και βασίζεται στη δημιουργία νέων δυικών όγκων ελέγχου γύρω από την εξεταζόμενη ακμή. Ο υπολογισμός τόσο των μη-συνεκτικών, όσο και των συνεκτικών διανυσμάτων ροής, εκτελείται με σάρωση των ακμών του πλέγματος, χρησιμοποιώντας κατάλληλες δομές δεδομένων, με στόχο τη μείωση του απαιτούμενου

υπολογιστικού κόστους. Επιπλέον, η παρούσα εργασία παρέχει μια λεπτομερή περιγραφή του συστήματος ιδιοδιανυσμάτων που χρησιμοποιείται στον επιλύτη του Roe, καλύπτοντας έτσι το αντίστοιχο κενό στην διεθνή βιβλιογραφία. Η χρονική ολοκλήρωση και τελική κατάσταση της ροής προσεγγίζεται επαναληπτικά, μέσω ενός ρητού σχήματος και της μεθόδου Runge-Kutta τεσσάρων βημάτων, και δεύτερης τάξης χρονικής ακρίβειας. Πέραν των κατάλληλων δομών δεδομένων, περαιτέρω μείωση του υπολογιστικού χρόνου επιτυγχάνεται μέσω της εφαρμογής της τεχνικής του τοπικού ψευδο-χρονικού βήματος (local time-stepping) καθώς και της μεθόδου πολυπλέγματος (multigrid). Η εγκυρότητα της παρούσας μεθοδολογίας, και του αντίστοιχου λογισμικού, επαληθεύονται μέσω της σύγκρισης των αποτελεσμάτων με πλήθος αριθμητικών και πειραματικών δεδομένων αναφοράς, τα οποία είναι διαθέσιμα στη βιβλιογραφία, καθώς και με τα αποτελέσματα του εμπορικού λογισμικού ANSYS Fluent, για διάφορους τύπους αξονοσυμμετρικών ασυμπίεστων ροών.

Επιπλέον, η παρούσα διδακτορική διατριβή περιγράφει την ανάπτυξη και επικύρωση των αποτελεσμάτων ενός αξονοσυμμετρικού μοντέλου RANS - BEM, για την ταυτόχρονη πρόλεξη της απόδοσης του ρότορα και των χαρακτηριστικών της περιβάλλουσας ροής. Η συγκεκριμένη μεθοδολογία βασίζεται ουσιαστικά στο συνδυασμό των λογισμικών BEM και IGal2D, τα οποία αναπτύχθηκαν στα πλαίσια της παρούσας διδακτορικής διατριβής. Η θεμελιώδης ιδέα πίσω από το προτεινόμενο μοντέλο συνοψίζεται στην αντικατάσταση της θεωρίας Δίσκου Ορμής εντός του κλασσικού μοντέλου BEM, με ένα πιο λεπτομερές μοντέλο ροής, όπως οι εξισώσεις Navier-Stokes, υποθέτοντας ότι η πραγματική γεωμετρία του ρότορα αναπαρίσταται από έναν απείρως λεπτό δίσκο ενέργειας (actuator disc). Τελικά, η επίδραση των πτερυγίων στο πεδίο ροής μοντελοποιείται μέσω των εξισώσεων της θεωρίας Στοιχείων Πτερύγωσης (Blade Element theory) και των όρων πηγής, που περιλαμβάνονται εντός των εξισώσεων διατήρησης της ορμής. Η διαδικασία σύζευξης συντονίζεται εξ' ολοκλήρου από το λογισμικό IGal2D, ενώ η αλληλεπίδραση μεταξύ των εμπλεκόμενων λογισμικών επιτυγχάνεται μέσω των αεροδυναμικών φορτίων/δυνάμεων κατά μήκος του πτερυγίου, και των συνιστωσών της ταχύτητας στο επίπεδο του ρότορα. Η παρεμβολή των παραπάνω ποσοτήτων, μεταξύ των κόμβων του πλέγματος και των στοιχείων της πτερύγωσης υλοποιείται μέσω κατάλληλα σχεδιασμένων Matlab scripts.

Πέραν των προαναφερθέντων λογισμικών ανάλυσης, η παρούσα διδακτορική διατριβή επικεντρώνεται επίσης στη σχεδίαση και την αεροδυναμική αξιολόγηση μιας πλήρους οικογένειας αεροτομών, για χαμηλούς αριθμούς Reynolds και ολόκληρο το εύρος πτερυγίων μικρών ανεμογεννητριών, με στόχο τη μείωση των επιπτώσεων της αποκόλλησης του οριακού στρώματος, τη βελτίωση της απόκρισης του ρότορα κατά την εκκίνηση, και την επίτευξη αποδεκτών επιπέδων δομικής ακεραιότητας. Συγκεκριμένα, η προτεινόμενη οικογένεια αεροτομών αποτελείται από έξι αεροτομές με διαφορετικό

σχετικό πάχος, οι οποίες σχεδιάστηκαν αυξάνοντας την κατανομή πάχους της αεροτομής RG15 έως και 50 τοις εκατό, και υιοθετώντας ένα στρογγυλεμένο χείλος εκφυγής (trailing edge) με διάμετρο ίση με 1 τοις εκατό του μήκους της χορδής. Αρχικά, η αεροδυναμική απόδοση της οικογένειας αεροτομών RG15 αξιολογείται μέσω του λογισμικού XFOIL, για διάφορους αριθμούς Reynolds και γωνίες προσβολής, ενώ στη συνέχεια πραγματοποιούνται πιο λεπτομερείς προσομοιώσεις RANS, μέσω του λογισμικού IGal2D, προκειμένου να ληφθούν πρόσθετες πληροφορίες για τα χαρακτηριστικά της περιβάλλουσας ροής. Επιπλέον, η παρούσα εργασία εξετάζει τη συμπεριφορά της περιοχής ανακυκλοφορίας πίσω από το στρογγυλεμένο χείλος εκφυγής, καθώς και αυτή της φουσαλίδας αποκόλλησης (separation bubble) κοντά στο χείλος προσβολής (leading edge), για διαφορετικές τιμές του σχετικού πάχους και της γωνίας προσβολής. Σύμφωνα με τα αριθμητικά αποτελέσματα, η αύξηση του πάχους των αεροτομών δείχνει να έχει ευεργετική επίδραση στην εμφάνιση φουσαλίδων αποκόλλησης, ενώ δεν παρατηρείται σημαντική επίδραση του στρογγυλεμένου χείλους εκφυγής στις τιμές της αεροδυναμικής άνωσης και αντίστασης.

Τέλος, η παρούσα διατριβή – όπως δηλώνει και ο τίτλος της – παρουσιάζει την ανάπτυξη και εφαρμογή μιας ενιαίας, σπονδυλωτής, υπολογιστικής μεθοδολογίας για τον αυτοματοποιημένο βέλτιστο σχεδιασμό ανεμογεννητριών υποβοηθούμενων από διαχύτη, η οποία συνδυάζει τα προαναφερθέντα λογισμικά/μοντέλα ανάλυσης με μια παράλληλη και ασύγχρονη έκδοση ενός Διαφορικού Εξελικτικού αλγορίθμου. Στις περιπτώσεις όπου απαιτείται η παραμετροποίηση και παραμόρφωση του υπολογιστικού πλέγματος, αυτές επιτυγχάνονται μέσω ενός λογισμικού το οποίο επίσης αναπτύχθηκε στα πλαίσια της παρούσας διδακτορικής διατριβής και βασίζεται στην τεχνική της Ελεύθερης Παραμόρφωσης (Free-Form Deformation). Η διαδικασία βελτιστοποίησης εφαρμόζεται επαναληπτικά μέχρι την ολοκλήρωση του προκαθορισμένου αριθμού γενεών, ενώ ο εξελικτικός αλγόριθμος αλληλεπιδρά με τα λογισμικά παραμετροποίησης, ανάλυσης και μετα-επεξεργασίας των αποτελεσμάτων, εντός ενός πλήρως αυτοματοποιημένου πλαισίου, χρησιμοποιώντας ειδικά σχεδιασμένα scripts. Τελικά, η προτεινόμενη μεθοδολογία εφαρμόζεται σε τρεις διαφορετικές περιπτώσεις βελτιστοποίησης σχεδιασμού, οι οποίες αφορούν:

- Τη βέλτιστη αεροδυναμική σχεδίαση πτερυγίων για μία δεδομένη γεωμετρία διαχύτη.
- Τη βέλτιστη αεροδυναμική σχεδίαση ενός διαχύτη υπό μηδενική φόρτιση ρότορα.
- Την ταυτόχρονη βέλτιστη αεροδυναμική σχεδίαση πτερυγίων και διαχύτη.

Acknowledgements

At this point, it is my sincere pleasure to thank all those who have contributed for the successful completion of this doctoral dissertation. First and foremost, I would like to honestly thank my doctoral advisor, Professor Ioannis K. Nikolos, for introducing me – when I was still an undergraduate student – to the fields of aerodynamic shape optimization, computational fluid dynamics and wind turbine design, while later providing me the opportunity to pursue a PhD on such an exciting and challenging research topic. His constant presence, time investment and effort, during the entire course of my undergraduate and doctoral studies, have been of paramount importance for the successful completion of this work. I am immensely grateful for his encouragement, support, kindness and ethics – as well as for the unforgettable hospitality during my visits in Epirus!

Besides my advisor, I would also like to deeply thank Professor Anargiros I. Delis and Associate Professor Fotios D. Kanellos for their constructive suggestions and valuable feedback, as members of the advisory committee. Moreover, I would like to honestly acknowledge all the members of the examination committee for their insightful comments, which helped me to significantly improve the quality of this dissertation.

With the completion of this work, I would also like to express the deepest gratitude to my dear colleagues Dr. Georgios N. Lygidakis and Dr. Giorgos A. Strofylas, for being a constant source of inspiration, knowledge, encouragement and support. I owe special thanks to Dr. Strofylas for providing the asynchronous and parallel version of the surrogate-assisted Differential Evolution algorithm that was employed within this study, as well as to Dr. Lygidakis for his substantial contribution during the development of the axisymmetric IGal2D solver and the constructive guidance towards completing this work.

Of course, I am also grateful to every member of the Turbomachines and Fluid Dynamics Laboratory, who I had the pleasure to meet and work with during all these years, and especially to: Alexandros Eskantar, Iason Dimitriou, Sofia Tavla, Maria Seremeti and Petros Zografos, who – besides pleasant colleagues – eventually became beloved friends. Moreover, at this point, I would definitely like to address a warm thank you to my friends Vangelis Salapatas, Tasos Platis, Thomas Stamoulis, Thanos Nastoulis and Antonis Halkitis, for the friendship we share and their support throughout the peaks and valleys.

In addition, special thanks should be addressed to several researchers and academics along the globe for providing useful data and essential information for the completion of this work; in particular, I would like to acknowledge Dr. Francesco Avallone and Dr. Vinit Dighe for providing the geometry of Donqi Urban Windmill, Dr. Rodolfo Bontempo for providing useful validation data that were used during the preliminary development of RANS - BEM methodology, Mr. Lee Fingersh for providing the experimental measurements of the NREL

Phase VI campaign, as well as Dr. Romeo Resiga and Dr. Constantin Popescu for proving a detailed benchmark case for the preliminary validation of IGal2D solver.

Moreover, I am deeply grateful to OGT GreenTech Ltd – and especially to Mr. Seth Larsson and Dr. Mark Venton – for partially funding this research study and offering me the opportunity to explore the field of diffuser-augmented wind turbines. Besides, I would like to acknowledge the General Secretariat for Research and Innovation (GSRI) for also partially funding this work, under the PhD Scholarships of the Hellenic Foundation for Research and Innovation (HFRI). Please note that all the funding sources of this doctoral dissertation are explicitly recognised in Financial Support.

Finally, I am most thankful to my beloved Konstantina for her love, encouragement and patience during the final stage of this journey. Last but certainly not least, my very special gratitude goes to my dear family for their unconditional love and support: my father Nikos, my mother Georgia, my sister Angeliki and my grandmother Angeliki, to whom I owe everything I have achieved in my life so far. This thesis is as much their hard work as it is mine.

Stavros N. Leloudas

March 2024

Chania, Greece

Short Biography



Stavros N. Leloudas was born in 1992 in Athens, Greece and received a Diploma in Production Engineering and Management in 2015 from Technical University of Crete (TUC), Greece. In addition, after the completion of his undergraduate studies, Stavros received Awards of Academic Excellence from Limmat Stiftung Foundation and Technical Chamber of Greece, as the graduate with the third highest GPA during the academic year of 2014/2015. Since 2015, Stavros has been a PhD candidate and research assistant at the Turbomachines and Fluid Dynamics Laboratory (TurboLab – TUC), while since 2016, he has been a teaching assistant for both undergraduate and graduate courses in the School of Production Engineering and Management. Moreover, he has participated in 6 research programs funded by the private sector and 2 research programs funded by the Greek Government and the European Union. His research interests are mainly focused on the fields of Computational Fluid Dynamics (CFD), Optimal Aerodynamic Design and Computational Engineering. Up to now, Stavros Leloudas has been the lead author of 5 international journal articles and a co-author of 12 conference papers. During his PhD studies, Stavros received a scholarship from the Hellenic Foundation for Research and Innovation, while since 2015 he is a member of Technical Chamber of Greece. Stavros has been working in the Aerodynamic Optimization and Validation team of Siemens Gamesa Renewable Energy Rotor Performance department since November 2021, mainly focused on advanced aerodynamics prototype testing and power curve modelling and validation.

 <https://www.linkedin.com/in/stavrosleloudas>

 <https://www.researchgate.net/profile/Stavros-Leloudas>

 <https://orcid.org/0000-0002-9352-9012>

Financial Support

This study has been financially supported by:

1. Omnilink GreenTech Ltd

Under the following research programs:

- a. **Design and optimization of a diffuser-augmented wind turbine – Stage 1**
OGT GreenTech Ltd, Duration: 15 February – 30 April 2016.
- b. **Design of new flaps and centrebody for a diffuser-augmented wind turbine**
OGT GreenTech Ltd, Duration: 10 June 2016 – 31 August 2016.
- c. **Design of new blades for a diffuser-augmented wind turbine**
OGT GreenTech Ltd, Duration: 10 June 2016 – 31 August 2016.
- d. **Design and optimization of a diffuser-augmented wind turbine – Stage 2**
OGT GreenTech Ltd, Duration: 1 July 2016 – 31 October 2016.

2. General Secretariat for Research and Innovation

Hellenic Foundation for Research and Innovation

PhD Scholarship – 1st Call for HFRI Scholarships for PhD Candidates

Scholarship Title: Design and Optimization of Diffuser Augmented Wind Turbines

Duration: 1 November 2017 – 28 February 2019

Scholarship Code: 624



3. Greek National Strategic Reference Framework (NSRF) 2014 – 2020

This study has been co-financed by the European Union and Greek national funds through the Operational Program “**Human Resources Development, Education and Lifelong Learning**”. **Project Title:** Development of a Computational Methodology for the Optimal Design of Ducted Rotors. **Duration:** 1 February 2020 – 30 April 2021. **MIS:** 5047362.



Table of Contents

Summary	v
Σύνοψη – Summary in Greek.....	ix
Acknowledgements.....	xiii
Short Biography.....	xv
Financial Support	xvi
Table of Contents	xvii
Nomenclature.....	xxiii
Latin Symbols	xxiii
Greek Symbols.....	xxv
Subscripts and Superscripts.....	xxvi
Abbreviations and Acronyms	xxvii
List of Figures.....	xxix
List of Tables.....	xli
Chapter 1 Introduction	1-1
1.1 Motivation.....	1-1
1.2 Aims and Objectives	1-5
1.3 Physics of Shrouded Wind Turbines.....	1-7
1.3.1 Cross-Wind Force Mechanism.....	1-8
1.3.2 Mixing of the Wake and the External Flow Mechanism	1-9
1.4 Shrouded Wind Turbines – A Brief Research Review	1-11
1.5 Thesis Outline	1-15
1.6 Contributions.....	1-17
1.7 List of Related Publications	1-18
A. International Journals.....	1-18
B. Proceedings of International Conferences	1-19
Chapter 2 Development of a Blade Element Momentum Code	2-1
2.1 Momentum Theory.....	2-1
2.1.1 Axial Momentum Theory for HAWTs.....	2-2

2.1.2 Axial Momentum Theory for Shrouded Wind Turbines	2-6
2.1.2.1 Zero Diffusive Losses.....	2-11
2.2 Blade Element Momentum Theory.....	2-14
2.2.1 Momentum Equations.....	2-15
2.2.2 Blade Element Equations	2-17
2.2.3 Combination of Blade Element and Momentum Equations.....	2-20
2.2.4 Extension of BEM Theory for Shrouded Rotors	2-21
2.2.5 Tip Loss Correction Model.....	2-23
2.2.5.1 Prandtl’s Correction Model.....	2-23
2.2.5.2 Shen’s Correction Model	2-24
2.2.6 Empirical Region Calculations.....	2-25
2.3 BEM Code Features.....	2-26
2.3.1 Blade Discretization.....	2-27
2.3.2 Aerodynamic Coefficients Calculation.....	2-27
2.3.2.1 Drag Correction for Reynolds Number.....	2-29
2.3.3 Relaxation Procedure	2-30
2.3.4 The Iterative Procedure.....	2-31
Chapter 3 Numerical Validation of the BEM Code	3-1
3.1 Conventional Horizontal-Axis Wind Turbines.....	3-1
3.1.1 NREL Phase VI Wind Turbine	3-1
3.1.1.1 Blade Characteristics and Simulation Parameters.....	3-2
3.1.1.2 BEM Simulation Results	3-4
3.1.2 NREL 5-MW Reference Wind Turbine	3-6
3.1.2.1 Blade Characteristics and Simulation Parameters.....	3-7
3.1.2.2 BEM Simulation Results	3-8
3.2 Shrouded Wind Turbines.....	3-11
3.2.1 Donqi Urban Windmills DAWT	3-11
3.2.1.1 BEM Simulation Results	3-14
3.2.2 A Multi-Slotted DAWT	3-15
3.2.2.1 BEM Simulation Results	3-17
Chapter 4 Development of an Axisymmetric RANS Solver	4-1

4.1 Axisymmetric Swirling Flows	4-1
4.2 Governing Equations	4-4
4.2.1 Axisymmetric Navier-Stokes Equations.....	4-4
4.2.1.1 Dimensionless Form of the Axisymmetric N-S Equations	4-6
4.2.1.2 Conservative Form of the Axisymmetric N-S Equations.....	4-8
4.2.2 Axisymmetric Reynolds-Averaged Navier-Stokes Equations	4-9
4.2.3 Artificial Compressibility and Pseudo-Cartesian Formulation.....	4-12
4.2.4 Turbulence Modeling	4-13
4.2.5 Coupling of Flow and Turbulence Models	4-15
4.3 Spatial Discretization.....	4-16
4.4 Numerical Fluxes	4-19
4.4.1 Inviscid Fluxes.....	4-19
4.4.1.1 Convective Flux Jacobian	4-20
4.4.1.2 Higher-Order Accurate Scheme	4-22
4.4.1.3 Slope Limiter	4-23
4.4.2 Viscous Fluxes	4-23
4.4.3 Turbulence Model's Fluxes	4-25
4.4.4 Boundary Conditions	4-25
4.4.5 Source Terms	4-27
4.5 Time Integration.....	4-27
4.5.1 Implicit Treatment of Turbulence Model Source Term.....	4-28
4.5.2 Acceleration Techniques	4-29
Chapter 5 Numerical Validation of IGal2D Solver	5-1
5.1 Non-Swirling Flows.....	5-1
5.1.1 Inviscid Flow over a Sphere	5-1
5.1.2 Viscous Laminar Flow over a Sphere.....	5-2
5.1.3 Turbulent Flow around a Flanged Diffuser	5-4
5.2 Swirling Flows	5-7
5.2.1 Inviscid Swirling Flow inside an S-Shaped Axisymmetric Tube.....	5-8
5.2.2 Laminar Swirling Flow inside an Axial Tube	5-17
5.2.3 Turbulent Swirling Flow inside a Conical Diffuser	5-23

Chapter 6 The RG15 Low-Reynolds Airfoil Family	6-1
6.1 Aerodynamics of Small Wind Turbine Blades.....	6-1
6.2 Review of Small Wind Turbine Airfoils.....	6-4
6.3 Motivation and Scope.....	6-6
6.4 The Original RG15 Airfoil.....	6-6
6.5 Thickening of the RG15 Airfoil	6-8
6.6 Trailing Edge Modification.....	6-11
6.7 RG15 Airfoil Family	6-13
Chapter 7 Numerical Analysis of the RG15 Airfoil Family	7-1
7.1 XFOIL Analysis.....	7-1
7.1.1 XFOIL Setup and Validation	7-1
7.2 RANS Analysis.....	7-3
7.2.1 IGal2D Setup and Validation	7-4
7.2.2 Lift and Drag Calculation	7-7
7.3 Numerical Results and Discussion.....	7-7
7.3.1 XFOIL Results.....	7-7
7.3.2 IGal2D Results.....	7-12
7.3.2.1 Aerodynamic Coefficients.....	7-12
7.3.2.2 Comparison with XFOIL	7-14
7.3.2.3 Flow Field Visualizations.....	7-18
7.4 Summary	7-22
Chapter 8 A Coupled RANS – BEM Model.....	8-1
8.1 Overview	8-1
8.2 Flow Modeling and Blade Representation	8-2
8.3 Coupling Approach	8-3
8.4 Numerical Validation of the RANS-BEM Model.....	8-5
8.4.1 NREL 5-MW Reference Wind Turbine	8-5
8.4.1.1 Numerical Setup.....	8-5
8.4.1.2 Numerical Results	8-7
8.4.2 NREL Phase VI Rotor	8-10
8.4.2.1 Numerical Setup.....	8-11

8.4.2.2 Numerical Results – Unshrouded Configuration.....	8-12
8.4.2.3 Numerical Results – Shrouded Configuration.....	8-13
Chapter 9 Optimization Framework for Shrouded Wind Turbines.....	9-1
9.1 The Differential Evolution Algorithm.....	9-1
9.1.1 Surrogate Models.....	9-2
9.1.2 Parallelization Strategy	9-2
9.1.3 Asynchronous Implementation	9-3
9.2 Mesh Parameterization and Deformation	9-4
9.3 Summary of the Optimization Framework	9-7
9.3.1 Design Evaluation.....	9-8
9.3.2 Genotype to Phenotype.....	9-9
9.3.3 Pre-processing Stage.....	9-10
9.3.4 Post-processing Stage	9-11
Chapter 10 Design Optimization Cases	10-1
10.1 Design of Improved Rotor Blades.....	10-1
10.1.1 Twist and Chord Parameterization.....	10-2
10.1.2 Cost Function and Constraint Formulation	10-3
10.1.3 Optimization Results.....	10-4
10.2 Design Optimization of an Unloaded Diffuser.....	10-7
10.2.1 Grid Independence Study.....	10-8
10.2.2 Mesh Parameterization and Design Variables.....	10-11
10.2.3 Objective Function and Constraints.....	10-12
10.2.3.1 Objectives.....	10-12
10.2.3.2 Constraints	10-13
10.2.3.3 Cost Function	10-13
10.2.4 Optimization Results.....	10-13
10.2.4.1 Optimal Shroud Design.....	10-15
10.3 Optimization of a Complete Shrouded Wind Turbine	10-20
10.3.1 Grid Independence Study.....	10-22
10.3.2 Geometry Parameterization and Design Variables.....	10-25
10.3.3 Objective Function and Implicit Constraints	10-28

10.3.3.1 Design Objectives	10-28
10.3.3.2 Implicit Constraints.....	10-28
10.3.3.3 Cost Function Formulation	10-29
10.3.4 Optimization Results.....	10-29
10.3.4.1 Optimal Blade	10-30
10.3.4.2 Optimal Shroud Geometry	10-31
10.3.5 Performance of the Optimal Design.....	10-33
Chapter 11 Conclusions and Future Work.....	11-1
11.1 Concluding Remarks	11-1
11.1.1 Development of a Blade Element Momentum Code	11-2
11.1.2 Development of an Axisymmetric RANS Solver	11-3
11.1.3 Development of a Coupled RANS – BEM Model	11-4
11.1.4 Design of a Low Reynolds Airfoil Family	11-5
11.1.5 Development of an Optimization Framework for Shrouded Wind Turbines.....	11-7
11.2 Further Research	11-9
References.....	R-1
Appendix A – Differential Operators in Cylindrical Coordinates	A-1
Appendix B – Conservative Form of the Axisymmetric Navier-Stokes.....	B-1
Appendix C - RG15 Airfoil Family	C-1
RG15-70-1 Airfoil.....	C-1
RG15-(10)-70-1	C-3
RG15-(20)-70-1	C-5
RG15-(30)-70-1	C-7
RG15-(40)-70-1	C-9
RG15-(50)-70-1	C-11

Nomenclature

Latin Symbols

A	Cross-sectional area of the stream tube [m ²]
α_α	Axial induction factor [-]
α_t	Tangential induction factor [-]
b	Reciprocal of the diffuser exit-area-ratio [-]
\mathcal{B}	External boundary of the computational domain
B_R	Number of rotor blades
c	Chord length [m]
C_n	Normal force coefficient [-]
C_p	Pressure coefficient [-]
C_P	Power coefficient [-]
C_t	Tangential force coefficient [-]
C_D	Drag coefficient [-]
C_L	Lift coefficient [-]
C_T	Thrust coefficient [-]
D	Drag force [N]
f_z, f_r, f_θ	Body force components
F	Total Prandtl's loss factor [-]
F_{hub}	Prandtl's hub loss factor [-]
F_{tip}	Prandtl's tip loss factor [-]
F_n	Normal force per unit length [N/m]
F_t	Tangential force per unit length [N/m]
F_D	Drag force per unit length [N/m]
F_L	Lift force per unit length [N/m]
Δh_L	Total pressure loss between the rotor plane and the diffuser exit plane
k	Turbulent kinetic energy [m ² /s ²]
L	Lift force [N]

L_{ref}	Reference Length [m]
L_s	Separation length
L_{sb}	Separation bubble length
\dot{m}	Mass flow rate [kg/s]
M	Torque [Nm]
$N_{i,p}, N_{j,q}$	B-Spline Basis functions
p	Static pressure [Pa]
Δp_d	Pressure loss across the rotor disc
P	Power [W]
Pr	Prandtl number [-]
\dot{q}	Volumetric flow rate [m ³ /s]
q_s	Total Shen's loss factor [-]
$q_{s,tip}$	Shen's tip loss factor [-]
$q_{s,hub}$	Shen's hub loss factor [-]
R	Rotor radius [m]
R_h	Hub radius [m]
R_x	x -component of total aerodynamic force
R_y	y -component of total aerodynamic force
Re	Reynolds number [-]
$S_N(P)$	Set of nodes that are directly connected to grid node P
t	Time [s]
T	Thrust force [N]
u_z, u_r, u_θ	Velocity components in cylindrical coordinates
u, v, w	Velocity components in Cartesian coordinates
V_{ref}	Reference velocity [m/s]
w_a	Axial velocity component at the rotor plane [m/s]
w_t	Tangential velocity component at the rotor plane [m/s]
x, y	Cartesian coordinates

z, r, θ	Cylindrical coordinates
\mathbf{A}_{PQ}	Jacobian matrix of the convective flux vector related to the edge PQ
$\mathbf{F}_i, \mathbf{G}_i$	Inviscid flux vectors of the flow model
$\mathbf{F}_i^t, \mathbf{G}_i^t$	Inviscid flux vectors of the turbulence model
$\mathbf{F}_v, \mathbf{G}_v$	Viscous flux vectors of the flow model
$\mathbf{F}_v^t, \mathbf{G}_v^t$	Viscous flux vectors of the turbulence model
\mathbf{H}	Source term vector of the flow model
\mathbf{H}^t	Source term vector of the turbulence model
\mathbf{I}	Identity matrix
\mathbf{L}_p^t	Jacobian matrix of the turbulence model source term
\mathbf{n}_{PQ}	Outward normal vector to ∂CV_{PQ}
$\hat{\mathbf{n}}_{PQ}$	Outward unit normal vector to ∂CV_{PQ}
\mathbf{R}	Total aerodynamic force vector
$\mathbf{R}_p^{(n)}$	Sum of the numerical fluxes at time step n
\mathbf{r}_{PQ}	Position vector that connects the mesh nodes P and Q
\mathbf{U}	Primitive variable vector of the flow model
\mathbf{U}^t	Primitive variable vector of the turbulence model
$\Delta \mathbf{U}_p^{(n)}$	Correction vector of primitive variables at time step n
$\boldsymbol{\tau}$	Viscous stress tensor
$\boldsymbol{\Phi}_i^{PQ}$	Inviscid flux vector related to edge PQ
$\boldsymbol{\Phi}_v^{PQ}$	Viscous flux vector related to edge PQ

Greek Symbols

α	Angle of attack [rad]
β	Artificial compressibility parameter [-]
γ	Velocity speed-up ratio for the unloaded diffuser [-]
η_d	Diffuser efficiency [-]
θ_B	Global pitch angle [rad]

θ_p	Local pitch angle [rad]
θ_T	Local twist angle [rad]
λ	Tip-speed ratio [-]
μ	Dynamic viscosity [N·s/m ²]
μ_t	Turbulent dynamic viscosity [N·s/m ²]
ν	Kinematic viscosity [m ² /s]
ν_t	Turbulent kinematic viscosity [m ² /s]
ν_{ref}	Reference kinematic viscosity [m ² /s]
ρ	Density [kg/m ³]
ρ_{ref}	Reference Density [kg/m ³]
σ	Rotor solidity [-]
τ_{ij}	Stress tensor components
ϕ	Angle between the relative velocity and rotor plane [rad]
ψ_r	Relaxation factor [-]
ω_R	Rotational speed of the rotor [rad/s]
ω_α	Axial induced velocity [m/s]
ω_t	Tangential induced velocity [m/s]

Subscripts and Superscripts

∞	Free-stream quantities
0	Station in the ambient free-stream (undisturbed flow)
1	Station at the shroud's inlet plane
2	Station immediately upstream of the rotor plane
3	Station immediately downstream of the rotor plane
4	Station at the shroud's exit plane
5	Station in the ultimate (far) wake
d	Station at the actuator disc (rotor plane)
i	Inviscid quantities

<i>in</i>	Quantities at the inlet of the computational domain
<i>v</i>	Viscous quantities
<i>z</i>	Axial direction component
<i>r</i>	Radial direction component
θ	Circumferential direction component
<i>t</i>	Quantities related to turbulence model
<i>x</i>	<i>x</i> – direction component
<i>y</i>	<i>y</i> – direction component

Abbreviations and Acronyms

ACM	Artificial Compressibility Method
BEM	Blade Element Momentum
CAD	Computer-Aided Design
CFD	Computational Fluid Dynamics
CFL	Courant-Friedrichs-Lewy Number
CV	Control Volume
DAWT	Diffuser-Augmented Wind Turbine
DE	Differential Evolution
DoF	Degrees of Freedom
EARSM	Explicit Algebraic Reynolds Stress Model
ERCOTAC	European Research Community on Flow, Turbulence and Combustion
FFD	Free-Form Deformation
GWEC	Global Wind Energy Council
HAWT	Horizontal-Axis Wind Turbine
IEC	International Electrotechnical Commission
IRENA	International Renewable Energy Agency
LES	Large Eddy Simulation
LBM	Lattice – Boltzmann Method

MAE	Mean Absolute Error
MAPE	Mean Absolute Percentage Error
MLP	Multi-Layer Perceptron
MPI	Message Parsing Interface
NACA	National Advisory Committee for Aeronautics
NASA	National Aeronautics and Space Administration
NCFV	Node-Centered Finite Volume
NREL	National Renewable Energy Laboratory
RANS	Reynolds-Averaged Navier-Stokes
REmap	Renewable Energy Roadmap
RBF	Radial Basis Function
TSR	Tip-Speed Ratio
UAE	Unsteady Aerodynamics Experiment
WESC	Wind Energy Conversion System
YoY	Year-Over-Year

List of Figures

Figure 1.1: Overview of the key milestones in wind power industry since 1982 (IRENA, 2019).	1-2
Figure 1.2: The IRENA’s wind roadmap to 2050 (REmap). The target values of wind generation share and total installed capacity, in order to achieve the global energy transformation (IRENA, 2019).	1-3
Figure 1.3: The full-scale prototypes of Hummingbird H15 DAWT model designed by OGT Greentech Ltd, with a rated capacity of 15 kW [Source: https://www.omnilinkgreentech.com].	1-4
Figure 1.4: The commercial Halo 6 kW model of Halo Energy [Source: https://www.halo.energy].	1-4
Figure 1.5: The main objectives of the current doctoral dissertation.	1-6
Figure 1.6: The energy extraction scheme for a conventional horizontal-axis wind turbine.	1-7
Figure 1.7: Schematic representation of the diffuser-augmented wind energy extraction scheme.	1-8
Figure 1.8: Schematic representation of the diffuser-augmented wind energy extraction scheme, combined with wake and external flow mixing.	1-10
Figure 1.9: The storyline of the current doctoral dissertation.	1-17
Figure 2.1: Schematic representation of the stream tube passing through the rotor of a conventional (unshrouded) horizontal-axis wind turbine. Illustration of the reference stations for the description of axial momentum theory.	2-2
Figure 2.2: Meridian section of the reference stream tube.	2-3
Figure 2.3: Schematic representation of the stream tube passing through the rotor of a shrouded wind turbine. Illustration of the reference stations employed for the application of axial momentum theory.	2-7

Figure 2.4: Meridian section of the reference stream tube for the case of a shrouded rotor.....	2-11
Figure 2.5: Illustration of the annular stream tube for the extraction of elementary momentum equations describing an unshrouded rotor.....	2-16
Figure 2.6: Schematic representation of blade discretization and definition of blade elements.....	2-18
Figure 2.7: Schematic representation of the local velocities and forces on a blade element.....	2-19
Figure 2.8: Illustration of the annular stream tube for the extraction of elementary momentum equations describing a shrouded rotor.....	2-23
Figure 2.9: The adopted blade discretization concept.....	2-27
Figure 2.10: Extrapolation of the lift coefficient curve for a NACA 0012 airfoil at 1,000,000 Re.....	2-29
Figure 2.11: Extrapolation of the drag coefficient curve for a NACA 0012 airfoil at 1,000,000 Re.....	2-29
Figure 2.12: Fluctuating behavior of the axial induction factor due to change of loading state. Reproduced from (Maheri et al., 2006).....	2-30
Figure 2.13: Damped fluctuation of the axial induction factor for different relaxation factors. Reproduced from (Maheri <i>et al.</i> , 2006).....	2-31
Figure 3.1: The NREL Phase VI wind turbine configuration (Hand et al., 2001).....	3-2
Figure 3.2: The planform of NREL Phase VI wind turbine blade (Hand <i>et al.</i> , 2001).	3-3
Figure 3.3: Comparison of the predicted and experimentally measured aerodynamic power and thrust for the NREL Phase VI wind turbine rotor – Test Sequence I (Low Pitch Setup).....	3-5
Figure 3.4: Comparison of the predicted and experimentally measured aerodynamic power and thrust for the NREL Phase VI wind turbine rotor – Test Sequence H (Baseline Setup).....	3-6

Figure 3.5: Comparison of the predicted and experimentally measured aerodynamic power and thrust for the NREL Phase VI wind turbine rotor – Test Sequence J (High Pitch Setup).	3-6
Figure 3.6: CAD representation of the NREL 5-MW blade.	3-7
Figure 3.7: Comparison of the axial (a) and tangential (b) force distribution over the NREL 5MW blade at 11.4 m/s, as obtained by the current BEM model and three-dimensional RANS simulations.	3-11
Figure 3.8: The three blade designs of Donqi Urban Windmill (van Dorst, 2011).	3-12
Figure 3.9: (a) The experimentally measured and numerically predicted velocity speed-up distribution over the rotor plane for the unloaded Donqi Urban Windmill (Kesby et al., 2016). (b) Comparison of the BEM results obtained from the measured and numerically predicted velocity speed-up.	3-13
Figure 3.10: Experimental data and BEM predictions for the power output of the Donqi Urban Windmill rotor. (a) Old blade; (b) Optimal blade; (c) Linear blade.	3-14
Figure 3.11: A schematic representation of the flow behaviour through the multi-slotted diffuser-augmented wind turbine (Phillips, 2003).	3-16
Figure 3.12: The experimentally measured and computational predicted power curve of the multi-slotted diffuser-augmented wind turbine at the optimum pitch angle of 6.7 degrees.	3-18
Figure 4.1: Definition of the median dual control volume CV_P for an internal grid node P	4-17
Figure 4.2: Definition of the median dual control volume CV_P for a boundary grid node P	4-17
Figure 4.3: Vectors definition for the cases of internal and boundary nodes.	4-18
Figure 4.4: Edge-dual volume examples, obtained by different types of faces.	4-24
Figure 5.1: Inviscid flow over a sphere: (a) Distribution of pressure coefficient on the surface of the sphere. (b) Distribution of dimensionless velocity magnitude on the surface of the sphere.	5-2

Figure 5.2: Streamlines over a sphere at various Reynolds numbers.	5-3
Figure 5.3: Laminar flow over a sphere: (a) Variation of drag coefficient with Reynolds number, (b) Pressure distribution on the surface of the sphere at $Re = 100$	5-3
Figure 5.4: Schematic representation of the examined flanged diffuser.	5-4
Figure 5.5: The computational grid for the simulation of the flow field around the flanged diffuser.	5-5
Figure 5.6: Turbulent flow around a flanged diffuser: (a) Dimensionless contours of the axial velocity component, (b) Dimensionless pressure contours, (c) Velocity streamlines, (d) Axial velocity contour lines.	5-6
Figure 5.7: Turbulent flow around a flanged diffuser: (a) On-axis velocity speed-up distribution, (b) On-axis pressure coefficient distribution.	5-7
Figure 5.8: Geometric characteristics of the S-shaped axisymmetric tube.	5-8
Figure 5.9: Curved part of the coarsest resolution (M1) of each grid type.	5-9
Figure 5.10: Contours of dimensional pressure and velocity components inside the S-shaped tube, derived by IGal2D and Fluent solvers.	5-13
Figure 5.11: Isolines of pressure and velocity components, derived by IGal2D and Fluent solvers.	5-13
Figure 5.12: Dimensional velocity components and pressure distributions along the centerline of the S-shaped tube, obtained with IGal2D and Fluent solvers.	5-14
Figure 5.13: Dimensional velocity components and pressure distributions along the cross-sections S1, S2 and S3 of the S-shaped axisymmetric tube, produced by IGal2D and Fluent solvers.	5-15
Figure 5.14: Pressure convergence history per number of iterations for the densest triangular-unstructured grid, derived by single-grid (L1), three-level (L3) and four-level (L4) multigrid runs.	5-17
Figure 5.15: Geometric details of the axial tube.	5-17

Figure 5.16: Density of the utilized grid for the axial tube.....	5-18
Figure 5.17: Convergence history per number of iterations for static pressure and velocity components (Laminar flow – IGal2D simulation).	5-19
Figure 5.18: Contours of axial velocity (laminar flow – axial tube).	5-20
Figure 5.19: Contours of swirl velocity (laminar flow – axial tube).....	5-20
Figure 5.20: Dimensional axial and swirl velocity components’ distributions along the cross-sections S1, S2, S3 and S4 of the axial tube, obtained by IGal2D and Fluent solvers.	5-21
Figure 5.21: Dimensional axial velocity distributions along the cross-sections S1, S2, S3 and S4 of the axial tube, obtained by IGal2D, in comparison to those reported by Rocha <i>et al.</i> (2015).	5-22
Figure 5.22: Dimensional relative pressure distribution along the centerline of the axial tube.....	5-22
Figure 5.23: Geometric details of the conical diffuser (Leloudas <i>et al.</i> , 2021).	5-23
Figure 5.24: Density of the utilized grid for the conical diffuser (Leloudas <i>et al.</i> , 2021).....	5-24
Figure 5.25: Experimentally obtained (Clausen <i>et al.</i> , 1993) distributions of axial and swirl velocity at the diffuser inlet (S0) along with the interpolated profiles of the corresponding velocity components.....	5-25
Figure 5.26: Distributions of axial and swirl velocity at cross-section S1 (conical diffuser).....	5-26
Figure 5.27: Distributions of axial and swirl velocity at cross-section S4 (conical diffuser).....	5-26
Figure 5.28: Distributions of axial and swirl velocity at cross-section S7 (conical diffuser).....	5-27
Figure 5.29: Distributions of pressure coefficient on the wall (conical diffuser).....	5-27

Figure 5.30: Turbulent flow inside the conical diffuser. Comparison of axial velocity contours.	5-28
Figure 5.31: Turbulent flow inside the conical diffuser. Comparison of swirl velocity contours.	5-29
Figure 5.32: Turbulent flow inside the conical diffuser. Comparison of pressure contours.	5-29
Figure 6.1: Schematic representation of laminar flow separation. (a) Subcritical flow regime. (b) Supercritical flow regime (Leloudas <i>et al.</i> , 2020b).	6-2
Figure 6.2: Velocity streamlines for different flow regimes. (a) Short separation bubble (supercritical regime). (b) Long separation bubble (supercritical regime). (c) Unattached shear layer (subcritical regime) (Leloudas <i>et al.</i> , 2020b).....	6-4
Figure 6.3: The RG15 airfoil. (a) Theoretical profile. (b) Actual profile (Broeren <i>et al.</i> , 1995).....	6-7
Figure 6.4: Aerodynamic characteristics of RG15 airfoil at several low Reynolds numbers, as measured at the UIUC wind tunnel (Broeren <i>et al.</i> , 1995). (a) $C_L - \alpha$. (b) $C_D - \alpha$. (c) $C_L/C_D - \alpha$. (d) $C_L - C_D$	6-8
Figure 6.5: The five thickened RG15 airfoils.....	6-9
Figure 6.6: Calculation of the RG15 mean camber line (blue line).	6-9
Figure 6.7: Calculation of the thickness line corresponding to a random point k along the chord line.....	6-10
Figure 6.8: Indicative thickness lines (magenta) of the RG15 airfoil.....	6-10
Figure 6.9: Indicative points of a thickened airfoil, constructed through the proper extension of the RG15 thickness lines.....	6-10
Figure 6.10: Schematic definition of the (a) trailing edge diameter and (b) blending distance.....	6-12
Figure 6.11: Schematic representation of the followed methodology for the creation of a rounded trailing edge.	6-12

- Figure 6.12:** The influence of the rounded trailing edge and blending distance parameter on the drag polar at $Re = 300,000$. (a) XFOIL results. (b) 2D RANS results. 6-14
- Figure 6.13:** The airfoils composing the low-Reynolds RG15 airfoil family. 6-15
- Figure 7.1:** Comparison of the XFOIL results for the lift and drag coefficients of the original RG15 airfoil at $Re = 60,000$ with the corresponding experimental measurements (Broeren *et al.*, 1995); (a) $C_L - \alpha$. (b) $C_D - \alpha$ 7-2
- Figure 7.2:** Comparison of the XFOIL results for the lift and drag coefficients of the original RG15 airfoil at $Re = 300,000$ with the corresponding experimental measurements (Broeren *et al.*, 1995); (a) $C_L - \alpha$. (b) $C_D - \alpha$ 7-3
- Figure 7.3:** (a) The computational domain used for the validation study of the RANS solver, (b) Wide view of the corresponding computational grid. 7-6
- Figure 7.4:** The hybrid computational grid used for the flow field simulation of the original RG15 airfoil at $\alpha = 6^\circ$ 7-6
- Figure 7.5:** The lift and drag coefficients of the original RG15 airfoil at $Re = 300,000$, as obtained by XFOIL software, IGal2D solver and the experimental measurements (Broeren *et al.*, 1995). 7-6
- Figure 7.6:** Aerodynamic characteristics of the RG15 airfoil family at $Re = 60,000$, as obtained through the XFOIL analysis. (a) $C_L - \alpha$. (b) $C_D - \alpha$. (c) $C_L/C_D - \alpha$. (d) $C_L - C_D$ 7-10
- Figure 7.7:** Aerodynamic characteristics of the RG15 airfoil family at $Re = 300,000$, as obtained through the XFOIL analysis. (a) $C_L - \alpha$. (b) $C_D - \alpha$. (c) $C_L/C_D - \alpha$. (d) $C_L - C_D$ 7-11
- Figure 7.8:** The hybrid computational grid used for the flow field simulation of the RG15-(30)-70-1 airfoil at $\alpha = 6^\circ$ 7-12
- Figure 7.9:** Aerodynamic characteristics of the RG15 airfoil family at $Re = 300,000$ (RANS analysis). (a) $C_L - \alpha$. (b) $C_D - \alpha$. (c) $C_L/C_D - \alpha$. (d) $C_L - C_D$ 7-14

Figure 7.10: Comparison of pressure coefficient distributions obtained by XFOIL software and IGal2D solver for the RG15-(40)-70-1 airfoil at $Re = 300,000$. (a) $\alpha = -5^\circ$. (b) $\alpha = 0^\circ$. (c) $\alpha = 5^\circ$. (d) $\alpha = 10^\circ$.	7-15
Figure 7.11: Comparison between the lift and drag curves obtained by XFOIL and IGal2D solvers for the RG15-(00)-70-1 airfoil at $Re = 300,000$.	7-16
Figure 7.12: Comparison between the lift and drag curves obtained by XFOIL and IGal2D solvers for the RG15-(10)-70-1 airfoil at $Re = 300,000$.	7-16
Figure 7.13: Comparison between the lift and drag curves obtained by XFOIL and IGal2D solvers for the RG15-(20)-70-1 airfoil at $Re = 300,000$.	7-17
Figure 7.14: Comparison between the lift and drag curves obtained by XFOIL and IGal2D solvers for the RG15-(30)-70-1 airfoil at $Re = 300,000$.	7-17
Figure 7.15: Comparison between the lift and drag curves obtained by XFOIL and IGal2D solvers for the RG15-(40)-70-1 airfoil at $Re = 300,000$.	7-17
Figure 7.16: Comparison between the lift and drag curves obtained by XFOIL and IGal2D solvers for the RG15-(50)-70-1 airfoil at $Re = 300,000$.	7-18
Figure 7.17: Recirculation area behind the rounded trailing edges of the proposed airfoils at $\alpha = 0^\circ$ and $Re = 300,000$.	7-18
Figure 7.18: Variation of the recirculation zone behind the trailing edge of the RG15-(30)-70-1 airfoil with the angle of attack at $Re = 300,000$.	7-19
Figure 7.19: The variation of laminar separation bubble with thickness-to-chord ratio at $\alpha = 12^\circ$.	7-20
Figure 7.20: The pressure contours around each one of the airfoils composing the RG15 family at the angle of attack leading to the maximum lift-to-drag ratio ($Re = 300,000$).	7-21
Figure 7.21: The axial velocity contours around each one of the airfoils composing the RG15 family at the angle of attack leading to the maximum lift-to-drag ratio ($Re = 300,000$).	7-21
Figure 8.1: Flow chart of the RANS - BEM methodology	8-4

Figure 8.2: The adopted computational domain for the simulation of NREL 5-MW wind turbine.....	8-6
Figure 8.3: Illustration of the quadrilateral computational mesh, employed for the simulation of NREL 5-MW wind turbine.	8-6
Figure 8.4: Axial momentum deficit predicted by IGal2D and SOWFA for the NREL 5-MW rotor at $u_\infty = 8 \text{ m/s}$	8-8
Figure 8.5: Axial momentum deficit predicted by IGal2D and SOWFA for the NREL 5-MW rotor at $u_\infty = 11 \text{ m/s}$	8-9
Figure 8.6: Axial momentum deficit predicted by IGal2D and SOWFA for the NREL 5-MW rotor at $u_\infty = 15 \text{ m/s}$	8-9
Figure 8.7: Axial and tangential force distribution over the NREL 5-MW blade at 11.4 m/s and 12.06 RPM.....	8-10
Figure 8.8: Shroud configuration for the NREL Phase VI wind turbine rotor.	8-11
Figure 8.9: Overview of the hybrid computational mesh adopted for the simulation of the shrouded NREL Phase VI wind turbine rotor.....	8-12
Figure 8.10: Axial and tangential force distributions over the bare NREL Phase VI rotor at 7 m/s.	8-13
Figure 8.11: Axial momentum deficit for the shrouded NREL Phase VI rotor at 5 m/s.	8-14
Figure 8.12: Axial and tangential force distribution over the NREL Phase VI blade for the shrouded configuration at 5 m/s.....	8-14
Figure 9.1: Flowcharts of the parallel differential evolution algorithm (Leloudas <i>et al.</i> , 2020a).....	9-3
Figure 9.2: Application of the FFD technique to a hybrid computational mesh around a NACA 0012 airfoil.	9-5
Figure 9.3: Overview of the proposed optimization framework.....	9-7
Figure 9.4: The available analysis tools for the design evaluation module.	9-8

Figure 9.5: The available computational tools for translating the genotype into the phenotype.....	9-10
Figure 9.6: The major steps of the pre-processing stage depending on the adopted analysis tool.....	9-11
Figure 10.1: Illustration of several Donqi Urban Windmill models within the urban environment [Source: http://www.jetsongreen.com/2011/08/donqi-urban-windmill-residentia.html].	10-2
Figure 10.2: Parameterization strategy for chord and twist distributions.	10-3
Figure 10.3: The convergence history of the differential evolution algorithm.....	10-4
Figure 10.4: History of the testing error for the employed surrogate models.....	10-4
Figure 10.5: Twist and chord distributions of the optimized blade <i>BD1</i>	10-5
Figure 10.6: Twist and chord distributions of the optimized blade <i>BD2</i>	10-5
Figure 10.7: Comparison between the twist and chord distributions of <i>BD1</i> and <i>BD2</i>	10-6
Figure 10.8: The increased power output of the rotor, utilizing the optimized blade geometries <i>BD1</i> and <i>BD2</i>	10-6
Figure 10.9: Three dimensional drawings of the (a) original blade, (b) optimized blade <i>BD1</i> and (c) optimized blade <i>BD2</i>	10-7
Figure 10.10: The aerodynamic profile of the baseline shroud design (Leloudas, Lygidakis, <i>et al.</i> , 2020).	10-8
Figure 10.11: The computational meshes used for the grid independence study: (a) coarse, (b) medium and (c) fine.	10-9
Figure 10.12: Grid independence study: (a) On-axis velocity speed-up ratio distribution, (b) On-axis pressure coefficient distribution, (c) Velocity speed-up ratio distribution over the rotor plane, (d) Distribution of the pressure coefficient over the surface of the shroud profile.	10-10
Figure 10.13: The initial FFD lattice.	10-11

Figure 10.14: (a) The testing error for the two surrogate modes; (b) the convergence history of the DE algorithm.	10-14
Figure 10.15: The aerodynamic profiles of the baseline design, SD1, and SD2.	10-15
Figure 10.16: The aerodynamic profile of the SD2 shroud design (Leloudas, Lygidakis, <i>et al.</i> , 2020).	10-16
Figure 10.17: Comparison between the baseline design, SD1, and SD2. (a) Velocity speed-up ratio distribution over the rotor plane; (b) on-axis velocity speed-up ratio distribution; (c) on-axis pressure coefficient distribution; (d) distribution of the pressure coefficient over the surface of the shroud profile (fine meshes).....	10-17
Figure 10.18: 3D representation of the (a) baseline design, (b) SD1, and (c) SD2.	10-18
Figure 10.19: The dimensionless contours of axial velocity component (top), radial velocity component (middle), and static pressure (bottom), for the baseline design, SD1, and SD2, for a Reynolds number equal to 2,200,000 (fine meshes).....	10-19
Figure 10.20: The velocity streamlines around the (a) baseline design, and (b) SD1 (fine meshes).	10-20
Figure 10.21: The velocity streamlines around the (a) baseline design, and (b) SD2 (fine meshes).	10-20
Figure 10.22: The Donqi DAWT with the linearized blade.	10-21
Figure 10.23: Geometric characteristics of the Donqi Urban Windmill shroud.	10-21
Figure 10.24: Chord and twist distributions of the linearized blade configuration (van Dorst, 2011).....	10-22
Figure 10.25: The computational grids used for the grid independence study: (a) coarse, (b) medium, and (c) fine.	10-23
Figure 10.26: Wide view of the coarse (QM1) computational grid.	10-24
Figure 10.27: Results of the grid independence study.	10-24
Figure 10.28: Parameterization strategy for chord and twist distributions.	10-25

Figure 10.29: Definition of the FFD lattice employed for the parameterization of the computational mesh. 10-26

Figure 10.30: (a) The convergence history of the DE algorithm; (b) The testing error for the two surrogate modes. 10-30

Figure 10.31: The chord and twist distributions of the optimal blade design against the chord and twist distribution of the linear blade, reported by van Dorst (2011). 10-30

Figure 10.32: The aerodynamic profiles of the baseline and optimized shroud designs. 10-31

Figure 10.33: Three-dimensional representation of (a) the baseline and (b) optimal shrouds. 10-32

Figure 10.34: The axial and tangential force distributions along the optimized and baseline blade designs. 10-34

Figure 10.35: The contours of dimensionless axial velocity component around the optimal and baseline shrouds. 10-34

Figure 10.36: The contours of dimensionless swirl velocity component around the optimal and baseline shrouds. 10-35

Figure 10.37: The contours of dimensionless pressure around the optimal and baseline shrouds. 10-35

Figure 10.38: The contour lines of dimensionless pressure around the optimal and baseline shrouds. 10-36

Figure 10.39: The velocity streamlines around the optimal and baseline shrouds. 10-36

List of Tables

Table 3.1: Simulation cases for the NREL Phase VI wind turbine rotor.	3-2
Table 3.2: Geometric characteristics of the NREL Phase VI wind turbine blade.	3-4
Table 3.3: Simulation cases for the NREL 5-MW reference wind turbine.	3-7
Table 3.4: Characteristics of the NREL 5-MW wind turbine blade.	3-8
Table 3.5: Comparison of predicted power by different turbine simulation tools for the NREL 5-MW Reference Wind Turbine at various operational points.	3-9
Table 3.6: Comparison of predicted thrust by different turbine simulation tools for the NREL 5-MW Reference Wind Turbine at various operational points.	3-10
Table 3.7: Simulation cases for the Donqi Urban Windmill rotor.	3-13
Table 3.8: The mean absolute error (MAE) and the mean absolute percentage error (MAPE) between the experimental data and the BEM results for each blade of the Donqi Urban Windmill.	3-15
Table 3.9: The velocity speed-up ratio distribution over the rotor plane for the unloaded diffuser of the multi-slotted diffuser-augmented wind turbine (Phillips, 2003).	3-16
Table 3.10: Blade characteristics for the multi-slotted DAWT (Phillips, 2003).	3-17
Table 5.1: Comparison of separation length and drag coefficient at $Re = 100$	5-4
Table 5.2: Control points of the cubic B-spline curve, used for the design of the centerline of the S-shaped tube.	5-9
Table 5.3: Density data of the employed grids.	5-9
Table 5.4: P_t and rw metrics extracted from quadrilateral grids.	5-11
Table 5.5: P_t and rw metrics extracted from triangular-regular grids.	5-11
Table 5.6: P_t and rw metrics extracted from triangular-unstructured grids.	5-12

Table 5.7: Number of DoFs at every agglomerated level ($L1 - L5$) for each of the utilized grids for the S-shaped axisymmetric tube.....	5-16
Table 5.8: Number of iterations, required to decrease pressure log(residual) to 10^{-13} , depending on grid-type, grid density and number of employed multigrid levels.....	5-16
Table 5.9: Pressure drop between solid walls points at inlet and outlet positions of the axial tube.	5-23
Table 6.1: The modified RG15 airfoils with a thickened and rounded trailing edge.....	6-13
Table 6.2: Geometrical characteristics of the airfoils composing the RG15 airfoil family.	6-15
Table 7.1: Meshing parameters used for the grid independence study.....	7-5
Table 7.2: The results of the grid independence study. The flow simulations were performed for RG15 airfoil at $Re = 300,000$ and $\alpha = 0^\circ$	7-5
Table 7.3: The maximum lift coefficient and lift-to-drag ratio for each one of the examined airfoils, at various Reynolds numbers, resulting from the XFOIL analysis.....	7-8
Table 7.4: Increase rate of $(L/D)_{max}$ and C_{Lmax} with Re using the slope linear regression through data points.....	7-9
Table 7.5: Lift-to-drag ratio as a function of angle of attack at $Re = 300,000$ (RANS analysis).	7-13
Table 7.6: Comparison between the results of XFOIL and RANS solvers, in terms of the maximum lift-to-drag ratio.	7-16
Table 8.1: Summary of the simulation cases for the NREL 5-MW reference wind turbine.....	8-5
Table 8.2: Comparison of predicted power using different turbine simulation tools, for the NREL 5-MW reference wind turbine at various operational points.	8-7

Table 8.3: Comparison of predicted thrust by different turbine simulation tools, for the NREL 5-MW reference wind turbine at various operational points.	8-8
Table 8.4: Summary of the simulation cases for the NREL Phase VI rotor.	8-11
Table 8.5: Numerical predictions and experimental data for power and thrust.	8-12
Table 8.6: Numerical predictions for power and thrust, for the shrouded NREL Phase VI rotor.	8-13
Table 10.1: Overview of the design optimization cases encountered in this study.	10-1
Table 10.2: The main geometrical characteristics of the baseline shroud design.	10-8
Table 10.3: Drag variation for different mesh resolutions.	10-9
Table 10.4: Wall-clock computation time, number of exact evaluations, and number of total evaluations.	10-14
Table 10.5: The main geometrical characteristics of SD1 and SD2.....	10-16
Table 10.6: Drag and velocity speed-up variation for the different shroud designs (fine meshes).	10-16
Table 10.7: The main geometrical characteristics of the baseline shroud.	10-22
Table 10.8: Characteristics of the mesh employed in the grid independence study.	10-23
Table 10.9: Results of the grid independence study.	10-25
Table 10.10: Comparison of the predicted and experimentally measured values of power.	10-25
Table 10.11: The adopted bounds for the control points of the FFD lattice.....	10-27
Table 10.12: The main geometrical characteristics of the baseline and optimal shroud designs.....	10-32
Table 10.13: Performance characteristics of the initial and optimal designs.....	10-33
Table C.1: Cartesian coordinates of RG15-70-1 airfoil.....	C-2

Table C.2: Cartesian coordinates of RG15-(10)-70-1 airfoil..... C-4

Table C.3: Cartesian coordinates of RG15-(20)-70-1 airfoil..... C-6

Table C.4: Cartesian coordinates of RG15-(30)-70-1 airfoil..... C-8

Table C.5: Cartesian coordinates of RG15-(40)-70-1 airfoil..... C-10

Table C.6: Cartesian coordinates of RG15-(50)-70-1 airfoil..... C-12

Chapter 1

Introduction

The first chapter aims to familiarize the reader with the concept of shrouded or diffuser-augmented wind turbines and introduce him/her to the subject of the current research study. In particular, Section 1.1 presents the motivation underlying this doctoral dissertation, while Section 1.2 presents the main objectives and the respective approaches. Subsequently, Section 1.3 unravels the core physical principles governing the operation of shrouded wind turbines and Section 1.4 provides a detailed overview of the major theoretical, numerical and experimental investigations reported in literature. Finally, Section 1.5 outlines the structure and Section 1.6 summarizes the contributions of this doctoral dissertation, while Section 1.7 lists all the related publications.

1.1 Motivation

In recent years, the escalating awareness about the adverse environmental impact of carbon dioxide emissions and global climate change has been the main factor pushing for the systematic revision of the conventional energy paradigm and actively promoting the massive deployment of sustainable energy technologies, based on renewable energy sources – a process widely referred to as energy transition (Creutzig *et al.*, 2014). Under these global circumstances, the wind power sector has been experiencing remarkable rates of growth since the early years of the twenty-first century, by capitalizing on supportive government policies and international climate treaties (such as the Kyoto Protocol, the Paris Climate Agreement and the European Green Deal), along with significant technological and scientific developments (see Figure 1.1). As a matter of fact, and according to the latest annual report released by the Global Wind Energy Council (GWEC), 2020 was recorded as the best year in history for the global wind power industry, which – despite the adverse impact of COVID-19 pandemic on the sectors of supply chain and project construction execution – witnessed a year-over-year (YoY) growth of approximately 53 percent (GWEC, 2021). In particular, more than 93 GW of new onshore and offshore wind power came online around the world during the course of 2020, contributing for an overall installed capacity of approximately 743 GW (GWEC, 2021). Moreover, future projections and estimates indicate that this exciting growth will carry on. According to the Renewable Energy Roadmap (REmap) of the International Renewable Energy Agency (IRENA) – which represents a climate resilient pathway characterized by a relatively ambitious, yet achievable, uptake of renewable energy sector and energy efficiency measures – the global wind energy market has the potential to reach 2,000 GW until 2030 and

6,000 GW until 2050, thus providing up to 21 and 35 percent of the worldwide energy demand, respectively (IRENA, 2019). Figure 1.2 summarizes the REmap targets for the wind generation share and total installed capacity (two of the key wind energy indicators) in order to achieve the global energy transformation or transition.

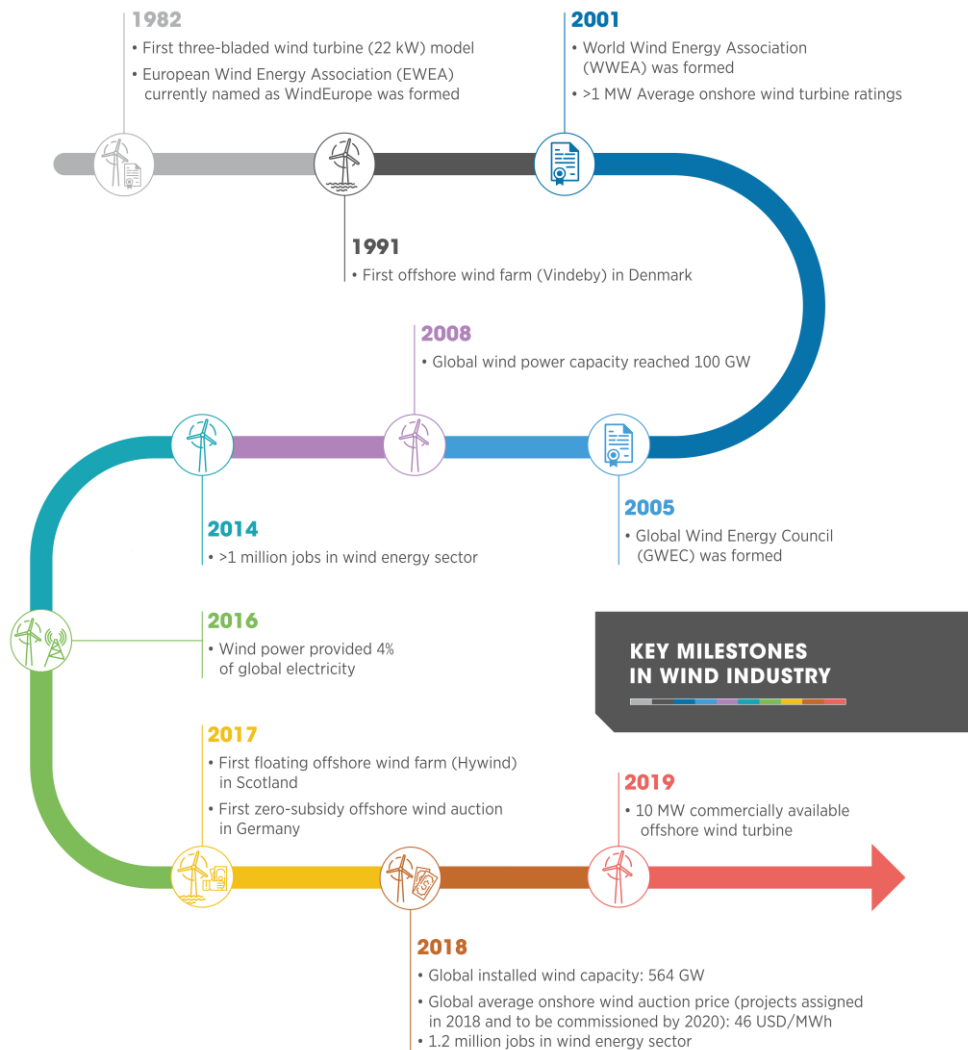


Figure 1.1: Overview of the key milestones in wind power industry since 1982 (IRENA, 2019).

However, the constant expansion of large wind farm installations, in combination with several technical, economic and social limitations, has caused a considerable reduction in the available sites with high quality wind resources (Mathew *et al.*, 2016). Therefore, exploiting the full wind potential, increasing the wind generation share and eventually, meeting the future energy targets, call for the development of innovative and more versatile wind energy conversion systems that are capable of operating effectively in unconventional installation sites and under poor wind conditions, such as those usually encountered within the urban environment (Dighe, 2020).

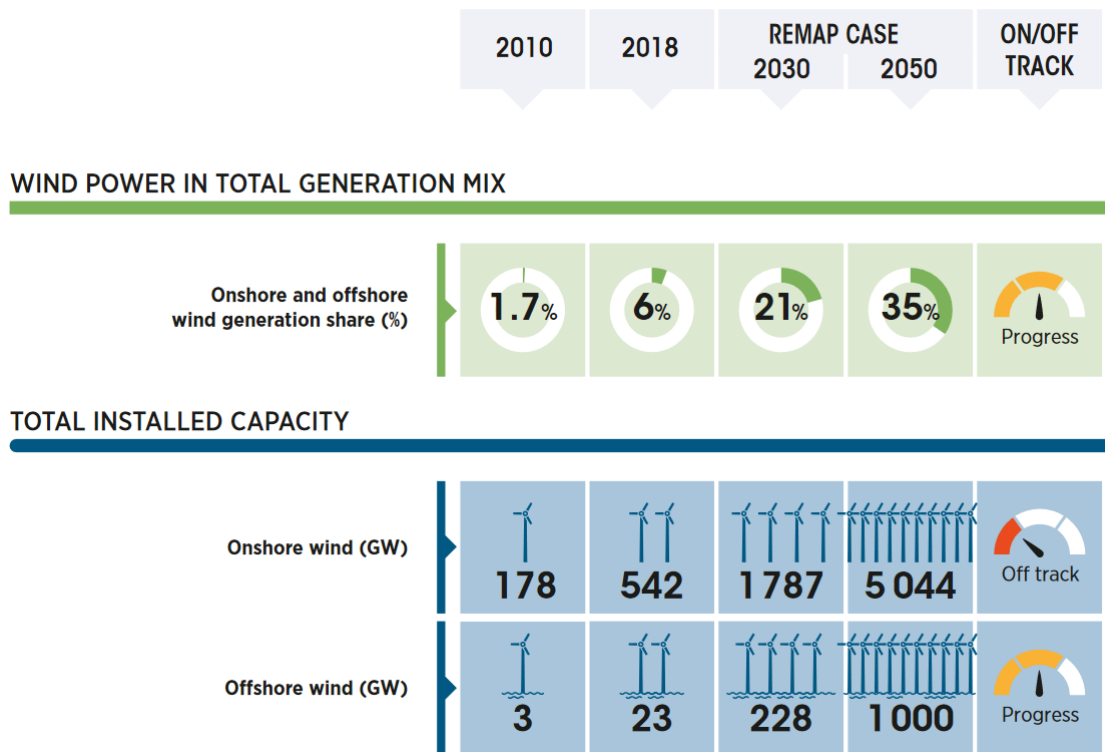


Figure 1.2: The IRENA's wind roadmap to 2050 (REmap). The target values of wind generation share and total installed capacity, in order to achieve the global energy transformation (IRENA, 2019).

Against this background, **shrouded or diffuser-augmented wind turbines** (also abbreviated as DAWTs) have recently attracted renewed attention from the international engineering community, and have become a significant part of the current research agendas, since they represent a promising solution for improving the efficiency and economic feasibility of power production from low energy density flows (Nunes *et al.*, 2020). The fundamental concept characterizing the operation of these wind energy concentrators can be summarized on the addition of a static diffuser around the rotor, which essentially serves as a mechanism to control the expansion of the wake, and create a region of high subatmospheric pressure near the exit plane of the diffuser – a phenomenon that eventually results in augmenting the mass flow rate passing through the turbine (Hansen *et al.*, 2000). Consequently, under the condition of a well-designed diffuser, shrouded wind turbines have the ability to yield power performance coefficients well in excess of the Betz limit (Betz, 2013) and thus, to extract additional power from the wind, as compared to a conventional horizontal-axis wind turbine (HAWT) with the same rotor diameter (Leloudas *et al.*, 2018a). Figure 1.3 illustrates the full-scale prototype of Hummingbird H15 DAWT model designed by OGT Greentech Ltd, with a rated capacity of 15 kW, while Figure 1.4 presents the commercially available Halo 6 kW DAWT solution of Halo Energy, which was specifically designed to address the energy needs within the expansive telecom industry.



Figure 1.3: The full-scale prototypes of Hummingbird H15 DAWT model designed by OGT Greentech Ltd, with a rated capacity of 15 kW [Source: <https://www.omnilinkgreentech.com>].

In contrast to their conventional and larger counterparts, shrouded wind turbines provide a considerably higher level of flexibility, both in terms of required space and wind speed conditions (van Dorst, 2011). Therefore, they could possibly be integrated within a much broader spectrum of rural and remote areas (Zhu *et al.*, 2019), operating either in a stand-alone mode or in combination with other small-scale energy solutions – for example, within the context of a distributed energy system (Evans *et al.*, 2020) – not only for on-grid but also for off-grid power generation, usually directly where the power is required, rather than where the wind is most favourable. In addition to that, the casing of the rotor has been proved to drastically reduce the emitted noise levels, the danger from broken blades and the sensitivity of the turbine to turbulence (Phillips, 2003). Hence, these wind energy conversion systems could form an attractive solution for urban or residential applications as well, especially in terms of direct small-scale energy production (Dighe, 2020).



Figure 1.4: The commercial Halo 6 kW model of Halo Energy [Source: <https://www.halo.energy>].

In summary, shrouded wind turbines represent a potentially efficient energy solution that could improve the feasibility of renewable energy production in regions with small wind potential, and eventually enable significant opportunities for more geographic dispersion of

wind technology applications, growth in distributed energy deployments and further expansion of renewable energy utilization on a global scale (Evans *et al.*, 2020; Yang *et al.*, 2019). Even though their ability to result in acceptable levels of energy production cost (levelized cost of energy – LCoE) had been the subject of severe criticism for many years, mainly because of the Vortec Energy collapse in the early 2000s, the recent success stories of several companies across the world, such as the Halo Energy, proves that shrouded wind turbines could actually form a sustainable energy option, and finally reach broad commercialization. Yet, the achievement of a widely adopted implementation and the consolidation of this promising technological application in the renewable energy market can only be realized on the condition of highly efficient designs. Consequently, the development of effective computational tools and optimization methodologies, applicable to shrouded or diffuser-augmented wind turbines, still remains of major importance.

1.2 Aims and Objectives

The primary aim of the current doctoral dissertation involves the development and validation of effective computational tools and numerical methodologies for, but not restricted to, the aerodynamic analysis, performance prediction and shape optimization of diffuser-augmented wind turbines. In this direction, the following objectives, which are schematically illustrated in Figure 1.5, have been accomplished:

- Development and validation of a computational **Blade Element Momentum (BEM) code**, for the aerodynamic analysis and power output prediction of both conventional (unshrouded) horizontal-axis wind turbine and diffuser-augmented wind turbine rotors (see Chapter 2 and Chapter 3).
- Development and validation of an **axisymmetric Reynolds-Averaged Navier-Stokes (RANS) solver** – named IGal2D – for the numerical prediction of incompressible fluid motion that involves swirling (see Chapter 4 and Chapter 5).
- Development and validation of an **axisymmetric RANS - BEM model**, which relies on the combination of the in-house BEM and IGal2D codes, for the simultaneous prediction of the wind turbine rotor performance and surrounding flow characteristics (see Chapter 8).
- Development of a **computational tool** for the **parameterization and deformation of two-dimensional grids** (mesh morphing), based on Free-Form Deformation (FFD) technique (see Section 9.2).

- Development, validation, and application of a complete **optimization framework for the design of diffuser-augmented wind turbines**, which combines the aforementioned computational tools with an asynchronous and meta-model assisted Differential Evolution (DE) algorithm (see Chapter 9 and Chapter 10).
- Finally, this doctoral dissertation features the design and aerodynamic evaluation of a **low-Reynolds number airfoil family**, for the entire blade span of small wind turbines, aiming to reduce the effects related to laminar separation, improve startup response, and meet acceptable levels of structural integrity (see Chapter 6 and Chapter 7).

A Design Optimization Framework for Diffuser-Augmented Wind Turbines

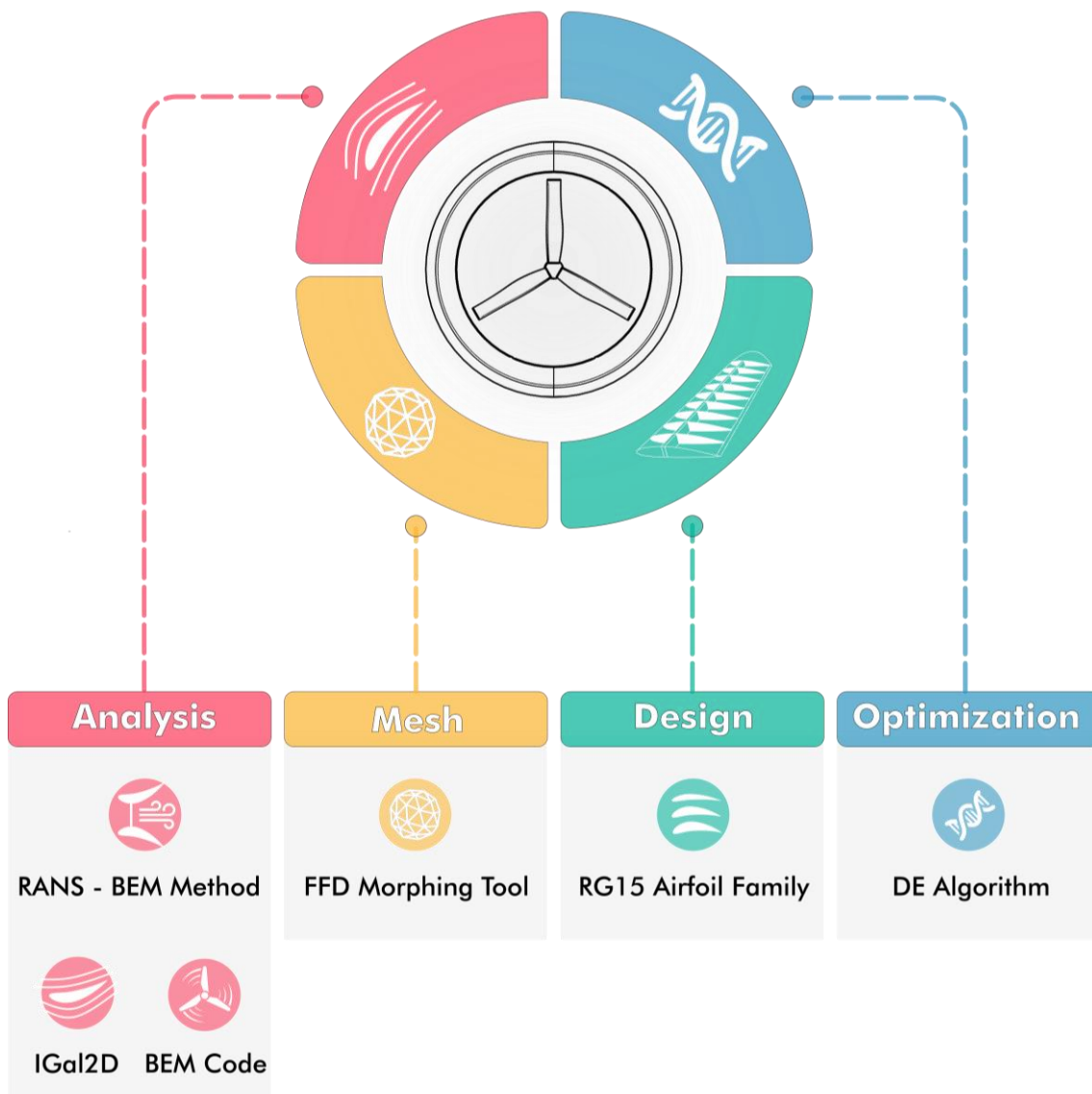


Figure 1.5: The main objectives of the current doctoral dissertation.

1.3 Physics of Shrouded Wind Turbines

The process of extracting mechanical power from the wind is inherently related to the application of a thrust force on the primary mass flow, pointing in the upwind direction (Hansen *et al.*, 2000). In terms of horizontal-axis wind turbines, the corresponding thrust force is the direct outcome of the static pressure drop across the rotor plane, which in turn is induced by the rotation of the blades. Ultimately, the aerodynamic power output can be calculated by multiplying the mass flow rate through the rotor with the corresponding pressure drop (Manwell *et al.*, 2010). At first glance, the power output of the system could be increased by increasing the thrust force and the associated pressure drop; however, that would also result in decreasing the mass flow rate through the rotor. Therefore, yielding the maximum power coefficient, that is the ratio between the rotor power output and the total wind energy input, requires the proper compromise of the involved quantities. According to momentum theory, the optimal operating conditions for an unshrouded horizontal-axis wind turbine dictate that the axial velocity component at the rotor plane should equal to $2/3$ of the ambient wind velocity, and the dimensionless thrust coefficient should equal to $8/9$ (Manwell *et al.*, 2010). Under these conditions, the power coefficient takes its maximum theoretical value, which is widely known as the Betz limit (Betz, 2013). In practice, the Betz limit indicates that the maximum energy amount that an unshrouded horizontal-axis wind turbine can extract from the wind equals to 59.3 percent of the total energy contained within the stream tube passing through the rotor (see Section 2.1.1). The energy extraction scheme for a conventional horizontal-axis wind turbine is illustrated in Figure 1.6.

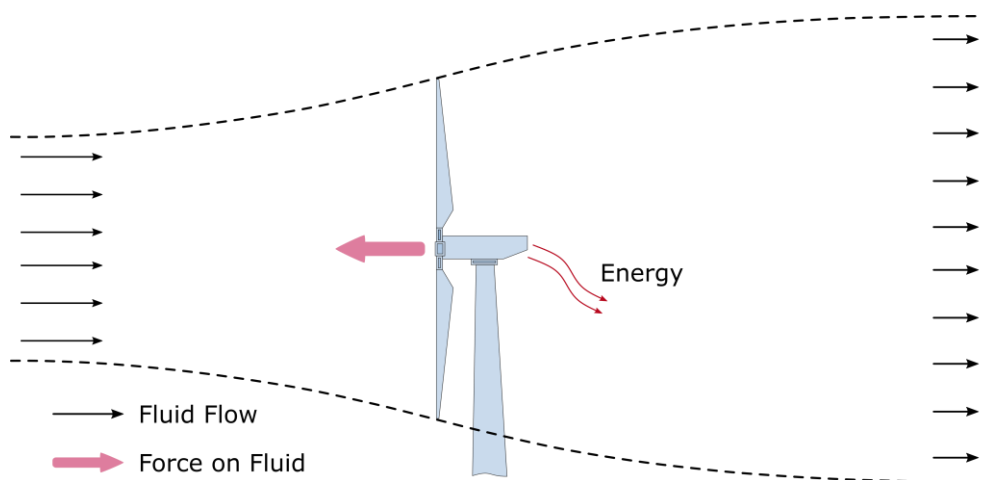


Figure 1.6: The energy extraction scheme for a conventional horizontal-axis wind turbine.

Evidently, the Betz limit represents a natural barrier within the power extraction process. However, under the presence of mechanism that increases the mass flow rate through the

rotor, the Betz limit could be exceeded. According to the study of van Holten (1981), enhancing the mass flow rate through the rotor can be achieved by means of two separate mechanisms. The first augmentation mechanism relies on the application of a cross-wind force on the primary mass flow (see Section 1.3.1), while the second one is based on mixing the wake and the external flow behind the rotor, in sub-atmospheric pressure (see 1.3.2).

1.3.1 Cross-Wind Force Mechanism

At first, let us recall that according to momentum theory, the axial velocity component over the rotor plane for an unshrouded horizontal-axis wind turbine that operates at the Betz limit equals to $2/3$ of the ambient wind velocity (Manwell *et al.*, 2010). Therefore, under the assumptions of incompressible fluid motion and no mass flow crossing the lateral boundary of the stream tube passing through the rotor, the continuity equation implies that the far upstream cross-sectional area of the reference stream tube should equal to $2/3$ of the rotor swept area; in other words, when the rotor operates at the Betz limit, it basically captures the kinetic energy contained in the wind, from an effective surface that is $2/3$ of the rotor swept area (Ten Hoopen, 2009). A detailed application of momentum theory for unshrouded horizontal-axis wind turbines can be found in Section 2.1.1.

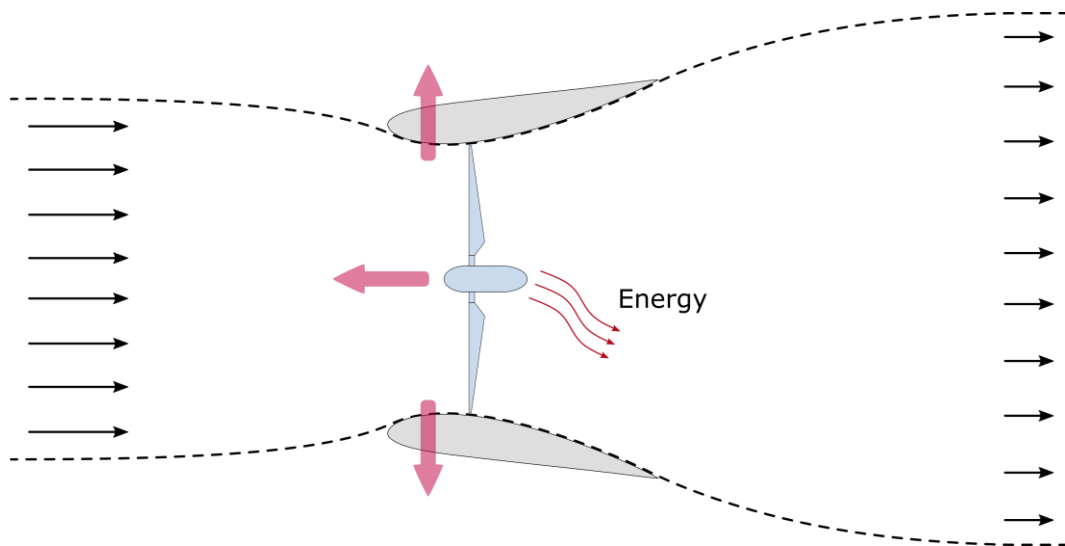


Figure 1.7: Schematic representation of the diffuser-augmented wind energy extraction scheme.

One of the available mechanisms to increase the effective area of the reference stream tube, as well as the mass flow rate through the rotor, relies on the application of a force perpendicular to the primary mass flow (van Holten, 1981). In practice, this perpendicular force can be realized by placing an annular lifting device – for example, a shroud or a diffuser

– around the rotor, with its suction side pointing towards the hub. Now, according to the third law of Newton, the mass within the reference stream tube will naturally exert a reaction force on the lifting device, in order to achieve a force equilibrium; a schematic representation of the described situation is provided in Figure 1.7. However, this reaction force can only be exerted by the flow, if more air mass is enforced to pass through the annular lifting device. Consequently, the ultimate effect of placing a diffuser or shroud around the rotor can be summarized on augmenting the effective area of the reference stream tube, and thus, the mass flow rate.

From a different standpoint, the augmented levels of mass flow rate through the rotor of a shrouded wind turbine could also be described by means of vortex theory (Ten Hoopen, 2009). To this end, let us consider a shroud geometry in the shape of a simple annular airfoil, with the suction or convex side pointing towards the rotor hub, similar to the one illustrated in Figure 1.7. Eventually, such an annular airfoil apparatus will cause – like any airfoil configuration – the air flow in the suction side, which in this case represents the internal surface of the shroud, to accelerate. Evidently, the levels of pressure suction and flow acceleration are tightly related to the lift force generated by the airfoil and therefore, according to the Kutta-Joukowski theorem, to the bound vorticity on the airfoil surface. Essentially, the inward radial force generated by the airfoil is accompanied by a ring vortex, which in turn, according to the Biot-Savart law, will induce a higher velocity on the suction surface. Ultimately, these higher velocity levels increase the mass flow rate through the wind turbine rotor; the bound vorticity increases the effective area of the stream tube in front of the rotor and consequently, the volumetric flow capability (also termed as swallowing capacity) of the wind turbine (Ten Hoopen, 2009).

1.3.2 Mixing of the Wake and the External Flow Mechanism

In addition to the first augmentation mechanism, described in Section 1.3.1, the operation of modern shrouded wind turbines is also characterized by mixing effects between the rotor wake and the external flow (van Holten, 1981) – a momentum transfer mechanism that eventually results in higher mass flow rates and power augmentation levels. In order to explain the fundamentals of the second augmentation mechanism, let us initially consider the flow situation behind the rotor. When a wind turbine rotor extracts energy from a moving fluid stream, it will induce – like every other obstacle in a flow – a wake; the wake field behind the rotor is characterized by both a static pressure and a velocity deficit, as compared to the undisturbed flow stream. Even though a low pressure region behind the rotor is favourable, this is not the case for the low wake velocity. According to the study of Igra (1981), the power augmentation obtained by a shrouded wind turbine is a direct outcome of the subatmospheric

pressure at the exit plane of the shroud. Therefore, an ideal situation, in terms of power production, would be that in which the pressure behind the rotor is low and the mass flow rate still high.

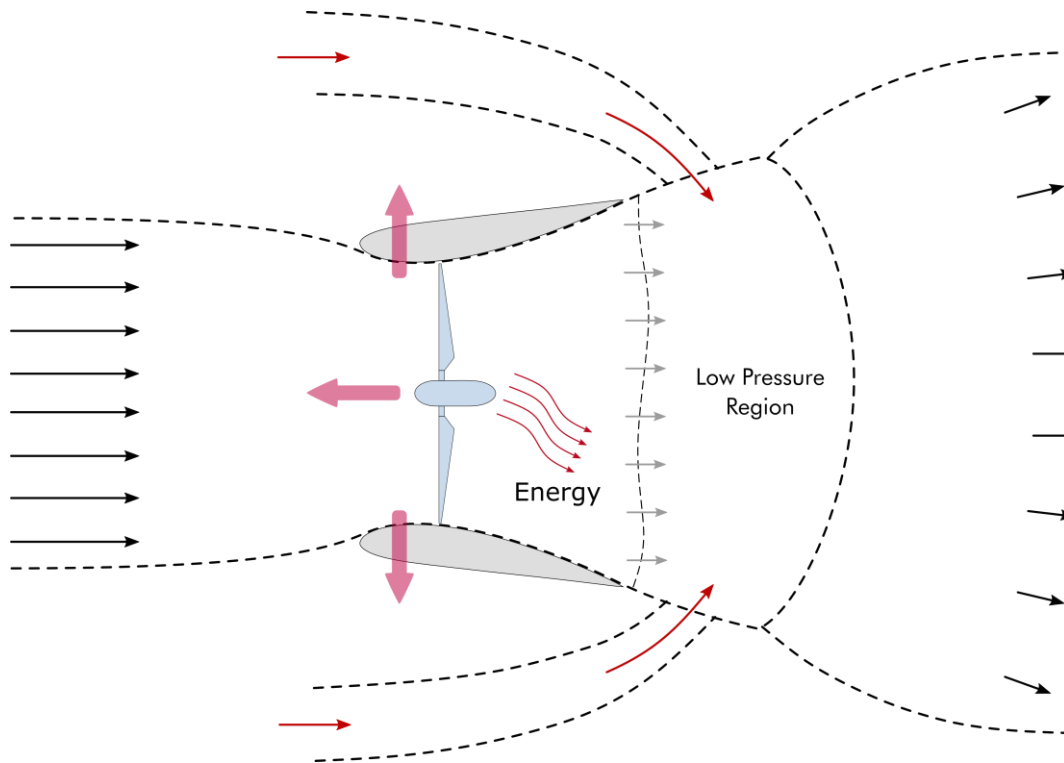


Figure 1.8: Schematic representation of the diffuser-augmented wind energy extraction scheme, combined with wake and external flow mixing.

In practice, increased levels of mass flow rate can be achieved either by means of wake expansion or by increasing the wake velocity (Lilley and Rainbird, 1956). The fundamental concept underlying the second augmentation mechanism is actually based on restoring the momentum deficit behind the rotor, by mixing the wake flow with the undisturbed flow stream, as schematically illustrated in Figure 1.8; the undisturbed flow will in turn provide the extra momentum for the rotor wake flow to recover from the velocity deficit, caused by the energy extraction process. Moreover, another reasoning behind the present augmentation mechanism is that the mixing effect between the rotor wake and the external flow will eventually cause the wake to have an additional expansion and thus, providing the rotor wake flow with more volume. Apparently, increased wake volume levels for the same mass flow rate through the shroud will result in lower exit pressure behind the rotor and therefore, more suction (Ten Hoopen, 2009).

1.4 Shrouded Wind Turbines – A Brief Research Review

The basic theoretical background of shrouded or diffuser-augmented wind turbines was originally established by Lilley and Rainbird (1956) during the 1950s, by means of axial or one-dimensional momentum theory, while the first experimental investigations were conducted by Kogan and Nissim (1962), Kogan and Seginer (1962, 1963), Igra (1976, 1977, 1981), Gilbert and Foreman (1979, 1983), Foreman and Gilbert (1983), Gilbert *et al.* (1978) and Oman *et al.* (1977). In addition, Igra (1977) and Foreman *et al.* (1978) devised some useful theoretical models as well, which were based on one-dimensional momentum theory, aiming to analyze the obtained experimental data and prove the ability of diffuser-augmented wind turbines to exceed the Betz limit. Recently, these early models were upgraded by Khamlaj and Rumpfkeil (2017); according to these latter researchers, the improved semi-empirical formulas that they proposed have been proved quite effective, especially during the preliminary design stage of shrouded rotors. In brief, the most important outcome of these initial studies was a remarkable reduction in the length-to-diameter ratio of the back then shroud designs – a parameter tightly associated with cost – by simultaneously maintaining high augmentation values. This is mainly attributed to the exploitation of several innovative approaches for that certain period of time; these include the replacement of straight-wall diffusers with high-lift producing annular airfoils (Igra, 1981), the application of boundary layer control techniques (Gilbert *et al.*, 1978) and the substitution of exit flaps with exit flanges (Loeffler, 1981). In summary, these investigations provided a much deeper understanding of the fundamental principles governing shrouded wind turbines. Therefore, they succeeded to establish some valuable preliminary design criteria, such as low static pressure at the exit plane of the shroud, high velocity acceleration over the rotor plane, minimum drag levels, and large pressure recovery.

Around the same period, significant research on the development of effective computational models has been reported as well. In particular, Fletcher (1981) developed a low-fidelity computational model, based on the blade element theory, by introducing two empirical parameters – namely, the diffuser efficiency and the diffuser exit pressure coefficient – in order to include the effect of the diffuser within the rotor analysis. In addition, Fletcher (1981) enriched the particular model by the addition of wake rotation and blade Reynolds number effects; thus, he achieved a good agreement between the computational results and the experimental data, in terms of the turbine power coefficient and axial velocity. Furthermore, significant research was carried out by Koras and Georgalas (1988) and Georgalas *et al.* (1991). These latter studies were mostly focused on evaluating the influence of several geometrical characteristics of wing shaped shrouds, including the angle of attack, the chord length and the maximum camber, on the power output of the turbine. Eventually, by applying the lifting line theory, and by representing the shroud geometry as a superposition

of source and vortex rings, Koras and Georgalas (1988) reached to the conclusion that power output increases linearly with the chord length and the angle of attack. Later on, Phillips (2003) proposed a modified Blade Element Momentum (BEM) model, by introducing an empirically-derived formula for calculating the radial distribution of the axial velocity component over the rotor plane. That simplified computational model – along with high-fidelity Computational Fluid Dynamics (CFD) simulations and wind tunnel experiments – was then extensively applied during a research program on a full-scale prototype built by Vortec Energy Limited (Phillips *et al.*, 1999); that was the first private company that attempted to commercialize the diffuser-augmented wind turbine concept. Nevertheless, the particular prototype failed to achieve an accepted LCoE, mostly because of the intense flow separation phenomena and the heavy supportive structures required to endure the expected loads. Thus, unfortunately, the aftermath of the subsequent collapse of Vortec Energy Limited, and the economic aspects associated with the high cost of the shroud, led to the disappearance of shrouded wind turbines from the back then research agendas (Khamlaj and Rumpfkeil, 2017).

However, in recent years, there has definitely been renewed interest in shrouded wind turbine applications, along with substantial attempts towards commercialization (Khamlaj and Rumpfkeil, 2017). In this context, Hansen *et al.* (2000) performed a numerical study to explore the impact of placing a diffuser around a wind turbine. By using momentum theory and CFD simulations, they demonstrated that power augmentation is proportional to the increased mass flow rate passing through the rotor. A similar momentum analysis was also carried out by van Bussel (1999); this study indicated that the optimal thrust coefficient of a shrouded wind turbine is equal to $8/9$, as exactly for the case of conventional (unshrouded) horizontal-axis wind turbines. The same value for the optimal thrust coefficient was later suggested by Jamieson (2009), who employed an ideal limiting model, based on a generalization of one-dimensional momentum theory. Eventually, van Bussel (1999) reached to similar conclusions with Hansen *et al.* (2000), as he reported that power augmentation is proportional to the increased mass flow rate, while he emphasized on the necessity of substantially reducing the back pressure, in order to achieve power performance coefficients far beyond the Betz limit.

In view of the preceding literature review, it is evident that momentum or actuator disk theory has always been a valuable tool for the analysis and preliminary design of shrouded wind turbines. Yet, this simplified model lacks the ability to estimate the system's performance for a prescribed value of thrust coefficient and a given shroud geometry (Bontempo and Manna, 2016). Therefore, in efforts to address the limitations of classical momentum theory, as well as those of other linearized and simplified models, Bontempo and Manna (2013, 2014, 2016) recently devised an accurate nonlinear and semi-analytical actuator disk theory. That model was capable of taking under consideration the shape of the examined shroud and

accounting for the interaction between the shroud and the rotor, the slipstream rotation and the non-uniform distribution of thrust over the rotor plane. Subsequently, Bontempo and Manna (2016) applied this nonlinear theory to investigate the impact of thrust coefficient and shroud's camber on power output; according to their findings, the increase of shroud's camber favours the overall system performance.

Further computational investigations were reported by Bet and Grassmann (2003); in fact, they used CFD simulations to assess the potential of a shrouded wind turbine with a wing profiled diffuser, while Grassmann *et al.* (2003) carried out an experimental study on this particular design. The experimental results revealed that power output augmentation could reach 1.55 and 2, for high and low wind speeds respectively. In addition, Wang F. *et al.* (2008) investigated the possibility of improving wind energy harvesting under low wind speed conditions in built-up areas. In this direction, they employed experimental tests and CFD computations to evaluate the effect of a converging-diverging nozzle on the power output of a small wind turbine for domestic use in such locations. Later on, Aranake *et al.* (2015) assessed numerically the performance of several shroud configurations, based on the criterion of highest mass flow rate. According to Aranake *et al.* (2015), the improvement in power extraction beyond the unshrouded wind turbine was substantial, even for particularly low wind speeds. Ultimately, they concluded their study by supporting the fact that the concept of diffuser-augmented wind turbine could actually form a promising alternative for sustainable energy production under low wind speed regimes.

A considerable number of studies have been also focused on the practice of using a brimmed or flanged diffuser. The most representative works on this concept were made by Abe and Ohya (2004), Ohya and Karasudani (2010), Kosasih and Tondelli (2012), Kardous *et al.* (2013), Mansour and Meskinkhoda (2014), Toshimitsu *et al.* (2008) and Takahashi *et al.* (2012). The majority of these studies indicated that the low pressure area and the strong vortex formation caused by the presence of the flange could increase the wind speed approaching the turbine by a factor ranging up to 2.6. Moreover, Abe and Ohya (2004) identified the turbine loading and the opening angle of the diffuser as the parameters with the highest impact on the overall performance. In particular, they suggested that low-loaded turbines, the elimination of large flow separations and the conservation of high pressure recovery, could significantly improve the power output levels.

Lately, Rio Vaz *et al.* (2014) proposed an extension to the classical BEM theory, and developed a modified BEM model of low computational cost, for the rotor analysis of shrouded wind turbines. The accuracy of the particular computational model was successfully validated, against both numerical and experimental data, by Leloudas *et al.* (2017), while a similar model was subsequently utilized by Vaz and Wood (2016) and Leloudas *et al.* (2018a,

2019a) for the aerodynamic optimization of diffuser-augmented wind turbine blades. Besides, several additional optimization schemes have been recently developed and successfully applied for the design of improved shrouded wind turbines (Alpman, 2018; Aranake and Duraisamy, 2017; Bagheri-Sadeghi *et al.*, 2018; Dighe, 2020; Foote and Agarwal, 2013; Khamlaj and Rumpfkeil, 2018; Leloudas *et al.*, 2018a, 2018b, 2019a, 2020a; Liu J. *et al.*, 2016; Oka *et al.*, 2014, 2016; Sorribes-Palmer *et al.*, 2017; Venters *et al.*, 2018). These optimization methodologies can be generally classified into three main categories: (i) those that exclusively involve the design of the shroud – either by imposing a predetermined turbine loading (Foote and Agarwal, 2013; Venters *et al.*, 2018) or even by considering an unloaded shroud configuration (Leloudas *et al.*, 2018b, 2020a; Liu J. *et al.*, 2016); (ii) those that investigate the rotor design for a given and fixed shroud geometry (Leloudas *et al.*, 2018a, 2019a); and finally, (iii) those exploring the simultaneous optimization of the coupled rotor/shroud system (Alpman, 2018; Aranake and Duraisamy, 2017; Khamlaj and Rumpfkeil, 2018; Oka *et al.*, 2014, 2016). Among the aforementioned approaches, the latter has been generally considered as the most effective one, while the individual optimization of the shrouded wind turbine components could possibly lead to sub-optimal solutions, as characteristically reported by Khamlaj and Rumpfkeil (2018). This is mainly attributed to the fact that the flow field inside the diffuser, and therefore, its overall aerodynamic performance, are strongly dependent upon the presence and the geometrical characteristics of the rotor blades. In particular, the circumferential velocity component that is induced by the rotating turbine blades has the tendency to suppress possible flow recirculation in the downstream diffuser wall, while the pressure drop across the rotor causes a natural tendency of the pressure to recover, and the wake to expand (Hjort and Larsen, 2015). Eventually, these flow features could result in increasing the mass flow rate and the power output performance. Therefore, as Khamlaj and Rumpfkeil (2018) suggested, it is vital that the aerodynamic optimization of the shroud and rotor blades are simultaneously performed, in order to achieve a highly performing shrouded wind turbine design.

Finally, significant research on shrouded wind turbines was also made by Venters *et al.* (2018), who explored the influence of several design parameters (thrust coefficient, angle of attack, rotor gap and axial position of the rotor) on power output. Among the examined ones, thrust coefficient was found as the parameter with the greatest impact on power output. In addition, Venters *et al.* (2018) highlighted that the optimal angle of attack of the shroud was much larger than the separation angle of attack for the corresponding airfoil in a freestream, as well as that large angles of attack did not necessary induce flow separation within the shroud, since the swirling velocity induced by the rotor helps to energize the boundary layer of the internal diffuser wall and maintain the flow attached. Conclusively, this work indicated that shrouded wind turbines are capable of exceeding the Betz limit, even if the power coefficient is calculated based on the exit area of the shroud. In line with Venters *et al.* (2018),

Alpman (2018) noted that the pressure drop across the rotor would delay flow separation within the diffuser; however the optimal designs obtained from this study failed to overcome the Betz limit, when the power coefficient was calculated based on the exit area of the shroud.

1.5 Thesis Outline

The remaining part of the current doctoral dissertation has been organized as follows:

Chapter 2 – The first part of this chapter, namely Section 2.1, describes the application of axial momentum theory for both conventional horizontal-axis and diffuser-augmented wind turbine rotors, while the second part, namely Section 2.2 and 2.3, provides a detailed overview on the theoretical background and the major features of an in-house BEM code, which was entirely developed in the context of the present doctoral dissertation.

Chapter 3 – This chapter provides a detailed validation study on the overall performance of the in-house BEM solver presented in Chapter 2. To this end, several benchmark cases have been selected, including both conventional horizontal-axis wind turbine (Section 3.1) and shrouded wind turbine (Section 3.2) rotors. The results of the current BEM simulations are compared against both numerical and experimental data available in the literature, as well as against the results obtained from the well-known QBlade software.

Chapter 4 – This chapter describes the development of an in-house developed RANS solver, named IGal2D, for the numerical prediction of incompressible axisymmetric flows involving swirling. In particular, Section 4.1 provides a general introduction into axisymmetric swirling flows, as well as the incentives for the development of IGal2D solver, while Section 4.2 presents the adopted form of the governing equations, defining the flow and turbulence models. Finally, the remaining sections of the current chapter outline the numerical methodology underlying the IGal2D solver, emphasizing on the spatial and temporal discretization schemes, the flux evaluation approaches, and the source term treatment.

Chapter 5 – This chapter aims to provide a detailed evaluation study on the numerical accuracy and performance of the in-house developed IGal2D solver. For this purpose, several incompressible and axisymmetric flows are considered, including both non-swirling (see Section 5.1) and swirling (see Section 5.2) regimes. The simulation results are compared against analytical, numerical and experimental data.

Chapter 6 – This chapter features a new low-Reynolds number airfoil family for the entire blade span of small horizontal-axis wind turbines, aiming to reduce the effects related to laminar separation, improve startup response and meet acceptable levels of structural integrity. The proposed RG15 low Reynolds airfoil family consists of six airfoil profiles of varying relative thickness, which were designed by increasing the thickness distribution of RG15 airfoil up to 50% and adopting a rounded trailing edge, with a diameter equal to 1% of the chord length.

Chapter 7 – This chapter involves the aerodynamic performance evaluation of the entire low Reynolds RG15 airfoil family. In order to obtain the aerodynamic characteristics of the involved airfoils, both the well-known XFOIL code and the in-house developed IGal2D solver are employed.

Chapter 8 – This chapter features the development and numerical validation of an axisymmetric RANS - BEM model, which relies on the combination of the in-house BEM and IGal2D codes, for the simultaneous prediction of the wind turbine rotor performance and surrounding flow characteristics. In particular, the first part of the current chapter provides an implementation overview of the coupled RANS - BEM model, while the second part includes a detailed validation study on the proposed methodology.

Chapter 9 – This chapter describes a modular optimization framework for the aerodynamic shape optimization of shrouded wind turbines, which combines the analysis tools developed within the current study, with a parallel and asynchronous version of a meta-model assisted Differential Evolution (DE) algorithm. The first part of this chapter (Section 9.1) outlines the major features of the in-house developed surrogate-assisted DE algorithm, employed as the optimizer. The particular asynchronous and parallel version of the current algorithm was developed at the Turbomachinery and Fluid Dynamics laboratory in the context of the doctoral dissertation of Giorgos A. Strofylas. Subsequently, Section 9.2 describes the development of a mesh parameterization and deformation tool that is based on Free-Form Deformation (FFD), while the last part of the current chapter (Section 9.3) provides an overview of the proposed optimization framework.

Chapter 10 – This chapter presents the application of the proposed optimization framework to the design of improved diffuser-augmented wind turbines.

Chapter 11 – Finally, this chapter summarizes the principal conclusions of the current doctoral dissertation. In particular, Section 11.1 provides a concise recap of the entire

study, focused on the most significant results and contributions, while Section 11.2 indicates possible directions for further research on the specific topic.

At this point, please note that, excluding Introduction and Conclusions chapters, the current doctoral dissertation has been divided into five thematic units that can, in one way or another, also be read independently. Nevertheless, they are part of a bigger storyline, illustrated in Figure 1.9.

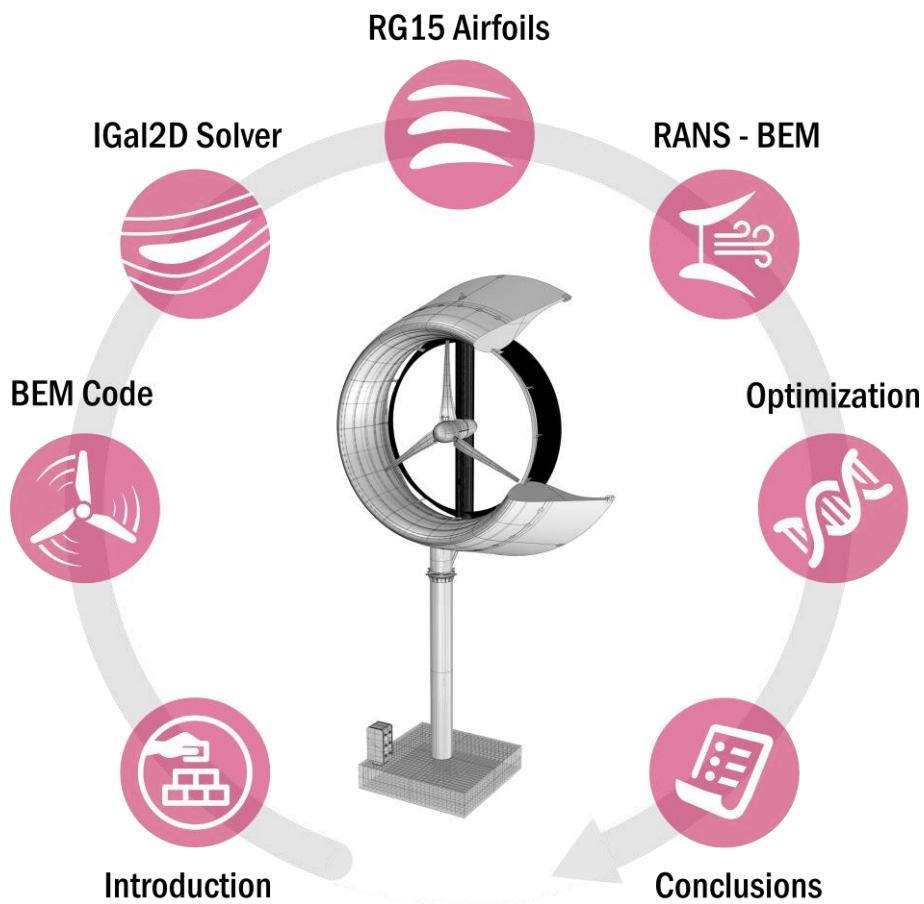


Figure 1.9: The storyline of the current doctoral dissertation.

1.6 Contributions

Considering similar studies available in the literature, the most significant contributions of this doctoral dissertation can be summarized as follows:

- The design and aerodynamic evaluation of a new low Reynolds airfoil family for the entire blade span of small horizontal-axis wind turbines, based on the RG15 airfoil (Leloudas *et al.*, 2019b, 2020b).

- The behavior investigation of the recirculation area behind the rounded trailing edge of the newly introduced RG15 airfoils for different angles of attack. In addition, this study involves the impact examination of the thickness-to-chord ratio on the separation bubbles near the leading edge of the RG15 airfoils (Leloudas *et al.*, 2020).
- The development and validation of an in-house Blade Element Momentum code for the performance prediction of shrouded wind turbines (Leloudas *et al.*, 2017).
- The development and numerical assessment of an academic flow solver that combines the artificial compressibility technique with the axisymmetric RANS equations for the accurate prediction of incompressible fluid motion that involves swirling (Leloudas *et al.*, 2018b, 2021).
- The detailed description of the convective flux Jacobian and the entire eigenvector system, used within Roe's approximate Riemann solver (Leloudas *et al.*, 2021).
- The development and application of a versatile computational framework for the aerodynamic shape optimization of diffuser-augmented wind turbines, which combines an asynchronous and meta-model assisted Differential Evolution algorithm with the currently developed analysis tools (Leloudas *et al.*, 2020).

1.7 List of Related Publications

The research findings of this dissertation have contributed to the following publications:

A. International Journals

1. Nikolos, I.K., Lygidakis, G.N., Leloudas, S.N., Tavla, S., "Application of B-spline Basis Functions as Harmonic Functions for the Concurrent Shape and Mesh Morphing of Airfoils", *GPPS Journal* (Accepted).
2. Leloudas, S.N., Lygidakis, G.N., Delis, A.I. and Nikolos, I.K. (2022), "Design Optimization of Shrouded Wind Turbines Using an Axisymmetric RANS-BEM Method and a Differential Evolution Framework", *SSRN Electronic Journal*. <https://www.doi.org/10.2139/ssrn.4014185>.
3. Leloudas, S.N., Lygidakis, G.N., Delis, A.I. and Nikolos, I.K. (2021), "An Artificial Compressibility Method for Axisymmetric Swirling Flows", *Engineering Computations*, Vol. 38, No. 10, pp. 3732-3767. <https://www.doi.org/10.1108/EC-10-2020-0594>.

4. Leloudas, S.N., Eskantar, A.I., Lygidakis, G.N. and Nikolos, I.K. (2020), "A Robust Methodology for the Design Optimization of Diffuser Augmented Wind Turbine Shrouds", *Renewable Energy*, Vol. 150, pp.722-742. <https://www.doi.org/10.1016/j.renene.2019.12.098>.
5. Leloudas, S.N., Eskantar, A.I., Lygidakis, G.N. and Nikolos, I.K. (2020), "Low Reynolds Airfoil Family for Small Horizontal Axis Wind Turbines Based on RG15 Airfoil", *SN Applied Sciences*, Vol. 2, No. 3. <https://www.doi.org/10.1007/s42452-020-2161-1>.
6. Leloudas, S.N., Strofylas, G.A. and Nikolos, I.K. (2018), "Constrained Airfoil Optimization Using the Area-Preserving Free-Form Deformation", *Aircraft Engineering and Aerospace Technology*, Vol. 90, No. 6, pp. 914-926. <https://doi.org/10.1108/AEAT-10-2016-0184>.

B. Proceedings of International Conferences

1. Leloudas, S.N., Lygidakis, G.N., Delis, A.I. and Nikolos, I.K. (2022), "Optimization of a Diffuser-Augmented Wind Turbine Utilizing a Differential Evolution Software and an Axisymmetric RANS-BEM Solver", *Proceedings of Global Power and Propulsion Society, GPPS Chania22*, 12-14 September 2022, Chania, Greece. <https://doi.org/10.33737/gpps22-tc-22>.
2. Nikolos, I.K., Lygidakis, G.N., Leloudas, S.N. and Tavla, S. (2022), "Application of B-Spline Basis Functions as Harmonic Functions for the Concurrent Shape and Mesh Morphing of Airfoils", *Proceedings of Global Power and Propulsion Society, GPPS Chania22*, 12-14 September 2022, Chania, Greece. <https://doi.org/10.33737/gpps22-tc-9>.
3. Lygidakis, G.N., Leloudas, S.N., Delis, A.I. and Nikolos, I.K. (2020), "Prediction of Turbulent Axisymmetric Flows Using an Artificial Compressibility Approach", *Proceedings of Global Power and Propulsion Society, GPPS Chania20* (Online Conference), 7-9 September 2020, Chania, Greece. <https://doi.org/10.33737/gpps20-tc-98>.
4. Leloudas, S.N. and Nikolos, I.K. (2019), "Design of a Low Reynolds Airfoil Family for Small Horizontal Axis Wind Turbine Applications Based on the RG15 Airfoil", *Proceedings of the 7th European Conference on Renewable Energy Systems*, 10-12 June 2019, Madrid, Spain.
5. Leloudas, S.N., Eskantar, A.I. and Nikolos, I.K. (2019), "Design of a Low Reynolds Airfoil Family for Small Horizontal Axis Wind Turbine Applications Based on the RG15 Airfoil", *Proceedings of the 7th European Conference on Renewable Energy Systems*, 10-12 June 2019, Madrid, Spain.

6. Leloudas, S.N., Strofylas, G.A. and Nikolos, I.K. (2018), "Aerodynamic Shape Optimization of Diffuser Augmented Wind Turbine Shrouds Using Asynchronous Differential Evolution", *Proceedings of the ASME 2018 International Mechanical Engineering Congress and Exposition*, Pittsburgh, PA, USA, November 9–14, 2018. <https://doi.org/10.1115/IMECE2018-86820>.
7. Lygidakis, G.N., Leloudas, S.N. and Nikolos, I.K. (2018), "Applying a Radiative Heat Transfer Finite-Volume Methodology to a Geometrically Complex Furnace", *Proceedings of the ASME 2018 International Mechanical Engineering Congress and Exposition*, Pittsburgh, Pennsylvania, USA, November 9–14, 2018. <https://doi.org/10.1115/IMECE2018-86831>.
8. Klothakis, A.G., Lygidakis, G.N., Leloudas, S.N. and Nikolos, I.K. (2018), "Revisiting Rarefied Gas Experiments with Recent Simulation Tools", *Proceedings of the 7th European Conference on Computational Fluid Dynamics*, Glasgow, Scotland, United Kingdom, 11 – 15 June, 2018. <https://api.semanticscholar.org/CorpusID:199428794>.
9. Klothakis, A.G., Lygidakis, G.N., Leloudas, S.N. and Nikolos, I.K. (2018), "Rarefied Gas Flow Analysis Over a Re-entry Space Capsule Geometry", *Proceedings of the 9th GRACM International Congress on Computational Mechanics*, Chania, Greece, June 4-6, 2018. [ISBN 978-618-81537-5-2](https://doi.org/10.1115/IMECE2018-86820).
10. Leloudas, S.N., Strofylas, G.A. and I.K. Nikolos, (2018), "Aerodynamic Shape Optimization of Diffuser Augmented Wind Turbine Blades Using Asynchronous Parallel Differential Evolution", *Proceedings of the 9th GRACM International Congress on Computational Mechanics*, Chania, Greece, June 4-6, 2018. [ISBN 978-618-81537-5-2](https://doi.org/10.1115/IMECE2018-86820).
11. Leloudas, S.N., Lygidakis, G.N. and Nikolos, I.K. (2017), "Assessment of a Modified Blade Element Momentum Methodology for Diffuser Augmented Wind Turbines", *Proceedings of the ASME 2017 International Mechanical Engineering Congress and Exposition*, Volume 7: Fluids Engineering, Tampa, FL, USA, November 3–9, 2017. <https://doi.org/10.1115/IMECE2017-70288>.

Chapter 2

Development of a Blade Element Momentum Code

The first part of the current chapter, namely Section 2.1, describes the application of axial momentum theory for both conventional horizontal-axis and diffuser-augmented wind turbine rotors, while the second part, namely Section 2.2 and 2.3, provides a detailed overview on the theoretical background and the major features of an in-house BEM solver, which was entirely developed in the context of the present doctoral dissertation.

2.1 Momentum Theory

Momentum theory represents one of the oldest, yet most widely adopted, theoretical tools for the aerodynamic analysis and performance prediction of wind turbine rotors, which is essentially based on control volume integrals for mass and energy conservation, along with axial and angular momentum balances (Sørensen, 2012). The origins of momentum theory can be traced back to the studies of Rankine (1865) and Froude (1889). However, several improvements and generalizations have been proposed since then, widening its applicability and boosting its accuracy (Sørensen, 2016; van Kuik, 2020). In general, the fundamental concept underlying momentum theory is that the actual rotor geometry can be represented by an infinitely thin, frictionless and permeable actuator disc with the same diameter as the rotor (see Figure 2.1 and Figure 2.3); the actuator disc operates under the assumptions of steady, inviscid, incompressible and axisymmetric flow (Burton *et al.*, 2001; van Kuik *et al.*, 2015). Besides, in the simplest form of momentum theory, the actuator disc is also considered ideal; that is, the disc – except from being frictionless – does not induce any azimuthal (rotational or circumferential) velocity component in the wake field. In that case, the resultant theory is referred to as axial or one-dimensional momentum theory, in order to be distinguished from the so-called generalized momentum theory (Sørensen, 2016), which is capable of accounting for wake rotation effects (Manwell *et al.*, 2010). The following sections (namely, Section 2.1.1 and Section 2.1.2) outline the application of axial momentum theory for both conventional (unshrouded) horizontal-axis and shrouded or diffuser-augmented wind turbines. As these sections indicate, even though the axial momentum theory is based on several simplifying assumptions, it can eventually provide very useful insights on the optimal operating conditions of the rotor, while it forms the basis for the development of the well-known BEM theory (see Section 2.2), which is nowadays the standard computational model for design applications in wind turbine industry (Malki *et al.*, 2013).

2.1.1 Axial Momentum Theory for HAWTs

In this section, the fundamental concepts and equations forming the one-dimensional or axial momentum theory, for the case of a conventional (unshrouded) horizontal-axis wind turbine, are recalled. Initially, let us consider a control volume, in the form of a long stream tube with circular cross section – such the one illustrated in Figure 2.1 and Figure 2.2 – that passes through the rotor disc and extends in both upstream and downstream directions. Herein, the following notations are adopted; subscript (0) refers to a station far upstream of the actuator disc, in the undisturbed flow; subscript (2) refers to a station immediately before the actuator disc; subscript (d) refers to a station at the actuator disc; subscript (3) refers to a station immediately after the actuator disc; finally, subscript (5) refers to a station downstream of the actuator disc, in the ultimate wake (also called as far wake). The term ultimate or far wake has been introduced to indicate the region where the air stream has fully recovered its undisturbed pressure value (Sørensen, 2016). Please note that subscripts (1) and (4) have intentionally been skipped, as they will be used during the one-dimensional analysis of shrouded wind turbines (see Section 2.1.2) to signify the stations corresponding to the inlet and exit planes of the diffuser. All the reference stations used for the description of axial momentum theory are illustrated in Figure 2.1 and Figure 2.2.

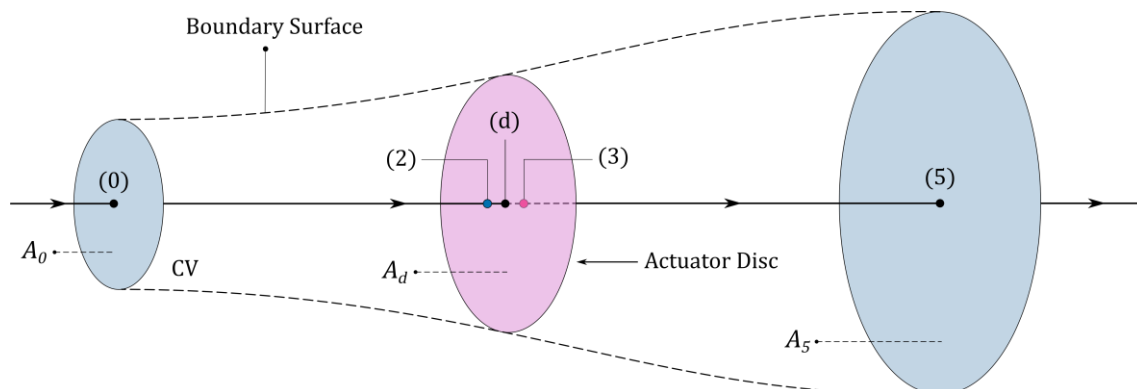


Figure 2.1: Schematic representation of the stream tube passing through the rotor of a conventional (unshrouded) horizontal-axis wind turbine. Illustration of the reference stations for the description of axial momentum theory.

Under the assumption of no mass flow crossing the lateral boundary surface of the reference control volume, which is represented by the dashed lines in Figure 2.1 and Figure 2.2, the fundamental law of mass conservation (continuity equation) enforces that the mass flow rate (\dot{m}) should be constant for each cross-section along the stream tube. Thus,

$$\dot{m} = \int \rho u_z dA = \rho A_0 u_{z,0} = \rho A_d u_{z,d} = \rho A_5 u_{z,5} . \quad (2.1)$$

Here, ρ stands for the air density, u_z stands for the axial velocity component and A stands for the cross-sectional area of the stream tube. In practice, the actuator disc, like the actual turbine rotor, acts as a drag device that applies a constant and uniform force (T_d) on the incoming flow. Basically, this drag force slows the wind speed down from $u_{z,0}$ upstream of the actuator disc, to $u_{z,d}$ at the actuator disc, and eventually, to $u_{z,5}$ in the ultimate wake (Hansen, 2008). As a result, given the assumption of incompressible fluid motion, the cross-sectional area of the stream tube must expand (as Figure 2.1 and Figure 2.2 characteristically demonstrate) from A_0 upstream of the actuator disc, to A_d at the actuator disc and finally, to A_5 in the far wake, in order to accommodate the slower moving air (Burton *et al.*, 2001).

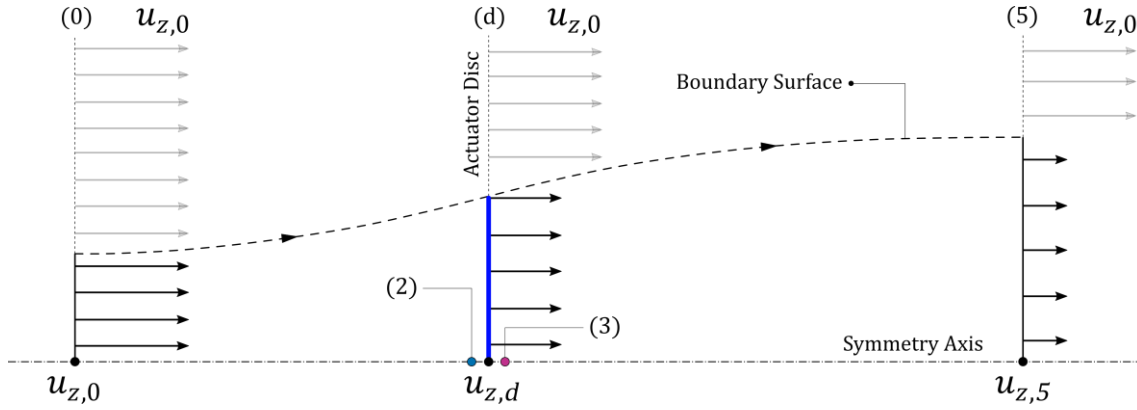


Figure 2.2: Meridian section of the reference stream tube.

At this point, let us note that stations (2) and (3) are practically coincide with station (d); hence, no variation in both axial velocity component (u_z) and cross-sectional area (A) of the stream tube among these particular stations is taken under consideration. Thus,

$$u_{z,2} = u_{z,d} = u_{z,3} , \quad (2.2)$$

$$A_2 = A_d = A_3 . \quad (2.3)$$

The only reason that stations (2) and (3) have been included within the current analysis is to signify the upstream and downstream sides of the wind turbine rotor, which are involved in the description of the static pressure jump (Δp_d) across the actuator disc (rotor).

The total thrust force on the rotor, which is equal and opposite to the drag force that the rotor exerts on the incoming flow, equals to the rate of linear momentum change along the stream tube at hand. Therefore, it can be obtained through the application of the integral form of momentum equation in the axial direction, for the reference control volume (Hansen, 2008).

Eventually, the axial momentum balance results in the following expression for the rotor thrust (Sørensen, 2016):

$$T_d = u_{z,0}(\rho A_0 u_{z,0}) - u_{z,5}(\rho A_5 u_{z,5}), \quad (2.4)$$

while under the assumption of steady-state or time-invariant flow, Eq. (2.4) recasts into:

$$T_d = \dot{m}(u_{z,0} - u_{z,5}) = \rho A_d u_{z,d}(u_{z,0} - u_{z,5}). \quad (2.5)$$

Here, it is recalled that the extraction of both Eq. (2.4) and Eq. (2.5) has been based on the hypothesis that the static pressure in the far wake (p_5) equals to the static pressure of the undisturbed flow (p_0), while the net action of pressure distribution on the lateral boundary of the stream tube is zero (Hansen, 2008; Manwell *et al.*, 2010).

Besides, the thrust force on the rotor disc can be expressed in terms of the total pressure loss or pressure jump (Δp_d) across the rotor, namely, between stations (2) and (3). Thus,

$$T_d = \Delta p_d \cdot A_d = (p_2 - p_3) \cdot A_d. \quad (2.6)$$

Moreover, since no work is done on either side of the actuator disc, Δp_d can be calculated by applying Bernoulli's equation, for both upstream and downstream sections of the reference stream tube. The application of Bernoulli's equation between station (0) and station (2) reads:

$$p_0 + \frac{1}{2} \rho u_{z,0}^2 = p_2 + \frac{1}{2} \rho u_{z,2}^2, \quad (2.7)$$

while for the stream tube section downstream of the actuator disc, that is, between station (3) and station (5), the application of Bernoulli's equation yields:

$$p_3 + \frac{1}{2} \rho u_{z,3}^2 = p_5 + \frac{1}{2} \rho u_{z,5}^2. \quad (2.8)$$

Accordingly, the combination of Eq. (2.7) and Eq. (2.8) with Eq. (2.6), results in the following expression for the rotor thrust:

$$T_d = \frac{1}{2} \rho A_d (u_{z,0}^2 - u_{z,5}^2). \quad (2.9)$$

Now, equating the thrust values from Eq. (2.5) and Eq. (2.9) results in the following expression:

$$u_{z,d} = u_{z,2} = u_{z,3} = \frac{1}{2} (u_{z,0} + u_{z,5}), \quad (2.10)$$

which is also known as the Froude's law (Bontempo and Manna, 2017). Therefore, according to axial momentum theory, the wind velocity experienced by the actuator disc (axial velocity

component at the rotor plane) equals to the average of the wind velocity in the undisturbed flow (free stream) and the ultimate wake (Burton *et al.*, 2001; Hansen, 2008; Manwell *et al.*, 2010).

At this point, let us introduce the axial induction factor (a_a), which practically represents the fractional decrease in axial velocity component between the undisturbed flow (0) and the rotor plane (d); in particular, the axial induction factor is defined as:

$$a_a = \frac{u_{z,0} - u_{z,d}}{u_{z,0}}. \quad (2.11)$$

Then, the axial velocity component at the rotor disc ($u_{z,d}$) and the axial velocity component in the ultimate wake ($u_{z,5}$) can be expressed in terms of the axial induction factor (a_a), as:

$$u_{z,d} = u_{z,0}(1 - a_a) = u_{z,0} - \omega_a, \quad (2.12)$$

$$u_{z,5} = u_{z,0}(1 - 2a_a) = u_{z,0} - 2\omega_a, \quad (2.13)$$

where the quantity $\omega_a = u_{z,0}a_a$ is often referred to as the axial induced velocity. Hence, the wind velocity at the rotor disc can be written as a combination of the free stream velocity and the induced wind velocity (Manwell *et al.*, 2010). Now, introducing Eq. (2.12) and Eq. (2.13) into Eq. (2.9), the rotor thrust can be expressed as a function of the axial induction factor:

$$T_d = 2\rho A_d u_{z,0}^2 a_a (1 - a_a). \quad (2.14)$$

Ultimately, the aerodynamic power output of the rotor (P) can be calculated by multiplying the rotor thrust force with the axial velocity component at the rotor plane. Thus,

$$P = u_{z,d} \cdot T_d = 2\rho A_d u_{z,0}^3 a_a (1 - a_a)^2. \quad (2.15)$$

Furthermore, the rotor thrust and power can be expressed in the form of the dimensionless thrust (C_T) and power (C_P) coefficients, which are respectively defined as:

$$C_T = T_d / (0.5\rho A_d u_{z,0}^2) = 4a_a(1 - a_a), \quad (2.16)$$

$$C_P = P / (0.5\rho A_d u_{z,0}^3) = 4a_a(1 - a_a)^2. \quad (2.17)$$

Conclusively, the most significant outcome of axial momentum theory can be summarized on the fact that the particular model allows for the extraction of the maximum theoretical power output for an ideal horizontal-axis wind turbine rotor. This is achieved by simply differentiating the power coefficient with respect to the axial induction factor, as follows:

$$\partial C_P / \partial a_a = 0 \rightarrow 4(1 - a_a)(1 - 3a_a) = 0 \rightarrow [a_a]_{opt} = 1/3. \quad (2.18)$$

Therefore, the value of axial induction factor (a_a) that maximizes the power coefficient of a horizontal-axis wind turbine equals to 1/3. The particular result indicates that, according to axial momentum theory, if an ideal horizontal-axis wind turbine rotor could possibly be designed, the point of maximum power production would be achieved for a value of wind velocity at the rotor plane that equals to 2/3 of the free stream velocity (Manwell *et al.*, 2010). Eventually, by simply introducing the optimal value of axial induction factor (1/3) into Eq. (2.16) and Eq. (2.17) the optimal rotor thrust coefficient is given as:

$$[C_T]_{opt} = 8/9. \quad (2.19)$$

while the maximum power coefficient reads:

$$[C_P]_{max} = 16/27 = 0.593. \quad (2.20)$$

The latter result is widely known as the Betz limit (Betz, 2013) and indicates that the maximum energy amount that an unshrouded horizontal-axis wind turbine can extract from the wind equals to 59.3 percent of the total energy contained within the stream tube passing through the rotor. However, in practice, this theoretical upper value of power coefficient can never be reached, due to energy losses associated with the rotation of the wake, the finite number of blades and non-zero aerodynamic drag. Typically, the value of power coefficient for an actual unshrouded wind turbine rotor ranges between 0.35 and 0.45 (Manwell *et al.*, 2010).

2.1.2 Axial Momentum Theory for Shrouded Wind Turbines

This section describes the application of axial momentum theory for the case of a shrouded or diffuser-augmented wind turbine, employing a similar approach to the one followed during the analysis of an unshrouded horizontal-axis wind turbine configuration (see Section 2.1.1). Initially, let us consider a control volume in the form of a long stream tube that passes through the shrouded rotor and extends in both upstream and downstream directions, such the one illustrated in Figure 2.3 and Figure 2.4. Here, the same notation strategy as for the case of an unshrouded wind turbine rotor has been adopted, with the only exception being the inclusion of two additional reference stations; station (1) refers to the inlet plane of the diffuser and station (4) refers to the exit plane of the diffuser. As for the case of an unshrouded horizontal-axis wind turbine, the flow field upstream of the shrouded rotor can be described by means of Bernoulli's equation. The application of Bernoulli's equation between station (0) and station (2) yields:

$$p_0 + \frac{1}{2}\rho u_{z,0}^2 = p_2 + \frac{1}{2}\rho u_{z,2}^2. \quad (2.21)$$

In a similar way, the Bernoulli's equation can be applied between station (3) and station (5), in order to describe the flow field downstream of the shrouded rotor. For this case, the Bernoulli's equation reads:

$$p_3 + \frac{1}{2} \rho u_{z,3}^2 = p_5 + \frac{1}{2} \rho u_{z,5}^2 + \Delta h_L, \quad (2.22)$$

where Δh_L denotes the total pressure loss between the rotor plane and the diffuser exit plane, due to friction effects and possible flow separation in the boundary layer of the downstream diffuser wall (Sørensen, 2016).

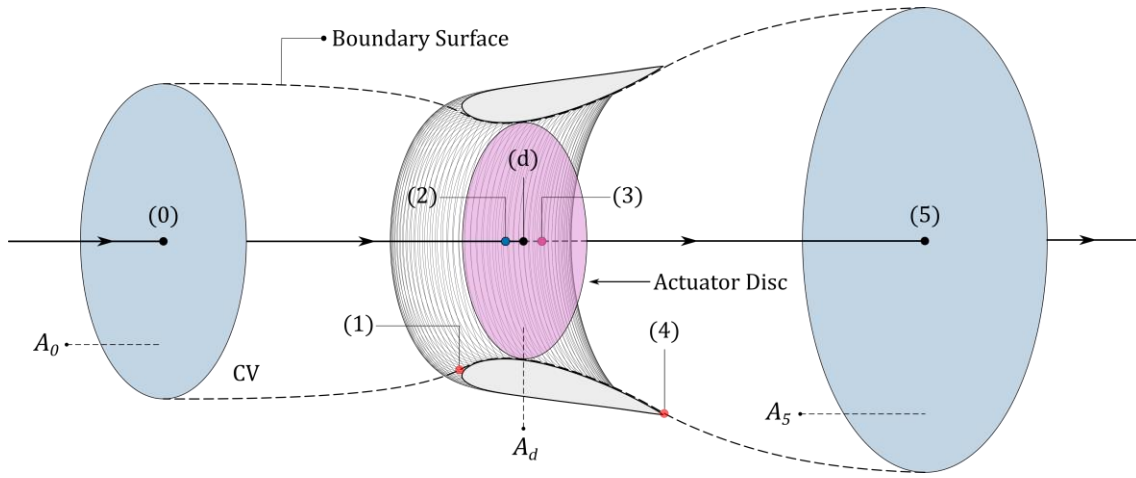


Figure 2.3: Schematic representation of the stream tube passing through the rotor of a shrouded wind turbine. Illustration of the reference stations employed for the application of axial momentum theory.

Please note that in the current analysis, the total pressure loss associated with the upstream diffuser part, which is defined as the region between the inlet plane of the diffuser (1) and the rotor plane (d), has been entirely neglected for the sake of simplicity. According to Phillips (2003), the validity of this approximation can reasonably hold for a well-designed diffuser with a smooth inlet section, where the rotor position is located near the inlet plane. Therefore, the total pressure loss along the diffuser is defined as:

$$\Delta h_L = \left(p_3 + \frac{1}{2} \rho u_{z,d}^2 \right) - \left(p_4 + \frac{1}{2} \rho u_{z,4}^2 \right). \quad (2.23)$$

Here, let us recall that the total thrust on the rotor can be calculated by multiplying the total pressure jump (Δp_d) between station (2) and station (3) with the rotor swept area (A_d). Thus,

$$T_d = \Delta p_d \cdot A_d = (p_2 - p_3) \cdot A_d. \quad (2.6)$$

Eventually, by combining the Bernoulli's equation for the upstream (2.21) and downstream (2.22) parts of the adopted control volume, along with the expressions providing the total pressure loss along the diffuser (2.23) and the rotor thrust (2.6), the energy balance for the stream tube at hand – which essentially represents the rate of energy loss between station (0) and station (5) – can be written as follows:

$$\dot{q} \left(\frac{1}{2} \rho u_{z,0}^2 - \frac{1}{2} \rho u_{z,5}^2 \right) = P + \dot{q} \Delta h_L, \quad (2.24)$$

where $\dot{q} = u_{z,d} \cdot A_d$ stands for the volumetric flow rate through the rotor disc and $P = u_{z,d} \cdot T_d$ denotes the aerodynamic power output of the shrouded rotor. Finally, rearranging Eq. (2.24), the power output for a shrouded wind turbine rotor can be calculated as:

$$P = \frac{1}{2} \rho u_{z,d} A_d \left(u_{z,0}^2 - u_{z,5}^2 - 2 \frac{\Delta h_L}{\rho} \right). \quad (2.25)$$

At this point, let us introduce the diffuser efficiency, denoted by η_d ; this dimensionless parameter that is related to the performance of the diffuser is defined as (Phillips, 2003):

$$\eta_d = \frac{p_4 - p_3}{0.5 \rho (u_{z,d}^2 - \rho u_{z,4}^2)}. \quad (2.26)$$

Accordingly, the total pressure loss can be expressed in terms of the diffuser efficiency, as:

$$\Delta h_L = (1 - \eta_d) \cdot \left(\frac{1}{2} \rho u_{z,d}^2 - \frac{1}{2} \rho u_{z,4}^2 \right), \quad (2.27)$$

while substituting Eq. (2.27) into Eq. (2.25), the latter one, providing the rotor power output, is reformed as follows:

$$P = \frac{1}{2} \rho u_{z,d} A_d \left[u_{z,0}^2 - u_{z,5}^2 - (1 - \eta_d) (u_{z,d}^2 - u_{z,4}^2) \right]. \quad (2.28)$$

In addition, the number of unknown quantities within Eq. (2.28) can be reduced, by expressing the axial velocity component at the exit plane of the diffuser ($u_{z,4}$) as a function of the axial velocity component at the rotor plane ($u_{z,d}$). In fact, this can be achieved by taking advantage of the mass conservation law, which reads:

$$A_d u_{z,d} = A_4 u_{z,4} \rightarrow u_{z,4} = (A_d / A_4) u_{z,d} = b \cdot u_{z,d}. \quad (2.29)$$

The dimensionless parameter b is the reciprocal of the diffuser exit-area-ratio; the diffuser exit-area-ratio is defined as the ratio between the exit area of the diffuser and the rotor swept area. Therefore, introducing Eq. (2.29) into Eq. (2.28) yields:

$$P = \frac{1}{2} \rho u_{z,d} A_d [u_{z,0}^2 - u_{z,5}^2 - (1 - \eta_d)(u_{z,d}^2 - b^2 u_{z,d}^2)]. \quad (2.30)$$

Ultimately, the power coefficient for a shrouded wind turbine rotor, calculated based on the rotor swept area, is given as (Phillips, 2003; Rio Vaz *et al.*, 2014; Sørensen, 2016):

$$C_p = P / (0.5 \rho A_d u_{z,0}^3) = \tilde{u}_{z,d} [1 - \tilde{u}_{z,5}^2 - (1 - \eta_d)(1 - b^2) \tilde{u}_{z,d}^2]. \quad (2.31)$$

Please note that the tilde superscript denotes the dimensionless velocity components, which have been normalized by means of the free-stream velocity ($u_{z,0}$). Apparently, except of the axial velocity component at the rotor plane ($\tilde{u}_{z,d}$), Eq. (2.31) also includes the diffuser efficiency parameter (η_d) and the axial velocity component in the ultimate wake ($\tilde{u}_{z,5}$). As long as the diffuser efficiency is concerned, which is essentially a measure of the total pressure loss along the diffuser, it has usually to be evaluated via experimental measurements for the diffuser configuration at hand (Sørensen, 2016). Besides, there is not a simple expression relating the axial velocity components in the rotor plane and ultimate wake, in contrast to the case of an unshrouded wind turbine rotor, where the induction in the rotor plane is half of the induction in the ultimate wake (see Section 2.1.1). Against this background, no simple closure for the equation providing the power coefficient of a shrouded wind turbine rotor is available, as in the case of an unshrouded horizontal-axis wind turbine rotor (Sørensen, 2016).

A common approach to alleviate the aforementioned closure problem relies on eliminating the axial velocity component from Eq. (2.31). In order to achieve that, let us initially introduce the dimensionless back pressure parameter or pressure recovery coefficient, which is denoted by $C_{p,4}$ and defined as (Phillips, 2003):

$$C_{p,4} = \frac{p_4 - p_5}{0.5 \rho u_{z,0}^2}. \quad (2.32)$$

Now, the application of Bernoulli's equation between the exit plane of the diffuser (4) and the ultimate wake (5) reads:

$$p_4 + \frac{1}{2} \rho u_{z,4}^2 = p_5 + \frac{1}{2} \rho u_{z,5}^2, \quad (2.33)$$

which can also be written by adopting a dimensionless formulation, as follows:

$$\tilde{u}_{z,5}^2 = \tilde{u}_{z,4}^2 + \frac{p_4 - p_5}{0.5 \rho u_{z,0}^2}. \quad (2.34)$$

Then, taking under consideration the definition of back pressure coefficient (2.32) and the expression connecting the axial velocity at the exit plane of the diffuser and the axial velocity in the far wake (2.29), Eq. (2.34) recasts into:

$$\tilde{u}_{z,5}^2 = b^2 \tilde{u}_{z,d}^2 + C_{p,4}. \quad (2.35)$$

Introducing Eq. (2.35) into Eq. (2.31), the equation for the power coefficient of a shrouded wind turbine rotor can be reformed as follows:

$$C_P = \tilde{u}_{z,d} [1 - C_{p,4} + [\eta_d(1 - b^2) - 1] \tilde{u}_{z,d}^2]. \quad (2.36)$$

Even though the two alternative expressions extracted within the current section for the power coefficient of a shrouded wind turbine rotor – namely, Eq. (2.31) and Eq. (2.36) – are mathematically equivalent, the latter one offers the opportunity to obtain the optimum operating conditions. This is attributed to the fact that near the optimum operating point, both the back pressure coefficient and the diffuser efficiency parameter are not strongly dependent upon the rotor velocity and mass flow rate (Sørensen, 2016). Therefore, the value of $\tilde{u}_{z,d}$ that maximizes the power coefficient can be calculated by differentiating Eq. (2.36) with respect to $\tilde{u}_{z,d}$, while assuming constant values for the back pressure coefficient and diffuser efficiency:

$$dC_P/d\tilde{u}_{z,d} = 0 \rightarrow 1 - C_{p,4} + 3\tilde{u}_{z,d}^2[\eta_d(1 - b^2) - 1] = 0. \quad (2.37)$$

Eventually, the value of axial velocity component at the rotor plane that maximizes the power output of a shrouded wind turbine (optimal value of axial velocity component) reads:

$$[\tilde{u}_{z,d}]_{opt} = \sqrt{\frac{1 - C_{p,4}}{3[1 - \eta_d(1 - b^2)]}}, \quad (2.38)$$

Therefore, introducing Eq. (2.38) into Eq. (2.36), the maximum power coefficient for the case of a shrouded wind turbine rotor is given as:

$$[C_P]_{max} = \frac{2}{3} \sqrt{\frac{1 - C_{p,4}}{3[1 - \eta_d(1 - b^2)]}} \cdot (1 - C_{p,4}). \quad (2.39)$$

while the optimal rotor loading can be obtained by:

$$[C_T]_{opt} = [C_P]_{max}/[\tilde{u}_{z,d}]_{opt} = \frac{2}{3}(1 - C_{p,4}). \quad (2.40)$$

In summary, the aforesaid equations provide a simple and useful model that describes the power output performance of a shrouded wind turbine. Nevertheless, the quantification of the involved parameters (namely, the diffuser efficiency and back pressure coefficient) in order to achieve the optimal operating conditions calls for experimental measurements for the diffuser design at hand (Sørensen, 2016).

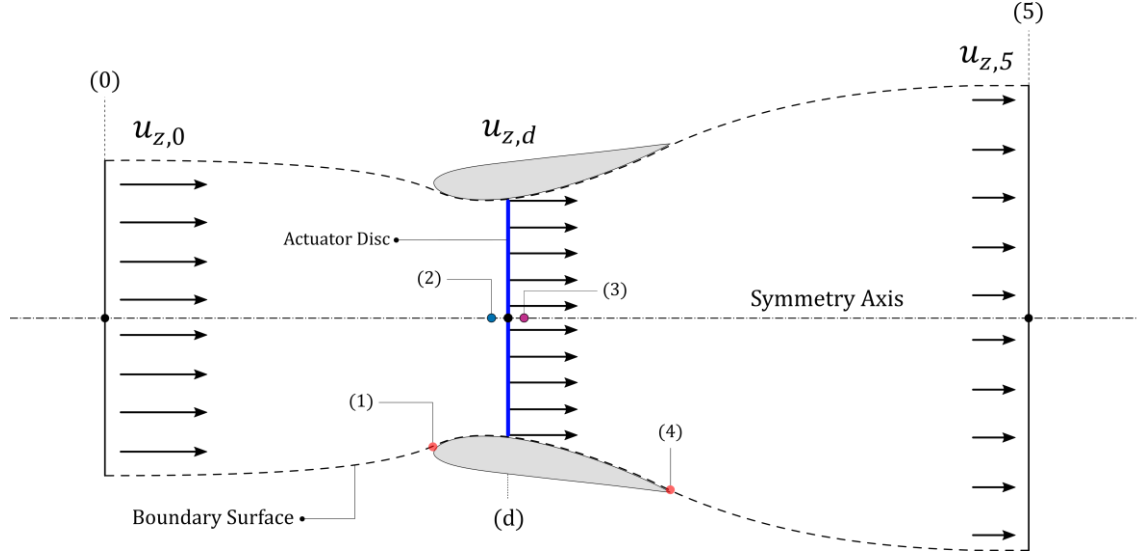


Figure 2.4: Meridian section of the reference stream tube for the case of a shrouded rotor.

2.1.2.1 Zero Diffusive Losses

In this section, we examine the modification of axial momentum theory for shrouded wind turbine rotors that was described in Section 2.1.2, under the simplifying assumption of zero diffusive losses – an approach also referred to as ideal diffuser case. The particular approach, which essentially considers that $\eta_d = 1$ and $\Delta h_L = 0$, represents a commonly adopted practice in the literature, aiming to simplify the expressions providing the optimal operating conditions. For the ideal diffuser case, the pressure jump across the rotor reads:

$$\Delta p_d = \frac{1}{2} \rho (u_{z,0}^2 - u_{z,5}^2), \quad (2.41)$$

which is equivalent to the expression for the total pressure loss across an unshrouded wind turbine rotor. Thus, the rotor thrust can be obtained as follows:

$$T_d = \Delta p_d \cdot A_d = \frac{1}{2} \rho A_d (u_{z,0}^2 - u_{z,5}^2). \quad (2.42)$$

In addition, the application of axial momentum balance (integral momentum equation) for the control stream tube illustrated in Figure 2.3 and Figure 2.4 yields:

$$T_d + T_s = \rho u_{z,d} A_d (u_{z,0} - u_{z,5}), \quad (2.43)$$

where T_s denotes the axial reaction force of the diffuser on the air within the control volume. Eventually, the combination of Eq. (2.42) and Eq. (2.43) results in the following equation:

$$u_{z,d} = \frac{1}{2}(u_{z,0} + u_{z,5})(1 + T_s/T_d), \quad (2.44)$$

which can also be expressed in a dimensionless formulation, as follows:

$$\tilde{u}_{z,d} = \frac{1}{2}(1 + \tilde{u}_{z,5})(1 + T_s/T_d). \quad (2.45)$$

Then, introducing Eq. (2.45) into Eq. (2.36), the rotor power coefficient for the ideal diffuser case reads:

$$C_P = \frac{1}{2}(1 + \tilde{u}_{z,5}) \cdot (1 - u_{z,5}^2) \cdot (1 + T_s/T_d), \quad (2.46)$$

while the thrust coefficient is given by:

$$C_T = C_P/\tilde{u}_{z,d} = (1 - u_{z,5}^2). \quad (2.47)$$

At this point, it is interesting to note that the comparison of the equations extracted during the axial momentum analysis for the ideal diffuser case to the corresponding ones for the case of an unshrouded wind turbine reveals that for a specified wake velocity, the pressure drop across the rotor is the same (Sørensen, 2016). Hence, the increase in power output for the case of a shrouded rotor stems from the augmented mass flow rate, which according to Eq. (2.45) is proportional to the diffuser force (T_s). Ultimately, under the assumption that the force ratio T_s/T_d does not depend upon the axial velocity component in the wake ($\tilde{u}_{z,5}$), the maximum power coefficient for the case of an ideal diffuser (zero diffusive losses $\rightarrow \eta_d = 1$ and $\Delta h_L = 0$) can be obtained by differentiating Eq. (2.46) with respect of $\tilde{u}_{z,5}$. In that situation, the maximum rotor power coefficient reads:

$$[C_P]_{max} = \frac{16}{27}(1 + T_s/T_d). \quad (2.48)$$

Here, the optimal value of axial velocity component in the ultimate wake equals to:

$$[\tilde{u}_{z,5}]_{opt} = 1/3 \quad (2.49)$$

and – as for the case of an unshrouded horizontal-axis wind turbine rotor – the optimal value of the rotor thrust coefficient equals to:

$$[C_T]_{opt} = 8/9. \quad (2.50)$$

The same value for the optimal thrust coefficient of a shrouded rotor was also derived from the studies of van Bussel (2007) and Jamieson (2009). In particular, van Bussel (2007) assumed that the velocity component in the ultimate wake of a shrouded wind turbine can be calculated

based on Eq. (2.13), which was actually derived during the one-dimensional analysis of an unshrouded rotor.

$$u_{z,5} = u_{z,0}(1 - 2a_a) = u_{z,0} - 2w_a. \quad (2.13)$$

The purpose of this hypothesis was the development of an axial momentum theory for shrouded wind turbine rotors resembling the momentum equations describing the operation of unshrouded wind turbines. Later on, Rio Vaz *et al.* (2014) were based on the work of van Bussel (2007) in order to modify the classic axial momentum theory and eventually, to propose an extension of BEM theory for shrouded wind turbines. To this end, Rio Vaz *et al.* (2014) expressed the axial velocity component at the rotor plane, as a function of the normalized velocity component at the rotor plane for the **unloaded diffuser** configuration (*i.e.*, $\Delta p_d = 0$), denoted by γ ; this parameter is mathematically defined as:

$$\gamma = \frac{[u_{z,d}]_{\Delta p_d=0}}{u_{z,0}}. \quad (2.51)$$

Thus, the axial velocity component at the rotor can be written in terms of γ and α_a , as follows:

$$u_{z,d} = \gamma(1 - \alpha_a)u_{z,0}, \quad (2.52)$$

while the dimensionless form of Eq. (2.52) reads:

$$\tilde{u}_{z,d} = \gamma(1 - \alpha_a). \quad (2.53)$$

Consequently, by combining Eq. (2.53) and Eq. (2.36), the power coefficient can be expressed in terms of the velocity speed-up for the unloaded diffuser (γ) as follows:

$$C_p = \gamma(1 - \alpha_a)^2 [4a_a + \gamma^2(1 - \alpha_a)(1 - \beta^2)(\eta_d - 1)], \quad (2.54)$$

which for the case of an ideal diffuser recasts into:

$$C_p = \gamma 4a_a(1 - \alpha_a)^2. \quad (2.55)$$

The corresponding thrust coefficient is given by:

$$C_T = 4a_a(1 - \alpha_a). \quad (2.56)$$

Apparently, if γ parameter equals to unity (zero velocity speed-up) the expression providing the aerodynamic power coefficient turns out to be identical to the one extracted during the one-dimensional analysis of an unshrouded horizontal-axis wind turbine (2.20). Nevertheless – in contrast to the case of a conventional wind turbine – a theoretical maximum power coefficient for the case of a shrouded wind turbine cannot be obtained, since the

differentiation of Eq. (2.59) with respect to the axial induction factor results in a value for the maximum power coefficient that is equal to:

$$[C_P]_{max} = \gamma \cdot 16/27 . \quad (2.57)$$

As a matter of fact, the maximum power coefficient is a linear and increasing function of the velocity speed-up (γ) for the unloaded diffuser configuration, which practically depends on the shroud geometry at hand, and has to be calculated either by numerical methods or experimental measurements (Bussel, 2007; Hansen *et al.*, 2000). In addition, please note that the latter expression for maximum power coefficient resembles Eq. (2.48). Both equations indicate that the maximum power coefficient is proportional to the mass flow rate, with the only difference being that in Eq. (2.48) this is expressed by means of the diffuser force, while in Eq. (2.60) it is expressed by means of the velocity speed-up ratio. Finally, an interesting remark can be drawn by observing the expression providing the rotor thrust coefficient; this expression is identical to the one of a conventional horizontal-axis wind turbine. However, van Bussel (2007) noted that – despite the similarity in the expressions for the rotor thrust – the reaction of a shrouded wind turbine is different, due to the significant impact of the diffuser on the axial induction factor.

Conclusively, the expressions presented within the current sub-section (2.1.2.1) can provide very useful insights on the optimal operating conditions of a shrouded wind turbine rotor. However, it should also be highlighted that these expressions have been extracted based on several simplifying assumptions, including:

- An ideal shroud design ($\eta_d = 1$ and $\Delta h_L = 0$).
- Independence of T_s/T_d upon $u_{z,5}$.
- The velocity in the far wake equals $u_{z,0} - 2w_d$.

Therefore, the particular expressions should only be used as indicative ones (in order to obtain a rough approximation of the system performance), since they may not accurately reflect the actual flow characteristics, especially when shrouds with large downstream expansions, which are usually associated with large flow separations and diffusive losses, are encountered.

2.2 Blade Element Momentum Theory

The Blade Element Momentum theory represents one of the most popular computational tools for the preliminary aerodynamic analysis and performance prediction of wind turbine rotors, in both academic and industrial design applications (Malki *et al.*, 2013). Essentially, the particular method – which over the years has been enhanced with the addition of various

empirical and analytical correction models (Branlard, 2017), dealing with many of its inherent limitations – relies on the combination of the well-established blade element and momentum theories, aiming to provide a rapid, yet reasonably accurate, prediction of the aerodynamic loads on the blade (Burton *et al.*, 2001). In terms of the blade element theory (Froude, 1878), the entire blade geometry is decomposed into a finite number of small blade elements along the spanwise (radial) direction, assuming that, from an aerodynamic point of view, each blade element operates independently of the surrounding ones and is represented by a two-dimensional blade section (Moriarty and Hansen, 2005); the radial distribution of axial and tangential forces on the rotor are estimated based on the local flow conditions and the geometric characteristics of the blade sections (namely, the local chord length and twist angle) using tabulated lift and drag coefficients. On the other hand, momentum theory refers to a control volume analysis of the forces acting on the blades, based on the fundamental conservation laws of axial and angular momentum, in order to provide the required axial and tangential induced velocities (local flow conditions) for the blade element calculations (Manwell *et al.*, 2010). Ultimately, the coupling of blade element and momentum models within the context of BEM theory is implemented by means of an iterative procedure (see Section 2.3.4), which eventually determines the aerodynamic forces and induced velocities over the rotor plane (Moriarty and Hansen, 2005). The following sections present the theoretical background and major features of an in-house BEM code that has been exclusively developed within the context of the current doctoral dissertation, for the aerodynamic analysis and performance prediction of both conventional and shrouded wind turbine rotors (Leloudas *et al.*, 2017).

2.2.1 Momentum Equations

In the framework of BEM theory, the reference stream tube that passes through the wind turbine rotor (see Figure 2.1) is divided into a finite number of independently operating concentric annuli or annular stream tubes, such the one illustrated in Figure 2.5; the loss of pressure or momentum in the rotor plane for each one of the annular stream tubes is attributed to the work done by the airflow passing through the rotor plane on the corresponding blade element (Moriarty and Hansen, 2005). In particular, the rate of change of the axial momentum along an elementary stream tube that starts far upstream of the rotor (0), passes through the rotor disc (d) and eventually, moves off into the ultimate wake (5), equals to the axial force on the corresponding blade element, while the rate of change of the angular momentum along the aforementioned stream tube equals to the tangential force on the blade element.

In order to derive the expressions for the elementary or differential forces on the rotor blades, from the standpoint of momentum theory, let us consider a control volume in the shape

of an annular stream tube, such the one depicted in Figure 2.5. The thrust force (dT) on the reference annulus – that is the axial reaction force by the corresponding blade element – can be obtained from the application of integral momentum equation, in the axial direction (Hansen, 2008). Thus, since the cross-sectional area of the control volume at the rotor plane equals $2\pi r dr$, the thrust for the examined annulus reads:

$$dT = (u_{z,0} - u_{z,5})d\dot{m} = 2\pi r \rho u_{z,d} (u_{z,0} - u_{z,5}) dr . \quad (2.58)$$

Please note that Eq. (2.58) is actually an alternative expression of the thrust equation (2.5) that was derived from the application of axial momentum balance to the entire stream tube (see Section 2.1.1), with the only difference being that the rotor swept area (A_d) has been replaced with the cross-sectional area of the annular stream tube at the rotor plane ($2\pi r dr$).

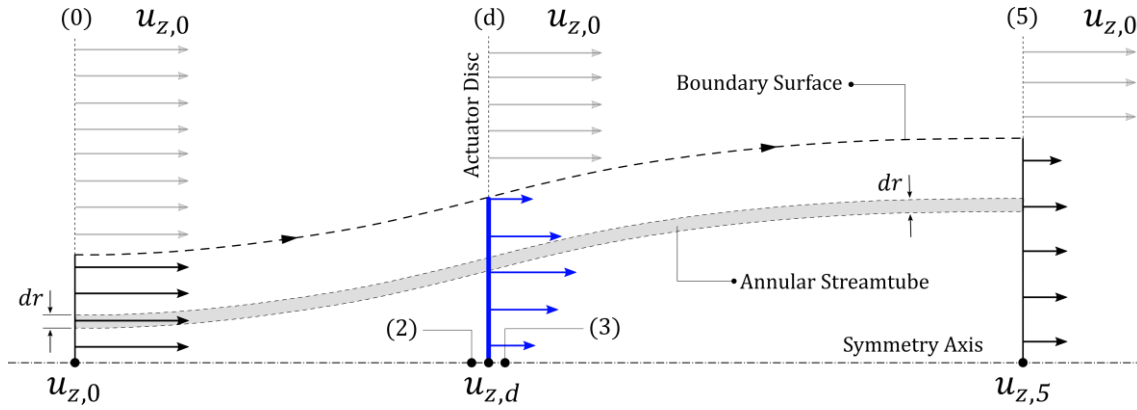


Figure 2.5: Illustration of the annular stream tube for the extraction of elementary momentum equations describing an unshrouded rotor.

In a similar way, the elementary tangential force on the reference stream tube – that is the circumferential reaction force by the corresponding blade element – can be obtained through the application of the integral momentum equation in the circumferential direction (Hansen, 2008). Eventually, by multiplying the tangential force with the radial position of the control volume at the rotor plane, the elementary torque (dM) reads:

$$dM = r(u_{\theta,5} - u_{\theta,0})d\dot{m} = r u_{\theta,3} d\dot{m} = 2\pi r^2 \rho u_{z,d} u_{\theta,3} dr , \quad (2.59)$$

where u_{θ} stands for the rotational velocity of the fluid. Herein, it should be noted that the final expression of Eq. (2.59) has been derived under the following assumptions (Burton *et al.*, 2001; Hansen, 2008): the rotational velocity of the flow upstream of the rotor equals to zero (*i.e.*, $u_{\theta,0} = u_{\theta,2} = 0$) and the rotation of the flow exiting the disc remains constant as the fluid progresses down the wake (*i.e.*, $u_{\theta,3} = u_{\theta,5}$).

At this point, let us recall that according to axial momentum theory (see Section 2.1.1), the axial velocity component at the rotor plane and the axial velocity component in the ultimate wake can be expressed in terms of the axial induction factor and ambient velocity, as follows:

$$u_{z,d} = (1 - a_a)u_{z,0} , \quad (2.12)$$

$$u_{z,5} = (1 - 2a_a)u_{z,0} , \quad (2.13)$$

where the axial (a_a) induction factor is defined as:

$$a_a = (u_{z,0} - u_{z,d})/u_{z,0} . \quad (2.11)$$

In addition, let us introduce the tangential induction factor (a_t), which practically provides a measure of change in tangential (also termed as rotational or circumferential) velocity (Burton *et al.*, 2001). The tangential induction factor is defined as:

$$a_t = u_{\theta,d}/\omega_R r = u_{\theta,3}/2\omega_R r , \quad (2.60)$$

where ω_R stands for the angular or rotational velocity of the wind turbine rotor. Ultimately, after the combination of the aforementioned equations, the elementary thrust and torque on the reference annulus, which are equal to the respective quantities on the matching blade element, can be expressed in terms of the induction factors, as follows:

$$dT = 4\pi r \rho u_{z,0}^2 a_a (1 - a_a) dr , \quad (2.61)$$

$$dM = 4\pi r^3 \rho u_{z,0} \omega_R (1 - a_a) a_t dr . \quad (2.62)$$

2.2.2 Blade Element Equations

In the previous section, the aerodynamic thrust and torque on the rotor blades were expressed in terms of the axial and tangential induction factors. Herein, an alternative formulation of the respective quantities is presented, this time by means of blade element theory. To this end, the wind turbine blades are divided or decomposed, along the spanwise direction, into a finite number of blade elements – as characteristically illustrated in Figure 2.6 – under the assumption that each blade element acts independently of the adjacent ones and operates aerodynamically as a two-dimensional airfoil (Manwell *et al.*, 2010). Then, the resulting values of sectional thrust and torque can be summed, in order to predict the overall performance of the rotor. Even though the particular theory does not include any secondary flow effects, such as the three-dimensional flow velocities induced on the rotor by the shed tip vortex or the radial velocity components induced by the angular acceleration, due to the

rotation of the blades, it still continues to be widely used for many wind turbine applications, such as initial aerodynamic analysis, conceptual design, loads and stability analysis, and controls design. In the following analysis, R denotes the rotor radius, R_h the hub radius and dr the length of each blade element, measured in the radial direction (r).

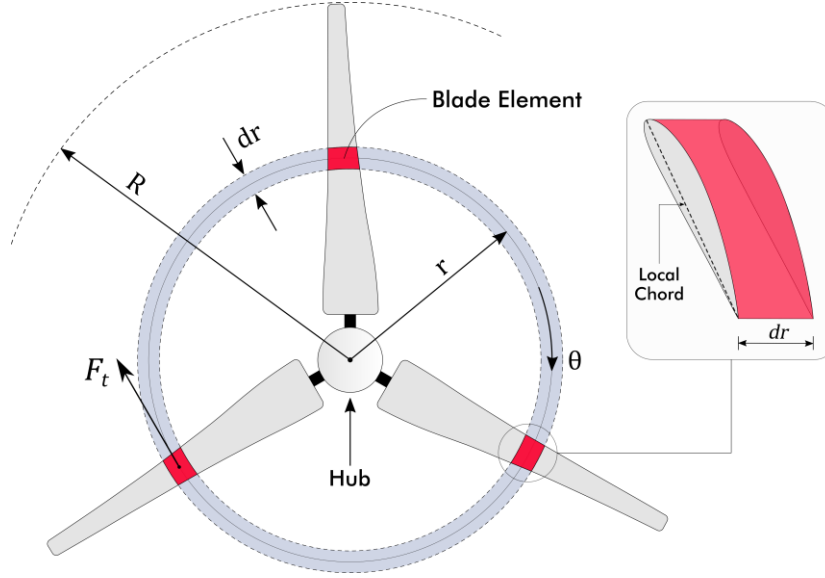


Figure 2.6: Schematic representation of blade discretization and definition of blade elements.

The local relative velocity (\mathbf{w}) experienced by each blade section along the rotating blade is a combination of the axial velocity component (w_a) and the tangential velocity component (w_t) at the rotor plane, which are illustrated in Figure 2.7 and defined as follows:

$$w_a = u_{z,d} = u_{z,0}(1 - a_a), \quad (2.63)$$

$$w_t = \omega_R r + u_{\theta,d} = \omega_R r(1 + \alpha_t). \quad (2.64)$$

Therefore, the measure of relative velocity for each blade element reads:

$$|\mathbf{w}|^2 = [u_{z,0}(1 - a_a)]^2 + [\omega_R r(1 + \alpha_t)]^2 = u_{z,d}^2 + (\omega_R r + u_{\theta,d})^2. \quad (2.65)$$

The relative velocity acts at an angle (ϕ) to the rotor plane, such that:

$$\tan\phi = \frac{u_{z,0}(1 - a_a)}{\omega_R r(1 + \alpha_t)} = \frac{u_{z,d}}{\omega_R r + u_{\theta,d}}. \quad (2.66)$$

Now, the local angle of attack (α) can be calculated by:

$$\alpha = \phi - \theta_T, \quad (2.67)$$

where θ_T is the local pitch angle, defined as the angle between the airfoil chord and the rotor plane (see Figure 2.7); the local pitch angle is calculated by adding the global pitch angle of the blade (θ_B) with the local twist angle of the blade (θ_P).

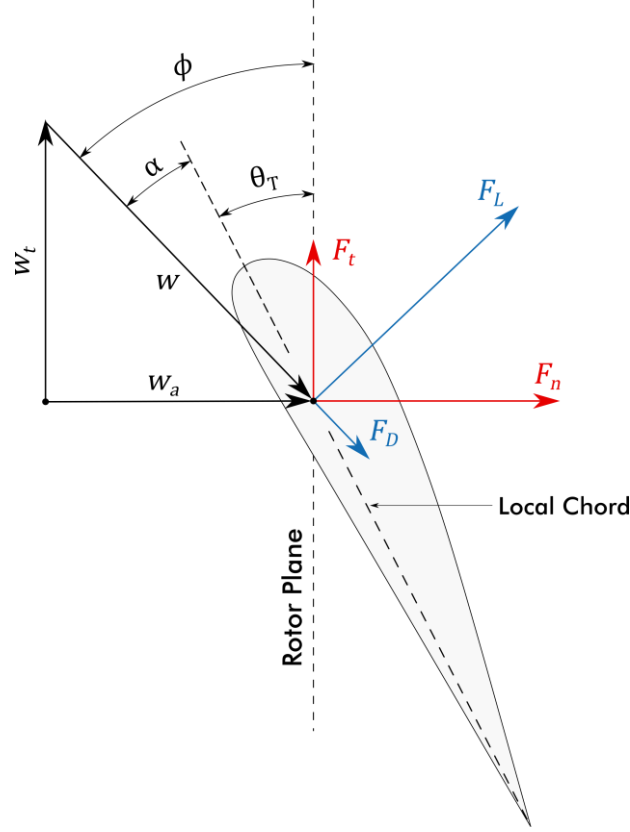


Figure 2.7: Schematic representation of the local velocities and forces on a blade element.

By introducing the lift (C_L) and drag (C_D) coefficients, the lift (F_L) and drag (F_D) force per unit length on the examined blade element can be expressed as:

$$F_L = C_L \cdot \frac{1}{2} \rho |\mathbf{w}|^2 c, \quad (2.68)$$

$$F_D = C_D \cdot \frac{1}{2} \rho |\mathbf{w}|^2 c, \quad (2.69)$$

where c denotes the local chord length. Consequently, the normal (F_n) and tangential (F_t) forces per unit radial length on each blade section can be obtained by simply adding the projections of F_L and F_D on the axial and tangential directions (see Figure 2.7). Thus,

$$F_n = F_L \cdot \cos\phi + F_D \cdot \sin\phi, \quad (2.70)$$

$$F_t = F_L \cdot \sin\phi - F_D \cdot \cos\phi. \quad (2.71)$$

Furthermore, the axial and tangential force per unit length can be expressed in a dimensionless form, by introducing the normal and tangential force coefficients, denoted by C_n and C_t , respectively. Thus,

$$C_n = C_L \cdot \cos\phi + C_D \cdot \sin\phi, \quad (2.72)$$

$$C_t = C_L \cdot \sin\phi - C_D \cdot \cos\phi, \quad (2.73)$$

where

$$C_n = F_n / (0.5\rho|\mathbf{w}|^2c), \quad (2.74)$$

$$C_t = F_t / (0.5\rho|\mathbf{w}|^2c). \quad (2.75)$$

Ultimately, the total axial (dF_n) and tangential (dF_t) forces exerted on the actuator disc by the annular streamtube swept by the examined blade element, can be calculated as:

$$dT = B_R \cdot F_n \cdot dr, \quad (2.76)$$

$$dM = r \cdot B_R \cdot F_t \cdot dr, \quad (2.77)$$

where B_R stands for the number of rotor blades. Then, taking into consideration Eq. (2.78) and Eq. (2.79), connecting the free stream velocity, the relative velocity, the inflow angle and the induction factors,

$$|\mathbf{w}| \cdot \sin\phi = u_{z,0}(1 - a_a), \quad (2.78)$$

$$|\mathbf{w}| \cdot \cos\phi = \omega_R r(1 + a_t), \quad (2.79)$$

Eq. (2.76) and Eq. (2.77) can recast into:

$$dT = \frac{1}{2}\rho B_R \frac{u_{z,0}^2(1 - a_a)^2}{\sin^2\phi} c C_n dr \quad (2.80)$$

$$dM = \frac{1}{2}\rho B_R \frac{u_{z,0}(1 - a_a)\omega_R r(1 + a_t)}{\sin\phi \cdot \cos\phi} c C_t r dr \quad (2.81)$$

2.2.3 Combination of Blade Element and Momentum Equations

In this section, the final expressions employed for the calculation of the axial and tangential induction factors during the iterative process of BEM theory are described, which practically tie together the blade element and momentum models. Initially, let us introduce the rotor solidity (σ) parameter, which is defined as:

$$\sigma = B_R c / 2\pi r \quad (2.82)$$

Then, by equating the RHS of Eq. (2.61) and Eq. (2.80), the axial induction factor reads:

$$a_a = 1 / [(4 \sin^2 \phi) / (\sigma C_n) + 1], \quad (2.83)$$

while equating the RHS of Eq. (2.62) and Eq. (2.81), the tangential induction factor reads:

$$a_t = 1 / [(4 \sin \phi \cos \phi) / (\sigma C_t) - 1]. \quad (2.84)$$

Please note that after the combination of blade element and momentum equations, both induction factors are expressed in terms of the inflow angle and aerodynamic coefficients, which in turn are non-linear functions of the induction factors; consequently, a direct solution to the aforementioned equations cannot be obtained. In the current in-house BEM code, the calculation of axial and tangential induced factors is achieved by applying the common approach of a fixed-point iteration scheme, in which the induction at the current iterative step is expressed as a function of the induction at the previous step (McWilliam and Crawford, 2011; Sun *et al.*, 2017). A detailed description of the adopted iterative procedure is provided in Section 2.3.4.

2.2.4 Extension of BEM Theory for Shrouded Rotors

One of the inherent shortcomings of classical BEM theory is related to the fact that the particular model is not capable of accounting for the shroud's effect on the calculation of the axial and tangential induced velocities at the rotor plane. Hence, in an effort to overcome this drawback, a number of studies have been undertaken, aiming to modify the classical BEM theory, and thus, make it applicable for the analysis of shrouded wind turbine rotors (Leloudas *et al.*, 2017).

In this direction, Fletcher (1981) developed an efficient computational model, based on the blade element theory, by introducing two empirical parameters – namely, the diffuser efficiency and the diffuser exit pressure coefficient – in order to include the effect of the diffuser within the rotor analysis. In addition, Fletcher (1981) enriched the particular model by the addition of wake rotation and blade Reynolds number effects; thus, he achieved a good agreement between the computational results and the experimental data, in terms of the turbine power coefficient and axial velocity.

Later on, a modified BEM model for the aerodynamic evaluation of a multi-slotted diffuser-augmented wind turbine was proposed by Phillips (2003). The fundamental idea characterizing the featured methodology was the replacement of the formula for the

calculation of the local axial velocity with an empirically-derived velocity equation, which is a function of the local disk loading coefficient. Eventually, this approach proved capable of accurately predicting the power output characteristics of the multi-slotted diffuser-augmented wind turbine at the design blade pitch angle. However, significant discrepancies between the computational results and the experimental measurements at off-design pitch angles were also reported, which were mainly attributed to the fact that the empirically-derived velocity equation fails to fully capture the flow behavior at the particular operating conditions (Phillips, 2003).

More recently, another extension of the classical BEM theory to the case of shrouded wind turbine rotors was introduced by Rio Vaz *et al.* (2014). According to the particular model, the equation providing the axial velocity component at the rotor plane (w_a) is enhanced by the addition of the velocity speed-up ratio (γ) for the unloaded shroud configuration, as follows:

$$w_a = u_{z,d} = \gamma u_{z,0}(1 - a_a), \quad (2.85)$$

Consequently, the resultant velocity for each blade section reads:

$$|\mathbf{w}|^2 = [\gamma u_{z,0}(1 - a_a)]^2 + [\omega_R r(1 + \alpha_t)]^2, \quad (2.86)$$

which now acts at an angle (ϕ) to the rotor plane, such that:

$$\tan \phi = \frac{\gamma u_{z,0}(1 - a_a)}{\omega_R r(1 + \alpha_t)}. \quad (2.87)$$

Subsequently, the equations providing the differential thrust and torque for an elementary annulus, such the one illustrated in Figure 2.8, from the standpoint of momentum theory, read:

$$dT = 4\pi r \rho u_{z,0}^2 a_a(1 - a_a) dr, \quad (2.88)$$

$$dM = 4\pi r^3 \rho u_{z,0} \omega_R (1 - a_a) a_t dr. \quad (2.89)$$

while the respective quantities from the standpoint of blade element theory can be written as:

$$dT = \frac{1}{2} \rho B_R \frac{\gamma^2 u_{z,0}^2 (1 - a_a)^2}{\sin^2 \phi} c C_n dr \quad (2.90)$$

$$dM = \frac{1}{2} \rho B_R \frac{\gamma u_{z,0} (1 - a_a) \omega_R r (1 + \alpha_t)}{\sin \phi \cdot \cos \phi} c C_t r dr \quad (2.91)$$

Eventually, by equating the RHS of Eq. (2.88) and Eq. (2.90), the axial induction factor reads:

$$a_a = 1 / [(4 \sin^2 \phi) / (\gamma^2 \sigma C_n) + 1], \quad (2.92)$$

while equating the RHS of Eq. (2.89) and Eq. (2.91), the tangential induction factor reads:

$$a_t = 1 / [(4 \sin \phi \cos \phi) / (\sigma C_t) - 1]. \quad (2.93)$$

Please note that these expressions are actually generalizations of those extracted for the case of an ideal unshrouded wind turbine.

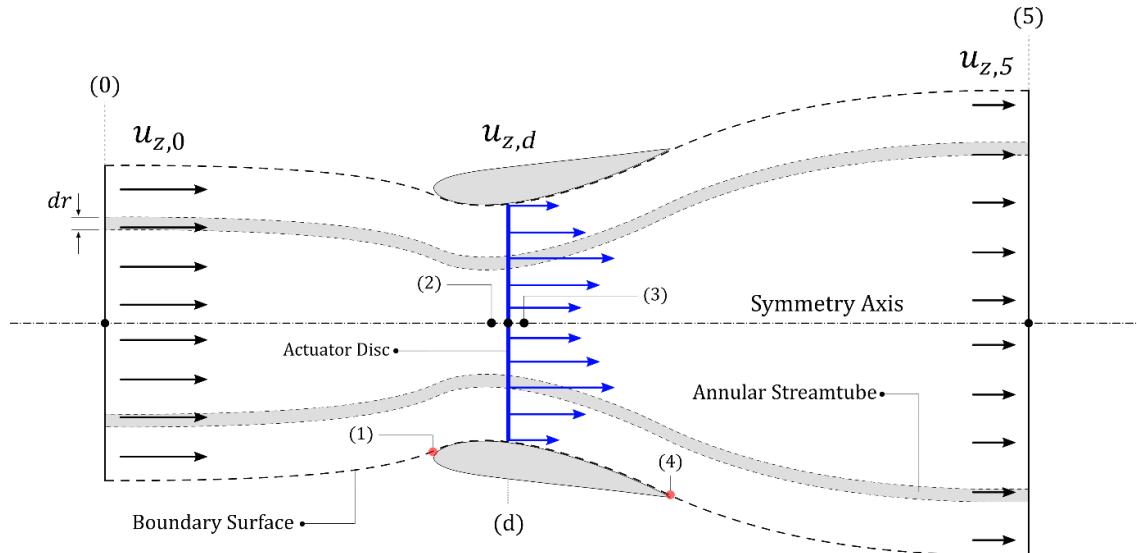


Figure 2.8: Illustration of the annular stream tube for the extraction of elementary momentum equations describing a shrouded rotor.

2.2.5 Tip Loss Correction Model

The addition of a correction model that accounts for tip and hub losses is a widely adopted practice in the context of BEM theory, which essentially deals with the simplistic assumption of azimuthally averaged loading and provides a more realistic representation of the actual wind turbine rotor, with a finite number of blades (Burton *et al.*, 2001). More precisely, such correction models compensate for the inability of classical BEM theory to capture the effects of the vortices shed from the blade tip and hub regions into the wake (helical structures) on the induced velocity field (Moriarty and Hansen, 2005). In this study, the modeling of tip and hub losses can be achieved by employing two different correction models; namely, the tip loss correction model of Prandtl (Glauert, 1935) and the tip loss correction model proposed by Shen *et al.* (2005).

2.2.5.1 Prandtl's Correction Model

The correction model proposed by Prandtl and Glauert (1935) is actually one of the earliest contributions on the specific topic of tip and hub losses. Essentially, the particular model involves the addition of a cumulative correction factor (F) in order to properly modify the

induced velocity field. The cumulative correction factor accounting for both tip and hub losses is defined as:

$$F = F_{tip} \cdot F_{hub} , \quad (2.94)$$

where

$$F_{tip} = \frac{2}{\pi} \cdot \arccos \left[\exp \left(-\frac{R-r}{2r \sin \phi} \cdot B_R \right) \right] , \quad (2.95)$$

$$F_{hub} = \frac{2}{\pi} \cdot \arccos \left[\exp \left(-\frac{r-R_h}{2r \sin \phi} \cdot B_R \right) \right] . \quad (2.96)$$

In practice, the proposed correction factor is applied to adapt the momentum part of BEM theory, by replacing the equations providing the elementary thrust (2.61) and torque (2.62) with the following ones:

$$dT = 4\pi r \rho u_{z,0}^2 a_a (1 - a_a) F dr , \quad (2.97)$$

$$dM = 4\pi r^3 \rho u_{z,0}^2 \omega_R (1 - a_a) a_t F dr . \quad (2.98)$$

Hence, the expression for the axial and tangential induction factors, including the Prandtl's losses model, read:

$$a_a^d = 1 / [(4F \sin^2 \phi) / (\gamma^2 \sigma C_n) + 1] , \quad (2.99)$$

$$a_t^d = 1 / [(4F \sin \phi \cos \phi) / (\sigma C_t) - 1] . \quad (2.100)$$

If the Prandtl's correction model is not active, F parameter equals to unity. Apparently, in that case, the modified equations for the axial and tangential induction factors reduce to those derived in Section 2.2.3.

2.2.5.2 Shen's Correction Model

More recently, another correction model that accounts for tip and hub losses was featured by Shen *et al.* (2005). The Shen's tip and hub loss correction model is implemented by introducing the cumulative loss factor q_s , which practically modifies the normal and tangential force coefficients as follows (Shen *et al.*, 2005):

$$C_n \rightarrow q_s \cdot C_n , \quad (2.101)$$

$$C_t \rightarrow q_s \cdot C_t . \quad (2.102)$$

The Shen's loss factor q_s reads:

$$q_s = q_{s,tip} \cdot q_{s,hub} , \quad (2.103)$$

where

$$q_{s,tip} = \frac{2}{\pi} \cdot \arccos \left[\exp \left(-g_s \cdot \frac{R-r}{2r \sin \phi} \cdot B_R \right) \right] , \quad (2.104)$$

$$q_{s,hub} = \frac{2}{\pi} \cdot \arccos \left[\exp \left(-g_s \cdot \frac{r-R_h}{2r \sin \phi} \cdot B_R \right) \right] . \quad (2.105)$$

Finally, the expression for the calculation of the g_s parameter reads (Shen *et al.*, 2005):

$$g_s = \exp[-0.125 \cdot (B_R \lambda - 21) + 0.1] , \quad (2.106)$$

where λ stands for the tip-speed ratio and B_R for the number of rotor blades; the rest of the coefficients in Eq. (2.106) have been determined based on experimental measurements (Shen *et al.*, 2005).

2.2.6 Empirical Region Calculations

Even though momentum theory provides a useful theoretical model for the performance prediction of wind turbine rotors, the particular method is no longer valid when the value of axial induction factor does not lie between 0 and 0.5 (Manwell *et al.*, 2010). Therefore, since momentum theory cannot longer describe the wind turbine performance, the application of alternative expressions for the axial induction factor is required.

In this study, the empirical expressions proposed by Ning (2014) are employed to accurately predict the wind turbine performance for the different operating states of the rotor. Furthermore, the original expressions have been enhanced with the addition of velocity speed-up ratio, so as they can be applied to the case of shrouded wind turbines as well. At first, let us introduce the following non-dimensional parameters:

$$k_a = \gamma^2 \sigma C_n / (4F \sin^2 \phi) , \quad (2.107)$$

$$k_t = \sigma C_t / (4F \sin \phi \cos \phi) . \quad (2.108)$$

At this point, let us also recall that ϕ stands for local inflow angle and F stands for the Prandtl's correction factor, quantifying the rotor tip and hub losses.

Now, if the local inflow angle (ϕ) is positive and the value of k_a parameter is less than or equal to 2/3, the solution falls into the momentum theory region (windmill state). Thus,

$$a_a = k_a / (1 + k_a). \quad (2.109)$$

Please note that Eq. (2.109) is identical to Eq. (2.83). If the local inflow angle (ϕ) is positive and the value of k_a parameter is greater than 2/3, the solution falls into the empirical estimation region, also termed as turbulent wake state. In that case, the expression for the calculation of axial induction factor reads:

$$a_a = (h_1 - \sqrt{h_2}) / h_3 \quad (2.110)$$

where

$$h_1 = 2Fk_a - (10/9 - F) \quad (2.111)$$

$$h_2 = 2Fk_a - F(4/3 - F) \quad (2.112)$$

$$h_3 = 2Fk_a - (25/9 - 2F) \quad (2.113)$$

On the other hand, if the local inflow angle (ϕ) is negative and the value of k_a parameter is greater than 1.0, the solution falls into the propeller brake region. The expression for the calculation of the axial induction factor becomes:

$$a_a = k_a / (k_a - 1) \quad (2.114)$$

Finally, if the local inflow angle (ϕ) is negative and the value of k_a parameter is less than or equal to 1.0, then the particular value of the inflow angle cannot possibly be a solution to the BEM equations; therefore, in this case, the axial induction factor should be set to any random value, different from its previous one. In any of the aforementioned cases, the tangential induction factor reads:

$$a_t = k_t / (1 - k_t) \quad (2.115)$$

2.3 BEM Code Features

This section outlines the major features of the in-house BEM code. The current software version has been implemented in Fortran 90, while the interaction between the user and the program is made by properly designed text files. Additionally, an updated version of the current software has been also developed in the context of Maria Seremeti's undergraduate diploma thesis (Seremeti, 2019), based on the Qt cross-platform and C++ programming language. The later employs the same computational subroutines developed for the current one; however it is further enhanced by the addition of a friendly graphical user interface.

2.3.1 Blade Discretization

The adopted strategy for the discretization of the rotor blades into a finite number of blade elements is illustrated in Figure 2.9, where the number of blade elements equals to the number of the airfoil sections defining the blade. Now, let us consider a wind turbine blade defined by N airfoil sections, where r_i denotes the radial position of the i^{th} airfoil section, measured from the rotation axis.

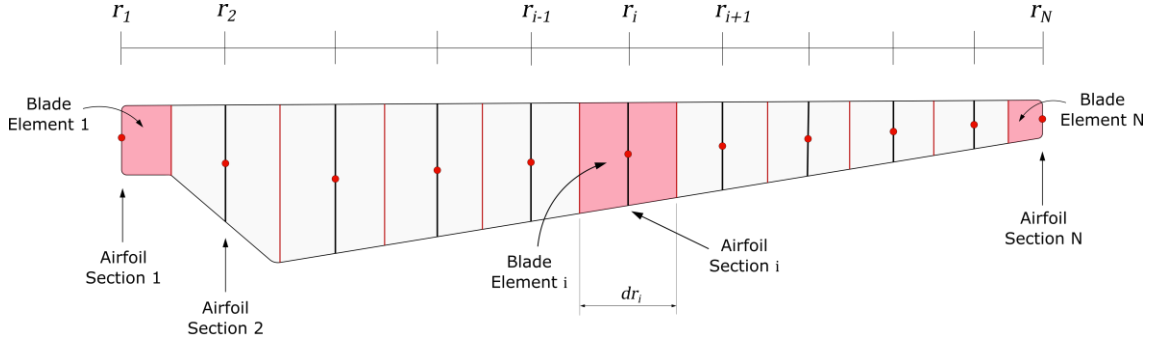


Figure 2.9: The adopted blade discretization concept.

Therefore, the radial length of each blade element (dr_i) is defined as:

$$\begin{aligned} dr_1 &= [r_2 - r_1]/2 \\ dr_i &= [r_{i+1} - r_i]/2 + [r_i - r_{i-1}]/2 \\ dr_N &= [r_N - r_{N-1}]/2 \end{aligned} \quad (2.116)$$

Please note that the radial position of each blade element, except of the first and the last ones, is set as the radial position of the corresponding airfoil. As long as the first and the last blade elements are concerned, their radial positions are the radial position of the first and the last airfoil section of the blade, respectively. In practice, the number of blade elements should be large enough to provide a good approximation of the variations in velocity, chord, and twist distributions along the examined blade geometry. Experience shows that typical performance analyses can be done accurately using a number of blade elements between 10 and 20 (Wood, 2011).

2.3.2 Aerodynamic Coefficients Calculation

According to BEM theory, the calculation of axial and tangential force distributions along the rotor plane relies on the aerodynamic characteristics of the airfoil sections defining the wind turbine blades, as they are expressed by the lift and drag coefficients. In the early versions of the current BEM code, the lift and drag coefficients for each blade element and each

step of the iterative procedure were being obtained by means of external calls to the well-known XFOIL code (Drela, 1989). In particular, after the calculation of the local angle of attack and the local Reynolds number, XFOIL code was automatically being called by the main calculation subroutine, so as to provide the aerodynamic data required for the estimation of the axial and tangential force coefficients. However, this approach was eventually rejected, since the XFOIL code was not always capable of achieving a converged solution for the prescribed flow conditions and thus, feeding back the required aerodynamic data, especially for angles of attack lying away from the linear lift region, causing the unexpected termination of BEM code. This problem was more intense during the simulation of low tip-speed ratios, where the angle of attack, in certain stations of the rotor blades, could be extremely high. Besides, such high angles of attack could also be encountered during the analysis of stall-regulated wind turbines, where deep stall is invited, in order to limit the excessive power in high winds.

In order to alleviate this shortcoming, two custom subroutines for the extrapolation of the aerodynamic curves, provided by XFOIL code, to the entire 360 range of angles of attack were later implemented and fully incorporated within the particular BEM code. The first extrapolation subroutine is based on the method proposed by Bjorn Montgomerie (Montgomerie, 2004), which actually combines the Thin Plate theory with the linear range behavior of the airfoil, under the assumption that an airfoil section operating at high angles of attack behaves like a thin plate with a sharp leading edge. The second extrapolation subroutine is based on the Viterna-Corrigan extrapolation method (Viterna and Corrigan, 1981). Subsequently, the entire procedure for the calculation of the aerodynamic coefficients was reformed. This time, the required XFOIL simulations for each blade section and each iterative step were being performed for a wider range of angles of attack, usually between -5 and 25, instead for the local angle of attack; then, the resulting lift and drag coefficient curves were automatically being passed to the selected extrapolation subroutine, which would finally output the lift and drag coefficients for the entire range between -180 and 180 degrees, with respect to the local Reynolds number. Nevertheless, since both extrapolation methods rely on fine-tuning parameters, the quality of the automatically extrapolated results was not always acceptable.

Ultimately, in order to assure that accurate values for the lift and drag coefficients would always be available during the entire iterative process, regardless the angle of attack, a third approach was finally adopted, which is the most common one in such applications. According to the followed approach the XFOIL simulations for each airfoil section are manually performed in a pre-processing stage, before the execution of BEM code, considering an average Reynolds number along the blade, which is empirically estimated based on the inflow velocity and average chord length. Then, both lift and drag coefficient curves are manually

extrapolated to the entire 360° range of angles of attack, by properly selecting the corresponding extrapolation parameters. The main advantage of this method is that the aerodynamic coefficients for each blade section have been already calculated and stored within the database, ready to be used when required. Nevertheless, this method calculates the aerodynamic coefficient based on an average (reference) Reynolds number, instead of the local Reynolds number for each blade section. Figure 2.10 and Figure 2.11 illustrate the lift and drag curves of a NACA 0012 airfoil at 1,000,000 Re, extrapolated to the entire range of angles of attack, using the Montgomerie (2004) extrapolation method.

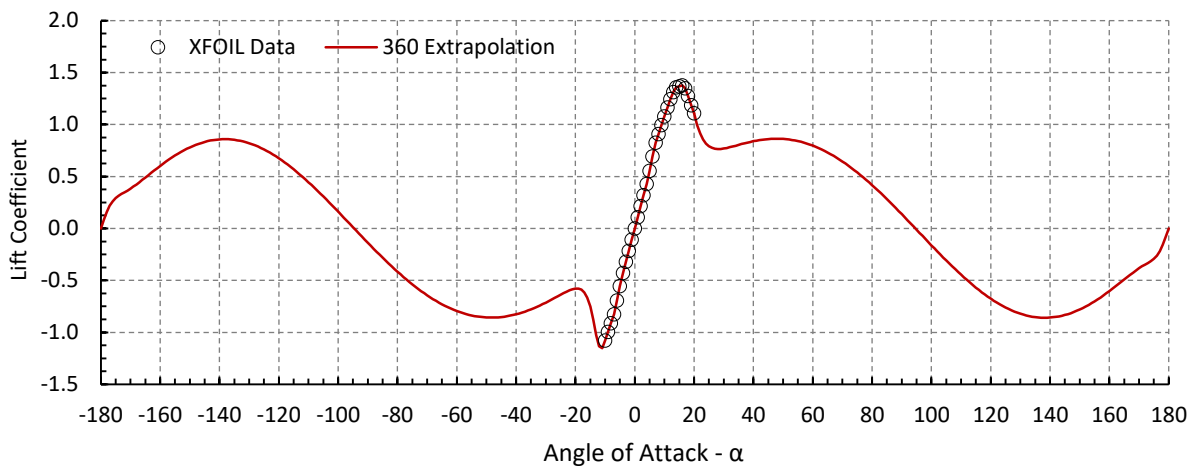


Figure 2.10: Extrapolation of the lift coefficient curve for a NACA 0012 airfoil at 1,000,000 Re.

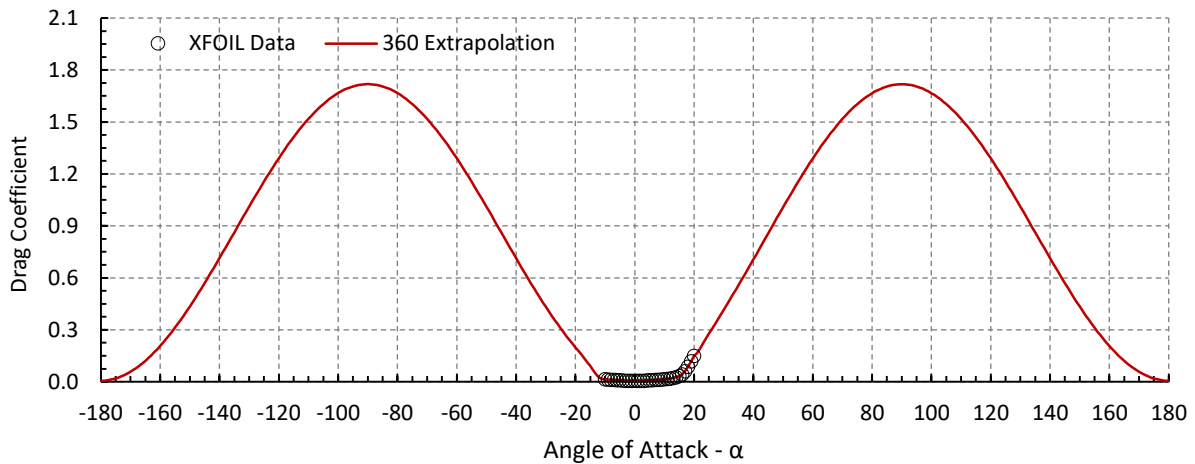


Figure 2.11: Extrapolation of the drag coefficient curve for a NACA 0012 airfoil at 1,000,000 Re.

2.3.2.1 Drag Correction for Reynolds Number

In the framework of BEM models, the aerodynamic performance of the rotor blades is completely determined by means of the lift and drag coefficients, for each blade section. Therefore, the accurate prediction of these aerodynamic parameters is crucial for the precision

of the final solution. However, the utilization of pre-calculated lift and drag coefficients, considering an average Reynolds number, instead of the actual local one, could introduce a significant amount of error. In efforts to improve the accuracy of the final solution, Hernandez and Crespo (1987) proposed a correction model accounting for the aforementioned problem, in which the drag polar is corrected by scaling the drag coefficient inversely with the Reynolds number, as follows:

$$C_D = C_{D,Ref} \cdot (Re_{Ref}/Re)^{0.2} \quad (2.117)$$

Here, Re stands for the local Reynolds number while Re_{Ref} denotes the average Reynolds number, for which the drag coefficient is available. In terms of the lift coefficient, no correction needs to be applied, since it is less sensitive to the Reynolds number than the drag coefficient.

2.3.3 Relaxation Procedure

The fluctuating behaviour of the axial induction factor, which is characteristically demonstrated in Figure 2.12, represents one of the most commonly encountered problems during the iterative process applied for the solution of BEM equations; in particular, these fluctuations stem from the periodically variation of the rotor loading state, practically quantified by the thrust coefficient, between light and heavy loading. Therefore, since convergence cannot be achieved, the iteration process is terminated after a pre-defined number of steps and the corresponding blade element is skipped. However, this impacts both the accuracy of the predicted results and the performance of the code.

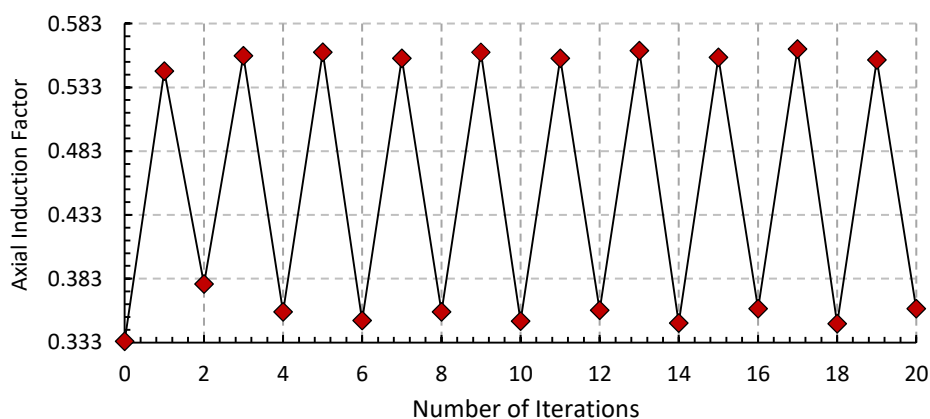


Figure 2.12: Fluctuating behavior of the axial induction factor due to change of loading state. Reproduced from (Maheri et al., 2006).

An efficient solution to the aforementioned fluctuating behaviour problem was eventually proposed by Maheri *et al.* (2006). According to this approach, a relaxation factor (ψ_r) is

introduced within the iterative solution process for each blade element; thus, the value of the axial induction factor for the current iterative step is calculated by using the value of the axial induction at the previous iterative step, as follows (Maheri *et al.*, 2006):

$$a_a^{k+1} = \psi_r \cdot a_a^{k+1} + (1 - \psi_r) \cdot a_a^k, \quad 0 < \psi_r < 1 \quad (2.118)$$

Moreover, Maheri *et al.* (2006) suggested that further acceleration of the iterative procedure could be achieved by adopting a value of ψ_r equal to unity for the first few iterations, so the first few oscillations to happen. Eventually, these oscillations will mark the boundaries of the final result's neighbourhood. By using a three-point-equation, the axial induction factor is then placed inside this neighbourhood as follows:

$$a_{k+1} = \frac{1}{4} a_{k+1} + \frac{1}{2} a_k + \frac{1}{4} a_{k-1} \quad (2.119)$$

Then, the iteration proceeds as normal, by applying Eq. (2.118) with the desired relaxation factor. Figure 2.13 demonstrates the behaviour of axial induction factor for different values of the relaxation parameter ψ_r . Accordingly, for all the simulations encountered in this study a values between 0.2 and 0.3 have been selected.

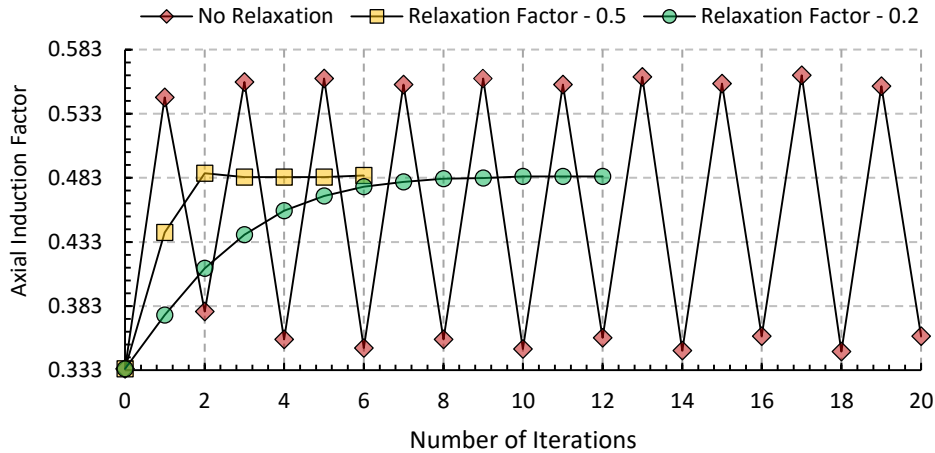


Figure 2.13: Damped fluctuation of the axial induction factor for different relaxation factors.

Reproduced from (Maheri *et al.*, 2006).

2.3.4 The Iterative Procedure

At this point, all the necessary equations of the current BEM model have been derived and the algorithm for the calculation of the axial and tangential induction factors can be summarized in the following steps. Due to the assumption of no aerodynamic interaction between the elements, each element can be treated separately. Therefore, the application of the

BEM algorithm at a specific radius can be computed before solving for another radius, while the sequence in which the elements are treated is irrelevant. Ultimately, for each blade element, the following algorithm is applied:

Step 1: Initialize axial (α_α) and tangential (α_t) induction factors. The initial value for both induction factors is typically zero.

Step 2: Compute the local inflow angle ϕ using Eq. (2.87).

Step 3: Compute the Prandtl's correction factor (F) using Eq. (2.94) or the Shen's correction factor (q_s) using Eq. (2.103), depending on which of the available tip and hub correction models has been selected.

Step 4: Compute the local angle of attack (α) using Eq. (2.67).

Step 5: Compute the relative inflow velocity (w) using Eq. (2.86); then calculate the local Reynolds number, based on the local inflow velocity (w) and chord length (c).

Step 6: Calculate the lift (C_L) and drag (C_D) coefficients for the examined airfoil section at the given flow conditions.

Step 7: If the drag correction model for Reynolds number is active, calculate the new value of drag coefficient applying Eq. (2.117).

Step 8: Compute the normal (C_n) and tangential (C_t) force coefficients using Eq. (2.72) and Eq. (2.73).

Step 9: Apply the Shen's correction model; compute the updated values for the normal (C_n) and tangential (C_t) force coefficients using Eq. (2.101) and Eq. (2.102).

Step 10: Calculate α_α and α_t based on the expressions provided in Section 2.2.6.

Step 11: If α_α or α_t has changed more than the adopted tolerance ε , go to Step 2. Else finish.

Step 12: Compute the local loads on the blade element.

Chapter 3

Numerical Validation of the BEM Code

This chapter provides a detailed validation study on the overall performance of the in-house BEM solver that was presented in Chapter 2. To this end, several benchmark cases have been selected, including both conventional horizontal-axis wind turbine (Section 3.1) and shrouded wind turbine (Section 3.2) rotors. The results of the current BEM simulations are compared against both numerical and experimental data available in literature, as well as against the results obtained from the well-known QBlade software.

3.1 Conventional Horizontal-Axis Wind Turbines

The current section aims to investigate, and eventually validate, the ability of the in-house developed BEM code to accurately predict the aerodynamic performance and power output of unshrouded horizontal-axis wind turbine rotors. For that purpose, two widely examined and well-documented benchmark cases have been selected, namely the NREL Phase VI wind turbine (Hand *et al.*, 2001) and the NREL 5-MW reference wind turbine (Jonkman *et al.*, 2009), which represent typical examples of small and large wind turbine configurations, respectively.

3.1.1 NREL Phase VI Wind Turbine

The first validation case considers the well-documented NREL Phase VI wind turbine, which was extensively investigated during the Unsteady Aerodynamics Experiment (UAE) conducted at the 24.4 m × 36.6 m wind tunnel facilities of the National Aeronautics and Space Administration (NASA) Ames Research Center (Hand *et al.*, 2001). The scope of that particular experimental campaign was to obtain accurate quantitative aerodynamic and structural data for the development and validation of enhanced engineering models. Essentially, the NREL Phase VI wind turbine refers to a stall-regulated configuration with full-span pitch control and a rated capacity of approximately 20 kW that is characterized by a two-bladed rotor of 10.058 m diameter; the rotor operates at a constant speed of 72 RPM (Hand *et al.*, 2001). The entire NREL Phase VI wind turbine system is presented in Figure 3.1.

Overall, the experimental campaign that conducted at the NASA Ames Research Center included thirty test sequences, which refer to various operating states and wind turbine setups (Hand *et al.*, 2001). In this research study, the assessment of the developed BEM code is performed by using the experimental results from test sequence **H**, test sequence **I** and test

sequence J. All the three test sequences refer to upwind operation and zero yaw angle, with the only difference between them being the adopted blade pitch angle. Specifically, the blade pitch angle for test sequence H equals to three degrees (baseline configuration), the blade pitch angle for test sequence I equals to zero degrees (low pitch configuration) and the blade pitch angle for test sequence J equals to six degrees (high pitch configuration). At this point, it should be noted that according to the experimental setup, the blade pitch angle is actually referred to the pitch angle of the blade tip, which is defined as the angle between the rotor plane and the chord of the blade tip. Table 3.1 provides a summary of the simulation cases encountered in the present study, while detailed technical characteristics for the entire experimental campaign can be found in the work of Hand *et al.* (2001).

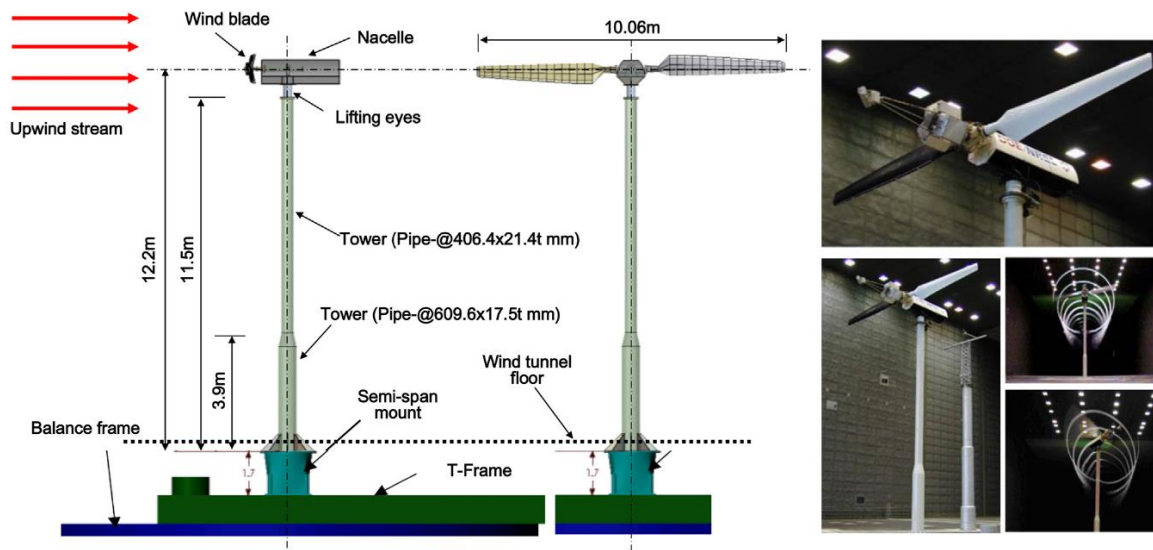


Figure 3.1: The NREL Phase VI wind turbine configuration (Hand *et al.*, 2001).

Case	Sequence	Wind Velocity	Rotor Speed	Blade Pitch	TSR (λ)
1	H	5.0 – 25.0 m/s	72 RPM	3.00 deg	7.6 – 1.5
2	I	5.0 – 25.0 m/s	72 RPM	0.00 deg	7.6 – 1.5
3	J	5.0 – 25.0 m/s	72 RPM	6.00 deg	7.6 – 1.5

Table 3.1: Simulation cases for the NREL Phase VI wind turbine rotor.

3.1.1.1 Blade Characteristics and Simulation Parameters

The main geometric characteristics of the aerodynamic profiles defining the NREL Phase VI wind turbine blade are provided in Table 3.2, while the blade planform is illustrated in Figure 3.2. The particular blade configuration is entirely based on the S809 airfoil, with the

only exception being the root region, where cylindrical profiles of varying chord length have been employed for the first 14 percent of the blade span. At this point, let us note that the blade region defined by the cylindrical profiles has been also included within the current BEM simulations, even though the aerodynamic contribution of that certain part of the blade to the overall rotor performance is practically negligible.

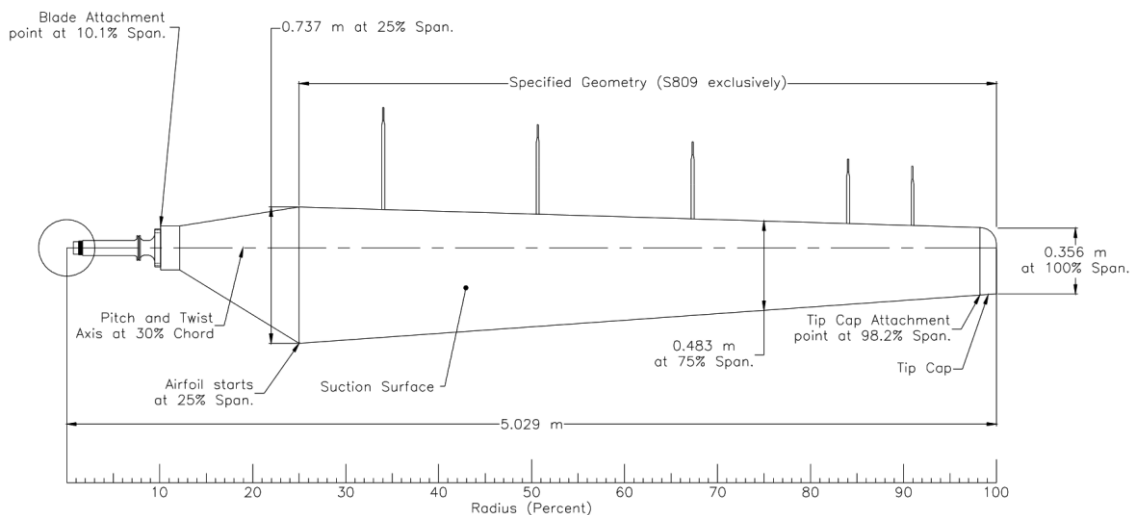


Figure 3.2: The planform of NREL Phase VI wind turbine blade (Hand *et al.*, 2001).

In addition, the NREL Phase VI blade is characterized by a linear chord distribution (linear taper) with a maximum chord length of 0.737 m and a minimum chord length of 0.356 m; the aspect ratio of the blade, that is the ratio of the square of the blade span to the projected blade area, is approximately equal to 7.2; according to the study of Lindenburg (2003), this aspect ratio value is less than half of the values usually adopted in modern large wind turbines. Finally, the maximum twist angle of the examined blade equals to 20.04 degrees, which decreases in a parabolic way as the blade tip is approached, until a minimum value of -1.815 degrees. Based on the particular blade characteristics, the solidity of the two-bladed NREL Phase VI rotor equals to 5.8 percent.

The aerodynamic characteristics of the S809 airfoil that were used during the current BEM simulations – namely, the lift and drag coefficients – were calculated by means of XFOIL code (Drela, 1989). Then, the lift and drag curves were extrapolated to the entire 360° range of angles of attack, by applying the Montgomerie’s extrapolation method (Montgomerie, 2004). On the other hand, constant values of the lift and drag coefficients for the cylindrical profiles forming the root region of the blade were adopted; in that case, the lift coefficient was set to zero, while the drag coefficient was set equal to unity. Finally, tip and hub losses were also included within the current analyses, by employing both Prandtl’s and Shen’s correction models.

Section	Airfoil	Radius [m]	Chord [m]	Twist Angle [deg]
1	Circular	0.508	0.218	0.00
2	Circular	0.660	0.218	0.00
3	Circular	0.883	0.189	0.00
4	Circular	1.008	0.349	6.70
5	Circular	1.067	0.441	9.90
6	Circular	1.133	0.544	13.40
7	S809	1.257	0.737	20.04
8	S809	1.343	0.728	18.07
9	S809	1.510	0.711	14.29
10	S809	1.648	0.697	11.91
11	S809	1.952	0.666	7.98
12	S809	2.257	0.636	5.31
13	S809	2.343	0.627	4.71
14	S809	2.562	0.605	3.42
15	S809	2.867	0.574	2.08
16	S809	3.172	0.543	1.15
17	S809	3.185	0.542	1.115
18	S809	3.476	0.512	0.494
19	S809	3.781	0.482	-0.015
20	S809	4.023	0.457	-0.381
21	S809	4.086	0.451	-0.475
22	S809	4.391	0.420	-0.920
23	S809	4.696	0.389	-1.352
24	S809	4.780	0.381	-1.469
25	S809	4.938	0.365	-1.689
26	S809	5.000	0.358	-1.775
27	S809	5.029	0.356	-1.815

Table 3.2: Geometric characteristics of the NREL Phase VI wind turbine blade.

3.1.1.2 BEM Simulation Results

Figure 3.3 until Figure 3.5 compare the results of the current BEM simulations, in terms of aerodynamic rotor power and thrust, against the corresponding data from the experimental campaign at the NASA Ames Research Center; please note that the experimental power and thrust data for the NREL Phase VI wind turbine rotor that are illustrated in the following figures refer to the mean experimental values. The entire set of experimentally measured data for each one of the encountered test sequences – including the minimum, maximum and mean experimental values, as well as standard deviation information – are openly available at the following link: <https://a2e.energy.gov/projects/uae6>.

According to the following comparisons, the in-house BEM code is capable of providing a reasonably accurate prediction of the entire power curve of the NREL Phase VI wind turbine rotor for the baseline (see Figure 3.4a) and high (see Figure 3.5a) pitch setups; however, at the same time, significant overestimations of the aerodynamic power for the low pitch setup (see Figure 3.3a) have been also identified, particularly for wind speed values greater than 9 m/s. In general, the predicted values of thrust and power are in good agreement with the experimentally measured ones for wind speeds below 10 m/s. Though, as the wind speed increases, the discrepancies between the BEM results and the experimentally measured data generally tend to increase as well, especially in terms of the rotor thrust.

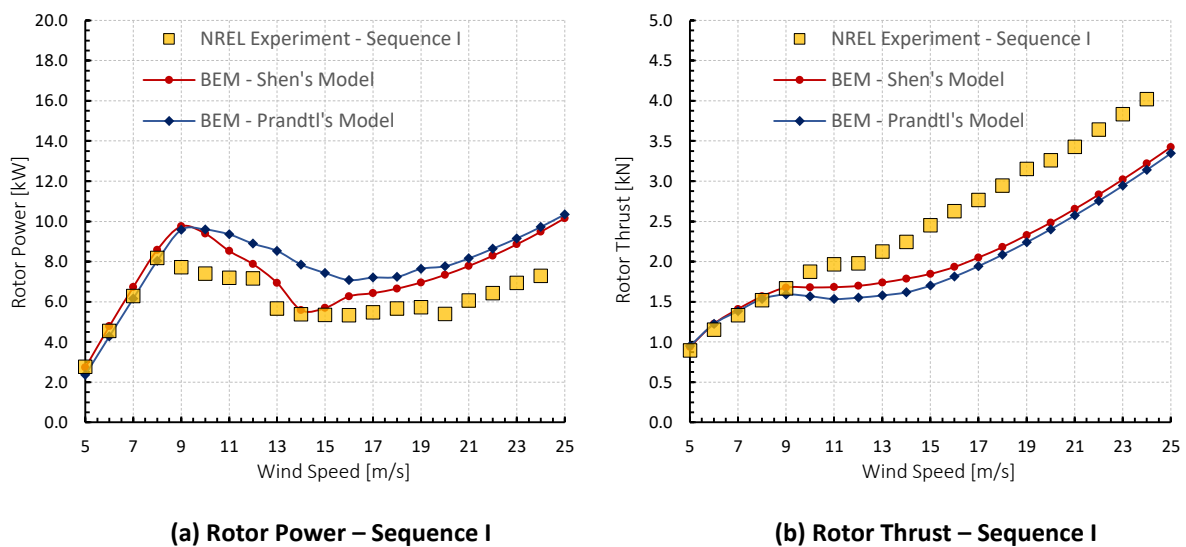
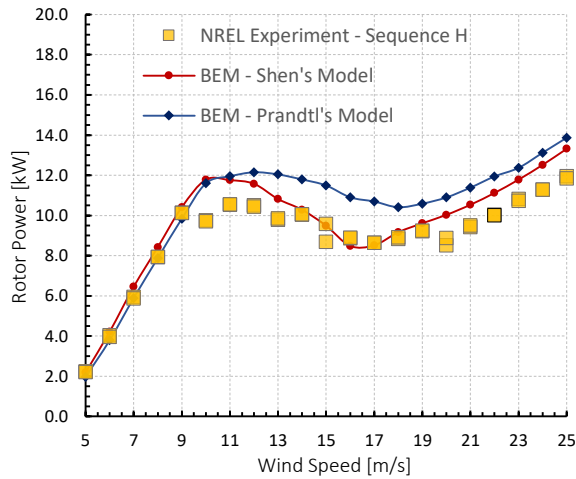
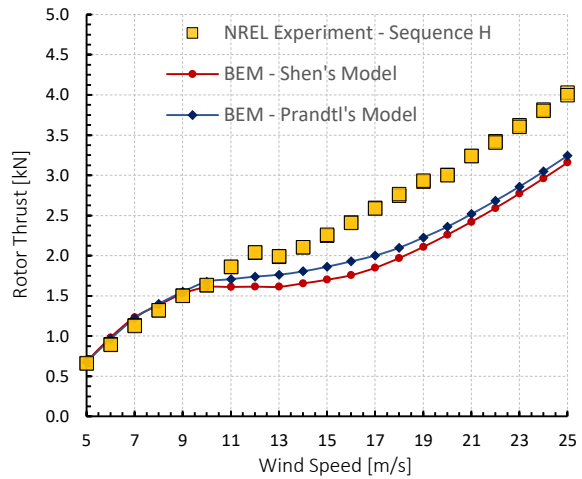


Figure 3.3: Comparison of the predicted and experimentally measured aerodynamic power and thrust for the NREL Phase VI wind turbine rotor – Test Sequence I (Low Pitch Setup).

According to several studies on the performance of NREL Phase VI rotor (Gur and Rosen, 2008; Arramach *et al.*, 2017; Bontempo and Manna, 2017; Lee *et al.*, 2017; Zhong *et al.*, 2019), the particular discrepancies are primarily attributed to the fact that when the value of ambient wind speed exceeds approximately 10 m/s the examined rotor configuration operates in dynamic or deep stall mode. In such operating situations, all the computational methods that rely on the actuator disk concept, inherently fail to properly capture the flow physics, unless a tuning procedure for the two-dimensional airfoil data (the lift and drag coefficients) is employed (Bontempo and Manna, 2017). In fact, during the stall operation, the flow becomes three-dimensional, thus violating the main assumption of the actuator disk approach. Hence, such discrepancies between the BEM results and the experimental measurements for high values of the wind speed are generally anticipated, to some extent.

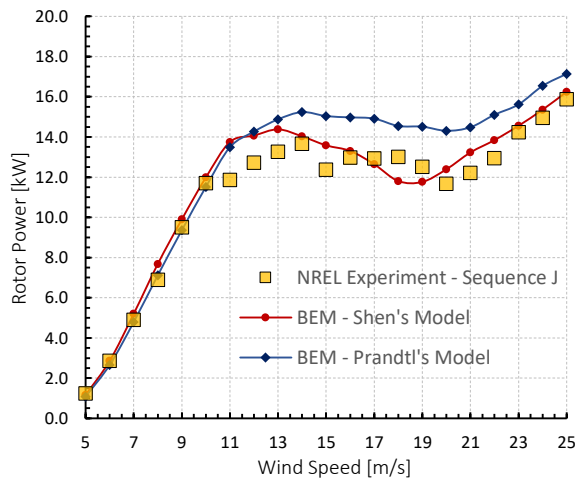


(a) Rotor Power – Sequence H

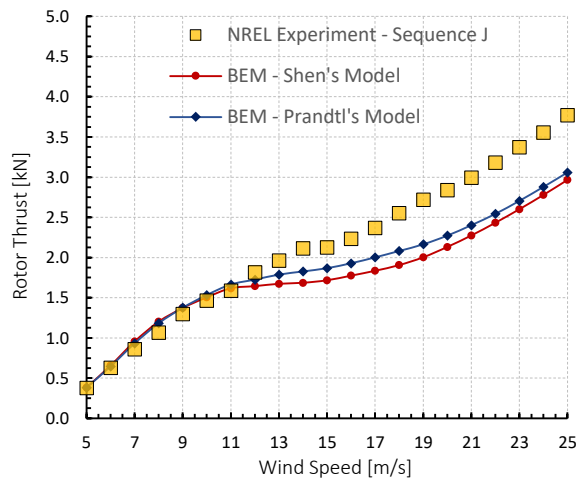


(b) Rotor Thrust – Sequence H

Figure 3.4: Comparison of the predicted and experimentally measured aerodynamic power and thrust for the NREL Phase VI wind turbine rotor – Test Sequence H (Baseline Setup).



(a) Rotor Power – Sequence J



(b) Rotor Thrust – Sequence J

Figure 3.5: Comparison of the predicted and experimentally measured aerodynamic power and thrust for the NREL Phase VI wind turbine rotor – Test Sequence J (High Pitch Setup).

3.1.2 NREL 5-MW Reference Wind Turbine

This validation case considers the NREL 5-MW reference wind turbine, which was originally developed by National Renewable Energy Laboratory and reflects the design specifications of a utility-scale system for offshore energy production, in the megawatt range (Jonkman *et al.*, 2009). The particular variable-speed and pitch-regulated wind turbine configuration is characterized by a three-bladed upwind rotor with a diameter of approximately 126 meters; detailed characteristics of the NREL 5-MW wind turbine can be found in the work of Jonkman *et al.* (2009). In this validation study four typical points within

the operating envelope of NREL 5-MW reference wind turbine are considered, covering the three major control regions of the encountered system, as shown in Table 3.3. In particular, Region 2 refers to variable speed control, Region 3 refers to variable pitch control and finally, Region 2.5 refers to the transitional region between variable speed and variable pitch control.

Case	Wind Velocity	Rotor Speed	Pitch Angle (θ_b)	TSR (λ)	Control Region
1	8.0 m/s	9.16 RPM	0.00 deg	7.55	2
2	11.0 m/s	11.89 RPM	0.00 deg	7.13	2.5
3	11.4 m/s	12.06 RPM	0.00 deg	6.97	2.5
4	15.0 m/s	12.10 RPM	10.45 deg	5.32	3

Table 3.3: Simulation cases for the NREL 5-MW reference wind turbine.

3.1.2.1 Blade Characteristics and Simulation Parameters

Table 3.4 provides a detailed overview of the main geometric characteristics of the NREL 5-MW wind turbine blade (Resor, 2013) – a CAD representation of which is also shown in Figure 3.6. The current blade configuration is defined by a blended distribution of nineteen cross-sectional blade stations, with variable chord length and twist angle values. The first eleven percent of the blade span is characterized by cylindrical cross-sections, while the remaining blade stations are based on five different profiles from the DU airfoil family and one profile from the NACA five-digit series.

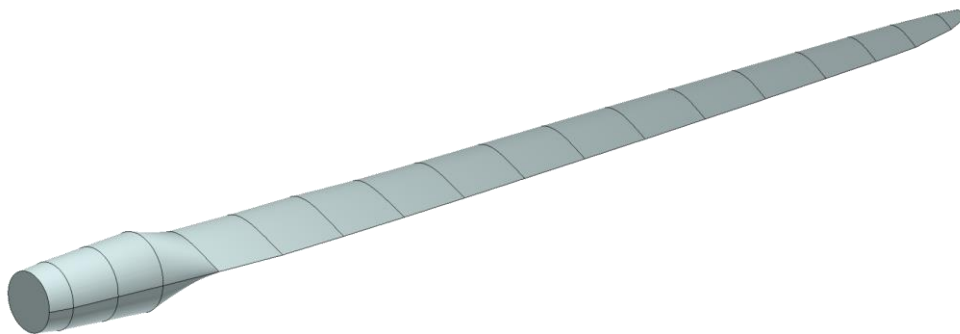


Figure 3.6: CAD representation of the NREL 5-MW blade.

Similar to the previous case study, the lift and drag coefficients for the airfoil sections forming the NREL 5-MW wind turbine blade were calculated using the XFOIL code, and then extrapolated to the entire range of angles of attack by means of Montgomerie (2004) method. As for the cylindrical profiles defining the root region of the blade, constant values of drag coefficient were adopted; for the first three cylindrical profiles, the drag coefficient was set at

0.5, while for the last one equal to 0.35. Finally, both the correction models proposed by Shen and Prandtl were used to account for the tip and hub losses.

Section	Airfoil	Radius [m]	Chord [m]	Twist Angle [deg]
1	Cylinder	1.50	3.542	13.308
2	Cylinder	2.87	3.542	13.308
3	Cylinder	5.60	3.854	13.308
4	Cylinder	8.33	4.167	13.308
5	DU40	11.75	4.557	13.308
6	DU35	15.85	4.652	11.480
7	DU35	19.95	4.458	10.162
8	DU30	24.05	4.249	9.011
9	DU25	28.15	4.007	7.795
10	DU25	32.25	3.748	6.544
11	DU21	36.35	3.502	5.361
12	DU21	40.45	3.256	4.188
13	NACA64618	44.55	3.010	3.125
14	NACA64618	48.65	2.764	2.310
15	NACA64618	52.75	2.518	1.526
16	NACA64618	56.17	2.313	0.863
17	NACA64618	58.90	2.086	0.370
18	NACA64618	61.63	1.400	0.160
19	NACA64618	62.90	0.700	0.000

Table 3.4: Characteristics of the NREL 5-MW wind turbine blade.

3.1.2.2 BEM Simulation Results

Unfortunately, no experimental data for the NREL 5-MW reference wind turbine are available. Thus, at this stage, an indirect validation of the developed model is performed by comparing the results of the current BEM simulations against the corresponding results of the following well-respected simulation tools:

- **SOWFA** – A computational fluid dynamics solver that is based on OpenFOAM toolbox and includes a version of the turbine model, coupled with FAST (Fleming *et al.*, 2013).
- **OVERFLOW2** – A numerical simulation method that is based on the unsteady three-dimensional RANS equations (Nichols and Buning, 2021).
- **FAST** – A comprehensive aeroelastic simulator for horizontal-axis wind turbines that combines modal and multibody dynamics formulation (Jonkman and Buhl, 2005).

- **QBlade** – An open source wind turbine calculation software based on Blade Element Momentum theory (Marten, 2015).

The results of the numerical simulations performed with SOWFA, OVERFLOW2 and FAST were obtained from the comparative study of Anderson *et al.* (2015), which examines the aerodynamic characteristics of the NREL 5-MW rotor; detailed information on the aforementioned simulation tools and the established simulation parameters can be found in the same study. On the other hand, the simulations of NREL 5-MW wind turbine rotor with QBlade was implemented within the current doctoral dissertation. The simulation parameters for QBlade simulations were set in line with those adopted in the simulations with the current BEM model.

Table 3.5 and Table 3.6 contain the predicted aerodynamic power and thrust, respectively, for the NREL 5-MW wind turbine rotor, at free-stream velocities equal to 8 m/s, 11 m/s and 15 m/s. In terms of aerodynamic power prediction, the results of the in-house BEM solver are generally in reasonable agreement with those of the reference simulation tools. In particular, the maximum percentage deviation between the power output estimation of the current BEM model and the respective predictions obtained from the reference computational tools was found for OVERFLOW2, at 8 m/s, and it was approximately equal to 8.8%. As long as the comparison between the current BEM model and the rest simulation tools – in terms of aerodynamic power prediction – is concerned, the percentage deviation for each one of the examined operational point was below 4.4%, following a decreasing trend as the free-stream velocity increases. Overall, the current simulations results for the power output of the NREL 5-MW rotor were found closer to those of FAST, since the mean percentage deviation for the three operational points was approximately equal to 1%; the corresponding percentages for SOWFA, OVERFLOW and QBlade were equal to 3.8%, 6% and 2.4%, respectively, validating the accuracy of our in-house methodology.

NREL 5MW Reference Wind Turbine – Power					
Wind Speed	BEM Code	SOWFA	OVERFLOW2	FAST	QBlade
8 m/s	1900 kW	1985 kW	1733 kW	1875 kW	1977 kW
11 m/s	4905 kW	5061 kW	4650 kW	4827 kW	5020 kW
15 m/s	5296 kW	5093 kW	5499 kW	5297 kW	5250 kW

Table 3.5: Comparison of predicted power by different turbine simulation tools for the NREL 5-MW Reference Wind Turbine at various operational points.

Similar levels of accuracy can be observed on the predictions of aerodynamic thrust for the NREL 5-MW wind turbine rotor, which are included in Table 3.6. In this case, the estimations of the proposed BEM model were found closer to those of SOWFA, deviating from them by only 1% (average percentage deviation for all the encountered operational points); the corresponding percentages for OVERFLOW2 and QBlade are equal to 6.4% and 1.5%, respectively. The only exception to the generally good agreement between the current model and the reference simulation tools is the case of FAST, the predictions of which – in terms of aerodynamic thrust – deviate by an average percentage of 21% from the current simulation results. However, since the same discrepancies can be observed between the results of FAST and those obtained from the other reference models, this is probably attributed to the parameters used in FAST simulation rather to the current BEM code.

NREL 5MW Reference Wind Turbine – Thrust					
Wind Speed	BEM Code	SOWFA	OVERFLOW2	FAST	QBlade
8 m/s	382 kN	382 kN	399 kN	477 kN	390 kN
11 m/s	695 kN	693 kN	733 kN	789 kN	705 kN
15 m/s	417 kN	405 kN	455 kN	520 kN	413 kN

Table 3.6: Comparison of predicted thrust by different turbine simulation tools for the NREL 5-MW Reference Wind Turbine at various operational points.

Finally, in order to provide further validation to the proposed computational tool, the results of the current BEM simulations – in terms of axial and tangential force distributions over the blade – are compared against those obtained by detailed three-dimensional RANS simulations with a fully resolved rotor geometry (Zhong *et al.*, 2019, 2020). The comparisons are performed for the operational conditions in which the NREL 5-MW wind turbine has been rated; namely, a freestream velocity of 11.4 m/s and a rotational speed of 12.06 RPM. According to Figure 3.7, the in-house BEM solver is capable to achieve similar levels of accuracy to those of RANS simulations, for both axial and tangential force distributions.

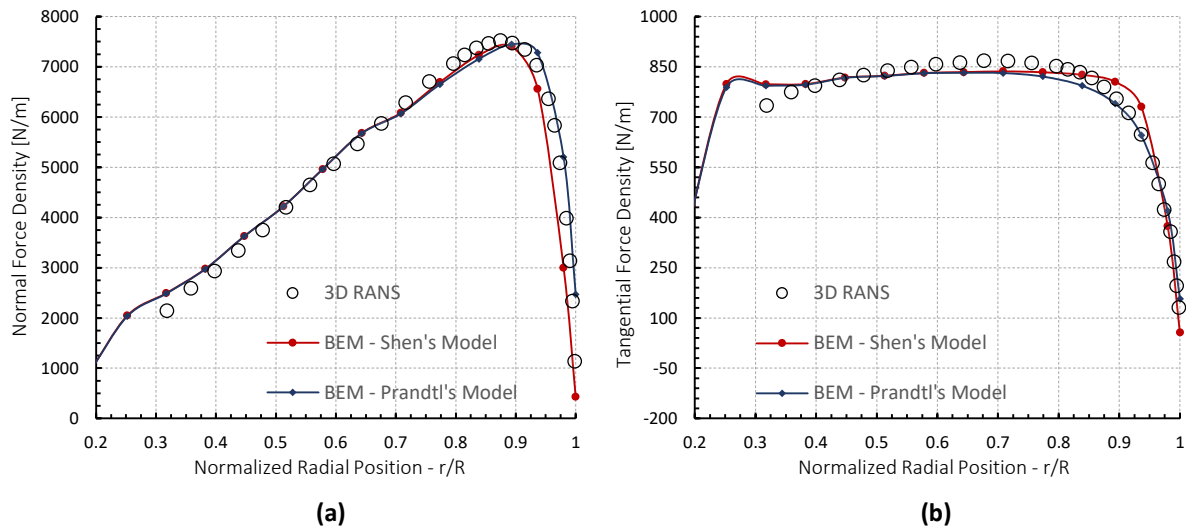


Figure 3.7: Comparison of the axial (a) and tangential (b) force distribution over the NREL 5MW blade at 11.4 m/s, as obtained by the current BEM model and three-dimensional RANS simulations.

3.2 Shrouded Wind Turbines

This section aims to investigate, and eventually validate, the ability of the current BEM code to accurately predict the aerodynamic performance and power output characteristics of shrouded or diffuser-augmented wind turbine rotors. For this reason, the computational results of the in-house developed BEM model are compared against the corresponding data obtained from the experimental investigations of two different shrouded wind turbine configurations; namely, the Donqi Urban Windmill ([van Dorst, 2011](#)) and a multi-slotted diffuser-augmented wind turbine ([Phillips, 2003](#)).

3.2.1 Donqi Urban Windmills DAWT

The present validation study involves the performance prediction of Donqi Urban Windmill, in terms of aerodynamic power output. The particular diffuser-augmented wind turbine, which essentially consists of a single element shroud and a three bladed rotor, with a tip radius of 0.75 m, was originally designed for small scale energy production within the urban environment by Donqi Independent Energy Company, in cooperation with the [Netherlands Aerospace Centre \(NLR\)](#) and [Delft University of Technology](#). Since then, the Donqi Urban Windmill has been the subject of several experimental and numerical research studies ([Ten Hoopen, 2009](#); [van Dorst, 2011](#); [Anselmi, 2017](#); [Avallone et al., 2020](#); [Dighe, 2020](#)), which have primarily been focused on improving the performance of the original design, but also on evaluating newly developed engineering models for shrouded wind turbines.

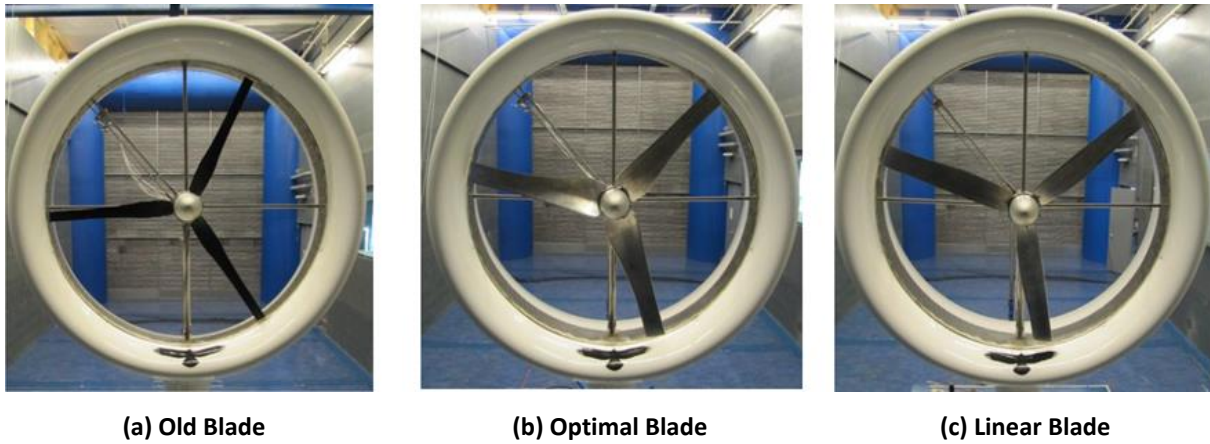


Figure 3.8: The three blade designs of Donqi Urban Windmill (van Dorst, 2011).

Herein, the evaluation of the in-house BEM model is made by using the experimental measurements conducted at the Open Jet Facility of [Delft University of Technology](#) during the Master of Science project of van Dorst (2011). In particular, the work of van Dorst (2011) was mainly focused on designing improved rotor blades for the Donqi Urban Windmill. Thus, in order to experimentally evaluate the performance of the involved blade designs, he conducted a series of wind tunnel measurements by using the same diffuser geometry but three different blade designs, which are labelled as: old, optimal and linear. The three blade designs that were experimentally tested by van Dorst (2011) are shown in Figure 3.8; detailed information about the chord and twist distributions of the blades, as well as for the entire Donqi Urban Windmill system, can be found in the Master of Science thesis of van Dorst (2011).

Actually, the old blade refers to the geometry that was originally manufactured for the Donqi Urban Windmill, based on the NACA 2207 airfoil (Ten Hoopen, 2009); the so-called optimal blade was designed through the chord and twist optimization of the old blade, while the third blade configuration, labelled as linear, was eventually resulted from linearizing the chord distribution of the optimal blade design, in an effort to reduce the material amount and the production costs (van Dorst, 2011). In this validation study, the assessment of the in-house BEM code is made by using experimental data that correspond to all the three blade designs. The current simulation cases are listed in Table 3.7; please note that the BEM calculations for each blade configuration were performed at the optimal TSR for the particular design, which is defined as the TSR yielding the maximum power coefficient.

Case	Blade Design	Wind Velocity	Rotor Speed	Blade Pitch	TSR (λ)
1	Old	5.0 – 8.0 m/s	340 – 545 RPM	10.0 deg	5.4
2	Optimal	5.0 – 8.0 m/s	363 – 581 RPM	10.0 deg	5.7
3	Linear	5.0 – 8.0 m/s	376 – 601 RPM	10.0 deg	5.9

Table 3.7: Simulation cases for the Donqi Urban Windmill rotor.

Now, as long as the single element diffuser of Donqi Urban Windmill is concerned, it is characterized by an exit-area-ratio (that is the ratio between the diffuser exit plane area and the rotor swept area) equal to 1.728 and an exit plane diameter equal to 2 m, while it is also equipped with a 0.04 m high Gurney flap (Ten Hoopen, 2009); more information about the geometrical characteristics of the diffuser design are provided in Section 10.3. The velocity speed-up distribution over the rotor plane for the unloaded diffuser case (input for the BEM calculations) is provided in Figure 3.9a. To be more precise, Figure 3.9a provides both the experimentally measured (van Dorst, 2011) and the numerically estimated (Kesby et al., 2016) distribution of the velocity speed-up ratio over the rotor plane for the unloaded diffuser case. The particular numerical prediction of the velocity speed-up distribution was originally reported in the study of Kesby et al. (2016) and it was obtained by means of ANSYS CFX solver for an ambient wind speed of 5 m/s.

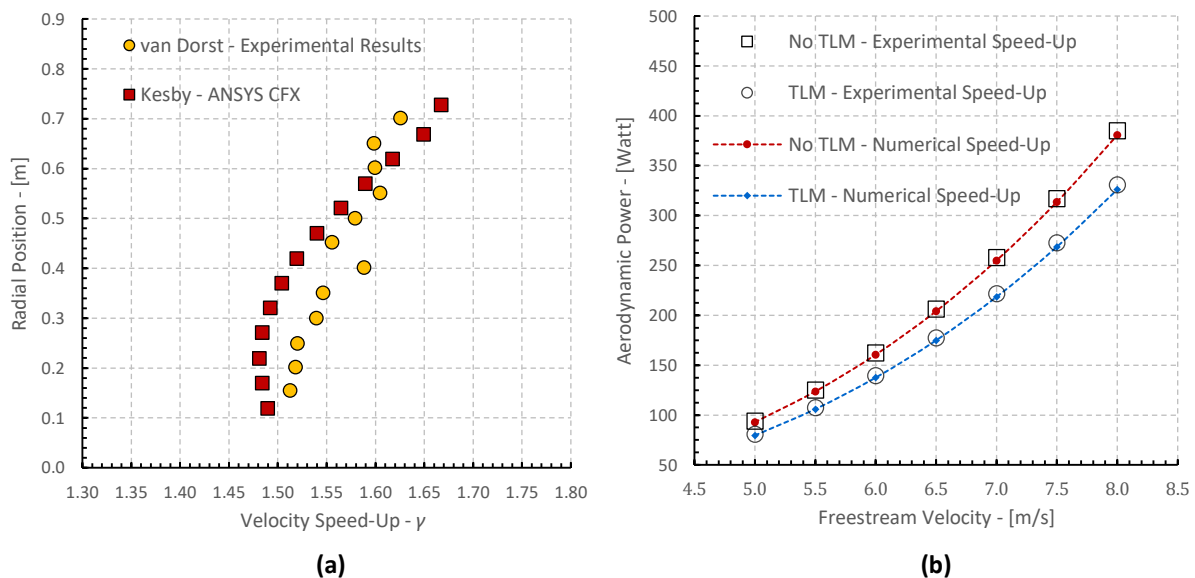


Figure 3.9: (a) The experimentally measured and numerically predicted velocity speed-up distribution over the rotor plane for the unloaded Donqi Urban Windmill (Kesby et al., 2016). (b) Comparison of the BEM results obtained from the measured and numerically predicted velocity speed-up.

3.2.1.1 BEM Simulation Results

Figure 3.10 illustrates the experimentally measured power output of the Donqi Urban Windmill rotor, for each one of the involved blade designs, in comparison with the results obtained from the in-house BEM code. Please note that the current BEM calculations for each blade design were performed both with and without the inclusion of a tip loss correction model. The aim of this strategy was to examine the effect of such a correction model on power output, and identify whether a tip loss correction model is necessary during the BEM analysis of shrouded wind turbines. As long as the power loss associated with the **0.15 m** radius hub of Donqi Urban Windmill are concerned, the Prandtl's hub loss correction model (see Section 2.2.5.1) was included for every BEM simulation, regardless of the tip loss correction model. It is also noted that in the current validation study, all BEM calculations were performed by employing the numerically predicted velocity speed-up distribution reported in the study of Kesby *et al.* (2016), instead of the velocity speed-up distribution measured by van Dorst (2011), since both the experimentally measured and numerically estimated velocity speed-up distributions – shown in Figure 3.9a – led to practically identical power output predictions. In order to support this claim, Figure 3.9b provides a comparison between the power output predictions obtained by using both of the aforementioned velocity speed-up distributions, for the old blade geometry. The maximum observed discrepancy was less than 1.5 percent; this was also the case for the optimal and linear blade designs.

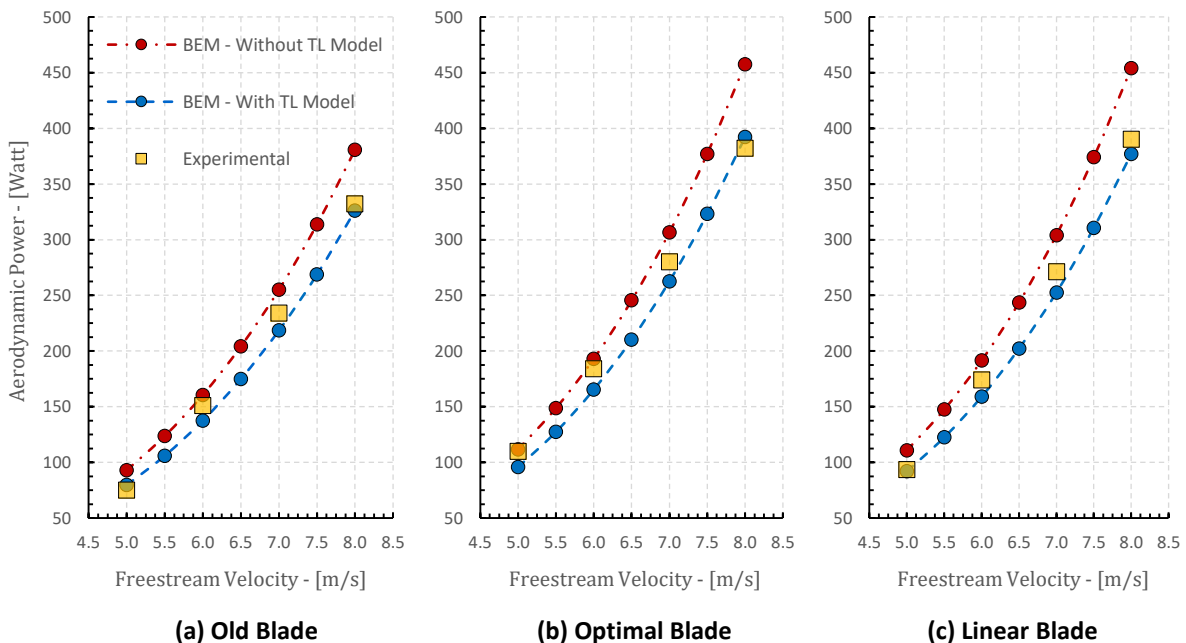


Figure 3.10: Experimental data and BEM predictions for the power output of the Donqi Urban Windmill rotor. (a) Old blade; (b) Optimal blade; (c) Linear blade.

Regarding the evaluation of the developed BEM code, in terms of accuracy, Figure 3.10 reveals a very good association between the computational results and the experimental values for the aerodynamic power output of Donqi Urban Windmill rotor; the accuracy of the computational results does not seem to be affected by the blade design at hand. Moreover, from a qualitative point of view, the comparisons illustrated in Figure 3.10 definitely indicate that the BEM results obtained by including the tip loss correction model are much closer to the experimental ones, as compared to those obtained from the opposite simulation case. In fact, the absence of a tip loss correction model results in notable discrepancies between the computational and experimental results (overestimation of the aerodynamic power output) that increase with the value of the ambient wind speed.

Furthermore, Table 3.8 provides the mean absolute error (MAE) and the mean absolute percentage error (MAPE) between the experimental and the computational results for the three blade designs of the Donqi Urban Windmill. Obviously, the quantitative information provided in Table 3.8 supports the inclusion of a tip loss correction model, since it result in notably smaller average deviations between the computational and the experimental results, even though it may generally leads to an underestimation of the measured power output. In general, the comparisons between the experimental measurements and BEM results reveal that the current model is able to reasonably predict the power output of such configurations, since the trend of the power curve has been adequately captured and the maximum mean absolute percentage error was found around 8 percent.

Blade	Old	Optimal	Linear
Without Prandtl's Tip Loss Model			
MAE	24.28 Watts	28.18 Watts	32.89 Watts
MAPE	13.47 %	8.92 %	14.27 %
With Prandtl's Tip Loss Model			
MAE	9.89 Watts	15.08 Watts	11.99 Watts
MAPE	5.87 %	7.99 %	5.08 %

Table 3.8: The mean absolute error (MAE) and the mean absolute percentage error (MAPE) between the experimental data and the BEM results for each blade of the Donqi Urban Windmill.

3.2.2 A Multi-Slotted DAWT

In order to add further validity to the results of the in-house BEM code, this section considers the power performance prediction of the multi-slotted diffuser-augmented wind turbine that was experimentally investigated during the doctoral thesis of Phillips (2003), at

the Twisted Flow Wind Tunnel of the University of Auckland. The 0.48 m diameter multi-slotted diffuser-augmented wind turbine is composed by a double surface diffuser. The outer skin of the particular diffuser design is formed by a single continuous surface, with its trailing edge to be fixed at an angle of 55 degrees relative to the centreline, while the inner surface has five boundary layer control slots, all positioned behind of the rotor plane. A schematic representation of the flow behaviour through the multi-slotted diffuser is provided in Figure 3.11. The examined diffuser geometry has an inlet-area-ratio (that is the ratio of the diffuser inlet area to the rotor swept area) equal to 1.2 and an exit-area-ratio equal to 3. The distribution of the velocity speed-up ratio over the rotor plane for the unloaded diffuser case is provided in Table 3.9, as obtained from wind tunnel measurements conducted by Phillips (2003).

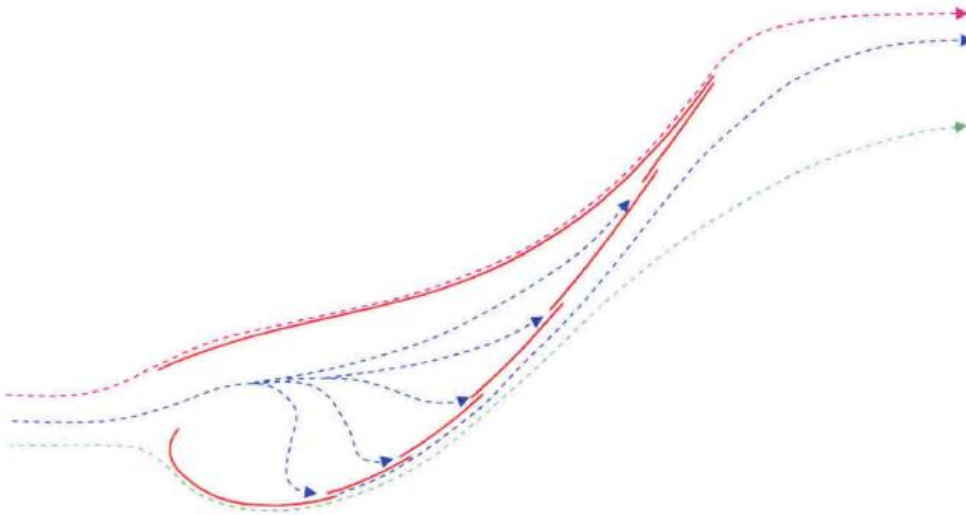


Figure 3.11: A schematic representation of the flow behaviour through the multi-slotted diffuser-augmented wind turbine (Phillips, 2003).

r/R_{tip}	0.32	0.44	0.54	0.62	0.69	0.75	0.81	0.87	0.92	0.97
γ	1.18	1.17	1.16	1.16	1.17	1.20	1.23	1.27	1.32	1.42

Table 3.9: The velocity speed-up ratio distribution over the rotor plane for the unloaded diffuser of the multi-slotted diffuser-augmented wind turbine (Phillips, 2003).

As long as the rotor of the multi-slotted diffuser-augmented wind turbine is concerned, the examined wind turbine configuration has a typical three bladed rotor. The geometrical characteristics of the rotor blades are presented in Table 3.10; the particular blade design was obtained by means of a single point optimization procedure, which was based on the modified BEM model developed by Phillips (2003). Eventually, the tip region of the blade has been formed by a Selig S-3021-095-84 airfoil with an approximate thickness-to-chord ratio of 10

percent, while a similar (scaled) airfoil with a thickness-to-chord ratio of 25 percent has been employed for the root region of the blade. The thickness-to-chord ratio of the airfoils defining the mid region of the blade varies linearly between 10 and 25 percent. The exact twist and chord distributions of the particular blade are reported in Table 3.10. Please note that all BEM calculations for this case study have been performed at the optimal blade pitch angle, which equals to 6.7 degrees (Phillips, 2003).

Section	Airfoil	Radius [m]	Chord [m]	Twist Angle [deg]
1	S-3021-095-84	0.058	0.0426	21.3
2	S-3021-095-84	0.076	0.0426	16.9
3	S-3021-095-84	0.094	0.0375	11.8
4	S-3021-095-84	0.112	0.0330	8.1
5	S-3021-095-84	0.130	0.0303	5.4
6	S-3021-095-84	0.148	0.0278	3.3
7	S-3021-095-84	0.166	0.0256	1.6
8	S-3021-095-84	0.184	0.0240	0.3
9	S-3021-095-84	0.202	0.0235	-0.6
10	S-3021-095-84	0.220	0.0235	-0.8
11	S-3021-095-84	0.238	0.0235	0.0

Table 3.10: Blade characteristics for the multi-slotted DAWT (Phillips, 2003).

3.2.2.1 BEM Simulation Results

Figure 3.12 illustrates the experimentally measured values of shaft augmentation for the multi-slotted diffuser-augmented wind turbine, at the optimal pitch angle of 6.7 degrees, in comparison to the predicted augmentation values that were obtained from the current BEM code and the modified BEM model developed by Phillips (2003). Apparently, the current BEM model seems able to provide a reasonably good approximation of the entire power curve. However, at the same time, significant underestimations of the measured augmentation values can be definitely observed, especially near the optimum tip speed ratio. According to our point of view, these discrepancies between the experimental and the computational values probably stem from the inaccurate values of the aerodynamic lift and drag coefficients reported within the reference study, and eventually employed during the current BEM calculations. In fact, Phillips (2003) provided only the aerodynamic data for the Selig S-3021-095-84 airfoil, as well as a manually modified version of them. However, the study of Phillips (2003) did not provide the respective aerodynamic characteristics for the scaled airfoils defining the root and mid regions of the blade. Therefore, being the only ones available, the aerodynamic lift and drag

coefficients of the root airfoil were eventually adopted for all the airfoil sections along the blade, even though there was a considerable change of the thickness-to-chord ratio along the blade.

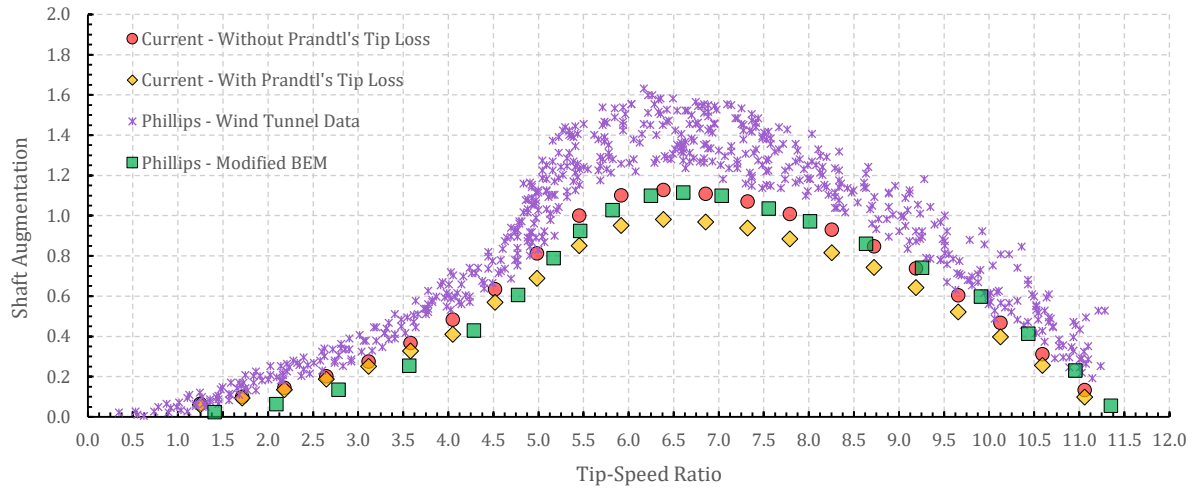


Figure 3.12: The experimentally measured and computational predicted power curve of the multi-slotted diffuser-augmented wind turbine at the optimum pitch angle of 6.7 degrees.

Finally, Figure 3.12 could also provide significant information about the effect of the tip loss correction model on the predicted shaft augmentation. In this case, the inclusion of such a correction model seems to cause an even greater underestimation of the experimental data. Nevertheless, a solid conclusion on whether the inclusion of a tip loss model during the analysis of shrouded wind turbines is required, cannot be established based on this case study, given the inaccuracies of the utilized lift and drag data.

Chapter 4

Development of an Axisymmetric RANS Solver

This chapter describes the development of an academic in-house RANS solver, called IGal2D, for the numerical prediction of incompressible axisymmetric flows involving swirling. In particular, Section 4.1 provides a general introduction into axisymmetric swirling flows, as well as the incentives for the development of IGal2D solver, while Section 4.2 presents the adopted form of the governing equations defining the flow and turbulence models. Finally, the remaining sections of the current chapter outline the numerical methodology underlying the IGal2D solver, emphasizing on the spatial and temporal discretization schemes, the flux evaluation approaches and the source term treatment.

4.1 Axisymmetric Swirling Flows

Axisymmetric flows that involve swirling or rotation represent a fundamental class of relatively complex fluid motion that is widely encountered in many engineering applications (e.g., pipeline systems, cooling devices, cyclone separators, combustion chambers and turbomachines), as well as in various natural phenomena (e.g., tornadoes, hurricanes and ocean circulations). Therefore, in recent decades, such flows have been consistently considered as an attractive subject of both scientific research and technical investigations.

In general, the interaction between the swirling and streamwise motions has been proved an effective technique to enhance heat and mass transfer, as well as to stabilize and intensify certain working processes, particularly in aviation and rocket technology (Algifri *et al.*, 1987). In addition, swirling motion has also been shown to improve the performance of shrouded wind turbines, since the tangential velocity component induced by the rotor blades helps to energize the velocity boundary layer of the internal diffuser wall and thus, to suppress possible flow separation (Leloudas *et al.*, 2020a; Venters *et al.*, 2018). However, large values of the swirl parameter or number – which is defined as a measure of the ratio between the azimuthal and axial velocities (Billant *et al.*, 1998; Ramos, 1984; Yang *et al.*, 2018) – can possibly result in adverse flow patterns. A characteristic example was reported during the experimental study of Billant *et al.* (1998) on swirling water jets. This investigation concluded that increasing the swirl parameter over a critical threshold, for a prescribed Reynolds number, is directly related to the emergence of vortex breakdown (Yang *et al.*, 2018). Negative implications of swirling, in terms of conventional diesel engines, were also reported by Ikegami and Kamimoto (2009), and although it was found that swirl itself may bring about favourable effects in fuel

distribution, air utilization, and acceleration of combustion, it was highlighted that large swirl numbers may not only decrease volumetric efficiency, but also cause poor combustion.

In any case, accurate predictions of axisymmetric swirling flows and deep understanding of the associated phenomena are essential to improve the performance of the applications and processes involved. In modern engineering practice, numerical methods, and particularly CFD, represent a class of highly valuable tools – sometimes the only viable ones, given the drawbacks related to experimental procedures – to serve that purpose (Mazzafarro *et al.*, 2005). From a macroscopic point of view, axisymmetric fluid motion, with or without the presence of swirling, can be predicted by means of the three-dimensional (3D) Navier-Stokes equations in cylindrical coordinates (Bird *et al.*, 2006). However, the application of numerical methods adopting that form of governing equations is usually associated with relatively high computational cost and pre-processing effort, whereas their implementation entails significant challenges as well, which mainly stem from the 3D nature of the problem.

On the other hand, the majority of the aforementioned shortcomings could be alleviated by taking advantage of the axisymmetric condition, dictating that the gradient for each flow variable in the azimuthal direction equals to zero. Consequently, by eliminating all the respective derivatives, the 3D Navier-Stokes equations in cylindrical coordinates can be reduced to a quasi-two-dimensional (2D) set of partial differential equations, defined over the meridional plane; these are widely known as the axisymmetric Navier-Stokes equations. As a matter of fact, the axisymmetric Navier-Stokes equations are usually arranged in a pseudo-Cartesian form, by treating all the redundant terms associated with axisymmetric effects as source ones (Zhang *et al.*, 2019). Ultimately, this approach allows for a significant reduction in both pre-processing effort and computational time, owned to the utilization of 2D grids and methods, instead of 3D ones, while at the same time providing reasonable levels of accuracy, when compared with the corresponding 3D models (Abedi *et al.*, 2020; Leloudas *et al.*, 2018b, 2020a, 2021; Susan-Resiga *et al.*, 2006).

To assess the accuracy of axisymmetric Navier-Stokes models, especially in comparison with their 3D counterparts, but also with experimental measurements, significant studies were carried out by Susan-Resiga *et al.* (2006) and Abedi *et al.* (2020). In particular, Susan-Resiga *et al.* (2006) compared the numerical results of an axisymmetric solver for the incompressible Navier-Stokes equations, against the time-averaged solution of an unsteady 3D simulation, regarding the swirling flow inside the draft tube cone of Francis turbines at partial discharge. On the other hand, Abedi *et al.* (2020) performed a series of steady-state simulations on a supersonic inlet, using both axisymmetric and 3D flow solvers that were based on the compressible RANS equations and $k-\omega$ Shear Stress Transport (SST) turbulence model. Both research teams reached to the conclusion that numerical simulations, performed by means of

the axisymmetric models, could provide adequate levels of accuracy, especially in the absence of intense 3D effects; a valid assumption of a purely axisymmetric flow. Nevertheless, for the detailed prediction of strongly rotating flows that involve unsteady and intense 3D phenomena, associated with the collapse of the axisymmetric condition – such as the rotating vortex rope in the draft tube cone of Francis turbines (Susan-Resiga *et al.*, 2006; Yang *et al.*, 2018) – 3D simulations were found rather appropriate (Li *et al.*, 2014). Yet, the axisymmetric models could still capture the major flow aspects with reasonable accuracy for practical applications.

Besides the aforementioned studies, many numerical models that employ the axisymmetric form of Navier-Stokes equations have been developed, for both compressible (Clain *et al.*, 2010; Gokhale and Suresh, 1997; Musa *et al.*, 2016) and incompressible flows (Dağtekin and Ünsal, 2011; Durkish, 2006; Lee and Lee, 2011; Leloudas, 2018b, 2020a; Morsi *et al.*, 1995; Moshkin *et al.*, 2010; Saiac, 1990; Semião and Carvalho, 1997), featuring various discretization methods, flux evaluation schemes and turbulence models. Moreover, axisymmetric flow modelling has lately become a highly attractive topic in the context of mesoscopic approaches as well, such as the lattice Boltzmann Method (LBM) (Hajabdollahi *et al.*, 2019; Huang *et al.*, 2007; Lee *et al.*, 2005; Li *et al.*, 2018; Liu H. *et al.*, 2016; Liu Q. *et al.*, 2019; Zhang *et al.*, 2019). However, to the best of our knowledge, the implementation of an axisymmetric Navier-Stokes solver for incompressible swirling flows that employs Artificial Compressibility Method (ACM) is not available.

The artificial compressibility approach, which is also termed as pseudo-compressibility approach, was originally introduced by Chorin (1967), in order to overcome pressure decoupling. Essentially, ACM involves the addition of a temporal derivative of pressure to the continuity equation, allowing the incompressible system of equations to be relaxed within the framework of a time-marching compressible flow solver (Anderson *et al.*, 1996). In particular, the ACM transforms the incompressible Navier-Stokes equations of mixed elliptic/parabolic type, into a pseudo-temporal set of hyperbolic or parabolic partial differential equations (Kiris *et al.*, 2006; Stokos *et al.*, 2015). Additionally, in cases that the prediction of temperature distribution is not required (*i.e.*, fluid motion characterized by negligible temperature gradients) ACM can provide significant advantages, especially over preconditioning methods; namely, energy equation isn't solved, hence the corresponding flow solver is enhanced with substantial memory and time savings (Anderson *et al.*, 1996). Furthermore, according to the comprehensive study of Tamamidis *et al.* (1996), ACM could outperform the pressure-based method (PBM) in terms of convergence rates, while according to Tanno *et al.* (2013), ACM has been proved faster than LBM on GPUs, for a properly selected value of the artificial compressibility parameter.

Therefore, against this background, and given the overall goal of the current doctoral dissertation to propose a computational framework for the design optimization of shrouded wind turbines, the remainder of this chapter features the development of an academic in-house flow solver that combines the ACM with the axisymmetric RANS equations, for the prediction of incompressible swirling flows. In particular, Section 4.2 describes the detailed derivation of the adopted form of the governing equations, defining the flow and turbulence models, while Section 4.3 until Section 4.5 outline the numerical methodology underlying the current flow solver, emphasizing on the spatial and temporal discretization schemes, the flux evaluation approaches and the source term treatment. Ultimately, the developed flow solver, called **IGal2D** (Leloudas *et al.*, 2021; Lygidakis *et al.*, 2020), is validated against relevant demanding benchmark test cases, which include both non-swirling and swirling flows with axial symmetry; the numerical validation of the proposed axisymmetric solver is included in Chapter 5. The obtained results are compared with available experimental and numerical data reported in the literature, as well as with those of the commercial software ANSYS Fluent (Fluent, 2009), aiming to confirm the potential of the proposed ACM-based methodology to predict such pseudo-3D flows in terms of accuracy.

4.2 Governing Equations

4.2.1 Axisymmetric Navier-Stokes Equations

The axisymmetric Navier-Stokes equations for incompressible fluid motion can be derived in a relatively straightforward manner from the fundamental laws of mass, momentum and energy conservation – when they are expressed in cylindrical coordinates (r, θ, z) – through the application of axisymmetric invariance assumption (Clain *et al.*, 2010); essentially, the axisymmetric invariance assumption considers no flow variation in the azimuthal direction (θ) and therefore, eliminates all the respective partial derivatives $(\partial/\partial\theta)$. At this point, let us note that the scope of this study is exclusively restricted to practically incompressible and isothermal flows, which are characterized by uniform density (ρ) and kinematic viscosity (ν) values. Under these conditions, the energy equation is irrelevant, due to negligible temperature gradients and thermodynamic effects (Wang, 2015). Consequently, fluid motion is entirely governed by the continuity (4.1) and momentum (4.2) equations, which respectively read:

$$\nabla \cdot \mathbf{u} = 0, \quad (4.1)$$

$$\frac{\partial \mathbf{u}}{\partial t} + \mathbf{u} \cdot \nabla \mathbf{u} = -\frac{1}{\rho} \nabla p + \nu \Delta \mathbf{u} + \mathbf{f}. \quad (4.2)$$

Here, p stands for static pressure, t stands for time, $\mathbf{u} = (u_r, u_\theta, u_z)$ stands for the fluid velocity vector and $\mathbf{f} = (f_r, f_\theta, f_z)$ stands for the vector of external body forces. Therefore, by implementing all the differential operators included within Eqs. (4.1) and (4.2) in terms of cylindrical coordinates (see Appendix A) while eliminating all the partial derivatives related to azimuthal (θ) direction, the **non-conservative form of the incompressible axisymmetric Navier-Stokes equations** can be emerged, as shown in Eqs. (4.3) – (4.6).

Continuity:

$$\frac{1}{r} \frac{\partial(ru_r)}{\partial r} + \frac{\partial u_z}{\partial z} = 0 \quad (4.3)$$

Radial Momentum (r):

$$\frac{\partial u_r}{\partial t} + u_r \frac{\partial u_r}{\partial r} + u_z \frac{\partial u_r}{\partial z} - \frac{u_\theta^2}{r} = -\frac{1}{\rho} \frac{\partial p}{\partial r} + \nu \frac{\partial}{\partial r} \left(\frac{1}{r} \frac{\partial(ru_r)}{\partial r} \right) + \nu \frac{\partial}{\partial z} \left(\frac{\partial u_r}{\partial z} \right) + f_r \quad (4.4)$$

Azimuthal Momentum (θ):

$$\frac{\partial u_\theta}{\partial t} + u_r \frac{\partial u_\theta}{\partial r} + u_z \frac{\partial u_\theta}{\partial z} + \frac{u_r u_\theta}{r} = \nu \frac{\partial}{\partial r} \left(\frac{1}{r} \frac{\partial(ru_\theta)}{\partial r} \right) + \nu \frac{\partial}{\partial z} \left(\frac{\partial u_\theta}{\partial z} \right) + f_\theta \quad (4.5)$$

Axial Momentum (z):

$$\frac{\partial u_z}{\partial t} + u_r \frac{\partial u_z}{\partial r} + u_z \frac{\partial u_z}{\partial z} = -\frac{1}{\rho} \frac{\partial p}{\partial z} + \nu \frac{1}{r} \frac{\partial}{\partial r} \left(r \frac{\partial u_z}{\partial r} \right) + \nu \frac{\partial}{\partial z} \left(\frac{\partial u_z}{\partial z} \right) + f_z \quad (4.6)$$

Apparently, the axisymmetric invariance assumption leads to the elimination of azimuthal velocity component (u_θ) from continuity equation (4.3). However, u_θ is still coupled to the axial (u_z) and radial (u_r) velocity components by means of momentum equations (4.4) – (4.6). In addition, axial symmetry condition removes the explicit effects of pressure from the azimuthal momentum equation (4.5). Nevertheless, u_θ remains coupled to the pressure field through the centrifugal acceleration term (u_θ^2/r), which is included within the radial momentum equation (4.4); the centrifugal acceleration term represents the effective acceleration in radial direction, resulting from fluid motion in azimuthal direction (Bird *et al.*, 2006; Siebert and Yocum, 1993). Finally, it should be noted that the body forces per unit volume in Eqs. (4.4) – (4.6), provide a convenient means by which the effect of external objects, such as wind turbine blades, can be introduced into the momentum equations. A detailed discussion on the proper modeling of body forces, as well as the development of a methodology coupling IGal2D and BEM solvers, is provided in Chapter 8.

4.2.1.1 Dimensionless Form of the Axisymmetric N-S Equations

IGal2D solver is based on a dimensionless formulation of the axisymmetric Navier-Stokes equations. Dimensionless analysis represents a common practice in the field of fluid mechanics, which allows for the utilization of dimensionless similarity parameters, such as the Reynolds (Re) and Prandtl (Pr) numbers. In that way, the data of several equivalent experiments at different scales, can be grouped together and analyzed efficiently, while the number of required variables for the simulation of similar flows can be significantly reduced. Besides, dimensionless or normalized variables could also be a better alternative, compared to the unscaled or dimensional ones, from a numerical point of view; since their values are usually scaled so that they lie between zero and one, the floating point errors associated with very large or small numbers can be diminished (Siebert and Yocum, 1993).

In this study, the governing equations (4.3) – (4.6) are normalized by introducing four reference quantities; namely, a reference length scale - L_{ref} , a reference velocity scale - V_{ref} , a reference density scale - ρ_{ref} and a reference kinematic viscosity scale - ν_{ref} . Consequently, the dimensionless length (\tilde{x}_i), velocity (\tilde{u}_i), density ($\tilde{\rho}$) and kinematic viscosity ($\tilde{\nu}$) are defined as:

$$\tilde{x}_i = \frac{x_i}{L_{ref}}, \quad \tilde{u}_i = \frac{u_i}{V_{ref}}, \quad \tilde{\rho} = \frac{\rho}{\rho_{ref}}, \quad \tilde{\nu} = \frac{\nu}{\nu_{ref}}. \quad (4.7)$$

The remaining parameters included in Eqs. (4.3) – (4.6) are normalized by combinations of the adopted reference quantities, as follows:

$$\tilde{p} = \frac{p}{\rho_{ref} \cdot V_{ref}^2}, \quad \tilde{f}_i = \frac{f_i}{\rho_{ref} \cdot V_{ref}^2 \cdot L_{ref}^2}, \quad \tilde{t} = \frac{t}{L_{ref} \cdot V_{ref}^{-1}}, \quad (4.8)$$

where the "~" superscript indicates the dimensionless quantities. Typically, the reference length scale (L_{ref}) is defined by using a characteristic length of the examined flow problem, whereas the reference velocity scale (V_{ref}) is selected as the magnitude of the free-stream velocity. On the other hand, the reference scale of density (ρ_{ref}) for incompressible flows is usually defined as the fluid's density (ρ), which is constant; thus, non-dimensional density ($\tilde{\rho}$) equals to unity. At last, the fluid's kinematic viscosity (ν) is the most convenient reference scale for viscosity (ν_{ref}). Consequently, for isothermal and laminar flows, the non-dimensional kinematic viscosity ($\tilde{\nu}$) is also equal to unity (Siebert and Yocum, 1993).

Ultimately, by introducing Eqs. (4.7) and (4.8) into Eqs. (4.3) – (4.6), the non-conservative form of the axisymmetric Navier-Stokes equations for incompressible fluid motion, in terms of **dimensionless** parameters, can be written as follows:

Continuity:

$$\frac{1}{\tilde{r}} \frac{\partial(\tilde{r}\tilde{u}_r)}{\partial\tilde{r}} + \frac{\partial\tilde{u}_z}{\partial\tilde{z}} = 0 \quad (4.9)$$

Radial Momentum (r):

$$\frac{\partial\tilde{u}_r}{\partial\tilde{t}} + \tilde{u}_r \frac{\partial\tilde{u}_r}{\partial\tilde{r}} + \tilde{u}_z \frac{\partial\tilde{u}_r}{\partial\tilde{z}} - \frac{\tilde{u}_\theta^2}{\tilde{r}} = -\frac{1}{\tilde{\rho}} \frac{\partial\tilde{p}}{\partial\tilde{r}} + \frac{\tilde{\nu}}{\text{Re}} \frac{\partial}{\partial\tilde{r}} \left(\frac{1}{\tilde{r}} \frac{\partial(\tilde{r}\tilde{u}_r)}{\partial\tilde{r}} \right) + \frac{\tilde{\nu}}{\text{Re}} \frac{\partial}{\partial\tilde{z}} \left(\frac{\partial\tilde{u}_r}{\partial\tilde{z}} \right) + \tilde{f}_r \quad (4.10)$$

Azimuthal Momentum (θ):

$$\frac{\partial\tilde{u}_\theta}{\partial\tilde{t}} + \tilde{u}_r \frac{\partial\tilde{u}_\theta}{\partial\tilde{r}} + \tilde{u}_z \frac{\partial\tilde{u}_\theta}{\partial\tilde{z}} + \frac{\tilde{u}_r\tilde{u}_\theta}{\tilde{r}} = \frac{\tilde{\nu}}{\text{Re}} \frac{\partial}{\partial\tilde{r}} \left(\frac{1}{\tilde{r}} \frac{\partial(\tilde{r}\tilde{u}_\theta)}{\partial\tilde{r}} \right) + \frac{\tilde{\nu}}{\text{Re}} \frac{\partial}{\partial\tilde{z}} \left(\frac{\partial\tilde{u}_\theta}{\partial\tilde{z}} \right) + \tilde{f}_\theta \quad (4.11)$$

Axial Momentum (z):

$$\frac{\partial\tilde{u}_z}{\partial\tilde{t}} + \tilde{u}_r \frac{\partial\tilde{u}_z}{\partial\tilde{r}} + \tilde{u}_z \frac{\partial\tilde{u}_z}{\partial\tilde{z}} = -\frac{1}{\tilde{\rho}} \frac{\partial\tilde{p}}{\partial\tilde{z}} + \frac{\tilde{\nu}}{\text{Re}} \frac{1}{\tilde{r}} \frac{\partial}{\partial\tilde{r}} \left(\tilde{r} \frac{\partial\tilde{u}_z}{\partial\tilde{r}} \right) + \frac{\tilde{\nu}}{\text{Re}} \frac{\partial}{\partial\tilde{z}} \left(\frac{\partial\tilde{u}_z}{\partial\tilde{z}} \right) + \tilde{f}_z \quad (4.12)$$

Although both the dimensionless scales of density ($\tilde{\rho}$) and kinematic viscosity ($\tilde{\nu}$) are equal to unity, they are deliberately retained within Eqs. (4.9) - (4.12) just for the sake of completeness. At this point, please note that the Reynolds number – which is defined as:

$$\text{Re} = \frac{L_{\text{ref}} \cdot V_{\text{ref}}}{\nu_{\text{ref}}} \quad (4.13)$$

and provides the ratio of inertial forces to viscous ones (Anderson, 2010) – appears naturally within momentum equations, when they are expressed in a dimensionless formulation. Apparently, in the current formulation of the non-dimensional Navier-Stokes equations, each viscous or diffusive term in the RHS of momentum equations (4.10) - (4.12) is divided by Re; an alternative to this could be to multiply every convective or inertial term, as well as the body force term, by Re. However, the former approach is generally preferred over the latter one, in order to minimize floating point errors during the numerical solution (Siebert and Yocum, 1993), especially in the case where high-Reynolds number flows are encountered. Finally, a concluding remark on the normalization procedure of the Navier-Stokes equations could be drawn by observing the continuity equation (4.9); its form is not reformed by the non-dimensionalization. This stems from the fact that all the terms within continuity equations are inviscid ones. In the rest of this thesis, the superscript "~" denoting the normalized variables is neglected for simplification reasons; every flow quantity is considered in its dimensionless form.

4.2.1.2 Conservative Form of the Axisymmetric N-S Equations

In this section, the conservative form of the incompressible axisymmetric Navier-Stokes equations is derived. According to Hoffmann and Chiang (1993), a differential equation is termed to be in conservative form if the coefficients of the derivatives are either constant, or if variable, their derivatives do not appear anywhere in the equation. Although, the conservative and non-conservative forms of the governing equations – as well as those of any other differential equation – are mathematically equivalent, this is not the case for their discretized counterparts. In general, a conservative formulation of the governing equations is usually preferred when a numerical solution is involved. This stems from the fact that the conservative form of the fundamental conservation laws could result in a discrete approximation of a similar form, which leads to discrete conservation almost naturally. On the other hand, numerical conservation can be proved quite challenging when a non-conservative formulation is employed (Oud, 2017). In fact, by solving the equations in their conservative form, the flux crossing one control volume face will be the same for each of the adjacent control volumes that share that face. Consequently, both local and global flux conservation is guaranteed (Siebert and Yocum, 1993).

In order to derive the conservative form of axisymmetric Navier-Stokes equations, Eq. (4.14) and Eq. (4.15) are initially introduced. Essentially, Eq. (4.14) is just an expression of the product rule for derivatives, while Eq. (4.15) results from the fact that cylindrical coordinate systems are orthogonal. Therefore, the radial coordinate (r) is independent of the axial coordinate (z) and, as such, it may be brought inside the partial derivatives with respect to z .

$$\frac{\partial u_r}{\partial r} + \frac{u_r}{r} = \frac{1}{r} \frac{\partial (ru_r)}{\partial r}, \quad (4.14)$$

$$\frac{\partial u_z}{\partial z} = \frac{1}{r} \frac{\partial (ru_z)}{\partial z}. \quad (4.15)$$

Thus, the conservative form of the axisymmetric Navier-Stokes equations can be derived from the non-conservative one, presented in Section 4.2.1.1, by adding the continuity equation to the LHS of each momentum equation while applying Eqs. (4.14) and (4.15). At this point, please note that besides the convective terms in the LHS of momentum equations, some of the viscous ones in the RHS have been properly recast as well, so as the components of the viscous stress tensor (τ_{ij}) to be emerged. Eventually, the conservative form of the incompressible axisymmetric Navier-Stokes equations, in terms of dimensionless parameters and viscous shear stress components, are shown through Eqs. (4.16) - (4.19). The equivalent (conservative and dimensionless) formulation of the axisymmetric Navier-Stokes equations, in terms of velocity gradients, is provided in Appendix B.

Continuity:

$$\frac{1}{r} \frac{\partial(ru_r)}{\partial r} + \frac{\partial u_z}{\partial z} = 0 \quad (4.16)$$

Radial Momentum (r):

$$\frac{\partial u_r}{\partial t} + \frac{1}{r} \frac{\partial(ru_r u_r)}{\partial r} + \frac{1}{r} \frac{\partial(ru_r u_z)}{\partial z} - \frac{u_\theta^2}{r} = -\frac{\partial p}{\partial r} + \frac{1}{r} \frac{\partial(r\tau_{rr})}{\partial r} + \frac{1}{r} \frac{\partial(r\tau_{rz})}{\partial z} - \frac{\tau_{\theta\theta}}{r} + f_r \quad (4.17)$$

Azimuthal Momentum (θ):

$$\frac{\partial u_\theta}{\partial t} + \frac{1}{r} \frac{\partial(ru_r u_\theta)}{\partial r} + \frac{1}{r} \frac{\partial(ru_\theta u_z)}{\partial z} + \frac{u_r u_\theta}{r} = \frac{1}{r^2} \frac{\partial(r^2 \tau_{r\theta})}{\partial r} + \frac{1}{r} \frac{\partial(r\tau_{\theta z})}{\partial z} + f_\theta \quad (4.18)$$

Axial Momentum (z):

$$\frac{\partial u_z}{\partial t} + \frac{1}{r} \frac{\partial(ru_z u_r)}{\partial r} + \frac{1}{r} \frac{\partial(ru_z u_z)}{\partial z} = -\frac{\partial p}{\partial z} + \frac{1}{r} \frac{\partial(r\tau_{zr})}{\partial r} + \frac{1}{r} \frac{\partial(r\tau_{zz})}{\partial z} + f_z \quad (4.19)$$

Now, the viscous stress tensor ($\boldsymbol{\tau}$) for incompressible flow of a Newtonian fluid is defined as:

$$\boldsymbol{\tau} = \frac{1}{\text{Re}} (\nabla \mathbf{u} + \nabla \mathbf{u}^T), \quad (4.20)$$

while under the axisymmetric invariance assumption, the stress tensor components (τ_{ij}) read:

$$\begin{aligned} \tau_{rr} &= 2 \frac{1}{\text{Re}} \frac{\partial u_r}{\partial r}, & \tau_{\theta\theta} &= 2 \frac{1}{\text{Re}} \frac{u_r}{r}, & \tau_{zz} &= 2 \frac{1}{\text{Re}} \frac{\partial u_z}{\partial z}, \\ \tau_{r\theta} = \tau_{\theta r} &= \frac{1}{\text{Re}} \left(\frac{\partial u_\theta}{\partial r} - \frac{u_\theta}{r} \right), & \tau_{\theta z} = \tau_{z\theta} &= \frac{1}{\text{Re}} \frac{\partial u_\theta}{\partial z}, & \tau_{rz} = \tau_{zr} &= \frac{1}{\text{Re}} \left(\frac{\partial u_z}{\partial r} + \frac{\partial u_r}{\partial z} \right). \end{aligned} \quad (4.21)$$

4.2.2 Axisymmetric Reynolds-Averaged Navier-Stokes Equations

The Reynolds-Averaged Navier-Stokes (RANS) equations represent one of the most widely adopted approaches for turbulence modeling in engineering applications, according to which, each instantaneous flow quantity is decomposed into an average and a fluctuating part (Blazek, 2015). The Reynolds decomposition of pressure (p), velocity components (u_i) and body force components (f_i) is described in Eq. (4.22), where the overbar denotes the average or mean part of the respective flow variable, while the prime denotes the fluctuating one.

$$p = \underbrace{\bar{p}}_{\text{average}} + \underbrace{p'}_{\text{fluctuating}} \quad (4.22)$$

$$u_i = \underbrace{\bar{u}_i}_{\text{average}} + \underbrace{u'_i}_{\text{fluctuating}}$$

$$f_i = \underbrace{\bar{f}_i}_{\text{average}} + \underbrace{f'_i}_{\text{fluctuating}}$$

In general, averaging of the main flow quantities can be performed by employing three different strategies; namely, time-averaging, spatial averaging and ensemble averaging (Blazek, 2015). In this study, the time-averaging approach is adopted, since the majority of the encountered flows are characterized by statistically steady turbulence (steady-state flows). Accordingly, the mean values of pressure, velocity and body force components are defined as:

$$\bar{p} = \lim_{T \rightarrow \infty} \frac{1}{T} \int_t^{t+T} p \, dt, \quad \bar{u}_i = \lim_{T \rightarrow \infty} \frac{1}{T} \int_t^{t+T} u_i \, dt, \quad \bar{f}_i = \lim_{T \rightarrow \infty} \frac{1}{T} \int_t^{t+T} f_i \, dt, \quad (4.23)$$

where $T \rightarrow \infty$ signifies that the time interval of integration should be larger than the typical time-scale of the turbulent fluctuations. Please note that the mean value of the fluctuating part for every flow quantity is zero, regardless of the employed averaging approach (Blazek, 2015). Consequently, the mean value of each flow variable does not vary in time, but only in space. Now, introducing Eq. (4.22) into Eqs. (4.16) - (4.19), the incompressible axisymmetric RANS equations, in terms of dimensionless parameters, can be expressed as:

Continuity:

$$\frac{1}{r} \frac{\partial(r\bar{u}_r)}{\partial r} + \frac{\partial\bar{u}_z}{\partial z} = 0 \quad (4.24)$$

Radial Momentum (r):

$$\frac{\partial\bar{u}_r}{\partial t} + \frac{1}{r} \frac{\partial(r\bar{u}_r\bar{u}_r)}{\partial r} + \frac{1}{r} \frac{\partial(r\bar{u}_r\bar{u}_z)}{\partial z} - \frac{\bar{u}_\theta^2}{r} = -\frac{\partial\bar{p}}{\partial r} + \frac{1}{r} \frac{\partial(r\hat{\tau}_{rr})}{\partial r} + \frac{1}{r} \frac{\partial(r\hat{\tau}_{rz})}{\partial z} - \frac{\hat{\tau}_{\theta\theta}}{r} + \bar{f}_r \quad (4.25)$$

Azimuthal Momentum (θ):

$$\frac{\partial\bar{u}_\theta}{\partial t} + \frac{1}{r} \frac{\partial(r\bar{u}_r\bar{u}_\theta)}{\partial r} + \frac{1}{r} \frac{\partial(r\bar{u}_\theta\bar{u}_z)}{\partial z} + \frac{\bar{u}_r\bar{u}_\theta}{r} = \frac{1}{r^2} \frac{\partial(r^2\hat{\tau}_{r\theta})}{\partial r} + \frac{1}{r} \frac{\partial(r\hat{\tau}_{\theta z})}{\partial z} + \bar{f}_\theta \quad (4.26)$$

Axial Momentum (z):

$$\frac{\partial\bar{u}_z}{\partial t} + \frac{1}{r} \frac{\partial(r\bar{u}_z\bar{u}_r)}{\partial r} + \frac{1}{r} \frac{\partial(r\bar{u}_z\bar{u}_z)}{\partial z} = -\frac{\partial\bar{p}}{\partial z} + \frac{1}{r} \frac{\partial(r\hat{\tau}_{zr})}{\partial r} + \frac{1}{r} \frac{\partial(r\hat{\tau}_{zz})}{\partial z} + \bar{f}_z \quad (4.27)$$

where

$$\hat{\tau} = \bar{\tau} - \overline{\mathbf{u}' \otimes \mathbf{u}'} = \frac{\nu}{\text{Re}} (\nabla \bar{\mathbf{u}} + \nabla \bar{\mathbf{u}}^T) - \overline{\mathbf{u}' \otimes \mathbf{u}'}. \quad (4.28)$$

Apparently, the form of axisymmetric RANS equations (4.24) - (4.28) is identical to that of the instantaneous or non-averaged axisymmetric Navier-Stokes equations (4.16) - (4.19); except of the additional non-linear term:

$$\overline{\mathbf{u}' \otimes \mathbf{u}'}, \quad (4.29)$$

which has been emerged after the averaging process and denotes the Reynolds stress tensor. Herein, the Reynolds stress tensor is evaluated by introducing the Boussinesq hypothesis or approximation, assuming a linear relationship between the turbulent shear stress and the mean rate strain. Thus,

$$-\overline{\mathbf{u}' \otimes \mathbf{u}'} = \nu_t (\nabla \bar{\mathbf{u}} + \nabla \bar{\mathbf{u}}^T) - \frac{2}{3} k \mathbf{I}, \quad (4.30)$$

where ν_t stands for the turbulent kinetic viscosity and k for the turbulent kinetic energy.

$$k = \frac{1}{2} \overline{\mathbf{u}' \cdot \mathbf{u}'} \quad (4.31)$$

Eventually, the total averaged stress tensor $\hat{\boldsymbol{\tau}}$ is given as:

$$\hat{\boldsymbol{\tau}} = \bar{\boldsymbol{\tau}} - \overline{\mathbf{u}' \otimes \mathbf{u}'} = \left(\frac{\nu}{\text{Re}} + \nu_t \right) \cdot (\nabla \bar{\mathbf{u}} + \nabla \bar{\mathbf{u}}^T) - \frac{2}{3} k \mathbf{I}, \quad (4.32)$$

and the averaged stress tensor components as:

$$\begin{aligned} \hat{\tau}_{rr} &= 2 \left(\frac{\nu}{\text{Re}} + \nu_t \right) \frac{\partial u_r}{\partial r} - \frac{2}{3} k & \hat{\tau}_{r\theta} &= \hat{\tau}_{\theta r} = \left(\frac{\nu}{\text{Re}} + \nu_t \right) \left(\frac{\partial u_\theta}{\partial r} - \frac{u_\theta}{r} \right) \\ \hat{\tau}_{\theta\theta} &= 2 \left(\frac{\nu}{\text{Re}} + \nu_t \right) \frac{u_r}{r} - \frac{2}{3} k & \hat{\tau}_{\theta z} &= \hat{\tau}_{z\theta} = \left(\frac{\nu}{\text{Re}} + \nu_t \right) \frac{\partial u_\theta}{\partial z} \\ \hat{\tau}_{zz} &= 2 \left(\frac{\nu}{\text{Re}} + \nu_t \right) \frac{\partial u_z}{\partial z} - \frac{2}{3} k & \hat{\tau}_{zr} &= \hat{\tau}_{rz} = \left(\frac{\nu}{\text{Re}} + \nu_t \right) \left(\frac{\partial u_z}{\partial r} + \frac{\partial u_r}{\partial z} \right) \end{aligned} \quad (4.33)$$

Finally, it is recalled that according to the adopted non-dimensionalization strategy, the value of laminar kinematic viscosity (ν) equals to unity.

4.2.3 Artificial Compressibility and Pseudo-Cartesian Formulation

The artificial compressibility method (ACM) was originally introduced by Chorin (1967) to overcome pressure decoupling. Essentially, the particular method involves the addition of a temporal derivative of pressure to the continuity equation, allowing the incompressible system of equations to be relaxed within the framework of a time-marching compressible flow solver (Anderson *et al.*, 1996). In particular, it transforms the incompressible Navier-Stokes equations of mixed elliptic/parabolic type into a pseudo-temporal set of hyperbolic or parabolic partial differential equations (Kiris *et al.*, 2006; Stokos *et al.*, 2015). Introducing the artificial compressibility parameter (β), the continuity equation recasts as follows:

Continuity:

$$\frac{\partial p}{\partial t} + \frac{\partial \beta u_r}{\partial r} + \frac{\partial \beta u_z}{\partial z} = -\frac{\beta u_r}{r} \quad (4.34)$$

Essentially, the artificial compressibility parameter (β) allows for the incorporation of the pressure term in continuity equation (Anderson *et al.*, 1996; Lygidakis *et al.*, 2016). At this point it is emphasized that special attention should be paid on the proper selection of its value, since it affects the artificial speed of sound and consequently the corresponding speed of artificial pressure wave and overall convergence rate (Kallinderis and Ahn, 2005). Although the value of β should be ideally chosen as high as possible to accelerate analogously the artificial pressure waves and consequently enforce incompressibility effects to the whole computational domain, values close to unit are typically chosen to assure good convergence rates, especially in viscous unsteady simulations (Cox *et al.*, 2016). The momentum equations are not affected by artificial compressibility method. However, in order to result in a pseudo-Cartesian formulation, they have been arranged into inviscid, viscous and source terms, as follows:

Radial Momentum (r):

$$\frac{\partial u_r}{\partial t} + \frac{\partial (u_r^2 + p)}{\partial r} + \frac{\partial (u_r u_z)}{\partial z} - \frac{\partial \tau_{rr}}{\partial r} - \frac{\partial \tau_{rz}}{\partial z} = -\frac{u_r^2}{r} + \frac{\tau_{rr}}{r} - \frac{\tau_{\theta\theta}}{r} + f_r \quad (4.35)$$

Azimuthal Momentum (θ):

$$\frac{\partial u_\theta}{\partial t} + \frac{\partial (u_r u_\theta)}{\partial r} + \frac{\partial (u_\theta u_z)}{\partial z} - \frac{\partial \tau_{r\theta}}{\partial r} - \frac{\partial \tau_{z\theta}}{\partial z} = \frac{2}{r} (\tau_{r\theta} - u_r u_\theta) + f_\theta \quad (4.36)$$

Axial Momentum (z):

$$\frac{\partial u_z}{\partial t} + \frac{\partial (u_r u_z)}{\partial r} + \frac{\partial (u_z^2 + p)}{\partial z} - \frac{\partial \tau_{rz}}{\partial r} - \frac{\partial \tau_{zz}}{\partial z} = \frac{\tau_{rz}}{r} - \frac{u_r u_z}{r} + f_z \quad (4.37)$$

Now, let us replace coordinates (z, r) with (x, y) and velocity components (u_z, u_r, u_θ) with (u, v, w); then, the system of partial differential equations defined by Eq. (4.34) – Eq. (4.37) can

be reformulated – arranged into inviscid, viscous and source terms – as follows (Cummings *et al.*, 1995; Gokhale and Suresh, 1997; Masatsuka, 2013; Mohammadi and Saiac, 1993):

$$\frac{\partial \mathbf{U}}{\partial t} + \frac{\partial \mathbf{F}_i}{\partial x} + \frac{\partial \mathbf{G}_i}{\partial y} - \frac{\partial \mathbf{F}_v}{\partial x} - \frac{\partial \mathbf{G}_v}{\partial y} = \mathbf{H} \quad (4.38)$$

where \mathbf{U} denotes the vector of primitive flow variables, \mathbf{F}_i and \mathbf{G}_i are the inviscid (convective) flux vectors, while \mathbf{F}_v and \mathbf{G}_v are the viscous (diffusive) flux vectors.

$$\mathbf{U} = \begin{pmatrix} p \\ u \\ v \\ w \end{pmatrix} \quad \mathbf{F}_i = \begin{pmatrix} \beta u \\ u^2 + p \\ uv \\ uw \end{pmatrix} \quad \mathbf{G}_i = \begin{pmatrix} \beta v \\ vu \\ v^2 + p \\ vw \end{pmatrix} \quad \mathbf{F}_v = \begin{pmatrix} 0 \\ \tau_{xx} \\ \tau_{yx} \\ \tau_{x\theta} \end{pmatrix} \quad \mathbf{G}_v = \begin{pmatrix} 0 \\ \tau_{xy} \\ \tau_{yy} \\ \tau_{y\theta} \end{pmatrix} \quad (4.39)$$

Finally, the source term vector \mathbf{H} , associated with axisymmetric swirling flows, is defined as:

$$\mathbf{H} = \frac{1}{y} \begin{pmatrix} -\beta v \\ u\tau_{xy} - uv \\ \tau_{yy} - \tau_{\theta\theta} - v^2 + w^2 \\ 2(\tau_{y\theta} - vw) \end{pmatrix} + \begin{pmatrix} 0 \\ f_x \\ f_y \\ f_\theta \end{pmatrix} \quad (4.40)$$

For axisymmetric flow simulations in which circumferential or swirl velocity is neglected, the corresponding partial differential equation (4.36) shall be excluded and the tangential velocity component (w) within the source term should be zeroed as well (Lee and Lee, 2011; Leloudas *et al.*, 2020a, 2021). Moreover, in cases of purely two-dimensional flow simulations, the whole source term should be neglected.

4.2.4 Turbulence Modeling

In the current version of IGal2D solver, turbulence modeling is achieved by means of k - ω Shear Stress Transport (SST) model (Menter, 1994; Menter *et al.*, 2003). The SST model is defined by adopting the same differential formulation used for the flow partial differential equations, but it is solved separately, following a loose coupling approach; interaction between the flow and turbulence models is succeeded via the turbulent kinematic viscosity. Please note that no additional model is included to simulate transition from laminar to turbulent flow. To this end, the SST model is described as (Leloudas *et al.*, 2021):

$$\frac{\partial \mathbf{U}^t}{\partial t} + \frac{\partial \mathbf{F}_i^t}{\partial x} + \frac{\partial \mathbf{G}_i^t}{\partial y} - \frac{\partial \mathbf{F}_v^t}{\partial x} - \frac{\partial \mathbf{G}_v^t}{\partial y} = \mathbf{H}^t, \quad (4.41)$$

where \mathbf{U}^t denotes the vector of turbulence model variables.

$$\mathbf{U}^t = \begin{bmatrix} k \\ \omega \end{bmatrix} \quad (4.42)$$

In accordance to the flux vectors of the Navier-Stokes equations, the convective vectors of the SST turbulence model are given as:

$$\mathbf{F}_i^t = \begin{bmatrix} uk \\ u\omega \end{bmatrix} \quad \mathbf{G}_i^t = \begin{bmatrix} vk \\ v\omega \end{bmatrix} \quad (4.43)$$

and the diffusive ones as:

$$\mathbf{F}_i^t = \begin{bmatrix} (v/\text{Re} + \nu_t \sigma_k) \cdot (\partial k / \partial x) \\ (v/\text{Re} + \nu_t \sigma_k) \cdot (\partial \omega / \partial x) \end{bmatrix} \quad \mathbf{G}_i^t = \begin{bmatrix} (v/\text{Re} + \nu_t \sigma_k) \cdot (\partial k / \partial y) \\ (v/\text{Re} + \nu_t \sigma_k) \cdot (\partial \omega / \partial y) \end{bmatrix} \quad (4.44)$$

Finally, the source term vector \mathbf{H}^t is defined as follows (Leloudas *et al.*, 2021):

$$\mathbf{H}^t = \begin{bmatrix} P_k - \beta^* \omega k \\ P_k \gamma / \nu_t - \gamma^* \omega^2 + 2(1 - F_1) \nabla k \nabla \omega \end{bmatrix} + \frac{1}{y} \cdot \begin{bmatrix} (v/\text{Re} + \nu_t \sigma_k) \cdot (\partial k / \partial y) - vk \\ (v/\text{Re} + \nu_t \sigma_k) \cdot (\partial k / \partial y) - v\omega \end{bmatrix} \quad (4.45)$$

The parameters $\sigma_k, \sigma_\omega, \beta^*, \gamma^*$ are obtained with regard to the equivalent constants of the k- ω and k- ϵ models, using the blending function F_1 in a way that the parameter from the k- ω model is multiplied by F_1 and the one from k- ϵ with $(1 - F_1)$ and then added together. Therefore, if q represents all coefficients of the SST model, q_1 the constants from k- ω and q_2 the ones from k- ϵ , then the first would be calculated as:

$$q = F_1 \cdot q_1 + (1 - F_1) \cdot q_2 \quad (4.46)$$

The parameters for k- ω and k- ϵ closures are:

Constants of k- ω closure:

$$\sigma_{k1} = 0.85, \quad \sigma_{\omega1} = 0.5, \quad \beta_1 = 0.075, \quad \gamma_1^* = 0.555 \quad (4.47)$$

Constants of k- ϵ closure:

$$\sigma_{k2} = 1.00, \quad \sigma_{\omega1} = 0.856, \quad \beta_2 = 0.0828, \quad \gamma_2^* = 0.44 \quad (4.48)$$

The blending function F_1 is defined as:

$$F_1 = \tanh(\arg_1^4), \quad (4.49)$$

where

$$\arg_1 = \min \left[\max \left(\frac{\sqrt{k}}{\beta^* \omega d}, \frac{500\nu}{d^2 \omega \text{Re}} \right), \frac{4\rho\sigma_{\omega_2} k}{CD_{k\omega} d^2} \right], \quad (4.50)$$

and

$$CD_{k\omega} = \max \left(2\sigma_{\omega_2} \frac{1}{\omega} \nabla k \nabla \omega, 10^{-10} \right), \quad (4.51)$$

where d is the distance of the point in space where the SST model is applied, from the nearest solid wall surface. The turbulent kinematic viscosity is also calculated with the help of a second blending function (F_2) as:

$$\nu_t = \frac{\alpha_1 k}{\max(a_1 \omega, SF_2)} \quad (4.52)$$

The blending function F_2 is defined as:

$$F_2 = \tanh(\arg_2^2), \quad (4.53)$$

where

$$\arg_2^2 = \max \left(\frac{\sqrt{k}}{\beta^* \omega d}, \frac{500 \cdot \nu}{d^2 \omega \text{Re}} \right). \quad (4.54)$$

Finally, the turbulent energy production term (P_k) is computed as:

$$P_k = \nu_t S^2, \quad (4.55)$$

where the invariant measure of the strain rate (S) for the case of an axisymmetric swirling flow is evaluated as follows:

$$\begin{aligned} S &= \sqrt{2(S_{ij}S_{ij})} = \sqrt{2 \left[\frac{1}{2} (\nabla \vec{V} + \nabla \vec{V}^T)_{ij} \frac{1}{2} (\nabla \vec{V} + \nabla \vec{V}^T)_{ij} \right]} \\ &= \sqrt{2 \left(\frac{\partial u}{\partial x} \right)^2 + 2 \left(\frac{\partial v}{\partial y} \right)^2 + \left(\frac{\partial u}{\partial y} + \frac{\partial v}{\partial x} \right)^2 + 2 \left(\frac{v}{y} \right)^2 + \left(\frac{\partial w}{\partial x} \right)^2 + \left(\frac{\partial w}{\partial y} - \frac{w}{y} \right)^2} \end{aligned} \quad (4.56)$$

4.2.5 Coupling of Flow and Turbulence Models

As already mentioned in the previous section, the coupling of the flow (4.38) and turbulence (4.41) models is achieved by adopting a so-called loose coupling approach, where the partial

differential equation defining the flow and turbulence models are resolved separately at each pseudo-time step, with the interaction between them to be realized by means of the turbulent kinetic viscosity (ν_t) and velocity components (u, v, w). In particular, since an intermediate solution of the flow equations has been obtained, the resulting velocity field is fed to the turbulence model equations; subsequently, the turbulent model equations are resolved and the resulting turbulent kinematic viscosity is fed back to the flow model. The process is repeated in the next pseudo-time step. Eventually, this approach allows for the effortless switch between various available turbulence models and favors the addition of new ones.

4.3 Spatial Discretization

The spatial discretization of the partial differential equations defining the flow and turbulence models, namely, Eq. (4.38) and Eq. (4.41), is performed by applying a conservative node-centered finite-volume scheme over general unstructured grids in two dimensions, including triangular, quadrilateral and hybrid ones. According to the adopted discretization approach, the entire computational domain is divided into a finite number of non-overlapping control volumes, which are essentially defined as the median dual volumes of the grid nodes (Kallinderis and Ahn, 2005). In particular, the boundary ∂CV_P of the control volume CV_P around a node P (which may be located either on the interior or the boundary of the computational domain) is formed by joining the line segments connecting the midpoints of the edges (M_i) and the barycenters of the primary elements (B_j) sharing this node (Leloudas et al., 2020a, 2021).

Now, let Q be a random node within the set of nodes that are directly connected to P via the grid edges, denoted as $S_N(P)$. By introducing ∂CV_{PQ} to signify the intersection of ∂CV_P and ∂CV_Q , as well as \mathcal{B} to symbolize the external boundary of the computational domain, ∂CV_P is mathematically defined as (Nikolos and Delis, 2009):

$$\partial CV_P = \bigcup_{\forall Q \in S_N(P)} \partial CV_{PQ} + \partial CV_P \cap \mathcal{B}. \quad (4.57)$$

Figure 4.1 and Figure 4.2 illustrate the definition of such median dual control volumes, constructed by different types of primary elements. In particular, Figure 4.1 refers to the case in which the examined grid node P is located on the interior of the computational domain, while Figure 4.2 describes the definition of the median dual control volume for the case of a boundary node. Herein, B_1 and B_2 denote the barycenters of the elements sharing the edge PQ . Please note that if the particular edge is a boundary one – as depicted in Figure 4.2 – B_2 is not

defined. Finally, M_Q and M_T stand for the midpoints of the edges PQ and PT (*i.e.*, the midpoints of the two boundary edges sharing the examined node P).

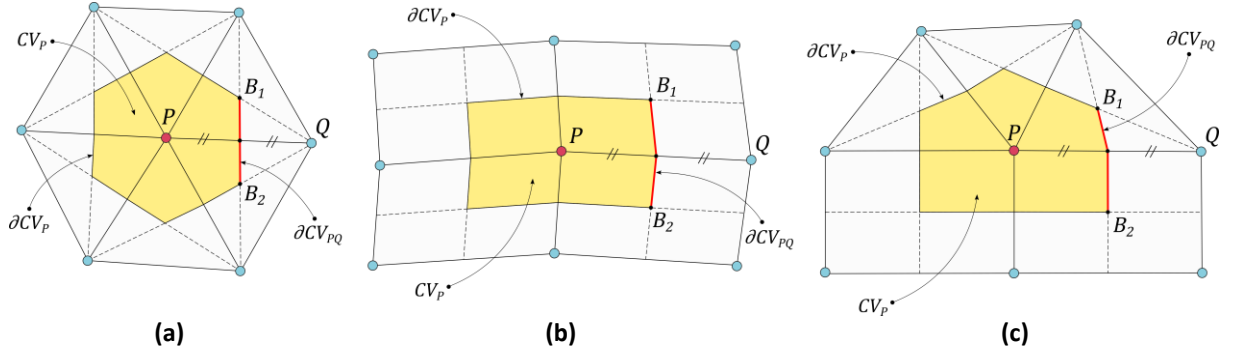


Figure 4.1: Definition of the median dual control volume CV_P for an internal grid node P .

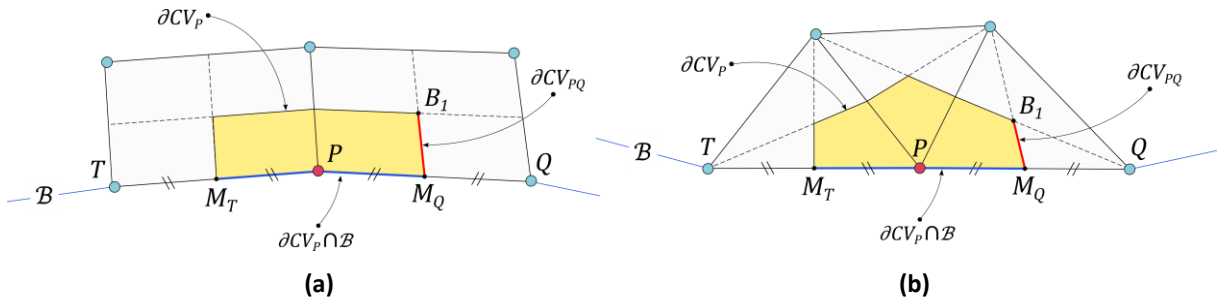


Figure 4.2: Definition of the median dual control volume CV_P for a boundary grid node P .

Based on the adopted finite-volume discretization technique, Eq. (4.38) can be integrated over the median dual control volume CV_P for each grid node P , as follows:

$$\iint_{CV_P} \frac{\partial \mathbf{U}}{\partial t} dx dy + \iint_{CV_P} \frac{\partial \mathbf{F}_i}{\partial x} + \frac{\partial \mathbf{G}_i}{\partial y} - \frac{\partial \mathbf{F}_v}{\partial x} - \frac{\partial \mathbf{G}_v}{\partial y} dx dy = \iint_{CV_P} \mathbf{H} dx dy. \quad (4.58)$$

Then, by applying the two-dimensional divergence theorem, which relates the divergence of a vector field within a region, to the flux of that vector field through the closed boundary of the region, Eq. (4.58) recasts into:

$$\iint_{CV_P} \frac{\partial \mathbf{U}}{\partial t} dx dy + \oint_{\partial CV_P} \Psi_i - \Psi_v ds = \iint_{CV_P} \mathbf{H} dx dy, \quad (4.59)$$

where Ψ_i and Ψ_v represent the vector of inviscid and viscous fluxes, respectively. At this point, let us define $\mathbf{n}_{PQ} = \mathbf{n}_1 + \mathbf{n}_2$ as the outward normal vector to ∂CV_{PQ} , where \mathbf{n}_1 is normal to $\overline{B_1 M_Q}$ with a norm equal to the length of $\overline{B_1 M_Q}$ and \mathbf{n}_2 is normal to $\overline{M_Q B_2}$ with a norm equal to the length of $\overline{M_Q B_2}$. In the same way, let us define $\mathbf{n}_{out} = \mathbf{n}_{out,1} + \mathbf{n}_{out,2}$ as the outward normal vector to $\partial CV_P \cap \mathcal{B}$, where $\mathbf{n}_{out,1}$ is normal to $\overline{M_Q P}$ with a norm equal to the length of $\overline{M_Q P}$ and

$\mathbf{n}_{out,2}$ is normal to $\overline{PM_T}$ with a norm equal to the length of $\overline{PM_T}$. Figure 4.3 provides a schematic representation of the aforementioned vectors.

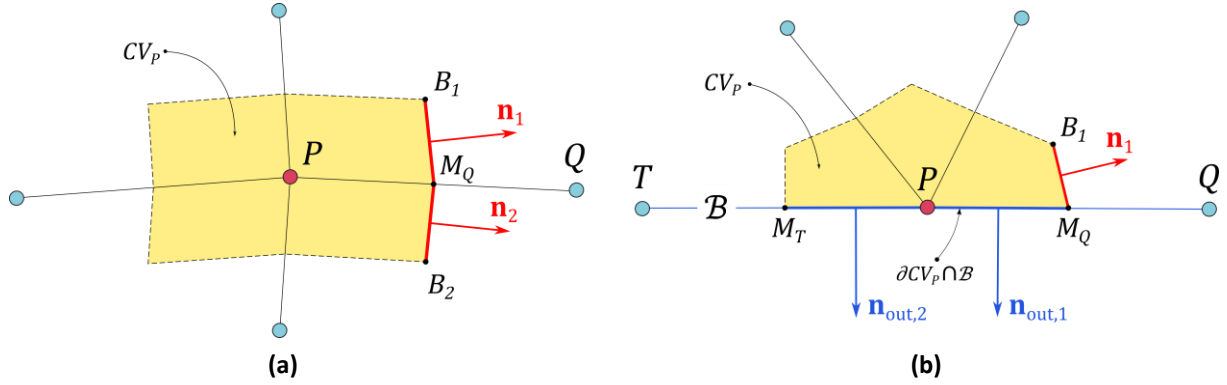


Figure 4.3: Vectors definition for the cases of internal and boundary nodes.

Subsequently, by introducing the outward unit normal vector $\hat{\mathbf{n}}_{PQ}$ to ∂CV_{PQ} and the outward unit normal vector $\hat{\mathbf{n}}_{out}$ to $\partial CV_P \cap \mathcal{B}$, which are defined as:

$$\hat{\mathbf{n}}_{PQ} = \frac{\mathbf{n}_{PQ}}{\|\mathbf{n}_{PQ}\|} = [\hat{n}_{PQ,x}, \hat{n}_{PQ,y}], \quad (4.60)$$

$$\hat{\mathbf{n}}_{out} = \frac{\mathbf{n}_{out}}{\|\mathbf{n}_{out}\|} = [\hat{n}_{out,x}, \hat{n}_{out,y}], \quad (4.61)$$

Ψ_i and Ψ_v can be expressed as follows:

$$\Psi_i = \hat{n}_{PQ,x} \mathbf{F}_i + \hat{n}_{PQ,y} \mathbf{G}_i, \quad (4.62)$$

$$\Psi_v = \hat{n}_{PQ,x} \mathbf{F}_v + \hat{n}_{PQ,y} \mathbf{G}_v.$$

Both inviscid and viscous fluxes are evaluated by using the values of primitive variables at the midpoint of the corresponding edge; in terms of the current discretization approach, this midpoint actually coincides with the interface between the adjacent control volumes of the computational nodes defining the respective edge (Lygidakis, 2015). Eventually, Eq. (4.59) can be reformulated as:

$$\iint_{CV_p} \frac{\partial \mathbf{U}}{\partial t} dx dy + \sum_{Q \in S_N(P)} \int_{\partial CV_{PQ}} \Psi_i - \Psi_v ds + \int_{\partial CV_P \cap \mathcal{B}} \Psi_i - \Psi_v ds = \iint_{CV_p} \mathbf{H} dx dy. \quad (4.63)$$

Under the assumption that the conservative variables at node P are equal to their mean values over CV_P , which is the fundamental concept underlying finite-volume method, the first term in the LHS of Eq. (4.63) becomes:

$$\iint_{CV_P} \frac{\partial \mathbf{U}}{\partial t} dx dy = \left(\frac{\partial \mathbf{U}}{\partial t} \right)_P \cdot \iint_{CV_P} dx dy = \frac{\partial \mathbf{U}_P}{\partial t} E_P, \quad (4.64)$$

where E_P denotes the area of the control volume CV_P around node P . Ultimately, by expressing the line integrals of the inviscid and viscous fluxes Ψ_i and Ψ_v , as algebraic summations of the fluxes through the faces composing the control volume of node P , Eq. (4.63) recasts into:

$$\left(\frac{\partial \mathbf{U}}{\partial t} \right)_P E_P + \sum_{Q \in S_N(P)} \Phi_i^{PQ} - \Phi_v^{PQ} + \sum_{(K_{out} \in \partial CV_P \cap B)} \Phi_i^{P,out} - \Phi_v^{P,out} = \iint_{CV_P} \mathbf{H} dx dy, \quad (4.65)$$

where

$$\Phi_i^{PQ} = \int_{\partial CV_{PQ}} \Psi_i ds = \mathbf{f}(\mathbf{U}_{PQ}^{(L)}, \mathbf{U}_{PQ}^{(R)}, \mathbf{n}_{PQ}), \quad (4.66)$$

$$\Phi_v^{PQ} = \int_{\partial CV_{PQ}} \Psi_v ds = \mathbf{g}(\mathbf{U}_{PQ}^{(L)}, \mathbf{U}_{PQ}^{(R)}, \mathbf{n}_{PQ}), \quad (4.67)$$

$$\Phi_i^{P,out} = \int_{\partial CV_P \cap B} \Psi_i ds = \mathbf{f}(\mathbf{U}_P, \mathbf{U}_{out}, \mathbf{n}_{out}), \quad (4.68)$$

$$\Phi_v^{P,out} = \int_{\partial CV_P \cap B} \Psi_v ds = \mathbf{g}(\mathbf{U}_P, \mathbf{U}_{out}, \mathbf{n}_{out}). \quad (4.69)$$

Herein, $\mathbf{U}_{PQ}^{(L)}$ and $\mathbf{U}_{PQ}^{(R)}$ denote the vectors of the conservative variables on the left and right side of the of point M_Q (*i.e.*, the midpoint of the edge PQ) respectively, while \mathbf{U}_{out} stands for the corresponding vector on the boundary.

4.4 Numerical Fluxes

4.4.1 Inviscid Fluxes

In order to evaluate the inviscid (also termed as convective) flux vector associated with the edge PQ , a one-dimensional Riemann problem (Laney, 1998) between the left (L) and right (R) states existing at the two sides of point M_Q (*i.e.*, the midpoint of the edge PQ) is assumed; these particular fluid states are defined by the vectors $\mathbf{U}_{PQ}^{(L)}$ and $\mathbf{U}_{PQ}^{(R)}$, respectively. In this study, the solution to the adopted Riemann problem is obtained by employing the well-known Roe's approximate Riemann solver (Roe, 1981), which – even though considers a simplified version of the original Riemann problem – can eventually provide an exact solution. The Roe's

approximate Riemann solver is based on the assumption that the Jacobian matrix is constant and calculated using consistency and conservation conditions (Nikolos and Delis, 2009). Thus, the inviscid or convective flux vector can be calculated as follows:

$$\Phi_i^{PQ} = \frac{1}{2} \left[\Psi_i(\mathbf{U}_{PQ}^{(L)}, \mathbf{n}_{PQ}) + \Psi_i(\mathbf{U}_{PQ}^{(R)}, \mathbf{n}_{PQ}) \right] - \frac{1}{2} |\bar{\bar{\mathbf{A}}}_{PQ}| \cdot (\mathbf{U}_{PQ}^{(R)} - \mathbf{U}_{PQ}^{(L)}), \quad (4.70)$$

where $\bar{\bar{\mathbf{A}}}_{PQ}$ stands for the Jacobian matrix of the convective flux vector, related to the edge PQ . Please note that $\bar{\bar{\mathbf{A}}}_{PQ}$ is evaluated at the midpoint (M_Q) of the corresponding edge by using the Roe-averaged values of the primitive variables, which are indicated by the double overbar and defined as:

$$\bar{\bar{\mathbf{U}}}_{PQ} = \frac{\sqrt{\rho^{(L)}} \cdot \mathbf{U}_{PQ}^{(L)} + \sqrt{\rho^{(R)}} \cdot \mathbf{U}_{PQ}^{(R)}}{\sqrt{\rho^{(L)}} + \sqrt{\rho^{(R)}}}. \quad (4.71)$$

Furthermore, by introducing the following expression (Laney, 1998; Roe, 1981):

$$\Psi_i(\mathbf{U}_{PQ}^{(R)}, \mathbf{n}_{PQ}) - \Psi_i(\mathbf{U}_{PQ}^{(L)}, \mathbf{n}_{PQ}) = \bar{\bar{\mathbf{A}}}_{PQ}^{(-)} (\mathbf{U}_{PQ}^{(R)} - \mathbf{U}_{PQ}^{(L)}), \quad (4.72)$$

an alternative, yet equivalent, formulation of Eq. (4.70) can be obtained, which reads:

$$\Phi_i^{PQ} = \Psi_i(\mathbf{U}_{PQ}^{(L)}, \mathbf{n}_{PQ}) + \bar{\bar{\mathbf{A}}}_{PQ}^{(-)} (\mathbf{U}_{PQ}^{(R)} - \mathbf{U}_{PQ}^{(L)}). \quad (4.73)$$

Eventually, the calculation of inviscid flux vector within the current implementation of the proposed flow solver is performed by means of Eq. (4.73), where $\bar{\bar{\mathbf{A}}}_{PQ}^{(-)}$ represents the Jacobian matrix of the convective flux vector, computed using the arithmetic averages of primitive variables at (L) and (R) positions and negative eigenvalues (Nikolos and Delis, 2009). The detailed procedure for the derivation of $\bar{\bar{\mathbf{A}}}_{PQ}^{(-)}$ is provided in the following section (4.4.1.1).

4.4.1.1 Convective Flux Jacobian

The Jacobian matrix $\bar{\bar{\mathbf{A}}}_{PQ}$ of the convective (inviscid) flux vector Φ_i^{PQ} related to the edge PQ can be expressed in terms of the Roe-averaged values of the primitive variables vector $\bar{\bar{\mathbf{U}}}$, as:

$$\bar{\bar{\mathbf{A}}}_{PQ} = \frac{\partial \Phi_i^{PQ}}{\partial \bar{\bar{\mathbf{U}}}_{PQ}} = \begin{pmatrix} 0 & \beta \cdot n_{PQ,x} & \beta \cdot n_{PQ,y} & 0 \\ n_{PQ,x} & \bar{\bar{\theta}} \cdot \|\mathbf{n}_{PQ}\| + u \cdot n_{PQ,x} & \bar{\bar{u}} \cdot n_{PQ,y} & 0 \\ n_{PQ,y} & \bar{\bar{v}} \cdot n_{PQ,x} & \bar{\bar{\theta}} \cdot \|\mathbf{n}_{PQ}\| + \bar{\bar{v}} \cdot n_{PQ,y} & 0 \\ 0 & \bar{\bar{w}} \cdot n_{PQ,y} & \bar{\bar{w}} \cdot n_{PQ,y} & \bar{\bar{\theta}} \cdot \|\mathbf{n}_{PQ}\| \end{pmatrix} \quad (4.74)$$

where $\bar{\mathbf{U}}$ is given by Eq. (4.71) and the parameter $\bar{\Theta}$ is defined as:

$$\bar{\Theta} = \bar{u} \cdot \hat{n}_{PQ,x} + \bar{v} \cdot \hat{n}_{PQ,y}. \quad (4.75)$$

At this point, let us recall that $\hat{n}_{PQ,x}$ and $\hat{n}_{PQ,y}$ are the components of the outward unit vector $\hat{\mathbf{n}}_{PQ}$ that is normal to ∂CV_{PQ} (see Section 4.3).

$$\hat{\mathbf{n}}_{PQ} = \frac{\mathbf{n}_{PQ}}{\|\mathbf{n}_{PQ}\|} = [\hat{n}_{PQ,x}, \hat{n}_{PQ,y}] \quad (4.60)$$

The flux Jacobian calculation is made by applying the following eigenvalue decomposition:

$$\bar{\mathbf{A}}_{PQ} = \bar{\mathbf{T}} \cdot \bar{\mathbf{\Lambda}} \cdot \bar{\mathbf{T}}^{-1}, \quad (4.76)$$

where $\bar{\mathbf{\Lambda}}$ is the diagonal eigenvalue vector, defined as:

$$\bar{\mathbf{\Lambda}} = \text{diag}\{\bar{\lambda}_1, \bar{\lambda}_2, \bar{\lambda}_3, \bar{\lambda}_4\} \cdot \|\mathbf{n}_{PQ}\| = \text{diag}\{\bar{\Theta}, \bar{\Theta}, \bar{\Theta} + \bar{c}, \bar{\Theta} - \bar{c}\} \cdot \|\mathbf{n}_{PQ}\| \quad (4.77)$$

and $\bar{\mathbf{T}}$ is the matrix of the right eigenvector, described as:

$$\bar{\mathbf{T}} = \begin{pmatrix} 0 & 0 & \bar{c} & -\bar{c} \\ \hat{n}_{PQ,y} & 0 & \hat{n}_{PQ,x} + \frac{(\bar{\Theta} + \bar{c}) \cdot \bar{u}}{\beta} & \hat{n}_{PQ,x} + \frac{(\bar{\Theta} - \bar{c}) \cdot \bar{u}}{\beta} \\ -\hat{n}_{PQ,x} & 0 & \hat{n}_{PQ,y} + \frac{(\bar{\Theta} + \bar{c}) \cdot \bar{v}}{\beta} & \hat{n}_{PQ,y} + \frac{(\bar{\Theta} - \bar{c}) \cdot \bar{v}}{\beta} \\ 0 & 1 & \frac{(\bar{\Theta} + \bar{c}) \cdot \bar{w}}{\beta} & \frac{(\bar{\Theta} - \bar{c}) \cdot \bar{w}}{\beta} \end{pmatrix} \quad (4.78)$$

while $\bar{\mathbf{T}}^{-1}$ is its inverse matrix, expressed as:

$$\bar{\mathbf{T}}^{-1} = \begin{pmatrix} \frac{\bar{v} \cdot \hat{n}_{PQ,x} - \bar{u} \cdot \hat{n}_{PQ,y}}{\bar{c}^2} & \frac{\beta \cdot \hat{n}_{PQ,y} + \bar{v} \cdot \bar{\Theta}}{\bar{c}^2} & -\frac{\beta \cdot \hat{n}_{PQ,x} + \bar{u} \cdot \bar{\Theta}}{\bar{c}^2} & 0 \\ -\frac{\bar{w}}{\bar{c}^2} & -\frac{\bar{w} \cdot \hat{n}_{PQ,x} \cdot \bar{\Theta}}{\bar{c}^2} & -\frac{\bar{w} \cdot \hat{n}_{PQ,y} \cdot \bar{\Theta}}{\bar{c}^2} & 1 \\ \frac{\bar{c} - \bar{\Theta}}{2\bar{c}^2} & \frac{\beta \cdot \hat{n}_{PQ,x}}{2\bar{c}^2} & \frac{\beta \cdot \hat{n}_{PQ,y}}{2\bar{c}^2} & 0 \\ -\frac{\bar{c} + \bar{\Theta}}{2\bar{c}^2} & \frac{\beta \cdot \hat{n}_{PQ,x}}{2\bar{c}^2} & \frac{\beta \cdot \hat{n}_{PQ,y}}{2\bar{c}^2} & 0 \end{pmatrix} \quad (4.79)$$

The artificial speed of sound \bar{c} , included in the above matrices, is computed as follows (Anderson *et al.*, 1996; Kallinderis and Ahn, 2005; Tai *et al.*, 2005; Tai and Zhao, 2003):

$$\bar{c} = \sqrt{\bar{\Theta}^2 + \beta} \quad (4.80)$$

Finally, for the discrete formulation of Roe's scheme – as is expressed by Eq. (4.73) – $\bar{\mathbf{A}}_{PQ}^{(-)}$ can be obtained as follows (Nikolos and Delis, 2009):

$$\bar{\mathbf{A}}_{PQ}^{(-)} = \bar{\mathbf{T}} \cdot \bar{\mathbf{A}}^{(-)} \cdot \bar{\mathbf{T}}^{-1}, \quad (4.81)$$

where $\bar{\mathbf{A}}^{(-)} = \text{diag}\{\bar{\lambda}_1^-, \bar{\lambda}_2^-, \bar{\lambda}_3^-, \bar{\lambda}_4^-\}$ and $\bar{\lambda}_i^- = \min(\bar{\lambda}_i, 0)$.

4.4.1.2 Higher-Order Accurate Scheme

At this point, please note that within the framework of a first-order spatial scheme, the quantities $\mathbf{U}_{PQ}^{(L)}$ and $\mathbf{U}_{PQ}^{(R)}$, which actually define the left (L) and right (R) states existing at the two sides of ∂CV_{PQ} , are approximated by using the vectors of the flow variables at points P and Q , *i.e.* $\mathbf{U}_{PQ}^{(L)} = \mathbf{U}_P$ and $\mathbf{U}_{PQ}^{(R)} = \mathbf{U}_Q$. However, in order to improve the accuracy of the final solution, the current flow solver has been enhanced by the addition of a second-order spatial scheme that is based on the well-known Monotonic Upstream Scheme for Conservation Laws (MUSCL) (van Leer, 1979). Accordingly, the values of the primitive flow variables at each side of ∂CV_{PQ} are properly reconstructed by means of the MUSCL interpolation; the required gradients at the corresponding nodes (P and Q) are computed using the Green-Gauss theorem, via an edge-based formulation (Barth, 1992). Thus,

$$\mathbf{U}_{PQ}^{(L)} = \mathbf{U}_P + \frac{1}{2} \cdot (\nabla \mathbf{U})^L \cdot \mathbf{r}_{PQ}, \quad (4.82)$$

$$\mathbf{U}_{PQ}^{(R)} = \mathbf{U}_Q - \frac{1}{2} \cdot (\nabla \mathbf{U})^R \cdot \mathbf{r}_{PQ}, \quad (4.83)$$

where \mathbf{r}_{PQ} denotes the position vector that connects the mesh nodes P and Q ; \mathbf{r}_{PQ} is directed from P to Q . Herein, the extrapolation gradients $(\nabla \mathbf{U})^L$ and $(\nabla \mathbf{U})^R$ are equal to the gradients $(\nabla \mathbf{U})_P$ and $(\nabla \mathbf{U})_Q$ of the flow vector at the nodes P and Q respectively and calculated by applying the Green-Gauss linear representation method, as follows:

$$(\nabla \mathbf{U})_P = \frac{1}{E_P} \sum_{Q \in S_N(P)} \frac{1}{2} \cdot (\mathbf{U}_P + \mathbf{U}_Q) \cdot \mathbf{n}_{PQ}. \quad (4.84)$$

where E_p stands for the area of the control volume around node P . Finally, in the case that the examined node is a boundary one, the respective expression for the calculation of $(\nabla\mathbf{U})_P$ reads:

$$(\nabla\mathbf{U})_P = \frac{1}{E_p} \left[\sum_{Q \in S_N(P)} \frac{1}{2} (\mathbf{U}_P + \mathbf{U}_Q) \cdot \mathbf{n}_{PQ} + \sum_{(K_{out} \in \partial CV_P \cap B)} \mathbf{U}_P \cdot \mathbf{n}_{out} \right]. \quad (4.85)$$

4.4.1.3 Slope Limiter

In order to minimize the total variation and suppress any occasional discontinuities in the reconstructed field after the application of the second-order scheme, the proposed flow solver has been enhanced by the addition of the Min-Mod slope limiter (Sweby, 1984). Essentially, the Min-Mod limiter ensures the smoothness of the resulting solution by means of choosing the slope with the smallest magnitude (Lygidakis, 2015). Initially, let us introduce the centered (c) and upwind (u) gradients, which are defined as:

$$(\nabla\mathbf{U})_{PQ}^c \cdot \mathbf{r}_{PQ} = \mathbf{U}_Q - \mathbf{U}_P \quad (4.86)$$

$$(\nabla\mathbf{U})_P^u = 2 \cdot (\nabla\mathbf{U})_P - (\nabla\mathbf{U})_{PQ}^c \quad (4.87)$$

$$(\nabla\mathbf{U})_Q^u = 2 \cdot (\nabla\mathbf{U})_Q - (\nabla\mathbf{U})_{PQ}^c \quad (4.88)$$

Then, according to the adopted limiting strategy, Eq. (4.82) and Eq. (4.83) recast into:

$$\mathbf{U}_{PQ}^{(L)} = \mathbf{U}_P + \frac{1}{2} \cdot \mathcal{L}((\nabla\mathbf{U})_P^u \cdot \mathbf{r}_{PQ}, (\nabla\mathbf{U})_{PQ}^c \cdot \mathbf{r}_{PQ}) \quad (4.89)$$

$$\mathbf{U}_{PQ}^{(R)} = \mathbf{U}_P - \frac{1}{2} \cdot \mathcal{L}((\nabla\mathbf{U})_Q^u \cdot \mathbf{r}_{PQ}, (\nabla\mathbf{U})_{PQ}^c \cdot \mathbf{r}_{PQ}) \quad (4.90)$$

where \mathcal{L} stands for the Min-Mod limiting function, defined as:

$$\mathcal{L}(a, b) = \begin{cases} a & \text{if } |a| < |b| \text{ and } ab > 0 \\ b & \text{if } |b| < |a| \text{ and } ab > 0 \\ 0 & \text{if } ab \leq 0 \end{cases} \quad (4.91)$$

4.4.2 Viscous Fluxes

The numerical approximation of the viscous fluxes included within the flow model requires the calculation of the spatial gradients of the velocity components (axial, radial and tangential) at the midpoint of every grid edge. In this study, the computation of the involved spatial

derivatives is implemented by adopting an element-based approach (Kallinderis and Ahn, 2005; Lygidakis *et al.*, 2016; Leloudas *et al.*, 2020a, 2021). According to this method, a new finite control volume, called edge-dual volume, is created around every edge of the computational mesh, in such a way that includes the adjacent cells (primary elements) sharing the examined edge. Figure 4.4 illustrates such edge-dual volume examples around an arbitrary edge PQ , composed by different types of primary elements. Then, the divergence theorem is applied over these newly introduced finite volumes; the spatial derivatives of the velocity components at the midpoint of the edge PQ are calculated by performing the surface integrals along the edge-dual boundaries, as follows:

$$\left(\frac{\partial u_i}{\partial x}\right)_{PQ} = \frac{1}{E_{PQ}} \oint_{PQ} u_i n_x ds = \frac{1}{E_{PQ}} \sum_{k=1}^m n_{x,k} \frac{u_{i,k}^L + u_{i,k}^R}{2}, \quad (4.92)$$

$$\left(\frac{\partial u_i}{\partial y}\right)_{PQ} = \frac{1}{E_{PQ}} \oint_{PQ} u_i n_y ds = \frac{1}{E_{PQ}} \sum_{k=1}^m n_{y,k} \frac{u_{i,k}^L + u_{i,k}^R}{2}. \quad (4.93)$$

Herein, E_{PQ} and m denote the area and the number of boundary edges of the edge-dual volume that corresponds to the examined edge PQ , respectively. In addition, $n_{x,k}$ and $n_{y,k}$ represent the components of the normal outward vector on the k -edge of the edge-dual volume, whereas $u_{i,k}^L$ and $u_{i,k}^R$ stand for the velocity component values at the endpoints of the k -edge. Ultimately, utilizing the edge-based data structure of IGal2D solver, the aforementioned fluxes are obtained with a single edge-loop, as no information is needed about the cell topology (Kallinderis and Ahn, 2005; Lygidakis *et al.*, 2016; Leloudas *et al.*, 2020a, 2021). Please note that the same approach is followed for the calculation of the viscous fluxes of the turbulence model as well.

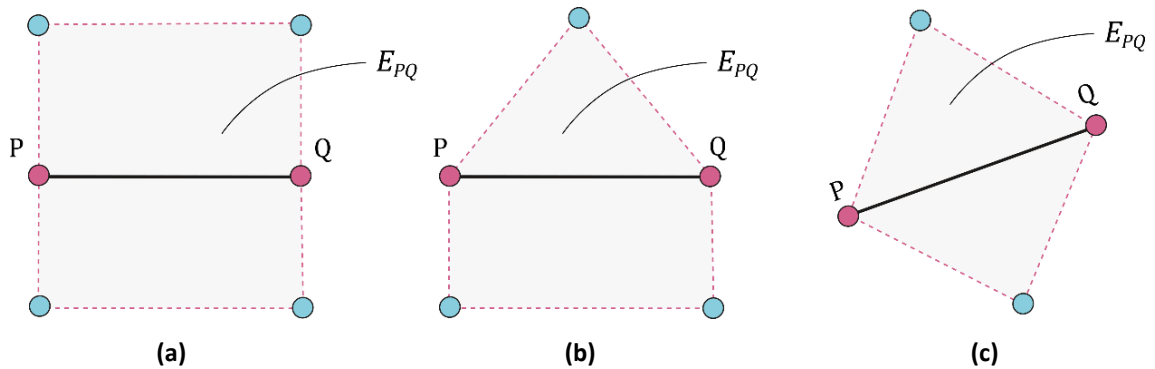


Figure 4.4: Edge-dual volume examples, obtained by different types of faces.

4.4.3 Turbulence Model's Fluxes

In the present study, the calculation of the numerical fluxes related to the turbulence model is implemented by adopting the same node-centered finite-volume discretization approach that was applied for the flow model equations. Especially, the convective (inviscid) fluxes of the SST turbulence model are evaluated at the midpoint of every edge PQ , by means of a simple first-order accurate upwind scheme (Anderson and Bonhaus, 1994); in that way stability of the numerical methodology is assured without reducing noticeably the accuracy of the final solution (Leloudas *et al.*, 2021; Lygidakis *et al.*, 2020). Thus,

$$(\Phi_i^t)_{PQ} = \int_{\partial CV_{PQ}} \Psi_i^t ds = \int_{\partial CV_{PQ}} \hat{n}_{PQ,x} \mathbf{F}_i^t + \hat{n}_{PQ,y} \mathbf{G}_i^t ds = \Theta^+ \cdot \mathbf{U}_P^t + \Theta^- \cdot \mathbf{U}_Q^t, \quad (4.94)$$

where denote \mathbf{U}_P^t and \mathbf{U}_Q^t the vectors of the turbulence model variables; the parameters Θ^+ and Θ^- are defined as:

$$\Theta^+ = \max(\Theta, 0), \quad (4.95)$$

$$\Theta^- = \min(\Theta, 0). \quad (4.96)$$

Now, in terms of calculating the diffusive fluxes of the turbulence model at the midpoint of every edge PQ , the spatial gradients of the respective primitive variables (namely, the turbulent kinetic energy and the specific rate of dissipation) have to be pre-evaluated. Practically, this is achieved by following a similar approach to the one adopted for the calculation of the velocity gradients, involved within the flow equations (see Section 4.4.2). Therefore, the spatial derivatives of turbulent kinetic energy (k) and the specific rate of dissipation (ω) are evaluated by applying an alternative form of Eq. (4.92) and Eq. (4.93), where the velocity components have been replaced by k and ω . Ultimately, since the required spatial derivatives have been obtained, the viscous fluxes of the SST model can be calculated as:

$$(\Phi_v^t)_{PQ} = \mathbf{F}_i^t \cdot n_{PQ,x} + \mathbf{G}_i^t \cdot n_{PQ,y} \quad (4.97)$$

4.4.4 Boundary Conditions

In order to complete the flux balance on each node of the computational mesh, appropriate boundary conditions have to be employed as well, either contributing corresponding values to the inviscid fluxes' sum of boundary nodes or defining explicitly their primitive variables' values. Herein, four different types of boundary conditions are encountered: solid wall, symmetry, inlet and outlet types of boundaries. At symmetry areas, *e.g.* axis of symmetry, or

solid walls for inviscid flows, free-slip conditions are imposed (Leloudas *et al.*, 2021; Lygidakis *et al.*, 2016; Ramos, 1986). In case of a viscous flow, the velocity components on solid wall nodes are set straightforward equal to zero (Leloudas *et al.*, 2021; Lygidakis *et al.*, 2016). Accordingly, at each inlet/outlet control volume, additional convective fluxes are taken into account, extracted by the corresponding normal to the boundary edge vector and the terms of the inviscid fluxes (4.39). The latter is calculated with primitive variables' values, taken either from inside or outside the computational field; velocity is taken from upstream free-flow in case of inflow boundaries and from inside the flow domain for outflow ones, while for pressure the opposite procedure is followed (Anderson *et al.*, 1996).

Furthermore, in terms of outlet area nodes and flow problems involving swirling, the radial equilibrium method (Wu and Wolfenstein, 1949) is also applied, which essentially defines the pressure distribution outside the computational domain. The corresponding relation, derived from the inviscid radial momentum equation after removing the radial velocity component, is described as follows (Susan-Resiga *et al.*, 2009):

$$\partial p / \partial y = w^2 / y. \quad (4.98)$$

In practice, Eq. (4.98) is implemented successively to the outlet nodes with a simple linear integration along the radial direction; at the starting point (closest to the axis of symmetry) the pre-defined outlet pressure is imposed. Additionally, a Laplacian smoothing technique is also applied to avoid odd-even decoupling phenomena at the outlet region; mathematically, it is expressed for each boundary node P and each primitive variable as:

$$\mathbf{U}_P = \frac{\mathbf{U}_P E_P + \varepsilon \sum_{Q \in S_N(P)} \mathbf{U}_Q E_Q}{E_P + \varepsilon \sum_{Q \in S_N(P)} E_Q}, \quad (4.99)$$

where ε is the smoothing coefficient, set equal to 0.5 in this study. Ultimately, depending on the encountered flow, the circumferential velocity component (w) at inlet (on the outside) can be computed via the free vortex flow approach, *i.e.* $w \cdot y = \text{const.}$, which stems from the conservation of angular momentum.

Finally, the boundary conditions of the SST turbulence model are implemented in the same way to those of the flow model. In particular, at inlet and solid wall regions turbulence model's variables are defined explicitly (Dirichlet conditions). Values at inlet boundaries are set equal to those upstream the computational domain, whereas at solid walls turbulent kinetic energy and turbulent kinematic viscosity are zeroed (low Reynolds approach) (Leloudas *et al.*, 2021; Lygidakis *et al.*, 2016). Please note that no special treatment is required for the symmetry area. Finally, a simple upwind scheme is employed for the outlet nodes, with data taken from inside

the computational domain similarly to the flow model (Leloudas *et al.*, 2021; Lygidakis *et al.*, 2016).

4.4.5 Source Terms

In this study, the source term vector of the flow model – containing both the term related to axial symmetry and external body forces – as well as the source term vector of turbulence model, is calculated by applying the finite volume discretization approach, expressed as:

$$\iint_{CV_p} \mathbf{H} \, dx dy = \mathbf{H}_P \cdot E_p \quad (4.100)$$

It is recalled that E_p stands for the area of the control volume formed around node P .

4.5 Time Integration

Following the calculation of numerical fluxes for each control volume, Eq. (4.65) can be reformed as follows (Leloudas *et al.*, 2021):

$$-E_p \frac{\Delta \mathbf{U}_P^{(n+1)}}{\Delta t_p} = \mathbf{R}_P^{(n)}, \quad (4.101)$$

where $\Delta \mathbf{U}_P^{(n+1)}$ stands for the correction vector of primitive variables at time step $n + 1$, $\mathbf{R}_P^{(n)}$ for the sum of the numerical fluxes at the previous time step n and Δt_p for the time step of the iterative procedure. Please note that IGal2D solver employs a local time-stepping methodology; thus, a different time step Δt_p is calculated for each computational node P , aiming to accelerate the overall convergence rate. Besides, different formulas for Δt_p are adopted for the cases of inviscid and viscous flow simulations. In particular, for an inviscid flow problem, the local time step reads:

$$\Delta t_p^{inv} = CFL \cdot \frac{0.5 l_p}{|\mathbf{U}_P| + c_p}, \quad (4.102)$$

while for the case of a viscous one, the local time step is calculates as:

$$\Delta t_p^{vis} = CFL \cdot \frac{E_p}{A_x + A_y + D}. \quad (4.103)$$

Herein, CFL stands for the Courant-Friedrichs-Lewy number and l_p denotes the length of the shortest edge connected to the examined node P . $|\mathbf{U}_P|$ and c_p denote the magnitude of the

velocity vector and the artificial speed of sound at the same point, respectively; the formula for the calculation of the artificial speed of sound is given in Section 4.4.1.1. Lastly, the terms A_x , A_y and D are expressed as follows (Kallinderis and Ahn, 2005):

$$A_x = (|u| + c_x)S_x \quad , \quad A_y = (|v| + c_y)S_y \quad , \quad D = \frac{2}{\text{Re}} \cdot \frac{E_P}{S_x + S_y} \quad . \quad (4.104)$$

where artificial speed of sound (c_x and c_y) and projection of dual-volume surfaces' normal vector (S_x and S_y) at point P along each Cartesian coordinate direction are calculated respectively as:

$$c_x = \sqrt{u^2 + \beta} \quad , \quad c_y = \sqrt{v^2 + \beta} \quad , \quad S_x = \frac{1}{2} \sum_e |S_x|_e \quad , \quad S_y = \frac{1}{2} \sum_e |S_y|_e \quad . \quad (4.105)$$

This method allows for the maximum acceptable time step to be used for each point and consequently accelerates the solution procedure (Blazek, 2015). Please note that the system of partial differential equation defining the SST turbulence model (4.41) is reformulated in exactly the same way, with the only exception being the implicit treatment of the corresponding source term (see Section 4.5.1). Finally, for the computation of the involved correction vectors an explicit second-order four-stage Runge-Kutta method (RK(4)) is applied, separately for flow and turbulence model equations (loose-coupling strategy) (Leloudas *et al.*, 2020a, 2021; Lygidakis *et al.*, 2016).

4.5.1 Implicit Treatment of Turbulence Model Source Term

The rapid change of turbulence models' source term can cause instability to the solution or even its complete failure; a remedy to this shortcoming appears to be the implicit handling of this component (Kim, 2003). While this treatment is a prerequisite for implicit methods, for explicit ones constitutes an additional technique, implemented by a similar Newton linearization procedure only for the source term (Blazek, 2015; Kim, 2003). Considering this approach, the differential equation for turbulence models becomes:

$$\begin{aligned} \frac{\Delta \mathbf{U}_P^{t(n+1)}}{\Delta t_P} \cdot E_P + \sum_{Q \in S_N(P)} (\Phi_i^t)_{PQ} - \sum_{Q \in S_N(P)} (\Phi_v^t)_{PQ} &= \mathbf{H}_P^t \cdot E_P \quad , \\ \frac{\Delta \mathbf{U}_P^{t(n+1)}}{\Delta t_P} \cdot E_P + \sum_{Q \in S_N(P)} (\Phi_i^t)_{PQ} - \sum_{Q \in S_N(P)} (\Phi_v^t)_{PQ} &= (\mathbf{H}_P^t + L_P^t \cdot \Delta \mathbf{U}_P^{t(n+1)}) \cdot E_P \quad , \end{aligned} \quad (4.106)$$

$$\left(\frac{\Delta \mathbf{U}_P^{t(n+1)}}{\Delta t_P} - L_P^t \cdot \Delta \mathbf{U}_P^{t(n+1)} \right) \cdot E_P + \sum_{Q \in S_N(P)} (\Phi_i^t)_{PQ} - \sum_{Q \in S_N(P)} (\Phi_v^t)_{PQ} = \mathbf{H}_P^t \cdot E_P,$$

$$\left(\frac{\mathbf{I}}{\Delta t_P} - L_P^t \right) \Delta \mathbf{U}_P^{t(n+1)} = -\frac{\mathbf{R}_P^{(n)}}{E_P},$$

where \mathbf{I} is a 2×2 identity matrix and L_P^t denotes the Jacobian matrix of the SST turbulence model's source term, including only the negative main source term components; the iterative step of the Runge-Kutta method is transformed accordingly (Kim, 2003). Ultimately, the computation of the inverse $(\mathbf{I}/\Delta t_P - L_P^t)$ matrix is implemented as follows:

$$\left(\frac{\mathbf{I}}{\Delta t_P} - L_P^t \right)^{-1} = \begin{array}{cc} \frac{y\Delta t_P}{y + \beta^* \omega y \Delta t_P + \nu \Delta t_P} & 0 \\ 0 & \frac{y\Delta t_P}{y + 2\beta \omega y \Delta t_P + \nu \Delta t_P} \end{array} \quad (4.107)$$

4.5.2 Acceleration Techniques

Besides local time-stepping approach and edge-based data structure, the proposed numerical solver is enhanced with an agglomeration multigrid scheme to further improve its computational performance, especially in large-scale problems (Blazek, 2015; Lygidakis *et al.*, 2016; Nishikawa *et al.*, 2010). Although it was initially developed for three-dimensional simulations (Lygidakis *et al.*, 2016), its edge-wise framework allowed for, almost, a straightforward implementation to the two-dimensional approach presented in the current work. According to this scheme the final solution is approximated on successively coarser meshes, in order the low-frequency errors to be damped more efficiently. The sequence of aforementioned coarser grids, comprised of irregular polyhedral cells, is generated with either isotropic or directional (full- or semi-coarsening) fusion of neighbouring control volumes on a topology-preserving framework (Lygidakis *et al.*, 2016). Independently of the agglomeration type, fusion procedure begins from solid wall surfaces following pre-defined rules, and extends successively to the interior domain resembling in that way the advancing-front technique (Lygidakis *et al.*, 2016). The whole procedure is repeated if an even coarser resolution is required. A number of four to five levels is usually adequate. The multigrid accelerated solution is succeeded with the Full Approximation Scheme (FAS) in a V-cycle process, according to which Eq. (4.101) is solved only at the initial finest grid; at the coarser ones, approximate versions of it are relaxed (Blazek, 2015; Lygidakis *et al.*, 2016; Nishikawa *et al.*, 2010). Data exchange between each two successive spatial levels is performed with the restriction of the variables and flux balances, computed at the centers of control cells, from the finer to the coarser resolution, as well as with the prolongation of the corresponding updated

variables' corrections from the coarser to the finer one (Lygidakis *et al.*, 2016). Additional acceleration is gained with a combined (Full Multigrid) FMG/FAS approach, according to which the whole procedure begins from the coarsest mesh and as the number of iterative cycles increases, it extends gradually to the finer grids up to the initial finest one (Lygidakis *et al.*, 2016).

Chapter 5

Numerical Validation of IGal2D Solver

This chapter aims to provide a detailed evaluation study on the numerical accuracy and performance of the in-house developed IGal2D solver. For this purpose, several incompressible axisymmetric flows are considered, including both non-swirling (see Section 5.1) and swirling flow (see Section 5.2) regimes. The flow simulation results are compared against analytical, numerical and experimental data.

5.1 Non-Swirling Flows

The first part of the current validation study aims to investigate the performance of the proposed RANS solver, by means of three widely adopted benchmark cases that involve axisymmetric flow without the presence of swirl velocity. In particular, the encountered case studies include the prediction of the inviscid flow over a sphere (see Section 5.1.1), the viscous laminar flow over a sphere (see Section 5.1.2) and the turbulent flow around a flanged diffuser (see Section 5.1.3).

5.1.1 Inviscid Flow over a Sphere

The first benchmark case for the evaluation of IGal2D solver considers the inviscid, incompressible and irrotational flow (potential flow) around a sphere. In this case, the spatial discretization of the computational domain was made with a two-dimensional triangular mesh, composed by 14,819 triangular primary elements and 7,648 nodes. The numerical simulation of the axisymmetric flow field around the sphere was achieved by setting the value of the artificial compressibility parameter equal to 10, while the steady-state solution was reached with a CFL number equal to 0.5. For the evaluation of the solver's performance, the numerical results are compared against the analytical solution provided by potential theory. In particular, according to potential theory, pressure (p_s) and pressure coefficient (C_{p_s}) distributions on the surface of the sphere read:

$$p_s - p_\infty = \frac{1}{2}\rho u_\infty^2 - \frac{9}{8}\rho u_\infty^2 \sin^2 \theta \rightarrow c_{p_s} = \frac{p_s - p_\infty}{0.5\rho u_\infty^2} = 1 - \frac{9}{4}\sin^2 \theta, \quad (5.1)$$

while the velocity magnitude distribution on the surface of the sphere (u_s) is calculated as:

$$u_s = \frac{3}{2} \cdot u_\infty \sin \theta, \quad (5.2)$$

where θ denotes the angle between a random point on the surface of the sphere and the stagnation point. Figure 5.1 illustrates the comparison of the numerical results against the analytical solution, in terms of both pressure coefficient (C_{p_s}) and dimensionless velocity magnitude (u_s/u_∞). Apparently, an almost perfect agreement between the analytically calculated and numerically predicted distributions can be observed.

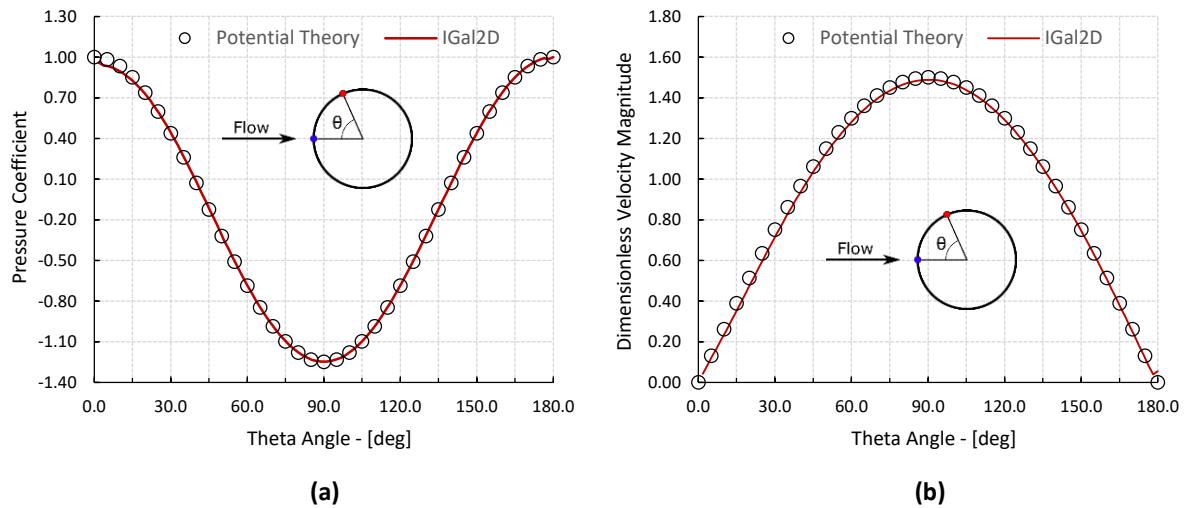


Figure 5.1: Inviscid flow over a sphere: (a) Distribution of pressure coefficient on the surface of the sphere. (b) Distribution of dimensionless velocity magnitude on the surface of the sphere.

5.1.2 Viscous Laminar Flow over a Sphere

In order to assess the ability of the developed flow solver to accurately predict drag force, as well as flow separation and vortex formation phenomena, the current section involves the simulation of viscous laminar flow around a sphere. Flow separation behind a sphere is generally anticipated when Reynolds number becomes greater than 24, resulting in the development of an attached axisymmetric vortex ring. The flow remains steady and axisymmetric up to a Reynolds number of approximately 220, while it finally starts to become unsteady and three-dimensional when the Reynolds number exceeds the aforementioned limit (Lee and Lee, 2011). Herein, the axisymmetric (steady-state) viscous laminar flow around a sphere is examined for Reynolds numbers equal to 30, 50, 100 and 150. The simulation of the incompressible flow field around the sphere was achieved by setting the value of the artificial compressibility parameter (β) equal to 10. Figure 5.2 illustrates the streamlines around the sphere, for the different Reynolds numbers considered in this work, revealing that the size of the separation bubble behind the sphere increases proportionally to the Reynolds number, as expected.

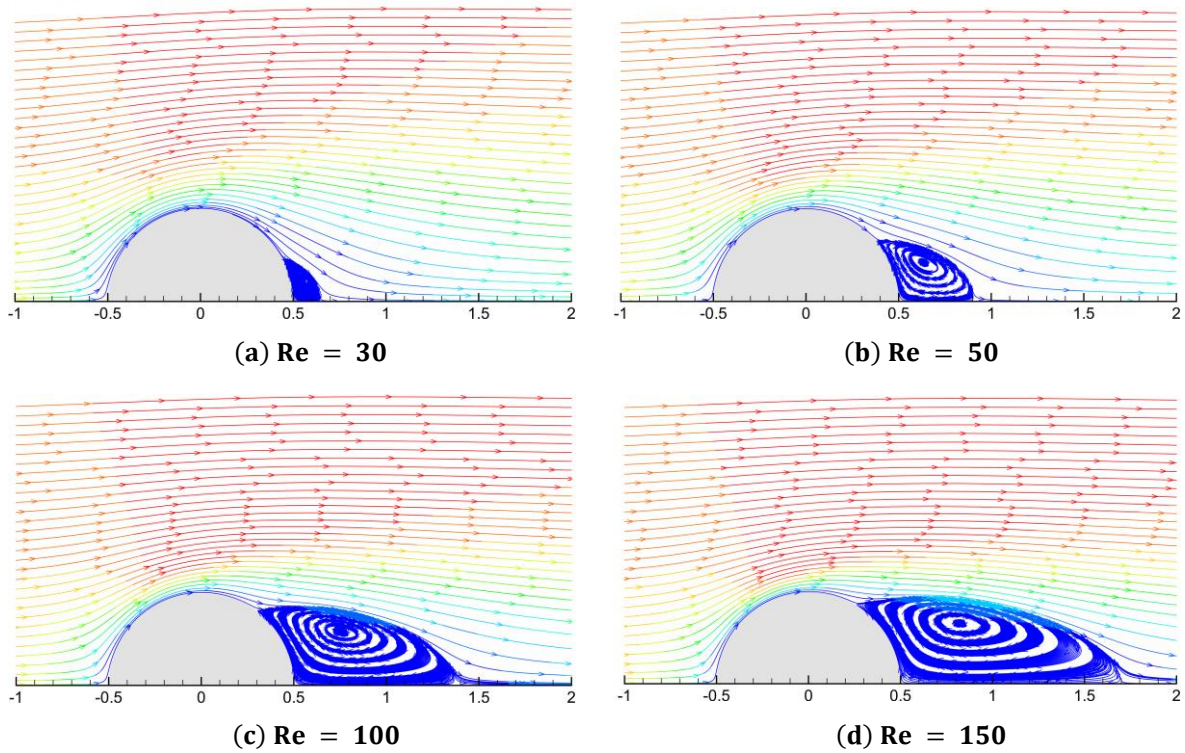


Figure 5.2: Streamlines over a sphere at various Reynolds numbers.

As long as the quantitative evaluation of the obtained results is concerned, Figure 5.3a presents the variation of drag coefficient (C_D) with Reynolds number, in comparison to the corresponding data derived from the numerical study of Mittal (1999) and the experimental work of Roos and Wilmarth (1971).

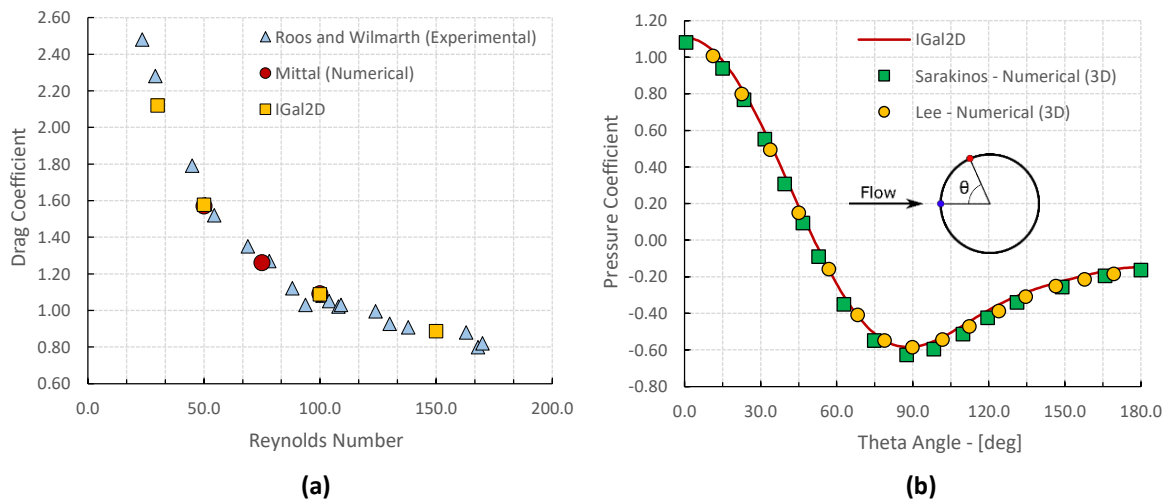


Figure 5.3: Laminar flow over a sphere: (a) Variation of drag coefficient with Reynolds number, (b) Pressure distribution on the surface of the sphere at $Re = 100$.

In addition, the pressure coefficient distribution over the sphere surface at $Re = 100$ is also provided in Figure 5.3b, along with the pressure distributions obtained from the numerical works of Lee (2000) and Sarakinos (2016). Evidently, the results of the present study match well with the corresponding ones of previous research. Finally, Table 5.1 compares the drag coefficient and the length of the recirculation zone (L_s) behind the sphere at $Re = 100$, with those of other researchers. The particular comparison indicates that the present solver is capable of simulating accurately such flows, since both L_s and C_D have been well predicted.

Method	Separation Length - L_s	Drag Coefficient - C_D
IGal2D	0.84D	1.090
Wang Y. <i>et al.</i> (2008)	0.86D	1.108
Vrahliotis <i>et al.</i> (2012)	0.87D	1.093
Kallinderis and Ahn (2005)	-	1.084

Table 5.1: Comparison of separation length and drag coefficient at $Re = 100$.

5.1.3 Turbulent Flow around a Flanged Diffuser

The current section considers the numerical simulation of the turbulent flow field around an unloaded flanged diffuser; the particular case study was selected in order to assess and eventually validate the ability of the in-house IGal2D solver – and particularly that of the employed SST turbulence model – to accurately predict such complex turbulent flows, which are characterized by massive flow separations. The diffuser geometry under examination is one of the initial designs investigated, both numerically and experimentally, by Abe and Ohya (2004); essentially, it is composed by a straight-wall diffuser that is connected to an exit flange, as shown in Figure 5.4.

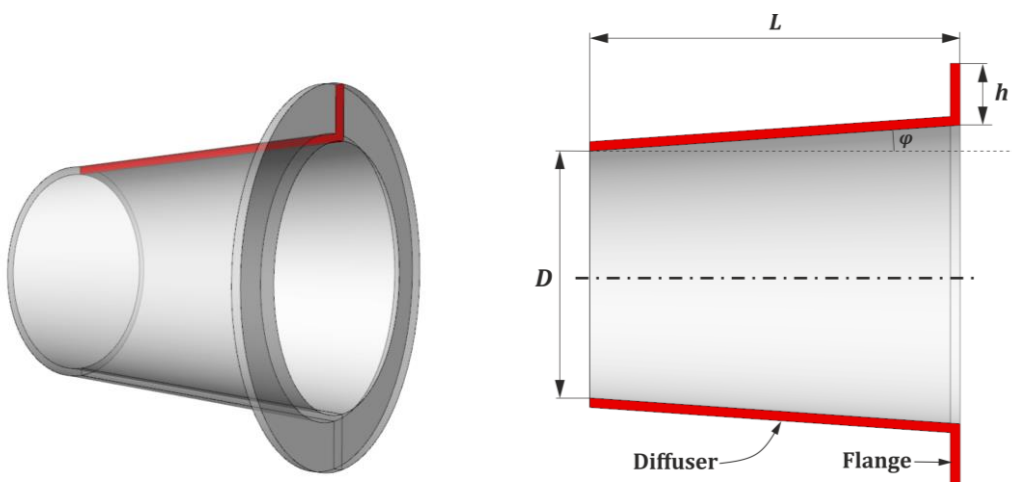


Figure 5.4: Schematic representation of the examined flanged diffuser.

In fact, Abe and Ohya (2004) explored the performance characteristics of an entire family of similar configurations, which were obtained by varying the corresponding design parameters, such as the height of the flange and the opening angle of the diffuser. The diffuser model considered in this study has a throat diameter (D) equal to 0.2 m, an opening angle (φ) equal to 4 degrees, a total length (L) of 0.3 m, while the ratio of the flange height to the throat diameter (h/D) equals to 0.25.

A detailed description of the simulation parameters adopted during this validation study (Reynolds number, computational domain, boundary conditions) can be found in the study of Abe and Ohya (2004). Please note that special attention was also given to the generation of the hybrid computational grid, which was eventually created by adopting a y^+ value below 1. In addition, a relatively high mesh resolution was applied around the solid walls and the symmetry axis, in order to accurately resolve the turbulent flow field within the diffuser, as well as the strong flow separation phenomena anticipated behind the flange. The particular computational grid, partially illustrated in Figure 5.5, was finally composed by 106,997 triangular and 15,640 quadrilateral elements; the total number of nodes was equal to 69,918. As in the previous benchmark case, the artificial compressibility parameter (β) was set equal to 10.

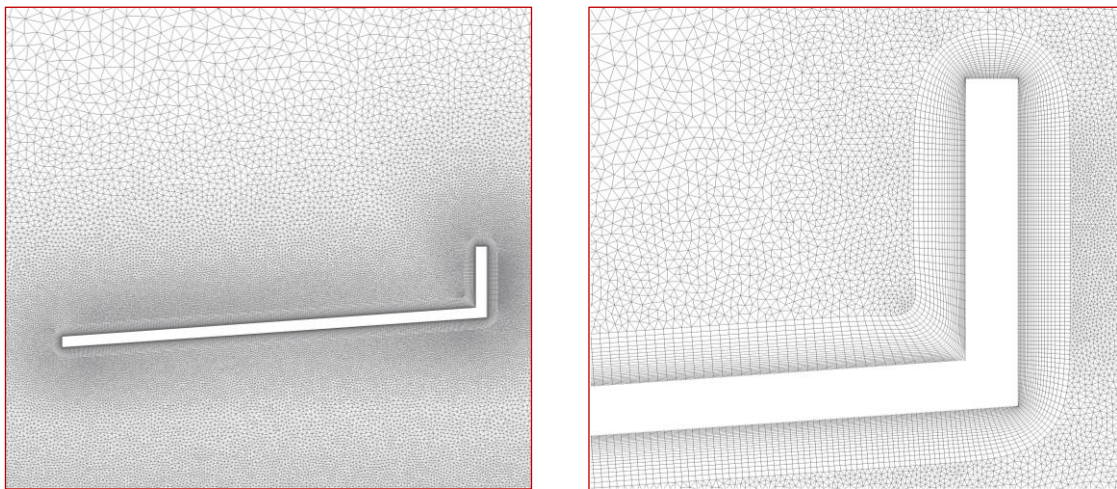


Figure 5.5: The computational grid for the simulation of the flow field around the flanged diffuser.

Figure 5.6 presents the flow streamlines and the dimensionless contours of pressure and axial velocity component around the examined diffuser geometry. Good agreement is found by comparing these qualitative results with the corresponding ones provided within the numerical study of Abe and Ohya (2004). In addition, by observing Figure 5.6, it is evident that the streamlines flow smoothly inside the diffuser, while the axial velocity does not vary significantly in the radial direction, except for the boundary layer region close to the diffuser

wall. In view of these remarks, Abe and Ohya (2004) noted that on-axis distributions of the flow variables can successfully explain the fundamental aspects of such diffuser flows. Therefore, they used such on-axis distributions of the velocity speed-up and the pressure coefficients to evaluate the diffuser performance and assess their numerical models.

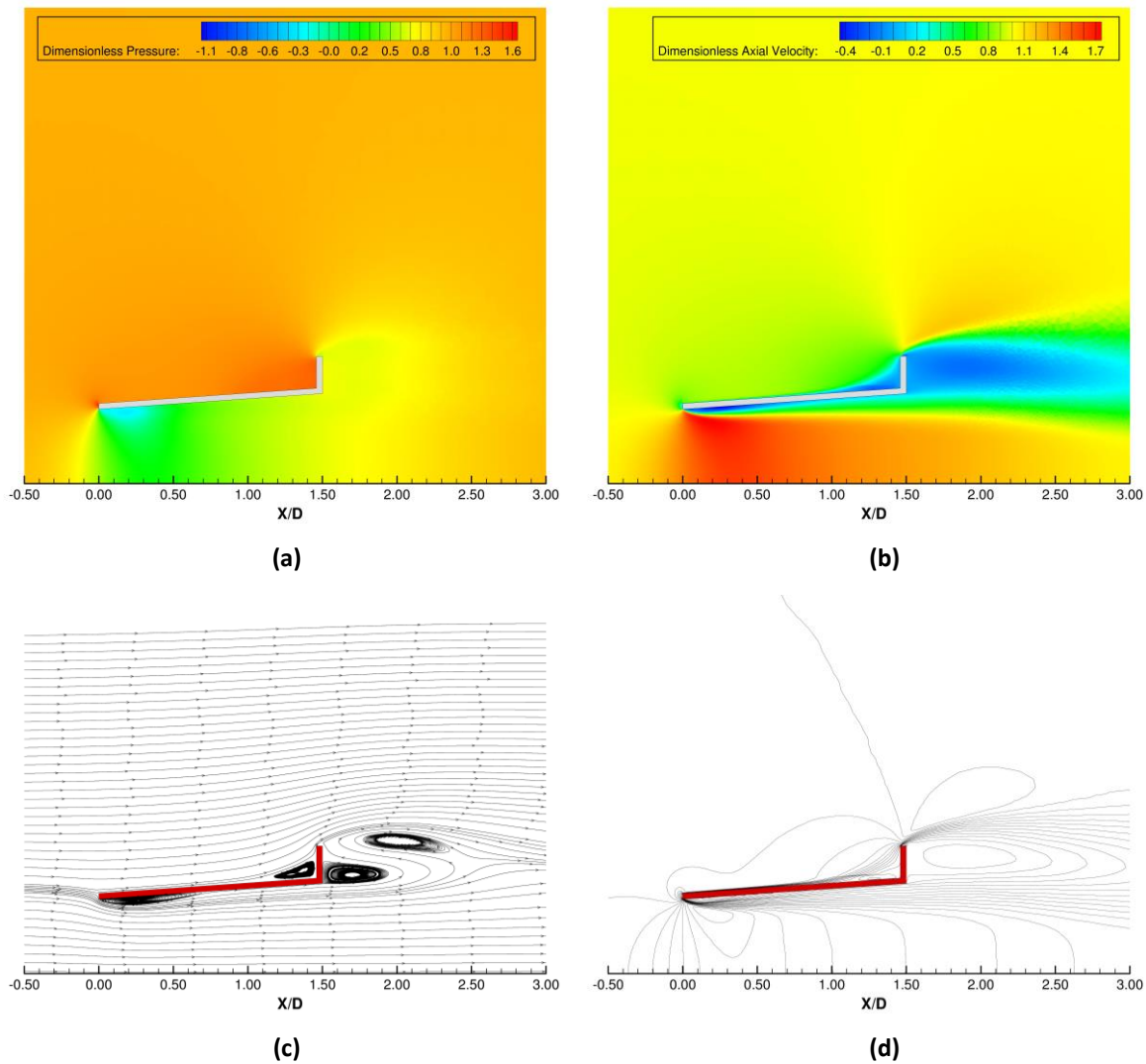


Figure 5.6: Turbulent flow around a flanged diffuser: (a) Dimensionless contours of the axial velocity component, (b) Dimensionless pressure contours, (c) Velocity streamlines, (d) Axial velocity contour lines.

Accordingly, for the quantitative evaluation of the results of the developed axisymmetric flow solver, Figure 5.7 contains the on-axis distributions of the velocity speed-up and pressure coefficient, comparatively to the corresponding distributions resulted by the numerical and experimental studies of Abe and Ohya (2004). It is demonstrated that the proposed axisymmetric flow solver is capable of predicting the flow field inside the diffuser with reasonable accuracy, both in terms of the on-axis velocity speed-up and pressure coefficient distributions, even

though a small underprediction of the experimental data is observed for the particular region (internal diffuser area). In addition, more significant discrepancies between the numerical and the experimental results have been detected in the region far downstream of the diffuser exit, as shown in Figure 5.7.

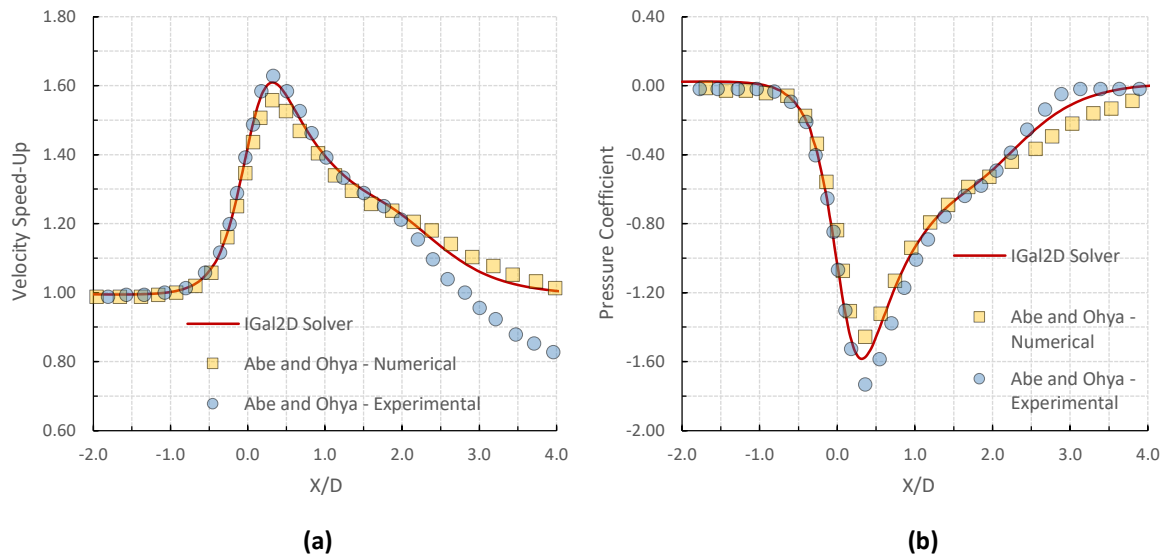


Figure 5.7: Turbulent flow around a flanged diffuser: (a) On-axis velocity speed-up distribution, (b) On-axis pressure coefficient distribution.

According to our conclusions, this is mainly attributed to the steady-state flow assumption that was made during this study, even though unsteady flow phenomena are actually expected in the wake region. Such unsteady phenomena are associated with vortex shedding. Therefore, the turbulent wake behind the flange is more active in the experiments than in the numerical simulations. A similar explanation was also provided by Abe and Ohya (2004), since such discrepancies were also found in their numerical results. Nevertheless, by considering the reasonable trends for both on-axis velocity speed-up and pressure coefficient distributions and the fact that the fundamental flow field characteristics within the diffuser were predicted with reasonable accuracy, the proposed solver seems to be capable of successfully encountering such turbulent flow fields.

5.2 Swirling Flows

The second part of this chapter aims to investigate and eventually validate the ability of IGal2D solver to accurately predict the characteristics of axisymmetric swirling flows. For this purpose, three relevant case studies have been considered; namely, the inviscid swirling flow inside an S-shaped axisymmetric tube (see Section 5.2.1), the laminar swirling flow inside an

axial tube (see Section 5.2.2) and finally, the turbulent swirling flow inside a conical diffuser (see Section 5.2.3).

5.2.1 Inviscid Swirling Flow inside an S-Shaped Axisymmetric Tube

This benchmark case considers the inviscid incompressible flow inside an S-shaped axisymmetric tube. The geometric characteristics of the 2.0 m long test section are illustrated in Figure 5.8. The design of the particular flow apparatus has been based on a cubic (third order) B-spline curve, which is defined over an open uniform knot vector. The B-Spline control points, used to define the centerline of the S-shaped tube, are included in Table 5.2. Following the centerline definition, the internal and external boundaries (walls) of the S-shaped tube were defined by simply offsetting the centerline in both directions by 0.06 m.

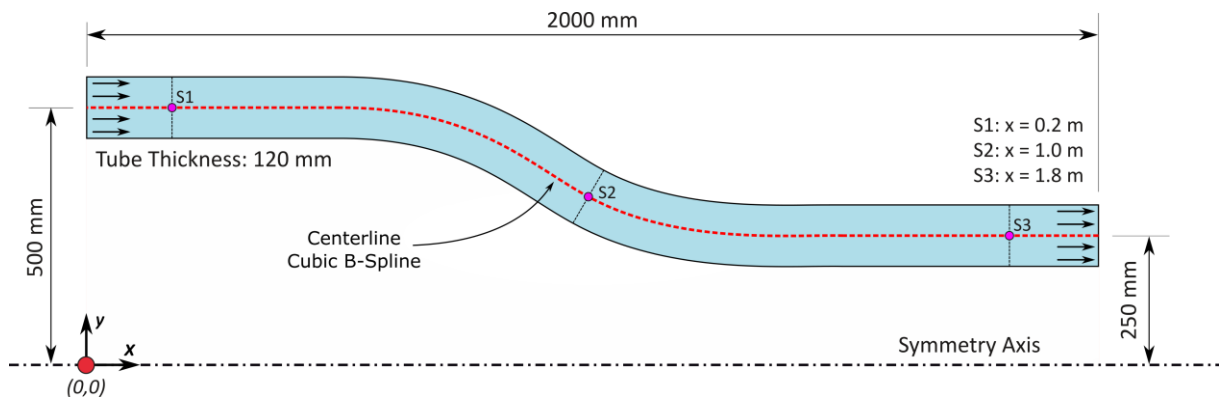


Figure 5.8: Geometric characteristics of the S-shaped axisymmetric tube.

Considering the main goal of this chapter, that is to assess the ability of the proposed methodology in swirling flow prediction, especially in terms of accuracy, a thorough study was conducted against this test case. Therefore, three different grid types were constructed for the representation of the computational field: (a) a grid composed of quadrilateral primary elements, (b) a regular triangular grid, which was derived by diagonalizing all the quadrilateral elements of type (a) grid, and finally, (c) an unstructured triangular grid. Furthermore, to achieve grid independency in the presented solutions, three different grids (denoted as M1, M2 and M3) were generated for each one of the aforementioned types, increasing successively their density. Here, for each denser resolution, the Degrees of Freedom (DoFs) – which actually are represented by the number of grid nodes (node-centered scheme) – were quadruplicated compared to the coarser one. Table 5.3 contains the density data of all the utilized grids, whereas Figure 5.9 presents the curved part of the coarsest resolution (M1) of each grid type (quadrilateral, triangular-regular and triangular-unstructured).

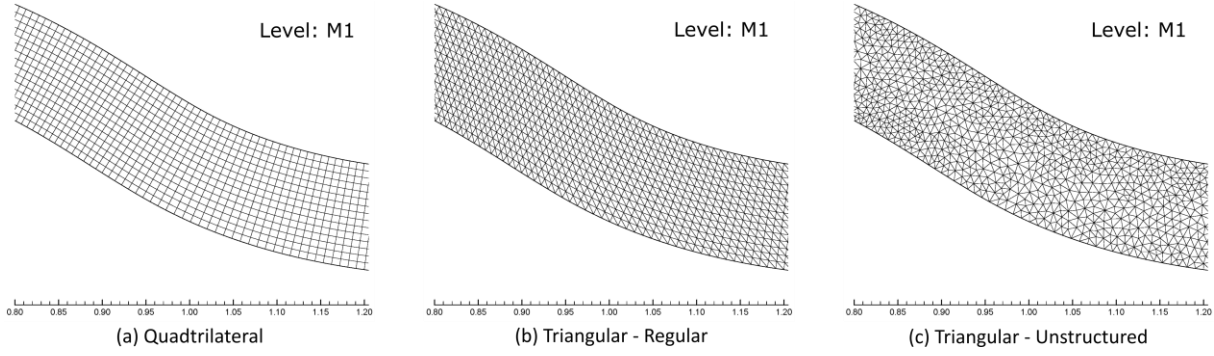


Figure 5.9: Curved part of the coarsest resolution (M1) of each grid type.

P_i	X_i	Y_i	P_i	X_i	Y_i	P_i	X_i	Y_i
P_0	0.00000	0.50000	P_{10}	0.68237	0.48103	P_{20}	1.39235	0.24914
P_1	0.02532	0.50000	P_{11}	0.75505	0.45840	P_{21}	1.46830	0.25045
P_2	0.07596	0.50000	P_{12}	0.82430	0.42684	P_{22}	1.54426	0.24988
P_3	0.15191	0.50000	P_{13}	0.88986	0.38837	P_{23}	1.62021	0.25004
P_4	0.22787	0.50000	P_{14}	0.95349	0.34698	P_{24}	1.69617	0.24999
P_5	0.30383	0.49999	P_{15}	1.01991	0.30979	P_{25}	1.77213	0.25000
P_6	0.37979	0.50004	P_{16}	1.09135	0.28331	P_{26}	1.84809	0.25000
P_7	0.45574	0.49985	P_{17}	1.16526	0.26541	P_{27}	1.92404	0.25000
P_8	0.53171	0.50057	P_{18}	1.24055	0.25483	P_{28}	1.97468	0.25000
P_9	0.60754	0.49472	P_{19}	1.31639	0.24994	P_{29}	2.00000	0.25000

Table 5.2: Control points of the cubic B-spline curve, used for the design of the centerline of the S-shaped tube.

Level	Quadrilateral			Triangular - Regular			Triangular - Unstructured		
	M1	M2	M3	M1	M2	M3	M1	M2	M3
Number of Nodes	4,000	16,000	64,000	4,000	16,000	64,000	4,055	16,082	64,051
Number of Elements	3,735	15,469	62,937	7,470	30,938	125,874	7,580	31,102	125,976

Table 5.3: Density data of the employed grids.

Regarding the inlet boundary conditions, a uniform profile was imposed for the axial velocity component (u), with a fixed value of $u_{in} = 0.966 \text{ m/s}$. At this point, please note that the subscript “in” is used to signify the flow quantities at the inlet of the computational domain. Furthermore, a free vortex approach was adopted for the calculation of the circumferential velocity profile over the inlet, using the following expression:

$$w_{in}(y) = w_m \cdot y_m / y, \quad (5.3)$$

where $y_m = 0.5 \text{ m}$ corresponds to the mean radius of the inlet annulus; the corresponding tangential velocity w_m was set equal to 0.259 m/s . Finally, zero radial velocity component (v_{in}) was imposed over the inlet. The particular values for the velocity components were selected in such a way that the magnitude of the total velocity vector over the inlet, which is denoted by V_{in} and calculated using w_m , to be equal to 1.0; thus, no re-dimensionalization of the obtained velocity field was required. Similarly, a unit dimensionless relative static pressure was considered at the outlet (0.0 Pa relative pressure for dimensional simulations with ANSYS Fluent), whereas free-slip conditions were imposed to the remaining boundaries. Ultimately, no re-dimensionalization of the grid was required due to the unitary mean diameter of the computational domain at the inlet. Independently of the grid used, an artificial compressibility parameter and a CFL number equal to 1.0 and 0.5, respectively, were used for the iterative approximation of the final steady-state solution; the latter was obtained after the $\log(\text{residual})$ of pressure was decreased more than ten orders of magnitude. Acceleration of the procedure was succeeded by implementing the incorporated multigrid scheme with up to five levels, *i.e.* with up to four agglomerated resolutions.

In order to evaluate the performance of IGal2D solver, the obtained results were compared with those of ANSYS Fluent. Moreover, specific metrics were obtained from the results of both solvers and compared with those stemming analytically from conservation of total pressure in case of inviscid incompressible steady-state flow, *i.e.* Bernoulli theorem, and conservation of angular momentum (moment of momentum). The following Table 5.4 - Table 5.6 present the extracted differences in total pressure P_t and rw quantity, between inlet and outlet boundaries at respective points at tip, mid and hub, *i.e.* between starting and ending points of corresponding streamlines. The aforementioned metrics were calculated for each resolution of the utilized grid types for both IGal2D and Fluent software.

The metrics of both solvers reveal a very good agreement with the corresponding theoretical values, *i.e.* almost zero differences between inlet and outlet, which tend to improve with increasing grid resolution. Simultaneously, no significant differences are identified between the results of IGal2D with those of Fluent. P_t or rw errors obtained by IGal2D code become slightly larger or smaller than those extracted by Fluent, depending on the computational grid type, grid density and streamline position. Independently of the code as well as the grid type, the best results are derived with the finer grid (M3-level) at mid streamline. Considering the value of rw at inlet, the errors for the aforementioned resolution and position are considered negligible as they correspond to less than 0.01% of the inlet value. The next better results are obtained at tip, whereas the worst at hub. Regarding the relatively small improvement of the above-mentioned errors by quadruplicating the DoFs of M2-level

meshes, grid independency is considered to be reached with the M3-level ones. Ultimately, no substantial differentiations are noticed between the results derived with the three different grid types.

Mid	$P_{t,2} - P_{t,1} [Pa]$			$r_2 w_2 - r_1 w_1 [m^2/s]$		
Quadrilateral	M1	M2	M3	M1	M2	M3
IGal2D	-5.60E-04	-2.79E-04	-7.53E-05	3.78E-05	3.29E-06	-8.91E-08
Ansys Fluent	-2.15E-04	1.80E-05	-2.92E-06	7.89E-05	1.71E-05	2.65E-06
Tip	$P_{t,2} - P_{t,1} [Pa]$			$r_2 w_2 - r_1 w_1 [m^2/s]$		
Quadrilateral	M1	M2	M3	M1	M2	M3
IGal2D	-1.33E-01	-6.70E-02	-3.36E-02	-1.47E-03	-6.82E-04	-3.27E-04
Ansys Fluent	-3.63E-02	-2.90E-02	-2.07E-02	-1.02E-03	-2.34E-04	-3.05E-04
Hub	$P_{t,2} - P_{t,1} [Pa]$			$r_2 w_2 - r_1 w_1 [m^2/s]$		
Quadrilateral	M1	M2	M3	M1	M2	M3
IGal2D	-6.27E-02	-3.15E-02	-1.55E-02	-1.64E-03	-8.08E-04	-4.81E-04
Ansys Fluent	-6.02E-02	-5.11E-02	-4.39E-02	-1.66E-02	-1.25E-02	-8.32E-03

Table 5.4: P_t and rw metrics extracted from quadrilateral grids.

Mid	$P_{t,2} - P_{t,1} [Pa]$			$r_2 w_2 - r_1 w_1 [m^2/s]$		
Triangular - Regular	M1	M2	M3	M1	M2	M3
IGal2D	1.16E-02	3.57E-04	6.28E-04	8.80E-04	-1.97E-04	-7.32E-05
Ansys Fluent	6.40E-05	3.76E-05	1.98E-05	5.07E-05	1.18E-05	2.85E-06
Tip	$P_{t,2} - P_{t,1} [Pa]$			$r_2 w_2 - r_1 w_1 [m^2/s]$		
Triangular - Regular	M1	M2	M3	M1	M2	M3
IGal2D	-8.33E-04	6.18E-04	6.42E-04	5.88E-03	3.43E-03	1.97E-03
Ansys Fluent	-1.32E-02	-6.61E-03	-3.40E-03	6.58E-04	3.17E-04	1.55E-04
Hub	$P_{t,2} - P_{t,1} [Pa]$			$r_2 w_2 - r_1 w_1 [m^2/s]$		
Triangular - Regular	M1	M2	M3	M1	M2	M3
IGal2D	-6.63E-02	-4.11E-02	-2.50E-02	-1.18E-02	-6.95E-03	-4.06E-03
Ansys Fluent	-9.77E-03	-4.89E-03	-3.30E-03	-3.15E-03	-1.55E-03	-7.87E-04

Table 5.5: P_t and rw metrics extracted from triangular-regular grids.

Mid						
	$P_{t,2} - P_{t,1} [Pa]$			$r_2 w_2 - r_1 w_1 [m^2/s]$		
Triangular – Unstruct.	M1	M2	M3	M1	M2	M3
IGal2D	9.49E-04	-3.08E-05	-2.08E-04	7.89E-04	3.70E-06	1.98E-05
Ansys Fluent	-9.14E-04	-2.62E-04	-1.64E-04	2.20E-04	7.22E-05	1.80E-05
Tip						
	$P_{t,2} - P_{t,1} [Pa]$			$r_2 w_2 - r_1 w_1 [m^2/s]$		
Triangular – Unstruct.	M1	M2	M3	M1	M2	M3
IGal2D	-8.12E-03	-3.17E-03	-1.38E-03	4.96E-03	2.86E-03	1.85E-03
Ansys Fluent	-2.62E-03	-7.53E-04	-7.70E-04	3.18E-03	2.10E-03	1.38E-03
Hub						
	$P_{t,2} - P_{t,1} [Pa]$			$r_2 w_2 - r_1 w_1 [m^2/s]$		
Triangular – Unstruct.	M1	M2	M3	M1	M2	M3
IGal2D	-5.26E-02	-2.95E-02	-2.35E-02	-9.27E-03	-5.61E-03	-3.65E-03
Ansys Fluent	-1.44E-02	-9.24E-03	-8.08E-03	-5.80E-03	-3.66E-03	-2.36E-03

Table 5.6: P_t and rw metrics extracted from triangular-unstructured grids.

Considering the previous state, the triangular-unstructured M3-level grid was selected for further evaluation of the proposed methodology as being the less biased and at the same time the most generic grid type. Figure 5.10 depicts the contours of dimensional pressure and velocity components, obtained with IGal2D, in comparison with those of Fluent; a perfect qualitative agreement is achieved between the employed software. The same agreement is observed in Figure 5.11, which presents comparatively isolines (contour lines) of pressure and radial velocity component, provided by both the aforementioned solvers.

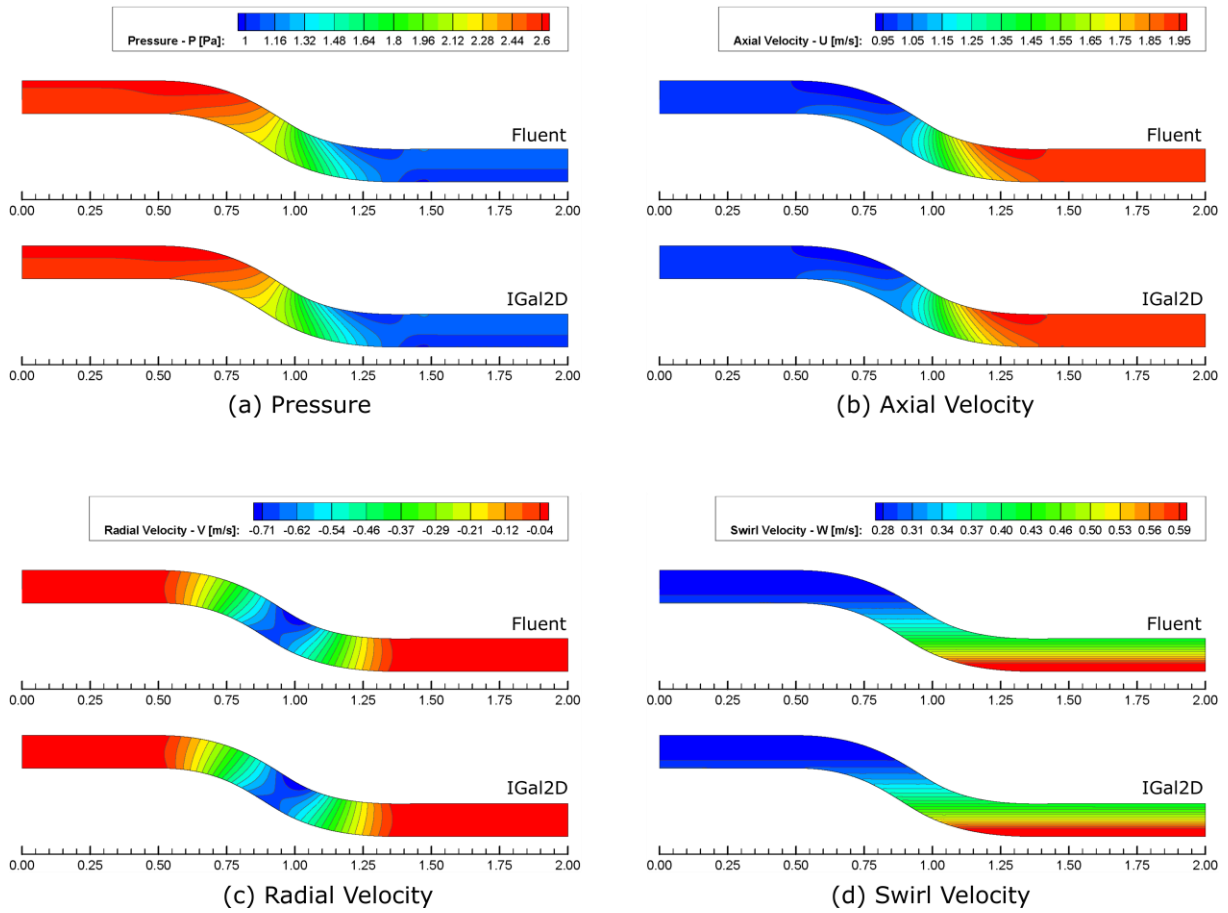


Figure 5.10: Contours of dimensional pressure and velocity components inside the S-shaped tube, derived by IGal2D and Fluent solvers.

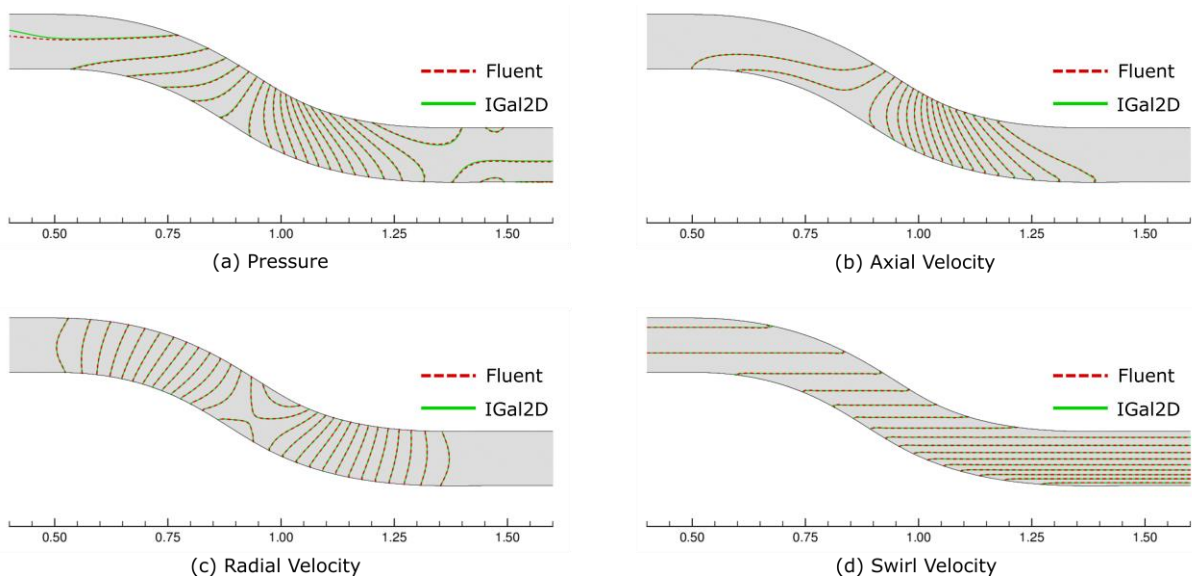


Figure 5.11: Isolines of pressure and velocity components, derived by IGal2D and Fluent solvers.

In addition to the qualitative assessment of the in-house solver, a quantitative one was completed as well, by comparing the dimensional velocity components and pressure distributions along the centerline of the S-shaped axisymmetric tube. Figure 5.12 illustrates these distributions, whereas Figure 5.13 presents the corresponding ones at three different cross-sections of the S-shaped tube; the aforementioned sections S1 ($x = 0.2 \text{ m}$), S2 ($x = 1.0 \text{ m}$), and S3 ($x = 1.8 \text{ m}$) are defined in Figure 5.8. The actually identical results confirm the equal potential of the proposed solver for such internal inviscid incompressible steady-state flows in terms of accuracy.

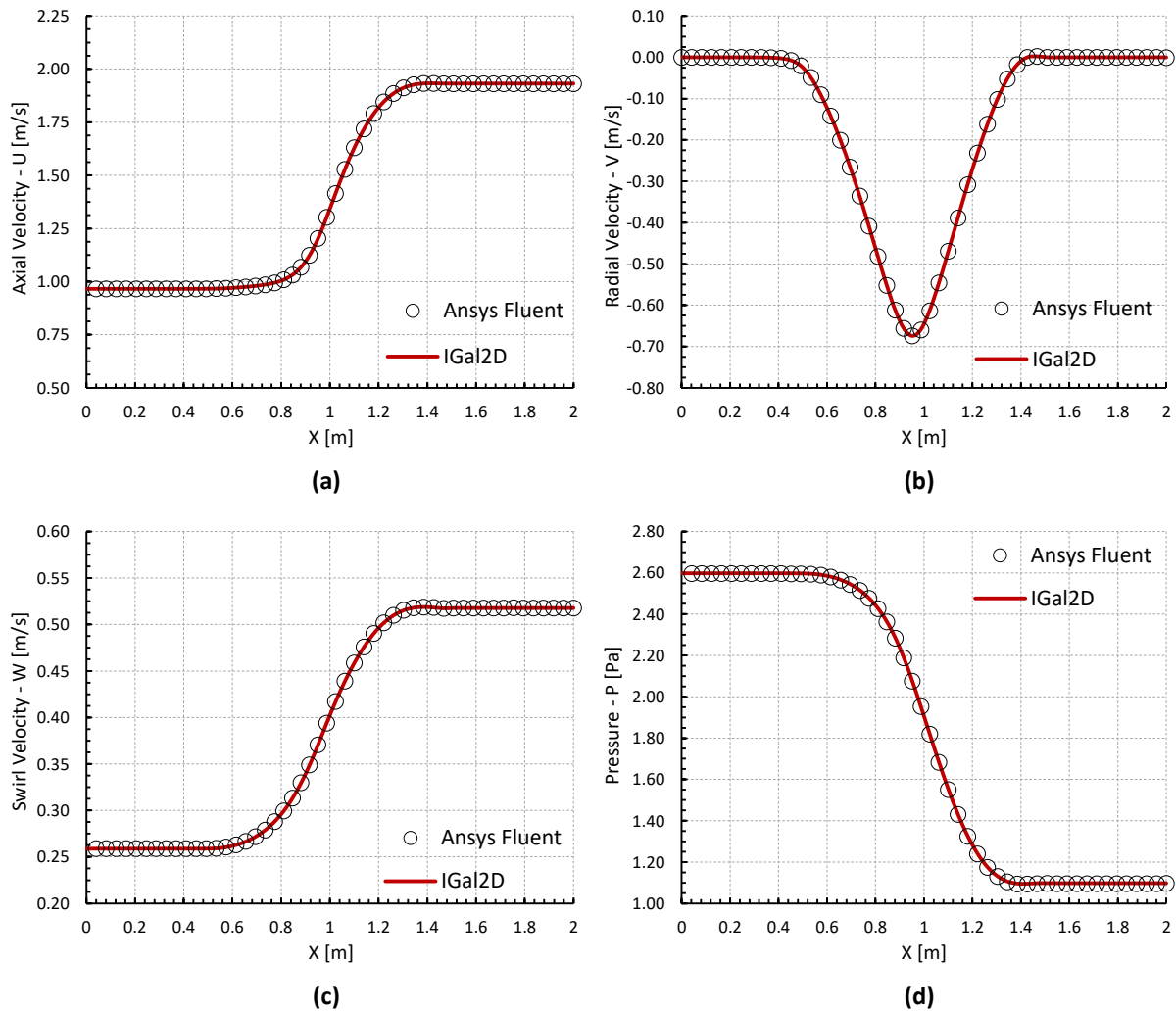


Figure 5.12: Dimensional velocity components and pressure distributions along the centerline of the S-shaped tube, obtained with IGal2D and Fluent solvers.

In addition to the accuracy of the final steady-state solution, the efficiency of the proposed solver was also assessed. In particular, the acceleration induced by the incorporated agglomeration multigrid methodology was evaluated. As mentioned above, up to five levels were utilized with the aforementioned scheme, which correspond to up to four agglomerated

resolutions, created following an isotropic fusion strategy (Lygidakis *et al.*, 2016). In case of triangular-unstructured grids, up to four levels were constructed, as highly distorted control cells were generated at coarser resolutions. Table 5.7 contains the number of DoFs at every agglomerated level ($L_1 - L_5$) for each of the utilized grids; L_1 corresponds to the initial grid. As it can be observed, at each successively coarser grid the number of included control volumes was reduced approximately by 3.5 to 4 times.

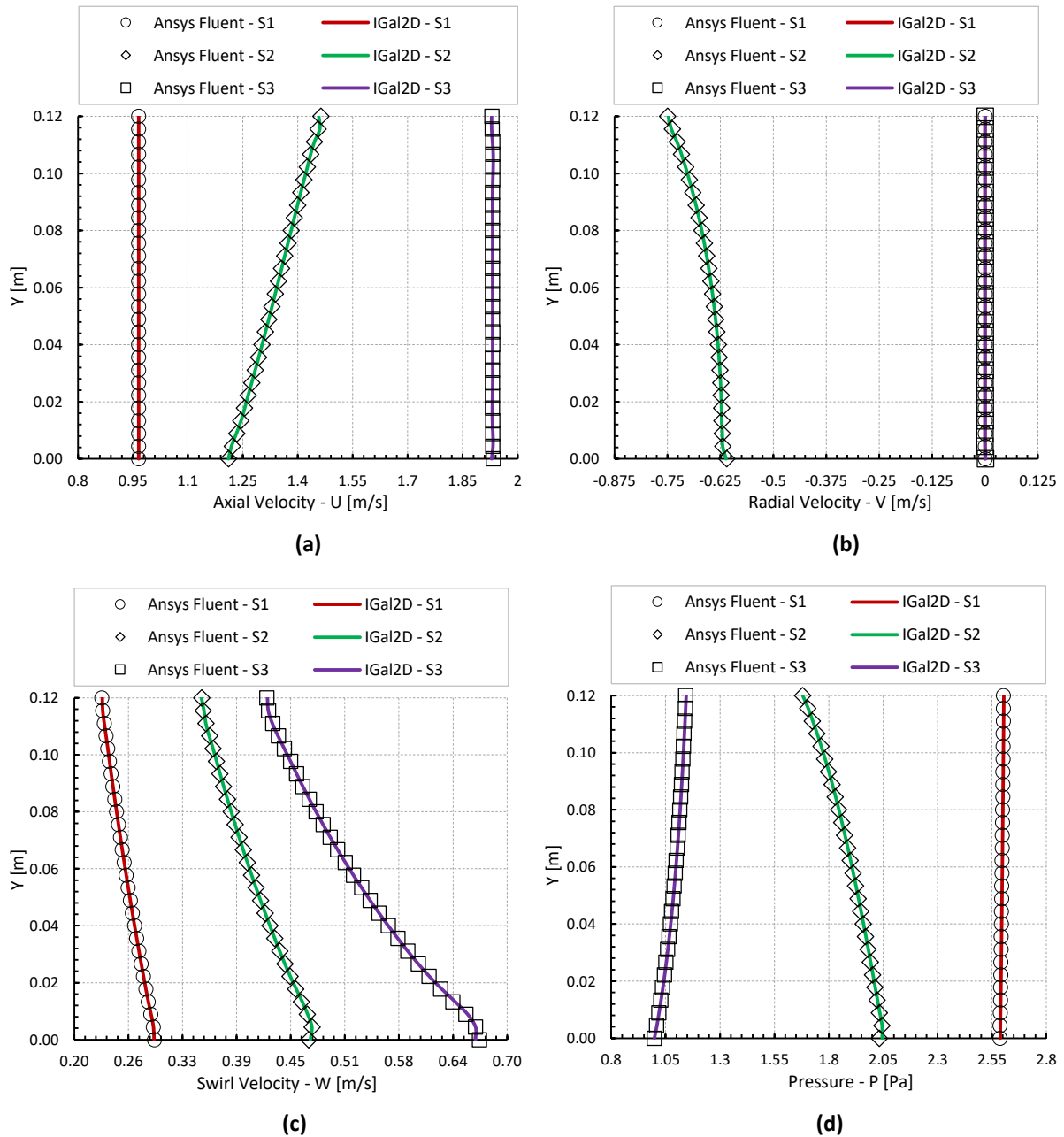


Figure 5.13: Dimensional velocity components and pressure distributions along the cross-sections S1, S2 and S3 of the S-shaped axisymmetric tube, produced by IGal2D and Fluent solvers.

	Quadrilateral			Triangular - Regular			Triangular - Unstructured		
	M1	M2	M3	M1	M2	M3	M1	M2	M3
DoFs – L_1	4,000	16,000	64,000	4,000	16,000	64,000	4,055	16,082	64,051
DoFs – L_2	1,876	7,751	31,501	1,136	4,276	16,559	1,248	4,728	18,349
DoFs – L_3	506	2,011	8,023	381	1,264	4,537	358	1,365	5,183
DoFs – L_4	160	570	2,140	129	385	1,272	98	390	1,471
DoFs – L_5	63	161	573	53	130	386	-	-	-

Table 5.7: Number of DoFs at every agglomerated level ($L_1 - L_5$) for each of the utilized grids for the S-shaped axisymmetric tube.

For all the constructed grids, the FAS approach (Lygidakis *et al.*, 2016; Nishikawa *et al.*, 2010) was implemented in a $V(1, 0)$ process using three and the maximum number of created levels. Besides multigrid simulations, single-grid ones were performed for comparison. Table 5.8 presents the number of iterations, required to decrease pressure $\log(\text{residual})$ to 10^{-13} , depending on grid-type, grid density and number of employed multigrid levels; L_1 corresponds to singlegrid, L_3 to three-level and L_{max} to five-level (four-level for triangular unstructured meshes) multigrid simulations. Regarding the single-grid simulations, only those using the coarser initial grids M1 were fully completed, *i.e.* the residual was reduced to the desired minimum value. Multigrid scheme speeded up the solution procedure more than 20 times for this grid density, whereas for denser ones the corresponding acceleration is estimated even higher, as it cannot be exactly calculated. In addition, Figure 5.14 illustrates the pressure convergence history per number of iterations for the densest triangular-unstructured grid (M3), derived by singlegrid L_1 , three-level (L_3) and four-level (L_4) multigrid runs, where a significant efficiency improvement can be visualized. Finally, the obtained results reveal crucial acceleration of the IGal2D solver with the implementation of the aforementioned multigrid scheme, independently of the employed grid type and its density.

	Quadrilateral			Triangular - Regular			Triangular - Unstructured		
	M1	M2	M3	M1	M2	M3	M1	M2	M3
Iter. – L_1	268,040	>5.0E+5	>5.0E+5	207,955	>5.0E+5	>5.0E+5	264,574	>5.0E+5	>5.0E+5
Iter. – L_3	24,485	164,185	>5.0E+5	19,659	37,292	381,611	20,422	39,396	234,868
Iter. – L_{max}	8,030	11,821	28,367	5363	9,318	16,921	9,900	18,907	36,392

Table 5.8: Number of iterations, required to decrease pressure $\log(\text{residual})$ to 10^{-13} , depending on grid-type, grid density and number of employed multigrid levels.

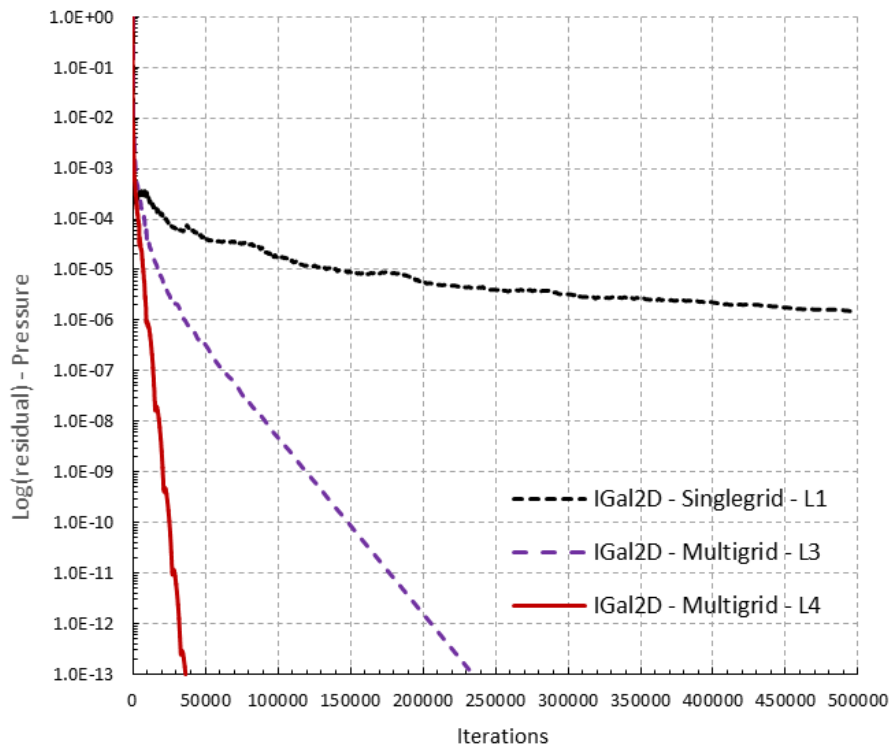


Figure 5.14: Pressure convergence history per number of iterations for the densest triangular-unstructured grid, derived by single-grid (L_1), three-level (L_3) and four-level (L_4) multigrid runs.

5.2.2 Laminar Swirling Flow inside an Axial Tube

The next test case, used for the evaluation of IGal2D, concerns viscous laminar flow in an axial tube following an experimental swirl generator device. The aforementioned test apparatus, introduced by Rocha *et al.* (2015), allows for the study of swirling flows similar to those met in industrial in-inline flow phase segregators. The geometric characteristics of the 3.0 m long and 0.05 m size (i.d.) pipe, including details of its major sections, are illustrated in Figure 5.15.

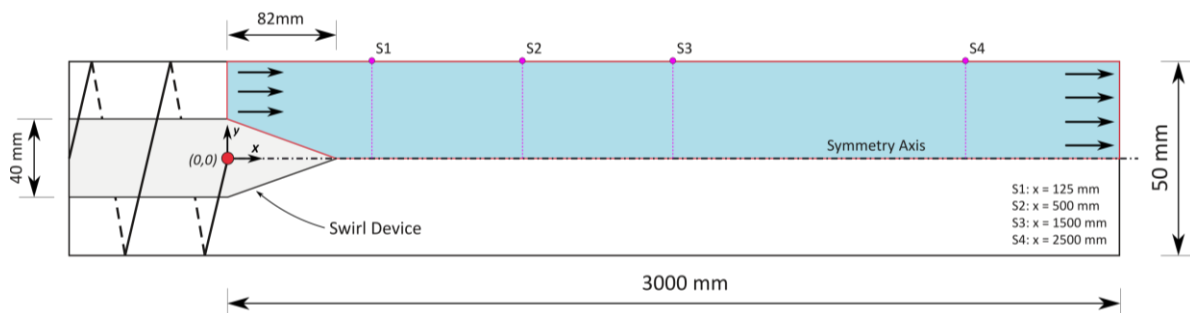


Figure 5.15: Geometric details of the axial tube.

As it can be observed, the examined flow domain (coloured in blue) includes also the conical trailing edge of the swirl generator. This conical part of 0.082 m height, base diameter 0.040 m and deflection angle $\alpha = 63.5^\circ$, has been added to reduce flow reversal in the central region (Rocha *et al.*, 2015). The respective flow domain was discretized in this work with the grid presented in Figure 5.16 (consisting of triangular elements). It is composed of 59,960 nodes and 116,844 triangular elements. In order to use it with the proposed dimensionless solver, it was non-dimensionalized with the internal diameter of the tube.

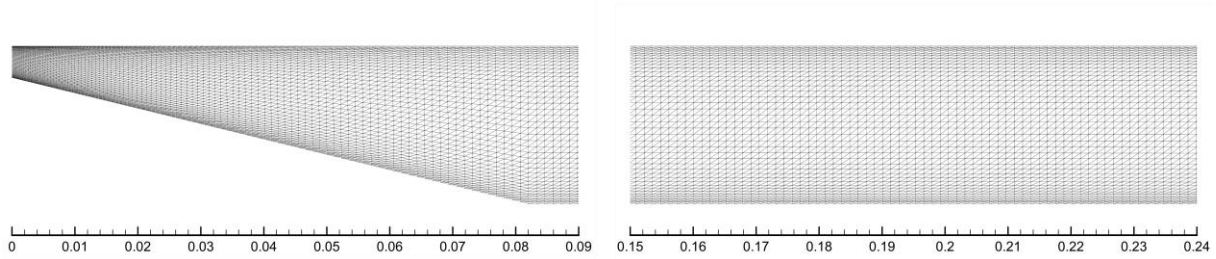


Figure 5.16: Density of the utilized grid for the axial tube.

In the reference work of Rocha *et al.* (2015) the flow inside the aforementioned geometry was studied for various volumetric rates \dot{q} , ranging from $3\text{ m}^3/\text{h}$ to $7.5\text{ m}^3/\text{h}$. However, in the current validation study a single volumetric rate of $\dot{q} = 3\text{ m}^3/\text{h}$ was examined. A uniform profile was adopted for both axial and tangential velocity over the inlet of the pipe; the corresponding values were obtained with the following expressions (Rocha *et al.*, 2015):

$$u_{in} = \dot{q}/\pi[R_o^2 - (R_o - \delta)^2], \quad (5.4)$$

$$w_{in} = u_{in} \cdot \tan(\alpha), \quad (5.5)$$

where $R_o = 0.025\text{ m}$ and $\delta = 0.005\text{ m}$. To this end, the axial and circumferential velocity components, u_{in} and w_{in} , at the inlet were computed equal to 1.178 m/s and 2.364 m/s , respectively, whereas they were re-dimensionalized with the total inflow velocity. Zero radial velocity was considered at the same boundary. At the outlet dimensionless relative static pressure was defined equal to unity; in dimensional simulations with Fluent it was correspondingly set to 0.0 Pa (relative pressure). The radial equilibrium method, without Laplacian smoothing, was applied at the outflow. Ultimately, no-slip and free-slip conditions were imposed to solid wall and symmetry axis, respectively. As far as the properties of the working fluid are concerned, its density and dynamic viscosity were set equal to $\rho = 1210\text{ kg/m}^3$ and $\mu = 0.04877\text{ kg/m/s}$ (Rocha, 2013). Taking into account the above mentioned values, the Reynolds number was computed as 3,277.6. Steady-state solution (obtained after the log(residual) of pressure was decreased more than eight orders of magnitude) was

approximated iteratively with an artificial compressibility parameter and a CFL number equal to 1.0 and 0.15, respectively. Although a relatively small CFL number was used for convergence reasons, the solution procedure was accelerated considerably with the proposed multigrid scheme. In particular, a three-level scheme was implemented, i.e. with two agglomerated coarser resolutions, derived using the incorporated isotropic fusion methodology (Lygidakis *et al.*, 2016). The convergence history per number of iterations for pressure and velocity components are illustrated in Figure 5.17.

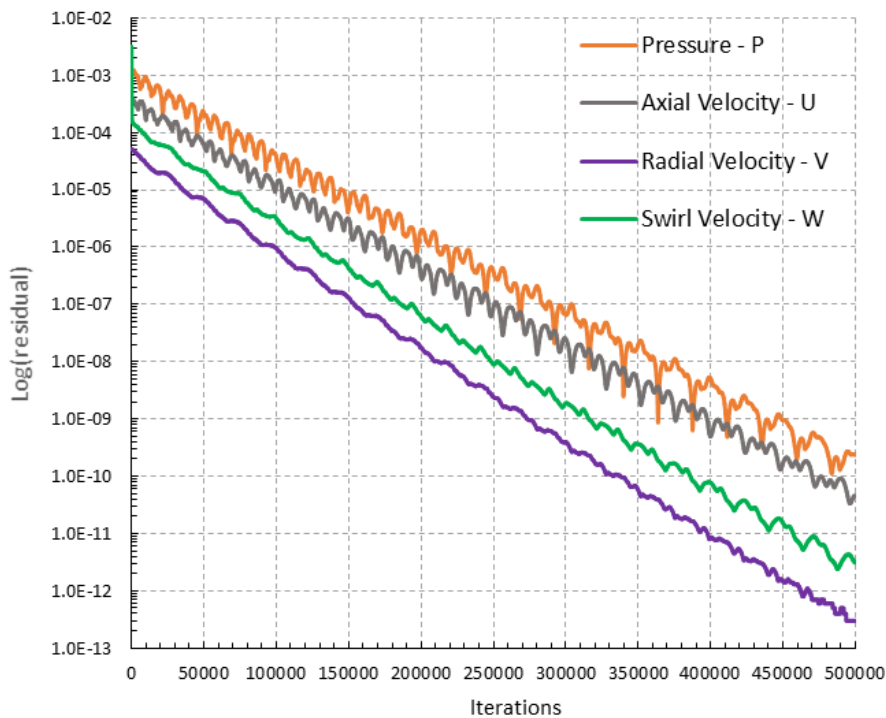


Figure 5.17: Convergence history per number of iterations for static pressure and velocity components (Laminar flow – IGal2D simulation).

Analogously to the previous inviscid test case, for this laminar case simulations were performed using both the IGal2D and the Fluent solvers, while the obtained results were compared between them, as well as with those reported by Rocha *et al.* (2015). Figure 5.18 and Figure 5.19 depict the contours of dimensional axial and swirl velocity up to $x = 1\text{ m}$, as extracted by both solvers. No qualitative difference can be identified between them. Both axial and circumferential velocities are zero on the centerline, increase with the radial coordinate and go back to zero near the solid walls due to the no-slip boundary conditions. Hence, a centrifugal flow field is generated along with the axial motion, restricting less dense fluid in the core region and consequently allowing for phase segregation in corresponding industrial applications.

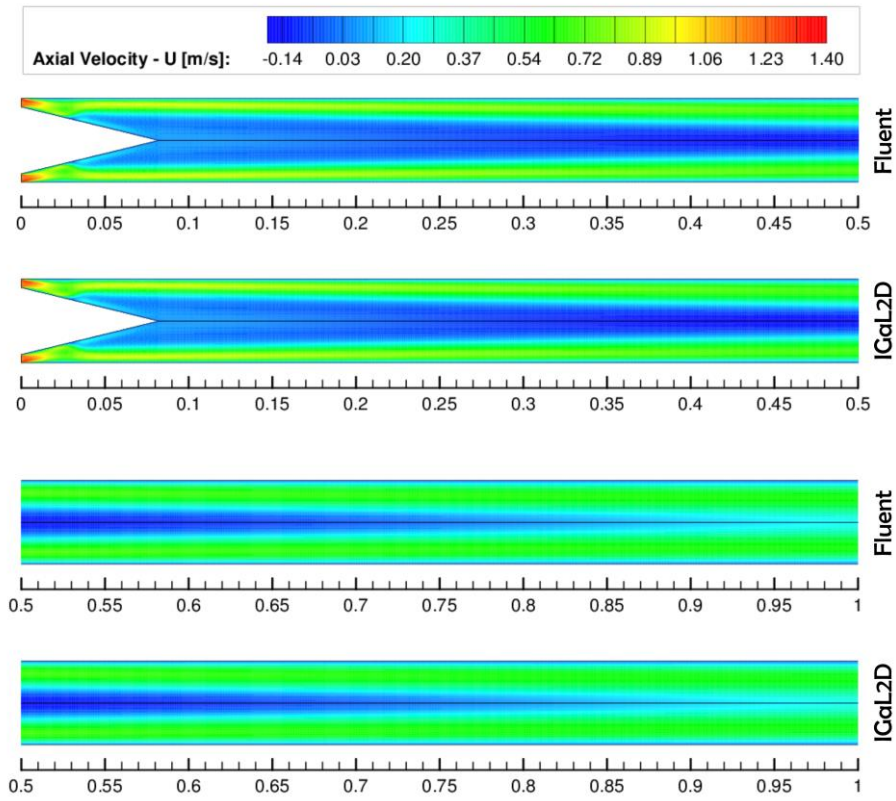


Figure 5.18: Contours of axial velocity (laminar flow – axial tube).

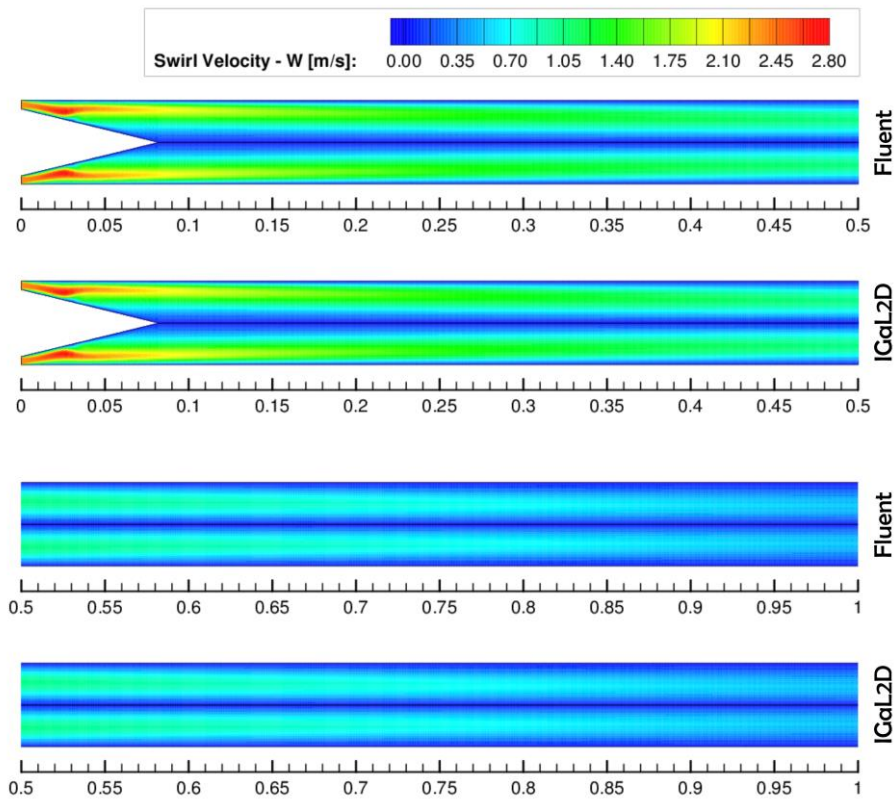


Figure 5.19: Contours of swirl velocity (laminar flow – axial tube).

Besides the previously presented qualitative assessment, a quantitative one was performed comparing initially the dimensional velocity components at four different cross-sections of the axial tube, namely S1 ($x = 0.125\text{ m}$), S2 ($x = 0.5\text{ m}$), S3 ($x = 1.5\text{ m}$) and S4 ($x = 2.5\text{ m}$), which are depicted in Figure 5.15. Figure 5.20 illustrates the aforementioned distributions, produced by IGal2D, in comparison with those derived by the Fluent solver. Axial velocity has positive and negative values; the latter are observed for both codes near the centerline region at cross-section S2, indicating that the vortex breakdown gets near the entrance and axis of symmetry. The same conclusion is drawn from the gradual dissipation of tangential component along the axial direction (from S1 to S4 cross-section) due to the viscous effects, hence the initial swirling flow approximates progressively a purely axial one. Ultimately, the actually identical results of IGal2D and Fluent, included in the following Figure 5.20, confirm the ability of the proposed CFD software to simulate accurately such internal incompressible steady-state flows.

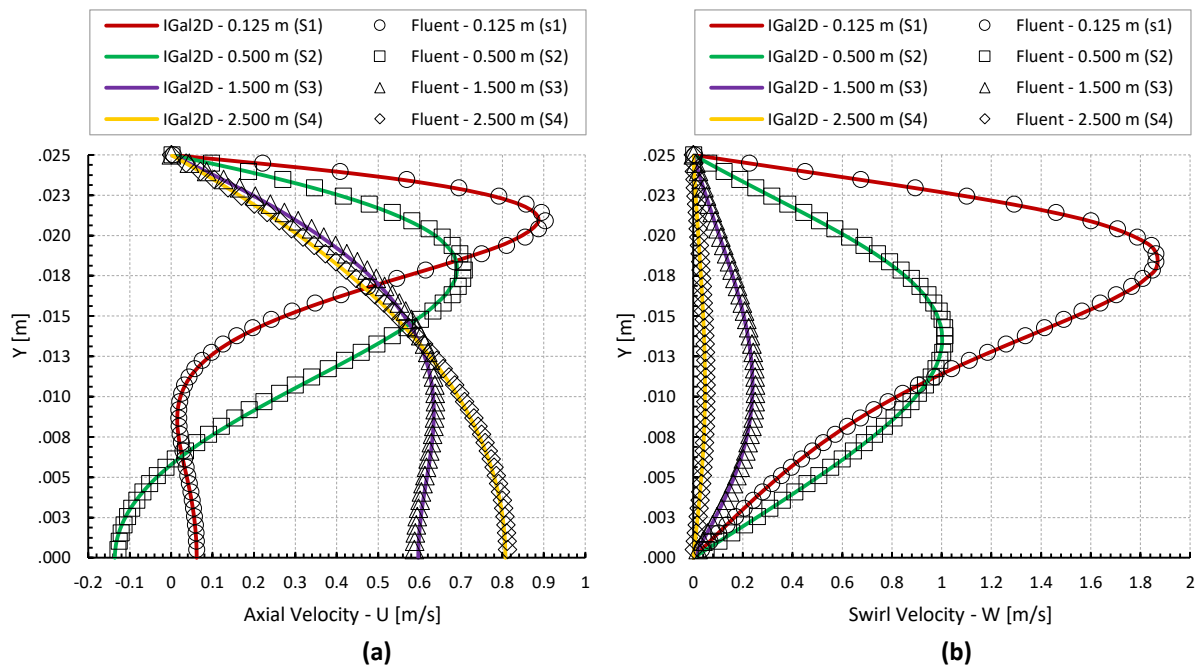


Figure 5.20: Dimensional axial and swirl velocity components' distributions along the cross-sections S1, S2, S3 and S4 of the axial tube, obtained by IGal2D and Fluent solvers.

Almost the same agreement is observed in Figure 5.21, which depicts the aforementioned distributions of axial velocity obtained with IGal2D in comparison with those reported by (Rocha *et al.*, 2015). Similarly, Figure 5.22 includes the dimensional relative pressure distributions along the centerline of the axial tube, produced by both the employed solvers. In addition, they are presented comparatively with this of the reference study (Rocha *et al.*, 2015). As expected (due to the previous matching velocity results), an almost perfect agreement is succeeded. Independently of the utilized solver, an adverse pressure gradient is obtained due to the pressure raising along the centerline, which consequently derives the above mentioned

negative axial velocity values. Finally, Table 5.9 contains the values of pressure drop between solid wall points at inlet and outlet of the axial tube under examination ($y = 0.025 \text{ m}$, $x_{inlet} = 0 \text{ m}$ and $x_{outlet} = 3 \text{ m}$), derived by both the utilized solvers, as well as by Rocha *et al.* (2015) (measured and computed). The value extracted by IGal2D compares close with the experimental and numerical ones of the reference work (Rocha *et al.*, 2015); regarding the measured one, it is approximately over-predicted by 4 %. Its accurate prediction is of crucial importance, especially in petroleum industrial lines, as excessive frictional pressure drops at high flow rates can lead to uneconomic operations (Rocha *et al.*, 2015).

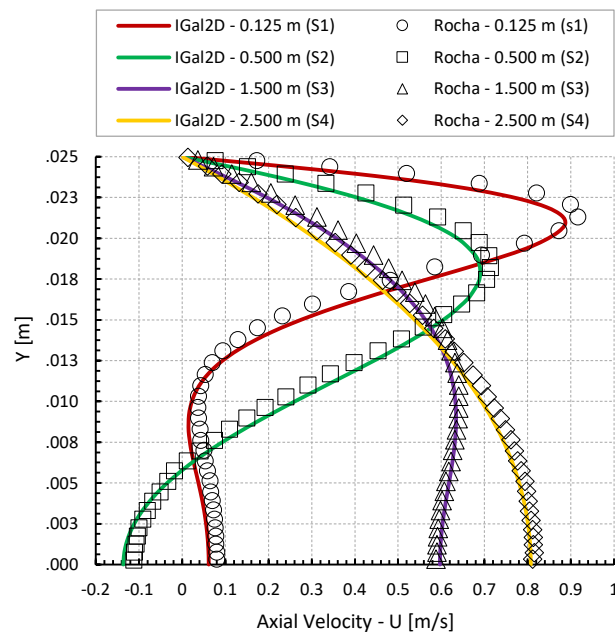


Figure 5.21: Dimensional axial velocity distributions along the cross-sections S1, S2, S3 and S4 of the axial tube, obtained by IGal2D, in comparison to those reported by Rocha *et al.* (2015).

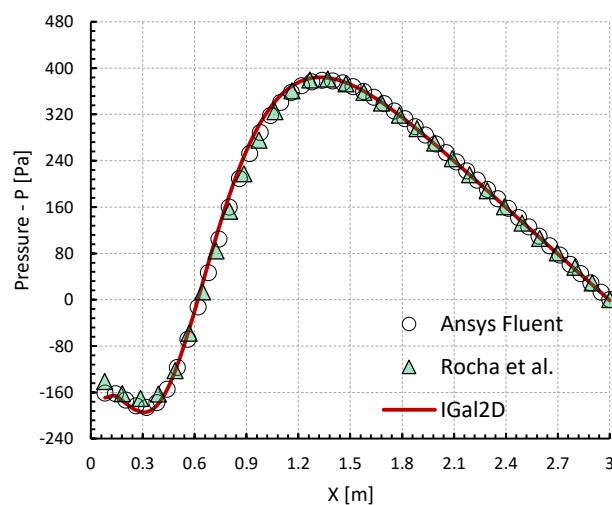


Figure 5.22: Dimensional relative pressure distribution along the centerline of the axial tube.

	IGal2D	Ansys Fluent	Rocha – Numerical	Rocha – Experimental
Pressure Drop	4320.28 Pa	4319.13 Pa	4325.51 Pa	4193.54 Pa

Table 5.9: Pressure drop between solid walls points at inlet and outlet positions of the axial tube.

5.2.3 Turbulent Swirling Flow inside a Conical Diffuser

The current benchmark case concerns the turbulent swirling flow inside a conical diffuser that resembles those usually employed in shrouded or diffuser augmented wind turbine applications, in order to recover pressure and increase turbine efficiency. Optimizing the performance of a diffuser is revealed to be of dramatically crucial importance for the overall efficiency of diffuser augmented wind turbines and in general, of analogous industrial confined geometries. This is the main motivation to study this test case, considering our objective to develop a numerical software platform for the design and optimization of shrouded wind turbines.

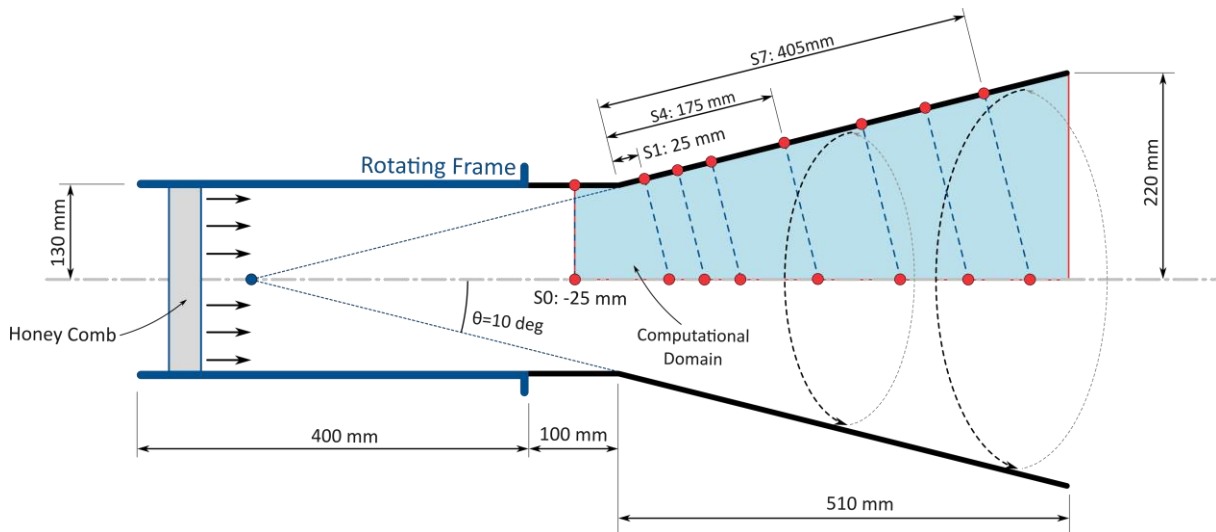


Figure 5.23: Geometric details of the conical diffuser (Leloudas *et al.*, 2021).

To this end, the diffuser examined in this work is the ERCOFTAC (European Research Community on Flow, Turbulence and Combustion) swirling conical diffuser, which has been extensively studied in the literature (Armfield *et al.*, 1990; Bounous, 2008; Cho and Fletcher, 1991; Clausen *et al.*, 1993; From *et al.*, 2017; Rodi *et al.*, 1995). The geometric characteristics of the 0.51 m long diffuser – also reported by Clausen *et al.* (1993) – are provided in Figure 5.23. The diffuser has a half-cone angle $\theta = 10^\circ$ and an area ratio of 2.84; the inlet radius is equal to 0.13 m, while the exit one is equal to 0.22 m. A swirl generator with a rotating velocity of

550 rpm (composed of a straight pipe with an internal honeycomb) has been placed upstream of the diffuser (see Figure 5.23) to produce a solid body rotation type swirl. The computational domain (coloured in blue) along with details for its major sections are illustrated in the same figure. For its representation a quadrilateral grid was utilized, consisted of 15,720 nodes and 15,470 quadrilateral elements. Its density is depicted in Figure 5.24; in order to use it with the proposed dimensionless solver, it was non-dimensionalized with the diameter at diffuser's intake.

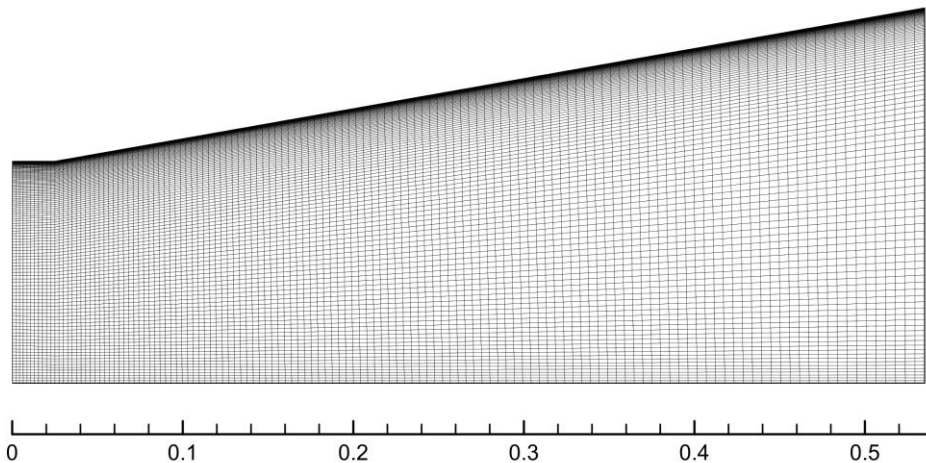


Figure 5.24: Density of the utilized grid for the conical diffuser (Leloudas *et al.*, 2021).

Similarly to the previous test cases, simulations were performed by both the IGal2D and the Fluent solver, whereas their results were compared between them, as well as with the available experimental ones (Clausen *et al.*, 1993). Axial and swirl velocities at the inlet boundary were imposed by interpolating the available experimental measurements (Clausen *et al.*, 1993), presented in Figure 5.25. In addition, the experimentally obtained Reynolds stresses ($\overline{u^2}, \overline{v^2}, \overline{w^2}$) were used to calculate the distribution of turbulent kinetic energy $k = \frac{1}{2}(\overline{u^2} + \overline{v^2} + \overline{w^2})$ over the inlet (S0), and therefore, to define the inflow turbulence magnitude. The particular distribution of turbulent kinetic energy results in an average value of inflow turbulence intensity \bar{T}_u of approximately 4%, which is similar to the value of turbulence intensity ($\bar{T}_u = 5\%$) adopted during the numerical study of From *et al.* (2017). The experimentally obtained values for Reynolds stresses can be also found in the study of Clausen *et al.* (1993) and Digital ERCOFTAC Database. The small peak of axial velocity component next to the boundary layer region is caused by the proximity to the diffuser inlet (Clausen *et al.*, 1993). Zero radial velocity component was considered at the inlet. At the outlet relative static pressure was defined equal to zero for both Fluent and IGal2D solvers (in dimensional and non-dimensional formulation, respectively). Moreover, at the outlet radial equilibrium was

applied, while no-slip and free-slip conditions were employed to solid wall and symmetry axis, respectively. Regarding the working fluid, its density and dynamic viscosity were set equal to 1.225 kg/m^3 and $1.8375 \cdot 10^{-5} \text{ kg/m/s}$. Based on the above mentioned values the Reynolds number was calculated as 206,153.581. A steady-state solution was obtained after the log(residual) of pressure was decreased more than five orders of magnitude. An artificial compressibility parameter and a CFL number equal to 1.0 and 0.2, respectively, were used. For the acceleration of the solution procedure a three-level multigrid scheme was implemented; two agglomerated coarser resolutions were constructed following the incorporated isotropic fusion procedure (Lygidakis *et al.*, 2016).

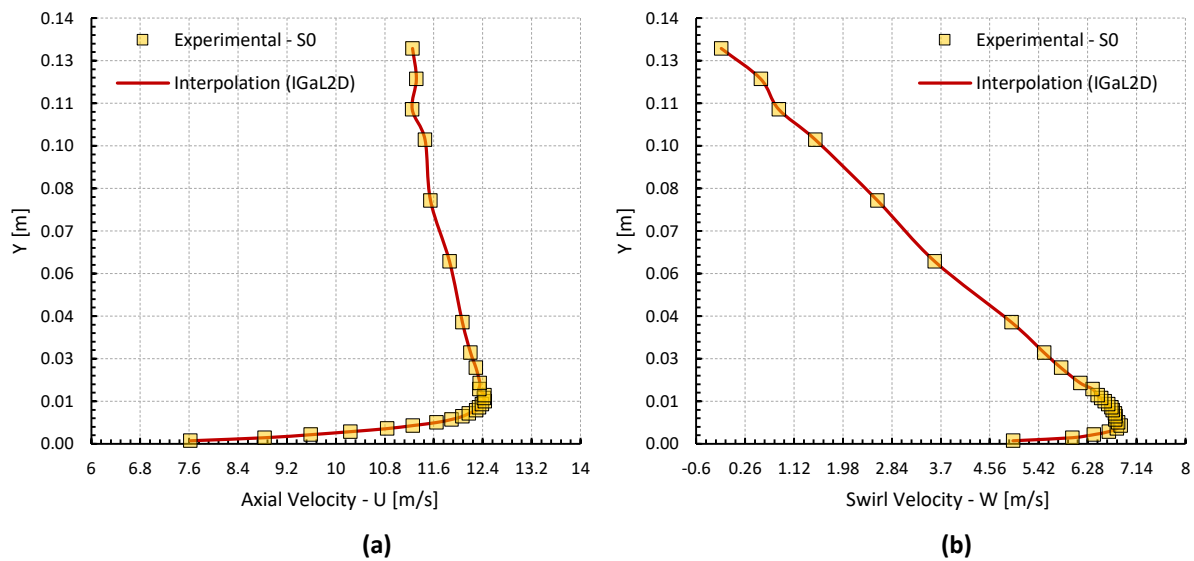


Figure 5.25: Experimentally obtained (Clausen *et al.*, 1993) distributions of axial and swirl velocity at the diffuser inlet (S0) along with the interpolated profiles of the corresponding velocity components, used for the numerical simulations.

In Figure 5.26 to Figure 5.28 the numerical results, obtained by IGal2D and ANSYS Fluent solvers (both using the $k - \omega$ SST turbulence model), are compared against the experimental measurements provided by Clausen *et al.* (1993), for reference sections S1, S4 and S7 (which are shown in Figure 5.23 and cover the largest part of the diffuser). The aforementioned comparisons are made in terms of axial and swirling velocity components. An almost perfect agreement between IGal2D and Fluent solvers can be observed for both velocity components at each one of the examined sections. However, some non-trivial discrepancies between the numerical and experimental data are identified, especially when moving towards the exit of the diffuser. In particular, IGal2D and Fluent solvers were found to over-predict the axial velocity component for each one of the examined sections. This over-prediction tends to increase as the symmetry axis is approached, hence failure to capture the actual velocity deficit

within the core diffuser region is indicated. Yet both near-wall intensity and the peak position of axial velocity have been reasonably predicted, especially at sections S1 and S4. At section S7 a relatively small under-estimation of axial velocity at the solid wall area is also noticed. In contrast to axial velocity component, a much better numerical computation of swirl velocity for every reference section was achieved, though the peak values at sections S1 and S7 have been slightly under-estimated. Nevertheless, an accurate prediction of the experimentally obtained pressure coefficient distribution over the diffuser wall (pressure recovery) was achieved by IGal2D solver as shown in Figure 5.29 – an anticipated result due to the aforementioned sufficiently matching velocity distributions. The axial pressure gradient gets high values near the entrance, while it decreases rapidly along the axial direction.

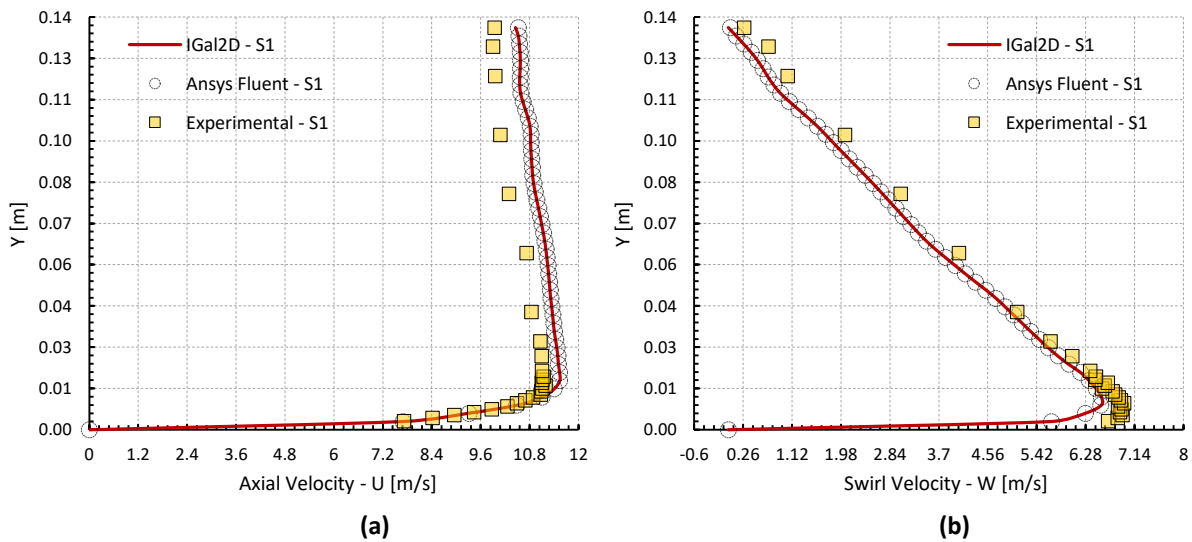


Figure 5.26: Distributions of axial and swirl velocity at cross-section S1 (conical diffuser).

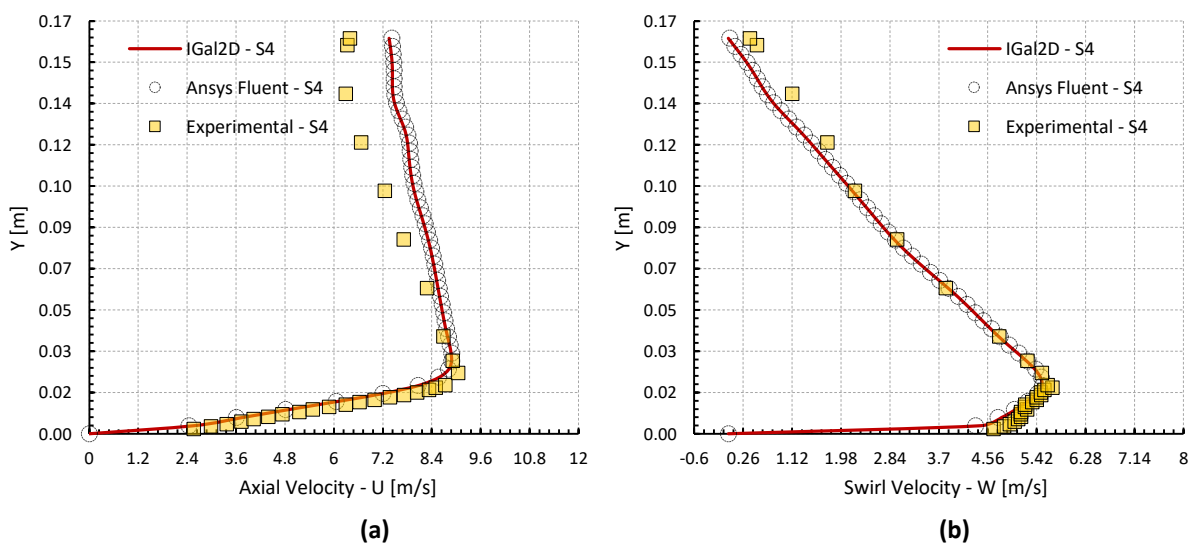


Figure 5.27: Distributions of axial and swirl velocity at cross-section S4 (conical diffuser).

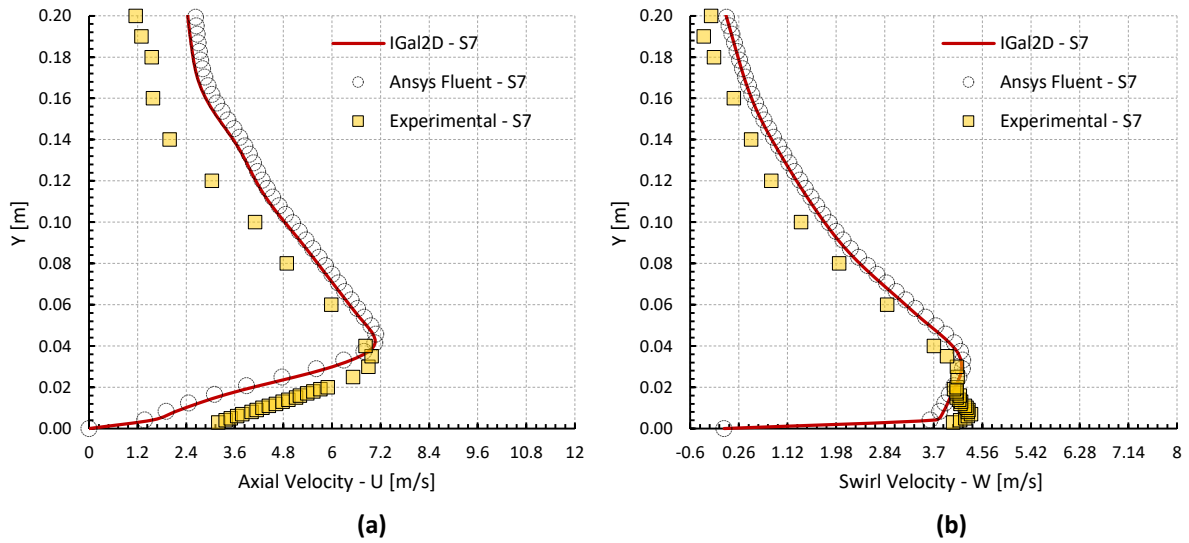


Figure 5.28: Distributions of axial and swirl velocity at cross-section S7 (conical diffuser).

Conclusively, despite some notable discrepancies between the numerical prediction of IGal2D and/or Fluent solvers and the experimental results, according to previous numerical studies (Rodi *et al.*, 1995) on the same benchmark test case, as well as to the authors' perspective, such discrepancies are almost entirely attributed to the inability of $k - \omega$ SST model to predict accurately turbulent kinetic energy k in such swirling flows along with the sensitivity of velocity components upon k , which increases as the diffuser exit is approached.

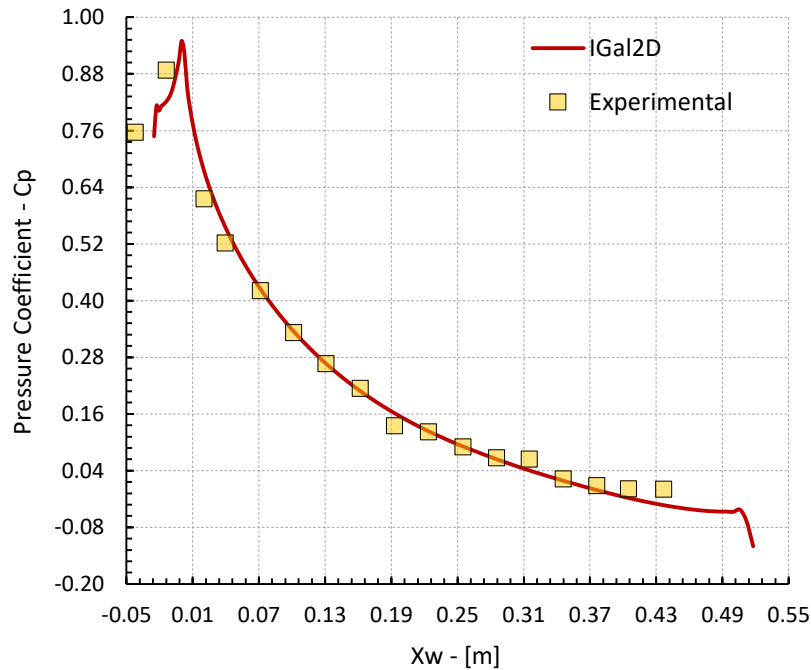


Figure 5.29: Distributions of pressure coefficient on the wall (conical diffuser).

A similar behaviour can be found in the literature for the standard $k - \varepsilon$ turbulence model (Rodi *et al.*, 1995), which provides globally better k results, compared to the $k - \omega$ one (Rodi *et al.*, 1995). Miscalculation of k is enlarged near the diffuser corner, due to the adverse pressure gradient and curvature effects, as well as with the implementation of low Reynolds approach instead of wall functions (Rodi *et al.*, 1995). Therefore, this calls for the incorporation of more advanced turbulent models within the current solver. Such an example could be the BSL_{k ω} EARSM model, which – according to the study of From *et al.* (2017) – proved capable of predicting the flow characteristics throughout the entire diffuser with high accuracy.

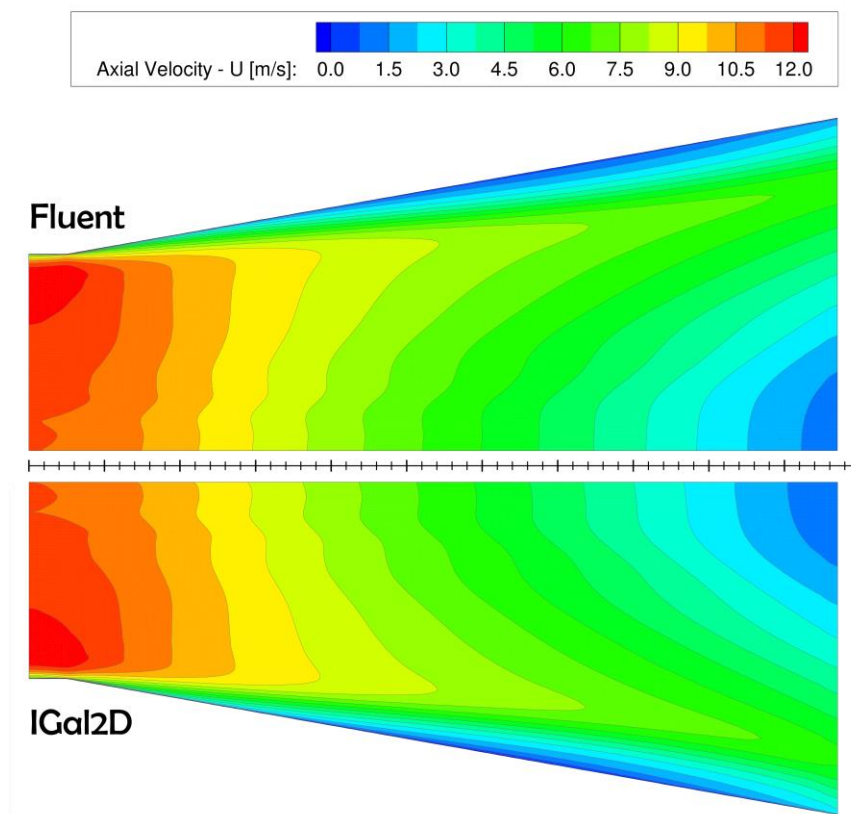


Figure 5.30: Turbulent flow inside the conical diffuser. Comparison of axial velocity contours.

Finally, Figure 5.30 and Figure 5.31 illustrate the axial and tangential velocity contours, while Figure 5.32 illustrates the static pressure contours, as they obtained from IGal2D and Fluent solvers. These comparisons confirm the good agreement between the two solvers, when the same turbulence model is employed. Both numerical codes predict reasonably the total velocity reduction, associated with constant mass flow, as well as the decrease of the centerline axial velocity and the increase of the near-wall one, caused by the tangential velocity component.

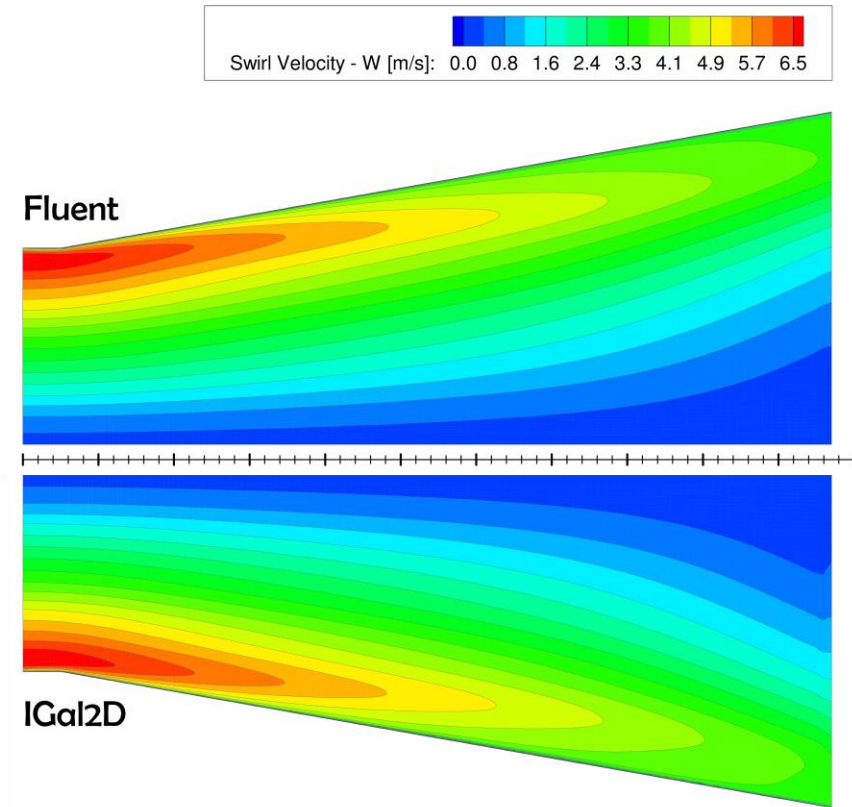


Figure 5.31: Turbulent flow inside the conical diffuser. Comparison of swirl velocity contours.

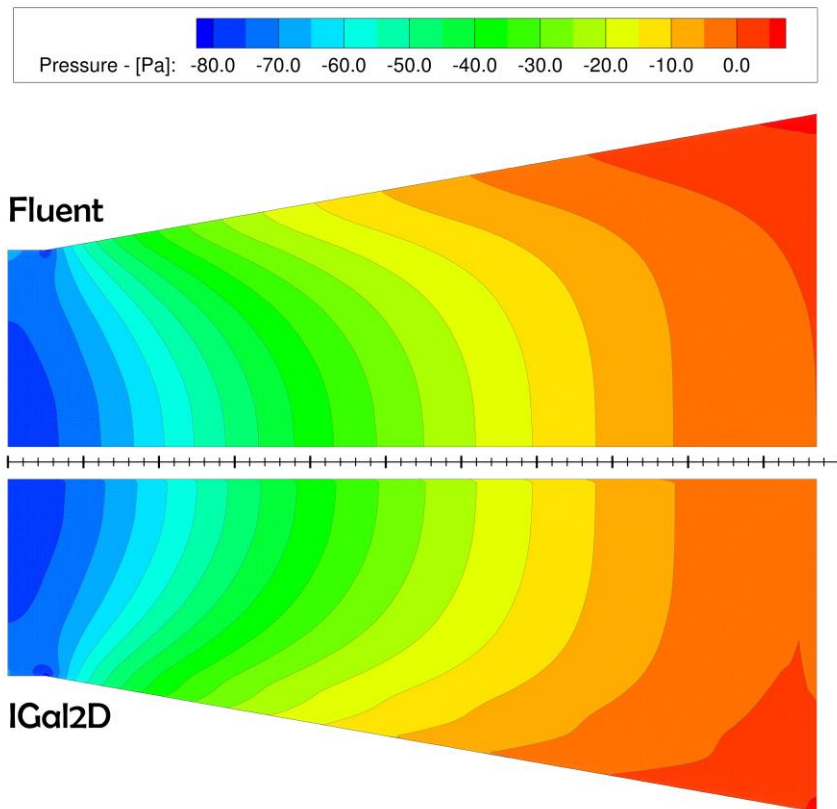


Figure 5.32: Turbulent flow inside the conical diffuser. Comparison of pressure contours.

Chapter 6

The RG15 Low-Reynolds Airfoil Family

This chapter features a new low Reynolds number airfoil family for the entire blade span of small horizontal-axis wind turbines, aiming to reduce the effects related to laminar separation, improve startup response and meet acceptable levels of structural integrity. The proposed RG15 low Reynolds airfoil family consists of six airfoil profiles of varying relative thickness, which were designed by increasing the thickness distribution of RG15 airfoil up to 50% and adopting a rounded trailing edge with a diameter equal to 1% of the chord length.

6.1 Aerodynamics of Small Wind Turbine Blades

On account of global efforts to reduce greenhouse gases emissions and combat climate change, small-scale wind energy conversion systems have recently attracted renewed attention from the international engineering community, since they represent a promising solution for sustainable energy production in site-specific cases. In contrast to their larger counterparts, small wind turbines provide a considerably higher level of flexibility, both in terms of required space and wind speed conditions (Singh *et al.*, 2012). Therefore, they can be integrated within a much broader spectrum of residential, rural and remote areas for either on-grid or off-grid power generation – usually directly where the power is required, rather than where the wind is most favourable. Consequently, they could enable significant opportunities for more geographic dispersion of wind technology applications (Yang *et al.*, 2019), growth in distributed energy deployments, and further expansion of renewable energy utilization on a global scale.

Small horizontal-axis wind turbines, which according to the standards issued by the International Electrotechnical Commission (IEC, 2013) are characterized by a rotor swept area of less than 200 m^2 , rely on the same aerodynamic principles governing the operation of larger HAWT systems. However, the chord Reynolds numbers (Re) prevailing along the entire blade span of the former applications are considerably lower – generally below 500,000 – as a consequence of the smaller blade radius (Shah *et al.*, 2012). One of the major aspects of high Reynolds number flows over airfoils is that the transition from laminar to turbulent flow inside the velocity boundary layer is realized earlier than laminar separation. Eventually, this early transition prevents the appearance of undesirable aerodynamic effects related to the latter phenomenon (Giguère and Selig, 1997), since a turbulent boundary layer is capable of withstanding an adverse pressure gradient (that is an increase of static pressure in the

direction of the flow) better than an equivalent laminar one. On the contrary, at low Reynolds number regimes – typically defined by a chord Reynolds number lower than approximately 500,000 – the boundary layer is predominantly laminar and therefore, relatively fragile (Shah *et al.*, 2012). In that case, the existence of a large adverse pressure gradient may force the flow to detach prematurely from the surface of the airfoil, that is, prior to the development of a fully turbulent flow. Even though the resultant free shear layer (detached boundary layer) remains laminar shortly after the separation point, it eventually transits to the turbulent state due to the intensification of the velocity disturbances in the flow (Alam and Sandham, 2000) (separation-induced transition). From that point on, two distinct flow regimes may result; the so-called subcritical and supercritical flow regimes (Mulleners *et al.*, 2008), which are represented in Figure 6.1 and Figure 6.2.

In a supercritical flow, the detached (now turbulent) shear layer does reattach to the surface of the airfoil, causing the formation of a laminar separation bubble, the size and chordwise location of which are functions of the airfoil profile, Reynolds number, turbulence intensity (T_u) and angle of attack (α) (Swift, 2009). Typically, a separation bubble moves towards the leading edge as the angle of attack increases (Giguère and Selig, 1997). In terms of size, laminar separation bubbles can be roughly classified as either short or long ones, depending on their chordwise extent (L_{sb}) and consequent effects on the pressure and velocity distributions about the airfoil (Tani, 1961). A short separation bubble encompasses a chordwise extent ranging up to approximately one percent; therefore, it does not influence the pressure distribution around the airfoil to a large degree. However, a long separation bubble (usually produced by the burst of a short one, because of either the reduction in Reynolds number or the increase in angle of attack) may cover a significantly larger percent of the airfoil chord, affecting severely the pressure distribution and the aerodynamic forces developed on the airfoil (Choudhry *et al.*, 2015).

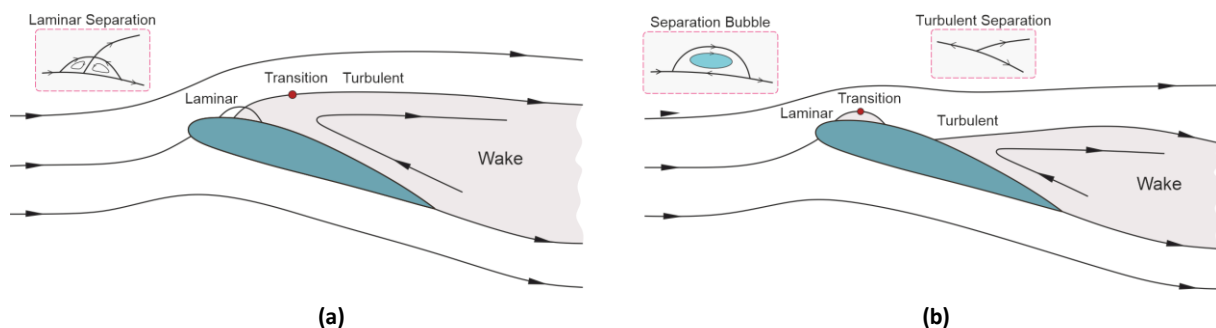


Figure 6.1: Schematic representation of laminar flow separation. (a) Subcritical flow regime. (b) Supercritical flow regime (Leloudas *et al.*, 2020b).

Although the existence of a laminar separation bubble near the leading edge at high angles of attack may increase the apparent camber of the airfoil and improve the lift (L) generation capacity (Hansen *et al.*, 2014), it ultimately thickens (locally) the velocity boundary layer on the suction side, increasing considerably the drag coefficient (C_D) as well. In addition to that, the presence of laminar separation bubble is also associated with a turbulent flow separation near the trailing edge of the airfoil, as exemplified in Figure 6.2a and Figure 6.2b; this characteristic phenomenon of the supercritical flow regime is known as trailing edge stall (Mulleners *et al.*, 2008). Besides, the potential premature burst of a laminar separation bubble could cause an even larger growth of the drag coefficient, which is accompanied by a sudden and severe loss of the generated lift (Hansen *et al.*, 2014). Now, in contrast to the supercritical regime, if the turbulent transition takes place far away from the surface of the airfoil, there is a possibility that the turbulent shear layer may not be able to reattach to the airfoil surface, creating an open separation area (subcritical flow) instead of a separation bubble. In that case, a thicker and extremely unstable wake region is produced, as shown in Figure 6.2c, resulting in much higher drag (D) levels and further reduction in the aerodynamic performance of the airfoil, compared to the supercritical flow regime. However, such an unattached free shear layer (open separation area) may also be produced by the bursting of a laminar separation bubble.

Therefore, to optimize the aerodynamic performance of small wind turbine blades, operating at low Reynolds numbers, the effects related to laminar separation have to be minimized. One of the available methods to reduce or even eliminate bubble drag (that is drag induced by a laminar separation bubble) – as well as to delay the possible chances of separation at higher angles of attack – is related to the promotion of early transition on the upper surface (suction side) of the airfoil, through the installation of a mechanical turbulator or trip (Singh *et al.*, 2012). However, the particular technique, which is the only one applicable to existing airfoils (Giguère and Selig, 1997), requires adequate experience in selecting the proper location and thickness of the trip, so as to maximize the reduction in bubble drag while minimizing the drag produced by the trip (Lyon *et al.*, 1997). On the other hand, according to Giguère and Selig (1997), the suppression of laminar separation effects could also be achieved by means of specially designed airfoils with a very gradual upper-surface pressure recovery (bubble ramp), which can decrease significantly the additional drag induced by separation bubbles. Currently, the majority of low Reynolds number airfoils are designed based on the latter technique, providing reduced amounts of drag and higher maximum lift-to-drag ratios (also termed as glide ratios), as compared with those of traditional airfoils that have been mainly designed for high Reynolds numbers and, therefore, they usually suffer from severe laminar separation effects when operating at low Reynolds number regimes.

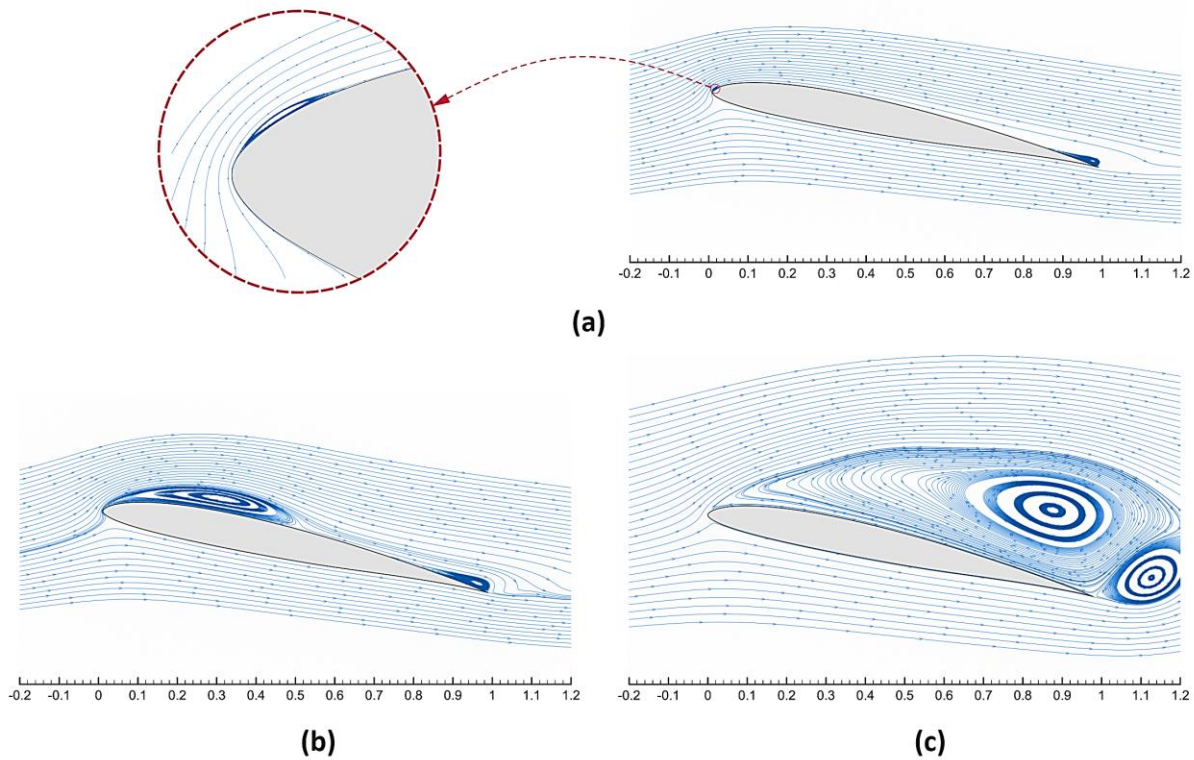


Figure 6.2: Velocity streamlines for different flow regimes. (a) Short separation bubble (supercritical regime). (b) Long separation bubble (supercritical regime). (c) Unattached shear layer (subcritical regime) (Leloudas *et al.*, 2020b).

6.2 Review of Small Wind Turbine Airfoils

The first airfoils for small wind turbines were introduced by the National Renewable Energy Laboratory (NREL); the S822 and S823 airfoils (Somers, 2005) were particularly designed for small stall-regulated wind turbines with a rotor diameter between 3 and 10 meters, based on the following criteria: restrained maximum lift, insensitivity to roughness and low profile drag. Nevertheless, the first systematic attempt to establish a wide database of low Reynolds number airfoils for small wind turbine blades was made by Giguere and Selig (1997). In that study, the aerodynamic performance of 15 already existing low Reynolds number airfoils (most of them had been originally designed for small unmanned aerial vehicles) was thoroughly evaluated, based on the results of a large-scale testing program undertaken in the University of Illinois at Urbana-Champaign (UIUC) low-turbulence subsonic wind tunnel (Broeren *et al.*, 1995). Besides, Giguere and Selig (1997) provided useful guidelines to facilitate the airfoil selection process for each one of the different operational modes of small wind turbines (variable-speed, variable-pitch, stall regulated). Later on, Giguere and Selig (1998) introduced the SG604x airfoil family, which was designed by taking into consideration the special requirements of small variable-speed wind turbines with a rated

capacity up to 5 kW. The SG604x airfoil family was formed by three primary airfoils (SG6041, SG6042 and SG6043) with a maximum relative thickness of 10% and by one root airfoil (SG6040) with a maximum relative thickness of 16%, to accommodate possible large root bending moment and large blade stiffness requirements. According to both experimental and numerical data reported in (Giguere and Selig, 1998), the SG604x family could achieve high lift-to-drag ratios (L/D) over a broad range of lift conditions. Moreover, Selig and McGranahan (2004) conducted detailed wind tunnel experiments in order to examine the performance characteristics of six low Reynolds number airfoils (E387, FX 63-137, S822, S834, SD2030 and SH3055) for small wind turbines, at various Reynolds numbers up to 500,000.

Significant research on small wind turbine airfoils was also made by Ram *et al.* (2013), who employed a Genetic Algorithm to design a low Reynolds number airfoil with high roughness insensitivity and maximum relative thickness of 10%. The resultant USPT2 airfoil was evaluated both numerically and experimentally. According to the corresponding results reported in (Ram *et al.*, 2013), USPT2 seemed to overperform the SG6043 airfoil in terms of lift-to-drag ratio for angles of attack greater than 10 degrees, while a smoother stall region, as compared to that of similar airfoils, was also observed. On the other hand, Henriques *et al.* (2009) applied a pressure-load prescription method to design a new airfoil (T.Urban 10/193) with high lift performance (C_L value around 2) for urban wind turbines. In comparison with conventional blade section designs, the T.Urban 10/193 airfoil demonstrated increased maximum lift, reduced leading edge suction peak and controlled soft-stall behavior, due to a reduction of the adverse pressure gradient on the suction side (Henriques *et al.*, 2009). More recent research on small wind turbine airfoil design can also be found in the studies of Singh *et al.* (2012), Shah *et al.* (2012), Islam *et al.* (2008), Marnett *et al.* (2010) and Shen *et al.* (2016). In particular, the study of Singh *et al.* (2012) was focused on the design of a new low Reynolds number airfoil, aiming to improve the startup behavior and low wind speed performance of small wind turbines. Compared with other low Reynolds number airfoils suited for small wind turbines, the proposed AF300 airfoil showed good aerodynamic performance, attaining the highest combinations of optimum C_L and lift-to-drag ratios. Moreover, Singh *et al.* (2012) highlighted that the flatback trailing edge of the AF300 airfoil had improved the aerodynamic properties of AF300 by delaying flow separation and increasing C_L . Finally, they noted that the structural strength added by the thick trailing edge would require lighter blade materials and decrease the rotor inertia. Therefore, the startup could be significantly improved and the rotor could operate at lower cut-in wind speeds (Singh *et al.*, 2012).

6.3 Motivation and Scope

Apart from the suppression of laminar separation effects, the achievement of a good starting behavior (startup response) and low cut-in speeds can also enhance significantly the overall performance of small wind turbines intended for low/moderate wind speeds and fluctuating regimes. According to Sathyajith and Philip (2011), a good startup can be succeeded by selecting root airfoils with high maximum lift coefficients (C_L) and high lift-to-drag ratios, since most of the starting torque is caused by the blade root, whereas the tip region generates most of the power producing torque (Wright and Wood, 2004). The RG15 is one of the attractive low Reynolds number airfoils – both in terms of aerodynamic performance and low Reynolds behavior – that were examined during the testing program at UIUC low-turbulence subsonic wind tunnel (Broeren *et al.*, 1995). However, the particular airfoil is rather unsuitable for the root region of the blade, because of its limited structural integrity (limited rigidity and stiffness), stemming from the small value of the thickness-to-chord ratio (t/c) and cross-sectional area (A). Against this background, this work presents the development and application of a methodology for the design of a low Reynolds number airfoil family, suitable for the entire blade span of small wind turbines, through the proper thickening of the RG15 airfoil. Moreover, since the original RG15 airfoil geometry has a knife-sharp trailing edge, which does not meet the current blade manufacturing and transportation limitations, the original and the thickened airfoils are further modified, to result in a rounded trailing edge, without truncating the provided airfoil geometries. Ultimately, the aim of this study is to extend the use of this promising low Reynolds number airfoil and provide an adequate airfoil family for the entire blade span (including the root region as well) of small wind turbine blades, capable of significantly improving the overall power performance.

6.4 The Original RG15 Airfoil

The RG15 low Reynolds number airfoil was designed by Rolf Girsberger in an attempt to provide a superior alternative – in terms of maximum C_L – to the Eppler E180 airfoil and meet the special requirements of the FAI-F3B class that is the World Championship for Model Gliders. Even though RG15 was initially intended exclusively for radio controlled sailplanes and model gliders, including slope soaring and electric powered gliders, it currently represents an attractive low Reynolds number airfoil for the design of small wind turbine blades as well. Figure 6.3a presents the theoretical profile of the RG15 airfoil, which has a maximum relative thickness of 8.92% located at 30.2% of the chord from the leading edge and a maximum relative camber of 1.8% located at 39.7% of the chord from the leading edge.

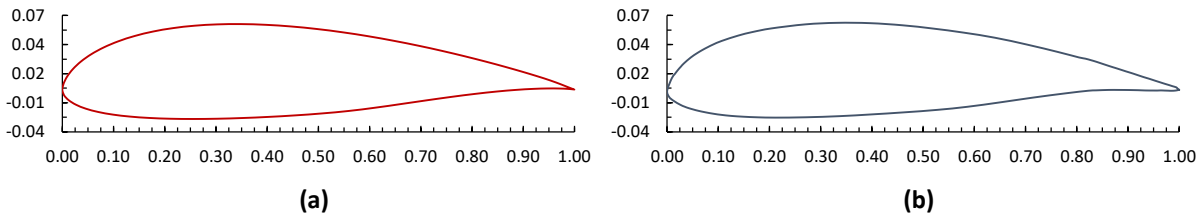


Figure 6.3: The RG15 airfoil. (a) Theoretical profile. (b) Actual profile (Broeren *et al.*, 1995).

The theoretical profile of the RG15 airfoil was generated by means of the Eppler airfoil code, according to the following criteria:

- a. Section drag for low lift (C_L between 0 and 0.4) comparable to E180 airfoil.
- b. Lower edge of laminar drag bucket at slightly negative lift.
- c. Higher maximum lift than E180 airfoil.
- d. Critical Reynolds number well below 100,000.
- e. Higher absolute value of pitching moment than E180 airfoil.
- f. Lower absolute value of pitching moment than E193 airfoil.
- g. Relative airfoil thickness between 8.5% and 9.5%.

In addition, Figure 6.3b illustrates the actual airfoil profile used during the experimental study at the UIUC low-turbulence subsonic wind tunnel (Broeren *et al.*, 1995). Since low Reynolds number airfoil performance is highly dependent on the laminar boundary layer behavior, low turbulence levels within the wind tunnel were necessary to ensure that laminar flow does not prematurely transition to the turbulent state over the airfoil surface. To this end, the wind-tunnel settling chamber had been equipped with a 4-in thick honeycomb and four anti-turbulence screens; the turbulence intensity was measured to be less than 0.1%, which was considered sufficient for low Reynolds number airfoil measurements (Broeren *et al.*, 1995). In Figure 6.4, the aerodynamic characteristics of the RG15 airfoil for various Reynolds numbers from $Re = 60,000$ to $Re = 300,000$ are illustrated, as obtained from the testing program at the UIUC low-turbulence subsonic wind tunnel (Broeren *et al.*, 1995). As expected, the increase of Re is associated with a reduction in drag coefficient and therefore, an increase of the lift-to-drag ratio, since no significant variation of the lift curve with Re was observed for the examined angles of attack.

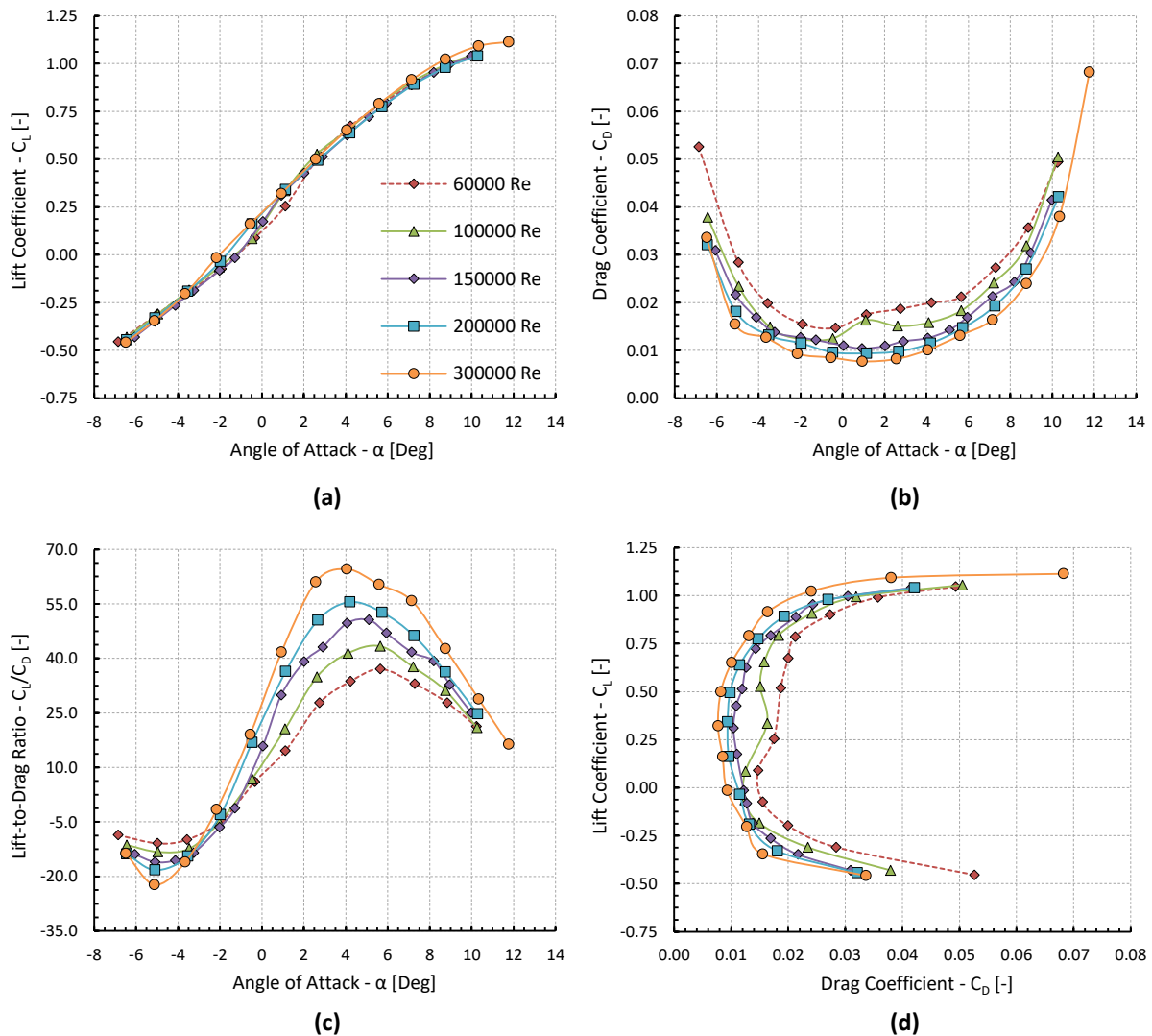


Figure 6.4: Aerodynamic characteristics of RG15 airfoil at several low Reynolds numbers, as measured at the UIUC wind tunnel (Broeren *et al.*, 1995). (a) $C_L - \alpha$. (b) $C_D - \alpha$. (c) $C_L/C_D - \alpha$. (d) $C_L - C_D$.

6.5 Thickening of the RG15 Airfoil

During the selection of the airfoil sections for the optimum wind turbine blade design, the specific requirements of the different blade regions should be considered as well. In particular, structural requirements have higher priority than the aerodynamic ones for airfoil sections that form the root region of the blade, due to the high stresses they go through. However, increased aerodynamic efficiency is essential for airfoil sections located in the mid span and tip regions, because of their great impact on the rotor power output. Consequently, even though RG15 airfoil seems appropriate for the mid span and tip regions, because of its promising aerodynamic characteristics, it appears unsuitable for the root region, due to its limited structural integrity (limited rigidity and stiffness), resulting from the small value of the thickness-to-chord ratio and cross-sectional area. To this end, five new thickened airfoils

have been designed, based on the original RG15 geometry, in order to create an airfoil database suitable for the root region formation of small wind turbine blades.

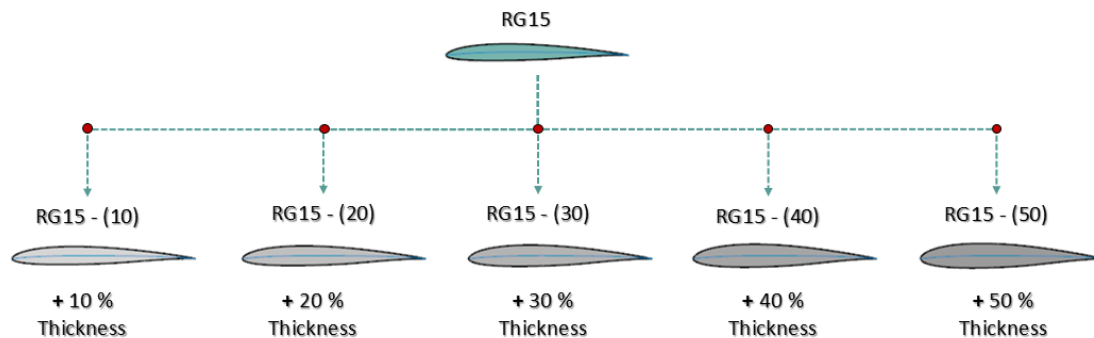


Figure 6.5: The five thickened RG15 airfoils.

The five thickened airfoils have been constructed in such a way that they have the same mean camber line (MCL) compared to the original RG15 airfoil (in order to retain its desirable aerodynamic characteristics), but an increased thickness-to-chord ratio distribution by 50%, 40%, 30%, 20% and 10% respectively, compared to the base airfoil design (see Figure 6.5). The construction of the five thickened airfoils, which from now on will be denoted as RG15-(50), RG15-(40), RG15-(30), RG15-(20) and RG15-(10), was implemented by the utilization of Rhinoceros 3D Computer-Aided Design (CAD) application software, developed by Robert McNeel & Associates, as well as Grasshopper visual programming language, which runs within Rhinoceros. Initially, the mean camber line of the original RG15 airfoil was calculated, by interpolating a smooth curve (blue line) through the centers (blue squares) of the inscribed circles (red circles) to the RG15 airfoil, as shown in Figure 6.6 (standard procedure for calculating the MCL).

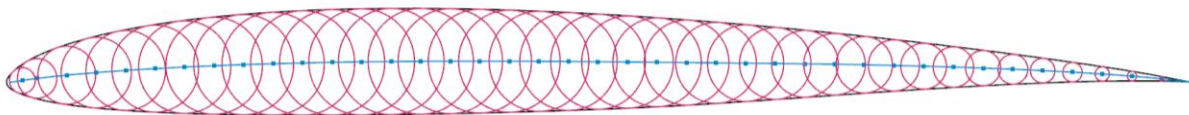


Figure 6.6: Calculation of the RG15 mean camber line (blue line).

Then, the thickness distribution of the RG15 airfoil was calculated, according to the following procedure, which is schematically represented in Figure 6.7; for a point k along the chord line (c), the thickness value corresponding to k is equal to the length of the line segment (thickness line – magenta) perpendicular to the MCL (blue) that passes through the projection of k on the MCL.

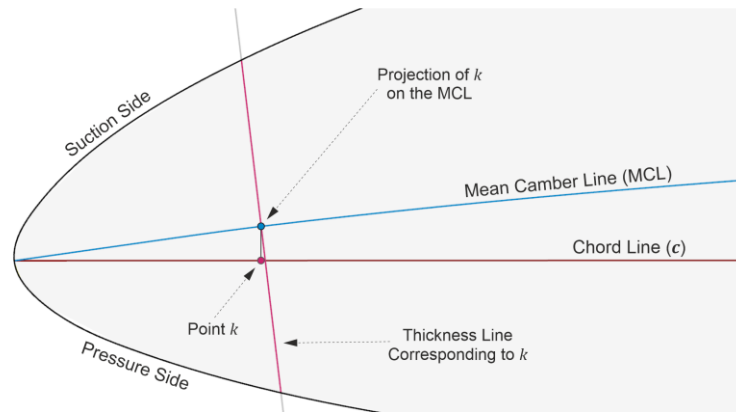


Figure 6.7: Calculation of the thickness line corresponding to a random point k along the chord line.

In Figure 6.8, only a few indicative thickness lines (magenta) of the RG15 airfoil are depicted for clarity purposes. Finally, as illustrated in Figure 6.9, for the construction of the points of the new thickened airfoils, each thickness line of the original RG15 was extended equally from both sides by the appropriate percentage, depending on the desirable rate of thickness increase. The start and end points of the extended thickness lines (magenta squares – Figure 6.9) are the points of the new thickened airfoil.

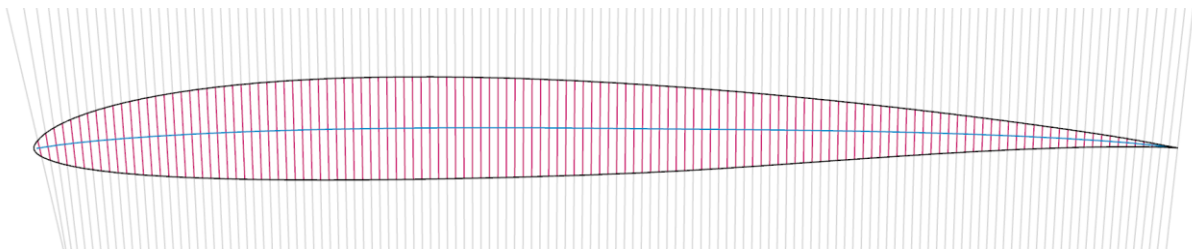


Figure 6.8: Indicative thickness lines (magenta) of the RG15 airfoil.

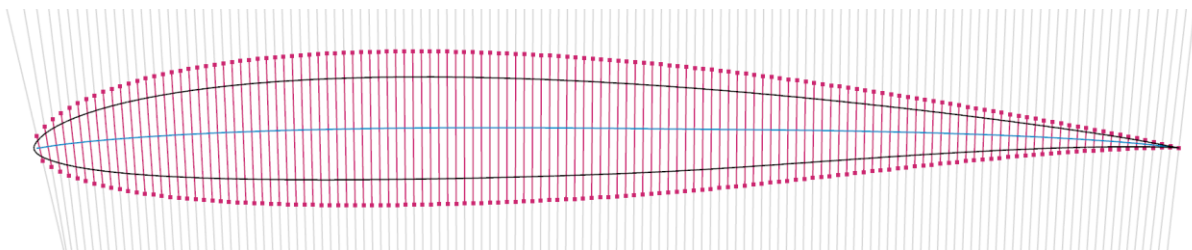


Figure 6.9: Indicative points of a thickened airfoil, constructed through the proper extension of the RG15 thickness lines.

6.6 Trailing Edge Modification

The Kutta-Zhukovsky theorem dictates that a lift producing airfoil should have a knife-sharp trailing edge and therefore, it considers the practical necessity of manufacturing blades and wings with rounded trailing edges as a divergence from the ideal case. However, some early experiments (Herrig *et al.*, 1951; Stack and Lindsey, 1938), which were carried out to determine the lift and drag dependence upon the trailing edge radius, revealed that a rounded trailing edge of radius less than 1% of the chord length produces essentially the same lift and drag as a maximally sharp trailing edge, while a notable increase in drag was observed for rounded trailing edges of radius above 2% of the chord length. In this context and given that the current blade manufacturing and transportation limitations do not allow sharp trailing edges to be constructed, the trailing edges of the original and thickened RG15 airfoils were locally thickened and rounded. For the generation of a blunt trailing edge without truncating the airfoil, QBlade software (Marten, 2015) provides the built-in Trailing Edge Gap function, where the desired gap and blending distance from the leading edge (i.e., the absolute percentage of the airfoil chord, downstream of which the smoothing code is free to modify the airfoil shape in order to accommodate the modified trailing edge) are specified as percentages of the chord length. Nevertheless, as it was observed during the utilization of the Trailing Edge Gap function, the user-defined blending distance was not being completely respected by the code; while additionally, the airfoil thickness was being measured and applied perpendicular to the center line (as utilized by QBlade instead of the actual MCL), which is a rough and generally incorrect approximation of the MCL.

Therefore, in order to overcome the aforementioned shortcomings, a custom script was created within Grasshopper, to be used for the generation of a blunt trailing edge without truncating the airfoil, through the proper modification (local thickening) of the provided (baseline) airfoil geometry under consideration. As long as the features of the developed script are concerned, the user is permitted to precisely define the trailing edge diameter and blending distance from the leading edge as in QBlade, while conversely to QBlade, the airfoil thickness is measured and applied perpendicular to the airfoil's MCL, as it should be, so the resultant airfoil to have the exact same MCL with the baseline, so as to retain its aerodynamic characteristics as far as possible. Once the baseline airfoil geometry (with a sharp trailing edge) and the required software parameters (blending distance and trailing edge diameter) have been provided, the modified airfoil geometry is constructed through the application of an additional parabolic thickness distribution to the baseline airfoil, starting from the point along the chord that corresponds to the established blending distance and ending at the airfoil's trailing edge; in such a way that the defined trailing edge diameter to be exactly achieved and the resultant airfoil geometry to fulfil all the required continuity, curvature and smoothness

criteria. The blending distance and trailing edge diameter are schematically defined in Figure 6.10.

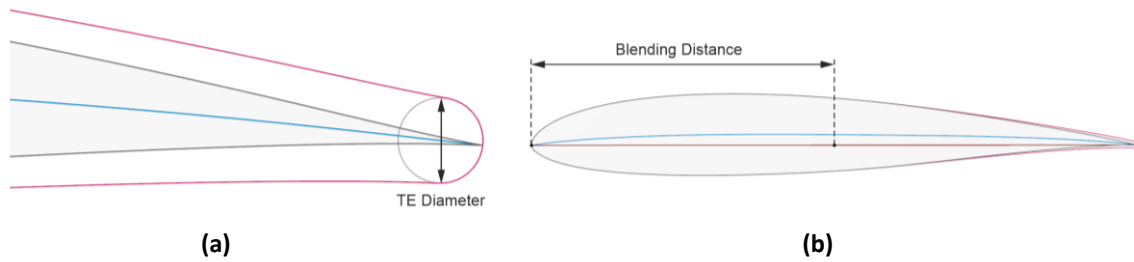


Figure 6.10: Schematic definition of the (a) trailing edge diameter and (b) blending distance.

Figure 6.11 presents an indicative application of the developed methodology to the RG15 airfoil; in the particular application, the trailing edge diameter and the blending distance from the leading edge were set equal to 1% and 50% of the chord length respectively.

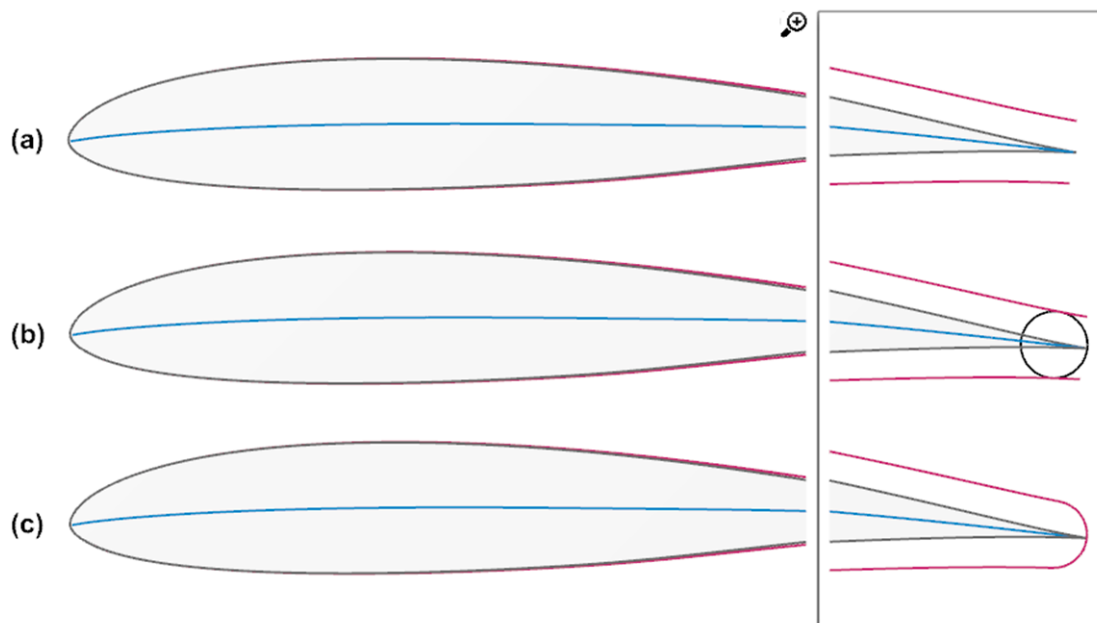


Figure 6.11: Schematic representation of the followed methodology for the creation of a rounded trailing edge.

As it seems, the baseline (RG15 - black) and the modified (red) airfoil geometries coincide from the leading edge until the point that corresponds to the 50% of the chord, while the differentiation between the two airfoils lies only in the region downstream of the 50% of the chord; increasing smoothly and parabolically as the trailing edge is approached, to

attain the desirable thickness. Subsequently, in order to create a rounded trailing edge geometry, a circle (black) is fitted to the thickened trailing edge of the modified airfoil, in such a way that is tangent to its upper and lower surfaces and passes through the sharp trailing edge of the baseline airfoil, as depicted in Figure 6.11b; so as the reformed airfoil to have the same chord line with the baseline one. Finally, the leftover edges are properly cut off, to result in the final modified airfoil with a rounded trailing edge.

6.7 RG15 Airfoil Family

In this work, the methodology developed for the conversion of sharp trailing edges to rounded ones, was applied to all the original and thickened RG15-(xx) airfoils. For each one of the six airfoils (denoted as “parent” airfoils), four modified configurations were generated (Table 6.1), by setting the trailing edge radius equal to 0.5% of the chord length (i.e., trailing edge diameter equal to 1%) and the blending distance equal to 0%, 50%, 60% and 70% of the chord length respectively. Regarding the notation used for the modified airfoils, the RG15-(xx)-yy-z refers to an airfoil with an increased thickness-to-chord ratio by xx% compared to the original RG15, whose rounded trailing edge was created by setting the trailing edge diameter equal to z% and the blending distance from the leading edge equal to yy% of the chord length.

“Parent” Airfoils - Sharp Trailing Edge					
RG15	RG15 – (10)	RG15 – (20)	RG15 – (30)	RG15 – (40)	RG15 – (50)
Modified Airfoils - Rounded Trailing Edge					
RG15-(00)-00-1	RG15-(10)-00-1	RG15-(20)-00-1	RG15-(30)-00-1	RG15-(40)-00-1	RG15-(50)-00-1
RG15-(00)-50-1	RG15-(10)-50-1	RG15-(20)-50-1	RG15-(30)-50-1	RG15-(40)-50-1	RG15-(50)-50-1
RG15-(00)-60-1	RG15-(10)-60-1	RG15-(20)-60-1	RG15-(30)-60-1	RG15-(40)-60-1	RG15-(50)-60-1
RG15-(00)-70-1	RG15-(10)-70-1	RG15-(20)-70-1	RG15-(30)-70-1	RG15-(40)-70-1	RG15-(50)-70-1

Table 6.1: The modified RG15 airfoils with a thickened and rounded trailing edge.

The four variants for each one of the “parent” airfoils, corresponding to the different blending distance values, as well as their “parent” airfoil, were then evaluated using XFOIL software (Drela, 1989), at various low Reynolds numbers, in order to examine the influence of the blending distance parameter on the developed aerodynamic forces. Figure 6.12a illustrates the drag polar for the RG15, RG15-(00)-00-1, RG15-(00)-50-1 and RG15-(00)-70-1 airfoils at $Re = 300,000$. Apparently, no significant variation of the drag polar was detected with different

values of the blending distance parameter, while the same outcome was observed by examining the rest of low Reynolds numbers considered during the experimental study at UIUC (Broeren *et al.*, 1995). In addition, Figure 6.12a indicates that the adoption of a rounded trailing edge (instead of a maximally sharp one) did not result in a substantial reduction in the aerodynamic performance of the airfoil, since the comparison between the drag polars (XFOIL solver) of RG15 and RG15-(00)-70-1 airfoils reveal a high level of similarity.

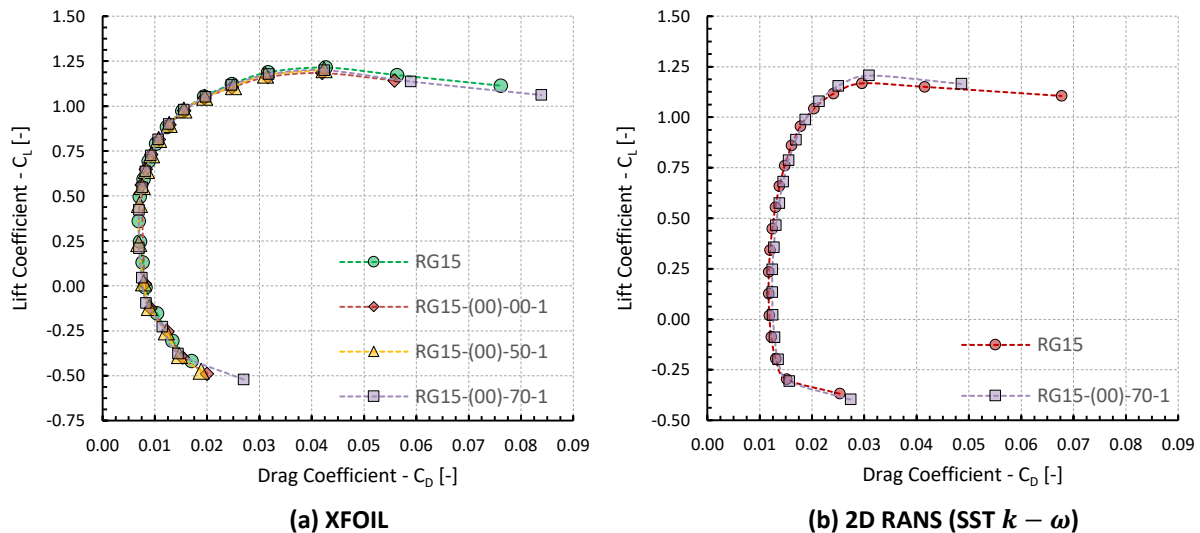


Figure 6.12: The influence of the rounded trailing edge and blending distance parameter on the drag polar at $Re = 300,000$. (a) XFOIL results. (b) 2D RANS results.

To further support the latter deduction, RG15 and RG15-(00)-70-1 airfoils were also evaluated at $Re = 300,000$, using the IGal2D solver (see Chapter 4) instead of XFOIL; turbulence simulation was achieved by means of the standard two-equation Shear Stress Transport (SST) turbulence model. The comparison between the resultant drag polars is provided in Figure 6.12b, verifying that a rounded trailing edge with a radius equal to 0.5% of the chord does not affect the aerodynamic performance of the airfoil to a large degree, as only minor differences were detected, especially in the upper high-drag region. The simulation parameters for both XFOIL and RANS solvers are equal to the ones adopted during the detailed evaluation of the entire RG15 airfoil family, which are presented in Chapter 7.

Consequently, since no significant impact of the blending distance parameter on the aerodynamic performance was found, the airfoils that were produced by setting the blending distance equal to 70% have been selected to form the RG15 airfoil family, as they are the ones with the lesser deviation from the “parent” airfoils. The final airfoil family RG15-(xx)-70-1 generated through this work is illustrated in Figure 6.13, whereas Table 6.2 contains the major geometrical characteristics of the corresponding airfoils. Given that all the airfoils have been

constructed using the same MCL (the MCL of the original RG15 airfoil), the maximum camber, the position of maximum camber and the position of maximum thickness are mutual for all members of the family. The dimensionless coordinates of the airfoils composing RG15 airfoil family are provided in [Appendix C](#).

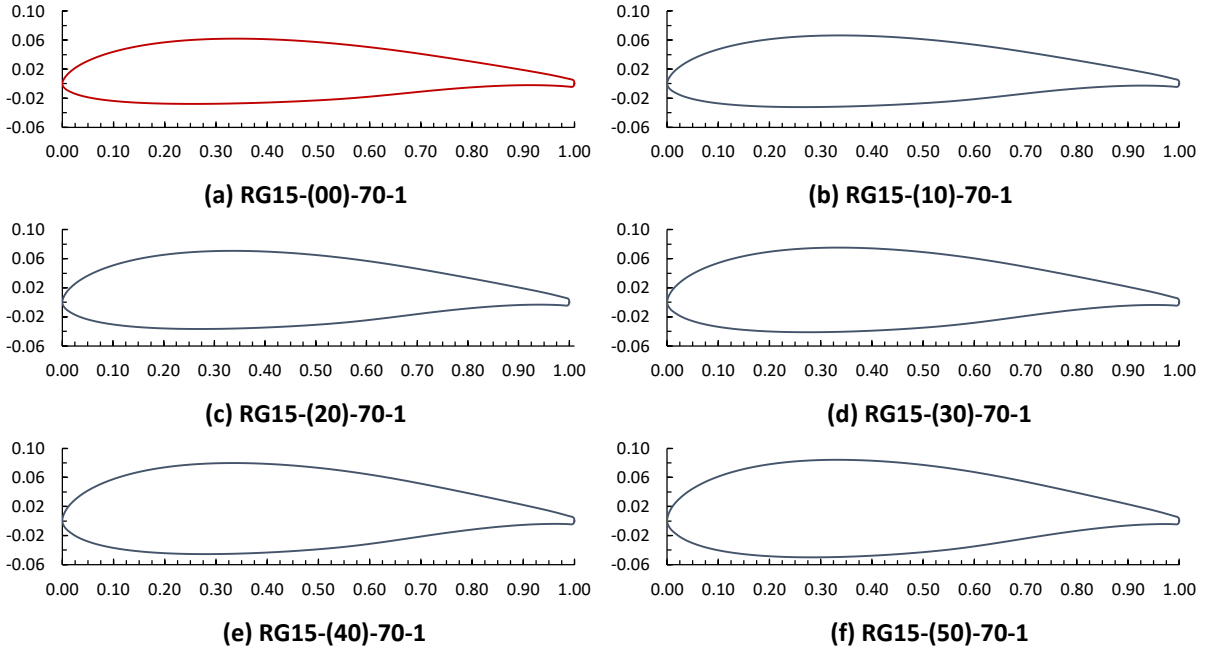


Figure 6.13: The airfoils composing the low-Reynolds RG15 airfoil family.

Airfoil	Maximum Thickness	Maximum Camber	Sectional Area
Original RG15	0.0892 c	0.018 c	0.0595 c^2
RG15-(00)-70-1	0.0892 c	0.018 c	0.0605 c^2
RG15-(10)-70-1	0.0981 c	0.018 c	0.0664 c^2
RG15-(20)-70-1	0.1070 c	0.018 c	0.0724 c^2
RG15-(30)-70-1	0.1160 c	0.018 c	0.0784 c^2
RG15-(40)-70-1	0.1249 c	0.018 c	0.0843 c^2
RG15-(50)-70-1	0.1338 c	0.018 c	0.0903 c^2

Table 6.2: Geometrical characteristics of the airfoils composing the RG15 airfoil family.

Chapter 7

Numerical Analysis of the RG15 Airfoil Family

This chapter involves the aerodynamic performance evaluation of the entire low-Reynolds RG-15 airfoil family. In order to obtain the aerodynamic characteristics of the involved airfoils, both the well-known XFOIL code and the in-house developed IGal2D solver are employed.

7.1 XFOIL Analysis

The aerodynamic performance of the RG15 airfoils was initially evaluated by means of XFOIL software, which relies on the combination of a potential flow panel method with an integral boundary layer formulation, for the analysis of subsonic isolated airfoils (Drela, 1989). The final solution is achieved through the implementation of an iterative procedure between the inner and outer flow solutions on the boundary layer displacement thickness, until an appropriate convergence criterion is reached; accordingly, the viscous pressure distributions (which capture the effects of laminar separation bubbles and trailing edge separation) can be predicted with reasonable accuracy (Coder and Maughmer, 2014). During an XFOIL analysis, the transition from laminar to turbulent state is predicted by applying an approximate e^N envelope method (Drela and Giles, 1987), according to which, only the most amplified frequency at a given point on the airfoil downstream from the point of instability is tracked (instead of tracking the amplification rates of all frequencies), in order to obtain the amplitude of the entire frequency envelope (Coder and Maughmer, 2014). Transition is assumed when this integrated amplitude N reaches an empirically determined value, denoted as N_{crit} . The appropriate value of N_{crit} parameter can be calculated as a function of the absolute value of turbulence intensity T_u , as follows (Van Ingen, 2008):

$$N_{crit} = -8.43 - 2.4 \ln(T_u) \quad (7.1)$$

7.1.1 XFOIL Setup and Validation

Prior to the aerodynamic evaluation of the proposed RG15 airfoil family, the accuracy of XFOIL was validated against the available experimental data for the original RG15 airfoil (Broeren *et al.*, 1995). In this study, a value of 9 was adopted for N_{crit} , in order to match the turbulence levels reported during the wind tunnel testing (that is a turbulence intensity value less than 0.001 or 0.1%) (Broeren *et al.*, 1995). As long as the geometry description is concerned,

the study of Morgado *et al.* (2016) concluded that no significant variation in the aerodynamic coefficients should be detected by increasing the number of points (panel resolution) on the airfoil surface over 150. However, XFOIL documentation advises that a fine panel resolution is required, if the appearance of laminar separation bubbles is expected. To this end, 300 points were used to describe the RG15 airfoil geometry, by applying a denser point distribution near the leading and trailing edges. The Mach number was set to zero.

Figure 7.1 and Figure 7.2 provide the lift and drag coefficients of the RG15 airfoil, as a function of the angle of attack, for $Re = 60,000$ and $Re = 300,000$ respectively, as they resulted from both the testing program at the UIUC low-turbulence subsonic wind tunnel (Broeren *et al.*, 1995) and XFOIL software; the particular Reynolds numbers correspond to the lower and upper values of the Reynolds number spectrum examined during the experimental studies at UIUC (Broeren *et al.*, 1995).

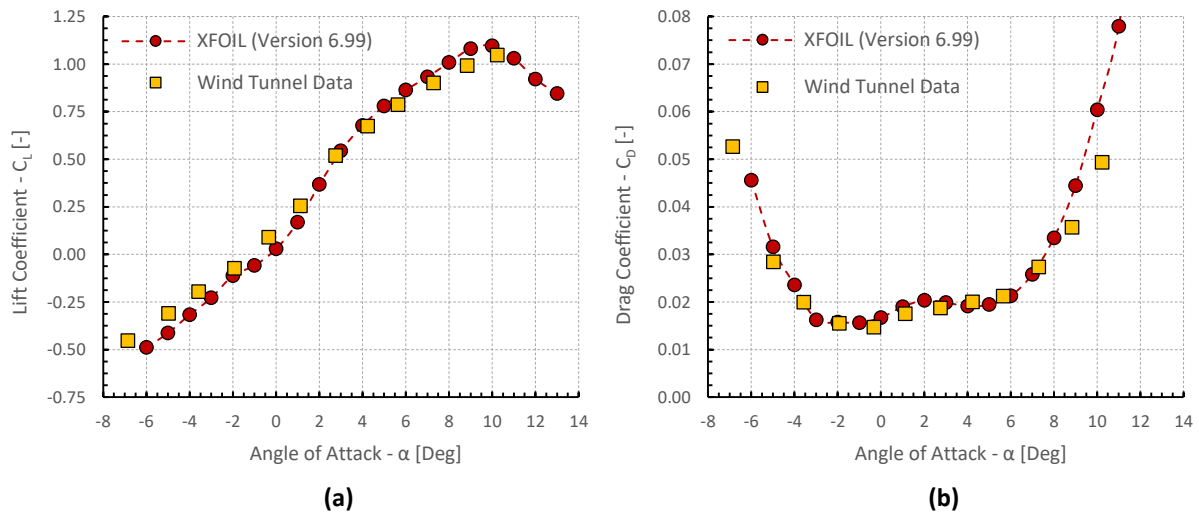


Figure 7.1: Comparison of the XFOIL results for the lift and drag coefficients of the original RG15 airfoil at $Re = 60,000$ with the corresponding experimental measurements (Broeren *et al.*, 1995); (a) $C_L - \alpha$. (b) $C_D - \alpha$.

As it can be observed, the experimental lift and drag curves have been predicted with reasonable accuracy for both Reynolds numbers; similar levels of accuracy were found during the comparisons made for the rest of the available experimental data, corresponding to the different Reynolds numbers (within the particular range) that were examined during the experimental study at UIUC (Broeren *et al.*, 1995). However, some notable discrepancies between the experimental and numerical results were also detected, especially in terms of the drag coefficient. In particular, XFOIL seems to over-predict the drag coefficient at $Re = 60,000$ for angles of attack higher than 8° , while an evident under-prediction of the drag coefficient at $Re = 300,000$ was also observed, regarding the angles of attack higher than 10° . Nevertheless, the approximation of the experimental data is considered acceptable, since the

trend and major aspects of both curves have been well captured. Consequently, XFOIL can be used for the evaluation of the RG15 airfoil family within the particular low Reynolds numbers range.

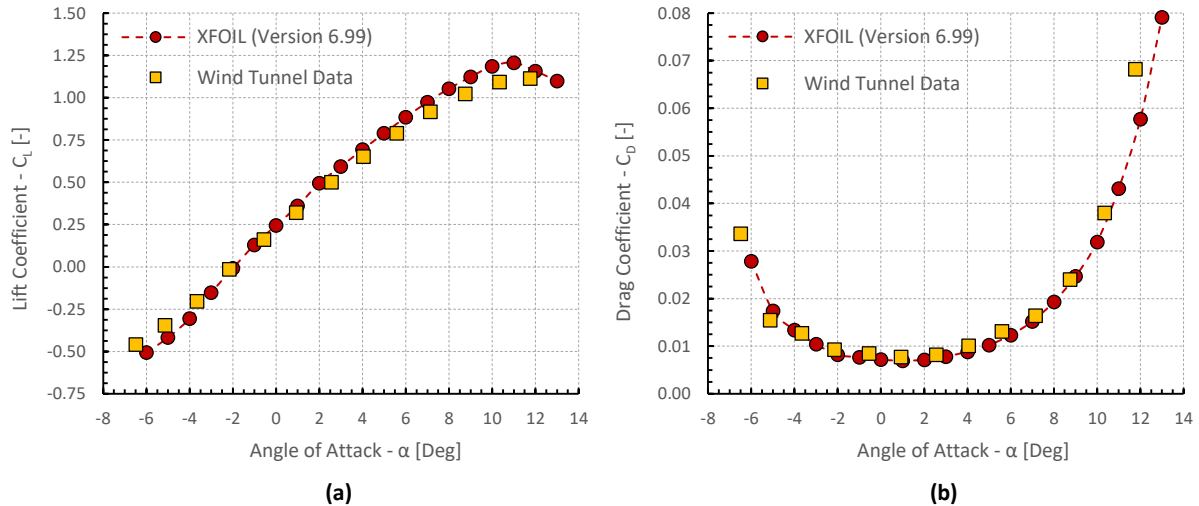


Figure 7.2: Comparison of the XFOIL results for the lift and drag coefficients of the original RG15 airfoil at $Re = 300,000$ with the corresponding experimental measurements (Broeren *et al.*, 1995); (a) $C_L - \alpha$. (b) $C_D - \alpha$.

7.2 RANS Analysis

Apart from the XFOIL analysis, the aerodynamic performance of the entire RG15 family was further evaluated by means of the in-house IGal2D solver, so as to have a better understanding of the respective flow fields and the associated phenomena. Herein, it is recalled that the particular flow solver is based on a dimensionless formulation of the RANS equations, modified by the artificial compressibility method; space discretization is based on node-centered finite volume formulation, utilizing a second order MUSCL (Monotonic Upstream Scheme for Conservation Laws) scheme; turbulence simulation is succeeded through the standard two-equation Shear Stress Transport (SST) $k - \omega$ turbulence model (Menter, 1994), which is a combination of the $k - \epsilon$ and $k - \omega$ turbulence models. The SST $k - \omega$ model was preferred over the alternative two-equation turbulence models because of the beneficial features that provides, since it combines the advantages of both $k - \epsilon$ and $k - \omega$ models, while disregarding their major shortcomings (Menter *et al.*, 2003). Furthermore, according to the study of Morgado *et al.* (2016), the SST $k - \omega$ model seems capable of accurately predicting a wide spectrum of low Reynolds number flows over airfoils. The limitations of this approach should be taken into account, as no transition model or low-Re corrections are considered in this study. The spatial discretization of the flow and turbulence models is performed over two-dimensional unstructured grids, comprised of both triangular

and quadrilateral elements, along with a node-centered finite-volume scheme. A detailed description of the employed solver (IGal2D) can be found in Chapter 4.

7.2.1 IGal2D Setup and Validation

Prior to the aerodynamic evaluation of the RG15 airfoil family, the ability of the IGal2D solver to accurately predict the lift and drag forces was validated against the available experimental data for the original RG15 airfoil (Somers, 2005). However, a grid independence study was also performed before the validation study, in order to guarantee that the grid resolution does not affect the simulation results. For this purpose, three computational grids with different resolutions were constructed, denoted as Mesh 1 (coarse), Mesh 2 (medium) and Mesh 3 (fine), by considering an angle of attack equal to 0° . At this point, it is noted that the desired angle of attack for each flow simulation was achieved by properly rotating the airfoil geometry instead of changing the inflow angle; then the updated computational domain was re-meshed. Therefore, a different computational grid was constructed for each one of the considered airfoils and angles of attack. This procedure was adopted in order to retain a high grid density in the wake region for all different angles of attack.

All three grids were generated by adopting a computational domain, such as the one depicted in Figure 7.3a, in which the inflow boundary was placed at a distance of 25 chord lengths upstream the airfoil's leading edge and the outflow boundary at a distance of 40 chord lengths downstream the airfoil's trailing edge. Mesh 1 (which is the coarsest among the examined ones) was composed of 164,345 triangular and 25,284 quadrilateral elements, with a total number of nodes equal to 107,927. For the description of the airfoil geometry 602 points were used along the airfoil surface, by applying a denser distribution near the leading and trailing edges. Mesh 2 was constructed by applying a denser points distribution on the airfoil surface (804 points), accompanied by increasing mesh resolution within the entire computational domain; it comprises of 380,032 triangular and 28,140 quadrilateral elements, with a total number of nodes equal to 218,765. Finally, an even finer mesh resolution and denser points distribution on the airfoil surface was adopted for the construction of Mesh 3, which is composed of 686,556 triangular and 47,920 quadrilateral elements, with a total number of nodes equal to 392,160. The wall spacing of the first inflation layer, created on the airfoil surface for all the three grids, was calculated by considering a y^+ value of approximately 1. The corresponding meshing parameters are also provided in Table 7.1.

Mesh Parameter	Mesh 1	Mesh 2	Mesh 3
Number of Nodes	107,927	218,765	392,160
Triangular Elements	164,345	380,032	686,556
Quadrilateral Elements	25,284	28,140	47,920
Points on Airfoil	602	804	1200
Target y^+	≈ 1.0	≈ 1.0	≈ 1.0

Table 7.1: Meshing parameters used for the grid independence study.

Table 7.2 presents the numerical lift and drag coefficients of the RG15 airfoil at $Re = 300,000$ and $\alpha = 0^\circ$, as obtained by using Mesh 1, Mesh 2 and Mesh 3. Apparently, no significant variation of the lift and drag coefficients was found by increasing the mesh resolution over the levels provided by Mesh 2; the percentage difference in both lift and drag obtained through the utilization of Mesh 2 and Mesh 3 was below 0.3%, even though the number of nodes has been almost doubled. Therefore, the resolution provided by Mesh 2 is considered sufficient to result in a mesh independent solution. Consequently, a computational mesh of analogous resolution was constructed for each one of the different angles of attack that were encountered during this validation study. Such a computational mesh is presented in Figure 7.3a and Figure 7.4.

	Number of Nodes	C_L	C_D	Percentage Diff. - C_L	Percentage Diff. - C_D
Mesh 1	107,927	0.2355460	0.0117844	-	-
Mesh 2	218,765	0.2353327	0.0116944	0.09%	0.76%
Mesh 3	392,160	0.2353510	0.0116699	0.01%	0.21%

Table 7.2: The results of the grid independence study. The flow simulations were performed for RG15 airfoil at $Re = 300,000$ and $\alpha = 0^\circ$.

The RANS simulations were conducted at $Re = 300,000$ for angles of attack ranging from -6° to 12° (using an increment of 1°); therefore, 19 computational grids were constructed in total. In Figure 7.5, the lift and drag coefficients of the RG15 airfoil as a function of the angle of attack are illustrated, as obtained from the testing program at the UIUC low-turbulence subsonic wind tunnel (Broeren *et al.*, 1995), XFOIL code and IGal2D solver. As it seems, the trend of both experimental curves have been well predicted by the RANS solver; however, an over-prediction of the drag coefficient was observed (typical characteristic of the SST $k - \omega$ turbulence model), especially for the angles of attack lying between -3° and 6° . According to the results presented in the study of Morgado *et al.* (2016), a better match of the experimental

drag coefficients could be achieved by the utilization of low Reynolds number correction to the standard SST $k - \omega$ turbulence model..

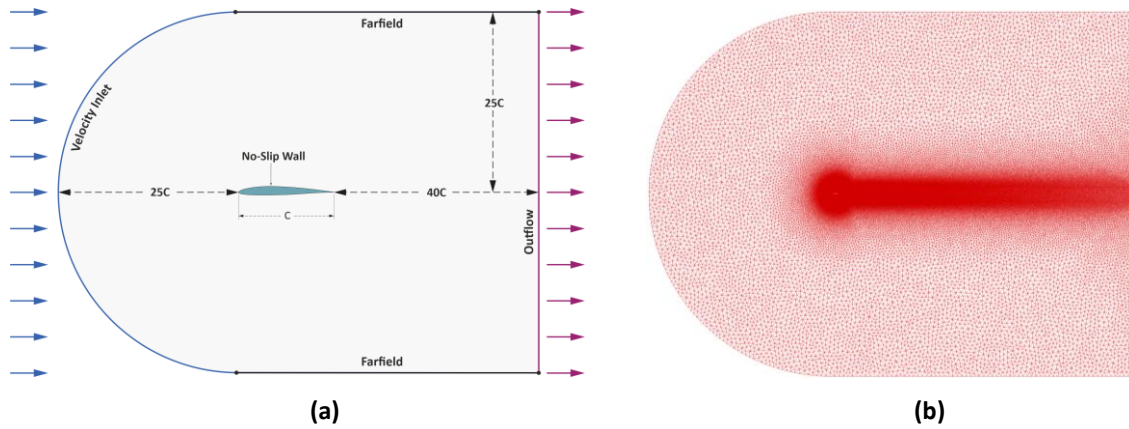


Figure 7.3: (a) The computational domain used for the validation study of the RANS solver, (b) Wide view of the corresponding computational grid.

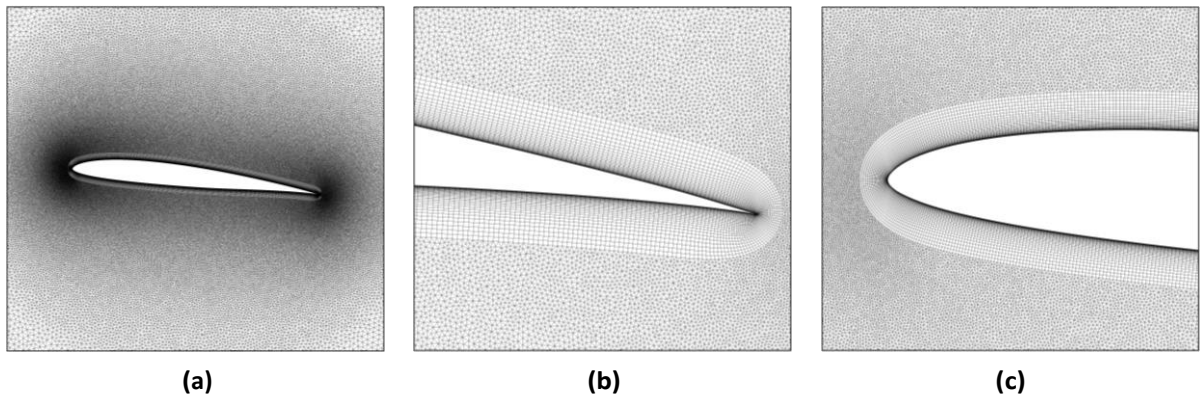


Figure 7.4: The hybrid computational grid used for the flow field simulation of the original RG15 airfoil at $\alpha = 6^\circ$.

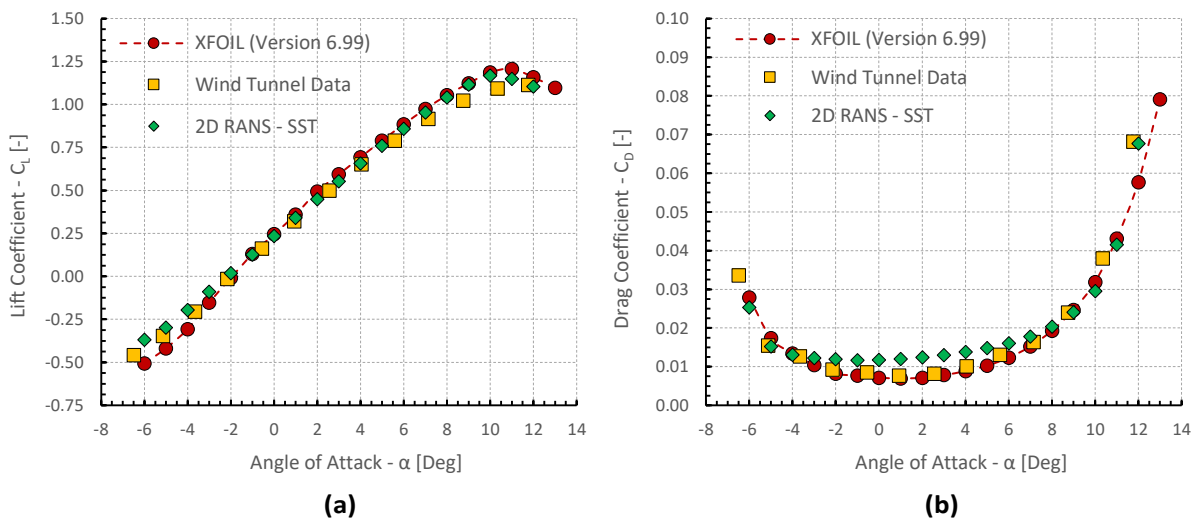


Figure 7.5: The lift and drag coefficients of the original RG15 airfoil at $Re = 300,000$, as obtained by XFOIL software, IGal2D solver and the experimental measurements (Broeren *et al.*, 1995).

7.2.2 Lift and Drag Calculation

The components of the total aerodynamic force $\mathbf{R} = (R_x, R_y)$ on the airfoil are calculated by integrating the pressure (p) and shear stress (τ) distributions over the airfoil contour (C_s) (Anderson, 2010). Thus,

$$R_x = - \oint_{C_s} p n_x ds + \oint_{C_s} (\tau_{xx} n_x + \tau_{xy} n_y) ds, \quad (7.2)$$

$$R_y = - \oint_{C_s} p n_y ds + \oint_{C_s} (\tau_{xy} n_x + \tau_{yy} n_y) ds. \quad (7.3)$$

Herein, n_x and n_y denote the components of the unit vector \hat{n} normal to the airfoil surface; τ_{xx} , τ_{xy} , τ_{yx} and τ_{yy} represent the components of the viscous stress tensor. Subsequently, the lift and drag forces on the airfoil can be obtained through the following equations (Anderson, 2010):

$$L = R_y \cos(\varphi) - R_x \sin(\varphi), \quad (7.4)$$

$$D = R_x \cos(\varphi) + R_y \sin(\varphi), \quad (7.5)$$

where φ is the angle between the inflow velocity vector and the x axis. In this study, φ angle is zero, since the desired angle of attack is simulated by rotating the airfoil geometry. Eventually, the lift and drag coefficients are calculated as follows (Anderson, 2010):

$$C_L = 2L/\rho u_\infty c, \quad (7.6)$$

$$C_D = 2D/\rho u_\infty c, \quad (7.7)$$

where ρ represents the air density, u_∞ the ambient wind speed and c the airfoil chord.

7.3 Numerical Results and Discussion

7.3.1 XFOIL Results

Similarly to the preceding validation study, the analysis of RG15 airfoil family was performed by setting the value of N_{crit} parameter equal to 9 and Mach number equal to 0, while the same panel resolution was adopted (300 points on each airfoil surface). The aerodynamic performance of the proposed RG15 airfoil family was evaluated for each one of the Reynolds numbers examined during the wind tunnel experiments (Broeren *et al.*, 1995), by considering a range of angles of attack between -6° and 20° . Table 7.3 contains the

maximum lift-to-drag ratio $(L/D)_{max}$ and the maximum lift coefficient C_{Lmax} for the RG15 airfoil and the entire RG15 airfoil family at the corresponding Reynolds numbers, ranging from $Re = 60,000$ to $Re = 300,000$. Apparently, the decrease of Re results in the reduction of $(L/D)_{max}$ for each one of the examined airfoils, while for a fixed Re value, a reduction in $(L/D)_{max}$ was also detected by increasing the thickness distribution. Therefore, all airfoils of the RG15 family exhibit a $(L/D)_{max}$ loss, for every Re , as compared with the original RG15 airfoil. However, the percentage loss of $(L/D)_{max}$ between a thickened and the original RG15 airfoil seems to decrease with increasing Re . In particular, the maximum reduction in $(L/D)_{max}$ was found for the RG15-(50)-70-1 airfoil at $Re = 60,000$; it was equal to 12.68%. The corresponding reduction at $Re = 300,000$ was equal to 4.13%, while the percentage reductions for the rest of Reynolds numbers lie within the range defined by the aforementioned values. Apparently, the particular range decreases as the thickness-to-chord ratio is reduced. For example, the reduction in the maximum lift-to-drag ratio for the RG15-(30)-70-1 airfoil was found equal to 7.52% and 2.09%, at $Re = 60,000$ and $Re = 300,000$ respectively. Conclusively, the impact of thickness distribution on the maximum lift-to-drag ratio tends to deteriorate as the Re increases.

Airfoil	60,000 Re		100,000 Re		150,000 Re		200,000 Re		300,000 Re	
	$(L/D)_{max}$	C_{Lmax}								
Original RG15	39.89	1.088	52.57	1.133	62.38	1.162	68.88	1.169	78.39	1.207
RG15-(00)-70-1	39.50	1.073	52.38	1.109	62.01	1.139	69.22	1.155	78.28	1.195
RG15-(10)-70-1	38.88	1.127	51.53	1.167	61.58	1.203	68.28	1.213	77.57	1.252
RG15-(20)-70-1	38.05	1.162	50.52	1.218	60.93	1.243	67.51	1.258	77.03	1.289
RG15-(30)-70-1	36.89	1.220	49.92	1.274	60.12	1.284	67.06	1.293	76.75	1.319
RG15-(40)-70-1	35.91	1.222	49.09	1.276	59.29	1.293	66.49	1.304	76.00	1.342
RG15-(50)-70-1	34.83	1.250	48.24	1.302	58.44	1.324	65.53	1.325	75.15	1.351

Table 7.3: The maximum lift coefficient and lift-to-drag ratio for each one of the examined airfoils, at various Reynolds numbers, resulting from the XFOIL analysis.

RG15-(50)-70-1 airfoil demonstrated the maximum reduction in $(L/D)_{max}$ at $Re = 60,000$ (Table 7.3) because this is the airfoil with the maximum geometrical deviation (thickness) from the original RG15 airfoil (compared to all the airfoils in the family) and the Reynold number is low enough to considerably affect the drag production. The $(L/D)_{max}$ for all the examined airfoils is observed in the range of angle of attack (α) between (approximately) 3 and 7 degrees. At this range of α , lift is not affected by the increase in maximum thickness of the airfoil, for constant Re (see Figure 7.6a and Figure 7.7a). However,

drag is increased with increasing the maximum airfoil thickness and decreasing Re (see Figure 7.6b and Figure 7.7b). At this Re range, as the Re decreases below 100,000 there is an increase in drag, particularly because of premature flow separation and failure to reattach, resulting in a reduced drag bucket and a large decrease in lift (Winslow *et al.*, 2018). At Re in the range between 50,000 and 100,000 the separation bubble and turbulent boundary-layer thickness both increase in size (compared to higher Re), a consequence of the higher contribution of the viscous forces, resulting in increased parasitic drag (Winslow *et al.*, 2018). Nevertheless, at such low Re , the increase in airfoil thickness results in considerable increase in form drag, due to trailing edge separation, while simple flat plates outperform conventional airfoils for Re lower than 50,000 (Winslow *et al.*, 2018).

Although the thickening of the RG15 airfoil results in reduced maximum glide ratios, an opposite behaviour was observed for the maximum lift coefficient, which seems to increase by increasing the thickness-to-chord ratio, for a fixed Re value. Apart from Table 7.3, the particular effect is characteristically demonstrated in Figure 7.6a and Figure 7.7a, which provide the lift coefficient for the entire RG15 airfoil family, as a function of the angle of attack. Additional information about the behaviour of $(L/D)_{max}$ and $C_{L_{max}}$ with Re can be obtained by observing Table 7.4, which presents the increase rate of $(L/D)_{max}$ and $C_{L_{max}}$ due to the increase of Re (*i.e.*, the rate of change in $(L/D)_{max}$ and $C_{L_{max}}$ as Re changes) for each airfoil of the RG15 family, using the slope of the linear regression line through data points suggested in (Animasaun *et al.*, 2019; Shah *et al.*, 2018). According to Table 7.4, Re has a higher impact on $(L/D)_{max}$, as the relative thickness of the airfoil increases. Unfortunately, such a conclusion cannot be drawn for $C_{L_{max}}$, since the slope of the linear regression line for $C_{L_{max}}$ is not a monotonic function of the relative thickness.

Airfoil	RG15	RG15-(00)-70-1	RG15-(10)-70-1	RG15-(20)-70-1	RG15-(30)-70-1	RG15-(40)-70-1	RG15-(50)-70-1
$(L/D)_{max}$	1.536E-04	1.552E-04	1.548E-04	1.563E-04	1.594E-04	1.605E-04	1.610E-04
$C_{L_{max}}$	4.536E-07	4.853E-07	4.910E-07	4.796E-07	3.532E-07	4.437E-07	3.634E-07

Table 7.4: Increase rate of $(L/D)_{max}$ and $C_{L_{max}}$ with Re using the slope linear regression through data points.

Furthermore, an extension of the high-lift region to higher angles of attack has been also detected for both $Re = 60,000$ and $Re = 300,000$, while the increase of the thickness distribution leads to a smoother stall behavior, especially at $Re = 300,000$. This latter deduction is further supported by observing the performance of the entire RG15 airfoil family in terms of the drag coefficient, which is represented in Figure 7.6a and Figure 7.7a. Even though the drag coefficient at $Re = 60,000$ is analogous to the airfoil thickness for

the angles of attack ranging from -3° to 7° , an opposite behaviour was found for the angles of attack higher than 7° , where the airfoils with a larger thickness-to-chord ratio exhibit a smaller drag coefficient. A similar behaviour was also identified at $Re = 300,000$; however, in the latter case, the drag dependence upon the thickness-to-chord ratio for the angles of attack below 7° was much weaker.

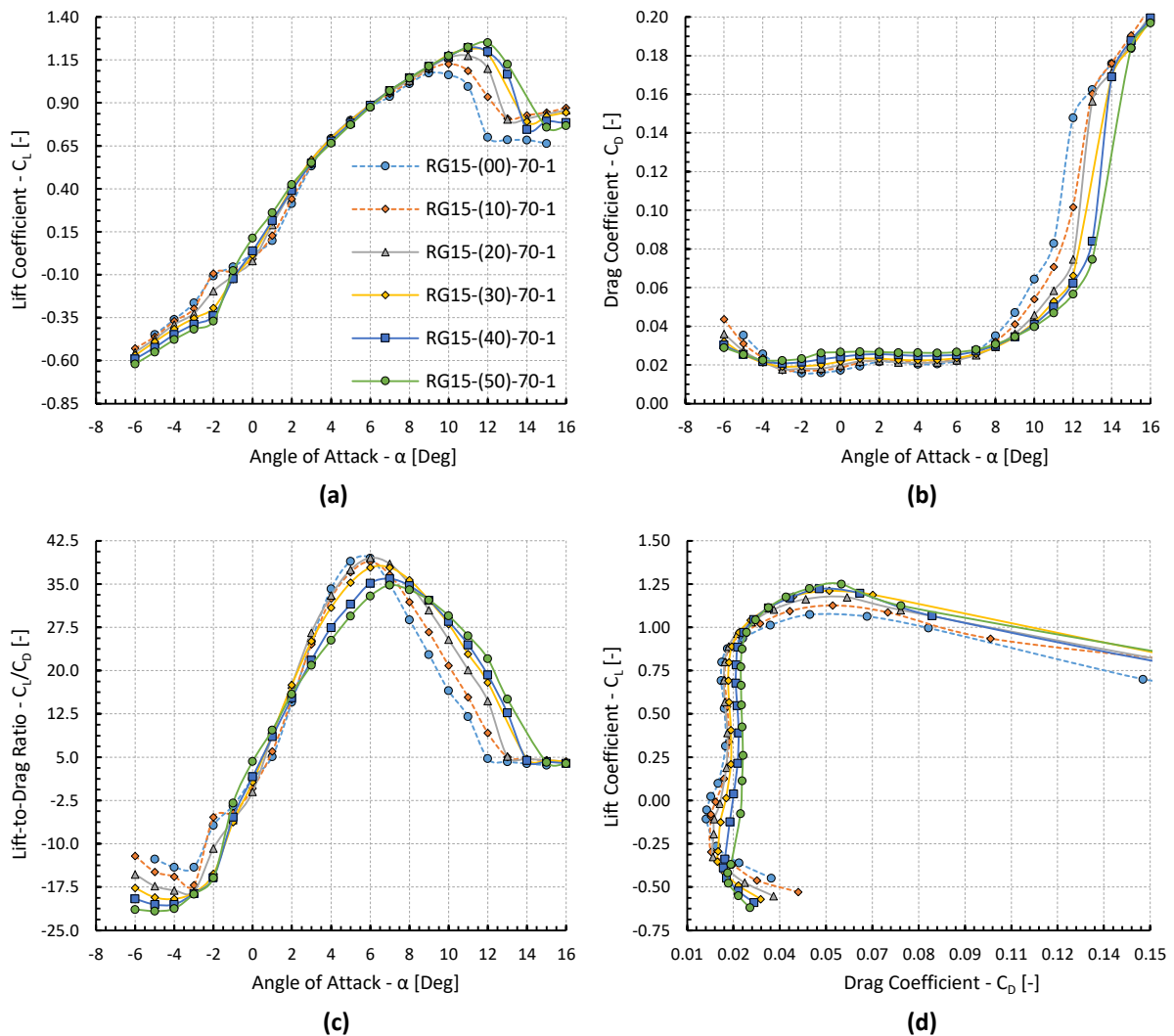


Figure 7.6: Aerodynamic characteristics of the RG15 airfoil family at $Re = 60,000$, as obtained through the XFOIL analysis. (a) $C_L - \alpha$. (b) $C_D - \alpha$. (c) $C_L/C_D - \alpha$. (d) $C_L - C_D$.

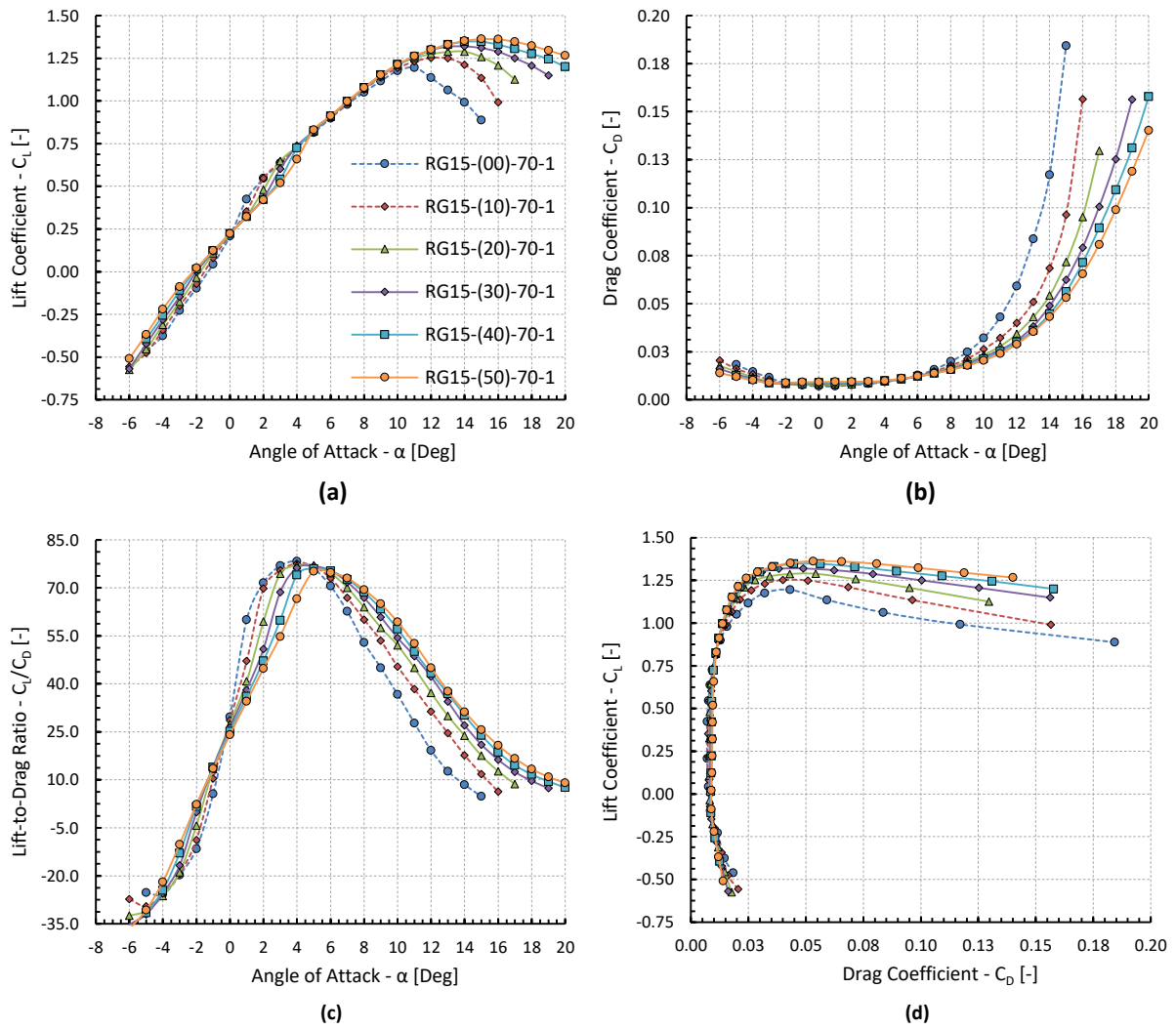


Figure 7.7: Aerodynamic characteristics of the RG15 airfoil family at $Re = 300,000$, as obtained through the XFOIL analysis. (a) $C_L - \alpha$. (b) $C_D - \alpha$. (c) $C_L/C_D - \alpha$. (d) $C_L - C_D$.

7.3.2 IGal2D Results

RANS simulations were performed for each airfoil composing the RG15 airfoil family at $Re = 300,000$, considering a range of angles of attack from -6° to 12° . As previously noted, a new computational grid of similar resolution to Mesh 2 was generated for each airfoil and angle of attack. Thus, by including the original RG15 airfoil, 133 different computational grids were constructed during this study. Such a computational grid (for the flow simulation around RG15-(30)-70-1 airfoil at $\alpha = 6^\circ$) is presented in Figure 7.8.

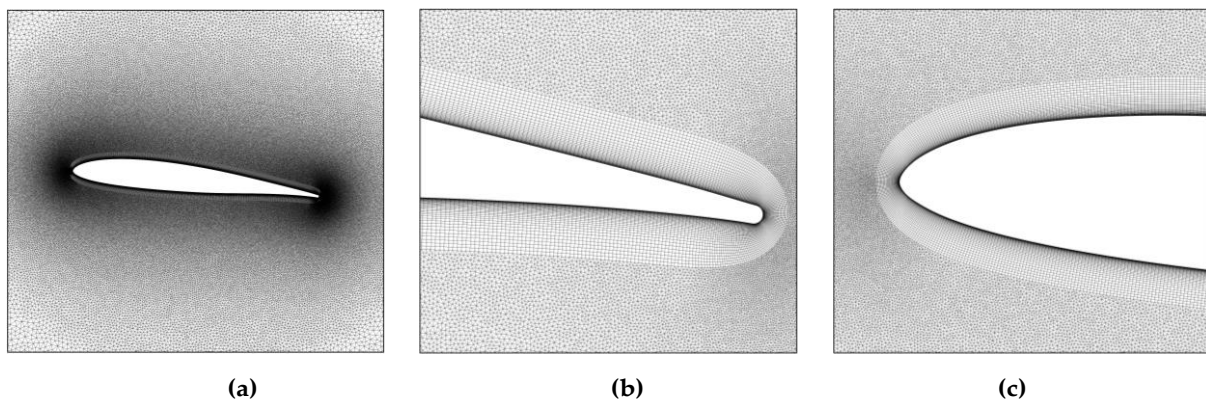


Figure 7.8: The hybrid computational grid used for the flow field simulation of the RG15-(30)-70-1 airfoil at $\alpha = 6^\circ$.

7.3.2.1 Aerodynamic Coefficients

Figure 7.9 illustrates the aerodynamic characteristics of the RG15 airfoil family at $Re = 300,000$, as obtained by the RANS simulations. In accordance to the results of XFOIL analysis, no significant variation in the linear region of the lift coefficient has been observed with increasing thickness-to-chord ratio, as shown in Figure 7.9a; a similar behavior in terms of drag coefficient was also found. Even though the drag coefficient seems to be proportional to the thickness-to-chord ratio, for the angles of attack ranging between -5° and 8° , a trend reversal was detected for the angles of attack higher than 8° , in which the airfoils with a larger thickness-to-chord ratio exhibit a smaller drag coefficient. This is probably attributed to the ability of the thicker airfoils of the RG15 family to maintain the flow attached at higher angles of attack (later and smoother stall). The quantification of the relationship between lift-to-drag ratio and angle of attack (Figure 7.9c) is provided in Table 7.5.

300,000 Reynolds Number							
AoA	RG15	RG15-(00)-70-1	RG15-(10)-70-1	RG15-(20)-70-1	RG15-(30)-70-1	RG15-(40)-70-1	RG15-(50)-70-1
-6°	-14.56	-14.51	-23.60	-25.77	-26.82	-27.37	-28.51
-5°	-19.55	-19.62	-20.69	-21.66	-21.42	-21.42	-21.56
-4°	-14.90	-14.69	-14.55	-14.65	-14.74	-14.73	-14.40
-3°	-7.23	-6.95	-6.67	-6.77	-6.98	-6.83	-6.84
-2°	1.62	1.76	1.94	1.58	1.49	1.32	1.24
-1°	10.84	10.80	10.89	10.36	10.20	9.95	9.47
0°	19.97	19.83	19.26	18.90	18.76	18.14	17.80
1°	28.48	28.04	27.53	27.01	26.42	25.96	25.27
2°	36.15	35.50	34.89	34.38	33.39	32.56	32.37
3°	42.60	41.89	41.19	40.66	39.71	39.05	38.00
4°	47.74	46.99	46.22	45.94	45.01	44.60	43.32
5°	51.40	50.66	49.54	49.72	49.12	48.43	46.73
6°	53.42	52.46	51.54	52.01	51.65	50.37	49.65
7°	53.65	52.80	52.30	51.65	52.85	50.72	50.62
8°	51.18	50.51	52.31	52.34	52.06	50.68	51.89
9°	46.27	46.17	50.57	52.23	50.93	51.47	48.43
10°	39.49	39.04	45.97	47.05	48.60	47.20	47.18
11°	27.68	23.98	39.19	43.87	43.83	44.20	42.38
12°	16.32	-	31.29	37.71	38.92	40.42	38.93

Table 7.5: Lift-to-drag ratio as a function of angle of attack at $Re = 300,000$ (RANS analysis).

However, as the preceding validation study already revealed, the drag levels estimated by the RANS solver are higher than those predicted by XFOIL solver; this conclusion can be easily drawn by observing both Figure 7.9b and Figure 7.9d, as well as Table 7.6, which provides a comparison between the maximum lift-to-drag ratios resulted from XFOIL and RANS solvers, for each airfoil of the RG15 family. In particular, the RANS simulation resulted in maximum lift-to-drag ratios which are reduced by approximately 30%, as compared to those of XFOIL analysis, for each airfoil. Furthermore, significant differences can be detected on the prediction of the angle of attack in which the maximum lift-to-drag ratio is achieved. Nevertheless, a fairly good agreement on the prediction of the percentage reduction of the maximum lift-to-drag ratio between the original and the thickened airfoils was found. For example, XFOIL predicted that the maximum lift-to-drag ratio of the RG15-(50)-70-1 was reduced by 4.6%, as compared to the original RG15; the estimation of the RANS solver on the corresponding reduction was equal to 3.2%. A last remark on the RANS results concerns the high drag coefficient that was observed for the RG15-(00)-70-1 airfoil at -6° (Figure 7.7b). According to the examination of the respective flow field, this is attributed to the presence of a large

separation bubble on the lower surface of the particular airfoil, which encompasses a chordwise extend of approximately 9%. It should be emphasized that no transition model or low-Re corrections for the turbulence model were used for RANS simulations in this study, which can partially explain the discrepancies between the XFOIL and RANS results.

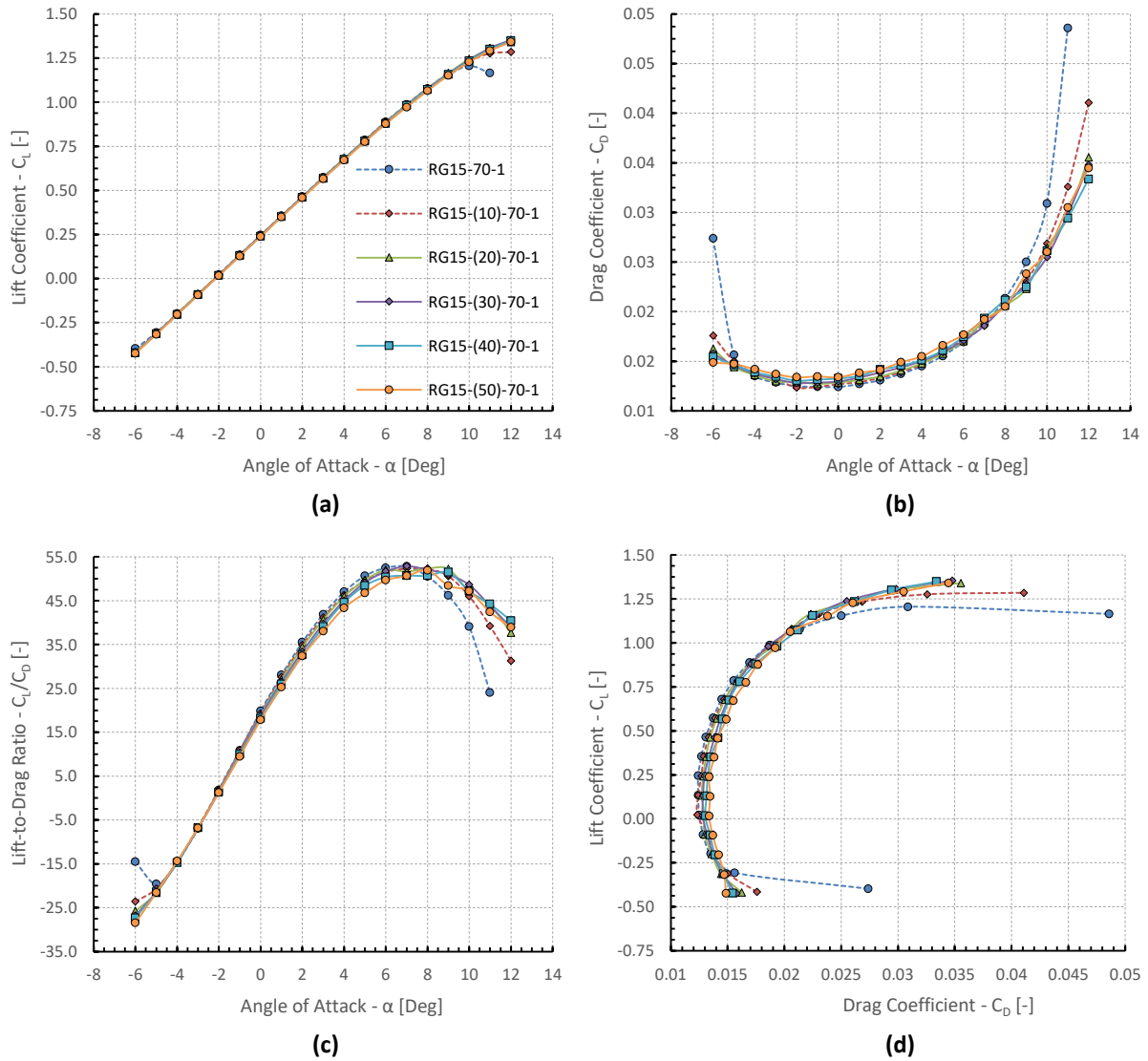


Figure 7.9: Aerodynamic characteristics of the RG15 airfoil family at $Re = 300,000$ (RANS analysis). (a) $C_L - \alpha$. (b) $C_D - \alpha$. (c) $C_L/C_D - \alpha$. (d) $C_L - C_D$.

7.3.2.2 Comparison with XFOIL

Further to the comparisons between the results of XFOIL and IGal2D solvers, Figure 7.10 provides the distribution of the pressure coefficient along the RG15-(40)-70-1 airfoil, as obtained by the IGal2D solver and XFOIL software, for various angles of attack between -5° and 10° . Although a good match is observed for the largest extend of the airfoil chord and

both suction and pressure sides, significant discrepancies have been found around the points in which laminar to turbulent transition is realized. Obviously, this is attributed to the inability of the standard SST $k - \omega$ model to predict the particular phenomenon. The calculation of pressure coefficient was implemented using Eq. (7.8). Thus,

$$C_p = (p - p_\infty)/(0.5\rho u_\infty^2) \quad (7.8)$$

where p_∞ is the free flow pressure.

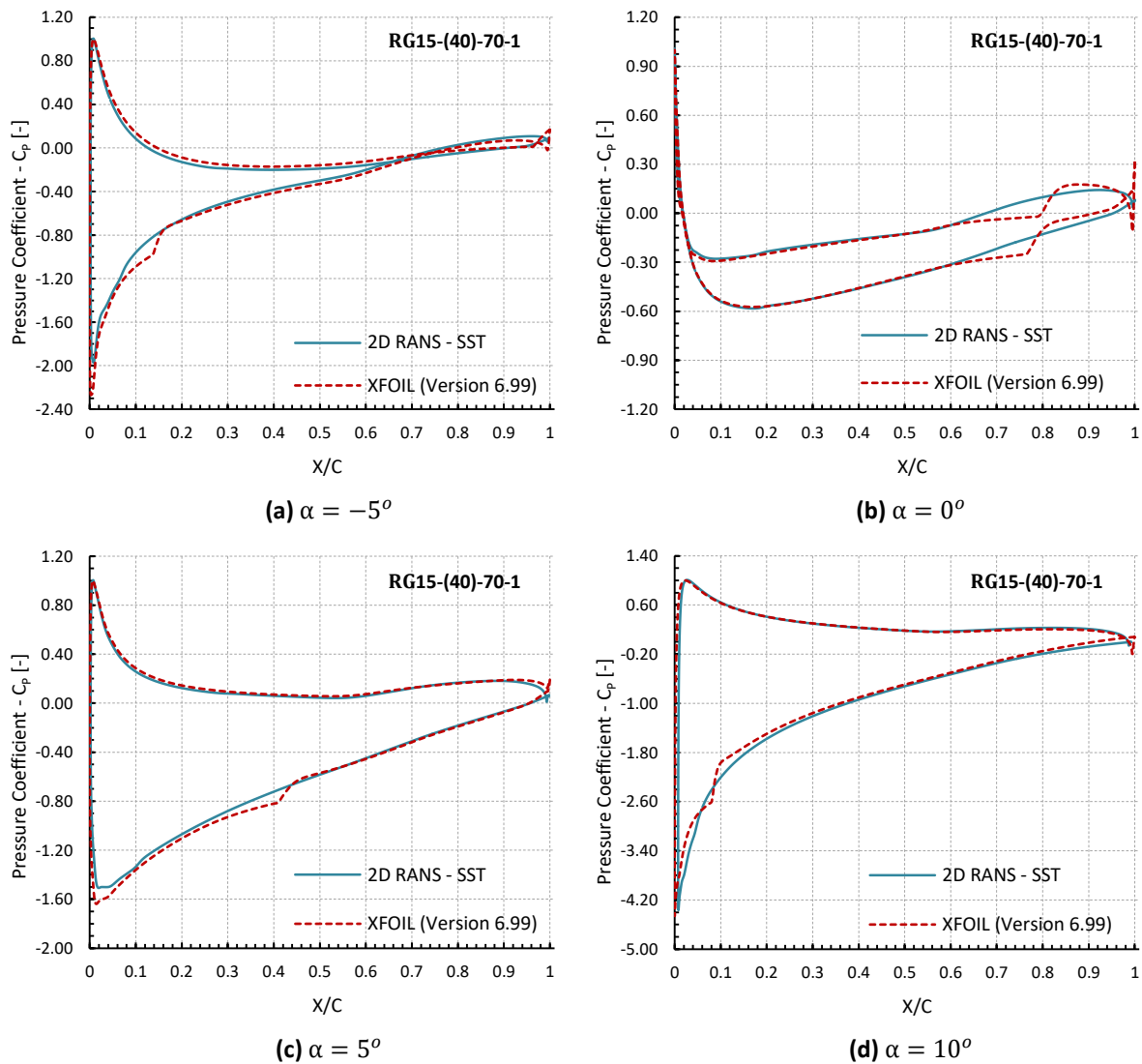


Figure 7.10: Comparison of pressure coefficient distributions obtained by XFOIL software and IGal2D solver for the RG15-(40)-70-1 airfoil at $Re = 300,000$. (a) $\alpha = -5^\circ$. (b) $\alpha = 0^\circ$. (c) $\alpha = 5^\circ$. (d) $\alpha = 10^\circ$.

Finally, a detailed comparison of the lift and drag curves for the entire RG15 airfoil family at $Re = 300,000$ is provided through Figure 7.11 until Figure 7.16. Apparently, the drag levels predicted by IGal2D solver are higher than those resulting from the XFOIL analysis for all the

airfoils composing the RG15 family. On the other hand, a better match is observed for the lift coefficient curves, which tends to improve as the thickness-to-chord ratio of the airfoil increases.

300,000 Reynolds Number							
Airfoil	RG15	RG15-(00)-70-1	RG15-(10)-70-1	RG15-(20)-70-1	RG15-(30)-70-1	RG15-(40)-70-1	RG15-(50)-70-1
XFOIL (L/D) _{max}	78.76	78.65	77.80	77.31	76.56	75.84	75.12
2D RANS (L/D) _{max}	53.64	52.80	52.31	52.34	52.85	51.47	51.89

Table 7.6: Comparison between the results of XFOIL and RANS solvers, in terms of the maximum lift-to-drag ratio.

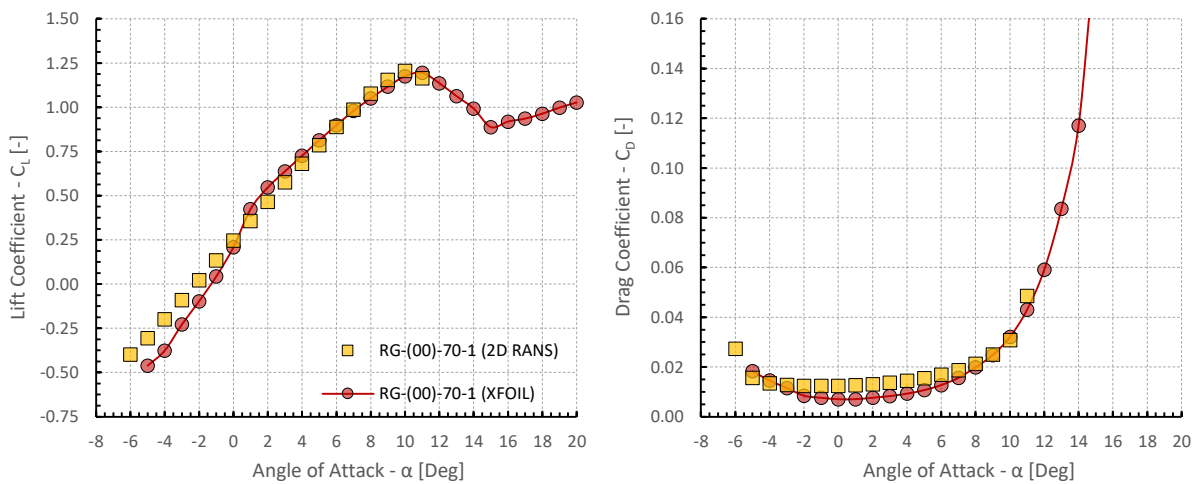


Figure 7.11: Comparison between the lift and drag curves obtained by XFOIL and IGal2D solvers for the RG15-(00)-70-1 airfoil at $Re = 300,000$.

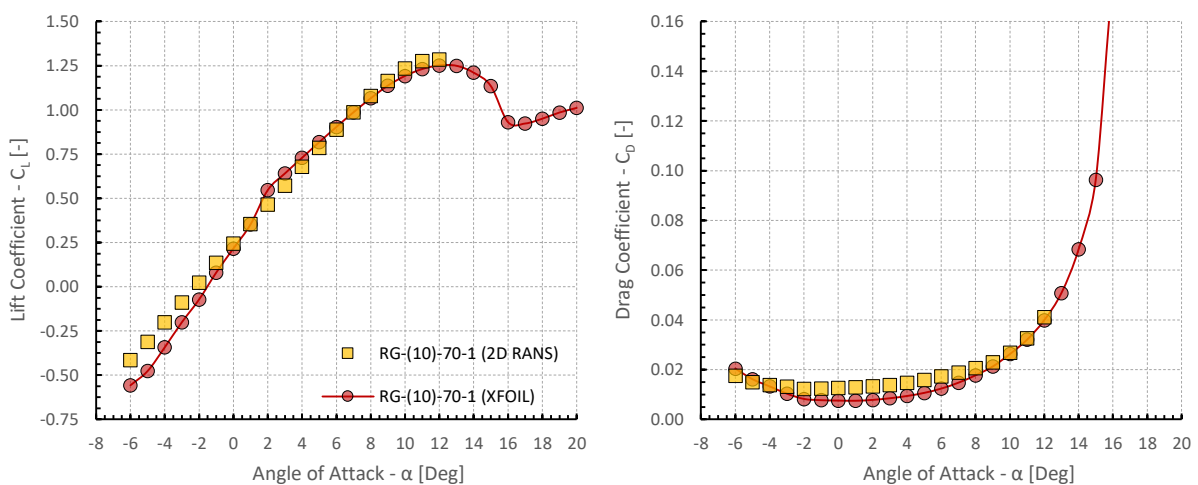


Figure 7.12: Comparison between the lift and drag curves obtained by XFOIL and IGal2D solvers for the RG15-(10)-70-1 airfoil at $Re = 300,000$.

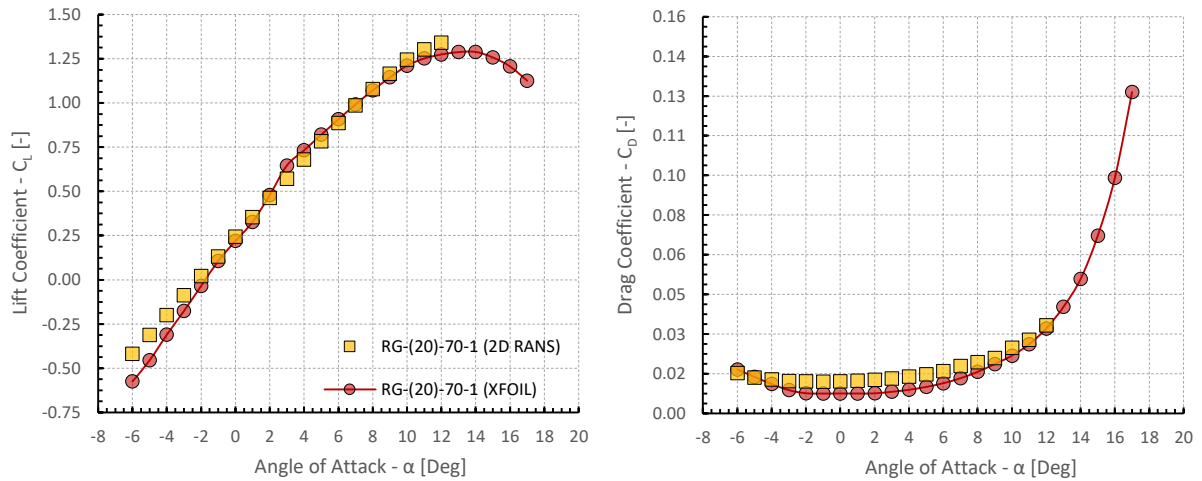


Figure 7.13: Comparison between the lift and drag curves obtained by XFOIL and IGal2D solvers for the RG15-(20)-70-1 airfoil at $Re = 300,000$.

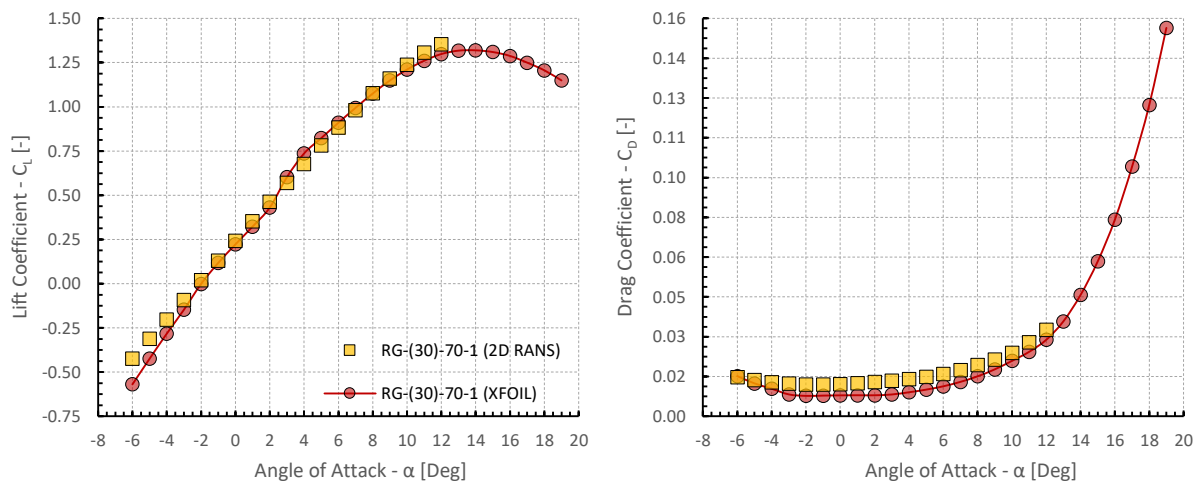


Figure 7.14: Comparison between the lift and drag curves obtained by XFOIL and IGal2D solvers for the RG15-(30)-70-1 airfoil at $Re = 300,000$.

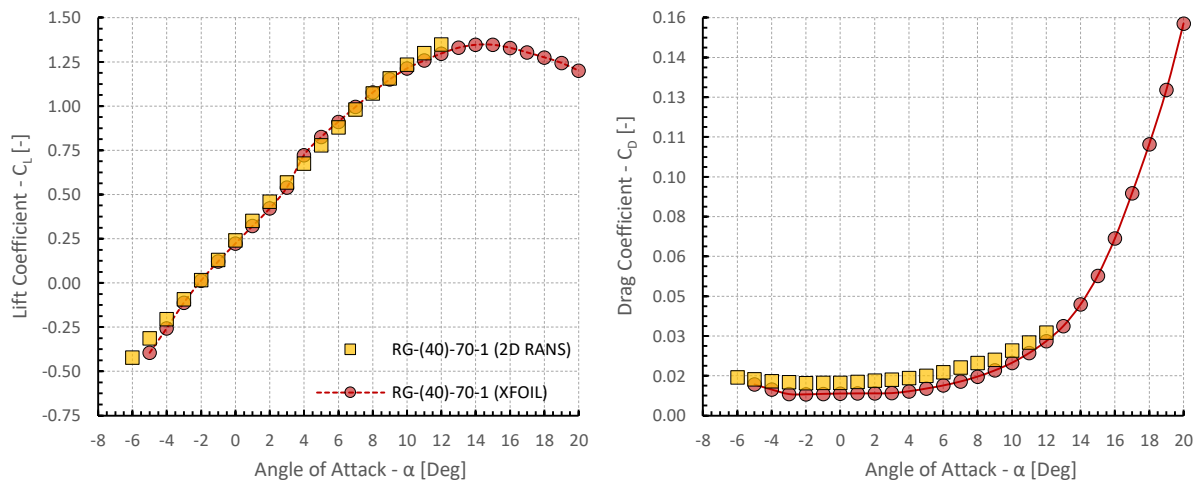


Figure 7.15: Comparison between the lift and drag curves obtained by XFOIL and IGal2D solvers for the RG15-(40)-70-1 airfoil at $Re = 300,000$.

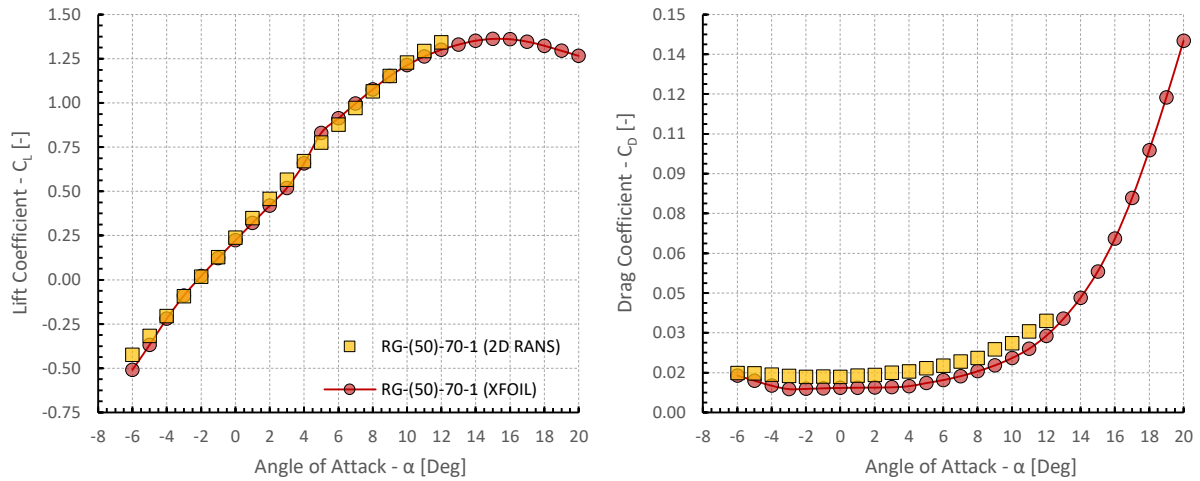


Figure 7.16: Comparison between the lift and drag curves obtained by XFOIL and IGal2D solvers for the RG15-(50)-70-1 airfoil at $Re = 300,000$.

7.3.2.3 Flow Field Visualizations

One of the most characteristic feature of the flow field around each one of the airfoils composing the RG15 family is the formation of a recirculation zone behind the rounded trailing edge, which is generally composed by two distinct vortex rings. Figure 7.17 illustrates the recirculation region behind the trailing edge of the proposed airfoils at $\alpha = 0^\circ$ and $Re = 300,000$. The vortex size is approximately equal to 1 percent of the chord length, while no variation in both size and behavior of the particular recirculation area has been observed by increasing the thickness-to-chord ratio of the airfoil.

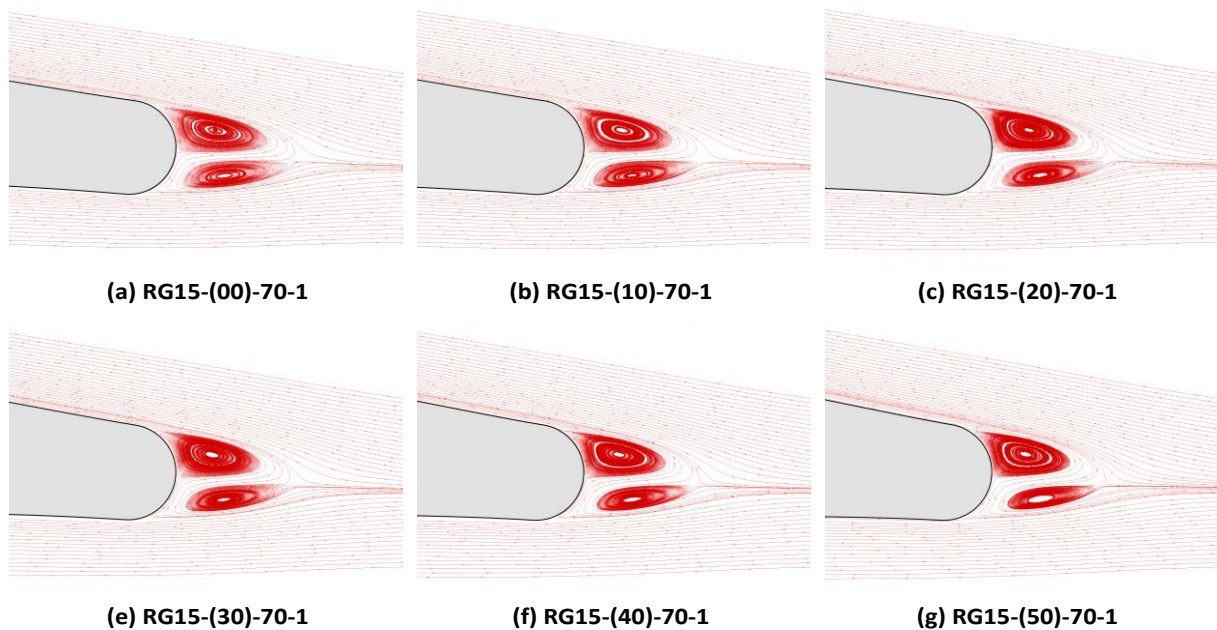


Figure 7.17: Recirculation area behind the rounded trailing edges of the proposed airfoils at $\alpha = 0^\circ$ and $Re = 300,000$.

Although the size of the recirculation zone seems not to be influenced by the thickness-to-chord ratio, it is highly dependent upon the angle of attack. Figure 7.18 presents the variation of the recirculation zone behind the trailing edge of the RG15-(30)-70-1 airfoil at $Re = 300,000$ for several angles of attack between -6° and 12° . As it can be observed, the recirculation zone size decreases as the angle of attack increases, until a trailing edge stall is established. Then, the recirculation region behind the trailing edge is substituted by a separated flow located on the suction side of the airfoil. According to the available numerical results, the first appearance of a trailing edge stall for the RG15-(30)-70-1 airfoil at $Re = 300,000$ was observed at an angle of attack between 10° and 11° . A similar behavior in terms of the recirculation zone behind the rounded trailing edge was found during the analysis of the numerical results for the rest airfoils of the RG15 family. However, in the cases of RG15-(40)-70-1 and RG15-(50)-70-1 airfoils, the first appearance of a trailing edge stall was observed at an angle of attack between 9° and 10° (that is slightly smaller than the corresponding angle of attack for the rest of the RG15 airfoils).

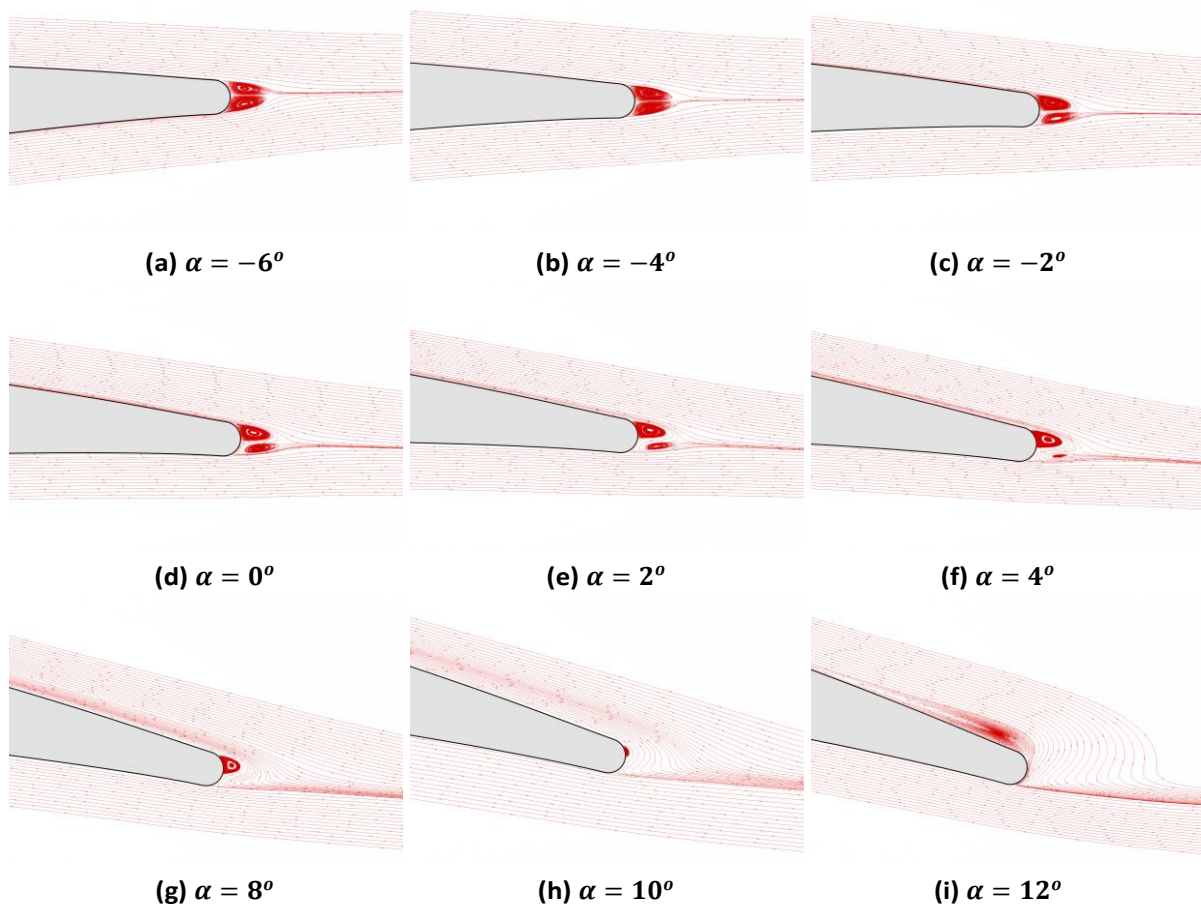


Figure 7.18: Variation of the recirculation zone behind the trailing edge of the RG15-(30)-70-1 airfoil with the angle of attack at $Re = 300,000$.

Apart from the improvement of the structural characteristics, the thickening of the RG15 airfoil seems to also have a beneficial impact on the appearance of separation bubbles. Especially, as the thickness-to-chord ratio increases the first appearance of a separation bubble moves to higher angles of attack. Figure 7.19 illustrates the velocity streamlines around the leading edge of the airfoils composing the proposed RG15 family at $\alpha = 12^\circ$. As it is observed, an open separation area has been formed on the suction side of RG15-(00)-70-1. However, by increasing the thickness-to-chord ratio, the open separation area is substituted by a short separation bubble (Figure 7.19b) covering a chordwise extend of approximately 1.6%. Further increase of the airfoil thickness results in the reduction of the bubble's size, accompanied by its movement away from the leading edge. Eventually, no separation bubble was detected on the upper surface of RG-(50)-70-1. Finally, Figure 7.20 and Figure 7.21 illustrate the pressure and axial velocity contours for each one of the airfoils composing the RG15 family at the angle of attack in which the maximum lift-to-drag ratio was detected.

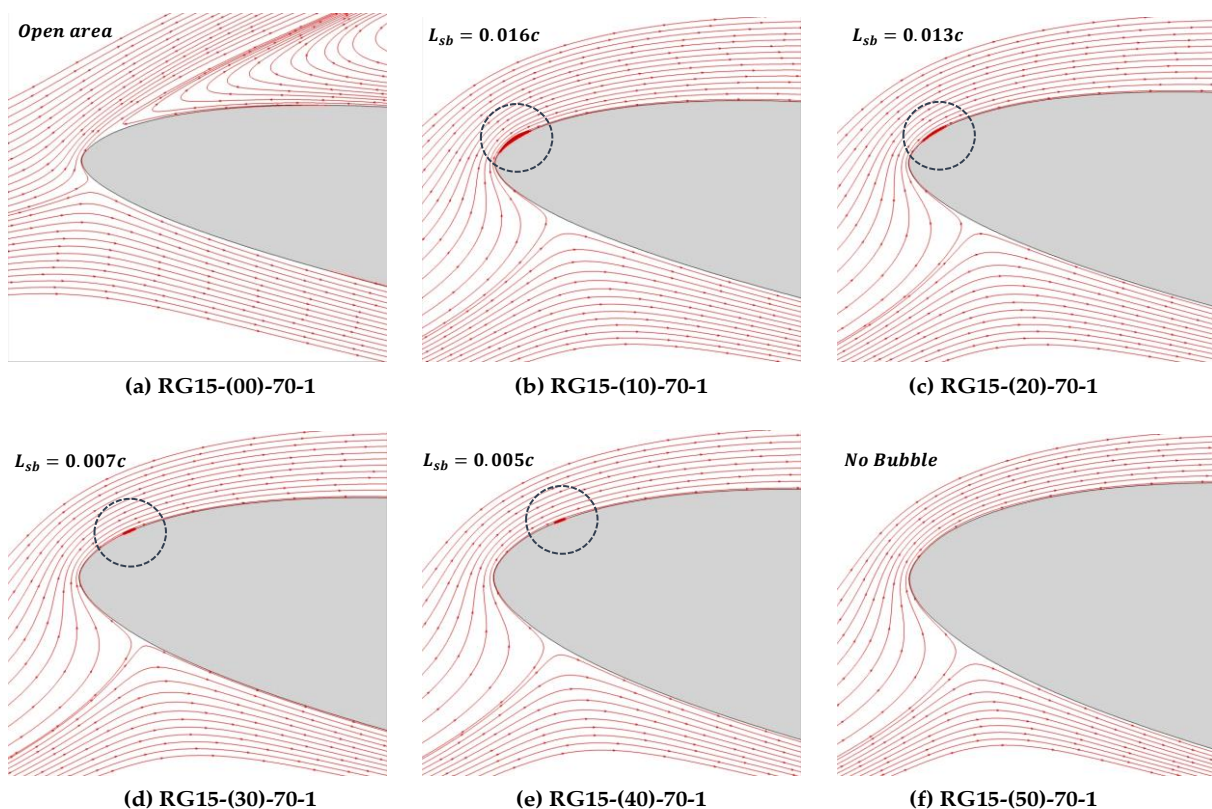


Figure 7.19: The variation of laminar separation bubble with thickness-to-chord ratio at $\alpha = 12^\circ$.

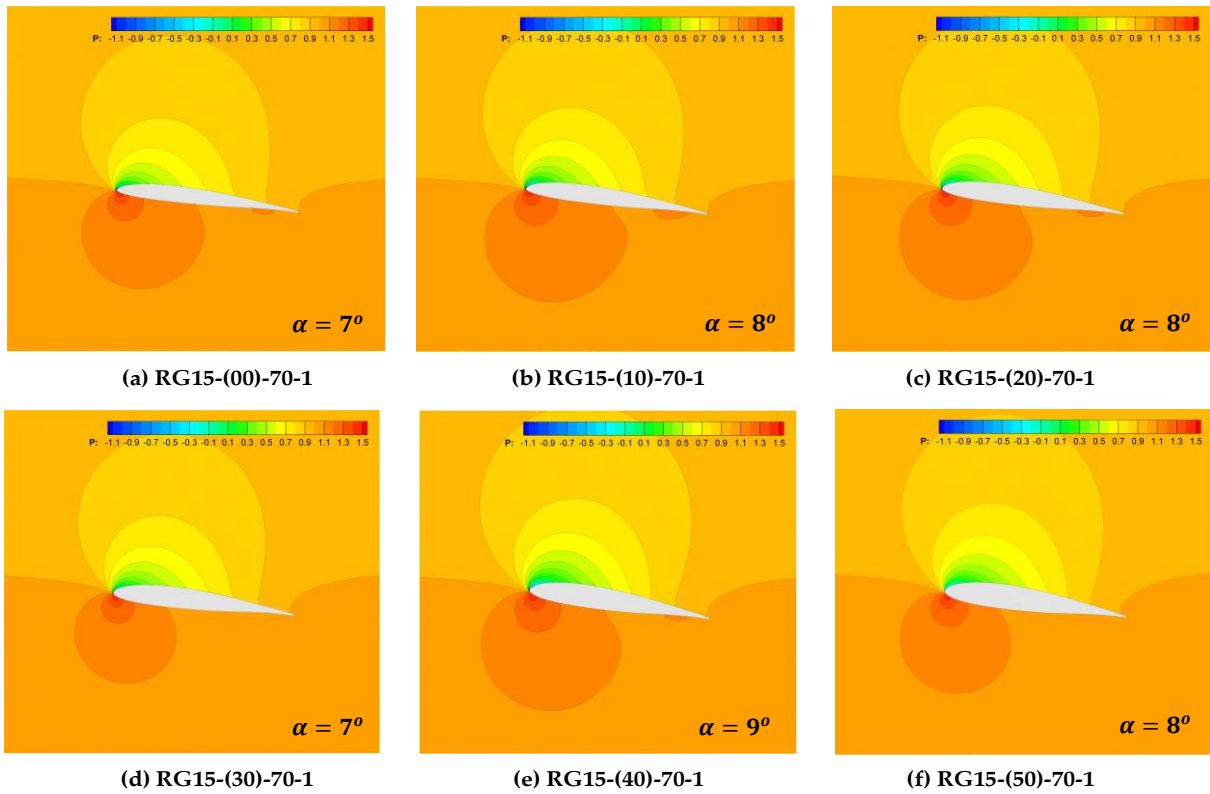


Figure 7.20: The pressure contours around each one of the airfoils composing the RG15 family at the angle of attack leading to the maximum lift-to-drag ratio ($Re = 300,000$).

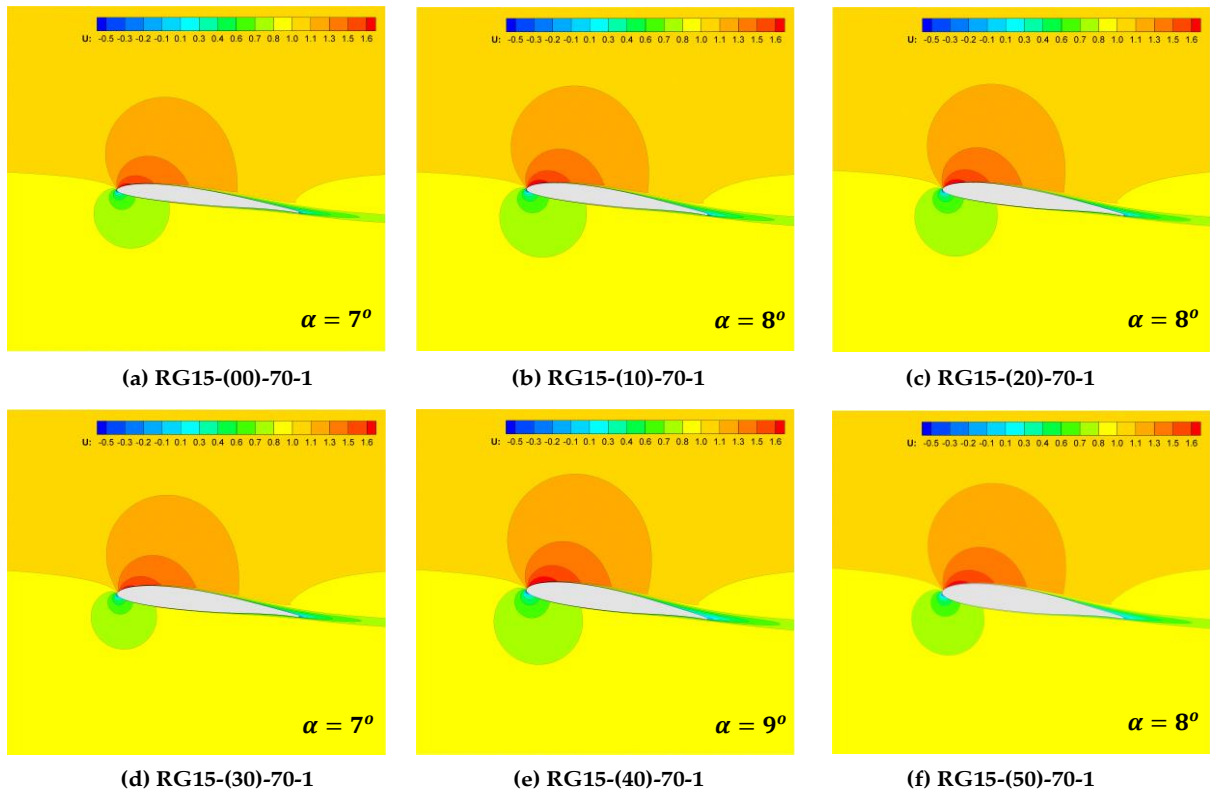


Figure 7.21: The axial velocity contours around each one of the airfoils composing the RG15 family at the angle of attack leading to the maximum lift-to-drag ratio ($Re = 300,000$).

7.4 Summary

In this study, a low-Reynolds airfoils family (consisted of six airfoils) suitable for the entire blade span of small horizontal-axis wind turbines has been designed, aiming to reduce the effects related to laminar separation, increase the structural integrity of the blade, enhance the startup behavior of the wind turbine and meet the current blade manufacturing limitations. Initially, 5 thickened airfoils were constructed based on the RG15 airfoil. According to the followed methodology, the thickened airfoils were designed in such a way that they have the same mean camber line (MCL), as compared to the one of the original RG15 airfoil (so as to retain its desirable aerodynamic characteristics), but an increased thickness-to-chord ratio distribution by 50%, 40%, 30%, 20% and 10% respectively. Then, another custom script was applied to the original and the thickened RG15 airfoils, for the generation of a rounded trailing edge without truncating the airfoil, through the proper modification (local thickening) of the provided airfoil geometries. The final airfoil family resulted through the application of a parabolic thickness distribution to the thickened airfoils, at their trailing edge region, setting the value for the blending distance equal to 70% and the trailing edge radius equal to 0.5% of the chord length respectively. According to the aerodynamic evaluations performed with XFOIL code at various low Reynolds numbers, the dependence of the blending distance on the lift and drag coefficients was found practically zero; the same conclusion was drawn for the dependence of the aerodynamic coefficients on the rounded trailing edge with a radius of 0.5% of the chord.

The aerodynamic performance of the entire RG15 airfoil family was initially evaluated by using XFOIL software for various low Reynolds numbers ranging from $Re = 60,000$ to $Re = 300,000$. The results of the XFOIL analysis revealed that the increase of the thickness-to-chord ratio leads to the reduction in the maximum lift-to-drag ratio for each one of the considered Reynolds numbers. However, as the Reynolds number increases the particular percentage reduction decreases. Apparently, the maximum reduction in the maximum lift-to-drag ratio, as compared to the one of the original RG15 airfoil, was found for the lowest Re examined (60,000) and the RG15-(50)-70-1 airfoil (the thicker airfoil of the RG15 family); this percentage reduction was equal to 12.68%. The corresponding percentage at $Re = 300,000$ was equal to 4.6%. Nevertheless, even the largest reduction of the maximum lift-to-drag ratio seems minor given that this airfoil has a maximum thickness-to-chord ratio that is 50% higher than the maximum thickness-to-chord ratio of the baseline RG15 airfoil, accompanied by cross-sectional area that has been increased by approximately 52%. On the other hand, a growth of the maximum lift coefficient for each Re was found by increasing the thickness-to-chord ratio.

Moreover, the performance of the RG15 airfoil family was further examined by employing an in-house 2D RANS solver, using the standard two-equation SST $k - \omega$ turbulence model.

The RANS simulations were performed at $Re = 300,000$. Although the results of the RANS simulation were generally in accordance with those of XFOIL, a notable over-estimation of the drag coefficient was detected, leading to the under-estimation of the lift-to-drag ratio. Such an outcome clearly indicates that a low Reynolds number correction model is essential, in order to increase the accuracy of the numerical results. Finally, the behavior of the recirculation area behind the rounded trailing edge for different angles of attack was examined, while the thickening of the airfoils was found to have a beneficial impact on the appearance of laminar separation bubbles.

Chapter 8

A Coupled RANS – BEM Model

This chapter features the development and numerical validation of an axisymmetric RANS - BEM model, which relies on the combination of the in-house BEM and IGal2D codes, for the simultaneous prediction of the wind turbine rotor performance and surrounding flow characteristics. In particular, the first part of the current chapter provides an implementation overview of the coupled RANS - BEM model, while the second part includes a detailed validation study on the proposed methodology.

8.1 Overview

In recent years, the ability of BEM models to adequately predict aerodynamic loads and rotor power curves for a wide range of wind turbine configurations and operating conditions has been successfully validated against experimental data (Bangga and Lutz, 2021; Xu *et al.*, 2019; Yang *et al.*, 2014), whereas their application has been extended to shrouded wind turbines as well (Leloudas *et al.*, 2017; Rio Vaz *et al.*, 2014). Nevertheless, momentum theory inherently fails to capture the rotor influence on the surrounding flow and, in turn, to predict wake characteristics (Malki *et al.*, 2013). Definitely, such information could be obtained by employing detailed computational fluid dynamics models, either RANS or Large Eddy Simulation (LES) ones, with a fully resolved rotor geometry (Aranake *et al.*, 2015; Watanabe and Ohya, 2019); however, these high-fidelity numerical approaches call for excessive computational cost, especially when integrated within iterative design optimization schemes. Besides, their implementation entails significant challenges stemming from the three-dimensional nature of the problem. Against this background, a wide family of hybrid models combining computational fluid dynamics techniques with BEM or actuator disc theory, have been recently proposed (Behrouzifar and Darbandi, 2019; Belloni *et al.*, 2017; Guo *et al.*, 2015; Khamlaj and Rumpfkeil, 2018; Malki *et al.*, 2013; Turnock *et al.*, 2011; Zhong *et al.*, 2019).

The fundamental idea behind the so-called CFD - BEM approaches relies on replacing the momentum part of the classical BEM theory with a more elaborate flow model, such as the Navier-Stokes or Euler equations, while assuming an actuator disc representation of the actual rotor geometry (Malki *et al.*, 2013). Eventually, the rotor blades are modelled by means of body force terms (naturally included within the momentum conservation laws) and blade element theory equations. The main advantage of this method is that the physical characteristics of the rotor blades can still be introduced within the analysis by using source terms, rather than being specifically resolved using an exact geometry, allowing for less complicated grids. Besides, the

representation of the rotor geometry with an actuator disc renders the entire flow field axisymmetric, enabling the utilization of time-saving axisymmetric solvers. Another significant advantage of this method is that it can be equally applied to the cases of unshrouded and shrouded wind turbines, in contrast to the stand-alone BEM method, where proper modification of the classical momentum theory is required in order to include the diffuser's effect (Leloudas *et al.*, 2017; Rio Vaz *et al.*, 2014). This chapter presents the development of an efficient RANS - BEM model, implemented by coupling the recently in-house developed axisymmetric RANS solver IGal2D (Leloudas *et al.*, 2021; Lygidakis *et al.*, 2020) with the also in-house developed BEM code (Leloudas *et al.*, 2017).

8.2 Flow Modeling and Blade Representation

Flow modelling is based on the axisymmetric formulation of the incompressible RANS equations, which essentially provide a time-averaged representation of mass and momentum conservation laws (Blazek, 2015). Eventually, by adopting a conservative formulation, and introducing the artificial compressibility approach (Chorin, 1967) for coupling pressure and velocity fields, the axisymmetric RANS equations for incompressible fluid motion, in terms of dimensionless parameters, can be expressed as (Leloudas *et al.*, 2021):

Continuity:

$$\frac{\partial p}{\partial t} + \frac{\partial \beta u_z}{\partial z} + \frac{\partial \beta u_r}{\partial r} = -\frac{\beta u_r}{r} \quad (8.1)$$

Radial Momentum (r):

$$\frac{\partial u_r}{\partial t} + \frac{\partial (u_z u_r)}{\partial z} + \frac{\partial (u_r^2 + p)}{\partial r} - \frac{\partial \tau_{zr}}{\partial z} - \frac{\partial \tau_{rr}}{\partial r} = -\frac{u_r^2}{r} + \frac{\tau_{rr}}{r} - \frac{\tau_{\theta\theta}}{r} + \frac{u_\theta^2}{r} + f_r \quad (8.2)$$

Azimuthal Momentum (θ):

$$\frac{\partial u_\theta}{\partial t} + \frac{\partial (u_z u_\theta)}{\partial z} + \frac{\partial (u_r u_\theta)}{\partial r} - \frac{\partial \tau_{z\theta}}{\partial z} - \frac{\partial \tau_{r\theta}}{\partial r} = \frac{2}{r} (\tau_{r\theta} - u_r u_\theta) + f_\theta \quad (8.3)$$

Axial Momentum (z):

$$\frac{\partial u_z}{\partial t} + \frac{\partial (u_z^2 + p)}{\partial z} + \frac{\partial (u_z u_r)}{\partial r} - \frac{\partial \tau_{zz}}{\partial z} - \frac{\partial \tau_{zr}}{\partial r} = \frac{\tau_{zr}}{r} - \frac{u_z u_r}{r} + f_z \quad (8.4)$$

Please recall that f_z, f_r, f_θ denote the momentum source terms (body forces per unit volume). These terms provide a convenient means by which the effect of external objects, such as wind turbine blades, can be introduced into the momentum equations (Siebert and Yocum, 1993),

actually forming the basis of RANS - BEM concept. Detailed information on the governing flow equations, as well as on the academic IGal2D solver employed for their numerical solution, can be found in Chapter 4.

The computation of axial and tangential force distributions over the actuator (rotor) disk, which are eventually fed into the flow model by means of the momentum source terms, is performed using BEM theory, and particularly by employing the in-house developed BEM code – a detailed description of the theoretical background underlying the current BEM model is given in Chapter 2. At this point, let us recall that in the framework of a stand-alone BEM simulation the calculation of induced velocities at the rotor plane is achieved by applying a fixed-point iteration scheme, in which the induction at the current iterative step is expressed as a function of the induction at the previous step (McWilliam and Crawford, 2011); an overview of the adopted iterative process is presented in Section 2.3.4. However, the implementation of such an iterative process during the application of a coupled RANS - BEM model is not actually required; in fact, a coupled RANS - BEM model allows for the direct calculation of the induced velocities by means of Eq. (2.63) and Eq. (2.64), since the values of axial and tangential velocity components at the disc are explicitly provided by the RANS solver. In this regard, the in-house developed BEM code has been properly modified so as to be capable of operating either in stand-alone mode or coupled with IGal2D solver, within the context of a RANS - BEM simulation. In the latter case, the source terms of the axial (f_z) and tangential (f_θ) momentum equations must be replaced with the total axial and tangential forces per unit volume. In the adopted axisymmetric coordinate system, a two-dimensional control cell with an axial length of dz and a radial length of dr represents a volume of $2\pi r dr dz$. Therefore, the forces per unit volume are given as:

$$f_z = B_R F_n dr / 2\pi r dr dz, \quad (8.5)$$

$$f_\theta = B_R F_t dr / 2\pi r dr dz. \quad (8.6)$$

Here, it is recalled that BEM theory neglects radial interaction between the blade elements, hence $f_r = 0$. In addition, please note that the aforementioned source terms are applied only to the computational cells within the actuator disc region.

8.3 Coupling Approach

The entire coupling procedure is coordinated by IGal2D software. After the initialization stage of the axisymmetric flow solver, a single stand-alone BEM simulation is performed, in order to provide an initial estimation of the aerodynamic loads; then, the axial and tangential force distributions (F_n and F_t) are transferred into the IGal2D software and the source term

formulation is implemented. At this point, please recall that IGal2D solver adopts a dimensionless formulation of the governing flow equations, while the BEM code a dimensional one. Therefore, prior to any force or velocity exchange, the respective flow quantities have to properly normalized. Given an initial approximation of the aerodynamic loads, the RANS solver initiates. Interaction between IGal2D and BEM software is not performed for every internal RANS iteration, since this proved to adversely affect convergence. Instead, interaction is enabled after the completion of a user-prescribed finite number of internal RANS iterations. At each interaction stage, the axial ($u_{z,d}$) and tangential ($u_{\theta,d}$) velocity components at the rotor plane are fed into the BEM solver. Subsequently, the BEM code runs in actuator disc mode and feeds back to IGal2D the updated force distributions, closing the interaction loop. For the interpolation of blade forces and velocities between the grid nodes and blade elements appropriate Matlab scripts are executed, implementing a B-Spline interpolation. The simulation is terminated when the established residual criteria are satisfied. A schematic overview of the adopted coupling methodology is provided by the flow chart in Figure 8.1.

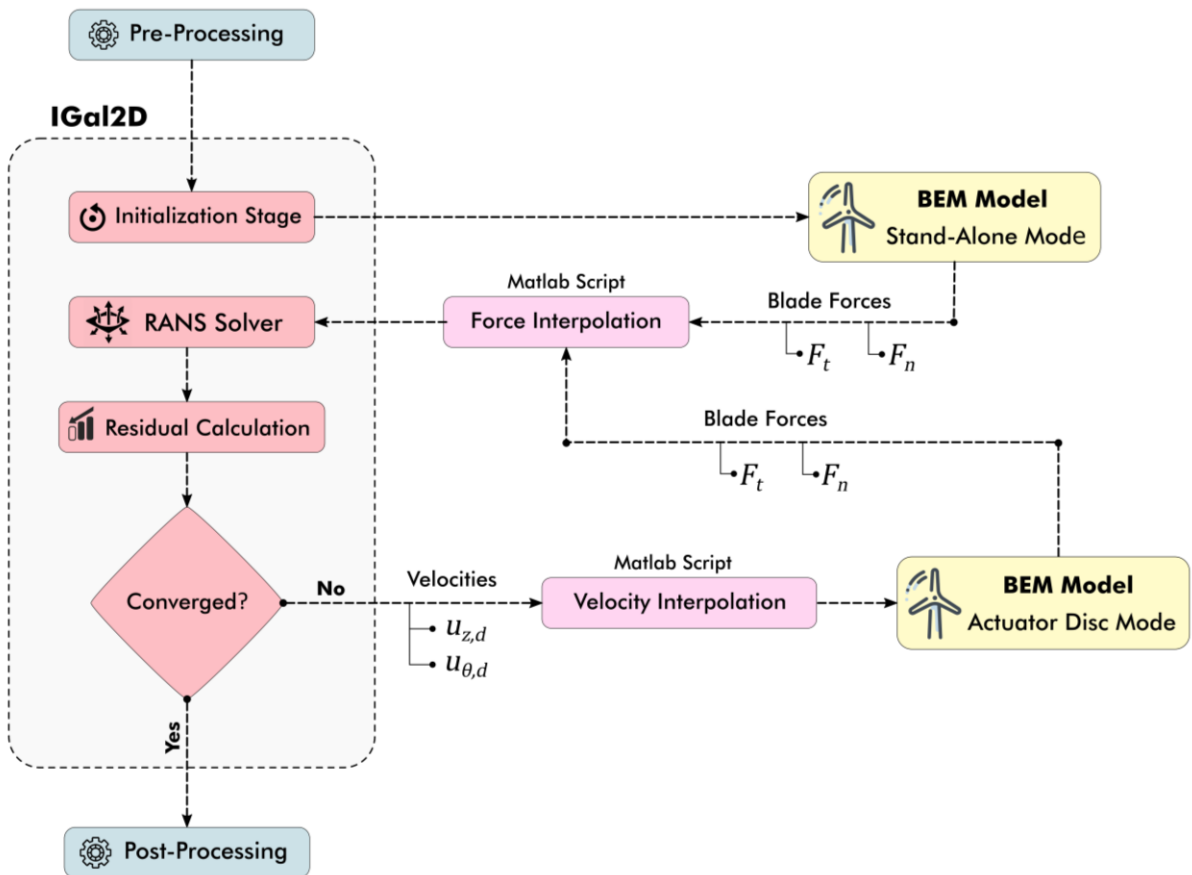


Figure 8.1: Flow chart of the RANS - BEM methodology.

8.4 Numerical Validation of the RANS-BEM Model

The current section aims to investigate and eventually validate the ability of the proposed RANS - BEM methodology to accurately predict the aerodynamic performance and power output of both conventional horizontal-axis and shrouded wind turbine rotors, as well as the characteristics of the surrounding flow field.

8.4.1 NREL 5-MW Reference Wind Turbine

The first validation case involves the performance prediction of the NREL 5-MW reference wind turbine, which was originally developed by National Renewable Energy Laboratory and reflects the design specifications of a utility-scale system for offshore energy production in the megawatt range (Jonkman *et al.*, 2009). The particular variable-speed and pitch-regulated wind turbine system is characterized by a three-bladed upwind rotor with a diameter of approximately 126 meters; detailed information on the geometric characteristics of the NREL 5-MW wind turbine blade are provided in Table 3.4. In this validation study, four typical points within the operating envelope of NREL 5-MW reference wind turbine are considered, covering the major control regions of the encountered system, as shown in Table 8.1. In particular, Region 2 refers to variable speed control, Region 3 refers to variable pitch control and finally, Region 2.5 refers to the transitional region between variable speed and variable pitch control.

Case	Wind Velocity	Rotor Speed	Pitch Angle	TSR	Control Region
1	8.0 m/s	9.16 RPM	0.00 deg	7.55	2
2	11.0 m/s	11.89 RPM	0.00 deg	7.13	2.5
3	11.4 m/s	12.06 RPM	0.00 deg	6.97	2.5
4	15.0 m/s	12.10 RPM	10.45 deg	5.32	3

Table 8.1: Summary of the simulation cases for the NREL 5-MW reference wind turbine.

8.4.1.1 Numerical Setup

The computational domain for the numerical simulation of the NREL 5-MW reference wind turbine is illustrated in Figure 8.2. The axial and radial sizes of the domain – as well as the distance of the actuator disc from the upstream and downstream boundaries – were determined based on the recent study of Behrouzifar and Darbandi (2019); in that work the results of previous computational studies were systematically compared in order to establish

suitable computational domain sizes and grid distributions. Accordingly, the axial size of the computational domain in this validation case was set equal to $22R$ and the radial one to $10R$, while the actuator disc was placed at a distance of $6R$ from the inflow boundary (Behrouzifar and Darbandi, 2019). Then, a quadrilateral computational mesh was built, composed by 96,354 cells and 96,976 nodes. The axial length of the grid elements within the actuator disc region was set equal to $1.59 \times 10^{-4}R$. Further refinement of the computational grid, illustrated in Figure 8.3, or further enlargement of the computational domain did not prove to affect the numerical results.

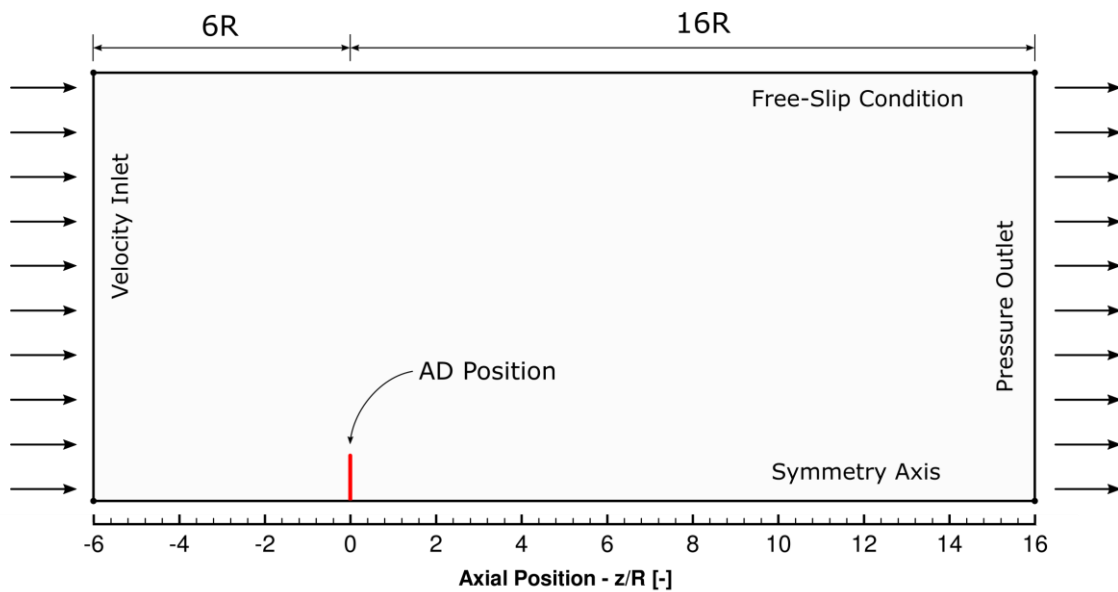


Figure 8.2: The adopted computational domain for the simulation of NREL 5-MW wind turbine.

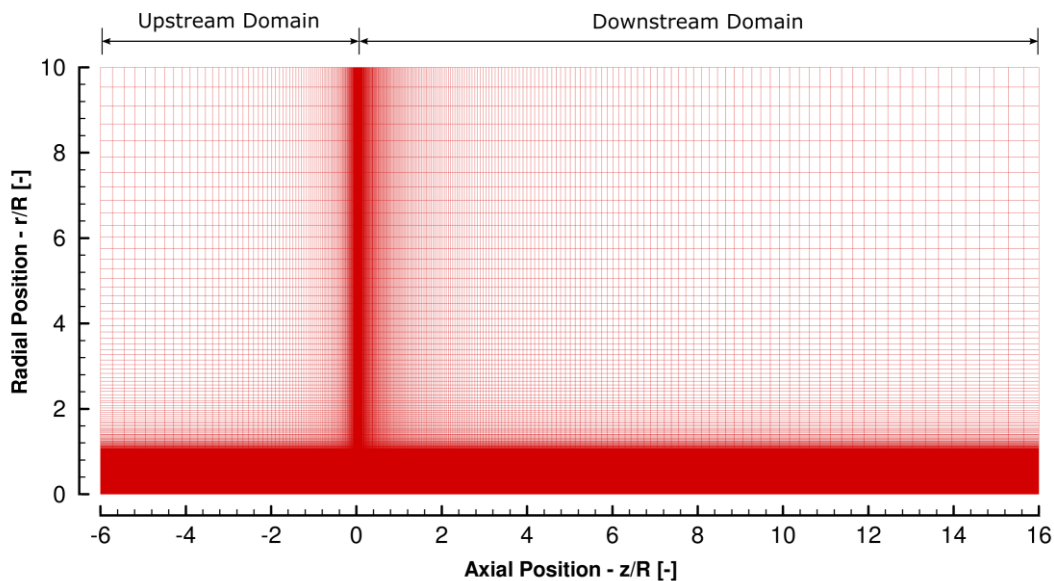


Figure 8.3: Illustration of the quadrilateral computational mesh, employed for the simulation of NREL 5-MW wind turbine.

Finally, regarding the adopted parameters and input data for the BEM calculations, please note that they have been the same with those employed during the stand-alone BEM analysis of the NREL 5-MW wind turbine configuration, presented in Section 3.1.2. The only difference is that in the coupled RANS - BEM simulations, the tip and hub losses are exclusively modelled by using the Shen's correction model (see Section 2.2.5.2).

8.4.1.2 Numerical Results

Unfortunately, no experimental data for the NREL 5-MW reference wind turbine are available, as already mentioned during the assessment of the in-house BEM code. Therefore, at this stage, an indirect validation of the proposed numerical model is performed by comparing the results of IGal2D simulations against the results of independent high-fidelity simulations, available in the literature. Table 8.2 and Table 8.3 contain the predicted aerodynamic power and thrust for the NREL 5-MW wind turbine rotor at free-stream velocities equal to 8 m/s, 11 m/s and 15 m/s. In particular, the results of IGal2D are compared against those reported in the study of Anderson *et al.* (2015), where the aerodynamic characteristics of the NREL 5-MW rotor were examined by employing two numerical simulation tools; namely, an unsteady Reynolds-Averaged Navier-Stokes method (OVERFLOW2) and a large eddy simulation method (SOWFA). Detailed information on the aforementioned simulation tools and the established simulation parameters can be found in the same study.

In terms of aerodynamic power prediction, the results of IGal2D are generally in reasonable agreement with those of SOWFA and OVERFLOW2. For each one of the encountered operating point the prediction of IGal2D lies between those of SOWFA and OVERFLOW2, with the only exception being the case of 11 m/s, where the power prediction of IGal2D is slightly higher than the respective one obtained from SOWFA. In general, the maximum percentage difference between IGal2D and SOWFA was observed at 15 m/s and it was approximately equal to 2.5%. On the contrary, the maximum percentage difference between IGal2D and OVERFLOW2 was observed for 8 m/s and it was approximately equal to 8.5%.

NREL 5MW Reference Wind Turbine – Aerodynamic Power				
Wind Speed	Rotor Speed	IGal2D	SOWFA	OVERFLOW2
8.0 m/s	9.16 RPM	1974 kW	1985 kW	1733 kW
11.0 m/s	11.89 RPM	5066 kW	5061 kW	4650 kW
15.0 m/s	12.10 RPM	5231 kW	5093 kW	5499 kW

Table 8.2: Comparison of predicted power using different turbine simulation tools, for the NREL 5-MW reference wind turbine at various operational points.

Similar levels of accuracy can be observed on the prediction of aerodynamic thrust. Once more, the predictions of IGal2D are between those of SOWFA and OVERFLOW2 for each one of the encountered operating points; yet, much closer to those of SOWFA. In this case, the maximum discrepancy between IGal2D and SOWFA was observed at 15 m/s and it was equal to approximately 1.7%. However, a significant deviation between IGal2D and OVERFLOW2 was found at 15 m/s, equal to 10%. Nevertheless, the percentage difference on thrust prediction results for both 8 m/s and 11 m/s was not larger than 4%.

NREL 5MW Reference Wind Turbine – Aerodynamic Thrust				
Wind Speed	Rotor Speed	IGal2D	SOWFA	OVERFLOW2
8.0 m/s	9.16 RPM	387 kN	382 kN	399 kN
11.0 m/s	11.89 RPM	703 kN	693 kN	733 kN
15.0 m/s	12.10 RPM	413 kN	405 kN	455 kN

Table 8.3: Comparison of predicted thrust by different turbine simulation tools, for the NREL 5-MW reference wind turbine at various operational points.

Figure 8.4 to Figure 8.6 provide a detailed comparison between the results of IGal2D and SOWFA (Anderson *et al.*, 2015) in terms of momentum deficit prediction in the wake of NREL 5-MW wind turbine. The comparisons refer to eight stations downstream of the rotor, corresponding to the following axial positions: 0.16R, 0.5R, 1R, 2R, 4R, 6R, 8R, and 12R. Overall, the results of IGal2D match well with those obtained by SOWFA.

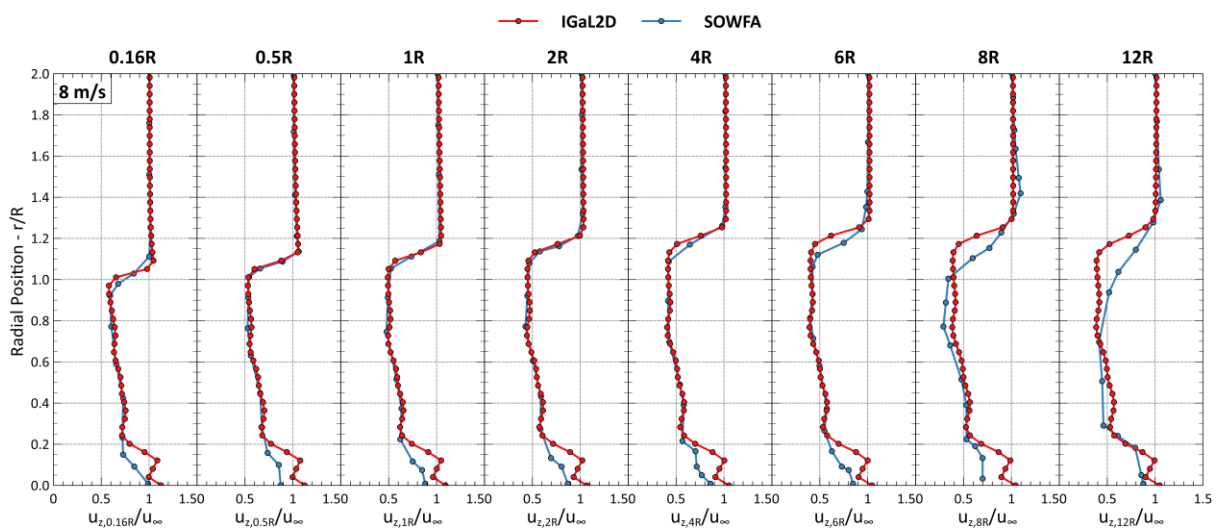


Figure 8.4: Axial momentum deficit predicted by IGal2D and SOWFA for the NREL 5-MW rotor at $u_{\infty} = 8 \text{ m/s}$.

However, some notable discrepancies can be identified as well, which are mainly located around the hub region. Since both models treat the rotor as if it had no hub, this discrepancies probably stem from different turbulence modeling approaches. Similar discrepancies can be also found for 8 m/s and 11 m/s at axial stations after 6R. Particularly, SOWFA seems to predict a larger axial momentum deficit around the radial position corresponding to the blade tip.

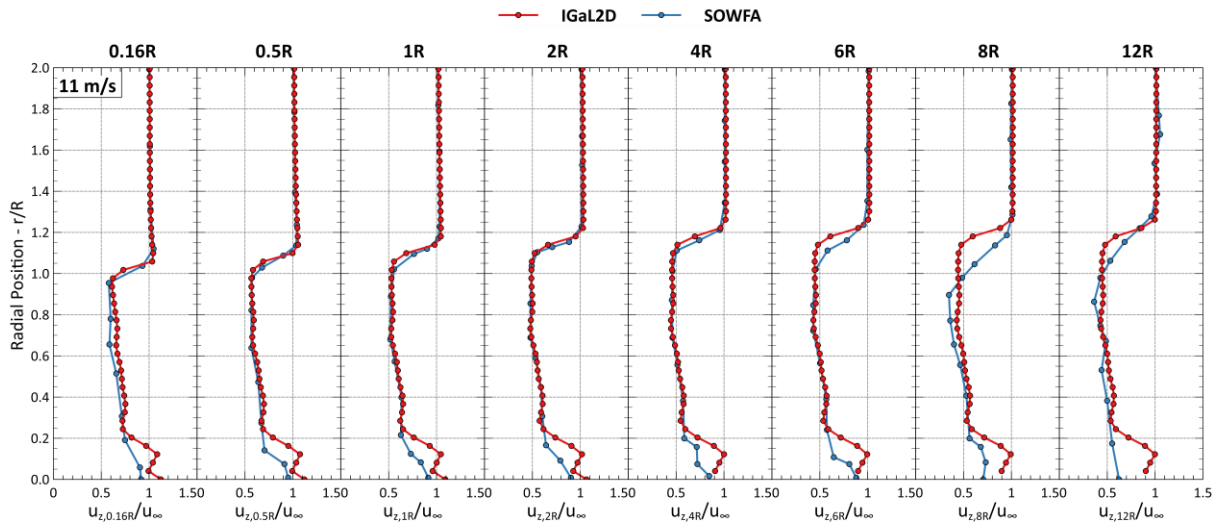


Figure 8.5: Axial momentum deficit predicted by IGA2D and SOWFA for the NREL 5-MW rotor at $u_\infty = 11 \text{ m/s}$.

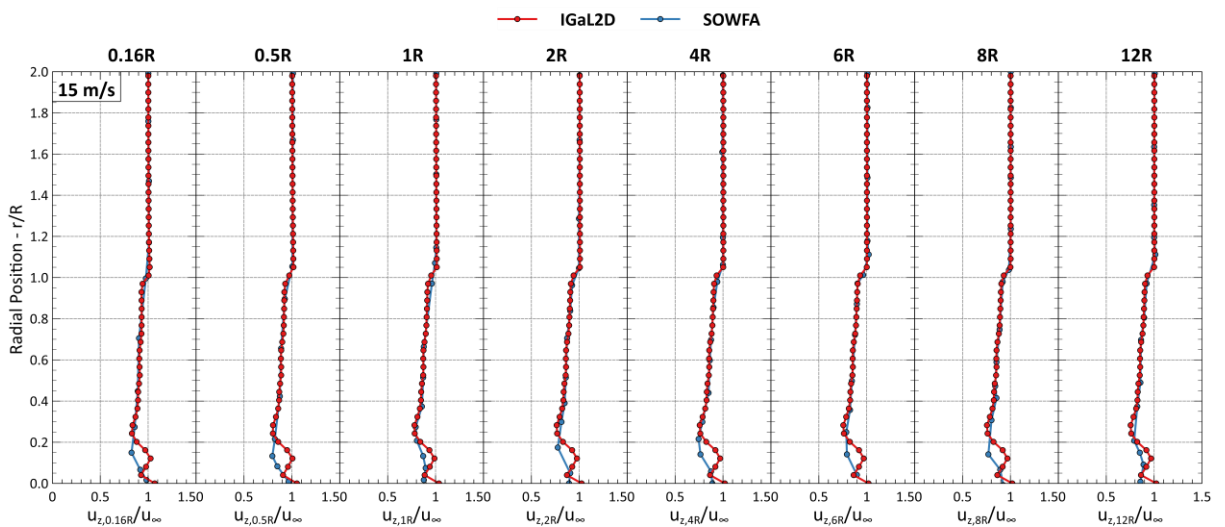


Figure 8.6: Axial momentum deficit predicted by IGA2D and SOWFA for the NREL 5-MW rotor at $u_\infty = 15 \text{ m/s}$.

Finally, in order to further validate the proposed computational model, the corresponding results in terms of axial and tangential force distributions over the NREL 5-MW blade, are compared against those obtained by detailed 3D RANS simulations with a fully resolved rotor

geometry, as they reported in the study of Zhong *et al.* (2019, 2020). The comparisons are performed for the operational conditions in which the particular wind turbine has been rated; namely, an ambient wind speed of 11.4 m/s and a rotational speed of 12.06 RPM. According to the results presented in Figure 8.7, the in-house axisymmetric model is capable of achieving similar levels of accuracy to the definitely much more elaborate reference model.

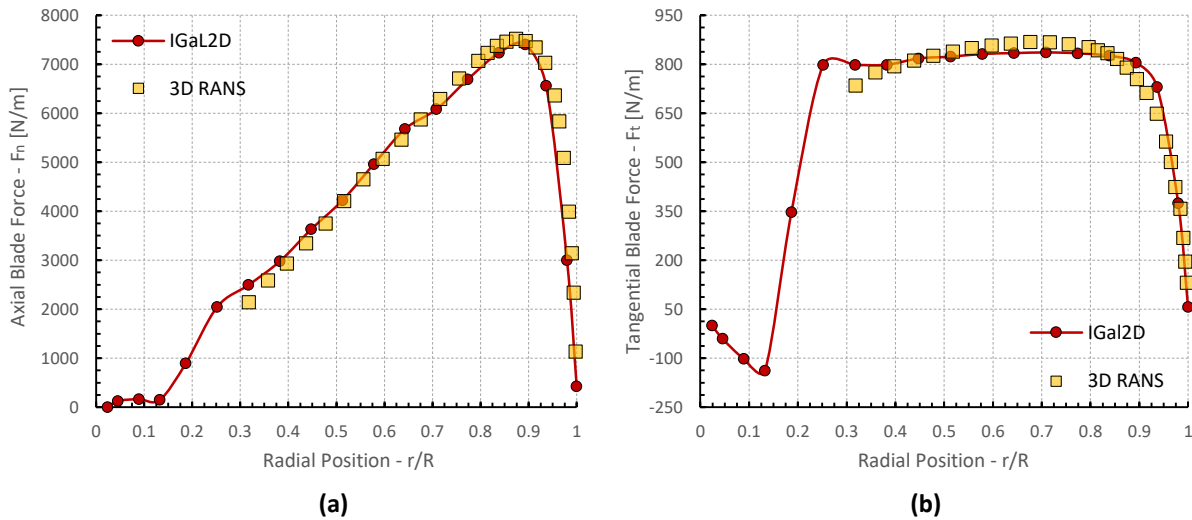


Figure 8.7: Axial and tangential force distribution over the NREL 5-MW blade at 11.4 m/s and 12.06 RPM.

8.4.2 NREL Phase VI Rotor

The second validation case considers the well-documented NREL Phase VI wind turbine, which was extensively investigated during the Unsteady Aerodynamics Experiment (UAE) conducted at the 24.4 m \times 36.6 m wind tunnel facilities of the National Aeronautics and Space Administration (NASA) Ames Research Center (Hand *et al.*, 2001). The scope of that experimental campaign was to obtain accurate quantitative aerodynamic and structural data for the development and validation of enhanced engineering models. The NREL Phase VI wind turbine refers to a stall-regulated configuration with full-span pitch control and a rated capacity of approximately 20 kW; the two-bladed rotor of the wind turbine has a diameter of 10.058 m and operates at a constant speed of 72 RPM (Hand *et al.*, 2001). Overall, the experimental campaign included 30 different operating states and configurations. In this study, the numerical validation of the RANS - BEM model is performed by using the experimental results that correspond to **test sequence S**; the particular test sequence refers to upwind operation, a blade pitch angle of three degrees and zero yaw angle. At this point, please recall that the blade pitch angle is actually referred to the pitch angle of the blade tip, which is defined as the angle between the rotor plane and the chord of the blade tip. Besides,

this validation study considers a shrouded NREL Phase VI wind turbine configuration that was numerically studied by Aranake *et al.* (2013). However, no experimental results are available for the case of shrouded wind turbine. Therefore, IGal2D is validated against the numerical results of 3D RANS simulations reported by Aranake *et al.* (2013). The operating points for both test cases are presented in Table 8.4.

Wind Velocity	Rotor Speed	Tip Pitch Angle	Yaw Angle	Shroud
5 m/s	72 RPM	3.0 Deg	0.0 Deg	NACA 0006
7 m/s	72 RPM	3.0 Deg	0.0 Deg	–

Table 8.4: Summary of the simulation cases for the NREL Phase VI rotor.

The examined shroud geometry is defined by a conventional NACA0006 airfoil with a chord length equal to the rotor radius (5.029 m) that has been placed at an angle of 15 degrees relative to the symmetry axis. The rotor (actuator disc) is located at an axial position of $0.1R$ downstream of the shroud's leading edge. A schematic representation of the shrouded rotor is presented in Figure 8.8. Finally, detailed information on the geometric characteristics of the NREL Phase VI wind turbine blade can be found in Section 3.1.1.

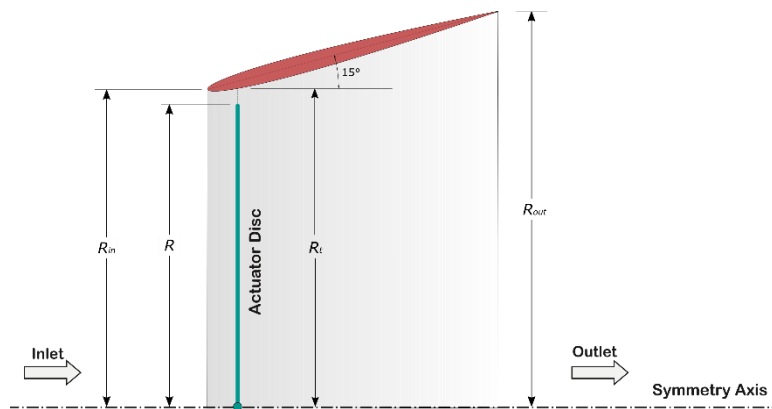


Figure 8.8: Shroud configuration for the NREL Phase VI wind turbine rotor.

8.4.2.1 Numerical Setup

For the numerical simulation of the unshrouded NREL Phase VI wind turbine rotor, the same computational domain and grid as for the previous validation case (Section 8.4.1) was employed. On the other hand, the simulation of the shrouded NREL Phase VI configuration was performed by adopting a larger computational field, which extends $15R$ upstream and $30R$ downstream the rotor; the radial size of the computational domain was set to $15R$. Besides,

a hybrid computational mesh was generated, including 436,116 triangular elements and 42,029 quadrilateral ones. The total number of grid nodes was 261,737 with a target y^+ value below unity. In particular, quadrilateral elements were generated around the shroud surface and the actuator disc regions, while the rest of the computational domain was filled with triangular ones. The domain size and grid resolution were finalized based on a grid independence study. An overview of the employed computational mesh is shown in Figure 8.9.

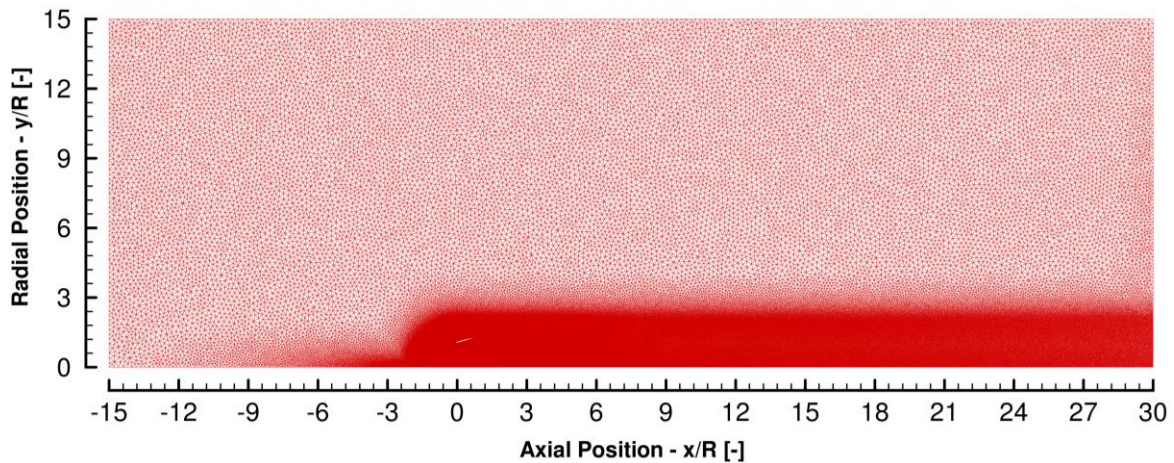


Figure 8.9: Overview of the hybrid computational mesh adopted for the simulation of the shrouded NREL Phase VI wind turbine rotor.

8.4.2.2 Numerical Results – Unshrouded Configuration

For the unshrouded NREL Phase VI rotor, Table 8.5 provides a comparison between the numerically predicted and experimental values of aerodynamic power and thrust at free stream velocity of 7 m/s. Apparently, both reference quantities have accurately been predicted. The percentage difference between the numerical prediction and experimental measurement of aerodynamic power is less than 1%, whereas the respective percentage difference for rotor thrust is approximately 3%. In addition, the axial and tangential force distributions over the NREL Phase VI are compared in Figure 8.10; both distributions have been accurately predicted for the entire blade span.

Wind Speed	IGal2D		NREL Experiment	
	Power [W]	Thrust [N]	Power [W]	Thrust [N]
7.00 m/s	6006	1158	6030	1120

Table 8.5: Numerical predictions and experimental data for power and thrust.

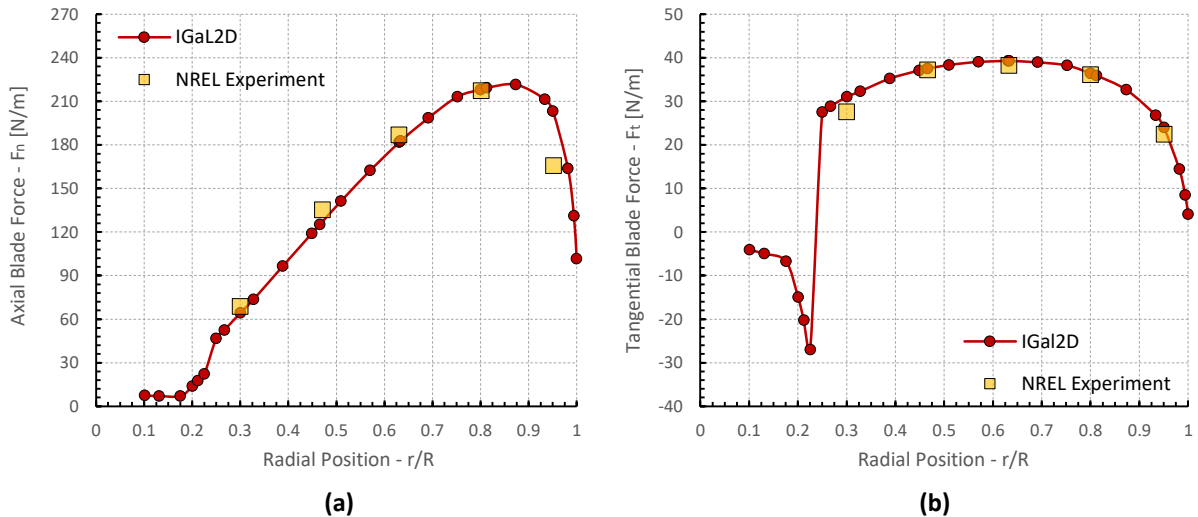


Figure 8.10: Axial and tangential force distributions over the bare NREL Phase VI rotor at 7 m/s.

8.4.2.3 Numerical Results – Shrouded Configuration

As previously mentioned, no experimental data for the shrouded NREL Phase VI rotor are available. Thus, the results of the proposed model are compared against the numerical results of the detailed three-dimensional RANS simulations, reported in the study of Aranake *et al.* (2013). Table 8.6 compares the numerical predictions for the aerodynamic power and thrust, revealing that despite the various simplistic assumptions within the RANS - BEM models, IGal2D is capable of reasonably approximating the results of high-fidelity simulation tools.

Wind Speed	IGal2D		3D RANS	
	Power [W]	Thrust [N]	Power [W]	Thrust [N]
5.00 m/s	4190	957	4013	927

Table 8.6: Numerical predictions for power and thrust, for the shrouded NREL Phase VI rotor.

In addition, Figure 8.11 illustrates the distribution of axial velocity for two upstream positions, three downstream positions and one position just before the rotor plane. As one can observe, the results of IGal2D match well with those of the reference study. Finally, Figure 8.12 provides the numerical predictions of axial and tangential forces along the NREL Phase VI blade. Once more, the prediction of IGal2D is consistent with that of the three-dimensional RANS simulation, even though it does not include a transitional turbulence model, such the one employed in the reference study of Aranake *et al.* (2013). Further validation of IGal2D using experimental data for a second shrouded wind turbine is provided in Section 10.3.1.

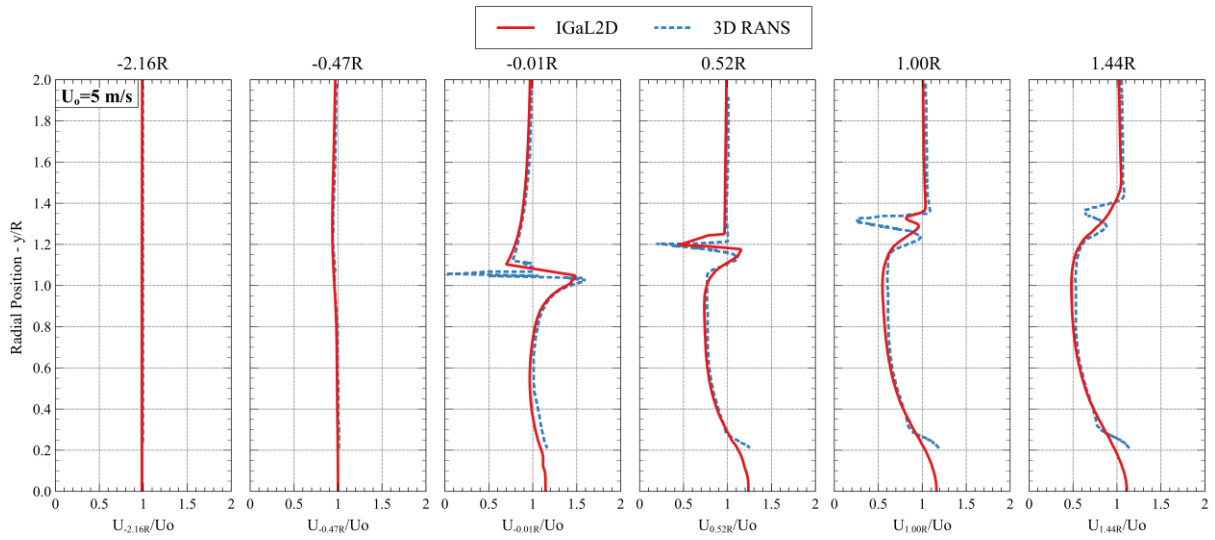


Figure 8.11: Axial momentum deficit for the shrouded NREL Phase VI rotor at 5 m/s.

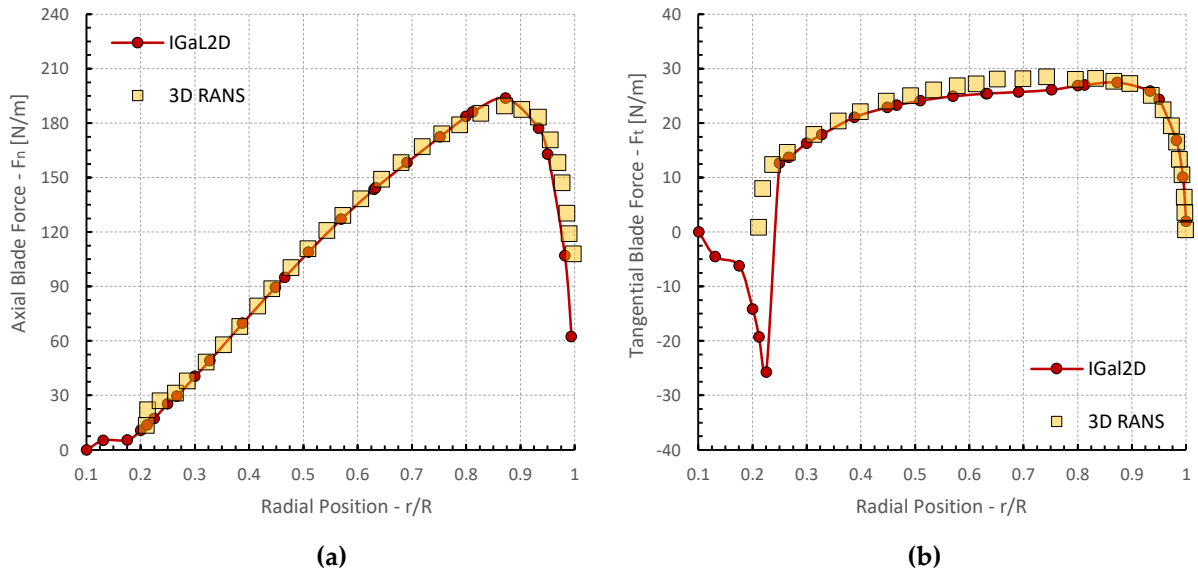


Figure 8.12: Axial and tangential force distribution over the NREL Phase VI blade for the shrouded configuration at 5 m/s.

Chapter 9

Optimization Framework for Shrouded Wind Turbines

This chapter describes a modular optimization framework for the aerodynamic shape optimization of shrouded wind turbines, which combines the analysis tools developed within the current study with a parallel and asynchronous version of a meta-model assisted Differential Evolution (DE) algorithm. The first part of this chapter (Section 9.1) outlines the major features of the in-house developed surrogate-assisted Differential Evolution algorithm employed as the optimizer. The particular asynchronous and parallel version of the current algorithm was developed at the Turbomachinery and Fluid Dynamics laboratory, in the context of the doctoral dissertation of Giorgos A. Strofylas. Subsequently, in Section 9.2, this chapter describes the development of an in-house mesh parameterization and deformation tool that is based on Free-Form Deformation, while the last part of the current chapter (Section 9.3) provides an overview of the proposed optimization framework.

9.1 The Differential Evolution Algorithm

Evolutionary Algorithms (EAs) represent a flexible and robust branch of heuristic methods, characterized by low sensitivity in terms of local minima treatment and efficient sense of balance between exploitation of the best solutions and exploration of the entire search space (Leloudas *et al.*, 2020a). From this perspective, a parallel and asynchronous version of a highly versatile Differential Evolution (DE) algorithm (Strofylas *et al.*, 2018) – that is further enhanced by the addition of two artificial neural networks – has been selected to form the basis of the optimization cases encountered in this study. The particular optimization algorithm is constantly developed within the Turbomachinery and Fluid Dynamics Laboratory (TurboLab – TUC), while the current implementation was mainly devised within the doctoral dissertation of Giorgos Strofylas (Strofylas, 2021).

One of the most characteristic features of the current implementation is “differential mutation”. According to this evolutionary operator, a new chromosome (called trial vector) is produced for each individual within the current population. The creation of a new trial vector relies on the combination of three distinct chromosomes, randomly selected among all the individuals of the current population; the combination strategy involves the addition of the weighted difference vector between the two members of the triplet to the third one, the so called donor. Subsequently, a crossover recombination is applied to the mutant and the parent chromosomes of the current population, which results in the final candidate (trial) vector.

Detailed information on the employed optimization algorithm can be found in the following studies (Leloudas *et al.*, 2018b, 2020a; Nikolos, 2011, 2013; Strofylas, 2021; Strofylas *et al.*, 2018).

9.1.1 Surrogate Models

In each generation of the DE algorithm, every single trial vector has to be initially evaluated and then, to be compared against its parent chromosome; the better-fitted among them will pass to the next generation. The incorporation of surrogate models (or meta-models) within this evaluation procedure provides the opportunity to avoid the costly CFD-based evaluations, using faster approximations instead (Nikolos, 2011). According to the followed approach, a surrogate model is employed to pre-evaluate each trial vector. In case that the result of the pre-evaluation indicates that the trial vector is lower-fitted than its parent chromosome, the latter one is directly passed to the next generation, while the trial vector is abandoned. On the contrary, if the pre-evaluation results that the trial vector is better-fitted than its parent chromosome, then an exact re-evaluation follows, accompanied by a second comparison between the trial and the parent chromosomes. If the trial is still better-fitted than the parent chromosome, then the former one is transferred to the next generation. Otherwise, the trial vector is rejected and the parent chromosome passes to the next generation.

In the current optimization study, the DE algorithm is combined with a Multilayer Perceptron (MLP) and a Radial-Basis Function (RBF) Artificial Neural Networks (ANNs). The utilized surrogate models are used as an ensemble. Even though the available models are re-trained and re-tested in every single generation, using the same training and testing data sets, only the best one between them is chosen to be used for the pre-evaluation of the trial vectors. The selection of the surrogate model (which may be different in each generation) is made using the criterion of the lower testing error.

9.1.2 Parallelization Strategy

The current parallelization strategy has been based on a master-slave architecture and implemented by means of the Message Passing Interface library functions. According to the adopted master-slave approach, all the chromosomes comprising the current population are scattered to the available slave processors (slave nodes). Each one of them is responsible for the evaluation of a single chromosome and the application of the required evolution operators (namely, mutation, crossover and selection). On the other hand, one of the available processors is chosen to be the master node; this master processor coordinates the entire optimization procedure and performs the inexact evaluations, through the use of a surrogate model. The flowcharts describing the parallel implementation of the DE algorithm are provided in Figure

9.1, while a thorough description of the adopted parallelization strategy can be found in the works of Stroyfylas (2021), Stroyfylas *et al.* (2018) and Leloudas *et al.* (2018a, 2018b, 2020a).

9.1.3 Asynchronous Implementation

In the synchronous implementation of the particular algorithm, the succession between two consecutive generations can only be achieved when all the slave processors have finished with the evaluation of their assigned chromosomes. However, as these evaluation times may generally differ, some of the slave processors remain idle, waiting for the last one to reach the so-called synchronization barrier. To overcome this deficiency and reduce the overall time required, an asynchronous update of the current DE algorithm has been developed. According to the asynchronous implementation, the generation is not strictly defined and the current population may include chromosomes that actually belong to different generations. Each newly generated trial vector can directly replace the parent chromosome (if better fitted) and become a member of the current population, just after the end of its evaluation process, without waiting for the end of the evaluation stages of the rest members of the auxiliary population (Stroyfylas *et al.*, 2018). Therefore, individuals can evolve independently (without full coordination between generations), while the improved solutions can contribute immediately to the evolution process, accelerating the convergence rate.

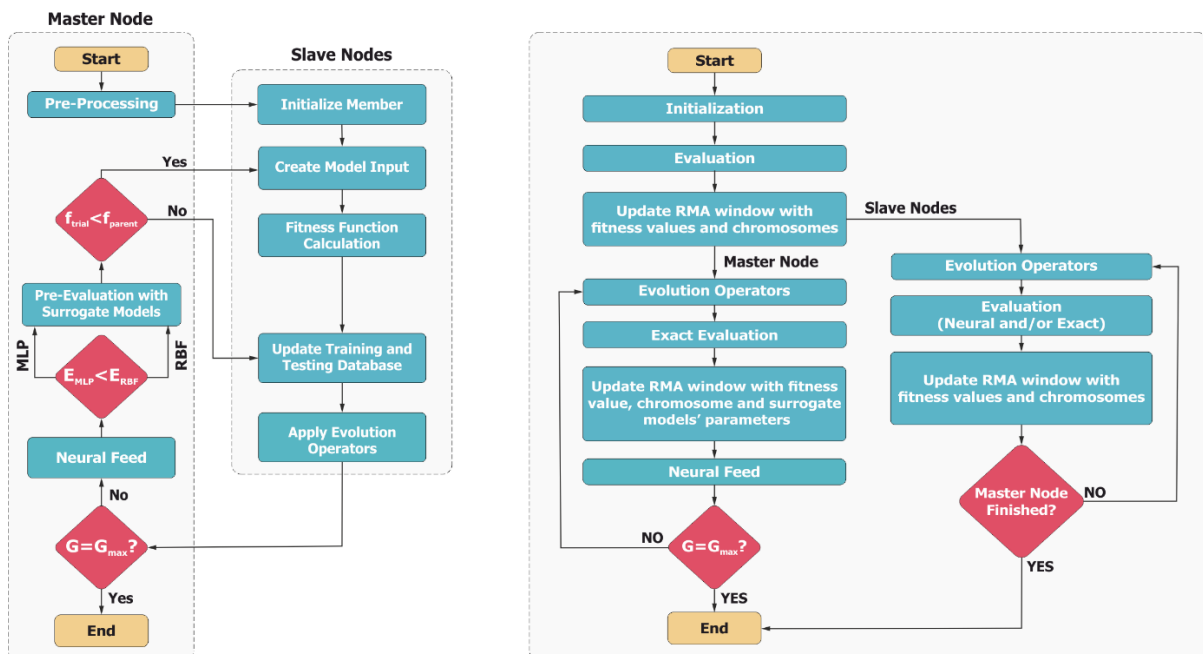


Figure 9.1: Flowcharts of the parallel differential evolution algorithm (Leloudas *et al.*, 2020a).

9.2 Mesh Parameterization and Deformation

Geometry parameterization is one of the most crucial components to any shape optimization methodology; the employed parameterization technique should take into consideration the specific characteristics of the optimization problem at hand, facilitating the detailed, robust and flexible definition of a wide range of potentially complex shapes (Yamazaki *et al.*, 2010). Besides, in the case of numerical shape optimization schemes in which design evaluation is performed by means of calls to a mesh-based solver, a new geometry definition should also be accompanied by either the proper deformation of the initial computational mesh or the generation of a completely new one (Morris *et al.*, 2008). Thus, in such optimization applications, two distinct parameterization strategies are generally followed; according to the first one, a parameterization technique can be used to exclusively control and modify the design geometry, from which a new computational mesh should be then generated, while according to the second one, a parameterization technique can alternatively be used to control and deform the computational mesh itself. Between these approaches, mesh parameterization and deformation techniques are generally preferred over regeneration ones, since they require less computational resources, do not involve the utilization of an automatic mesh generator and prevent the potential introduction of numerical errors within the analysis, due to the change in spatial discretization of the computational domain (Allen and Rendall, 2013; Morris *et al.*, 2008; Yamazaki *et al.*, 2010).

Within the current optimization framework, mesh and geometry parameterization are simultaneously succeeded by employing an in-house developed computational tool, based on the well-known Free-Form Deformation (FFD) technique (Sederberg and Parry, 1986); this is a versatile and powerful point-based methodology that does not require any information about the connectivity of the mesh nodes and results in deformed models with the same topology to the initial one. Consequently, it can equally and effortlessly be applied to both structured and unstructured computational meshes, composed by any type of elements. The fundamental idea underlying the FFD algorithm is to achieve an indirect deformation of the computational mesh by embedding the mesh nodes into a parametric control grid (lattice); then by transforming the geometry of the particular lattice, every node enclosed to it undergoes the corresponding deformation.

Step 1 – Construction of the Parametric Lattice

The first step for the implementation of the FFD method involves the construction of the parametric FFD lattice, which is actually consisted by an ordered mesh of control points, placed in such a way that wraps the design geometry and defines the mesh region to be deformed. Figure 9.2a presents the creation of such a control lattice, built around a NACA 0012

airfoil. Then, a parametric surface is created based on the control points of the particular lattice. Even though Bezier surfaces were used in the original version of FFD, a B-spline-based FFD can also be formulated easily by using the B-Spline basis functions instead of the Bernstein polynomials. In this application, a B-Spline based FFD version is employed, as the alteration of a control point does not modulate the entire B-Spline surface. Hence, a focused deformation can be achieved. The Cartesian coordinates of a mesh point lying within the 2D B-Spline surface may be calculated using the following formula (Piegl and Tiller, 1995):

$$\mathcal{S}(u_t, v_t) = \sum_{i=0}^n \sum_{j=0}^m N_{i,p}(u_t) N_{j,q}(v_t) \mathcal{P}_{ij} \quad (9.1)$$

Here, \mathcal{S} represents the Cartesian coordinate vector of the examined point, while \mathcal{P}_{ij} stand for the position vectors of the control points forming the FFD lattice. Moreover, $N_{i,p}$ and $N_{j,q}$ are the B-Spline basis functions; $N_{i,p}$ is applied in u parametric direction while $N_{j,q}$ is applied in v parametric direction.

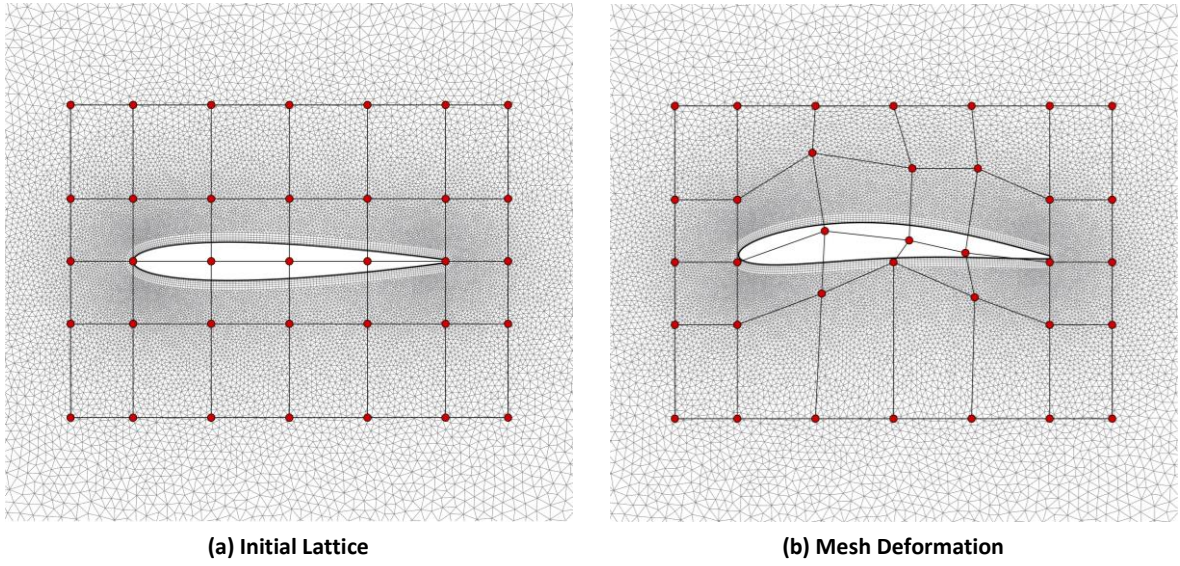


Figure 9.2: Application of the FFD technique to a hybrid computational mesh around a NACA 0012 airfoil.

Step 2 – Embedding the Object within the Lattice

After the construction of the initial FFD lattice and the corresponding B-Spline surface, a quadtree algorithm is implemented so a unique parametric pair of coordinates (u_t, v_t) to be assigned in every single node of the computational mesh to be deformed. For each grid node, the following algorithm is repeatedly applied (Amoiralis and Nikolos, 2008):

- a. The entire parametric area (surface) is divided into four equal subareas.

- b.** The Cartesian coordinates of each subarea vertex are calculated using Eq. (9.1).
- c.** The Cartesian coordinates of each subarea vertex are compared to the Cartesian coordinates of the object's point under consideration, in order to identify the subarea in which the corresponding point lies.
- d.** The latter subarea is divided into four new equal subareas and steps **b** until **d** are repeated for a prescribed number of subdivisions, or until a desirable accuracy is achieved. The desired parametric coordinates of the searched point are defined as the parametric coordinates of the center of the subarea, in which the point resides, resulting from the last subdivision (Patrikalakis and Maekawa, 2002).

Step 3 – Deformation of the Parametric Space

The deformation of the parametric B-Spline surface consists of changing the coordinates of the control points forming the FFD lattice (Figure 9.2b).

Step 4 – Evaluation of the deformation effects

The evaluation of the effects of the deformation consists of the straightforward process to calculate the new Cartesian coordinates of all the mesh points lying within the FFD lattice, using Eq. (9.1). In fact, during the deformation procedure, the parametric coordinates of each point of the computational mesh do not change, in contrast to their Cartesian coordinates, which are deformed due to the alteration of the control lattice. Finally, it is emphasized that the deformation will be applied only to the nodes of the computational mesh that are contained within the initial FFD lattice; the nodes lying outside this area will stay fixed. In consequence, the control points corresponding to the extreme right, left, up and down positions of the FFD lattice are not permitted to move, as a means of ensuring that the deformed computational mesh will be of accepted quality, in terms of overlapping edges.

9.3 Summary of the Optimization Framework

The flow chart shown in Figure 9.3 provides a description of the fundamental interactions between the main components of the modular optimization framework, proposed within the current doctoral dissertation for the design optimization of shrouded wind turbines. The entire optimization procedure is coordinated by the asynchronous DE algorithm, while the *pre-processing*, *genotype to phenotype*, *design evaluation* and *post-processing* modules are properly adjusted or replaced, depending on the optimization problem at hand.

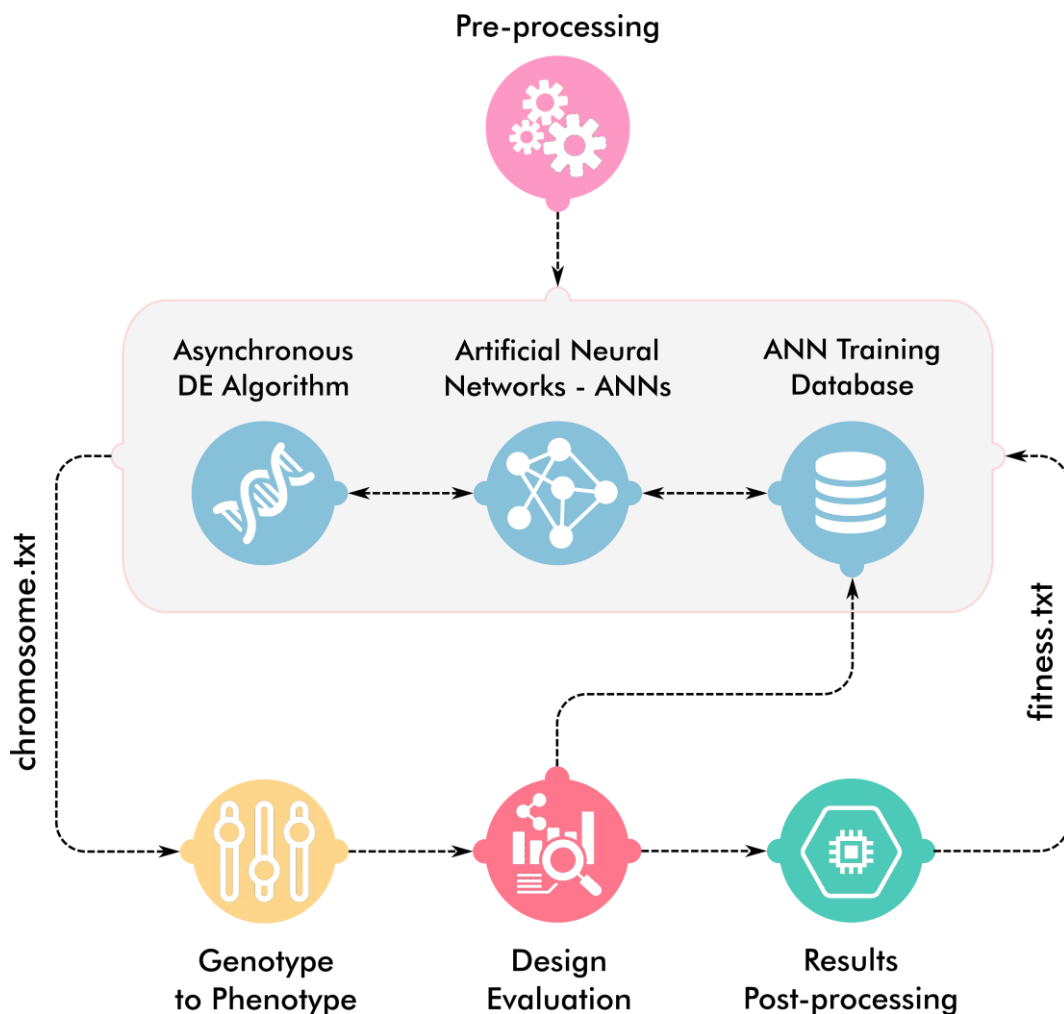


Figure 9.3: Overview of the proposed optimization framework.

Each individual member of the population, generated by the DE algorithm for each generation, is initially passed to the “*genotype to phenotype*” module, via a properly designed text file called `chromosome.txt`. After the generation of the phenotype, the respective information is fed to the “*design evaluation*” module, which – depending on the examined optimization problem – may be formed by one of the available analysis tools developed and

validated in the current study (see Section 9.3.1). Finally, a post-processing step is implemented, in order to extract the necessary quantities for the calculation of the fitness function. The fitness function value for each member of the current population is fed back to the DE algorithm by means of `fitness.txt` file. Then, the DE algorithm updates the members of the DE population through the application of the appropriate evolution operators (selection, crossover, mutation). This procedure is implemented iteratively up to the completion of the user-prescribed number of generations; during the course of the entire optimization process, the DE algorithm interacts with all the involved modules in a completely automated manner, by using specially developed scripts.

9.3.1 Design Evaluation

In this version of the proposed optimization platform, the evaluation of the candidate solutions is performed by using one of the three analysis tools that were developed and numerically validated within the context of the current doctoral study, as shown in Figure 9.4; namely, the BEM code (see Chapter 2 and Chapter 3), the IGal2D solver (see Chapter 4 and Chapter 5) and the coupled RANS-BEM model (see Chapter 8).

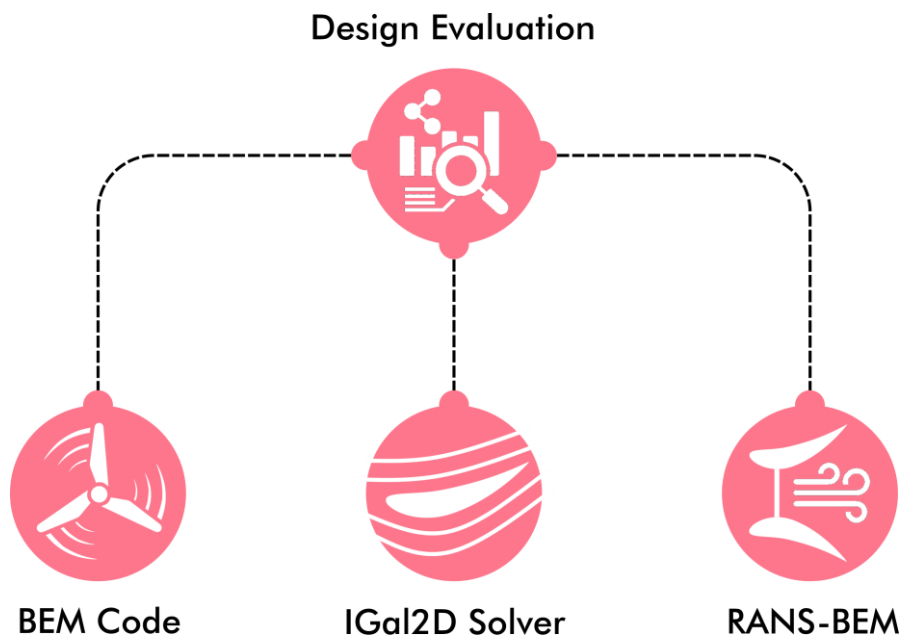


Figure 9.4: The available analysis tools for the design evaluation module.

Specifically, the stand-alone version of the in-house BEM code can be employed for the design optimization of improved rotor blades, either for the case of a shrouded wind turbine or even for that of an unshrouded horizontal-axis wind turbine. In the first case, the impact of

the diffuser on the performance of the turbine rotor is captured by means of the velocity speed-up over the rotor plane for the unloaded shroud configuration, as described in Section 2.2.4. At this point, let us note that due to the ability of the BEM theory to predict the rotor performance in a very short period of time, such optimization applications are generally characterized by high time efficiency, as shown in the respective application reported in Section 10.1.

On the other hand, the preliminary design optimization of improved shrouds can be achieved by using the stand-alone version of the axisymmetric IGal2D solver, while completely ignoring the presence of the turbine rotor and the associated effects on the surrounding flow, including the swirling velocity component as well (see Section 10.2). Even though such optimization applications may lead to reduced levels of computational time – due to the axisymmetric consideration of the actually three-dimensional flow field – they may usually result in suboptimal designs as well, since they disregard the favourable impact of the swirling velocity component on the downstream diffuser flow. As mentioned in Section 4.1, swirling motion has been shown to improve the performance of shrouded wind turbines, as the tangential or swirling velocity component, induced by the rotor blades, helps to energize the velocity boundary layer of the internal diffuser wall and thus, to avoid flow separation (Leloudas et al., 2020a; Venters et al., 2018).

Consequently, the performance optimization of the entire shrouded wind turbine system calls for the simultaneous analysis of both the rotor blades and the shroud geometry; this can be achieved by means of the proposed RANS-BEM model. The particular analysis method is capable of accounting for the effect of the rotor – such as the induced pressure drop and the swirling velocity component – on the flow field, as well as for counter effect of the shroud on the turbine rotor. Ultimately, it allows for the simultaneous design optimization of the coupled rotor/diffuser system (see Chapter 10.3). Nevertheless, this analysis method can be equally applied for the single optimization of the rotor blades or the shroud geometry.

9.3.2 Genotype to Phenotype

By the term *genotype to phenotype* we simply refer to the process of translating the design variables of the examined optimization problem, which are defined by the adopted parameterization technique, into the design geometry. In the current doctoral dissertation, the encountered optimization problems involve the design of improved rotor blades and shrouds. As long as the rotor blades are concerned, the parameterization of the twist and chord distribution – which is the only geometrical information used by the BEM model – is realized by employing B-Spline curves. On the other hand, the parameterization of the shroud geometry and that of the associated computational mesh are made by using the in-house mesh

morphing tool that is based on the FFD technique, which was presented in Section 9.2. In the former case, the twist and chord distribution of the blade can be described and controlled by the coordinates of the control points defining the respective B-Spline curves, while in the latter one, the shroud geometry and the computational mesh are controlled by the coordinates of the control points of the FFD lattice. Therefore, in optimization applications that involve only the design of improved rotor blades, the *genotype to phenotype* module is formed by a simple B-Spline generator that creates the twist and chord curves, based on the design variables (control points) outputted by the DE algorithm; similarly, in optimization applications that involve only the design of improved shrouds the particular module is formed by the mesh morphing tool, presented in Section 9.2, which is fed with the coordinates of the control points of the FFD lattice outputted by the DE algorithm and generates an updated shroud geometry (candidate solution), accompanied by the deformed computational mesh. Apparently, in optimization cases that involve the simultaneous design of the blades and shroud, both the B-Spline generator and FFD tools are executed successively.

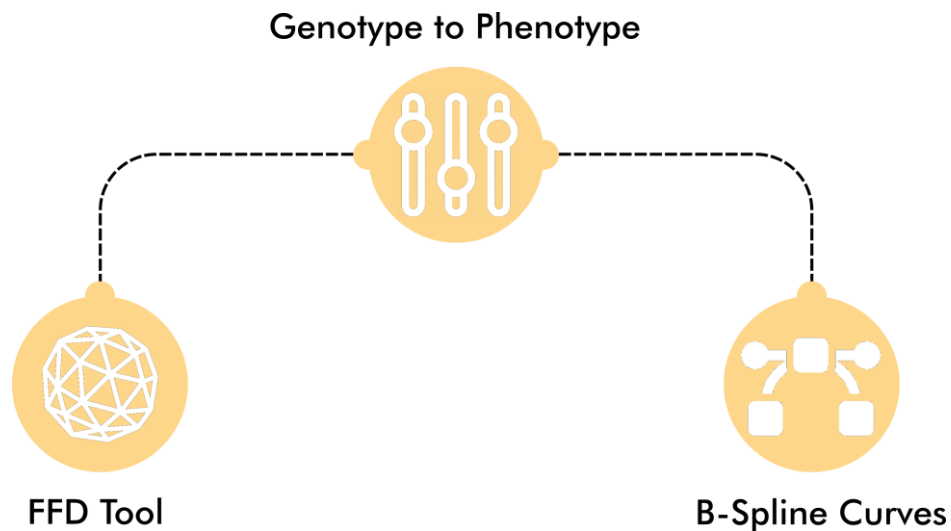


Figure 9.5: The available computational tools for translating the genotype into the phenotype.

9.3.3 Pre-processing Stage

The *pre-processing* stage of the optimization procedure is implemented manually prior to the execution of the optimization algorithm, as shown in Figure 9.3. Apparently, the steps included within the pre-processing phase differ, depending on the examined optimization problem, the adopted parameterization approach and the employed software for the design evaluation. Figure 9.6 presents the major steps of the pre-processing stage for each one of the available design evaluation tools. Please note that the solution of the flow field simulation around the initial design – for the cases in which design evaluation is achieved by means of

IGal2D solver or RANS - BEM model – is introduced as an initial condition for the flow field simulation of each candidate design; this approach aims to reduce the computational time required for each simulation to reach convergence.

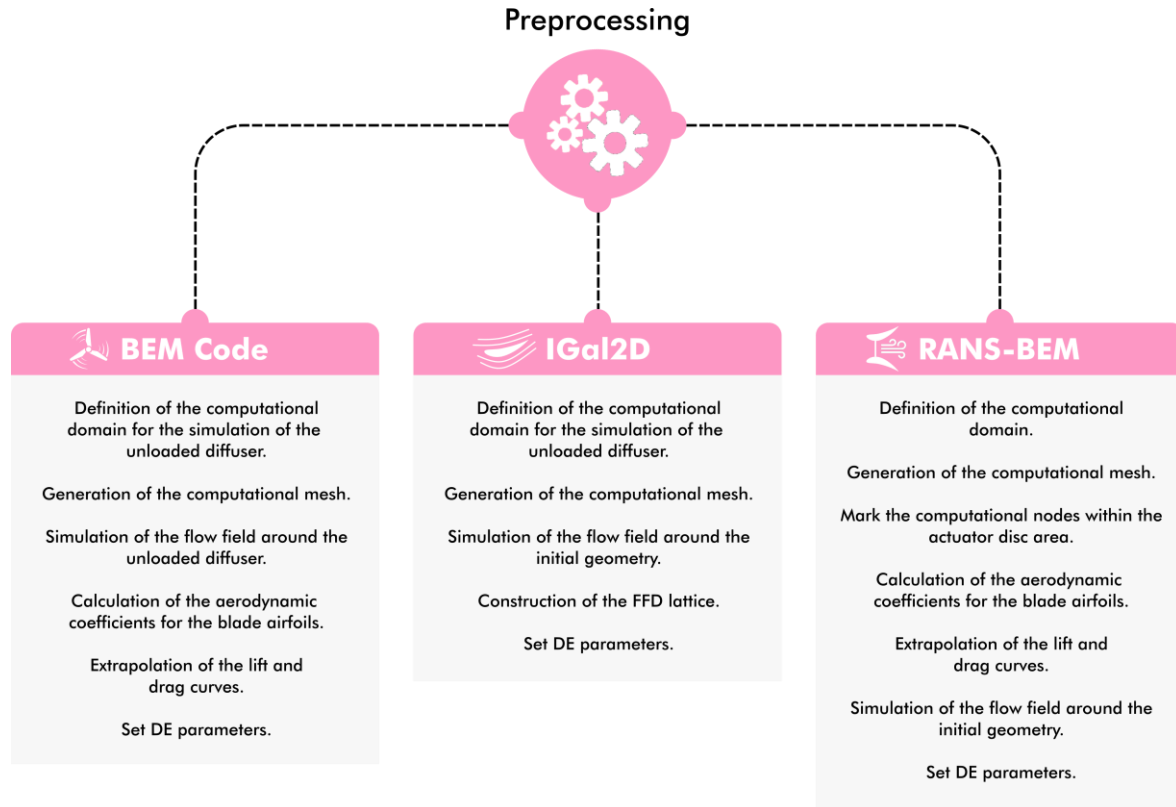


Figure 9.6: The major steps of the pre-processing stage depending on the adopted analysis tool.

9.3.4 Post-processing Stage

Finally, the *post-processing* module is essentially composed by properly made scripts, which are fed with the results of the design evaluation module and implement the fitness function of the examined optimization problem.

Chapter 10

Design Optimization Cases

This chapter presents the application of the proposed optimization framework, as described in Chapter 9, to the following design optimization problems:

OP1. Aerodynamic shape optimization of the rotor blades for a given shroud geometry.

OP2. Aerodynamic shape optimization of an unloaded diffuser configuration.

OP3. Simultaneous aerodynamic shape optimization of the blades and the diffuser.

Table 10.1 provides a summary of the encountered optimization cases.

Case	Component	Optimizer	Evaluation Software
OP1	Blade Optimization	DE Algorithm	BEM Code
OP2	Unloaded Shroud	DE Algorithm	IGal2D Solver
OP3	Blades and Shroud	DE Algorithm	IGal2D – BEM

Table 10.1: Overview of the design optimization cases encountered in this study.

10.1 Design of Improved Rotor Blades

In this section, the current optimization methodology is applied for the design of improved rotor blades for the Donqi Urban Windmill (Ten Hoopen, 2009). Please recall that the particular diffuser geometry, illustrated in Figure 10.1, was designed by the National Aerospace Laboratory in cooperation with Delft University of Technology; it has an exit-area-ratio equal to 1.728 and an exit plane diameter equal to 2 m, while it is further equipped with a 0.04 m high Gurney flap. The distribution of the velocity speed-up ratio over the rotor plane for the unloaded diffuser case is provided in Section 3.2.1, and especially in Figure 3.9a, as it was experimentally measured by van Dorst (2011) and numerically approximated by Kesby *et al.* (2016). The Donqi Urban Windmill has a three bladed rotor; the original blade was also designed by NLR, by adopting a tip diameter equal to 1.5 m and employing the NACA 2207 profile along the entire blade span. The original chord and twist distributions are available in the study of van Dorst (2011).



Figure 10.1: Illustration of several Donqi Urban Windmill models within the urban environment
 [Source: <http://www.jetsongreen.com/2011/08/donqi-urban-windmill-residentia.html>].

In this study, the proposed optimization method is applied to the design of improved rotor blades for the Donqui Urban Windmills by means of a twist and chord optimization procedure; in fact, the current optimization framework is applied for the design of two distinct blade geometries, as alternatives to the original blade configuration. For the first optimized blade, denoted as BD1, the NACA 2207 is employed for the entire span (similarly to the original blade), while for the second blade design, denoted as BD2, the RG15 airfoil is adopted; please recall that the RG15 is a low Reynolds number airfoil with a maximum thickness of 8.92% located at 30.2% of the chord and a maximum camber of 1.8% located at 39.7% of the chord. The lift and drag coefficients for the particular airfoil profiles (inputs to the BEM code) were calculated with XFOIL software (Drela, 1989) at 600,000 Reynolds, which is the diffuser Reynolds number (Ten Hoopen, 2009); subsequently, they were extrapolated to the full 360° range of angles of attack, applying the Montgomerie's 360° extrapolation method (Montgomerie, 2004). In this application, tip and hub losses were included within the analysis by employing the Prandtl's correction model. Finally, please note that the current twist and chord optimization was carried out by considering a zero blade pitch angle and a constant TSR value equal to 6.4.

10.1.1 Twist and Chord Parameterization

The parameterization of the twist and chord distributions is realized by means of two separate B-Spline curves of second degree; each B-Spline curve is defined by 5 control points, permitting the movement of each control point only in the y -direction. Therefore, the number of design variables for each one of the encountered optimization cases is 10, corresponding to

y coordinates of the B-Spline curves used to represent the twist and chord distributions. The adopted upper and lower bounds for each design variable are presented in Figure 10.2.

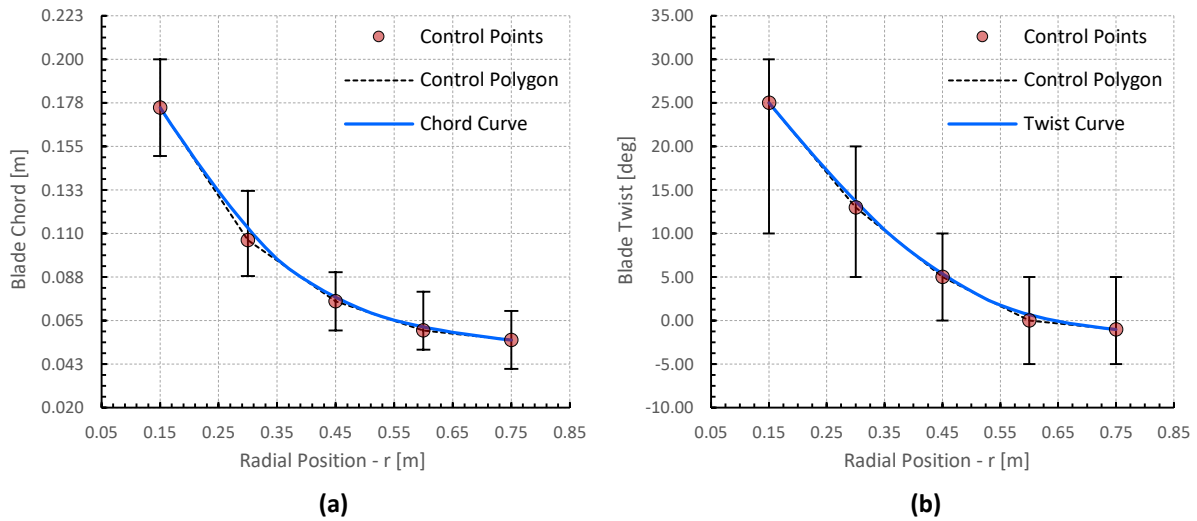


Figure 10.2: Parameterization strategy for chord and twist distributions.

10.1.2 Cost Function and Constraint Formulation

As long as the design objective is concerned, it is defined as the maximization of the rotor power output for a range of ambient wind speeds between 5 m/s and 8 m/s, using an increment of 1 m/s. Hence, considering that the current DE algorithm is designed to deal with minimization problems, the objective function is formed as follows:

$$f = 10 - (C_{p,5} + C_{p,6} + C_{p,7} + C_{p,8}) \quad (10.1)$$

where $C_{p,k}$ denotes the aerodynamic power coefficient of the rotor for an ambient wind speed of k m/s. In this optimization study only explicit constraints are employed, which are formed by the acceptable bounds of the considered design variables. The extraction of the particular ranges was based on a trial and error basis, in order to achieve upper and lower bounds that do not restrict or magnify inefficiently the search space and simultaneously do not permit undesirable twist and chord distributions to be created. Specifically, the bounds for the design variables corresponding to the chord B-Spline curve were set in such a way so the optimal chord distribution to result in a blade geometry as rigid as the current one; while regarding the bounds for the design variables corresponding to the twist B-Spline curve, they were set in such a way so the optimal twist distribution to be as smooth as possible, resulting in a less complicated geometry.

10.1.3 Optimization Results

The twist and chord optimization of both blade configurations was carried out on a DELL™ R815 PowerEdge™ server, with four AMD Opteron™ 6380 sixteen-core processors at 2.50 GHz (64 cores in total). The population size of the DE was set to 60, while the algorithm was executed for a total of 2000 “generations”. The overall elapsed computation time for the optimization of *BD1* and *BD2* blades was equal to 25.11 and 24.16 minutes respectively. Figure 10.3 provides the convergence history of the DE algorithm, while Figure 10.4 illustrates the history of the testing error for the employed surrogate models.

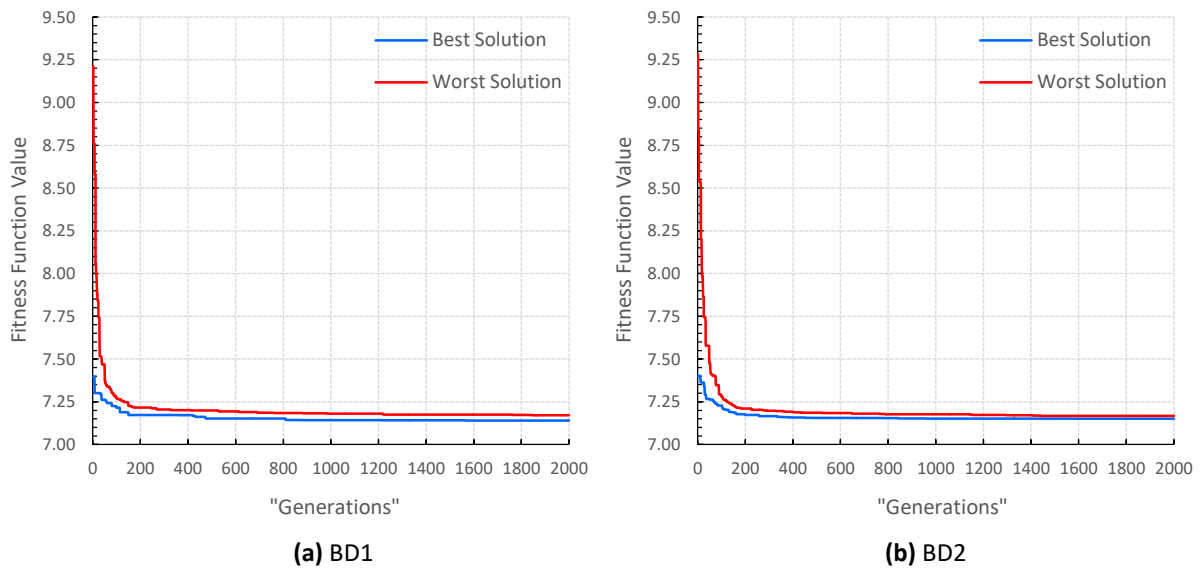


Figure 10.3: The convergence history of the differential evolution algorithm.

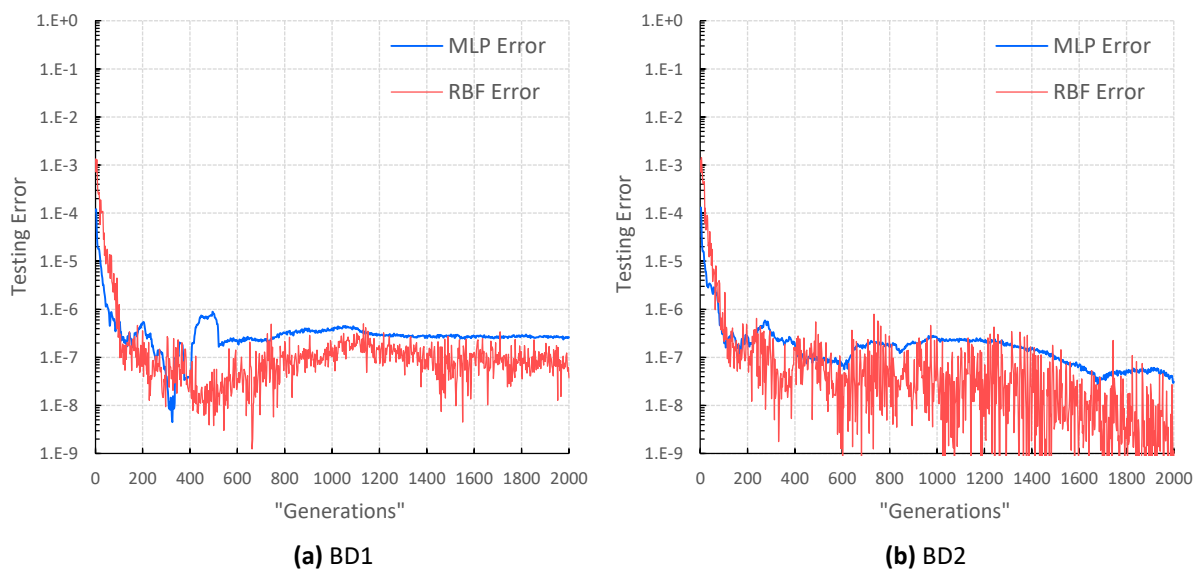


Figure 10.4: History of the testing error for the employed surrogate models.

The twist and chord distributions of the optimized blade designs BD1 and BD2, along with the twist and chord distributions of the original blade are presented in Figure 10.5 to Figure 10.7. It is evident that the optimization procedure resulted in blade designs that differ significantly from the original blade, with a much smoother and less complicated twist distribution; a fact that makes them quite attractive from a manufacturing point of view, as simpler geometries are easier to be constructed. As long as the comparison between the twist and chord distribution of BD1 and BD2 is concerned, no significant variation is observed, as shown in Figure 10.7. This is mainly attributed to the similarity between the lift and drag coefficient curves of the NACA 2207 and RG15 airfoils. However, since the RG15 airfoil has a maximum thickness that is 27.4 % larger than the maximum thickness of the NACA 2207, the corresponding BD2 blade is expected to provide better structural features.

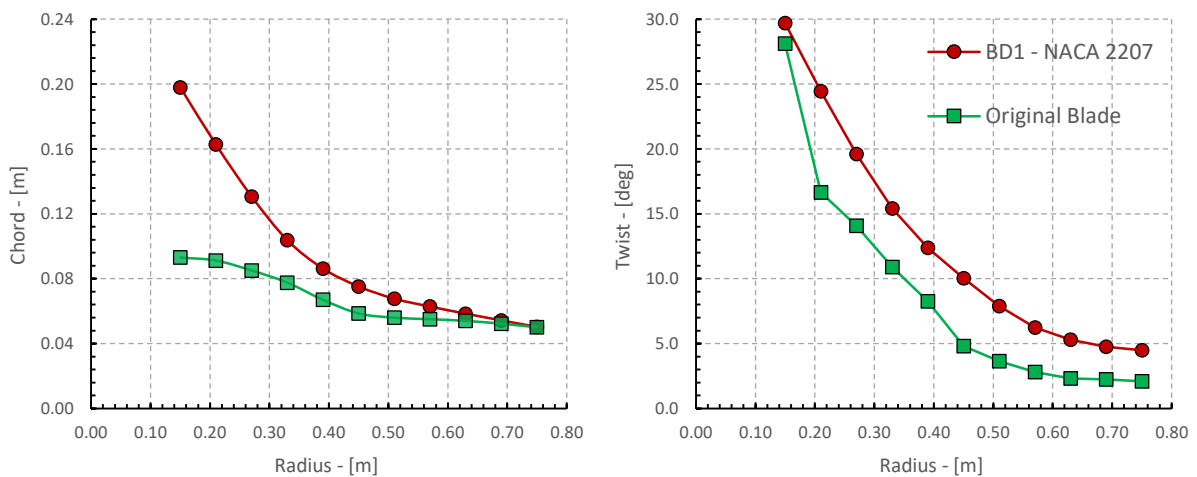


Figure 10.5: Twist and chord distributions of the optimized blade *BD1*.

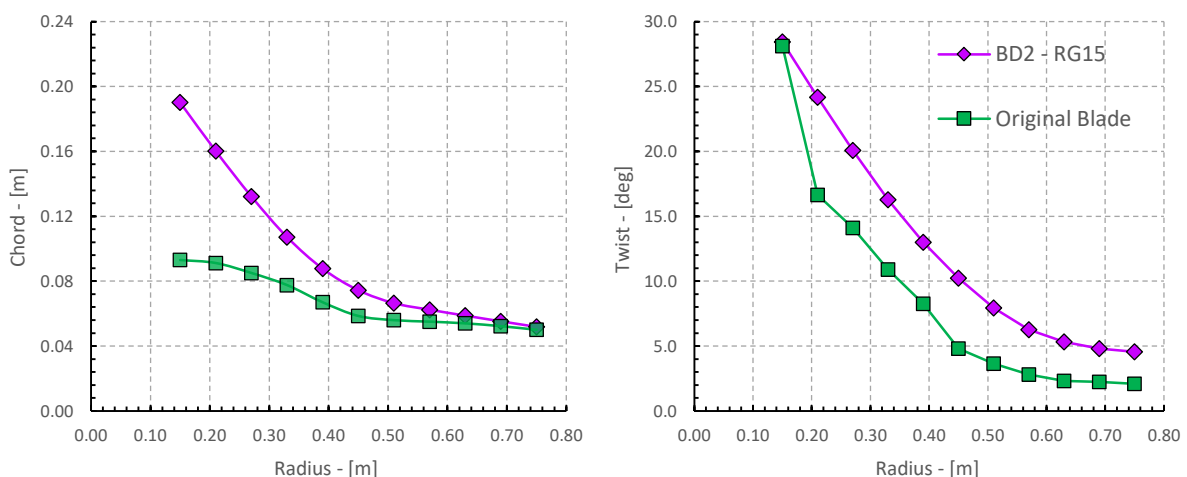


Figure 10.6: Twist and chord distributions of the optimized blade *BD2*.

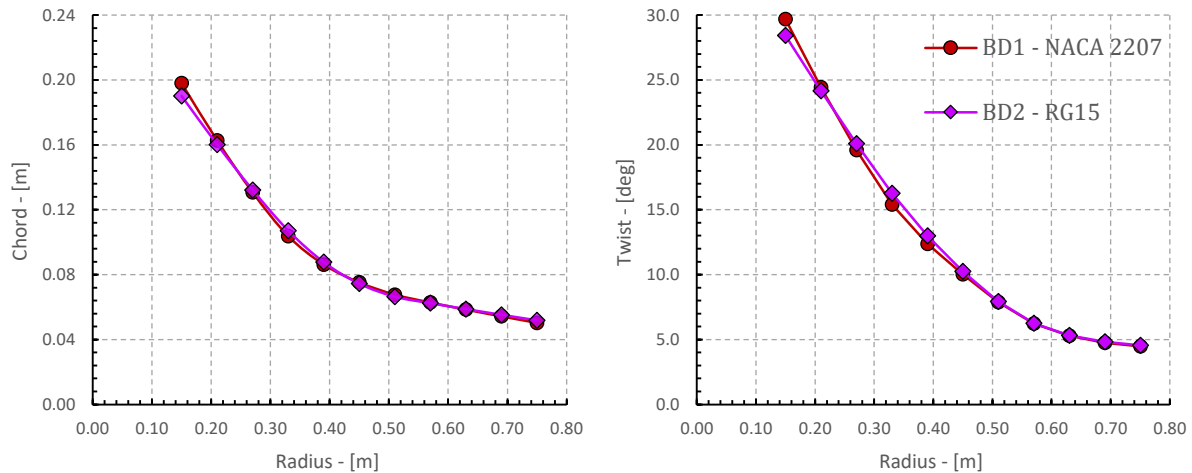


Figure 10.7: Comparison between the twist and chord distributions of BD1 and BD2.

The aerodynamic performance of the 3-bladed DAWT rotor under investigation is presented in Figure 10.8. As it can be observed, the utilization of BD1 and BD2, instead of the original blade geometry, results in a visible improvement of the aerodynamic power output for all the considered operational points. In particular, the BD1 leads to a mean increase of the aerodynamic power of the rotor of approximately 18.2 %, while the corresponding percentage for BD2 is 19.4 %. Furthermore, Figure 10.8 demonstrates the ability of the employed BEM code to approximate the experimental results for the original blade (van Dorst, 2011) with high accuracy.

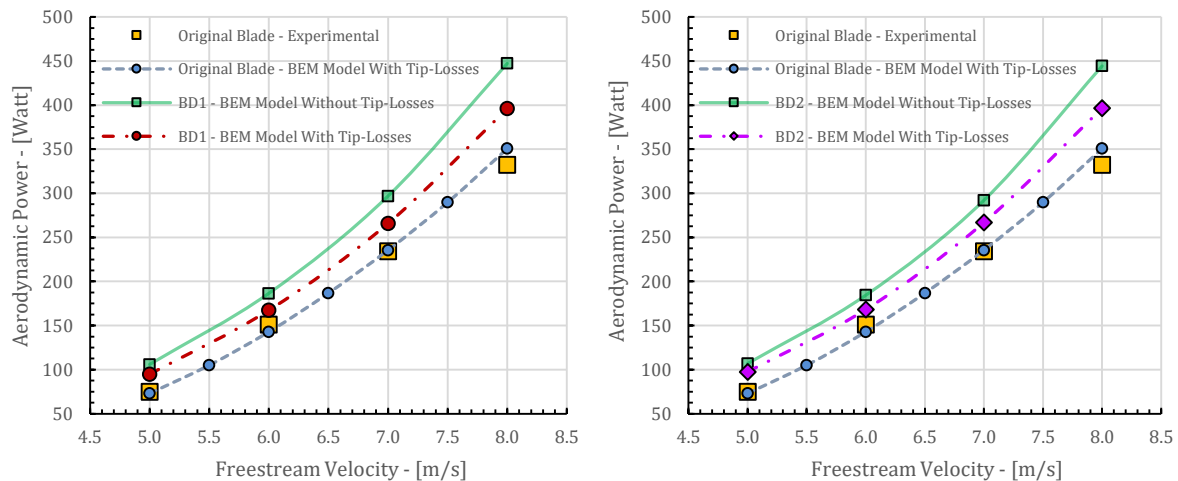


Figure 10.8: The increased power output of the rotor, utilizing the optimized blade geometries *BD1* and *BD2*.

At this point, it should be highlighted that the optimization of both *BD1* and *BD2* was conducted by including the correction model proposed by Prandtl to account for the blade tip losses, based on the findings of Phillips (2003), who noticed that tip losses exist on DAWT

blades as well, despite the relatively close proximity of the blades tips to the diffuser wall; a similar conclusion was also drawn by Kesby *et al.* (2016). Nevertheless, the inclusion of such a correction model during the BEM analysis of a DAWT rotor may result in an underestimation of the total power output, as the presence of the shroud around the rotor blades produces a noticeable reduction of the particular losses, compared to a bare wind turbine. For this reason, the aerodynamic performance of the examined DAWT rotor for *BD1* and *BD2* optimized blades without the application of a tip losses correction model, is also presented in Figure 10.8. Finally, Figure 10.9 illustrates the three-dimensional drawings of the optimized and original blade designs.

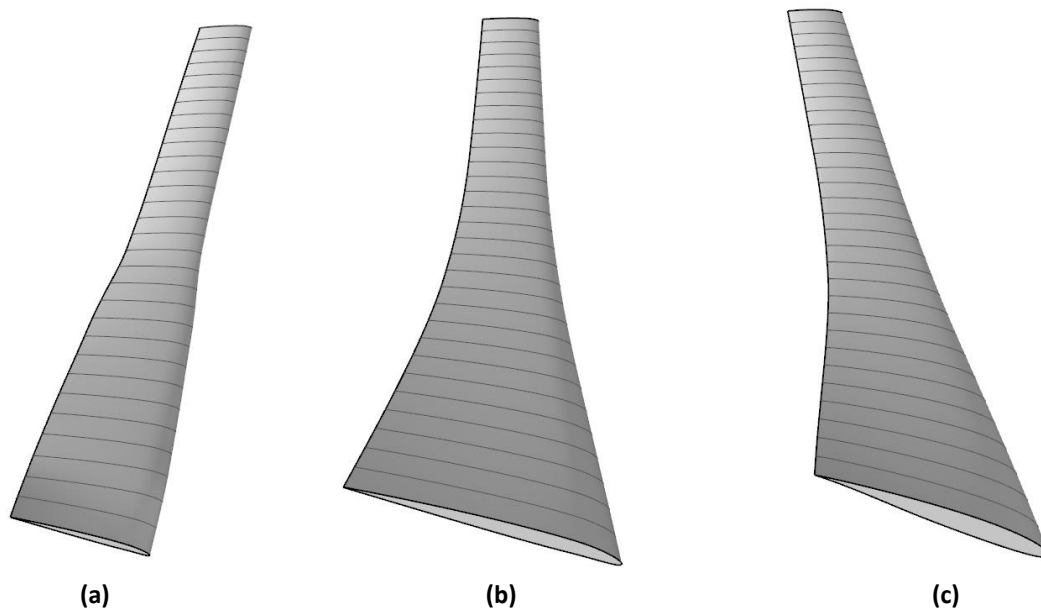


Figure 10.9: Three dimensional drawings of the (a) original blade, (b) optimized blade BD1 and (c) optimized blade BD2.

10.2 Design Optimization of an Unloaded Diffuser

In this section, the proposed optimization scheme is applied for the design of an aerodynamically improved shroud for a diffuser-augmented wind turbine application, with a rotor swept area of 22.9 m^2 and a rated capacity of approximately 15 kW. The aerodynamic profile of the original shroud design (denoted as baseline design) is illustrated in Figure 10.10; Table 10.2 contains some of its main geometrical characteristics. The aerodynamic shape optimization is performed for an isolated diffuser configuration (without the presence of the turbine), considering an ambient wind velocity V_∞ of 6 m/s and a Reynolds number equal to $2.2 \cdot 10^6$. The Reynolds number has been calculated based on the throat diameter D_t of the baseline shroud design (characteristic length scale).

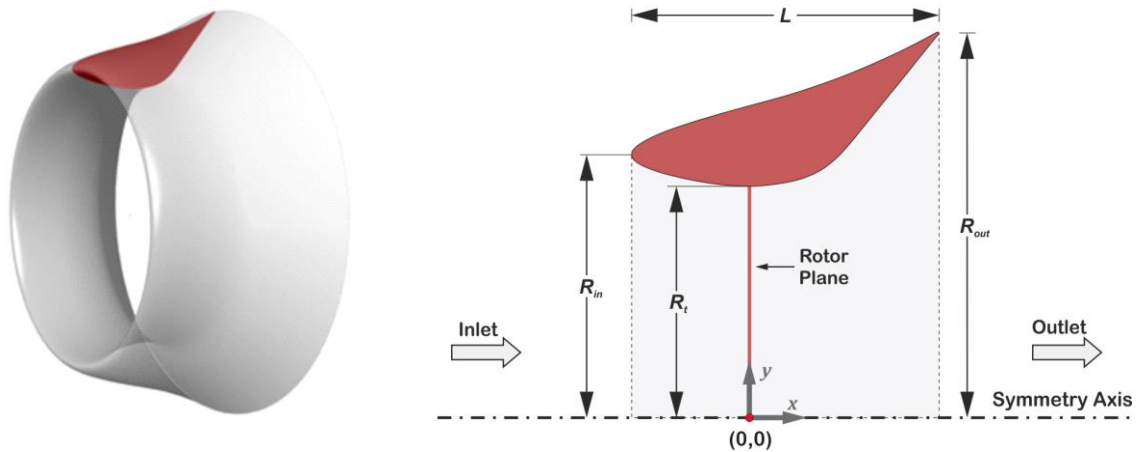


Figure 10.10: The aerodynamic profile of the baseline shroud design (Leloudas, Lygidakis, *et al.*, 2020).

Parameter	Value
Diffuser Length - L	3.660 m
Inlet Radius - R_{in}	3.112 m
Throat Radius - R_t	2.751 m
Exit Radius - R_{out}	4.570 m
Diffuser Volume - V	54.117 m ³

Table 10.2: The main geometrical characteristics of the baseline shroud design.

10.2.1 Grid Independence Study

To guarantee that the resolution of the computational grid does not have a significant impact on the simulation of the flow field around the diffuser and, therefore, on the objective function calculation, a grid independence study was initially made, by considering three distinct computational meshes (coarse, medium and fine). The adopted hybrid grids (composed by both triangular and quadrilateral elements) are characterized by a total number of nodes equal to 26,671, 49,992 and 68,809 respectively. In all the examined cases, regions of higher mesh resolution were generated around the shroud. At this point, it is emphasized that further refinement of the computational mesh (especially in the wake region) was not possible, since this was found to result in the appearance of unsteady flow phenomena, making the achievement of a steady-state solution unfeasible. The coarse and medium grids were constructed with a wall-spacing value of 0.00024 m, while the fine one with a wall-spacing value of 0.00015 m, leading to a y^+ value of 4 and 2.5 respectively. Since the current implementation of the axisymmetric RANS solver uses a dimensionless form of the governing

equations, the computational domain has been properly normalized by the throat diameter (characteristic length scale). Figure 10.11 illustrates the coarse, medium and fine meshes.

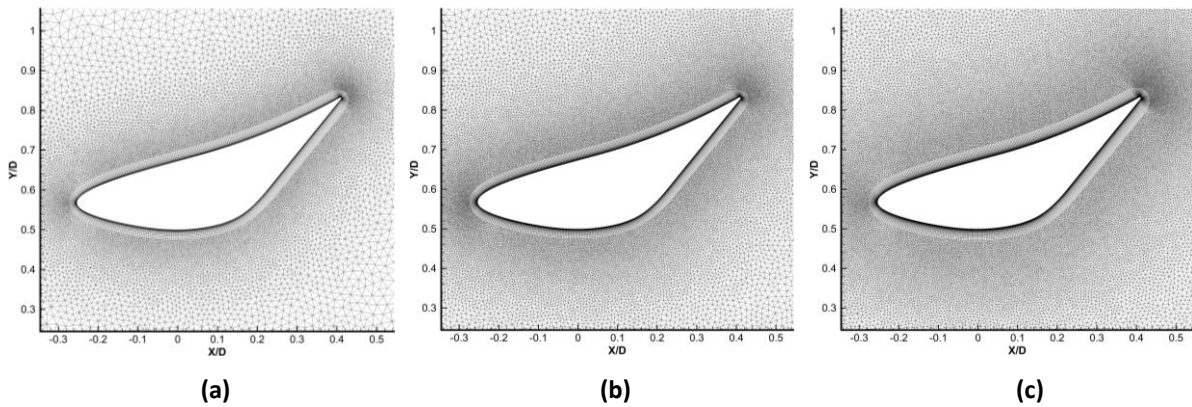


Figure 10.11: The computational meshes used for the grid independence study: (a) coarse, (b) medium and (c) fine.

The drag and the mean velocity speed-up ratio at the throat ($x = 0$) of the baseline diffuser design, by adopting each of the considered computational meshes, are presented in Table 10.3. The obtained results indicate that both computed drag and mean velocity speed-up are reduced by increasing grid resolution. In detail, the percentage difference, in terms of drag value, between the medium and fine meshes was found equal to 1.3%, while the respective percentage difference between the fine and coarse meshes is approximately equal to 6%. From a velocity speed-up standpoint, much smaller deviations were observed; the comparison revealed that the percentage difference between the fine and medium meshes is equal to 0.6% and the percentage difference between the solutions obtained from the fine and coarse meshes equal to 1.9%.

Mesh Resolution	Coarse	Medium	Fine
Target y^+ Value	4	4	2.5
Wall Spacing – [m]	0.00024	0.00024	0.00015
Drag Force – [N]	713.77	671.11	662.37
Mean Velocity SU Ratio	1.54	1.52	1.51

Table 10.3: Drag variation for different mesh resolutions.

In order to have a better understanding on the flow field dependence upon the mesh resolution, Figure 10.12 provides the variation of the on-axis velocity speed-up ratio distribution, the on-axis pressure coefficient distribution, the velocity speed-up distribution over the rotor plane, and the distribution of the pressure coefficient along the surface of the

shroud profile. Small, but noticeable, discrepancies have been observed between the distributions resulted from the use of the coarse and fine meshes, especially in the region around the rotor plane. On the other hand, no practical deviations were detected between the distributions resulted from the use of the medium and fine meshes. Accordingly, the solution obtained by adopting the mesh of medium resolution can be safely considered as mesh independent, and therefore, the particular grid should be ideally used during the optimization. However, owing to the limited computational resources available, the adoption of the medium grid within the current optimization procedure would excessively increase the total computational time. Therefore, the coarse mesh (26,671 nodes) has been selected instead. Although small discrepancies between the results obtained through the utilization of the coarse and fine meshes have been observed (the solution provided by the coarse grid is not mesh independent), the former computational mesh is capable of providing a reasonably accurate representation of the flow field, as shown in Figure 10.12.

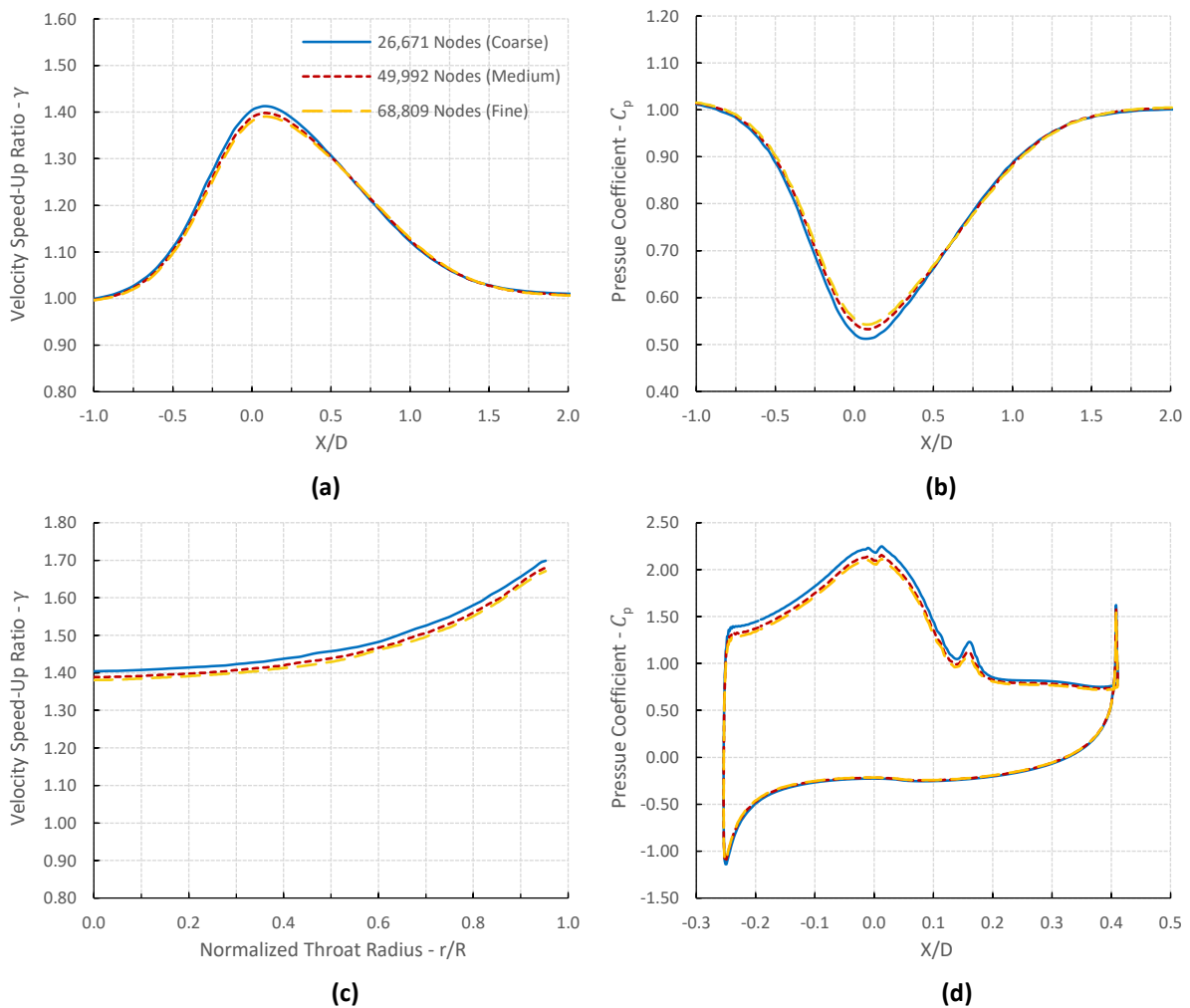


Figure 10.12: Grid independence study: (a) On-axis velocity speed-up ratio distribution, (b) On-axis pressure coefficient distribution, (c) Velocity speed-up ratio distribution over the rotor plane, (d) Distribution of the pressure coefficient over the surface of the shroud profile.

In addition, as Khamlaj and Rumpfkeil (2018) noted, the CFD model will always have some inherent error that is related to the modeling assumptions; hence, more reduction in truncation error with additional refinement seems insignificant when compared to the error associated with the model's simplification of physics. Nevertheless, even though the coarse mesh will be used to reach the optimal design, after the completion of the optimization procedure, a fine mesh will be also constructed for the optimal solution (having a similar resolution to the fine mesh for the baseline design), in order to perform an accurate and reliable comparison.

10.2.2 Mesh Parameterization and Design Variables

The parameterization of the computational mesh (coarse) was made by introducing the 2D lattice illustrated in Figure 10.24. The degree of the B-Spline basis function for both directions was set as the maximum possible, that is 6 and 5, for the (axial) x and (radial) y direction respectively, as a means to achieve smooth deformations. In addition, all the internal control points of the FFD lattice are free to move in both directions.

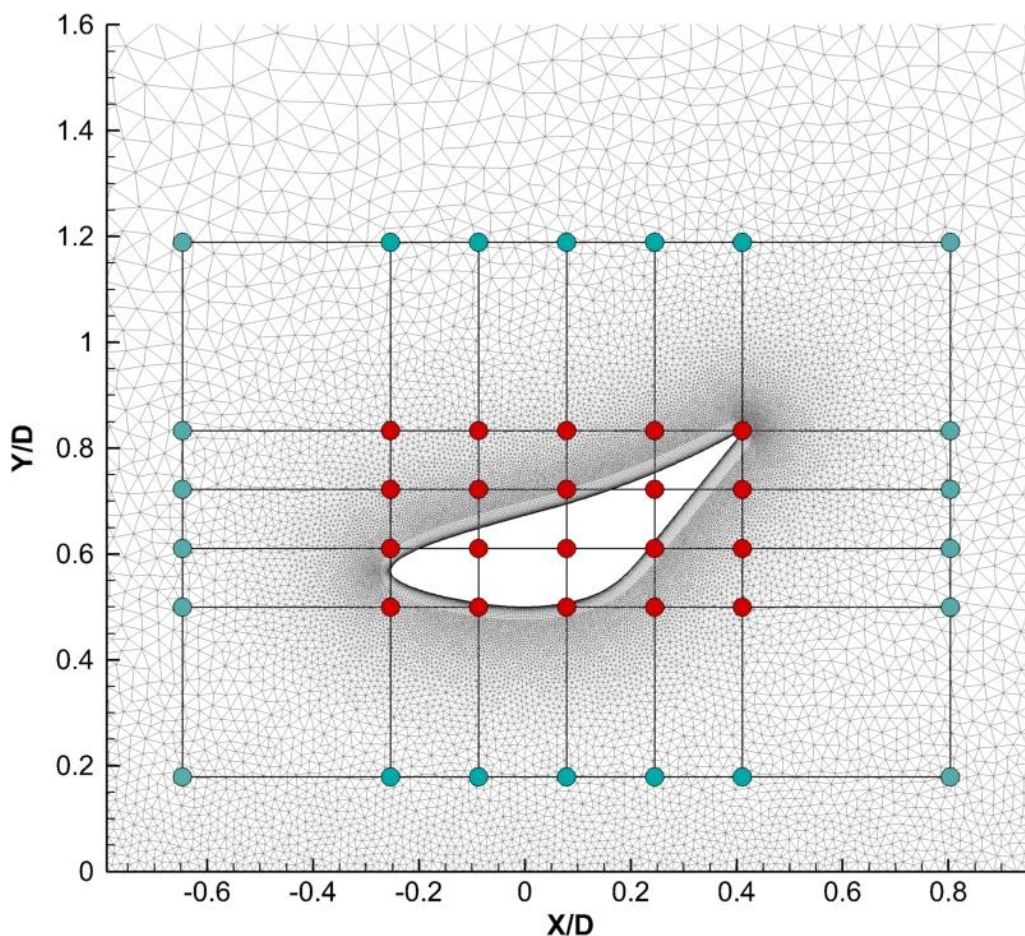


Figure 10.13: The initial FFD lattice.

On the other hand, the control points located at the extreme right, left, up and down positions (green points) have been fixed, as a means of ensuring that the deformed computational meshes will be of accepted quality, in terms of overlapping edges, as explained in Section 3. Consequently, a number of 40 design variables resulted, which correspond to x and y Cartesian coordinates of the 20 (internal) free-to-move control points of the FFD lattice.

10.2.3 Objective Function and Constraints

10.2.3.1 Objectives

Even though the diffuser is primarily used to accelerate the axial velocity over the rotor plane, and thus to increase the power output of the system, low levels of drag force are also desirable, to reduce the cost of the wind turbine (Liu J. *et al.*, 2016). Therefore, the design objectives in this optimization study are defined as the maximization of the mean velocity speed-up distribution $\gamma(r)$ over the rotor plane (turbine position) and the minimization of the total drag force \mathcal{D} . The value of the mean speed-up ratio at the rotor plane, averaged with the throat radius, is calculated as:

$$f_{su} = \frac{2\pi \int_0^R \gamma(r) dr}{\pi R_t^2} \quad (10.2)$$

The (non-dimensional) total drag force \mathcal{D} on the shroud surface E_S is computed by adding the pressure and viscous forces

$$\mathcal{D} = -2\pi \oint_{C_S} p n_x y ds + 2\pi \oint_{C_S} (\tau_{xx} n_x + \tau_{xy} n_y) y ds, \quad (10.3)$$

where C_S is the boundary curve of the shroud's cross-section (aerodynamic profile). The dimensionalization of the drag force \mathcal{D} is made by using the freestream density $\rho = 1.225 \text{ Kg/m}^3$, the freestream velocity $V_\infty = 6 \text{ m/s}$ and the throat diameter of the baseline design $D_t = 5.5 \text{ m}$ (characteristic length) as:

$$f_{\mathcal{D}} = \mathcal{D} \rho V_\infty^2 D_t^2 \quad (10.4)$$

Equation (10.4) was devised in line with the adopted strategy for the non-dimensionalization of the governing equations (see Section 4.2.1.1), according to which the scales of length and pressure have been normalized by means of the throat diameter D_t (characteristic length) and the freestream dynamic pressure ρV_∞^2 , respectively.

10.2.3.2 Constraints

In this optimization study, besides the explicit constraints formed by the acceptable bounds of the considered design variables, two additional geometrical constraints were imposed. The first one is related to the preservation of the throat radius of the baseline design, while the second one is imposed so as to ensure that the volume \mathcal{V} of the new shroud will be equal or less than the volume \mathcal{V}_{ref} of the baseline design. Thus,

$$\mathcal{V} \leq \mathcal{V}_{ref}, \quad (10.5)$$

$$R_t = R_{t,ref}. \quad (10.6)$$

where R_t is the throat radius of a candidate shroud design, while $\mathcal{V}_{ref} = 54.15 \text{ m}^3$, and $R_{t,ref} = 2.751 \text{ m}$ is the throat radius of the baseline shroud design. Both constraints were implemented following a penalty function approach. The two penalty functions were formed as:

$$f_{\mathcal{V}} = \begin{cases} \mathcal{V} - \mathcal{V}_{ref}, & \text{if } \mathcal{V} > \mathcal{V}_{ref} \\ 0, & \text{else} \end{cases} \quad (10.7)$$

$$f_{th} = |R_t - R_{t,ref}| \quad (10.8)$$

10.2.3.3 Cost Function

By combining the objective and penalty functions, the single cost (or fitness) function of the minimization problem at hand is formed as:

$$f = 5 - f_{su} + 0.0001f_D + 0.01f_{\mathcal{V}} + 10f_{th}. \quad (10.9)$$

The parameters shown in Eq. (10.9) have been empirically extracted in such a way that each function to have almost the same impact on the cumulative cost function.

10.2.4 Optimization Results

The aerodynamic shape optimization was made using a DELL™ R815 PowerEdge™ computing server that is equipped with four AMD Opteron™ 6380 sixteen-core processors. Regarding the parameters of the DE algorithm, the population for each generation was set equal to 50 and the optimal solution was obtained after the completion of 500 generations; the time required until the completion of 500 generations was approximately 722 hours. The convergence history of the optimization algorithm is presented in Figure 10.14. In addition,

Figure 10.14 provides the testing error progression for the two surrogate models (RBF and MLP) utilized within the current optimization study. Evidently, the testing error of the MLP model was considerably smaller (as compared to the one of the RBF model) for the great majority of the 500 generations. Accordingly, the MLP was almost exclusively used for the pre-evaluation of the trial vectors. This fact reveals that all the surrogate models cannot be adapt equally to any given problem. Thus, the incorporation of multiple surrogate models (operating as an ensemble) is important, as it provides the opportunity to treat efficiently a wide range of different optimization problems, through the achievement of higher approximation levels.

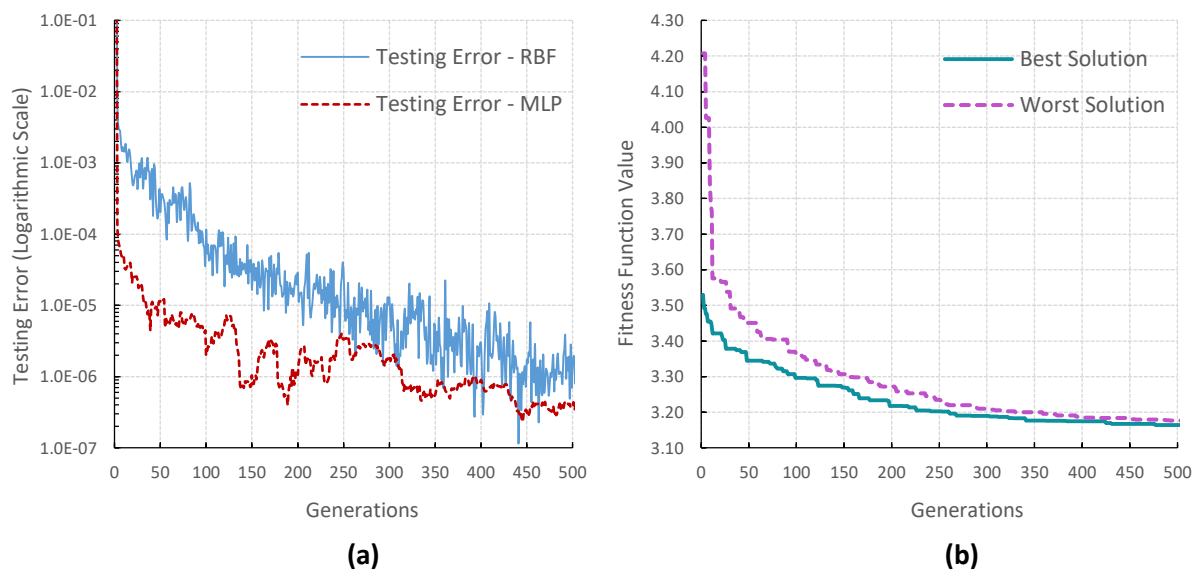


Figure 10.14: (a) The testing error for the two surrogate modes; (b) the convergence history of the DE algorithm.

Table 10.4 presents the number of the chromosome evaluations performed through the RANS solver (exact evaluations), as well as the number of the total evaluations (RANS and ANNs), completed during the entire optimization process. Table 10.4 reveals that the incorporation of the surrogate models resulted in a substantial reduction of the total number of exact evaluations by approximately 38%, accelerating considerably the design process.

Optimization Study	Wall-clock time (Hrs)	Exact evaluations	Total evaluations
Shroud Design	722	15401	25000

Table 10.4: Wall-clock computation time, number of exact evaluations, and number of total evaluations.

10.2.4.1 Optimal Shroud Design

The aerodynamic profile of the optimal shroud design (SD1) is shown in Figure 10.15, comparatively to the baseline aerodynamic profile. Through the comparison of the two aerodynamic profiles, it is evident that the optimization procedure resulted in a much thinner geometry (better aerodynamic performance) with a much smoother curvature in the region downstream of the rotor plane (throat). Another interesting remark is that the optimized geometry tends to approximate the shape of a flanged diffuser; this is attributed to the fact that such geometries are capable to create a region of high sub-atmospheric pressure near the exit plane, which increases the suction ability of the shroud and thus, the mass flow rate. However, the relatively small thickness distribution of SD1 downstream of $x/D = 0.2$, could be a critical point that reduces the structural integrity of the particular design and calls for the installation of additional supportive structures to prevent a possible failure. To overcome this problem, a modified shroud profile was created (SD2 – Figure 10.15 and Figure 10.16) by locally (manually) thickening SD1. Even though SD2 is probably a suboptimal solution, from an aerodynamic point of view (as the following CFD simulations will suggest), it is expected to have a better performance in terms of structural integrity, while the smoother curvature definitely makes it more attractive from a manufacturing standpoint. Some of the main geometrical characteristics of SD1 and SD2 are provided through Table 10.5, while a 3D representation of the new shroud designs is illustrated in Figure 10.18. Thanks to the efficient implementation of the throat constraint, both SD1 and SD2 have the same throat radius with the baseline shroud design.

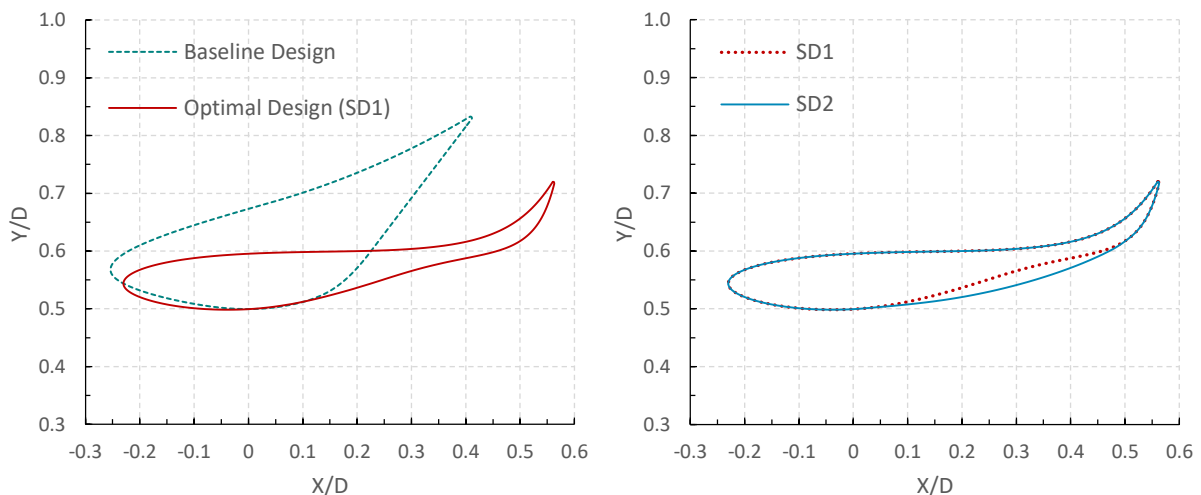


Figure 10.15: The aerodynamic profiles of the baseline design, SD1, and SD2.

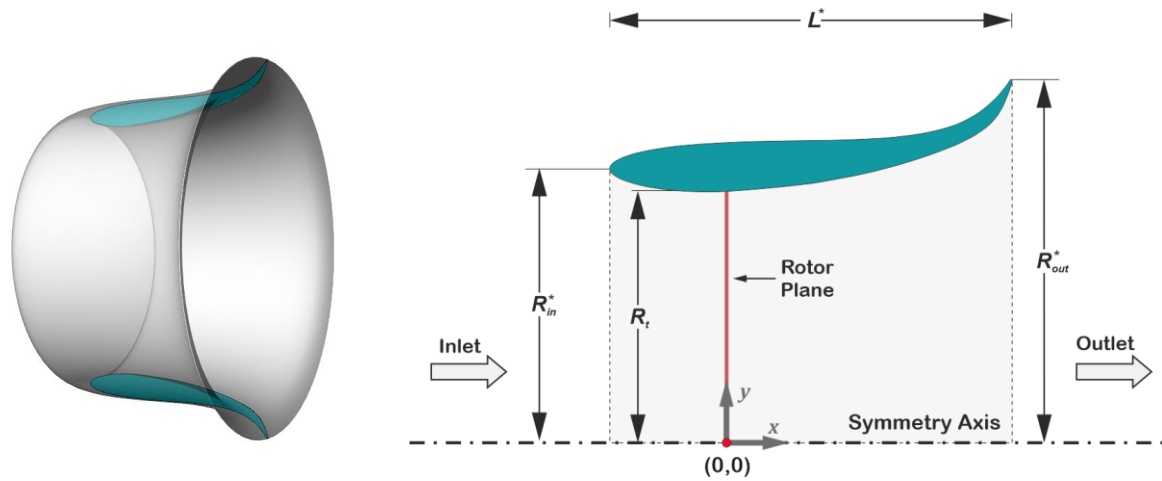


Figure 10.16: The aerodynamic profile of the SD2 shroud design (Leloudas, Lygidakis, *et al.*, 2020).

Parameter	Value
Diffuser Length - L^*	4.360 m
Inlet Radius - R_{in}^*	2.990 m
Throat Radius - R_t^*	2.750 m
Exit Radius - R_{out}^*	9.952 m

Table 10.5: The main geometrical characteristics of SD1 and SD2.

For the evaluation of the aerodynamic performance of both SD1 and SD2, comparatively to the baseline design, Table 10.6 provides the results of the objective functions, while a more detailed representation of the respective flow fields is given in Figure 10.17. At this point, it is highlighted that even though the optimization was performed with the coarser mesh (among the ones considered), a fine mesh of similar resolution to the fine mesh adopted during the grid independence study (with a y^+ value of 2) was used to obtain all the following results for both SD1 and SD2.

Design	Drag Force	Mean Velocity SU	Volume
Baseline Design	662.37 N	1.51	54.12 m ³
Shroud Design 1 (SD1)	409.45 N	1.90	28.18 m ³
Shroud Design 2 (SD2)	418.15 N	1.87	31.81 m ³

Table 10.6: Drag and velocity speed-up variation for the different shroud designs (fine meshes).

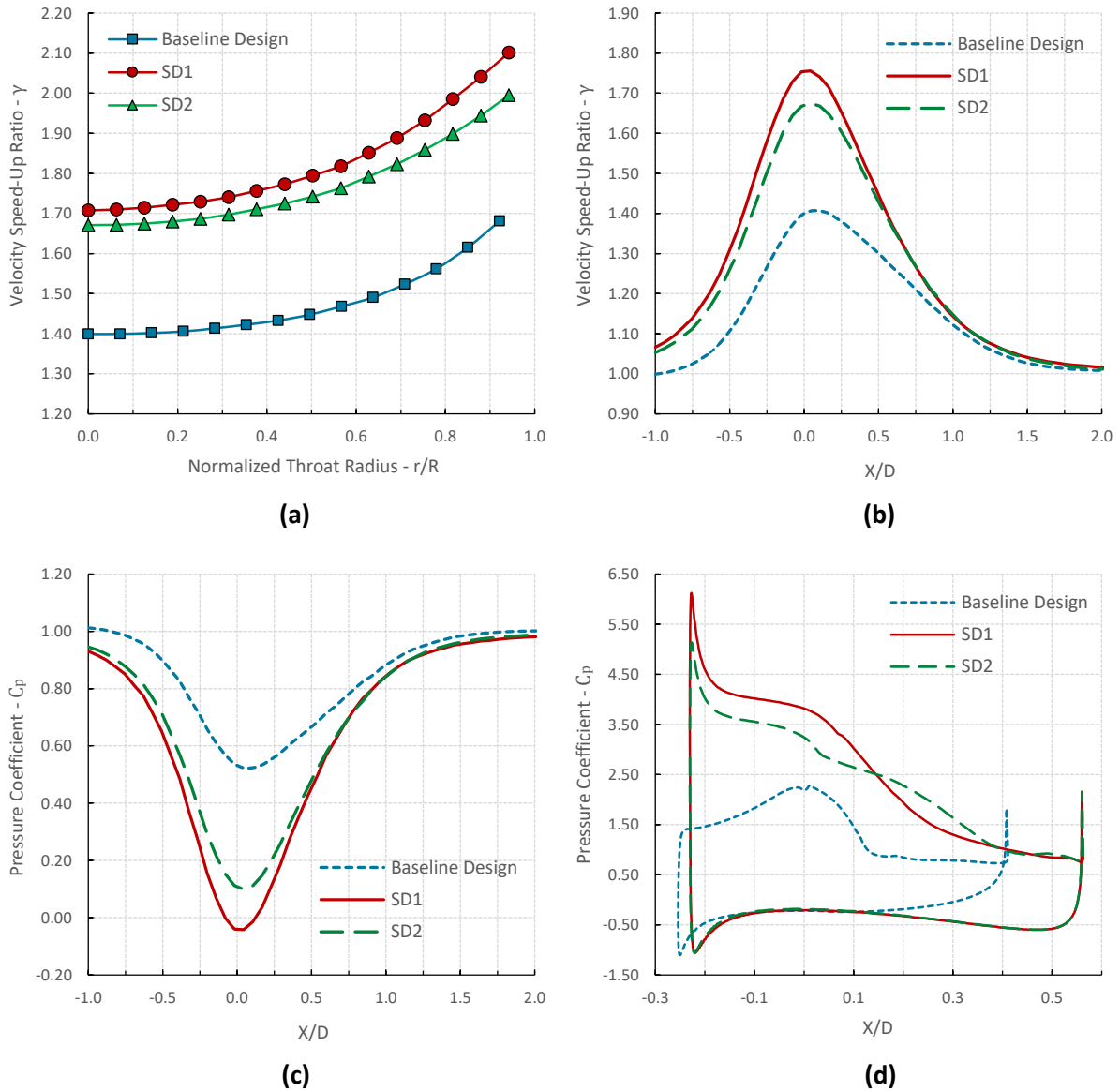


Figure 10.17: Comparison between the baseline design, SD1, and SD2. (a) Velocity speed-up ratio distribution over the rotor plane; (b) on-axis velocity speed-up ratio distribution; (c) on-axis pressure coefficient distribution; (d) distribution of the pressure coefficient over the surface of the shroud profile (fine meshes).

SD1 achieved a remarkable reduction of drag by approximately 47% accompanied by an increase of the mean velocity speed-up ratio by approximately 23%, comparatively to the initial design. The aerodynamic performance of SD2 is not much inferior. As a matter of fact, the drag reduction was equal to 45% and the increase of the mean velocity speed-up ratio equal to 21%. Therefore, the local thickening of SD1 caused a drag increase about 2% and a mean velocity speed-up reduction of almost 2%, which can practically considered negligible. In addition, a remarkable volume reduction, touching 48% and 41% for SD1 and SD2

respectively, was also achieved, allowing for huge cost reduction, even though the total length of the diffuser was increased.

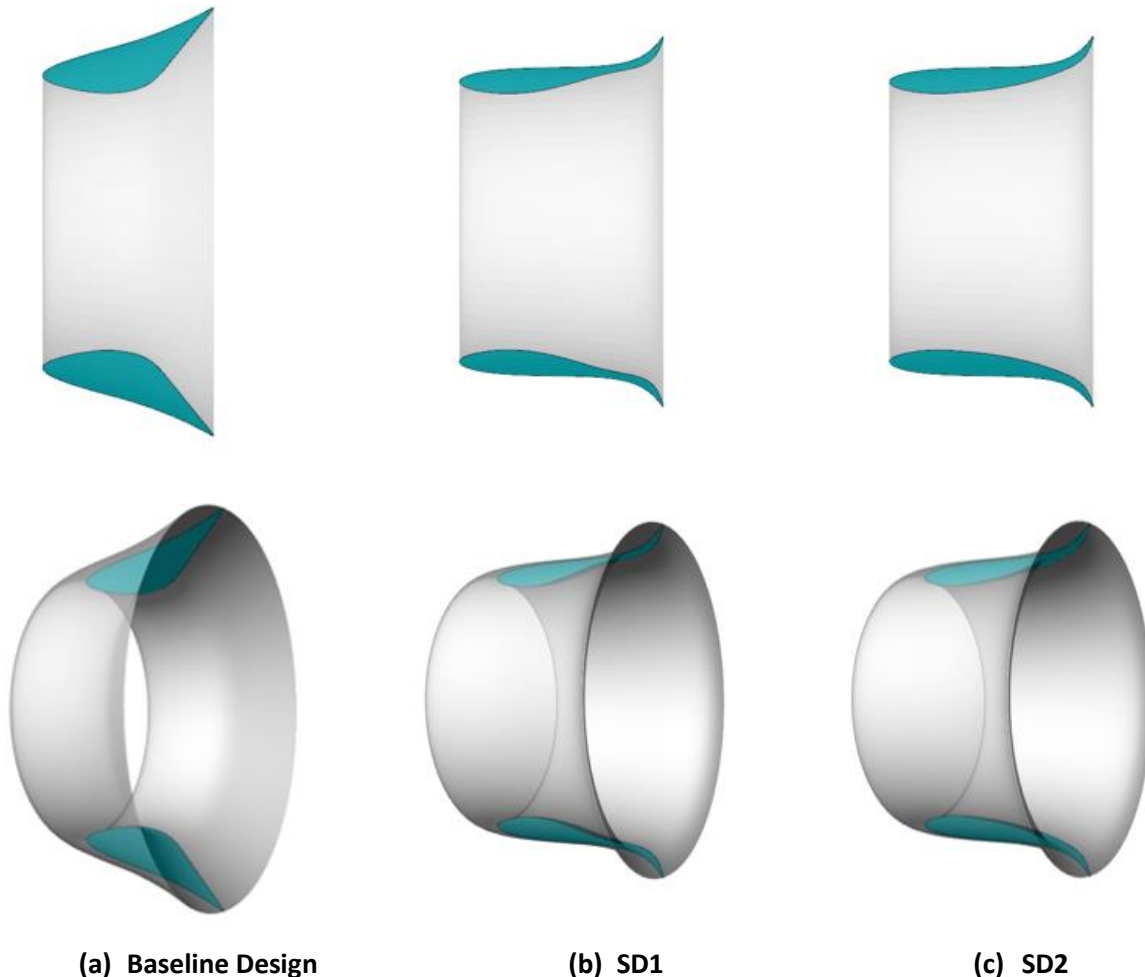


Figure 10.18: 3D representation of the (a) baseline design, (b) SD1, and (c) SD2.

Furthermore, in order to have a better understanding of the aerodynamic behavior of the baseline and optimized designs, the dimensionless contours of pressure and velocity components at the symmetry plane for the isolated diffusers are presented in Figure 10.19. As it can be observed, the major characteristic of the baseline design is the formation of a large recirculation area near the exit plane (attributed to its highly-curved shape), that produces a high pressure gradient in the flow direction. On the contrary, the recirculation area behind both SD1 and SD2 is considerably smaller (Figure 10.20 and Figure 10.21), while much higher acceleration of the flow inside the diffuser is observed as well. As a matter of fact, the recirculation region near the exit plane of SD1 and SD2 may be even smaller during the shroud

operation along with a rotating turbine, since the swirling velocity induced by the turbine tends to energize the velocity boundary layer; thus, delaying flow separation.

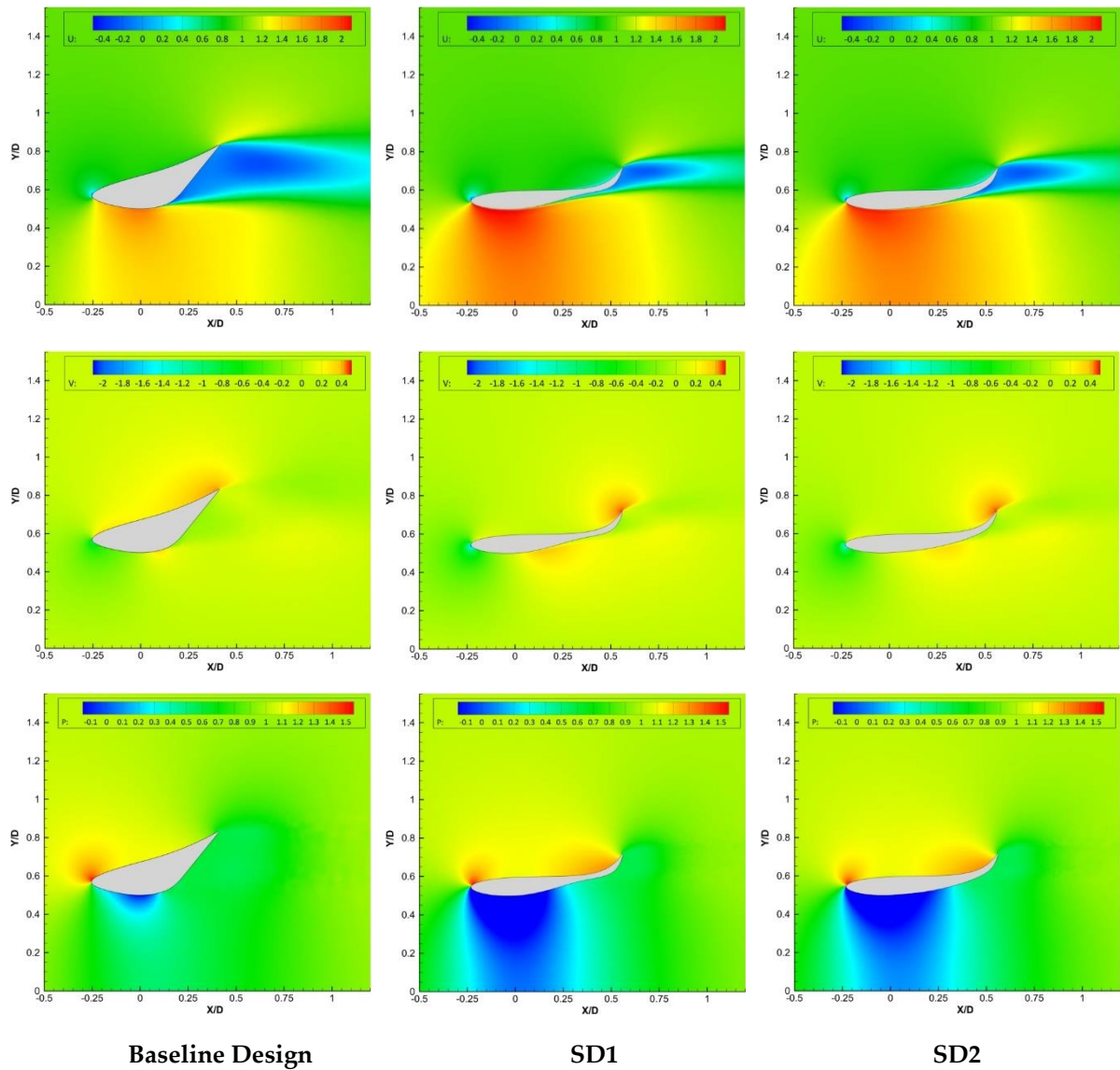


Figure 10.19: The dimensionless contours of axial velocity component (top), radial velocity component (middle), and static pressure (bottom), for the baseline design, SD1, and SD2, for a Reynolds number equal to 2,200,000 (fine meshes).

A more detailed representation of the recirculation areas for all the considered designs can be found in Figure 10.20 and Figure 10.21. It is evident that the streamlines flow smoothly inside the diffuser, while no recirculation areas exist along the high-pressure surface of the new diffusers. Even though SD1 and SD2 result in significantly smaller flow separations – which is identified as the main reason for the increase in velocity acceleration and drag reduction – these areas of recirculating flow tend to hamper their full aerodynamic potential.

A highly promising solution to alleviate this problem involves the addition of an internal flap near the exit plane.

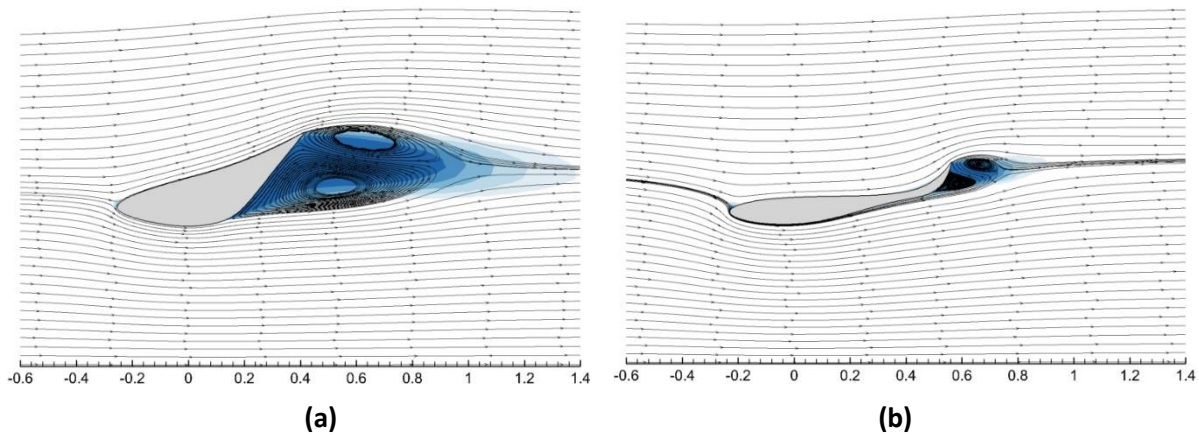


Figure 10.20: The velocity streamlines around the (a) baseline design, and (b) SD1 (fine meshes).

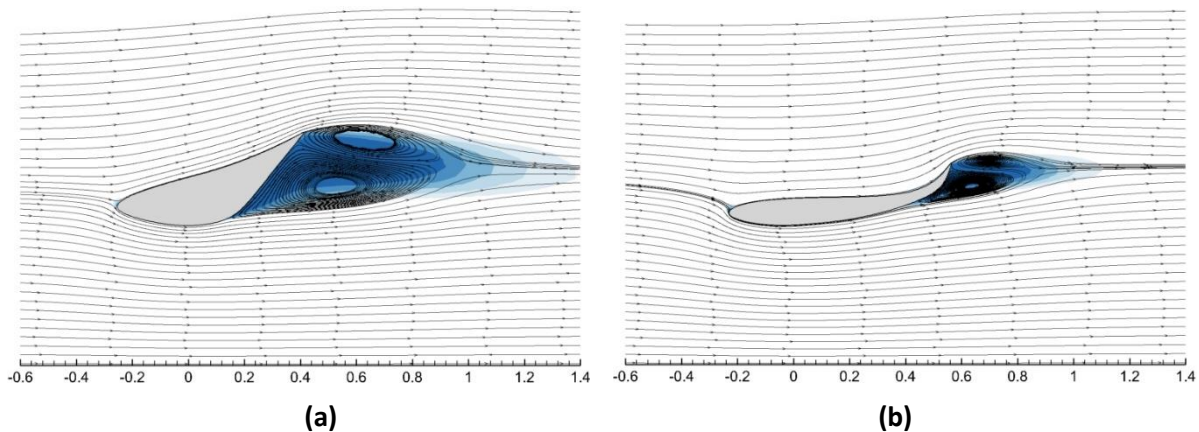


Figure 10.21: The velocity streamlines around the (a) baseline design, and (b) SD2 (fine meshes).

10.3 Optimization of a Complete Shrouded Wind Turbine

In this section, the proposed optimization scheme is applied for the simultaneous shroud and blade design improvement, considering the Donqi Urban Windmill as the baseline setup. The particular system for small energy production within urban environments was originally designed by Donqi Independent Energy Company, in cooperation with NRL and Delft University of Technology. It is consisted of a single-element shroud and a three-bladed rotor. To improve its performance many numerical and experimental studies have been performed since then (Ten Hoopen, 2009; van Dorst, 2011; Anselmi, 2017; Avallone *et al.*, 2020). One of the most important was that of van Dorst (2011), who designed a new blade configuration capable of significantly increasing power. Figure 10.22 illustrates a three-dimensional representation

of the shrouded rotor of Donqi Urban Windmill with the linearized blade, while a real Donqi Urban Windmill is presented in Figure 10.1.

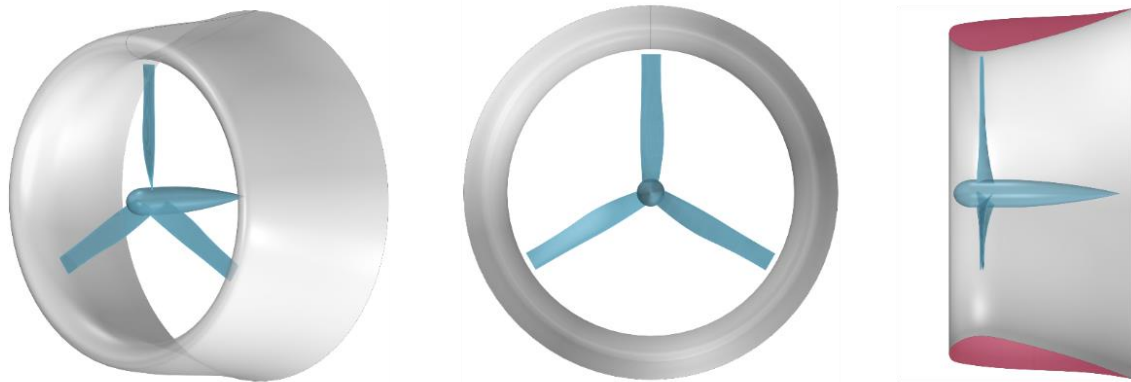


Figure 10.22: The Donqi DAWT with the linearized blade.

The diffuser is obtained as an axisymmetric revolution of an airfoil cross section, designed by NLR; the geometry was made available in the context of the DUCT4U project (Avallone *et al.*, 2020). The diffuser has a radius equal to $R_{in} = 0.87\text{ m}$ at inlet, $R_t = 0.77\text{ m}$ at throat, $R_{out} = 1\text{ m}$ at exit and an axial chord equal to 1 m. The aerodynamic profile of Donqi shroud is depicted in Figure 10.23, whereas its main geometrical characteristics are provided in Table 10.7.

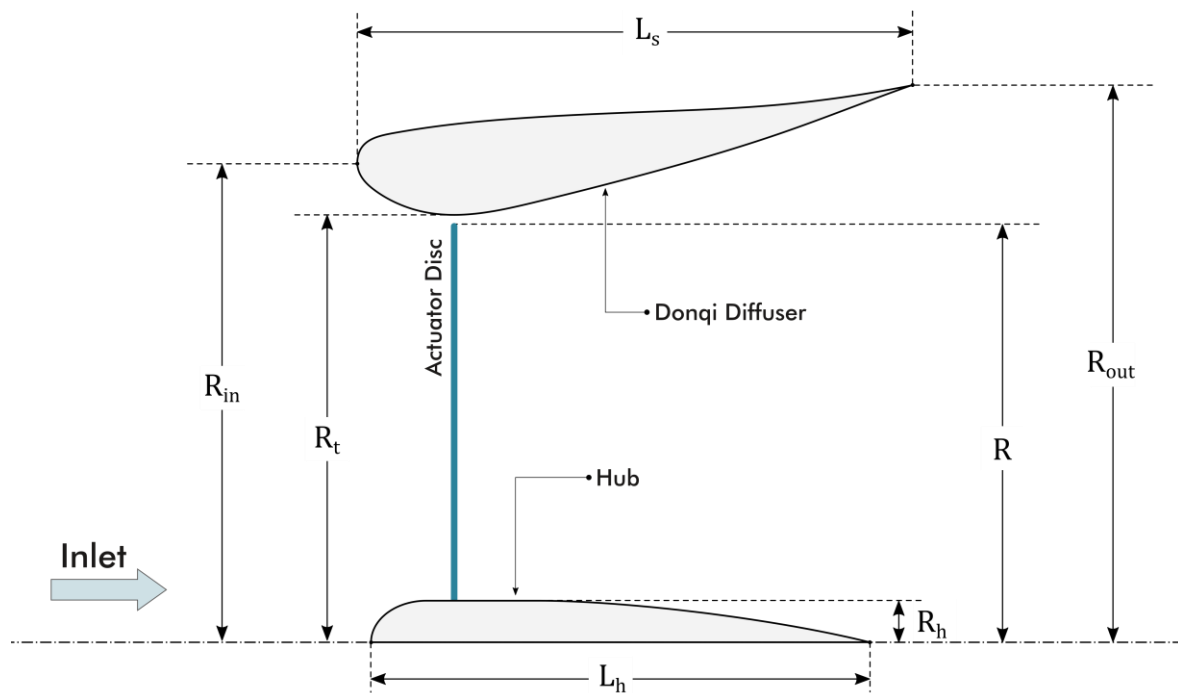


Figure 10.23: Geometric characteristics of the Donqi Urban Windmill shroud.

Parameter	Symbol	Value
Axial Diffuser Length	L_s	1.00 m
Axial Hub Length	L_h	0.90 m
Inlet Radius	R_{in}	0.87 m
Throat Radius	R_t	0.77 m
Exit Radius	R_{out}	1.00 m
Hub Radius	R_h	0.075 m
Shroud Volume	V_s	0.54 m^3

Table 10.7: The main geometrical characteristics of the baseline shroud.

The rotor has three blades with a NACA 2207 airfoil of chord length varying from 130 mm at root to 105 mm at tip; the rotor radius (R) equals to 0.75 m. The chord and twist angle distribution along the blade radius are plotted in Figure 10.24. Since no information of the hub geometry was available, a custom hub design was adopted in this study, resembling the one involved within the experimental studies. The radius of the hub at the rotor plane is equal to 0.075 m; the total length of the hub is equal to 0.9 m, while its leading edge has been placed 0.033R after the leading edge of the diffuser.

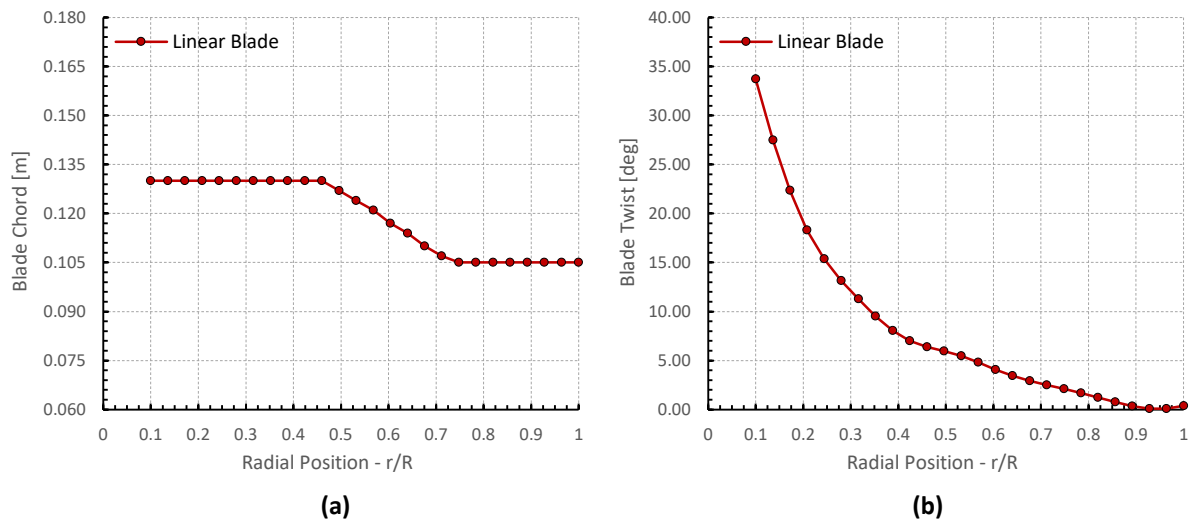


Figure 10.24: Chord and twist distributions of the linearized blade configuration (van Dorst, 2011).

10.3.1 Grid Independence Study

Before the application of the proposed optimization scheme, a detailed grid independence study is carried out, in order to assure that the resolution of the employed computational grid

does not have a significant impact on the simulation results and objective function value. To this end, three computational grids, exclusively composed by quadrilateral elements, were generated by increasing successively the mesh density; the involved computational grids are denoted by QM1, QM2 and QM3. For each denser resolution the degrees of freedom, *i.e.* the nodes (considering the vertex-centered scheme of the IGal2D solver), were doubled compared to the coarser one. Detailed characteristics for the involved computational grids are included in Table 10.8, while Figure 10.25 illustrates the region around the diffuser and hub walls, for each one of the three computational grids. Finally, Figure 10.26 provides a wide view of QM1.

Case	Nodes	Elements	Wall Spacing	y^+ Value
QM1	49,017	48,446	0.0000750 m	$\cong 1.45$
QM2	96,604	95,803	0.0000375 m	$\cong 0.70$
QM3	189,246	188,123	0.0000375 m	$\cong 0.70$

Table 10.8: Characteristics of the mesh employed in the grid independence study.

Values of aerodynamic power and thrust, as well as drag force, on the diffuser and the hub, regarding different mesh resolutions, are provided in Table 10.9. Apparently, the variation of each one of the adopted reference quantities is below 1%. In order to have a better understanding of the flow field and blade loading dependence upon the mesh density, Figure 10.27 provides the distribution of axial and tangential blade forces, as well as this of axial and tangential velocity components at an axial position $1.5R$ downstream the rotor plane. Once more, no deviations were detected between the distributions resulted from the use of the medium and fine grids. Consequently, the numerical solution, obtained by adopting QM1, can be safely considered as grid independent and the particular grid is used during the current optimization work.

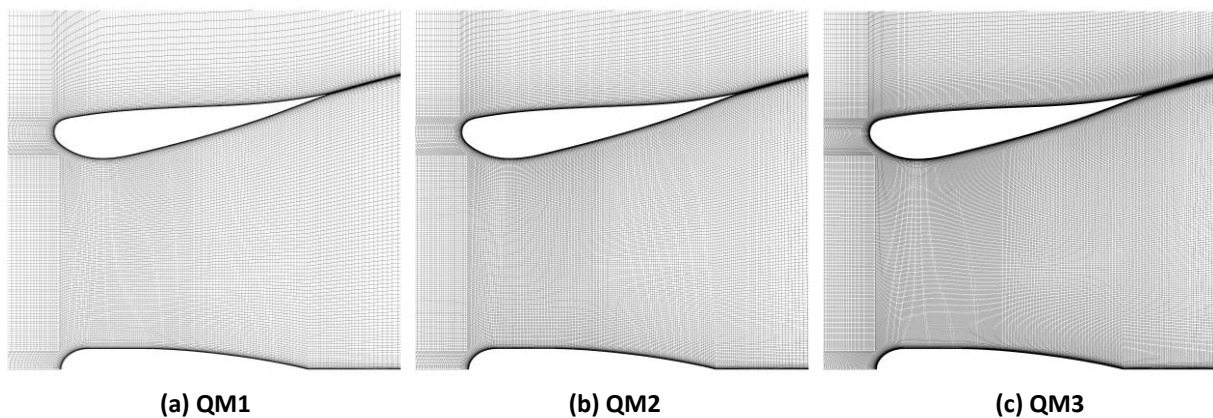


Figure 10.25: The computational grids used for the grid independence study: (a) coarse, (b) medium, and (c) fine.

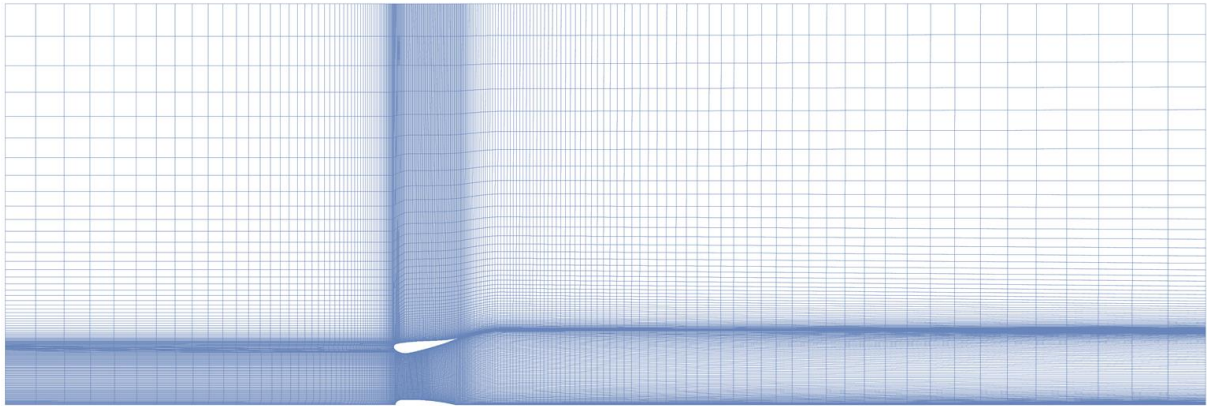


Figure 10.26: Wide view of the coarse (QM1) computational grid.

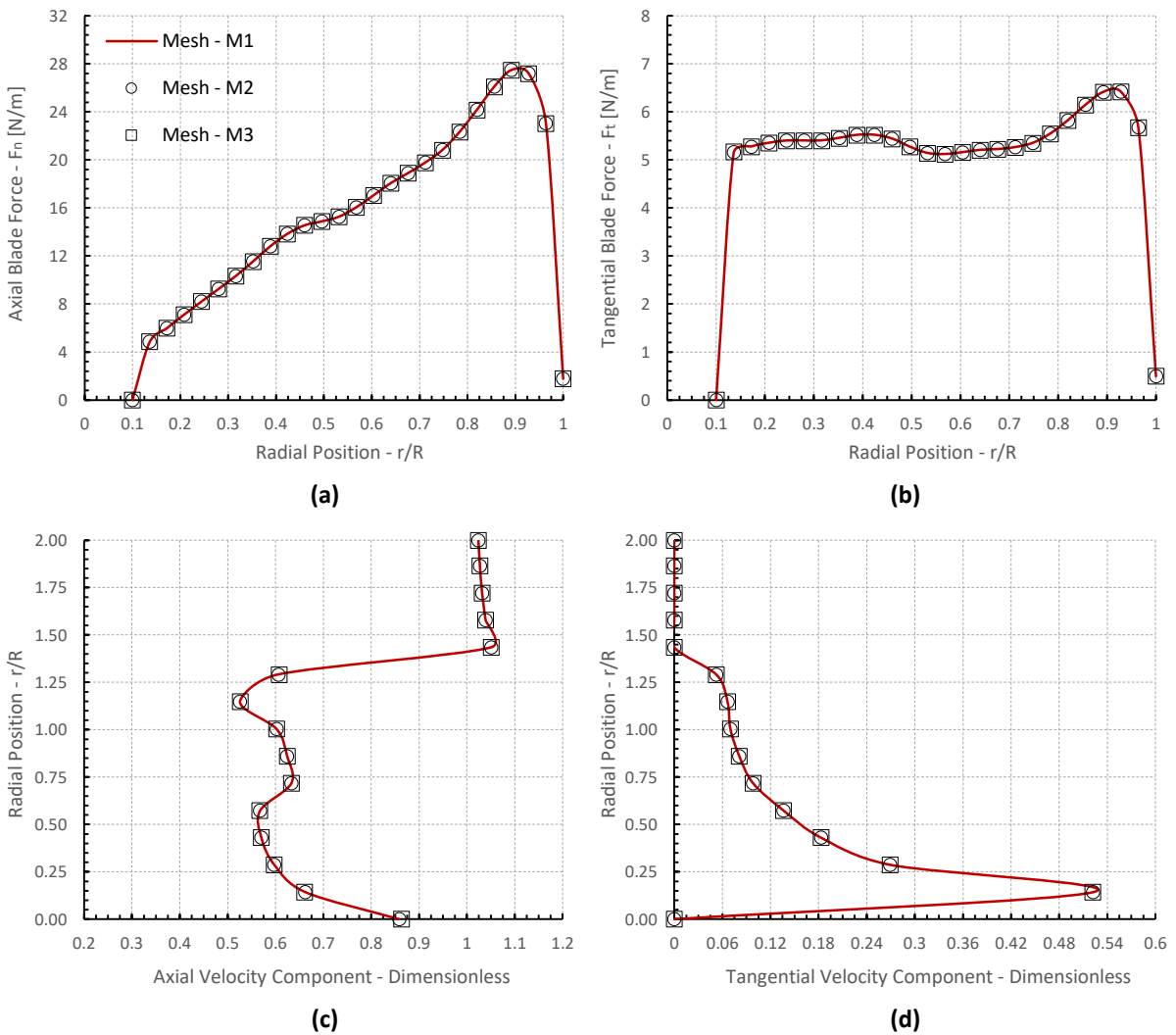


Figure 10.27: Results of the grid independence study.

Finally, the computed power with QM1 is compared against the experimentally obtained power output for values of ambient wind speed equal to 5 m/s, 6 m/s and 7 m/s, proving that

the proposed numerical model is capable of predicting the performance of the examined wind turbine configuration.

Case	Shroud – Drag [N]	Hub – Drag [N]	Rotor Power [W]	Rotor Thrust [N]
QM1	18.560	0.561	191.962	31.628
QM2	18.520	0.562	191.776	31.605
QM3	18.490	0.560	191.592	31.583

Table 10.9: Results of the grid independence study.

Linear Blade – Aerodynamic Power			
Wind Speed	Rotor Speed	IGal2D Prediction	Experiment
5 m/s	340.6 RPM	110.95 W	103.02 W
6 m/s	408.7 RPM	191.96 W	189.50 W
7 m/s	476.8 RPM	305.20 W	292.55 W

Table 10.10: Comparison of the predicted and experimentally measured values of power.

10.3.2 Geometry Parameterization and Design Variables

For the parameterization of the twist and chord distributions two B-Spline curves of second degree are employed, each one defined by 3 control points, as illustrated in Figure 10.28. The movement of B-Spline control points is allowed only in the vertical direction. Therefore, the blade chord and twist distributions can be fully defined by using 6 design variables, corresponding to the vertical coordinates of the respective control points. The upper and lower bounds for each design variable are presented in Figure 10.28.

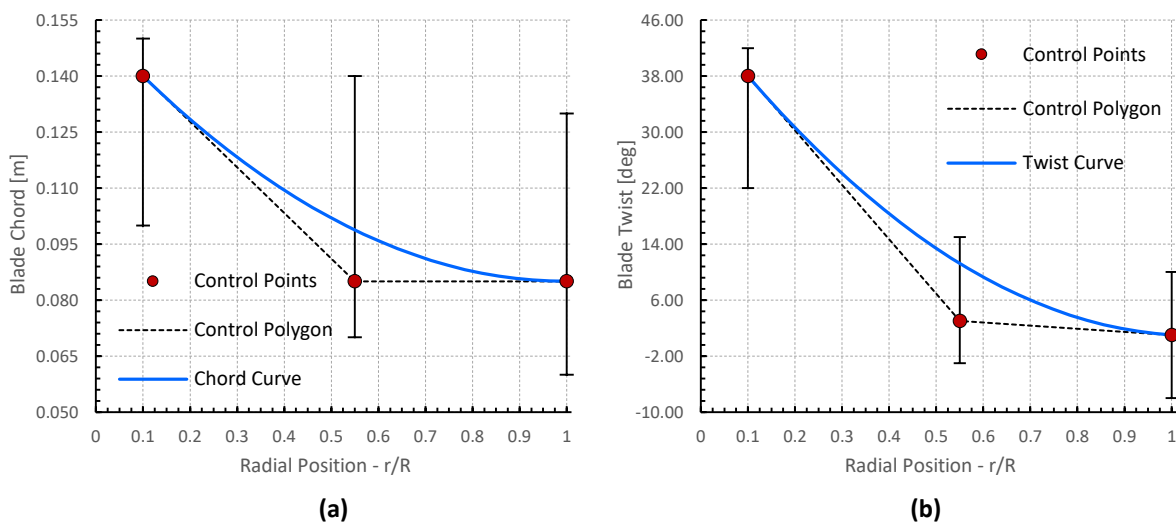


Figure 10.28: Parameterization strategy for chord and twist distributions.

In this optimization study, the parameterization and deformation of the computational grid is achieved by means of the in-house mesh deformation tool presented in Section 9.2. The employed two-dimensional lattice around the initial shroud geometry is depicted in Figure 10.29. The particular FFD lattice is defined by six control points in the radial direction and eight control points in the axial direction; in both parametric directions, fourth-degree basis function have been applied. Each control point of the FFD lattice is free to move in both directions, except of those positioned at the lattice boundaries; these points have been fixed, in order to avoid the formation of overlapping edges in the deformed computational grids. As a result, the number of design variables for the shroud geometry equals to 48, defined by the Cartesian coordinates of the 24 internal control points of the adopted FFD lattice. Ultimately, the total number of the design variables for the blade and shroud geometries within the current optimization study equals to 54. The upper and lower boundaries for the Cartesian coordinates of the FFD lattice are provided in Table 10.11. The enumeration of the control points goes from the bottom to top and left to right.

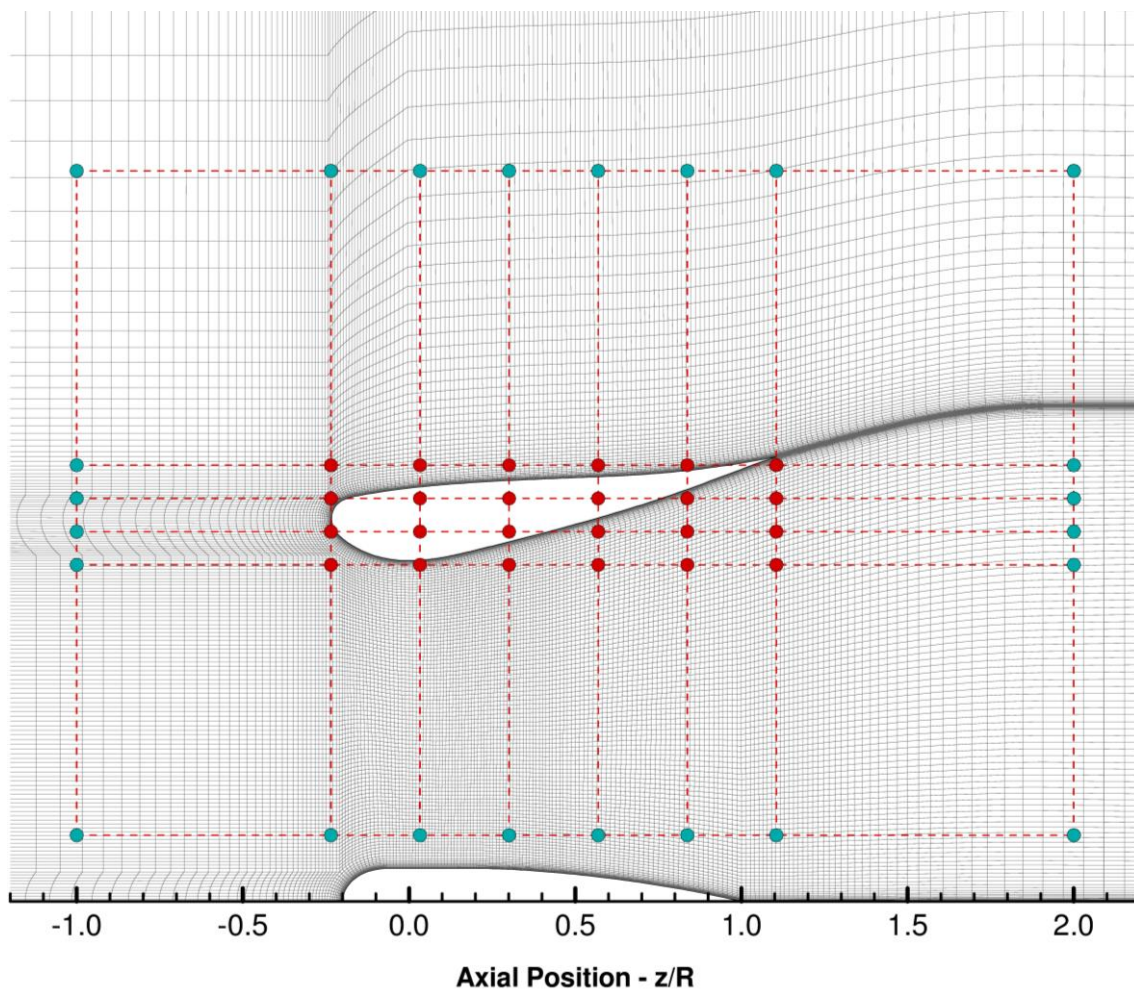


Figure 10.29: Definition of the FFD lattice employed for the parameterization of the computational mesh.

Point	Axial Direction		Radial Direction	
	Lower Bound	Upper Bound	Lower Bound	Upper Bound
CP ₁₁	-0.300	-0.200	1.014	1.014
CP ₁₂	-0.300	-0.200	1.100	1.140
CP ₁₃	-0.300	-0.170	1.100	1.220
CP ₁₄	-0.300	-0.170	1.160	1.350
CP ₂₁	-0.030	0.070	1.005	1.040
CP ₂₂	-0.030	0.080	1.090	1.130
CP ₂₃	-0.100	0.100	1.120	1.200
CP ₂₄	-0.080	0.120	1.100	1.350
CP ₃₁	0.200	0.440	0.850	1.070
CP ₃₂	0.200	0.440	0.980	1.180
CP ₃₃	0.200	0.440	1.000	1.300
CP ₃₄	0.150	0.480	1.070	1.380
CP ₄₁	0.350	0.900	0.800	1.150
CP ₄₂	0.350	0.900	0.800	1.170
CP ₄₃	0.350	0.850	0.990	1.370
CP ₄₄	0.300	0.850	1.000	1.400
CP ₅₁	0.500	1.200	0.850	1.180
CP ₅₂	0.500	1.200	0.800	1.180
CP ₅₃	0.500	1.200	1.050	1.400
CP ₅₄	0.500	1.200	1.100	1.450
CP ₆₁	0.800	1.400	0.800	1.300
CP ₆₂	0.800	1.400	0.800	1.350
CP ₆₃	0.800	1.400	0.850	1.500
CP ₆₄	0.800	1.400	1.100	1.600

Table 10.11: The adopted bounds for the control points of the FFD lattice.

10.3.3 Objective Function and Implicit Constraints

10.3.3.1 Design Objectives

The design objectives for the current application have been defined as the maximization of the rotor power coefficient and the minimization of the aerodynamic shroud drag. Thus, the design objectives are expressed as follows:

$$\max f_P = \max C_P \quad (10.10)$$

$$\min f_D = \min D_S \quad (10.11)$$

where C_P denotes the power coefficient of the three bladed rotor and D_S denotes the total drag force on the shroud at the design point.

10.3.3.2 Implicit Constraints

In this optimization study, besides the adopted explicit constraints, which are defined by means of the established bounds for the design variables, four additional implicit constraints have been introduced, to ensure that:

- C1. The rotor thrust coefficient of the optimal design will be less than a reference value.
- C2. The volume of the optimal shroud design will be less than the volume of the initial one.
- C3. The throat radius of the optimal shroud design will be equal to the initial one.
- C4. The local chord of the blade will be monotonically decreasing.

The implicit constraints are satisfied by introducing four penalty functions. The mathematical formulation of the penalty functions for the adopted constraints is described as:

C1 Constraint

$$f_T = \begin{cases} C_T - C_{T,ref} & \text{if } C_T > C_{T,ref} \\ 0 & \text{otherwise} \end{cases}, \quad (10.12)$$

C2 Constraint

$$f_V = \begin{cases} V_s - V_{s,ref} & \text{if } V_s > V_{s,ref} \\ 0 & \text{otherwise} \end{cases}, \quad (10.13)$$

C3 Constraint

$$f_{th} = |R_t - R_{t,ref}|, \quad (10.14)$$

C4 Constraint

$$f_c = f_{c12} + f_{c23}, \quad (10.15)$$

where

$$f_{c12} = \begin{cases} c(2) - c(1) & \text{if } c(2) > c(1) \\ 0 & \text{otherwise} \end{cases} \quad (10.16)$$

and

$$f_{c23} = \begin{cases} c(3) - c(2) & \text{if } c(3) > c(2) \\ 0 & \text{otherwise} \end{cases}. \quad (10.17)$$

Herein, $c(i)$ denotes the chord value corresponding to the i^{th} control point of the respective B-Spline curve (see Figure 10.28).

10.3.3.3 Cost Function Formulation

Eventually, the single cost function of the minimization problem at hand can be shaped by combining the objective and penalty functions:

$$f = 5 - 2 \cdot f_P + 0.1 \cdot f_D + 2 \cdot f_v + 4 \cdot f_{th} + f_T + 10 \cdot f_c. \quad (10.18)$$

The parameters multiplying the objectives and penalty functions in Eq. (10.18) have been finalized so that each individual function has similar impact on the cumulative cost function.

10.3.4 Optimization Results

Similar to the previous optimization cases that were reported in this doctoral dissertation, which are included in Section 10.1 and Section 10.2, the current design optimization study was performed on a DELL™ R815 PowerEdge™ computing server that is equipped with four AMD Opteron™ 6380 sixteen-core processors. As long as the parameters of the DE algorithm for this application are concerned, the population for each generation was set equal to 50 and the optimal solution was obtained after the completion of 70 generations. Figure 10.30a shows the convergence history of the optimization algorithm, in terms of the fitness function value.

In addition, Figure 10.30b provides the testing error progression for the two surrogate models that were employed in the current optimization study; namely, the MLP and the RBF artificial neural networks. Apparently, the testing error of the MLP model was lower than the corresponding error of the RBF model for the entire course of the optimization process, by approximately two orders of magnitude. Consequently, the pre-evaluation of the trial vectors in the current optimization application has been exclusively based on the MLP model.

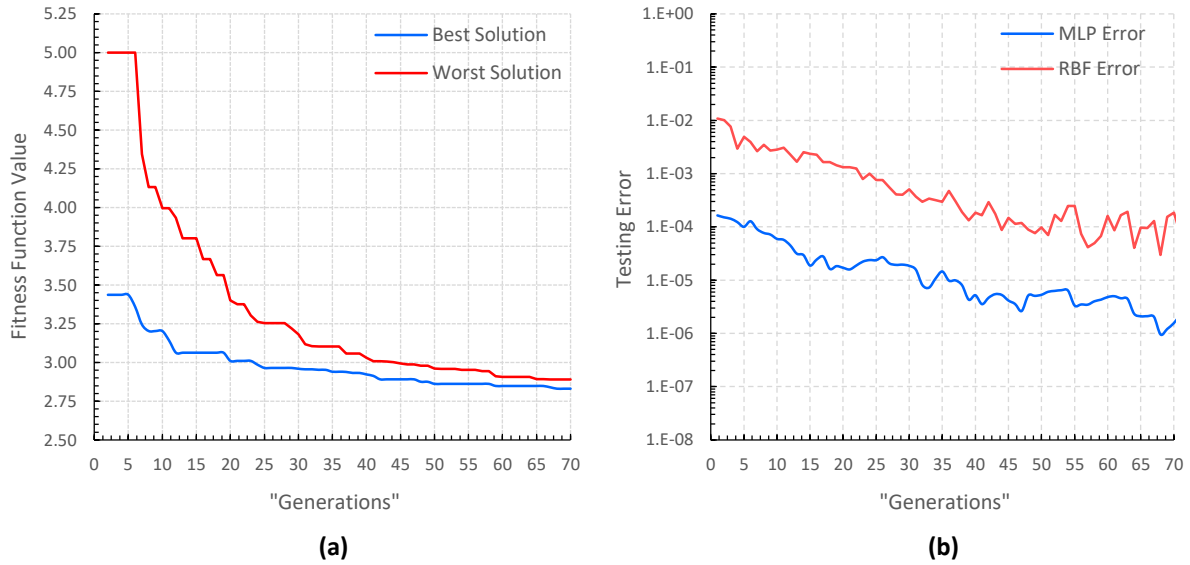


Figure 10.30: (a) The convergence history of the DE algorithm; (b) The testing error for the two surrogate modes.

10.3.4.1 Optimal Blade

Figure 10.31 illustrates the chord and twist distributions of the optimal blade design, in comparison with the respective distributions of the linear blade design (also denoted as baseline). By observing the optimized twist and chord distributions, it is evident that the new blade geometry has a much smoother twist distribution, as compared to the one of the linear blade; the maximum twist angle of the optimal blade equals to 24.95 degrees and decreases in a parabolic way as the blade tip is approached, until a minimum value of 1.22 degrees.

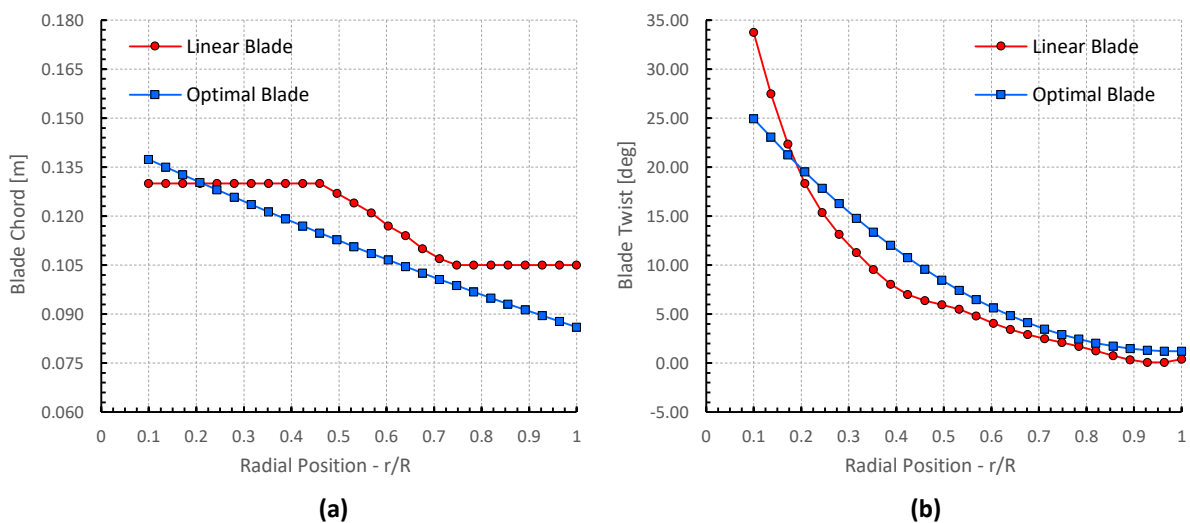


Figure 10.31: The chord and twist distributions of the optimal blade design against the chord and twist distribution of the linear blade, reported by van Dorst (2011).

On the other hand, the current optimization process resulted in a practically linear chord distribution along the entire span, with the maximum chord length to be 0.137 m and the minimum one 0.086 m. Please note that the linear chord distribution of the optimal blade is a truly desirable characteristic, as a simpler blade geometry is generally easier to be manufactured. Besides, the chord length of the optimal blade for almost the entire span is smaller than the respective value of the baseline one, allowing for significant material savings.

10.3.4.2 Optimal Shroud Geometry

Figure 10.32 illustrates the aerodynamic profile of the optimal shroud design along with the aerodynamic profile of the original Donqi Urban Windmill shroud, while Figure 10.33 provides a three-dimensional representation of the two axisymmetric designs. Initially, the visual comparison between the two aerodynamic shapes reveals that the optimization procedure resulted in a very smooth geometry (this is primarily attributed to the effective shape parameterization technique) that has a thinner cross-section and a higher camber that the baseline one. The main geometrical characteristics of the optimal shroud design are provided in Table 10.12.

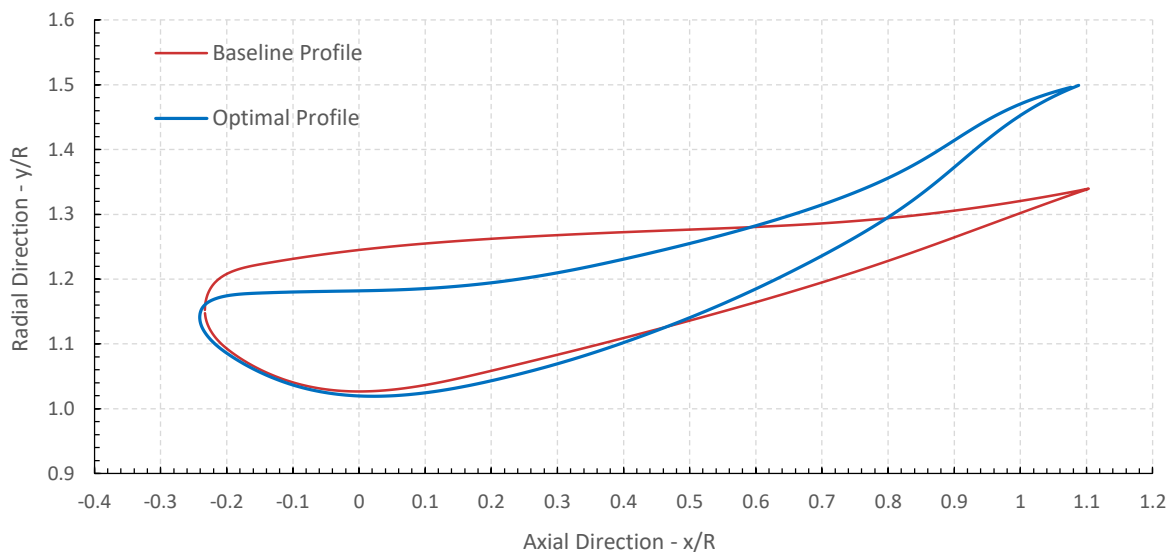


Figure 10.32: The aerodynamic profiles of the baseline and optimized shroud designs.

Please note that even though the axial length of the original and optimal shrouds is practically the same, the total volume of the optimal shroud has been reduced by approximately 24.7%, allowing for significant cost reduction. Furthermore, the optimal shroud design is characterized by a larger exit radius and – since the throat radius of the two designs is practically equal – by a larger exit-area-ratio, which according to Sorensen (2016) is

proportional to the maximum theoretical power coefficient. Finally, let us note that both the adopted geometrical constrains were successfully met, since the volume of the optimal shroud is lower than the original and the throat radius has been reduced by only 0.65 percent.

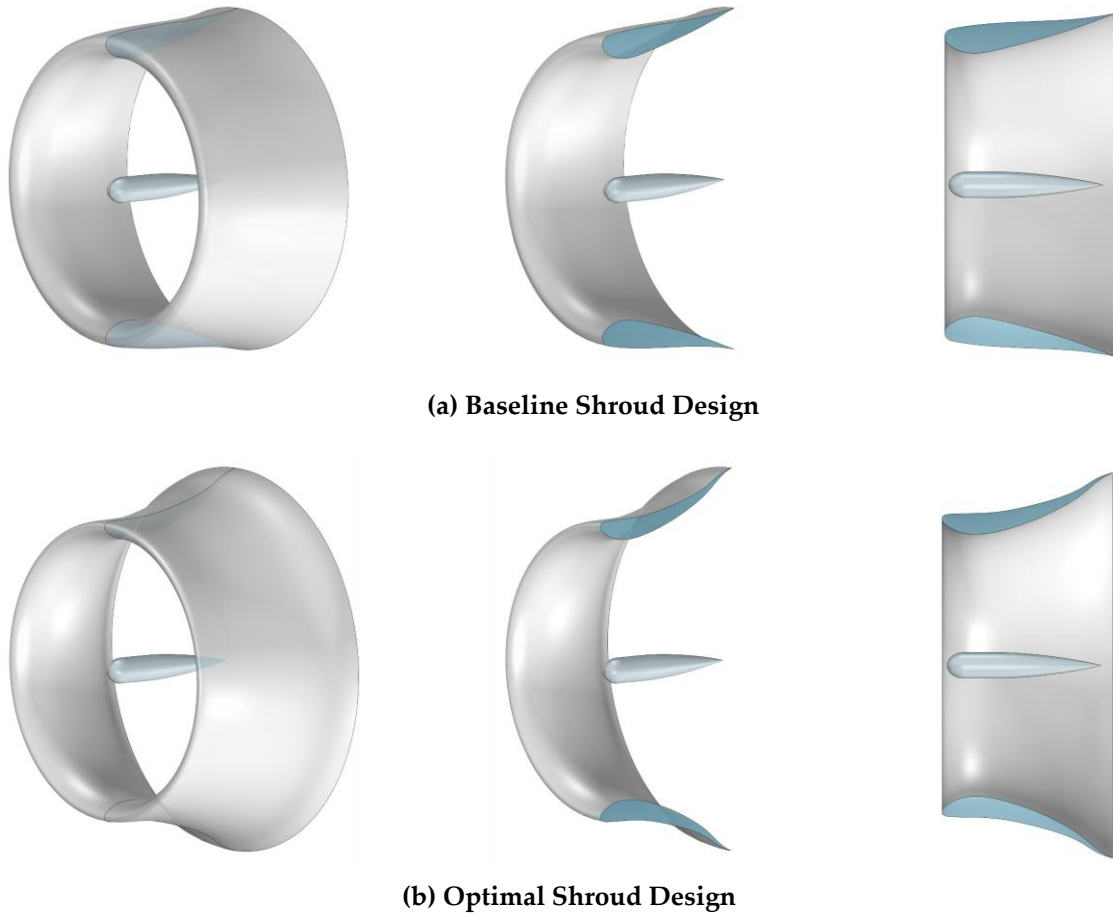


Figure 10.33: Three-dimensional representation of (a) the baseline and (b) optimal shrouds.

Parameter	Symbol	Baseline	Optimal
Axial Diffuser Length	L_s	1.000 m	0.997 m
Inlet Radius	R_{in}	0.870 m	0.856 m
Throat Radius	R_t	0.770 m	0.765 m
Exit Radius	R_{out}	1.000 m	1.124 m
Shroud Volume	V_s	0.545 m ³	0.425 m ³

Table 10.12: The main geometrical characteristics of the baseline and optimal shroud designs.

10.3.5 Performance of the Optimal Design

The current section involves the aerodynamic evaluation of the optimized wind turbine configuration. Initially, Table 10.13 compares the major performance characteristics of the optimal shrouded wind turbine design against the Donqi Urban Windmill; the latter one is also referred to as the baseline design. According to the numerical results presented in Table 10.13, the optimal design has the ability to reach significantly higher levels of power output; in particular, the aerodynamic power output of the rotor has been increased by approximately 33%. However, this is also accompanied by higher drag levels on the shroud. Yet, the increased value of drag force on the shroud was generally anticipated, since according to momentum theory – and more precisely according to Eq. (2.48) – the maximum power coefficient of a shrouded wind turbine is an increasing function of the shroud force. The power coefficient for the optimal configuration at the design point, calculated based on the rotor swept area, equals to 1.148; this is approximately 1.93 times higher than the Betz limit.

Design	Rotor Power	Rotor Thrust	Shroud – Drag	Hub – Drag
Baseline	191.9 Watts	31.628 N	18.560 N	0.561 N
Optimal	268.5 Watts	36.910 N	43.000 N	0.454 N

Table 10.13: Performance characteristics of the initial and optimal designs.

In addition, Figure 10.34 presents the axial and tangential force distributions along the entire blade span for the optimal and baseline designs. According to both Figure 10.34 and Table 10.13, the total axial loading – expressed by means of the thrust force – on the optimal rotor design is higher than the total axial loading on the baseline one, by approximately 15.5%; in particular, the thrust coefficient at the design point for the baseline rotor equals to 0.812, while the thrust coefficient for the optimal one equals to 0.947. Moreover, as long as the distribution of the axial or normal force along the blade span is concerned, no significant variation of the axial loading value between the involved designs is observed for the blade stations located among the rotor hub and 0.5R. However, the axial loading for the region corresponding between the 50 percent and 100 percent of the span, is considerably higher for the optimal design, with the maximum value of axial force to be increased by approximately 15%. Now, as long as the values of the tangential force on the blade are concerned, these are significantly higher for the case of the optimal design, almost along the entire blade span, as Figure 10.34b illustrates. Finally, no significant variation of the drag force on the rotor hub for the two involved designs has been observed.

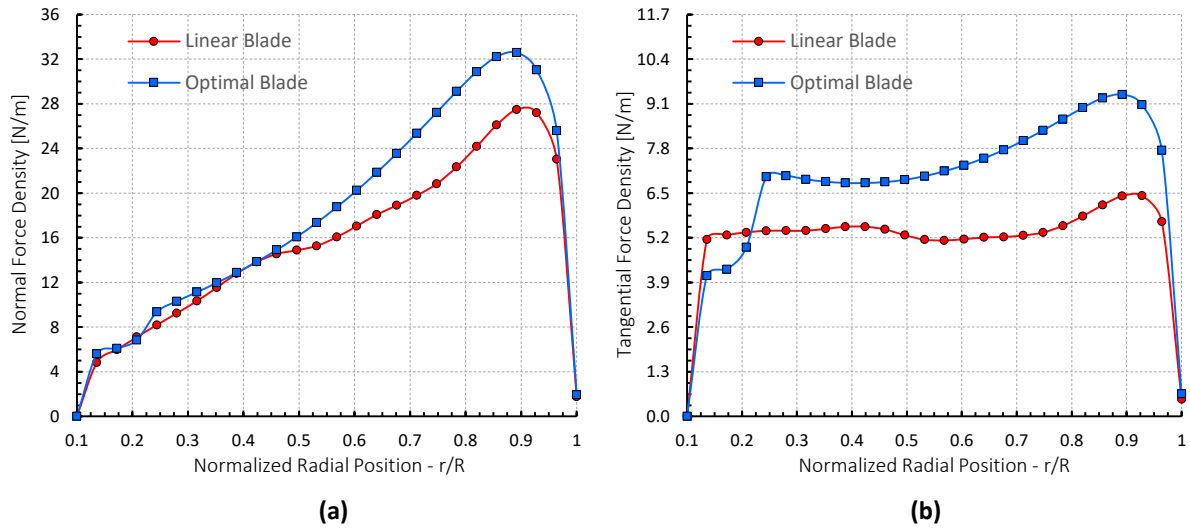


Figure 10.34: The axial and tangential force distributions along the optimized and baseline blade designs.

Furthermore, in order to have a better understanding of the aerodynamic behavior of the baseline and optimal designs, Figure 10.35 until Figure 10.37 present the dimensionless contours of axial velocity component, tangential velocity component and static pressure at the symmetry plane of the two shrouded wind turbine rotors. In particular, Figure 10.35 clearly displays the higher axial velocity levels within the diffuser, for the case of the optimal design, which eventually result in a higher mass flow rate, and therefore higher power output.

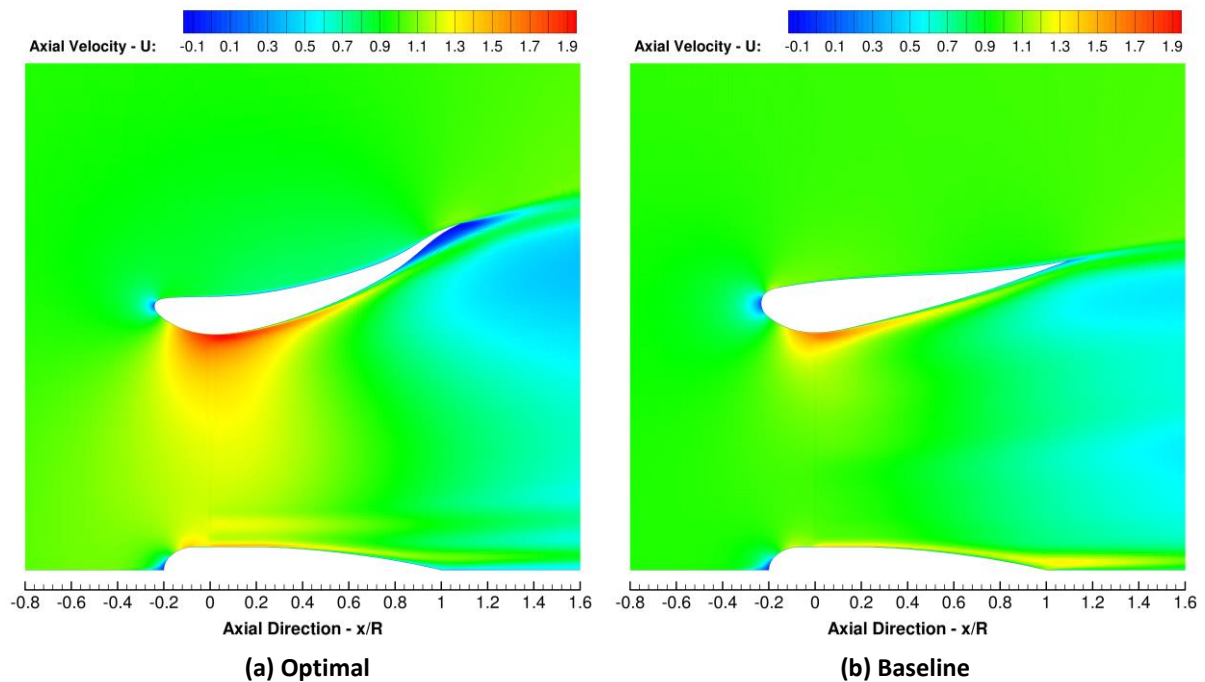


Figure 10.35: The contours of dimensionless axial velocity component around the optimal and baseline shrouds.

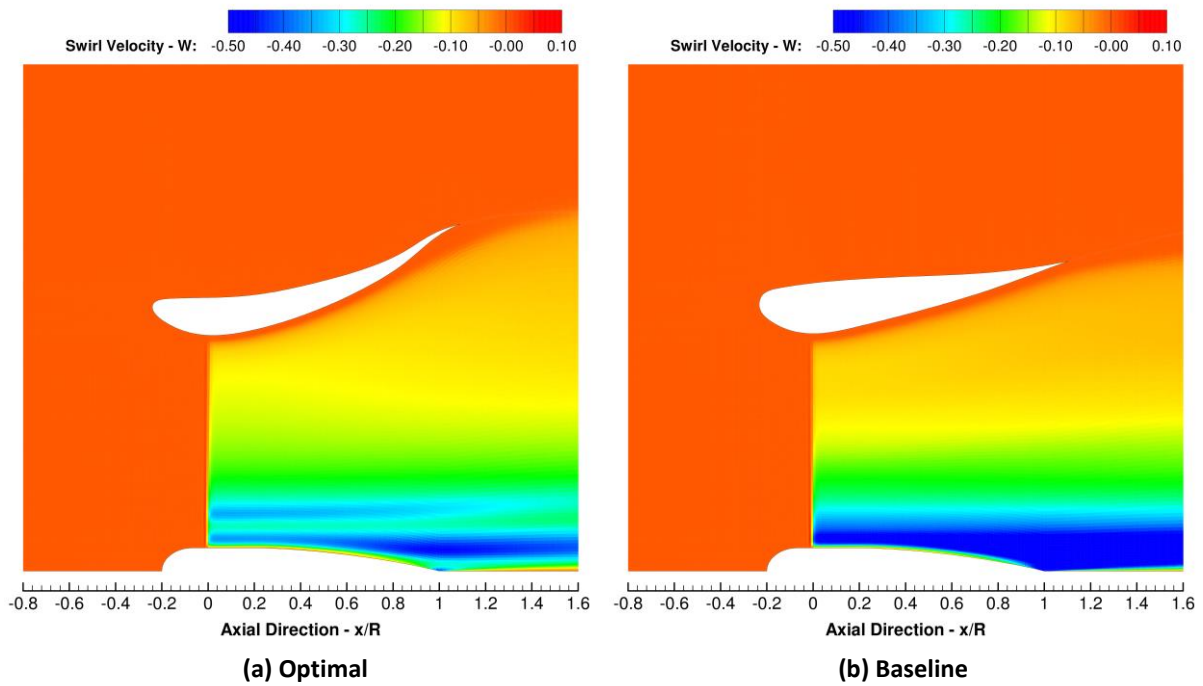


Figure 10.36: The contours of dimensionless swirl velocity component around the optimal and baseline shrouds.

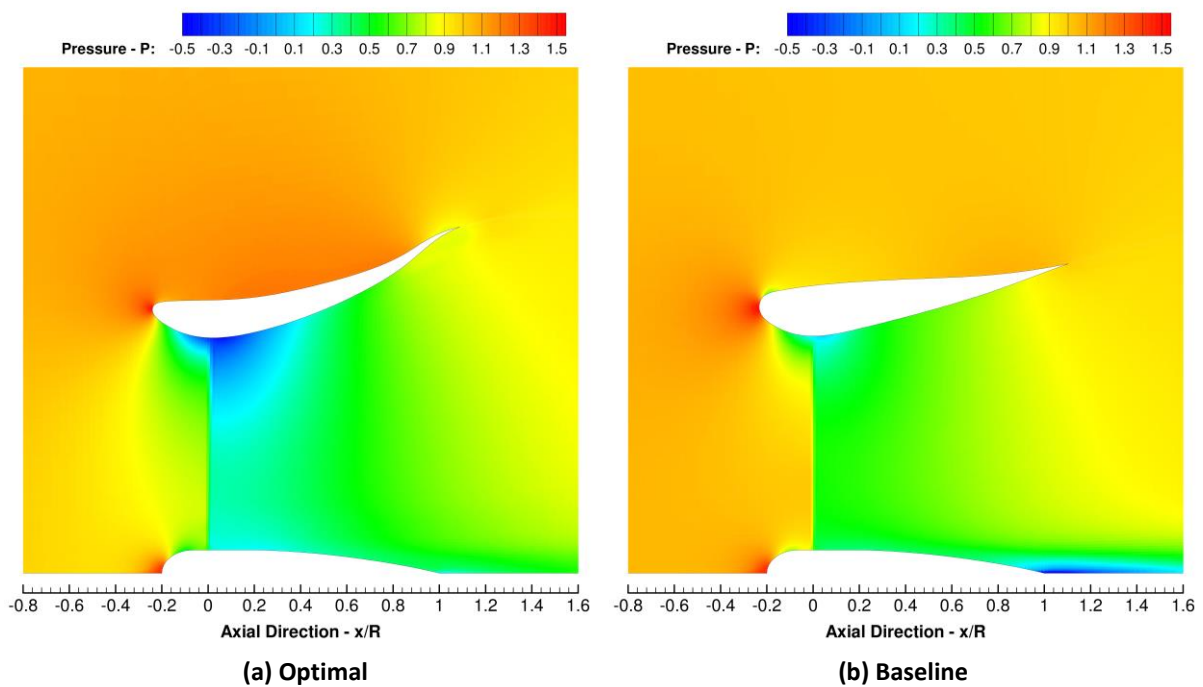


Figure 10.37: The contours of dimensionless pressure around the optimal and baseline shrouds.

Finally, Figure 10.38 displays the contour lines of the dimensionless static pressure and Figure 10.39 illustrates the velocity stream lines around the optimal and baseline shrouds. Moreover, the latter one reveals the presence of a small recirculation area near the trailing edge

of the optimal diffuser, which can be also identified by observing Figure 10.35a; even though the total length of the particular recirculation area equals to $0.3R$, it is not expected to have a significant impact on the overall system's performance.

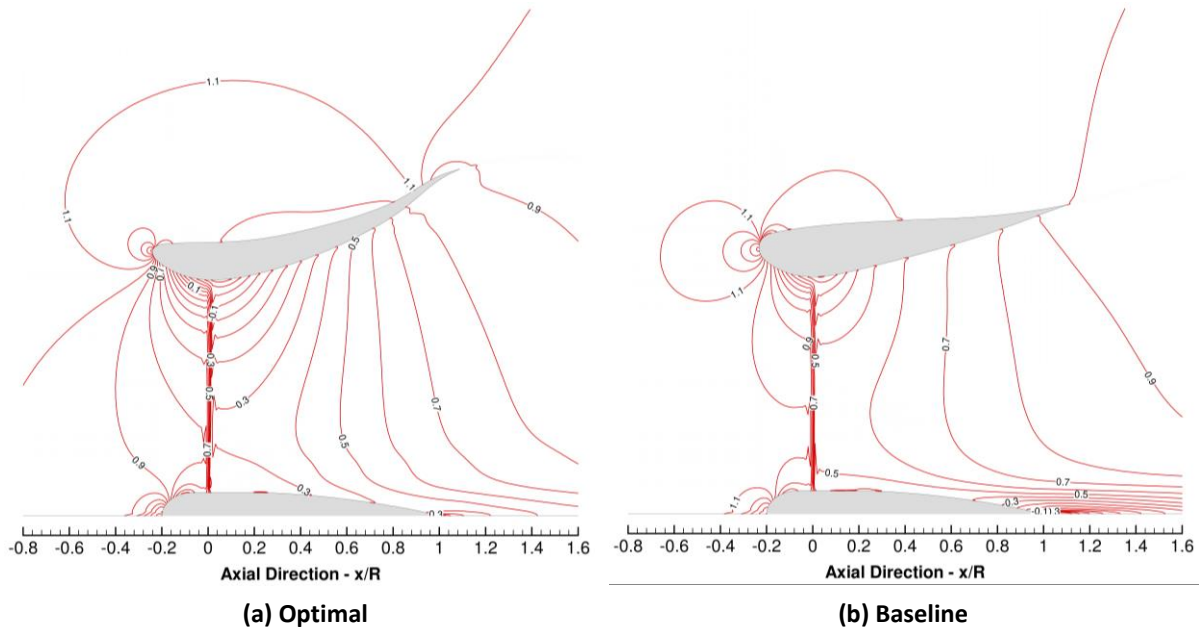


Figure 10.38: The contour lines of dimensionless pressure around the optimal and baseline shrouds.

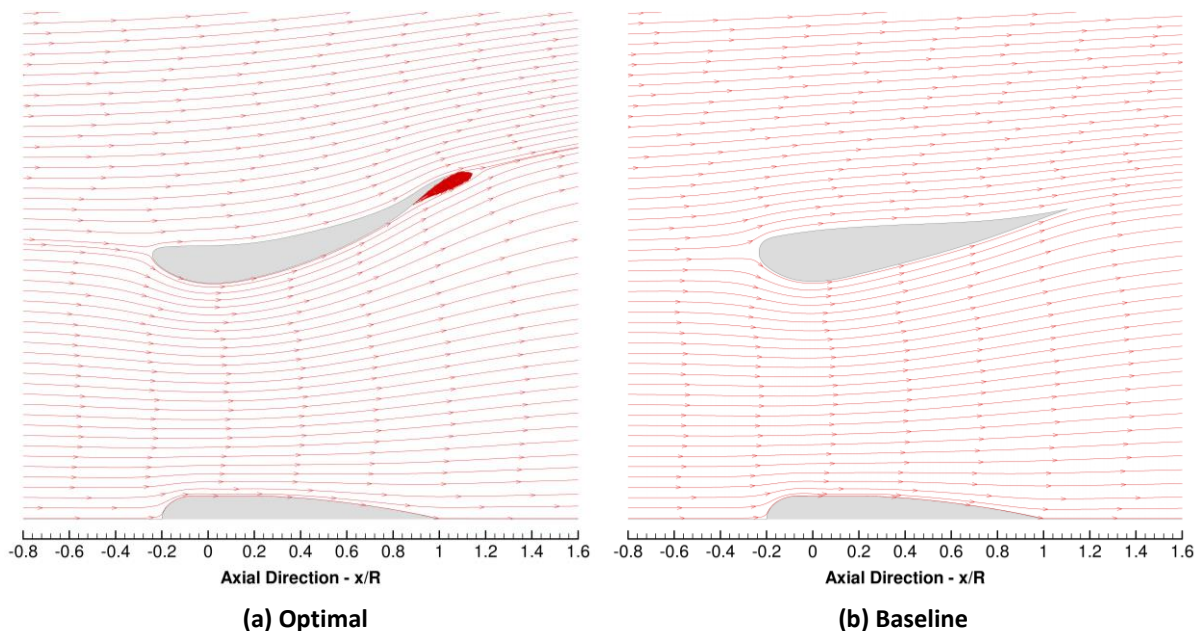


Figure 10.39: The velocity streamlines around the optimal and baseline shrouds.

Chapter 11

Conclusions and Future Work

This chapter summarizes the principal conclusions of the current doctoral dissertation. In particular, Section 11.1 provides a concise recap of the entire study, focused on the most significant results and contributions, while Section 11.2 indicates possible directions for further research on the specific topic.

11.1 Concluding Remarks

The concept of **diffuser-augmented or shrouded wind turbine** represents an attractive and highly versatile energy solution that has the potential to yield power performance coefficients exceeding the Betz limit, and therefore to improve the economic feasibility of renewable energy production under poor wind conditions, such as those prevailing within the urban environment. In that regard, shrouded wind turbines could eventually enable significant opportunities for more geographic dispersion of wind technology applications, growth in distributed energy deployments and further expansion of renewable energy utilization on a global scale, contributing to the so-called energy transition. However, the achievement of widely adopted implementations and the consolidation of this promising technological application in the renewable energy market call for highly efficient and economically sustainable designs. Against this background, the present doctoral dissertation has been primarily focused on the development and validation of effective computational tools and numerical methodologies for, but not restricted to, the aerodynamic analysis, performance prediction and design optimization of shrouded wind turbines. The remainder of this section summarizes the principal outcomes of this computational study; following the storyline of the entire doctoral dissertation, the major conclusions of the present research have been arranged into five thematic sub-sections:

-  **Development of a Blade Element Momentum Code**
-  **Development of an Axisymmetric RANS Solver**
-  **Development of a Coupled RANS-BEM Model**
-  **Design of a Low Reynolds Number Airfoil Family**
-  **Development of an Optimization Framework for Shrouded Wind Turbines**

11.1.1 Development of a Blade Element Momentum Code

In Chapter 2, the current doctoral dissertation has been focused on the development of an in-house **Blade Element Momentum code** for the aerodynamic analysis and performance prediction of both conventional horizontal-axis and shrouded wind turbine rotors. In particular, the proposed computational model has been based on the extension of classical BEM theory, to the case of shrouded rotors, which was originally proposed by Rio Vaz *et al.* (2014) and is actually implemented by properly modifying the original BEM expressions with the axial velocity speed-up distribution over the rotor plane, for the unloaded diffuser configuration. Furthermore, the current BEM code has been enhanced with several empirical and analytical correction models, dealing with many of the inherent limitations of BEM theory; namely, two different correction models for capturing the power losses related to the blade tip and rotor hub, a drag correction model that accounts for the effects of Reynolds number, and a detailed correction model for the accurate calculation of the axial induction factor, at the operating states of rotor in which the momentum theory is no longer valid. The latter one employs the expressions proposed by Ning (2014), specially tailored for the case of shrouded wind turbines (Leloudas *et al.*, 2017). Besides, two different models for the extrapolation of the aerodynamic coefficients to the entire range of angles of attack have been also implemented, based on the Montgomerie (2003) and Viterna-Corrigan (Viterna and Corrigan, 1981) extrapolation methods. Finally, the calculation of induced velocities at the rotor plane is achieved by applying a fixed-point iteration scheme, which is coupled with a typical relaxation procedure, aiming to dampen the fluctuating behaviour of the axial induction factor during the iterative process.

The performance evaluation of the proposed BEM code, in terms of accuracy, has been reported in Chapter 3, by considering several well-documented benchmark cases, which include both conventional horizontal-axis wind turbine and shrouded wind turbine rotors. The results of the current simulations were compared against numerical and experimental data available in the literature, as well as against the results obtained from the well-known QBlade software, validating the ability of the proposed BEM code to provide rapid and reasonably accurate predictions of the rotor characteristics, both for unshrouded and shrouded wind turbine configurations. However, at the same time, significant discrepancies between the computational and the experimental results were identified when the rotor blades operate in stall mode, which is a typical deficiency of BEM models and calls for the inclusion of so-called stall correction models or the proper modification of the two-dimensional aerodynamic coefficients. In addition, the effect of including a tip loss correction model on the power output prediction of shrouded rotors was also examined; the corresponding results indicated that the inclusion of such a correction model results in more accurate predictions of the experimental

data, especially as the value of the freestream velocity increases. However, in some cases, a possible underestimation of the actual power output should be also anticipated.

11.1.2 Development of an Axisymmetric RANS Solver

In Chapter 4, the current doctoral dissertation has been featuring the application of Artificial Compressibility Method (ACM) for the numerical prediction of incompressible axisymmetric flows that involve swirling. The respective numerical solver, named **IGal2D**, has been based on the axisymmetric formulation of the Reynolds-Averaged Navier-Stokes (RANS) equations, which were eventually arranged in a pseudo-Cartesian form and enhanced by the addition of the circumferential momentum equation. The discretization of spatial derivative terms within the governing equations has been performed via unstructured two-dimensional grid layouts, by means of a node-centered finite-volume scheme. For the evaluation of inviscid fluxes, the upwind Roe's approximate Riemann solver was applied, coupled with a higher-order accurate spatial reconstruction, whereas an element-based approach has been used for the calculation of gradients required for the viscous ones. In addition, a detailed description of the convective flux Jacobian and the entire eigenvector system used within the Roe's approximate Riemann solver was provided, filling a respective gap in research literature. Time integration has been relying on a second-order accurate four-stage Runge-Kutta method, adopting additionally a local time-stepping technique. Finally, further acceleration, in terms of computational time, was achieved by using an agglomeration multigrid scheme, incorporating the full approximation scheme in a V-cycle process, within an efficient edge-based data structure.

Subsequently, Chapter 5 has been presenting a detailed validation study on the performance of the proposed numerical methodology and the respective flow solver, by encountering several non-swirling and swirling flows with axial symmetry. As long as the numerical prediction of swirling flows is concerned – which are generally more demanding than their non-swirling counterparts – the proposed methodology was initially validated by considering the incompressible, inviscid and swirling flow inside a specially designed axisymmetric S-shaped tube. Detailed comparisons between IGal2D code and the commercial software ANSYS Fluent (which employs the SIMPLE algorithm) were made, regarding velocity components and pressure distributions at different reference sections of the tube. An excellent agreement between them was observed. Furthermore, IGal2D was successfully evaluated against properly established metrics, referring to the conservation of total pressure and angular momentum. Regarding the performance of the FAS V-cycle scheme, the multigrid scheme was found capable of speeding-up the solution procedure more than 20 times. Similar levels of accuracy were identified by encountering the second benchmark test case, concerning

incompressible laminar flow inside a straight-wall pipe equipped with swirl generator. The particular flow apparatus has been examined numerically and experimentally by Rocha *et al.* (2015). IGal2D was capable of accurately predicting both axial and tangential velocity component distributions along the entire length of the pipe, while excellent agreement between the results of IGal2D, those of ANSYS Fluent (axisymmetric simulation) and those reported in the study of Rocha *et al.* (2015) (3D simulation), in terms of pressure distribution along the axisymmetric line, was observed. As long as the comparison with the available experimental data is concerned, the proposed method resulted in a reasonably accurate prediction of the pressure drop; the experimental measurement was over-predicted by only 4%. Finally, the ERCOFTAC swirling conical diffuser (Clausen *et al.*, 1993) was examined. As in the previous case studies, an almost perfect agreement between IGal2D and ANSYS Fluent was succeeded for both axial and tangential velocity components at each one of the examined sections. However, some non-trivial discrepancies between the numerical and experimental data were identified; these are mainly attributed to the inability of $k-\omega$ SST model to accurately predict turbulent kinetic energy k in such swirling flows (Rodi *et al.*, 1995). Therefore, this calls for the incorporation of more advanced turbulence models within the current solver. Nevertheless, near-wall intensity, peak position of axial velocity and swirl velocity distributions along the entire length of the diffuser have been reasonably predicted. Furthermore, an accurate calculation of the experimentally obtained pressure coefficient distribution over the diffuser wall (pressure recovery) by IGal2D was achieved. Overall, the proposed numerical solver and consequently the corresponding axisymmetric-swirling ACM is revealed capable of accurately simulating a wide variety of axisymmetric swirling flows, whereas its performance may be further enhanced by the incorporation of alternative turbulence models, which will be the subject of further research.

11.1.3 Development of a Coupled RANS – BEM Model

Additionally, Chapter 8 reported the development and validation of an axisymmetric RANS - BEM model that is based on the combination of the in-house BEM and IGal2D codes, for the simultaneous prediction of the wind turbine rotor performance and surrounding flow characteristics. The fundamental idea behind the proposed model relies on replacing the momentum part of the classical BEM theory with a more elaborate flow model, such as the Navier-Stokes equations, while assuming an actuator disc representation of the actual rotor geometry. Eventually, the rotor blades are modelled by means of body force terms (naturally included within the momentum conservation laws) and blade element theory equations. The entire coupling procedure is coordinated by IGal2D software, while interaction is achieved by means of the aerodynamic blade loads and velocity components at the rotor plane. The

interpolation of the involved quantities between the mesh nodes and the blade stations is implemented by custom Matlab scripts.

The performance evaluation of the proposed methodology was initially investigated by considering the NREL 5-MW reference wind turbine, where the results of the in-house model were compared against those of other high-fidelity simulation tools. The comparisons between the involved software indicated that the current implementation has been capable of providing reasonably similar levels of accuracy, in terms of predicting the aerodynamic power and thrust of the wind turbine rotor, as well as the axial momentum deficit in the turbine wake field and the distribution of the aerodynamic loads along the blade span. Subsequently, in order to add further validity to the developed RANS - BEM methodology, two additional cases were studied, involving an unshrouded and a shrouded configuration of the NREL Phase VI rotor. As long as the unshrouded NREL Phase VI rotor is concerned, the current simulation results were successfully validated against the available experimental data, for the aerodynamic rotor power, aerodynamic rotor trust and loading distribution along the blade. According to the respective comparisons, all the reference quantities have been accurately predicted; in particular, the percentage difference between the numerical prediction and the experimental measurement for the aerodynamic power was less than 1%, whereas the respective percentage difference for the rotor thrust was approximately 3%. Finally, the accuracy of the current RANS - BEM implementation was assessed against a shrouded NREL Phase VI configuration, which was originally reported and studied by Aranake (2013). As for the previous cases, the proposed methodology was able to provide similar levels of accuracy, as compared to the detailed 3D RANS simulations with a fully resolved rotor geometry reported by Aranake (2013).

11.1.4 Design of a Low Reynolds Airfoil Family

Besides the aforementioned analysis tools, in Chapter 6 and Chapter 7, the current doctoral dissertation has been focused on the design and aerodynamic evaluation of a low-Reynolds airfoils family, which consists of six airfoils, for the entire blade span of small horizontal-axis wind turbines, aiming to reduce the effects related to laminar separation, increase the structural integrity of the blade, enhance the startup behavior of the wind turbine and meet the current blade manufacturing limitations. Initially, five thickened airfoils were constructed based on the RG15 airfoil. According to the followed methodology, the thickened airfoils were designed in such a way that they have the same mean camber line (MCL), as compared to the one of the original RG15 airfoil (so as to retain its desirable aerodynamic characteristics), but an increased thickness-to-chord ratio distribution by 50%, 40%, 30%, 20% and 10%, respectively. Then, another custom script was applied to the original and the thickened RG15

airfoils, for the generation of a rounded trailing edge without truncating the airfoil, through the proper modification (local thickening) of the provided airfoil geometries. The final airfoil family resulted through the application of a parabolic thickness distribution to the thickened airfoils, at their trailing edge region, setting the value for the blending distance equal to 70% and the trailing edge radius equal to 0.5% of the chord length respectively. According to the aerodynamic evaluations performed with XFOIL code at various low Reynolds numbers, the dependence of the blending distance on the lift and drag coefficients was found practically zero; the same conclusion was drawn for the dependence of the aerodynamic coefficients on the rounded trailing edge with a radius of 0.5% of the chord.

The aerodynamic performance of the entire RG15 airfoil family was initially evaluated by using XFOIL software for various low Reynolds numbers, ranging from 60,000 to 300,000. The results of the XFOIL analysis revealed that the increase of the thickness-to-chord ratio leads to a reduction in the maximum lift-to-drag ratio for each one of the considered Reynolds numbers. However, as the Reynolds number increases the particular percentage reduction decreases. Apparently, the maximum reduction in the maximum lift-to-drag ratio, as compared to the one of the original RG15 airfoil, was found for the lowest Reynolds number that was examined (*i.e.*, 60,000) and the RG15-(50)-70-1 airfoil (the thicker airfoil of the RG15 family); this percentage reduction was equal to 12.68%. The corresponding percentage at 300,000 Re was equal to 4.6%. Nevertheless, even the largest reduction of the maximum lift-to-drag ratio seems minor given that this airfoil has a maximum thickness-to-chord ratio that is 50% higher than the maximum thickness-to-chord ratio of the baseline RG15 airfoil, accompanied by cross-sectional area that has been increased by approximately 52%. On the other hand, a growth of the maximum lift coefficient for each Re was found by increasing the thickness-to-chord ratio.

Moreover, the performance of the RG15 airfoil family was further examined by employing the two-dimensional version of the in-house IGal2D solver, using the standard two-equation SST $k-\omega$ turbulence model. The RANS simulations were performed at 300,000 Re. Although the results of the RANS simulation were generally in accordance with those of XFOIL, a notable over-estimation of the drag coefficient was detected, leading to the under-estimation of the lift-to-drag ratio. Such an outcome clearly indicates that a low Reynolds number correction model is essential, in order to increase the accuracy of the numerical results. Finally, the behavior of the recirculation area behind the rounded trailing edge for different angles of attack was examined, while the thickening of the airfoils was found to have a beneficial impact on the appearance of laminar separation bubbles.

11.1.5 Development of an Optimization Framework for Shrouded Wind Turbines

Finally, this work presented the development and application of a modular optimization framework for the aerodynamic shape optimization of shrouded wind turbines, which combines the aforementioned analysis tools with a parallel and asynchronous version of a meta-model assisted Differential Evolution (DE) algorithm. The entire optimization process is implemented iteratively until the completion of the maximum number of generations, while the DE algorithm interacts with the parameterization, analysis and post-processing software in a completely automated manner, by utilizing specially developed scripts. Eventually, the proposed methodology was applied to three distinct design optimization cases, including:

- *The aerodynamic shape optimization of the rotor blades for a given shroud geometry – OP1.*
- *The aerodynamic shape optimization of an unloaded diffuser configuration – OP2.*
- *The simultaneous aerodynamic shape optimization of the blades and the diffuser – OP3.*

The first optimization problem (**OP1**) has been focused on the aerodynamic design of improved rotor blades for the Donqi Urban Windmills, by considering a fixed diffuser geometry; the performance evaluation of the candidate solutions was achieved by using the in-house BEM code that was developed in the context of the current doctoral dissertation, while the parameterization of the twist and chord distributions was accomplished using two distinct B-Spline curves. The proposed optimization methodology eventually resulted in two new blade designs for the particular shrouded wind turbine, capable of considerably increasing the power output performance of the examined application. In particular, the first optimized blade, which is denoted as **BD1** and has been based on the NACA 2207 airfoil, led to a mean increase of the aerodynamic power output of the rotor that approximates 18.2%, while the corresponding percentage for the second blade design, which is denoted as **BD2** and has been employing the RG15 airfoil for the entire span, was found equal to 19.4%. Besides, the optimization procedure resulted in blade designs that differ significantly from the original blade, with a much smoother and less complicated twist distribution; a fact that renders them quite attractive from a manufacturing point of view, as simpler geometries are easier to be manufactured.

The second optimization problem (**OP2**) has been focused on the design of an improved shroud for a 15 kW diffuser-augmented wind turbine, aiming to maximize the mean velocity speed-up ratio and minimize drag force, while maintaining the throat diameter of the baseline shroud design; in this application, the presence of the turbine was not included. The performance evaluation of the candidate design was made by using the in-house IGal2D

solver, while the mesh and geometry parameterization were simultaneously succeeded by employing an in-house developed computational tool, based on the well-known Free-Form Deformation (FFD) technique. In addition, a geometrical constraint ensuring that the volume of the optimal design will be less or equal to the volume of the baseline one, was also imposed. The optimization was performed for a freestream velocity of 6 m/s. Besides the utilization of a time-saving axisymmetric flow solver and an asynchronous version of the DE algorithm, further acceleration – by approximately 38% – was achieved through the combination of the optimization algorithm with two meta-models; namely, an MLP and an RBF ANNs. The optimization resulted in a shroud design (denoted as **SD1**) yielding a mean-velocity speed-up ratio of 1.9, which was 23% higher than the mean velocity speed-up ratio of the baseline design, accompanied by a remarkable reduction in surface drag by approximately 47%. However, the relatively small thickness distribution of **SD1**, in the region downstream the rotor plane, was identified as a critical point that could probably hamper the structural integrity of the particular design. To this end, a modified shroud profile, denoted as **SD2**, was created by locally thickening **SD1**. The aerodynamic performance of **SD2** was not much inferior. As a matter of fact, the drag reduction (comparatively to the baseline design) was equal to 45% and the increase in the mean velocity speed-up ratio equal to 21% (mean velocity speed-up ratio equal to 1.86). In addition, a remarkable volume reduction, touching 48% and 41% for **SD1** and **SD2** respectively, was also achieved, allowing for huge cost reduction, even though the total length of the diffuser was increased. Finally, both **SD1** and **SD2** resulted in significantly smaller flow separations near the exit plane, which is identified as the main reason for the increase in velocity acceleration and drag reduction, while no recirculation areas were observed along the high-pressure surface of the new diffusers.

Finally, the third design application (**OP3**) that was reported in the current doctoral study, has been focused on simultaneously optimizing the shape of the rotor blades and the shroud. For this purpose, the DE algorithm was coupled with the in-house developed RANS - BEM methodology, which combines the IGal2D solver and BEM code. In this application, the parameterization of the computational mesh and shroud geometry was made by using the FFD-based mesh morphing tool that was developed in the current study, while the parameterization of the twist and chord distributions of the blade was achieved by means of B-Spline curves. The optimization was performed for a free-stream velocity of 6 m/s, aiming to increase the rotor power output, while minimize the shroud drag. In addition, four explicit constraints were also imposed, in order to ensure that: (i) the rotor thrust coefficient of the optimal design will be less than unity; (ii) the volume of the optimal shroud design will be less than the volume of the initial one; (iii) the throat radius of the optimal shroud design will be equal to the initial one; (iv) the local chord of the blade will be monotonically decreasing. Eventually, the current optimization method was capable of providing a highly performing

solution to this challenging design problem, while respecting all the established constraints. Specifically, the optimal design was capable of increasing the power output of the baseline one by approximately 33% and yielding a power coefficient of approximately 1.93 times higher than the Betz limit.

11.2 Further Research

The current section indicates possible directions for the extension of the methodologies and computational tools that were developed within the context of this doctoral dissertation. The intention of the future work should be in the direction to enhance the usefulness, the applicability, and the accuracy of the developed methodology, and the corresponding computational tools. To this end, the following tasks may be applied:

- Apply additional validation to the proposed methodology and the corresponding computational tools.
- Develop a graphical interface, under which the aforementioned computational tools will be integrated, to provide a better working environment to the potential users.
- Import, validate and compare additional turbulence models to the IGal2D solver.
- Apply parallelization to the IGal2D solver, using OpenMP (a task under development).
- Extend the presented analysis and design optimization methodology for the case of shrouded propellers.

References

- Abe, K. and Ohya, Y. (2004), "An investigation of flow fields around flanged diffusers using CFD", *Journal of Wind Engineering and Industrial Aerodynamics*, Vol. 92, No. 3, pp. 315-330.
- Abedi, M., Askari, R., Sepahi-Younsi, J. and Soltani, M.R. (2020), "Axisymmetric and three-dimensional flow simulation of a mixed compression supersonic air inlet", *Propulsion and Power Research*, Vol. 9, No. 1, pp. 51-61.
- Alam, M. and Sandham, N.D. (2000), "Direct numerical simulation of 'short' laminar separation bubbles with turbulent reattachment", *Journal of Fluid Mechanics*, Vol. 410, pp. 1-28.
- Algifri, A.H., Bhardwaj, R.K. and Rao, Y.V.N. (1987), "Prediction of the decay process in turbulent swirl flow", *Proceedings of the Institution of Mechanical Engineers, Part C: Journal of Mechanical Engineering Science*, Vol. 201, No. 4, pp. 279-283.
- Allen, C.B. and Rendall, T.C.S. (2013), "CFD-based optimization of hovering rotors using radial basis functions for shape parameterization and mesh deformation", *Optimization and Engineering*, Vol. 14, No. 1, pp. 97-118.
- Alpman, E. (2018), "Multiobjective aerodynamic optimization of a microscale ducted wind turbine using a genetic algorithm", *Turkish Journal Of Electrical Engineering & Computer Sciences*, Vol. 26, No. 1, pp. 618-629.
- Amoiralis, E.I. and Nikolos, I.K. (2008), "Freeform deformation versus B-Spline representation in inverse airfoil design", *Journal of Computing and Information Science in Engineering*, Vol. 8, No. 2, pp. 024001-024001-13.
- Anderson, E.W., Chow, R. and Van Dam, C.P. (2015), "A comparison of the NREL 5-MW wake characteristics using both SOWFA and OVERFLOW2", *33rd Wind Energy Symposium*, American Institute of Aeronautics and Astronautics, 5-9 January 2015, Kissimmee, Florida, USA.
- Anderson, J.D. (2010), *Fundamentals of Aerodynamics*, 5th Edition, McGraw-Hill Education, New York.
- Anderson, W.K. and Bonhaus, D.L. (1994), "An implicit upwind algorithm for computing turbulent flows on unstructured grids", *Computers & Fluids*, Vol. 23, No. 1, pp. 1-21.

- Anderson, W.K., Rausch, R.D. and Bonhaus, D.L. (1996), "Implicit/Multigrid algorithms for incompressible turbulent flows on unstructured grids", *Journal of Computational Physics*, Vol. 128, No. 2, pp. 391-408.
- Animasaun, I.L., Ibraheem, R.O., Mahanthesh, B. and Babatunde, H.A. (2019), "A meta-analysis on the effects of haphazard motion of tiny/nano-sized particles on the dynamics and other physical properties of some fluids", *Chinese Journal of Physics*, Vol. 60, pp. 676-687.
- Anselmi, L. (2017), *Computational analysis of ducted wind turbines noise*, Master Thesis, Delft University of Technology, Delft, The Netherlands.
- Aranake, A. and Duraisamy, K. (2017), "Aerodynamic optimization of shrouded wind turbines", *Wind Energy*, Vol. 20, No. 5, pp. 877-889.
- Aranake, A., Lakshminarayan, V. and Duraisamy, K. (2013), "Computational analysis of shrouded wind turbine configurations", *Proceedings of the 51st AIAA Aerospace Sciences Meeting Including the New Horizons Forum and Aerospace Exposition*, American Institute of Aeronautics and Astronautics, 7-10 January 2013, Grapevine, Texas, USA.
- Aranake, A.C., Lakshminarayan, V.K. and Duraisamy, K. (2015), "Computational analysis of shrouded wind turbine configurations using a 3-dimensional RANS solver", *Renewable Energy*, Vol. 75, pp. 818-832.
- Armfield, S.W., Cho, N.-H. and Fletcher, C.A.J. (1990), "Prediction of turbulence quantities for swirling flow in conical diffusers", *AIAA Journal*, Vol. 28, No. 3, pp. 453-460.
- Arramach, J., Boutammachte, N., Bouatem, A. and Al Mers, A. (2017), "Prediction of the wind turbine performance by using a modified BEM theory with an advanced brake state model", *Energy Procedia*, Vol. 118, pp. 149-157.
- Avallone, F., Ragni, D. and Casalino, D. (2020), "On the effect of the tip-clearance ratio on the aeroacoustics of a diffuser-augmented wind turbine", *Renewable Energy*, Vol. 152, pp. 1317-1327.
- Bagheri-Sadeghi, N., Helenbrook, B.T. and Visser, K.D. (2018), "Ducted wind turbine optimization and sensitivity to rotor position", *Wind Energy Science*, Vol. 3, No. 1, pp. 221-229.
- Bangga, G. and Lutz, T. (2021), "Aerodynamic modeling of wind turbine loads exposed to turbulent inflow and validation with experimental data", *Energy*, Vol. 223, p. 120076.

- Barth, T. (1992), "Aspects of Unstructured Grids and Finite-Volume Solvers for the Euler and Navier-Stokes Equations", *Proceedings of the AGARD-FDP-VKI Special Course at VKI*, 2-6 March 1992, Rhode-Saint-Genese, Belgium, pp. 6.1-6.61.
- Behrouzifar, A. and Darbandi, M. (2019), "An improved actuator disc model for the numerical prediction of the far-wake region of a horizontal axis wind turbine and its performance", *Energy Conversion and Management*, Vol. 185, pp. 482-495.
- Belloni, C.S.K., Willden, R.H.J. and Houlby, G.T. (2017), "An investigation of ducted and open-centre tidal turbines employing CFD-embedded BEM", *Renewable Energy*, Vol. 108, pp. 622-634.
- Bet, F. and Grassmann, H. (2003), "Upgrading conventional wind turbines", *Renewable Energy*, Vol. 28, No. 1, pp. 71-78.
- Betz, A. (2013), "The Maximum of the theoretically possible exploitation of wind by means of a wind motor", *Wind Engineering*, Vol. 37, No. 4, pp. 441-446.
- Billant, P., Chomaz, J.-M. and Huerre, P. (1998), "Experimental study of vortex breakdown in swirling jets", *Journal of Fluid Mechanics*, Vol. 376, pp. 183-219.
- Bird, R.B., Stewart, W.E. and Lightfoot, E.N. (2006), *Transport Phenomena, Revised Second Edition*, John Wiley & Sons, New York, USA.
- Blazek, J. (2015), *Computational Fluid Dynamics: Principles and Applications*, 3rd Edition, Butterworth-Heinemann, Amsterdam, The Netherlands.
- Bontempo, R. and Manna, M. (2013), "Solution of the flow over a non-uniform heavily loaded ducted actuator disk", *Journal of Fluid Mechanics*, Vol. 728, pp. 163-195.
- Bontempo, R. and Manna, M. (2014), "Performance analysis of open and ducted wind turbines", *Applied Energy*, Vol. 136, pp. 405-416.
- Bontempo, R. and Manna, M. (2016), "Effects of the duct thrust on the performance of ducted wind turbines", *Energy*, Vol. 99, pp. 274-287.
- Bontempo, R. and Manna, M. (2017), "Effects of the approximations embodied in the momentum theory as applied to the NREL Phase VI wind turbine", *International Journal of Turbomachinery, Propulsion and Power*, Vol. 2, No. 2, p. 9.
- Bounous, O. (2008), *Studies of the ERCOFTAC Conical Diffuser with OpenFOAM*, Research Report No. 2008:05, Chalmers University of Technology, Goteborg, Sweden.

- Branlard, E. (2017), The Blade Element Momentum (BEM) method, *In: Wind Turbine Aerodynamics and Vorticity-Based Methods*, Springer International Publishing, Vol. 7, pp. 181-211.
- Broeren, A.P., Giguere, P., Selig, M.S. and Guglielmo, J.J. (1995), *Summary of Low-Speed Airfoil Data - Vol. 1*, SoarTech Publications, Virginia Beach, Virginia, USA.
- Burton, T., Sharpe, D., Jenkins, N. and Bossanyi, E. (2001), *Wind Energy Handbook*, John Wiley & Sons, Chichester, England.
- van Bussel, G.J.W. (2007), "The science of making more torque from wind: Diffuser experiments and theory revisited", *Journal of Physics: Conference Series*, Vol. 75.
- van Bussel, G.J.W. (1999), "An assessment of the performance of diffuser augmented wind turbines (DAWT's)", *Proceedings of the 1999 3rd ASME/JSME Joint Fluids Engineering Conference*, American Society of Mechanical Engineers, 18-23 July 1999, San Francisco, California, USA.
- Cho, N.-H. and Fletcher, C.A.J. (1991), "Computation of turbulent conical diffuser flows using a non-orthogonal grid system", *Computers & Fluids*, Vol. 19, No. 3, pp. 347-361.
- Chorin, A.J. (1967), "A numerical method for solving incompressible viscous flow problems", *Journal of Computational Physics*, Vol. 2, No. 1, pp. 12-26.
- Choudhry, A., Arjomandi, M. and Kelso, R. (2015), "A study of long separation bubble on thick airfoils and its consequent effects", *International Journal of Heat and Fluid Flow*, Vol. 52, pp. 84-96.
- Clain, S., Rochette, D. and Touzani, R. (2010), "A multislope MUSCL method on unstructured meshes applied to compressible Euler equations for axisymmetric swirling flows", *Journal of Computational Physics*, Vol. 229, No. 13, pp. 4884-4906.
- Clausen, P.D., Koh, S.G. and Wood, D.H. (1993), "Measurements of a swirling turbulent boundary layer developing in a conical diffuser", *Experimental Thermal and Fluid Science*, Vol. 6, No. 1, pp. 39-48.
- Coder, J.G. and Maughmer, M.D. (2014), "Comparisons of theoretical methods for predicting airfoil aerodynamic characteristics", *Journal of Aircraft*, Vol. 51, No. 1, pp. 183-191.
- Cox, C., Liang, C. and Plesniak, M.W. (2016), "A high-order solver for unsteady incompressible Navier–Stokes equations using the flux reconstruction method on

- unstructured grids with implicit dual time stepping”, *Journal of Computational Physics*, Vol. 314, pp. 414-435.
- Creutzig, F., Goldschmidt, J.C., Lehmann, P., Schmid, E., von Blucher, F., Breyer, C., Fernandez, B., *et al.* (2014), “Catching two European birds with one renewable stone: Mitigating climate change and Eurozone crisis by an energy transition”, *Renewable and Sustainable Energy Reviews*, Vol. 38, pp. 1015-1028.
- Cummings, R.M., Yang, H.T. and Oh, Y.H. (1995), “Supersonic, turbulent flow computation and drag optimization for axisymmetric afterbodies”, *Computers & Fluids*, Vol. 24, No. 4, pp. 487-507.
- Dagtekin, I. and Unsal, M. (2011), “Numerical analysis of axisymmetric and planar sudden expansion flows for laminar regime”, *International Journal for Numerical Methods in Fluids*, Vol. 65, No. 9, pp. 1133-1144.
- Dighe, V.V. (2020), *Ducted wind turbines revisited: A computational study*, Doctoral Dissertation, Delft University of Technology, Delft, The Netherlands.
- van Dorst, F.A. (2011), *An improved rotor design for a diffuser augmented wind turbine: Improvement of the Donqi Urban Windmill*, Master Thesis, Delft University of Technology, Delft, The Netherlands.
- Drela, M. (1989), “XFOIL: An Analysis and Design System for Low Reynolds Number Airfoils”, *In: Low Reynolds Number Aerodynamics. Lecture Notes in Engineering*, Vol 54, Springer, Berlin Heidelberg.
- Drela, M. and Giles, M.B. (1987), “Viscous-inviscid analysis of transonic and low Reynolds number airfoils”, *AIAA Journal*, Vol. 25, No. 10, pp. 1347-1355.
- Durkish, E. (2006), *A finite element formulation for axisymmetric swirling flows with an application to fuel slosh*, Master Thesis, Clarkson University, Potsdam, New York, USA.
- Evans, S.P., Kesby, J.E., Bradley, J. and Clausen, P.D. (2020), “Commercialization of a diffuser augmented wind turbine for distributed generation”, *Journal of Physics: Conference Series*, Vol. 1452, p. 012014.
- Fleming, P., Gebraad, P., Churchfield, M., Lee, S., Johnson, K., Michalakes, J., van Wingerden, J.W., *et al.* (2013), *SOWFA + Super Controller User’s Manual*, NREL/TP-5000-59197, National Renewable Energy Laboratory, Golden, Colorado, USA.

- Fletcher, C.A.J. (1981), "Computational analysis of diffuser-augmented wind turbines", *Energy Conversion and Management*, Vol. 21, No. 3, pp. 175-183.
- Fluent (2009), *ANSYS FLUENT 12.0 Theory Guide*.
https://www.afs.enea.it/project/neptunius/docs/fluent/html/th/main_pre.htm
- Foote, T. and Agarwal, R. (2013), "Optimization of Power Generation From Shrouded Wind Turbines", *Proceedings of the ASME 2012 6th International Conference on Energy Sustainability collocated with the ASME 2012 10th International Conference on Fuel Cell Science, Engineering and Technology*, 23-26 July 2013, San Diego, California, USA.
- Foreman, K.M., Gilbert, B. and Oman, R.A. (1978), "Diffuser augmentation of wind turbines", *Solar Energy*, Vol. 20, No. 4, pp. 305-311.
- Foreman, K.M. and Gilbert, B.L. (1983), *A Free Jet Wind Tunnel Investigation of DAWT Models*, Report RE-668, SERI/TR 01311-1, Grumman Research Department, New York, USA.
- From, C.S., Sauret, E., Armfield, S.W., Saha, S.C. and Gu, Y.T. (2017), "Turbulent dense gas flow characteristics in swirling conical diffuser", *Computers & Fluids*, Vol. 149, pp. 100-118.
- Froude, R.E. (1889), "On the part played in propulsion by difference in pressure", *Transactions of the Institution of Naval Architects*, pp. 390-423.
- Froude, W. (1878), "On the Elementary Relation Between Pitch, Slip and Propulsive Efficiency", *Transaction of the Institute of Naval Architects*, Vol. 19, pp. 22-33.
- Georgalas, C.G., Koras, A.D. and Raptis, S.N. (1991), "Parametrization of the power enhancement calculated for ducted rotors with large tip clearance", *Wind Engineering*, Vol. 15, No. 3, pp. 128-136.
- Giguère, P. and Selig, M.S. (1997), "Low Reynolds number airfoils for small horizontal axis wind turbines", *Wind Engineering*, Vol. 21, No. 6, pp. 367-380.
- Giguere, P. and Selig, M.S. (1998), "New airfoils for small horizontal axis wind turbines", *Journal of Solar Energy Engineering*, Vol. 120, No. 2, pp. 108-114.
- Gilbert, B.L. and Foreman, K.M. (1979), "Experimental demonstration of the diffuser-augmented wind turbine concept", *Journal of Energy*, Vol. 3, No. 4, pp. 235-240.
- Gilbert, B.L. and Foreman, K.M. (1983), "Experiments with a diffuser-augmented model wind turbine", *Journal of Energy Resources Technology*, Vol. 105, No. 1, pp. 46-53.

-
- Gilbert, B.L., Oman, R.A. and Foreman, K.M. (1978), "Fluid dynamics of diffuser-augmented wind turbines", *Journal of Energy*, Vol. 2, No. 6, pp. 368-374.
- Glauert, H. (1935), "Airplane Propellers", In: *Aerodynamic Theory: A General Review of Progress Under a Grant of the Guggenheim Fund for the Promotion of Aeronautics*, Springer, Berlin Heidelberg, pp. 169-360.
- Gokhale, S.S. and Suresh, R. (1997), "Numerical computations of internal flows for axisymmetric and two-dimensional nozzles", *International Journal for Numerical Methods in Fluids*, Vol. 25, No. 5, pp. 599-610.
- Grassmann, H., Bet, F., Cabras, G., Ceschia, M., Cobai, D. and DelPapa, C. (2003), "A partially static turbine—first experimental results", *Renewable Energy*, Vol. 28, No. 11, pp. 1779-1785.
- Guo, Q., Zhou, L. and Wang, Z. (2015), "Comparison of BEM-CFD and full rotor geometry simulations for the performance and flow field of a marine current turbine", *Renewable Energy*, Vol. 75, pp. 640-648.
- Gur, O. and Rosen, A. (2008), "Optimal design of horizontal axis wind turbine blades", *Proceedings the ASME 2008 9th Biennial Conference on Engineering Systems Design and Analysis*, 7-9 July 2008, Haifa, Israel, pp. 99-109.
- GWEC (2021), *Global Wind Report 2021*, Global Wind Energy Council, Brussels, Belgium.
- Hajabdollahi, F., Premnath, K.N. and Welch, S.W.J. (2019), "Cascaded lattice Boltzmann method based on central moments for axisymmetric thermal flows including swirling effects", *International Journal of Heat and Mass Transfer*, Vol. 128, pp. 999-1016.
- Hand, M.M., Simms, D.A., Fingersh, L.J., Jager, D.W., Cotrell, J.R., Schreck, S. and Larwood, S.M. (2001), *Unsteady Aerodynamics Experiment Phase VI: Wind Tunnel Test Configurations and Available Data Campaigns*, NREL/TP-500-29955, National Renewable Energy Laboratory, Golden, Colorado, USA.
- Hansen, K., Kelso, R., Choudhry, A. and Arjomandi, M. (2014), "Laminar separation bubble effect on the lift curve slope of an airfoil", *Proceedings of the 19th Australasian Fluid Mechanics Conference*, 8-11 December 2014, Melbourne, Australia.
- Hansen, M.O.L. (2008), *Aerodynamics of Wind Turbines*, 2nd Edition, Earthscan Publications, London.

- Hansen, M.O.L., Sørensen, N.N. and Flay, R.G.J. (2000), "Effect of placing a diffuser around a wind turbine", *Wind Energy*, Vol. 3, No. 4, pp. 207-213.
- Henriques, J.C.C., Marques da Silva, F., Estanqueiro, A.I. and Gato, L.M.C. (2009), "Design of a new urban wind turbine airfoil using a pressure-load inverse method", *Renewable Energy*, Vol. 34, No. 12, pp. 2728-2734.
- Hernández, J. and Crespo, A. (1987), "Aerodynamic calculation of the performance of horizontal axis wind turbines and comparison with experimental results", *Wind Engineering*, Vol. 11, No. 4, pp. 177-187.
- Herrig, L.J., Emery, J.C. and Erwin, J.R. (1951), *Effect of section thickness and trailing-edge radius on the performance of NACA 65-series compressor blades in cascade at low speeds*, Research Memorandum L51J16, National Advisory Committee for Aeronautics, Langley Aeronautical Laboratory, Langley Field, Virginia, USA.
- Hjort, S. and Larsen, H. (2015), "Rotor design for diffuser augmented wind turbines", *Energies*, Vol. 8, pp. 10736-10774.
- Hoffmann, K.A. and Chiang, S.T. (1993), *Computational Fluid Dynamics for Engineers*, 2nd Edition., Engineering Education System, Wichita, Kansas, USA.
- van Holten, Th. (1981), "Concentrator systems for wind energy, with emphasis on tipvanes", *Wind Engineering*, Vol. 5, No. 1, pp. 29-45.
- Huang, H., Lee, T.S. and Shu, C. (2007), "Hybrid lattice Boltzmann finite-difference simulation of axisymmetric swirling and rotating flows", *International Journal for Numerical Methods in Fluids*, Vol. 53, No. 11, pp. 1707-1726.
- IEC (2013), *IEC 61400-2:2013 Wind Turbines - Part 2: Design Requirements for Small Wind Turbines*, International Electrotechnical Commission.
- Igra, O. (1976), "Shrouds for Aerogenerators", *AIAA Journal*, Vol. 14, No. 10, pp. 1481-1483.
- Igra, O. (1977), "Compact shrouds for wind turbines", *Energy Conversion*, Vol. 16, No. 4, pp. 149-157.
- Igra, O. (1981), "Research and development for shrouded wind turbines", *Energy Conversion and Management*, Vol. 21, No. 1, pp. 13-48.
- Ikegami, M. and Kamimoto, T. (2009), "Conventional Diesel Combustion", *In: Flow and Combustion in Reciprocating Engines*, Springer Science & Business Media, pp. 309-351.

-
- IRENA (2019), *Future of Wind: Deployment, Investment, Technology, Grid Integration and Socio-Economic Aspects*, International Renewable Energy Agency, Abu Dhabi.
- Islam, M., Amin, M.R., Ting, D.S.-K. and Fartaj, A. (2008), "Selection of airfoils for straight-bladed vertical axis wind turbines based on desirable aerodynamic characteristics", *Proceedings of the ASME 2008 International Mechanical Engineering Congress and Exposition*, 31 October – 6 November 2008, Boston, Massachusetts, USA, pp. 3-12.
- Jamieson, P.M. (2009), "Beating Betz: Energy extraction limits in a constrained flow field", *Journal of Solar Energy Engineering*, Vol. 131, No. 3, pp. 031008-031008-6.
- Jonkman, J., Butterfield, S., Musial, W. and Scott, G. (2009), *Definition of a 5-MW Reference Wind Turbine for Offshore System Development*, NREL/TP-500-38060, National Renewable Energy Laboratory, Golden, Colorado, USA.
- Jonkman, J.M. and Buhl Jr., M.L. (2005), *FAST User's Guide - Updated August 2005*, NREL/TP-500-38230, National Renewable Energy Laboratory, Golden, Colorado, USA.
- Kallinderis, Y. and Ahn, H.T. (2005), "Incompressible Navier–Stokes method with general hybrid meshes", *Journal of Computational Physics*, Vol. 210, No. 1, pp. 75-108.
- Kardous, M., Chaker, R., Aloui, F. and Nasrallah, S.B. (2013), "On the dependence of an empty flanged diffuser performance on flange height: Numerical simulations and PIV visualizations", *Renewable Energy*, Vol. 56, pp. 123-128.
- Kesby, J.E., Bradney, D.R. and Clausen, P.D. (2016), "Determining diffuser augmented wind turbine performance using a combined CFD/BEM method", *Journal of Physics: Conference Series*, Vol. 753, p. 082033.
- Khamlaj, T.A. and Rumpfkeil, M.P. (2017), "Theoretical analysis of shrouded horizontal axis wind turbines", *Energies*, Vol. 10, No. 1, p. 38.
- Khamlaj, T.A. and Rumpfkeil, M.P. (2018), "Analysis and optimization of ducted wind turbines", *Energy*, Vol. 162, pp. 1234-1252.
- Kim, K. (2003), *Three-dimensional hybrid grid generator and unstructured flow solver for compressors and turbines*, Doctoral Dissertation, Texas A&M University, Texas, USA.
- Kiris, C., Housman, J. and Kwak, D. (2006), "Comparison of artificial compressibility methods", *In: Computational Fluid Dynamics 2004*, Springer, Berlin Heidelberg, pp. 475-480.

-
- Kogan, A. and Nissim, E. (1962), *Shrouded Aerogenerator Design Study, Two-Dimensional Shroud Performance*, Bulletin of the Research Council of Israel, Israel, pp. 67-88.
- Kogan, A. and Seginer, A. (1962), "Shrouded Aerogenerator Design Study II, Axisymmetrical Shroud Performance", *Fifth Israel Annual Conference on Aviation and Astronautics*, Israel.
- Kogan, A. and Seginer, A. (1963), *Shrouded Aerogenerator, Design Study II, Axisymmetric Shroud Performance*, Department of Aeronautical Engineering, Technion, Israel.
- Koras, A.D. and Georgalas, C.G. (1988), "Calculation of the influence of annular augmentors on the performance of a wind rotor", *Wind Engineering*, Vol. 12, No. 4, pp. 257-267.
- Kosasih, B. and Tondelli, A. (2012), "Experimental study of shrouded micro-wind turbine", *Procedia Engineering*, Vol. 49, pp. 92-98.
- van Kuik, G.A.M. (2020), "The Actuator Disc Concept", *In: Handbook of Wind Energy Aerodynamics*, Springer International Publishing, pp. 1-47.
- van Kuik, G.A.M., Sørensen, J.N. and Okulov, V.L. (2015), "Rotor theories by Professor Joukowsky: Momentum theories", *Progress in Aerospace Sciences*, Vol. 73, pp. 1-18.
- Laney, C.B. (1998), *Computational Gasdynamics*, 1st Edition, Cambridge University Press, New York.
- Lee, H.-R. and Lee, S.-S. (2011), "Convergence characteristics of upwind method for modified artificial compressibility method", *International Journal of Aeronautical and Space Sciences*, Vol. 12, No. 4, pp. 318-330.
- Lee, K., Huque, Z., Kommalapati, R. and Han, S.-E. (2017), "Fluid-structure interaction analysis of NREL Phase VI wind turbine: Aerodynamic force evaluation and structural analysis using FSI analysis", *Renewable Energy*, Vol. 113, pp. 512-531.
- Lee, S. (2000), "A numerical study of the unsteady wake behind a sphere in a uniform flow at moderate Reynolds numbers", *Computers & Fluids*, Vol. 29, No. 6, pp. 639-667.
- Lee, T.S., Huang, H. and Shu, C. (2005), "An axisymmetric incompressible lattice BGK model for simulation of the pulsatile flow in a circular pipe", *International Journal for Numerical Methods in Fluids*, Vol. 49, No. 1, pp. 99-116.
- van Leer, B. (1979), "Towards the ultimate conservative difference scheme. V. A second-order sequel to Godunov's method", *Journal of Computational Physics*, Vol. 32, No. 1, pp. 101-136.

-
- Leloudas, S.N., Lygidakis, G.N. and Nikolos, I.K. (2017), "Assessment of a modified blade element momentum methodology for diffuser augmented wind turbines", *Proceedings of the ASME 2017 International Mechanical Engineering Congress and Exposition*, 3-9 November 2017, Tampa, Florida, USA.
- Leloudas, S.N., Strofylas, G.A. and Nikolos, I.K. (2018a), "Aerodynamic shape optimization of diffuser augmented wind turbine blades using asynchronous parallel differential evolution", *Proceedings of the 9th GRACM International Congress on Computational Mechanics*, 4-6 June 2018, Chania, Greece.
- Leloudas, S.N., Lygidakis, G.N., Strofylas, G.A. and Nikolos, I.K. (2018b), "Aerodynamic shape optimization of diffuser augmented wind turbine shrouds using asynchronous differential evolution", *Proceedings of the ASME 2018 International Mechanical Engineering Congress and Exposition*, 9-15 November 2018, Pittsburgh, Pennsylvania, USA.
- Leloudas, S.N. and Nikolos, I.K. (2019a), "Design of improved rotor blades for a shrouded wind turbine using the RG15 airfoil family", *Proceedings of the 7th European Conference on Renewable Energy Systems*, 10-12 June 2019, Madrid, Spain.
- Leloudas, S.N., Eskantar, A.I. and Nikolos, I.K. (2019b), "Design of a low Reynolds airfoil family for small horizontal axis wind turbine applications based on the RG15 airfoil", *Proceedings of the 7th European Conference on Renewable Energy Systems*, 10-12 June 2019, Madrid, Spain.
- Leloudas, S.N., Lygidakis, G.N., Eskantar, A.I. and Nikolos, I.K. (2020a), "A robust methodology for the design optimization of diffuser augmented wind turbine shrouds", *Renewable Energy*, Vol. 150, pp. 722-742.
- Leloudas, S.N., Eskantar, A.I., Lygidakis, G.N. and Nikolos, I.K. (2020b), "Low Reynolds airfoil family for small horizontal axis wind turbines based on RG15 airfoil", *SN Applied Sciences*, Vol. 2, No. 3, p. 371.
- Leloudas, S.N., Lygidakis, G.N., Delis, A.I. and Nikolos, I.K. (2021), "An artificial compressibility method for axisymmetric swirling flows", *Engineering Computations*, Vol. ahead-of-print, No. ahead-of-print.
- Li, Y., Zhuo, Q. and You, W. (2018), "Axisymmetric lattice Boltzmann method for non-Newtonian flows", *International Journal for Numerical Methods in Fluids*, Vol. 88, No. 10-11, pp. 479-492.

-
- Li, Z., Huai, W., Yang, Z., Qian, Z. and Zeng, Y. (2014), "Numerical study on the dynamics and mass transfer characteristics of a radial offset jet", *Engineering Computations*, Vol. 31, No. 3, pp. 406-424.
- Lilley, G.M. and Rainbird, W.J. (1956), *A preliminary report on the design and performance of ducted windmills*, CoA Report No. I02, The College of Aeronautics, Cranfield.
- Lindenburg, C. (2003), *Investigation into rotor blade aerodynamics*, ECN-C-03-025, Energy Research Centre of the Netherlands, Petten, The Netherlands.
- Liu, H., Wu, L., Ba, Y., Xi, G. and Zhang, Y. (2016), "A lattice Boltzmann method for axisymmetric multicomponent flows with high viscosity ratio", *Journal of Computational Physics*, Vol. 327, pp. 873-893.
- Liu, J., Song, M., Chen, K., Wu, B. and Zhang, X. (2016), "An optimization methodology for wind lens profile using Computational Fluid Dynamics simulation", *Energy*, Vol. 109, pp. 602-611.
- Liu, Q., Feng, X.-B., He, Y.-L., Lu, C.-W. and Gu, Q.-H. (2019), "Multiple-relaxation-time lattice Boltzmann model for simulating axisymmetric thermal flows in porous media", *International Journal of Heat and Mass Transfer*, Vol. 137, pp. 1301-1311.
- Loeffler Jr., A.L., (1981), "Flow field analysis and performance of wind turbines employing slotted diffusers", *Journal of Solar Energy Engineering*, Vol. 103, No. 1, pp. 17-22.
- Lygidakis, G. (2015), *On the Numerical Solution of Compressible Fluid Flow and Radiative Heat Transfer Problems*, Doctoral Dissertation, Technical University of Crete, Chania, Greece.
- Lygidakis, G.N., Leloudas, S.N., Delis, A.I. and Nikolos, I.K. (2020), "Prediction of Turbulent Axisymmetric Flows Using an Artificial Compressibility Approach", *Proceedings of Global Power and Propulsion Society*, 7-9 September 2020, Chania, Greece.
- Lygidakis, G.N., Sarakinos, S.S. and Nikolos, I.K. (2016), "Comparison of different agglomeration multigrid schemes for compressible and incompressible flow simulations", *Advances in Engineering Software*, Vol. 101, pp. 77-97.
- Lyon, C., Selig, M. and Broeren, A. (1997), "Boundary layer trips on airfoils at low Reynolds numbers", *35th Aerospace Sciences Meeting and Exhibit*, 6-9 January 1997, Reno, Nevada, USA.

- Maheri, A., Noroozi, S., Toomer, C. and Vinney, J. (2006), "Damping the fluctuating behaviour and improving the convergence rate of the axial induction factor in the BEMT-based rotor aerodynamic codes", *Proceedings of the European Wind Energy Conference and Exhibition 2006*, 27 February – 2 March 2006, Athens, Greece.
- Malki, R., Williams, A.J., Croft, T.N., Togneri, M. and Masters, I. (2013), "A coupled blade element momentum – Computational fluid dynamics model for evaluating tidal stream turbine performance", *Applied Mathematical Modelling*, Vol. 37, No. 5, pp. 3006-3020.
- Mansour, K. and Meskinkhoda, P. (2014), "Computational analysis of flow fields around flanged diffusers", *Journal of Wind Engineering and Industrial Aerodynamics*, Vol. 124, pp. 109-120.
- Manwell, J.F., McGowan, J.G. and Rogers, A.L. (2010), *Wind Energy Explained: Theory, Design and Application*, 2nd Edition, John Wiley & Sons, Chichester, England.
- Marnett, M., Yang, S. and Schroder, W. (2010), "Lightweight airfoil design for a series of small vertical axis wind turbines", *Proceedings of the European Wind Energy Conference and Exhibition 2010*, 20 – 23 April 2010, Warsaw, Poland, Vol. 6, pp. 4232–4238.
- Marten, D. (2015), *QBlade Guidelines v0.9*, Technical University of Berlin, Germany.
- Masatsuka, K. (2013), *I Do like CFD, Vol. 1*, 2nd Edition.
- Mathew, S., Lim, C.M., Petra, M.I., Philip, G.S., Noorfathin, M., Mathew, M.S. and Raj, V. (2016), "Matching the characteristics of low wind speed turbines with candidate wind regimes", *Energy Procedia*, Vol. 95, pp. 286-293.
- Mazzaferro, G.M., Ferro, S.P. and Goldschmit, M.B. (2005), "An algorithm for rotating axisymmetric flows: model, validation and industrial applications", *International Journal for Numerical Methods in Fluids*, Vol. 48, No. 10, pp. 1101-1121.
- McWilliam, M. and Crawford, C. (2011), "The behavior of fixed point iteration and Newton-Raphson methods in solving the Blade Element Momentum equations", *Wind Engineering*, Vol. 35, No. 1, pp. 17-31.
- Menter, F.R. (1994), "Two-equation eddy-viscosity turbulence models for engineering applications", *AIAA Journal*, Vol. 32, No. 8, pp. 1598-1605.

-
- Menter, F.R., Ferreira, J.C., Esch, T. and Konno, B. (2003), "The SST turbulence model with improved wall treatment for heat transfer predictions in gas turbines", *Proceedings of the International Gas Turbine Congress*, 2-7 November 2003, Tokyo, Japan.
- Mittal, R. (1999), "A Fourier–Chebyshev spectral collocation method for simulating flow past spheres and spheroids", *International Journal for Numerical Methods in Fluids*, Vol. 30, No. 7, pp. 921-937.
- Mohammadi, B. and Saiaç, J.H. (1993), "Turbulent compressible axisymmetric flows computation with the k-epsilon model", *International Journal of Computational Fluid Dynamics*, Vol. 1, No. 2, pp. 115-133.
- Montgomerie, B. (2004), *Methods for root effects, tip effects and extending the angle of attack range to $\pm 180^\circ$, with application to aerodynamics for blades on wind turbines and propellers*, FOI-R-1305-SE, Swedish Defence Research Agency, Stockholm, Sweden.
- Morgado, J., Vizinho, R., Silvestre, M.A.R. and Páscoa, J.C. (2016), "XFOIL vs CFD performance predictions for high lift low Reynolds number airfoils", *Aerospace Science and Technology*, Vol. 52, pp. 207-214.
- Moriarty, P.J. and Hansen, A.C. (2005), *AeroDyn Theory Manual*, NREL/TP-500-36881, National Renewable Energy Laboratory, Golden, Colorado, USA.
- Morris, A.M., Allen, C.B. and Rendall, T.C.S. (2008), "CFD-based optimization of aerofoils using radial basis functions for domain element parameterization and mesh deformation", *International Journal for Numerical Methods in Fluids*, Vol. 58, No. 8, pp. 827-860.
- Morsi, Y.S.M., Holland, P.G. and Clayton, B.R. (1995), "Prediction of turbulent swirling flows in axisymmetric annuli", *Applied Mathematical Modelling*, Vol. 19, No. 10, pp. 613-620.
- Moshkin, N.P., Poochinapan, K. and Christov, C.I. (2010), "Numerical implementation of Aristov–Pukhnachev’s formulation for axisymmetric viscous incompressible flows", *International Journal for Numerical Methods in Fluids*, Vol. 62, No. 10, pp. 1063-1080.
- Mulleners, K., Henning, A. and Raffel, M. (2008), "Investigations of a trailing edge stall on 2D airfoils", *14th International Symposium on Application of Laser Technology to Fluid Mechanics*, 7-10 July 2008, Lisbon, Portugal.

- Musa, O., Changsheng, Z., Xiong, C. and Lunkun, G. (2016), "Prediction of swirling cold flow in a solid-fuel ramjet engine with a modified rotation/curvature correction SST turbulence model", *Applied Thermal Engineering*, Vol. 105, pp. 737-754.
- Nichols, R.H. and Buning, P.G. (2021), *User's Manual for OVERFLOW 2.3*.
<https://overflow.larc.nasa.gov/users-manual-for-overflow-2-3/>
- Nikolos, I.K. (2011), "Surrogate modeling in evolutionary based engineering design optimization", In: *Soft Computing Methods for Civil and Structural Engineering*, Saxe-Coburg Publications, Stirlingshire, United Kingdom, pp 173-203.
- Nikolos, I.K. (2013), "On the use of multiple surrogates within a differential evolution procedure for high-lift airfoil design", *International Journal of Advanced Intelligence Paradigms*, Vol. 5, No. 4, pp. 319-341.
- Nikolos, I.K. and Delis, A.I. (2009), "An unstructured node-centered finite volume scheme for shallow water flows with wet/dry fronts over complex topography", *Computer Methods in Applied Mechanics and Engineering*, Vol. 198, No. 47, pp. 3723-3750.
- Ning, S.A. (2014), "A simple solution method for the blade element momentum equations with guaranteed convergence", *Wind Energy*, Vol. 17, No. 9, pp. 1327-1345.
- Nishikawa, H., Diskin, B. and Thomas, J.L. (2010), "Critical study of agglomerated multigrid methods for diffusion", *AIAA Journal*, Vol. 48, No. 4, pp. 839-847.
- Nunes, M.M., Brasil Junior, A.C.P. and Oliveira, T.F. (2020), "Systematic review of diffuser-augmented horizontal-axis turbines", *Renewable and Sustainable Energy Reviews*, Vol. 133, p. 110075.
- Ohya, Y. and Karasudani, T. (2010), "A shrouded wind turbine generating high output power with wind-lens technology", *Energies*, Vol. 3, No. 4, pp. 634-649.
- Oka, N., Furukawa, M., Kawamitsu, K. and Yamada, K. (2016), "Optimum aerodynamic design for wind-lens turbine", *Journal of Fluid Science and Technology*, Vol. 11, No. 2.
- Oka, N., Furukawa, M., Yamada, K., Kawamitsu, K., Kido, K. and Oka, A. (2014), "Simultaneous optimization of rotor blade and wind-lens for aerodynamic design of wind-lens turbine", *Proceedings of the ASME Turbo Expo 2014: Turbine Technical Conference and Exposition*, 16 – 20 June 2014, Düsseldorf, Germany.

-
- Oman, R.A., Foreman, K.M. and Gilbert, B.L. (1977), *Investigation of diffuser-augmented wind turbines, Parts I & II*, Grumman Aerospace Corporation, Bethpage, New York, USA.
- Oud, G.T. (2017), *A dual interface method in cylindrical coordinates for two-phase pipe flows*, Doctoral Dissertation, Delft University of Technology, Delft, The Netherlands.
- Patrikalakis, N.M. and Maekawa, T. (2002), *Shape Interrogation for Computer Aided Design and Manufacturing*, Springer-Verlag, Berlin Heidelberg.
- Phillips, D.G. (2003), *An Investigation on Diffuser Augmented Wind Turbine Design*, Doctoral Dissertation, The University of Auckland, New Zealand.
- Phillips, D.G., Flay, R.G.J. and Nash, T.A. (1999), "Aerodynamic Analysis and Monitoring of the Vortec 7 Diffuser-augmented Wind Turbine", *Transactions of the Institution of Professional Engineers New Zealand: Electrical/Mechanical/Chemical Engineering Section*, Vol. 26, No. 1, pp. 13-19.
- Piegl, L. and Tiller, W. (1995), *The NURBS Book*, Springer-Verlag, Berlin Heidelberg.
- Ram, K.R., Lal, S. and Rafiuddin Ahmed, M. (2013), "Low Reynolds number airfoil optimization for wind turbine applications using genetic algorithm", *Journal of Renewable and Sustainable Energy*, Vol. 5, No. 5, p. 052007.
- Ramos, J.I. (1984), "Numerical solution of non-premixed reactive flows in a swirl combustor model", *Engineering Computations*, Vol. 1, No. 2, pp. 173-182.
- Ramos, J.I. (1986), "Incompressible swirling flows", *Engineering Computations*, Vol. 3, No. 1, pp. 53-63.
- Rankine, W.J.M. (1865), "On the Mechanical Principles of the Action of Propellers", *Transaction of the Institute of Naval Architects*, Vol. 6, pp. 13-39.
- Resor, B. (2013), *Definition of a 5MW/61.5m wind turbine blade reference model*, SAND2013-2569, Sandia National Laboratories, Albuquerque, New Mexico, USA.
- Rio Vaz, D.A., Amarante Mesquita, A.L., Pinheiro Vaz, J.R., Cavalcante Blanco, C.J. and Pinho, J.T. (2014), "An extension of the Blade Element Momentum method applied to diffuser augmented wind turbines", *Energy Conversion and Management*, Vol. 87, pp. 1116-1123.
- Rocha, A.D. (2013), *Estudo experimental e numérico de um escoamento com giro*, Doctoral Dissertation, University of Campinas, Brasil.

-
- Rocha, A.D., Bannwart, A.C. and Ganzarolli, M.M. (2015), "Numerical and experimental study of an axially induced swirling pipe flow", *International Journal of Heat and Fluid Flow*, Vol. 53, pp. 81-90.
- Rodi, W., Bonnin, J.C. and Buchal, T. (1995), "ERCOFTAC workshop on data bases and testing of calculation methods for turbulent flows", *Proceedings of the 4th ERCOFTAC/IAHR Workshop on Refined Flow Modelling*, 3 – 7 April 1995, University of Karlsruhe, Karlsruhe, Germany.
- Roe, P.L. (1981), "Approximate Riemann solvers, parameter vectors, and difference schemes", *Journal of Computational Physics*, Vol. 43, No. 2, pp. 357-372.
- Roos, F.W. and Willmarth, W.W. (1971), "Some experimental results on sphere and disk drag", *AIAA Journal*, Vol. 9, No. 2, pp. 285-291.
- Saiac, J.-H. (1990), "Finite element solutions of axisymmetric Euler equations for an incompressible and inviscid fluid", *International Journal for Numerical Methods in Fluids*, Vol. 10, No. 2, pp. 141-160.
- Sarakinos, S. (2016), *On the Simulation of Steady and Unsteady Incompressible Flows Using the Finite Volume Approach and Artificial Compressibility Concept on Hybrid Unstructured Grids*, Doctoral Dissertation, Technical University of Crete, Chania, Greece.
- Sathyajith, M. and Philip, G.S. (2011), *Advances in Wind Energy Conversion Technology*, Springer-Verlag, Berlin Heidelberg.
- Sederberg, T.W. and Parry, S.R. (1986), "Free-form deformation of solid geometric models", *ACM SIGGRAPH Computer Graphics*, Vol. 20, No. 4, pp. 151-160.
- Selig, M.S. and McGranahan, B.D. (2004), "Wind tunnel aerodynamic tests of six airfoils for use on small wind turbines", *Journal of Solar Energy Engineering*, Vol. 126, No. 4, pp. 986-1001.
- Semiao, V. and Carvalho, M.G. (1997), "LIMPO: an improved version of the PISO algorithm for turbulent swirling flows", *Engineering Computations*, Vol. 14, No. 3, pp. 325-341.
- Seremeti, M. (2019), *Graphical user interface development for a wind turbine analysis software*, Diploma Thesis, Technical University of Crete, Chania, Greece.

- Shah, H., Bhattarai, N., Mathew, S. and Lim, C.M. (2012), "Low Reynolds number airfoil for small horizontal axis wind turbine blades", *Proceeding of the Sustainable Future Energy 2012 and 10th SEE FORUM*, 21 – 23 November 2012, Brunei, Darussalam.
- Shah, N.A., Animasaun, I.L., Ibraheem, R.O., Babatunde, H.A., Sandeep, N. and Pop, I. (2018), "Scrutinization of the effects of Grashof number on the flow of different fluids driven by convection over various surfaces", *Journal of Molecular Liquids*, Vol. 249, pp. 980–990.
- Shen, W.Z., Mikkelsen, R., Sørensen, J.N. and Bak, C. (2005), "Tip loss corrections for wind turbine computations", *Wind Energy*, Vol. 8, No. 4, pp. 457-475.
- Shen, X., Avital, E., Paul, G., Rezaenia, M.A., Wen, P. and Korakianitis, T. (2016), "Experimental study of surface curvature effects on aerodynamic performance of a low Reynolds number airfoil for use in small wind turbines", *Journal of Renewable and Sustainable Energy*, Vol. 8, No. 5, p. 053303.
- Siebert, B. and Yocum, A. (1993), *An Incompressible Axisymmetric Through-Flow Calculation Procedure for Design and Off-Design Analyses of Turbomachinery*, Technical Report No. TR 93-05, The Pennsylvania State University.
- Singh, R.K., Ahmed, M.R., Zullah, M.A. and Lee, Y.-H. (2012), "Design of a low Reynolds number airfoil for small horizontal axis wind turbines", *Renewable Energy*, Vol. 42, pp. 66-76.
- Somers, D.M. (2005), *S822 and S823 Airfoils: October 1992--December 1993*, NREL/SR-500-36342, National Renewable Energy Laboratory, Golden, Colorado, USA.
- Sørensen, J.N. (2012), "Aerodynamic analysis of wind turbines", *In: Comprehensive Renewable Energy*, Elsevier, Oxford, England, pp. 225-241.
- Sørensen, J.N. (2016), *General Momentum Theory for Horizontal Axis Wind Turbines*, Springer International Publishing.
- Sorribes-Palmer, F., Sanz-Andres, A., Ayuso, L., Sant, R. and Franchini, S. (2017), "Mixed CFD-1D wind turbine diffuser design optimization", *Renewable Energy*, Vol. 105, pp. 386-399.
- Stack, J. and Lindsey, W.F. (1938), *Tests of N-85, N-86 and N-87 airfoil sections in the 11-inch high speed wind tunnel*, Technical Note No. 665, National Advisory Committee for Aeronautics, Washington, USA.

-
- Stokos, K., Vrahliotis, S., Pappou, T. and Tsangaris, S. (2015), "Development and validation of an incompressible Navier-Stokes solver including convective heat transfer", *International Journal of Numerical Methods for Heat & Fluid Flow*, Vol. 25, No. 4, pp. 861-886.
- Strofylos, G. (2021), *Development of Computational Tools, Based on Radial Basis Functions and Differential Evolution, for the Parametric Design of Aeroelastic Systems*, Doctoral Dissertation, Technical University of Crete, Chania, Greece.
- Strofylos, G.A., Porfyri, K.N., Nikolos, I.K., Delis, A.I. and Papageorgiou, M. (2018), "Using synchronous and asynchronous parallel Differential Evolution for calibrating a second-order traffic flow model", *Advances in Engineering Software*, Vol. 125, pp. 1-18.
- Sun, Z., Shen, W.Z., Chen, J. and Zhu, W.J. (2017), "Improved fixed point iterative method for blade element momentum computations", *Wind Energy*, Vol. 20, pp. 1585-1600.
- Susan-Resiga, R., Muntean, S., Stein, P. and Avellan, F. (2009), "Axisymmetric swirling flow simulation of the draft tube vortex in Francis turbines at partial discharge", *International Journal of Fluid Machinery and Systems*, Vol. 2, No. 4, pp. 295-302.
- Susan-Resiga, R.F., Muntean, S. and Bosioc, A. (2006), "Three-dimensional versus two-dimensional axisymmetric analysis for decelerated swirling flows", *Proceedings of the 13th International Conference on Fluid Flow Technologies*, 6 – 9 September 2006, Budapest, Hungary.
- Sweby, P.K. (1984), "High resolution schemes using flux limiters for hyperbolic conservation laws", *SIAM Journal on Numerical Analysis*, Vol. 21, No. 5, pp. 995–1011.
- Swift, K. (2009), *An Experimental Analysis of the Laminar Separation Bubble at Low Reynolds Numbers*, Master Thesis, University of Tennessee, Knoxville, Tennessee, USA.
- Tai, C.H. and Zhao, Y. (2003), "Parallel unsteady incompressible viscous flow computations using an unstructured multigrid method", *Journal of Computational Physics*, Vol. 192, No. 1, pp. 277-311.
- Tai, C.H., Zhao, Y. and Liew, K.M. (2005), "Parallel-multigrid computation of unsteady incompressible viscous flows using a matrix-free implicit method and high-resolution characteristics-based scheme", *Computer Methods in Applied Mechanics and Engineering*, Vol. 194, No. 36, pp. 3949-3983.

- Takahashi, S., Hata, Y., Ohya, Y., Karasudani, T. and Uchida, T. (2012), "Behavior of the blade tip vortices of a wind turbine equipped with a brimmed-diffuser shroud", *Energies*, Vol. 5, No. 12, pp. 5229-5242.
- Tamamidis, P., Zhang, G. and Assanis, D.N. (1996), "Comparison of pressure-based and artificial compressibility methods for solving 3D steady incompressible viscous flows", *Journal of Computational Physics*, Vol. 124, No. 1, pp. 1-13.
- Tani, I. (1961), *Critical Survey of Published Theories on the Mechanism of Leading-Edge Stall*, Report No. 367, Aeronautical Research Institute, Tokyo, Japan.
- Tanno, I., Hashimoto, T., Yasuda, T., Tanaka, Y., Morinishi, K. and Satofuka, N. (2013), "Simulation of turbulent flow by lattice Boltzmann method and conventional method on a GPU", *Computers & Fluids*, Vol. 80, pp. 453-458.
- Ten Hoopen, P.D.C. (2009), *An experimental and computational investigation of a diffuser augmented wind turbine: With an application of vortex generators on the diffuser trailing edge*, Master Thesis, Delft University of Technology, Delft, The Netherlands.
- Toshimitsu, K., Nishikawa, K., Haruki, W., Oono, S., Takao, M. and Ohya, Y. (2008), "PIV measurements of flows around the wind turbines with a flanged-diffuser shroud", *Journal of Thermal Science*, Vol. 17, No. 4, pp. 375-380.
- Turnock, S.R., Phillips, A.B., Banks, J. and Nicholls-Lee, R. (2011), "Modelling tidal current turbine wakes using a coupled RANS-BEMT approach as a tool for analysing power capture of arrays of turbines", *Ocean Engineering*, Vol. 38, No. 11, pp. 1300-1307.
- van Ingen, J.L. (2008), "The e^N method for transition prediction: Historical review of work at TU Delft", *Proceedings of the 38th AIAA Fluid Dynamics Conference and Exhibit*, 23 – 26 June 2008, Seattle, Washington, USA, pp. 1-49.
- Vaz, J.R.P. and Wood, D.H. (2016), "Aerodynamic optimization of the blades of diffuser-augmented wind turbines", *Energy Conversion and Management*, Vol. 123, pp. 35-45.
- Venters, R., Helenbrook, B.T. and Visser, K.D. (2018), "Ducted Wind Turbine Optimization", *Journal of Solar Energy Engineering*, Vol. 140, No. 1.
- Viterna, L.A. and Corrigan, R.D. (1981), "Fixed Pitch Rotor Performance of Large Horizontal Axis Wind Turbines", DOE/NASA Work-shop on Large Horizontal Axis Wind Turbines, 28 – 30 July 1981, Cleveland, Ohio, USA.

-
- Vrahliotis, S., Pappou, T. and Tsangaris, S. (2012), "Artificial Compressibility 3-D Navier-Stokes Solver for Unsteady Incompressible Flows with Hybrid Grids", *Engineering Applications of Computational Fluid Mechanics*, Vol. 6, No. 2, pp. 248-270.
- Wang, F., Bai, L., Fletcher, J., Whiteford, J. and Cullen, D. (2008), "The methodology for aerodynamic study on a small domestic wind turbine with scoop", *Journal of Wind Engineering and Industrial Aerodynamics*, Vol. 96, No. 1, pp. 1-24.
- Wang, X.Y., Yeo, K.S., Chew, C.S. and Khoo, B.C. (2008), "A SVD-GFD scheme for computing 3D incompressible viscous fluid flows", *Computers & Fluids*, Vol. 37, No. 6, pp. 733-746.
- Wang, Y. (2015), *Solving incompressible Navier-Stokes equations on heterogeneous parallel architectures*, Doctoral Dissertation, University of Paris-Saclay, France.
- Watanabe, K. and Ohya, Y. (2019), "Multirotor systems using three shrouded wind turbines for power output increase", *Journal of Energy Resources Technology*, Vol. 141, No. 5.
- Winslow, J., Otsuka, H., Govindarajan, B. and Chopra, I. (2018), "Basic Understanding of Airfoil Characteristics at Low Reynolds Numbers (104–105)", *Journal of Aircraft*, Vol. 55, No. 3, pp. 1050-1061.
- Wood, D. (2011), *Small Wind Turbines: Analysis, Design, and Application*, Springer-Verlag, London, England.
- Wright, A.K. and Wood, D.H. (2004), "The starting and low wind speed behaviour of a small horizontal axis wind turbine", *Journal of Wind Engineering and Industrial Aerodynamics*, Vol. 92, No. 14, pp. 1265-1279.
- Wu, C.-H. and Wolfenstein, L. (1949), *Application of Radial-Equilibrium Condition to Axial-Flow Compressor and Turbine Design*, Technical Note No. NACA-TR-955, National Advisory Committee for Aeronautics, Cleveland, Ohio, USA.
- Xu, J., Han, Z., Yan, X. and Song, W. (2019), "Design optimization of a multi-megawatt wind turbine blade with the NPU-MWA airfoil family", *Energies*, Vol. 12, No. 17, pp. 1-24.
- Yamazaki, W., Mouton, S. and Carrier, G. (2010), "Geometry parameterization and computational mesh deformation by physics-based direct manipulation approaches", *AIAA Journal*, Vol. 48, No. 8, pp. 1817-1832.

-
- Yang, H., Chen, J., Pang, X. and Chen, G. (2019), "A new aero-structural optimization method for wind turbine blades used in low wind speed areas", *Composite Structures*, Vol. 207, pp. 446-459.
- Yang, H., Shen, W., Xu, H., Hong, Z. and Liu, C. (2014), "Prediction of the wind turbine performance by using BEM with airfoil data extracted from CFD", *Renewable Energy*, Vol. 70, pp. 107-115.
- Yang, J., Hu, Q., Wang, Z., Ding, J. and Jiang, X. (2018), "Effects of inlet cavitation on swirling flow in draft-tube cone", *Engineering Computations*, Emerald Publishing Limited, Vol. 35, No. 4, pp. 1694-1705.
- Zhang, L., Chen, Z., Yang, L. and Zhang, M. (2019), "An improved axisymmetric lattice Boltzmann flux solver for axisymmetric isothermal/thermal flows", *International Journal for Numerical Methods in Fluids*, Vol. 90, No. 12, pp. 632-650.
- Zhong, W., Shen, W.Z., Wang, T. and Li, Y. (2020), "A tip loss correction model for wind turbine aerodynamic performance prediction", *Renewable Energy*, Vol. 147, pp. 223-238.
- Zhong, W., Wang, T.G., Zhu, W.J. and Shen, W.Z. (2019), "Evaluation of tip loss corrections to AD/NS simulations of wind turbine aerodynamic performance", *Applied Sciences*, Vol. 9, No. 22, p. 4919.
- Zhu, H., Sueyoshi, M., Hu, C. and Yoshida, S. (2019), "A study on a floating type shrouded wind turbine: Design, modeling and analysis", *Renewable Energy*, Vol. 134, pp. 1099-1113.

Appendix A – Differential Operators in Cylindrical Coordinates

At this point, let us consider a cylindrical coordinate system (r, θ, z) and a velocity vector field $\mathbf{u} = (u_r, u_\theta, u_z)$. The divergence of the velocity field in cylindrical coordinates reads:

$$\nabla \cdot \mathbf{u} = \frac{1}{r} \frac{\partial(ru_r)}{\partial r} + \frac{1}{r} \frac{\partial u_\theta}{\partial \theta} + \frac{\partial u_z}{\partial z}, \quad (\text{A.1})$$

Moreover, the gradient of the velocity vector field in cylindrical coordinates is expressed as:

$$\text{grad} \mathbf{u} = \nabla \mathbf{u} = \begin{pmatrix} \frac{\partial u_r}{\partial r} & \frac{1}{r} \frac{\partial u_r}{\partial \theta} - \frac{u_\theta}{r} & \frac{\partial u_r}{\partial z} \\ \frac{\partial u_\theta}{\partial r} & \frac{1}{r} \frac{\partial u_\theta}{\partial \theta} + \frac{u_r}{r} & \frac{\partial u_\theta}{\partial z} \\ \frac{\partial u_z}{\partial r} & \frac{1}{r} \frac{\partial u_z}{\partial \theta} & \frac{\partial u_z}{\partial z} \end{pmatrix} \quad (\text{A.2})$$

Finally, the Laplacian of the velocity vector field in cylindrical coordinates is given as:

$$\Delta \mathbf{u} = \nabla^2 \mathbf{u} = \begin{pmatrix} \frac{\partial^2 u_r}{\partial r^2} + \frac{1}{r^2} \frac{\partial^2 u_r}{\partial \theta^2} + \frac{\partial^2 u_r}{\partial z^2} + \frac{1}{r} \frac{\partial u_r}{\partial r} - \frac{2}{r^2} \frac{\partial u_\theta}{\partial \theta} - \frac{u_r}{r^2} \\ \frac{\partial^2 u_\theta}{\partial r^2} + \frac{1}{r^2} \frac{\partial^2 u_\theta}{\partial \theta^2} + \frac{\partial^2 u_\theta}{\partial z^2} + \frac{1}{r} \frac{\partial u_\theta}{\partial r} - \frac{2}{r^2} \frac{\partial u_r}{\partial \theta} - \frac{u_\theta}{r^2} \\ \frac{\partial^2 u_z}{\partial r^2} + \frac{1}{r^2} \frac{\partial^2 u_z}{\partial \theta^2} + \frac{\partial^2 u_z}{\partial z^2} + \frac{1}{r} \frac{\partial u_z}{\partial r} \end{pmatrix} \quad (\text{A.3})$$

Appendix B – Conservative Form of the Axisymmetric Navier-Stokes

The conservative form of the axisymmetric Navier-Stokes equations in terms of velocity gradients for incompressible fluid motion reads:

Continuity:

$$\frac{1}{r} \frac{\partial(ru_r)}{\partial r} + \frac{\partial u_z}{\partial z} = 0 \quad (\text{B.1})$$

Radial Momentum (r):

$$\begin{aligned} \frac{\partial u_r}{\partial t} + \frac{1}{r} \frac{\partial(ru_r u_r)}{\partial r} + \frac{1}{r} \frac{\partial(ru_r u_z)}{\partial z} - \frac{u_\theta^2}{r} \\ = -\frac{\partial p}{\partial r} + \frac{1}{r} \frac{\partial}{\partial r} \left(r \frac{2}{\text{Re}} \frac{\partial u_r}{\partial r} \right) + \frac{1}{r} \frac{\partial}{\partial z} \left[r \frac{1}{\text{Re}} \left(\frac{\partial u_z}{\partial r} + \frac{\partial u_r}{\partial z} \right) \right] - \frac{2}{\text{Re}} \frac{u_r}{r^2} + f_r \end{aligned} \quad (\text{B.2})$$

Azimuthal Momentum (θ):

$$\begin{aligned} \frac{\partial u_\theta}{\partial t} + \frac{1}{r} \frac{\partial(ru_r u_\theta)}{\partial r} + \frac{1}{r} \frac{\partial(ru_\theta u_z)}{\partial z} + \frac{u_r u_\theta}{r} \\ = \frac{1}{r} \frac{\partial}{\partial r} \left(r \frac{1}{\text{Re}} \frac{\partial u_\theta}{\partial r} \right) + \frac{1}{r} \frac{\partial}{\partial z} \left(r \frac{1}{\text{Re}} \frac{\partial u_\theta}{\partial z} \right) - \frac{1}{\text{Re}} \frac{u_\theta}{r^2} + f_\theta \end{aligned} \quad (\text{B.3})$$

Axial Momentum (z):

$$\begin{aligned} \frac{\partial u_z}{\partial t} + \frac{1}{r} \frac{\partial(ru_z u_r)}{\partial r} + \frac{1}{r} \frac{\partial(ru_z u_z)}{\partial z} \\ = -\frac{\partial p}{\partial z} + \frac{1}{r} \frac{\partial}{\partial r} \left[r \frac{1}{\text{Re}} \left(\frac{\partial u_z}{\partial r} + \frac{\partial u_r}{\partial z} \right) \right] + \frac{1}{r} \frac{\partial}{\partial z} \left(r \frac{2}{\text{Re}} \frac{\partial u_z}{\partial z} \right) + f_z \end{aligned} \quad (\text{B.4})$$

Appendix C - RG15 Airfoil Family

This chapter provides the dimensionless coordinates of the low-Reynolds RG15 airfoil family.

RG15-70-1 Airfoil

Point ID	x/c	y/c	Point ID	x/c	y/c
1	1.000000	0.000000	42	0.480370	0.058146
2	0.999615	0.002599	43	0.460770	0.059071
3	0.998459	0.004265	44	0.441231	0.059876
4	0.996534	0.005426	45	0.421783	0.060556
5	0.993844	0.005893	46	0.402455	0.061105
6	0.990393	0.006423	47	0.383277	0.061517
7	0.986185	0.007097	48	0.364280	0.061787
8	0.981228	0.007895	49	0.345492	0.061912
9	0.975528	0.008803	50	0.326941	0.061889
10	0.969096	0.009802	51	0.308658	0.061715
11	0.961940	0.010870	52	0.290670	0.061387
12	0.954072	0.011990	53	0.273005	0.060903
13	0.945503	0.013150	54	0.255689	0.060260
14	0.936248	0.014346	55	0.238751	0.059457
15	0.926320	0.015590	56	0.222215	0.058494
16	0.915735	0.016896	57	0.206107	0.057373
17	0.904508	0.018261	58	0.190453	0.056093
18	0.892658	0.019681	59	0.175276	0.054657
19	0.880203	0.021155	60	0.160600	0.053066
20	0.867161	0.022680	61	0.146447	0.051325
21	0.853553	0.024254	62	0.132839	0.049440
22	0.839400	0.025875	63	0.119797	0.047415
23	0.824724	0.027537	64	0.107342	0.045259
24	0.809547	0.029240	65	0.095492	0.042979
25	0.793893	0.030977	66	0.084265	0.040579
26	0.777785	0.032745	67	0.073680	0.038068
27	0.761249	0.034537	68	0.063752	0.035455
28	0.744311	0.036351	69	0.054497	0.032752
29	0.726995	0.038183	70	0.045928	0.029972
30	0.709330	0.040025	71	0.038060	0.027116
31	0.691342	0.041868	72	0.030904	0.024200
32	0.673059	0.043679	73	0.024472	0.021240
33	0.654508	0.045446	74	0.018772	0.018273
34	0.635720	0.047162	75	0.013815	0.015317
35	0.616723	0.048820	76	0.009607	0.012362
36	0.597545	0.050409	77	0.006156	0.009446
37	0.578217	0.051922	78	0.003466	0.006636
38	0.558769	0.053354	79	0.001541	0.004143
39	0.539230	0.054700	80	0.000385	0.001971
40	0.519630	0.055953	81	0.000000	0.000000

41	0.500000	0.057105	82	0.000385	-0.001864
----	----------	----------	----	----------	-----------

Point ID	x/c	y/c	Point ID	x/c	y/c
83	0.001541	-0.003636	124	0.558769	-0.020285
84	0.003466	-0.005424	125	0.578217	-0.019214
85	0.006156	-0.007242	126	0.597545	-0.018049
86	0.009607	-0.008942	127	0.616723	-0.016812
87	0.013815	-0.010544	128	0.635720	-0.015527
88	0.018772	-0.012175	129	0.654508	-0.014218
89	0.024472	-0.013793	130	0.673059	-0.012911
90	0.030904	-0.015339	131	0.691342	-0.011622
91	0.038060	-0.016775	132	0.709330	-0.010367
92	0.045928	-0.018105	133	0.726995	-0.009182
93	0.054497	-0.019356	134	0.744311	-0.008079
94	0.063752	-0.020523	135	0.761249	-0.007065
95	0.073680	-0.021600	136	0.777785	-0.006143
96	0.084265	-0.022583	137	0.793893	-0.005317
97	0.095492	-0.023472	138	0.809547	-0.004586
98	0.107342	-0.024273	139	0.824724	-0.003951
99	0.119797	-0.024987	140	0.839400	-0.003412
100	0.132839	-0.025617	141	0.853553	-0.002969
101	0.146447	-0.026164	142	0.867161	-0.002617
102	0.160600	-0.026631	143	0.880203	-0.002355
103	0.175276	-0.027018	144	0.892658	-0.002175
104	0.190453	-0.027330	145	0.904508	-0.002074
105	0.206107	-0.027565	146	0.915735	-0.002049
106	0.222215	-0.027729	147	0.926320	-0.002093
107	0.238751	-0.027823	148	0.936248	-0.002199
108	0.255689	-0.027850	149	0.945503	-0.002356
109	0.273005	-0.027814	150	0.954072	-0.002554
110	0.290670	-0.027716	151	0.961940	-0.002787
111	0.308658	-0.027556	152	0.969096	-0.003047
112	0.326941	-0.027338	153	0.975528	-0.003325
113	0.345492	-0.027062	154	0.981228	-0.003614
114	0.364280	-0.026730	155	0.986185	-0.003906
115	0.383277	-0.026343	156	0.990393	-0.004190
116	0.402455	-0.025903	157	0.993844	-0.004463
117	0.421783	-0.025410	158	0.996534	-0.004276
118	0.441231	-0.024865	159	0.998459	-0.003115
119	0.460770	-0.024266	160	0.999615	-0.001450
120	0.480370	-0.023612	161	1.000000	0.000000
121	0.500000	-0.022896	-	-	-
122	0.519630	-0.022113	-	-	-
123	0.539230	-0.021248	-	-	-

Table C.1: Cartesian coordinates of RG15-70-1 airfoil.

RG15-(10)-70-1

Point ID	x/c	y/c	Point ID	x/c	y/c
1	1.000000	0.000000	42	0.480370	0.062236
2	0.999615	0.002606	43	0.460770	0.063240
3	0.998459	0.004275	44	0.441231	0.064114
4	0.996534	0.005442	45	0.421783	0.064855
5	0.993844	0.005929	46	0.402455	0.065456
6	0.990393	0.006488	47	0.383277	0.065910
7	0.986185	0.007197	48	0.364280	0.066213
8	0.981228	0.008035	49	0.345492	0.066360
9	0.975528	0.008992	50	0.326941	0.066350
10	0.969096	0.010047	51	0.308658	0.066178
11	0.961940	0.011177	52	0.290670	0.065843
12	0.954072	0.012365	53	0.273005	0.065341
13	0.945503	0.013597	54	0.255689	0.064670
14	0.936248	0.014870	55	0.238751	0.063828
15	0.926320	0.016197	56	0.222215	0.062815
16	0.915735	0.017592	57	0.206107	0.061632
17	0.904508	0.019053	58	0.190453	0.060281
18	0.892658	0.020576	59	0.175276	0.058762
19	0.880203	0.022159	60	0.160600	0.057078
20	0.867161	0.023799	61	0.146447	0.055233
21	0.853553	0.025494	62	0.132839	0.053232
22	0.839400	0.027241	63	0.119797	0.051083
23	0.824724	0.029035	64	0.107342	0.048791
24	0.809547	0.030874	65	0.095492	0.046366
25	0.793893	0.032753	66	0.084265	0.043812
26	0.777785	0.034665	67	0.073680	0.041137
27	0.761249	0.036606	68	0.063752	0.038351
28	0.744311	0.038571	69	0.054497	0.035468
29	0.726995	0.040555	70	0.045928	0.032501
30	0.709330	0.042552	71	0.038060	0.029450
31	0.691342	0.044550	72	0.030904	0.026330
32	0.673059	0.046515	73	0.024472	0.023164
33	0.654508	0.048436	74	0.018772	0.019989
34	0.635720	0.050302	75	0.013815	0.016826
35	0.616723	0.052106	76	0.009607	0.013644
36	0.597545	0.053836	77	0.006156	0.010484
37	0.578217	0.055484	78	0.003466	0.007507
38	0.558769	0.057041	79	0.001541	0.004692
39	0.539230	0.058502	80	0.000385	0.002194
40	0.519630	0.059861	81	0.000000	0.000195
41	0.500000	0.061108	82	-0.000003	0.000000

Point ID	x/c	y/c	Point ID	x/c	y/c
83	0.000000	-0.000176	124	0.519630	-0.026012
84	0.000385	-0.001922	125	0.539230	-0.025041
85	0.001541	-0.003862	126	0.558769	-0.023963
86	0.003466	-0.005881	127	0.578217	-0.022766
87	0.006156	-0.007915	128	0.597545	-0.021467
88	0.009607	-0.009816	129	0.616723	-0.020088
89	0.013815	-0.011635	130	0.635720	-0.018656
90	0.018772	-0.013498	131	0.654508	-0.017195
91	0.024472	-0.015366	132	0.673059	-0.015734
92	0.030904	-0.017158	133	0.691342	-0.014289
93	0.038060	-0.018828	134	0.709330	-0.012878
94	0.045928	-0.020379	135	0.726995	-0.011538
95	0.054497	-0.021846	136	0.744311	-0.010280
96	0.063752	-0.023221	137	0.761249	-0.009114
97	0.073680	-0.024494	138	0.777785	-0.008044
98	0.084265	-0.025664	139	0.793893	-0.007073
99	0.095492	-0.026727	140	0.809547	-0.006200
100	0.107342	-0.027692	141	0.824724	-0.005429
101	0.119797	-0.028558	142	0.839400	-0.004759
102	0.132839	-0.029328	143	0.853553	-0.004189
103	0.146447	-0.030004	144	0.867161	-0.003718
104	0.160600	-0.030588	145	0.880203	-0.003341
105	0.175276	-0.031080	146	0.892658	-0.003053
106	0.190453	-0.031483	147	0.904508	-0.002850
107	0.206107	-0.031799	148	0.915735	-0.002729
108	0.222215	-0.032030	149	0.926320	-0.002685
109	0.238751	-0.032180	150	0.936248	-0.002708
110	0.255689	-0.032251	151	0.945503	-0.002789
111	0.273005	-0.032247	152	0.954072	-0.002915
112	0.290670	-0.032169	153	0.961940	-0.003081
113	0.308658	-0.032020	154	0.969096	-0.003278
114	0.326941	-0.031800	155	0.975528	-0.003501
115	0.345492	-0.031511	156	0.981228	-0.003742
116	0.364280	-0.031156	157	0.986185	-0.003995
117	0.383277	-0.030736	158	0.990393	-0.004245
118	0.402455	-0.030253	159	0.993844	-0.004488
119	0.421783	-0.029708	160	0.996534	-0.004288
120	0.441231	-0.029101	161	0.998459	-0.003121
121	0.460770	-0.028431	162	0.999615	-0.001452
122	0.480370	-0.027697	163	1.000000	0.000000
123	0.500000	-0.026893	-	-	-

Table C.2: Cartesian coordinates of RG15-(10)-70-1 airfoil.

RG15-(20)-70-1

Point ID	x/c	y/c	Point ID	x/c	y/c
1	1.000000	0.000000	42	0.480370	0.066327
2	0.999615	0.002614	43	0.460770	0.067409
3	0.998459	0.004288	44	0.441231	0.068353
4	0.996534	0.005462	45	0.421783	0.069154
5	0.993844	0.005967	46	0.402455	0.069806
6	0.990393	0.006551	47	0.383277	0.070303
7	0.986185	0.007292	48	0.364280	0.070638
8	0.981228	0.008174	49	0.345492	0.070808
9	0.975528	0.009182	50	0.326941	0.070811
10	0.969096	0.010293	51	0.308658	0.070642
11	0.961940	0.011485	52	0.290670	0.070300
12	0.954072	0.012740	53	0.273005	0.069780
13	0.945503	0.014044	54	0.255689	0.069080
14	0.936248	0.015394	55	0.238751	0.068199
15	0.926320	0.016804	56	0.222215	0.067136
16	0.915735	0.018288	57	0.206107	0.065893
17	0.904508	0.019846	58	0.190453	0.064470
18	0.892658	0.021472	59	0.175276	0.062869
19	0.880203	0.023164	60	0.160600	0.061092
20	0.867161	0.024919	61	0.146447	0.059143
21	0.853553	0.026734	62	0.132839	0.057029
22	0.839400	0.028607	63	0.119797	0.054754
23	0.824724	0.030534	64	0.107342	0.052328
24	0.809547	0.032510	65	0.095492	0.049760
25	0.793893	0.034529	66	0.084265	0.047052
26	0.777785	0.036586	67	0.073680	0.044214
27	0.761249	0.038675	68	0.063752	0.041256
28	0.744311	0.040791	69	0.054497	0.038194
29	0.726995	0.042929	70	0.045928	0.035042
30	0.709330	0.045080	71	0.038060	0.031798
31	0.691342	0.047233	72	0.030904	0.028474
32	0.673059	0.049352	73	0.024472	0.025103
33	0.654508	0.051425	74	0.018772	0.021723
34	0.635720	0.053443	75	0.013815	0.018354
35	0.616723	0.055393	76	0.009607	0.014954
36	0.597545	0.057264	77	0.006156	0.011551
37	0.578217	0.059046	78	0.003466	0.008323
38	0.558769	0.060728	79	0.001541	0.005276
39	0.539230	0.062305	80	0.000385	0.002567
40	0.519630	0.063769	81	0.000000	0.000547
41	0.500000	0.065112	82	-0.000011	0.000000

Point ID	x/c	y/c	Point ID	x/c	y/c
83	0.000000	-0.000248	124	0.519630	-0.029910
84	0.000385	-0.001998	125	0.539230	-0.028833
85	0.001541	-0.004109	126	0.558769	-0.027640
86	0.003466	-0.006317	127	0.578217	-0.026318
87	0.006156	-0.008557	128	0.597545	-0.024885
88	0.009607	-0.010677	129	0.616723	-0.023365
89	0.013815	-0.012709	130	0.635720	-0.021784
90	0.018772	-0.014802	131	0.654508	-0.020172
91	0.024472	-0.016920	132	0.673059	-0.018556
92	0.030904	-0.018961	133	0.691342	-0.016955
93	0.038060	-0.020867	134	0.709330	-0.015388
94	0.045928	-0.022641	135	0.726995	-0.013893
95	0.054497	-0.024325	136	0.744311	-0.012481
96	0.063752	-0.025909	137	0.761249	-0.011163
97	0.073680	-0.027379	138	0.777785	-0.009944
98	0.084265	-0.028736	139	0.793893	-0.008828
99	0.095492	-0.029976	140	0.809547	-0.007814
100	0.107342	-0.031105	141	0.824724	-0.006906
101	0.119797	-0.032124	142	0.839400	-0.006104
102	0.132839	-0.033035	143	0.853553	-0.005409
103	0.146447	-0.033841	144	0.867161	-0.004817
104	0.160600	-0.034542	145	0.880203	-0.004326
105	0.175276	-0.035139	146	0.892658	-0.003930
106	0.190453	-0.035635	147	0.904508	-0.003625
107	0.206107	-0.036032	148	0.915735	-0.003409
108	0.222215	-0.036331	149	0.926320	-0.003276
109	0.238751	-0.036537	150	0.936248	-0.003217
110	0.255689	-0.036652	151	0.945503	-0.003220
111	0.273005	-0.036680	152	0.954072	-0.003274
112	0.290670	-0.036623	153	0.961940	-0.003373
113	0.308658	-0.036483	154	0.969096	-0.003510
114	0.326941	-0.036261	155	0.975528	-0.003676
115	0.345492	-0.035960	156	0.981228	-0.003869
116	0.364280	-0.035582	157	0.986185	-0.004079
117	0.383277	-0.035130	158	0.990393	-0.004300
118	0.402455	-0.034603	159	0.993844	-0.004517
119	0.421783	-0.034005	160	0.996534	-0.004303
120	0.441231	-0.033336	161	0.998459	-0.003129
121	0.460770	-0.032596	162	0.999615	-0.001454
122	0.480370	-0.031782	163	1.000000	0.000000
123	0.500000	-0.030889	-	-	-

Table C.3: Cartesian coordinates of RG15-(20)-70-1 airfoil.

RG15-(30)-70-1

Point ID	x/c	y/c	Point ID	x/c	y/c
1	1.000000	0.000000	42	0.480370	0.070419
2	0.999615	0.002622	43	0.460770	0.071578
3	0.998459	0.004301	44	0.441231	0.072591
4	0.996534	0.005482	45	0.421783	0.073453
5	0.993844	0.006006	46	0.402455	0.074157
6	0.990393	0.006617	47	0.383277	0.074695
7	0.986185	0.007390	48	0.364280	0.075063
8	0.981228	0.008315	49	0.345492	0.075256
9	0.975528	0.009371	50	0.326941	0.075272
10	0.969096	0.010539	51	0.308658	0.075106
11	0.961940	0.011793	52	0.290670	0.074756
12	0.954072	0.013115	53	0.273005	0.074219
13	0.945503	0.014492	54	0.255689	0.073491
14	0.936248	0.015919	55	0.238751	0.072571
15	0.926320	0.017412	56	0.222215	0.071458
16	0.915735	0.018986	57	0.206107	0.070155
17	0.904508	0.020640	58	0.190453	0.068661
18	0.892658	0.022369	59	0.175276	0.066978
19	0.880203	0.024170	60	0.160600	0.065109
20	0.867161	0.026039	61	0.146447	0.063057
21	0.853553	0.027976	62	0.132839	0.060829
22	0.839400	0.029975	63	0.119797	0.058431
23	0.824724	0.032034	64	0.107342	0.055871
24	0.809547	0.034146	65	0.095492	0.053159
25	0.793893	0.036307	66	0.084265	0.050298
26	0.777785	0.038509	67	0.073680	0.047299
27	0.761249	0.040746	68	0.063752	0.044171
28	0.744311	0.043013	69	0.054497	0.040930
29	0.726995	0.045303	70	0.045928	0.037594
30	0.709330	0.047608	71	0.038060	0.034158
31	0.691342	0.049916	72	0.030904	0.030632
32	0.673059	0.052190	73	0.024472	0.027058
33	0.654508	0.054416	74	0.018772	0.023475
34	0.635720	0.056584	75	0.013815	0.019902
35	0.616723	0.058681	76	0.009607	0.016287
36	0.597545	0.060693	77	0.006156	0.012642
37	0.578217	0.062608	78	0.003466	0.009163
38	0.558769	0.064415	79	0.001541	0.005881
39	0.539230	0.066107	80	0.000385	0.002963
40	0.519630	0.067677	81	0.000000	0.000887
41	0.500000	0.069117	82	-0.000017	0.000000

Point ID	x/c	y/c	Point ID	x/c	y/c
83	0.000000	-0.000279	124	0.519630	-0.033809
84	0.000385	-0.002068	125	0.539230	-0.032625
85	0.001541	-0.004347	126	0.558769	-0.031316
86	0.003466	-0.006742	127	0.578217	-0.029869
87	0.006156	-0.009185	128	0.597545	-0.028302
88	0.009607	-0.011522	129	0.616723	-0.026640
89	0.013815	-0.013766	130	0.635720	-0.024912
90	0.018772	-0.016088	131	0.654508	-0.023148
91	0.024472	-0.018456	132	0.673059	-0.021377
92	0.030904	-0.020748	133	0.691342	-0.019621
93	0.038060	-0.022893	134	0.709330	-0.017898
94	0.045928	-0.024889	135	0.726995	-0.016247
95	0.054497	-0.026792	136	0.744311	-0.014681
96	0.063752	-0.028586	137	0.761249	-0.013211
97	0.073680	-0.030256	138	0.777785	-0.011844
98	0.084265	-0.031801	139	0.793893	-0.010581
99	0.095492	-0.033217	140	0.809547	-0.009427
100	0.107342	-0.034512	141	0.824724	-0.008382
101	0.119797	-0.035685	142	0.839400	-0.007449
102	0.132839	-0.036738	143	0.853553	-0.006627
103	0.146447	-0.037675	144	0.867161	-0.005915
104	0.160600	-0.038493	145	0.880203	-0.005310
105	0.175276	-0.039196	146	0.892658	-0.004806
106	0.190453	-0.039786	147	0.904508	-0.004399
107	0.206107	-0.040263	148	0.915735	-0.004088
108	0.222215	-0.040631	149	0.926320	-0.003866
109	0.238751	-0.040893	150	0.936248	-0.003725
110	0.255689	-0.041052	151	0.945503	-0.003652
111	0.273005	-0.041113	152	0.954072	-0.003634
112	0.290670	-0.041077	153	0.961940	-0.003666
113	0.308658	-0.040946	154	0.969096	-0.003740
114	0.326941	-0.040723	155	0.975528	-0.003851
115	0.345492	-0.040410	156	0.981228	-0.003996
116	0.364280	-0.040009	157	0.986185	-0.004166
117	0.383277	-0.039523	158	0.990393	-0.004355
118	0.402455	-0.038954	159	0.993844	-0.004546
119	0.421783	-0.038303	160	0.996534	-0.004317
120	0.441231	-0.037571	161	0.998459	-0.003137
121	0.460770	-0.036760	162	0.999615	-0.001457
122	0.480370	-0.035866	163	1.000000	0.000000
123	0.500000	-0.034885	-	-	-

Table C.4: Cartesian coordinates of RG15-(30)-70-1 airfoil.

RG15-(40)-70-1

Point ID	x/c	y/c	Point ID	x/c	y/c
1	1.000000	0.000000	42	0.480370	0.074510
2	0.999615	0.002634	43	0.460770	0.075748
3	0.998459	0.004321	44	0.441231	0.076830
4	0.996534	0.005512	45	0.421783	0.077753
5	0.993844	0.006043	46	0.402455	0.078507
6	0.990393	0.006678	47	0.383277	0.079088
7	0.986185	0.007490	48	0.364280	0.079488
8	0.981228	0.008454	49	0.345492	0.079704
9	0.975528	0.009561	50	0.326941	0.079733
10	0.969096	0.010785	51	0.308658	0.079570
11	0.961940	0.012101	52	0.290670	0.079212
12	0.954072	0.013491	53	0.273005	0.078658
13	0.945503	0.014940	54	0.255689	0.077901
14	0.936248	0.016444	55	0.238751	0.076943
15	0.926320	0.018020	56	0.222215	0.075781
16	0.915735	0.019684	57	0.206107	0.074418
17	0.904508	0.021434	58	0.190453	0.072853
18	0.892658	0.023266	59	0.175276	0.071089
19	0.880203	0.025176	60	0.160600	0.069128
20	0.867161	0.027161	61	0.146447	0.066973
21	0.853553	0.029218	62	0.132839	0.064632
22	0.839400	0.031344	63	0.119797	0.062111
23	0.824724	0.033534	64	0.107342	0.059418
24	0.809547	0.035783	65	0.095492	0.056564
25	0.793893	0.038085	66	0.084265	0.053552
26	0.777785	0.040432	67	0.073680	0.050392
27	0.761249	0.042817	68	0.063752	0.047094
28	0.744311	0.045235	69	0.054497	0.043676
29	0.726995	0.047679	70	0.045928	0.040157
30	0.709330	0.050138	71	0.038060	0.036532
31	0.691342	0.052600	72	0.030904	0.032805
32	0.673059	0.055028	73	0.024472	0.029029
33	0.654508	0.057407	74	0.018772	0.025244
34	0.635720	0.059725	75	0.013815	0.021471
35	0.616723	0.061969	76	0.009607	0.017644
36	0.597545	0.064122	77	0.006156	0.013759
37	0.578217	0.066170	78	0.003466	0.010026
38	0.558769	0.068103	79	0.001541	0.006508
39	0.539230	0.069911	80	0.000385	0.003382
40	0.519630	0.071586	81	0.000000	0.001242
41	0.500000	0.073121	82	-0.000021	0.000000

83	0.000000	-0.000297	124	0.519630	-0.037707
84	0.000385	-0.002133	125	0.539230	-0.036417
85	0.001541	-0.004577	126	0.558769	-0.034992
86	0.003466	-0.007155	127	0.578217	-0.033420
87	0.006156	-0.009801	128	0.597545	-0.031719
88	0.009607	-0.012352	129	0.616723	-0.029915
89	0.013815	-0.014806	130	0.635720	-0.028040
90	0.018772	-0.017354	131	0.654508	-0.026124
91	0.024472	-0.019975	132	0.673059	-0.024198
92	0.030904	-0.022519	133	0.691342	-0.022286
93	0.038060	-0.024904	134	0.709330	-0.020406
94	0.045928	-0.027125	135	0.726995	-0.018600
95	0.054497	-0.029248	136	0.744311	-0.016880
96	0.063752	-0.031254	137	0.761249	-0.015258
97	0.073680	-0.033124	138	0.777785	-0.013742
98	0.084265	-0.034858	139	0.793893	-0.012334
99	0.095492	-0.036452	140	0.809547	-0.011039
100	0.107342	-0.037913	141	0.824724	-0.009858
101	0.119797	-0.039242	142	0.839400	-0.008793
102	0.132839	-0.040437	143	0.853553	-0.007845
103	0.146447	-0.041505	144	0.867161	-0.007013
104	0.160600	-0.042442	145	0.880203	-0.006294
105	0.175276	-0.043251	146	0.892658	-0.005681
106	0.190453	-0.043934	147	0.904508	-0.005173
107	0.206107	-0.044493	148	0.915735	-0.004766
108	0.222215	-0.044929	149	0.926320	-0.004456
109	0.238751	-0.045248	150	0.936248	-0.004232
110	0.255689	-0.045452	151	0.945503	-0.004083
111	0.273005	-0.045546	152	0.954072	-0.003992
112	0.290670	-0.045531	153	0.961940	-0.003957
113	0.308658	-0.045410	154	0.969096	-0.003970
114	0.326941	-0.045185	155	0.975528	-0.004026
115	0.345492	-0.044859	156	0.981228	-0.004122
116	0.364280	-0.044436	157	0.986185	-0.004253
117	0.383277	-0.043916	158	0.990393	-0.004406
118	0.402455	-0.043304	159	0.993844	-0.004580
119	0.421783	-0.042600	160	0.996534	-0.004339
120	0.441231	-0.041807	161	0.998459	-0.003148
121	0.460770	-0.040924	162	0.999615	-0.001461
122	0.480370	-0.039951	163	1.000000	0.000000
123	0.500000	-0.038880	-	-	-

Table C.5: Cartesian coordinates of RG15-(40)-70-1 airfoil.

RG15-(50)-70-1

Point ID	x/c	y/c	Point ID	x/c	y/c
1	1.000000	0.000000	42	0.480370	0.078602
2	0.999615	0.002642	43	0.460770	0.079917
3	0.998459	0.004334	44	0.441231	0.081069
4	0.996534	0.005532	45	0.421783	0.082052
5	0.993844	0.006082	46	0.402455	0.082858
6	0.990393	0.006744	47	0.383277	0.083480
7	0.986185	0.007588	48	0.364280	0.083913
8	0.981228	0.008595	49	0.345492	0.084152
9	0.975528	0.009751	50	0.326941	0.084194
10	0.969096	0.011032	51	0.308658	0.084033
11	0.961940	0.012410	52	0.290670	0.083669
12	0.954072	0.013868	53	0.273005	0.083097
13	0.945503	0.015389	54	0.255689	0.082313
14	0.936248	0.016970	55	0.238751	0.081316
15	0.926320	0.018629	56	0.222215	0.080105
16	0.915735	0.020383	57	0.206107	0.078682
17	0.904508	0.022230	58	0.190453	0.077047
18	0.892658	0.024164	59	0.175276	0.075202
19	0.880203	0.026183	60	0.160600	0.073149
20	0.867161	0.028283	61	0.146447	0.070893
21	0.853553	0.030462	62	0.132839	0.068439
22	0.839400	0.032714	63	0.119797	0.065796
23	0.824724	0.035036	64	0.107342	0.062971
24	0.809547	0.037422	65	0.095492	0.059975
25	0.793893	0.039864	66	0.084265	0.056813
26	0.777785	0.042356	67	0.073680	0.053493
27	0.761249	0.044890	68	0.063752	0.050026
28	0.744311	0.047458	69	0.054497	0.046431
29	0.726995	0.050055	70	0.045928	0.042732
30	0.709330	0.052668	71	0.038060	0.038918
31	0.691342	0.055285	72	0.030904	0.034992
32	0.673059	0.057867	73	0.024472	0.031014
33	0.654508	0.060398	74	0.018772	0.027030
34	0.635720	0.062867	75	0.013815	0.023060
35	0.616723	0.065257	76	0.009607	0.019025
36	0.597545	0.067551	77	0.006156	0.014902
37	0.578217	0.069733	78	0.003466	0.010914
38	0.558769	0.071791	79	0.001541	0.007158
39	0.539230	0.073714	80	0.000385	0.003824
40	0.519630	0.075495	81	0.000000	0.001619
41	0.500000	0.077126	82	-0.000025	0.000000

Point ID	x/c	y/c	Point ID	x/c	y/c
83	0.000000	-0.000309	124	0.519630	-0.041604
84	0.000385	-0.002194	125	0.539230	-0.040208
85	0.001541	-0.004798	126	0.558769	-0.038668
86	0.003466	-0.007558	127	0.578217	-0.036971
87	0.006156	-0.010404	128	0.597545	-0.035135
88	0.009607	-0.013167	129	0.616723	-0.033190
89	0.013815	-0.015830	130	0.635720	-0.031167
90	0.018772	-0.018603	131	0.654508	-0.029098
91	0.024472	-0.021475	132	0.673059	-0.027018
92	0.030904	-0.024274	133	0.691342	-0.024950
93	0.038060	-0.026902	134	0.709330	-0.022914
94	0.045928	-0.029348	135	0.726995	-0.020952
95	0.054497	-0.031692	136	0.744311	-0.019078
96	0.063752	-0.033912	137	0.761249	-0.017304
97	0.073680	-0.035982	138	0.777785	-0.015639
98	0.084265	-0.037907	139	0.793893	-0.014086
99	0.095492	-0.039680	140	0.809547	-0.012649
100	0.107342	-0.041309	141	0.824724	-0.011332
101	0.119797	-0.042793	142	0.839400	-0.010135
102	0.132839	-0.044132	143	0.853553	-0.009062
103	0.146447	-0.045331	144	0.867161	-0.008110
104	0.160600	-0.046388	145	0.880203	-0.007276
105	0.175276	-0.047304	146	0.892658	-0.006555
106	0.190453	-0.048081	147	0.904508	-0.005946
107	0.206107	-0.048721	148	0.915735	-0.005443
108	0.222215	-0.049227	149	0.926320	-0.005044
109	0.238751	-0.049603	150	0.936248	-0.004739
110	0.255689	-0.049851	151	0.945503	-0.004513
111	0.273005	-0.049978	152	0.954072	-0.004351
112	0.290670	-0.049984	153	0.961940	-0.004249
113	0.308658	-0.049873	154	0.969096	-0.004200
114	0.326941	-0.049647	155	0.975528	-0.004201
115	0.345492	-0.049309	156	0.981228	-0.004249
116	0.364280	-0.048862	157	0.986185	-0.004339
117	0.383277	-0.048310	158	0.990393	-0.004461
118	0.402455	-0.047654	159	0.993844	-0.004609
119	0.421783	-0.046898	160	0.996534	-0.004354
120	0.441231	-0.046042	161	0.998459	-0.003156
121	0.460770	-0.045088	162	0.999615	-0.001463
122	0.480370	-0.044035	163	1.000000	0.000000
123	0.500000	-0.042875	-	-	-

Table C.6: Cartesian coordinates of RG15-(50)-70-1 airfoil.